Experimental Investigation of Gouges and Cataclasites, Alpine Fault, New Zealand

Carolyn Jeanne Boulton

A thesis submitted in partial fulfilment
of the requirements for
the Degree
of
Doctor of Philosophy
in
The Faculty of Postgraduate Studies
Geological Sciences

University of Canterbury
November 2013

Abstract

The upper 8-12 km of the Alpine Fault, South Island, New Zealand, accommodates relative Australian-Pacific plate boundary motion through coseismic slip accompanying large-magnitude earthquakes. Earthquakes occur due to frictional instabilities on faults; earthquake nucleation, propagation, and arrest are governed by tectonic forces and fault zone properties. A multidisciplinary dataset is presented on the lithological, microstructural, mineralogical, geochemical, hydrological, and frictional properties of Alpine Fault rocks collected from natural fault exposures and from Deep Fault Drilling Project (DFDP-1) drillcore. Results quantify and describe the physical and chemical processes that affect seismicity and slip accommodation.

Oblique dextral motion on the central Alpine Fault in the last 5-8 Myr has exhumed garnet-oligoclase facies mylonites from depths of up to 35 km. During the last phase of exhumation, brittle deformation of these mylonites, accompanied by fluid infiltration, has resulted in complex mineralogical and lithological fault rock variations. Petrophysical, geochemical, and lithological data reveal that the fault comprises a central alteration zone of protocataclasites, foliated and nonfoliated cataclasites, and fault gouges bounded by a damage zone containing fractured ultramylonites and mylonites. Mineralogical results suggest that at least two stages of chemical alteration have occurred. At, or near, the brittle-to-ductile transition (c. < 320°C), metasomatic alteration reactions resulted in plagioclase and feldspar replacement by muscovite, sericite, and sausserite, and biotite (phlogopite), hornblende (actinolite) and/or epidote replacement by chlorite (clinochlore). At lower temperatures (c. < 120°C), primary minerals were altered to kaolinite, smectite and pyrite, or kaolinite, smectite, Fe-hydroxide (goethite) and carbonate, depending on redox conditions. Ultramylonites, nonfoliated and foliated cataclasites, and gouges in the hanging wall and footwall contain the high-temperature phyllosilicates chlorite and muscovite/illite. Brown principal slip zone (PSZ) gouges contain the low-temperature phyllosilicates kaolinite and smecite.

The frictional and hydrological properties of saturated intact samples of central Alpine Fault surface-outcrop gouges and cataclasites were investigated in room temperature experiments conducted at 30-33 MPa effective normal stress (σ_n') using the double-direct shear configuration and controlled pore fluid pressure in a triaxial pressure vessel. Surface-outcrop samples from Gaunt Creek, location of DFDP-1, displayed, with increasing distance (up to 50 cm) from the contact with footwall fluvioglacial gravels: (1) an increase in fault normal permeability ($k = 7.45 \times 10^{-20}$ m^2 to $k = 1.15 \times 10^{-16}$ m^2), (2) a transition from frictionally weak ($\mu = 0.44$) fault gouge to frictionally strong ($\mu = 0.50$–0.55) cataclasite, (3) a change in friction rate dependence (a–b) from solely velocity strengthening to velocity strengthening and weakening, and (4) an increase in the rate of frictional healing. The frictional and hydrological properties of saturated intact samples of southern Alpine Fault surface-outcrop gouges were also investigated in room temperature double-direct shear experiments conducted at $\sigma_n' = 6 - 31$ MPa. Three complete cross-sections logged from outcrops of the southern Alpine Fault at Martyr River, McKenzie Creek, and Hokuri Creek show that dextral-normal slip is localized to a single 1-12 m-thick fault core comprising impermeable ($k = 10^{-20}$ to 10^{-22} m^2), frictionally weak ($\mu = 0.12$–0.37), velocity-strengthening, illite-chlorite and trioctahedral smectite (saponite)-chlorite-lizardite fault gouges. In low velocity room temperature experiments, Alpine Fault gouges have behaviours associated with aseismic creep.

In a triaxial compression apparatus, the frictional properties of PSZ gouge samples recovered from DFDP-1 drillcore at 90 and 128 m depths were tested at temperatures up to $T = 350$°C and effective normal stresses up to $\sigma_n' = 156$ MPa to constrain the fault's strength and stability under conditions representative of the seismogenic crust. The chlorite/white mica-bearing DFDP-1A blue gouge is frictionally strong ($\mu = 0.61$–0.76) across a range of experimental conditions ($T = 70$–350°C, $\sigma_n' = 31.2$–156 MPa) and undergoes a stability transition from velocity strengthening to velocity weakening as T increases past 210°C, $\sigma_n' = 31.2$–156 MPa. The coefficient of friction of smecite-bearing DFDP-1B brown gouge increases from $\mu = 0.49$ to $\mu = 0.74$ with increasing temperature and pressure ($T = 70$–210°C, $\sigma_n' = 31.2$–93.6 MPa); it undergoes a transition from velocity strength-

ening to velocity weakening as T increases past 140°C, σ_n' = 62.4 MPa. In low velocity hydrothermal experiments, Alpine Fault gouges have behaviours associated with potentially unstable, seismic slip at temperatures $\geq$ 140°C, depending on mineralogy.

High-velocity (v = 1 m/s), low normal stress (σ_n = 1 MPa) friction experiments conducted on a rotary shear apparatus showed that the Alpine Fault gouges and cataclasites have consistently high peak friction coefficients (mean $\mu_p = 0.69 \pm 0.06$) in room-dry experiments. Variations in fault rock mineralogy and permeability were more apparent in experiments conducted with pore fluid, wherein the peak coefficient of friction of the cataclasites (mean $\mu_p = 0.64 \pm 0.04$) was higher than the fault gouges (mean $\mu_p = 0.24 \pm 0.16$). All fault rocks exhibited very low steady state coefficients of friction (μ_{ss}) (room-dry mean $\mu_{ss} = 0.18 \pm 0.04$; saturated mean $\mu_{ss} = 0.10 \pm 0.04$). Three high-velocity experiments conducted on saturated smectite-bearing principal slip zone (PSZ) fault gouges had the lowest peak friction coefficients ($\mu_p = 0.13 - 0.18$), lowest steady state friction coefficients ($\mu_{ss} = 0.02 - 0.10$), and lowest breakdown work values ($W_B = 0.07 - 0.11$ MJ/m^2) of all the experiments performed.

Lower strength ($\mu <$ c. 0.62) velocity-strengthening fault rocks comprising a realistically heterogeneous fault plane represent barriers to rupture propagation. A wide range of gouges and cataclasites exhibited very low steady state friction coefficients in high-velocity friction experiments. However, earthquake rupture nucleation in frictionally strong ($\mu \geq$ c. 0.62), velocity-weakening material provides the acceleration necessary to overcome the low-velocity rupture propagation barriers posed by velocity-strengthening gouges and cataclasites. Mohr-Coulomb theory stipulates that sufficient shear stress must be resolved on the Alpine Fault, or pore fluid pressure must be sufficiently high, for earthquakes to nucleate in strong, unstable fault materials. A three-dimensional stress analysis was conducted using the average orientation of the central and southern Alpine Fault, the experimentally determined coefficient of friction of velocity-weakening DFDP-1A blue gouge, and the seismologically determined stress tensor and stress shape ratio(s). Results reveal that for a coefficient of friction of $\mu \geq$ c. 0.62, the

Alpine Fault is unfavourably oriented to severely misoriented for frictional slip.

Acknowledgments

The State College story perhaps best sums up the essential elements of my PhD. After labouring to rebuild and re-instrument a rotary shear apparatus at the University of Canterbury, I received a Claude McCarthy Fellowship from the New Zealand Vice Chancellors' Committee in 2010. Research funds in hand, I traveled to Penn State University, Pennsylvania, USA, to conduct my first experiments on Alpine Fault gouges and cataclasites. Upon arriving, I found helpful colleagues, friendly flatmates, and a charming college town replete with good food, cheap beer, and a bike shop with technicians who built me a pro bono bike from an assortment of spare parts. My experience at Penn State, a concoction of locomotion, data, lab work, great places, and fantastic people, was integral to the successful completion of this thesis.

Altogether, I am immeasurably grateful to the following people: my family, James and Anna, for their unwavering love and support, and my parents, John and Lynette Phillips and the late June Boulton; my supervisors and mentors, Tim Davies, Travis Horton, Virginia Toy, and Marlène Villenueve (and Rick Sibson); my colleagues and co-authors, Nic Barth, Brett Carpenter, John Townend, Rupert Sutherland, David Lockner, Diane Moore, Chris Marone, Yao Lu, Toshi Shimamoto, Shengli Ma, André Niemeijer, and Henri Leclère; my fellow graduate students, Tom Brookman, Louise Vick, Brendan Duffy, Flo Bégué, Paul Siratovich, Nic Riordan, Tim Stahl, Sharon Hornblow, Jackie Dohaney, Felix von Aulock, Hannah Scott, Carolin Boese, Marco Scuderi, Andy Rathbun, Catriona Menzies, and many others, for wiffle ball, soccer, beers, and insight; the skilled technicians, everyday heroes, Mark Raven, Peter Jones, Wallace Weideman, Steve Swavely, Damian Walls, Brent Pooley, Kat Lilly, Luke Easterbrook-Clarke, Mike Flaws, Rob Spiers, Chris Grimshaw, Cathy Higgins, Anekant Wandres, Kerry Swanson and Matt Cockroft; UC Department of Geological Sciences secretaries, Pat Roberts and Janet Warburton; Assoc. Professor David Shelley for help with complicated microstructures; the Mason Trust and University of Canterbury field

stations for research money and accommodation; the New Zealand Federation of Graduate Women and the New Zealand Earthquake Commission for conference travel funds; and last, but not least, the staff and community at Montana Early Education Center, Avonhead Kindercare, and Russley School, for taking excellent care of my favourite person.

Special thanks to the following people and places, who, as Christchurch was leveled by earthquakes, found time and money to enable me to work on some of the best rock deformation apparatuses in the world. It is impossible to adequately express my gratitude to: The Sediment and Rock Mechanics Lab, Penn State University, USA (Chris Marone and Brett Carpenter); the Institute of Geology, China Earthquake Administration, Beijing, China (Toshi Shimamoto and Shengli Ma); and the United State Geological Survey, Menlo Park, USA (David Lockner and Diane Moore). The staff and students at the Geology Department, University of Otago, also kindly lent me desk space, access to excellent research equipment, and housing (many thanks to Ewan Fordyce, Virginia Toy, Dave Prior, and Nic Barth). Additional thanks to the people, companies, communities, and institutions that made the Deep Fault Drilling Project possible: Horizon Drilling, Alex Pyne, the New Zealand Department of Conservation, the Whataroa Community, GNS Science, Victoria University of Wellington, the University of Otago, the University of Auckland, the University of Canterbury, the Marsden Fund, the University of Bremen, National Environment Research Council, and the University of Liverpool.

Another collection of spare parts finally worked in October 2012, after five years of tinkering and tears. Thank you to Peter Jones, Wallace Weideman, James Boulton, Tim Davies, and André Niemeijer for your help in getting good data out of the University of Canterbury ring shear (frontispiece). All the tasks that seemed insurmountable for so long were accomplished with the help, encouragement, and goodwill of a large number of skillful people who I am proud to call friends and colleagues.

Frontispiece (over). Experimental rock deformation apparatus used during this dissertation. Clockwise from top: double direct shear apparatus (the biax) with pressure vessel and jacketed sample, Pennsylvania State University, Pennsylvania, USA; unconfined compression testing apparatus with acoustic emission sensors, University of Canterbury, Christchurch, New Zealand; triaxial compression apparatus, machine #5, United States Geological Survey (USGS), California, USA (pictured are David Lockner, me, and Diane Moore); experimental fault along a sawcut, with lead jacket, USGS; experimental shear cell, University of Canterbury ring shear, Christchurch, New Zealand; low-to-high velocity (LHV) rotary shear apparatus, Institute of Geology, China Earthquake Administration, Beijing, China. Lower centre: the University of Canterbury ring shear, Christchurch, New Zealand, developed, tested, and calibrated in the course of my PhD research.

apparatus quos dilexi et apparatus quos odisse dilexi

To the people who would not let me give up, especially James and Anna.

Thesis Prologue

Understanding seismogenesis requires detailed descriptions of active faults, laboratory measurements of the physical properties of fault rocks, and numerical and theoretical models that incorporate these observations and values (e.g., Sibson 1977a, 1986, 2003; Noda & Lapusta 2013). New Zealand's Alpine Fault accommodates 65-75% of the total relative Australian-Pacific plate boundary motion, ruptures quasi-periodically in large magnitude ($M_w \sim$ 8) earthquakes, and represents the largest known onshore seismic hazard in New Zealand (e.g., Berryman et al. 2012a; Sutherland et al. 2007). Along the central Alpine Fault, dextral-oblique displacement has exhumed amphibolite-facies mylonites from c. 35 km depth over the past 5-8 Myr (Little et al. 2005). During exhumation, mylonitic fabrics have been overprinted by multiple episodes of brittle deformation involving frictional sliding, solution-assisted mass transfer, and fluid migration. Thus, rapid uplift has exposed a full suite of fault rocks formed in the presence of disparate crustal fluids at varying temperatures, pressures, and strain rates (e.g., Reed 1964; Norris & Cooper 2007; Sibson et al. 1979, 1981). Because previous field studies of Alpine Fault rocks have relied on composite sections constructed from discontinuous stream exposures, a complete description (on 0.1-100 m scale) of Alpine Fault cataclasites and gouges spanning the hanging wall-footwall interval has never before been presented. Furthermore, few publications on the mineralogical and microstructural characteristics of fault gouges and cataclasites, and no measurements of the permeability and frictional strength of Alpine Fault materials, existed prior to this dissertation (e.g., Warr & Cox 2001; Norris & Cooper 2007; Toy 2007). This thesis, set out in seven chapters and seven appendices, presents a multi-disciplinary dataset on the lithological, microstructural, mineralogical, geochemical, hydrological, and frictional properties of Alpine Fault rocks studied at field localities distributed 230 km along-strike. *Taken together, these data elucidate physical and chemical processes that drive seismicity and accommodate slip on the Alpine Fault.*

Thesis format

Questions addressed in each chapter of the thesis are listed below. Because much of the work documented was carried out collaboratively, this outline also details my personal contribution to the chapters. Formal co-authorship forms that verify the accuracy of this outline are found in the appendix that corresponds to each chapter.

Chapter 1 outlines fault mechanics and earthquake physics theory. It includes material published in two original manuscripts that I authored and co-authored during the course of my doctoral programme (Boulton et al. 2009; Davies et al. 2012). It also presents an overview of the Alpine Fault and the topics covered in the subsequent chapters.

Chapter 2 summarizes previous research conducted on the Alpine Fault and presents new data on the architecture of the fault at Gaunt Creek, a catchment of the Waitangi-taona River. Questions addressed include:

- What is the nature of fault zone materials on the 0.1-100 m scale?
- How do damage zone and fault core lithologies differ?
- What are microstructural characteristics of damage zone and fault core lithologies?
- What is the major element geochemistry of the fault rock lithologies?
- What is the mineralogy of fault rocks comprising the high strain fault core?
- How do mechanical and chemical processes influence fault zone hydrological and petrophysical properties?
- What are the rheological implications of the mechanical and chemical processes acting on the Alpine Fault?
- Do fault zone properties vary with time in the seismic cycle?

- Are these results applicable to other localities of the fault mapped along strike?

Chapter 2 contains data derived largely from the internationally funded Deep Fault Drilling Project (DFDP-1), with which I worked extensively for over three years. Before the drilling project, I collected background information on properties of the fault rocks exposed in field localities along strike of the central Alpine Fault. During the drilling project, I spent two weeks on site helping with core recovery, core logging, and core handling. Following the drilling project, I spent six weeks making detailed structural and lithological logs of the recovered core. Since January 2011, I have also worked closely with Virginia Toy to: formally describe the core lithologies, collect representative samples of core lithologies; obtain initial data on the bulk rock mineralogy and major element geochemistry of the core lithologies; ensure a complete set of reprentative fault rocks were collected and prepared for thin section making and imaging; interpret and document results. Chapter 2 includes material published in the following co-authored manuscripts: Sutherland et al. (2012); Townend et al. (2013); Toy et al. (in prep). However, I focus on the data that I collected and the words, interpretations, and synthesis are my own.

Chapter 3 presents new data on the hydrological and frictional properties of central Alpine Fault surface outcrop cataclasite and gouge samples collected at two well-known localities, Gaunt Creek and Waikukupa River (e.g., Read 1994; Cooper & Norris 1994; Norris & Cooper 1997, 2003; Warr & Cox 2001; Toy 2007). Questions addressed include:

- What are the structural and microstructural characteristics of surface outcrop cataclasites and fault gouges?

- What is the mineralogy of Alpine Fault surface outcrop cataclasites and fault gouges?

- How did the cataclasites and gouges form?

- How does fault zone permeability vary with proximity to the highly comminuted, striated fault gouges?

- What are the low velocity ($v = 1 - 300\mu$m/s), room temperature, low effective normal stress ($\sigma'_n \sim 30$ MPa) frictional properties of saturated Alpine Fault gouges and cataclasites?

- What are the steady state friction coefficients of these materials?

- Are these materials velocity strengthening or velocity weakening? That is, are earthquakes likely to nucleate and propagate through these materials?

- Do these materials heal with time during static holds? That is, what are the healing properties of the cataclasites and gouges?

- What are the implications of these measurements and observations for the nucleation and propagation of Alpine Fault earthquakes?

The data presented in this chapter represent the combined results of two weeks of fieldwork and sample collection, several weeks of sample preparation, and seven weeks of laboratory experiments at Pennsylvania State University, Pennsylvania, USA. I conducted all the fieldwork and sample preparation. Another PhD student at Penn State University, Brett Carpenter, assisted with running experiments on the double direct shear apparatus ("the biax") and with data reduction. I conducted all of the data analysis and interpretation. Chapter 3 is the Boulton et al. (2012) manuscript reprinted in its entirety. In total, I drafted, wrote, and revised, 85% of the manuscript.

Chapter 4 presents new data on the lithological, structural, microstructural, mineralogical, geochronological, frictional and hydrological properties of southern Alpine Fault surface outcrop gouges collected at three new localities only described before at the reconnaissance level (Wellman & Willett 1942; Clark & Wellman 1959; Hull & Berryman 1986; Berryman et al. 1992; Campbell 2005; Sutherland & Norris 1995). This chapter represents an integrated approach to fault zone research only achievable through collaboration with another PhD student at the University of Otago, Nic Barth, who conducted a largely field-based PhD on the southern Alpine Fault (Barth 2013). Questions addressed include:

- How does the southern Alpine Fault differ structurally from the central Alpine Fault?
- What is the architecture of the southern Alpine Fault?
- To what extent is slip localized in fault gouges?
- What is the timing of slip localization?
- What is the origin of the fault gouges?
- What microstructures are evident in the fault gouges?
- What is the mineralogy of the fault gouges?
- What is the permeability of the fault gouges?
- What are the low velocity ($v = 1 - 300\mu$m/s), room temperature, low effective normal stress ($\sigma_n' \sim 6$ MPa) frictional properties of saturated southern Alpine Fault gouges?
- What are the steady state friction coefficients of the gouges?
- Are these gouges velocity strengthening or velocity weakening? That is, are earthquakes likely to nucleate and propagate through these materials?
- Do these materials heal with time during static holds? That is, what are the healing properties of the cataclasites and gouges?
- What are the implications of these measurements and observations for the nucleation and propagation of Alpine Fault earthquakes?

Chapter 4 is the Barth et al. (2013) manuscript reprinted in its entirety. Of the field work documented in the manuscript, I went to two of the three localities described in detailed cross sections, collected samples, and took independent field notes, measurements, and photographs. Of the laboratory

work conducted, I prepared fault rock samples for the double direct shear experiments, ran one of the experiments (the others were done by Brett Carpenter), and did all of the data analysis. I prepared all the samples for quantitative X-ray diffraction, which was done by Mark Raven at the Commonwealth Scientific and Industrial Research Organisation (CSIRO), Australia. Nic Barth prepared all the samples for $^{40}Ar/^{39}Ar$ dating, which was done by Geoff Batt at the University of Western Australia. Nic Barth and I collaboratively did the data interpretation, manuscript drafting, writing, and revisions. Specifically, I contributed 40% to the final manuscript, including writing all of the following sections: 4.2; 4.4.2; 4.6; 4.8.2.

At the conclusion of Chapter 4, it is noted that the frictional properties of many crustal materials change with temperature and pressure. In **Chapter 5**, variations in the frictional properties of two DFDP-1 fault gouges are investigated in hydrothermal friction experiments conducted at in situ crustal conditions. Questions addressed include:

- What are the mineralogical, lithological, and microstructural characteristics of Alpine Fault gouges recovered in DFDP-1?

- What are the low velocity ($v = 0.01 - 3\mu$m/s), low to high temperature ($T = 23 - 350$°C), low to high effective normal stress ($\sigma'_\eta = 31 - 156$ MPa), frictional properties of saturated gouges?

- How does the steady state coefficient of friction of the gouges change with increasing temperature and effective normal stress?

- How does fault gouge stability change with depth? That is, at what conditions (temperature and effective normal stress) is the transition from velocity strengthening to velocity weakening observed?

- What mechanisms are responsible for the change in fault gouge stability with increasing temperature and effective normal stress?

- What are the implications of these results for Alpine Fault seismicity?

Chapter 5 is a longer version of a manuscript accepted by Geophysical Research Letters (Boulton et al. 2014). Experiments were conducted on a triaxial compression apparatus during five weeks of research at the United States Geological Survey (USGS), Menlo Park, California, USA. Diane Moore and David Lockner helped with experimental methods, equipment, and data corrections. I did all of the data processing and data analysis. Mark Raven, CSIRO Australia, did the quantitative X-ray diffraction analyses. In total, I drafted, wrote, and revised, 80% of the manuscript.

Chapter 6 presents new data on the high velocity frictional properties of cataclasites and gouges recovered during DFDP-1; data on southern Alpine Fault gouge are also presented. Questions addressed include:

- What are the high velocity, low normal stress (v = 1 m/s, σ_n=1 MPa) frictional properties of DFDP-1 gouges and cataclasites?

- What are the high velocity, low normal stress (v = 1 m/s, σ_n=1 MPa) frictional properties frictional properties of southern Alpine Fault gouge?

- How does high velocity frictional behaviour change with the addition of pore fluid?

- What microstructures are produced during high velocity frictional sliding in the dry cataclasites and gouges?

- What dynamic weakening mechanisms occur during sliding at coseismic slip rates?

- What are the implications of these data for earthquake rupture propagation?

Chapter 6 is a manuscript in preparation (Boulton et al. in prep). Experiments were conducted on a low-to-high velocity rotary shear apparatus at the Institute of Geology, China Earthquake Administration, Beijing, China. I conducted all the sample preparation, experiments, data processing, and data analysis. A PhD student at the Institute of Geology, Yao Lu, assisted

with the rotary shear experiments and answered my questions about experimental methods and results. In total, I drafted, wrote, and revised 100% of the manuscript.

Chapter 7 presents a summary of the results, a synthesis of the data obtained, and suggestions for future research.

Scientific contributions

Publications

Boulton C, Moore DE, Lockner DA, Toy VG, Townend J, Sutherland R (2014). Frictional strength and stability of exhumed fault gouges in DFDP-1 cores, Alpine Fault, New Zealand. Geophysical Research Letters, doi:10.1002/2013GL058236.

Townend J, Sutherland R, Toy VG, Eccles JD, **Boulton C**, Cox SC, McNamara D 2013. Late-interseismic state of a continental plate-bounding fault: Petrophysical results from DFDP-1 wireline logging and core analysis, Alpine Fault, New Zealand. Geochemistry, Geophysics, Geosystems: doi:10.1002/ggge.20236.

Barth NC, **Boulton C**, Carpenter BM, Batt GE, Toy VG 2013. Slip localization on the southern Alpine Fault, New Zealand. Tectonics 32: 1-21, doi:10.1002/tect.20041.

Sutherland R, Toy VG, Townend J, Cox SC, Eccles JD, Faulkner DR, Prior DJ, Norris RJ, Mariani E, **Boulton C**, Carpenter BM, Menzies CD, Little TA, Hasting M, De Pascale G, Langridge RM, Scott HR, Reid-Lindroos Z, Fleming B 2012. Drilling reveals fluid control on architecture and rupture of the Alpine Fault, New Zealand. Geology 40: 1143-1146, doi:10.1130/G33614.1.

Boulton C, Carpenter BM, Toy V, Marone C 2012. Physical properties of surface outcrop cataclastic fault rocks, Alpine Fault, New Zealand. Geochemistry Geophysics Geosystems 13: Q01018, doi:10.1029/2011GC003872.

Davies TRH, McSaveney MJ, **Boulton C** 2012. Elastic strain energy release from fragmenting grains: Effects on fault rupture. Journal of Structural Geology 38: 265-277, doi:10.1016/j.jsg.2011.11.004.

Boulton C, Davies TRH, McSaveney MJ 2009. The frictional strength of granular fault gouge: application of theory to the mechanics of low-angle normal faults. In: Ring U, Wernicke B eds. Extending a Continent: Architecture, Rheology, and Heat Budget. London, Geological Society Special Publications 321: 9-31.

Publications in preparation

Toy VG, **Boulton C**, Sutherland R, Townend J, Norris RJ, Little TA, Prior DJ, Mariani E, Faulkner D, Menzies C, Scott H, Carpenter BM (in prep). Rock types, deformation mechanisms, and architecture of the Alpine Fault, revealed by DFDP-1 drilling, New Zealand.

Boulton C, Yao L, Ma S, Shimamoto T (in prep) High velocity frictional properties of DFDP-1 core, Alpine Fault, New Zealand.

Conference presentations

Boulton C, Moore DE, Lockner DA, Toy VG, Townend J, Sutherland R 2013. High T-P frictional strength and stability of exhumed fault core gouges, Alpine Fault, New Zealand. EOS Transactions AGU Fall Meeting Supplement.

Boulton C, Toy VG, DFDP-1 Scientific Party 2013. Rheological implications of fluid-rock interaction revealed in fault rock recovered during the Alpine Fault-Deep Fault Drilling Project (DFDP-1). 19th International Conference on Deformation Mechanisms, Rheology and Tectonics, 16-18 September, Leuven, Belgium.

Boulton C, Toy VG, Barth NC, Carpenter BM 2012. Along strike applicability of results from the Deep Fault Drilling Project, Alpine Fault, New Zealand. EOS Transactions AGU Fall Meeting Supplement: Abstract T31C-2617.

Boulton C, Barth NC, Carpenter BM, Toy VG 2012. Weak Fault Cores, Alpine Fault, New Zealand. In: Pittari A, Hansen RJ eds. Abstracts, Geosciences 2012 Conference, Hamilton, New Zealand, Geological Society of New Zealand Misc. Publication 134A: 10.

Boulton C, Barth NC, Carpenter BM, Toy VG 2012. Weak Fault Cores, Alpine Fault, New Zealand. Feedback Processes in Rock Deformation, Gordon Research Conference, 19-24 August, Andover, New Hampshire, USA.

Boulton C, Villeneuve M, Goodin C 2012. Acoustic emissions generated during uniaxial compressive strength tests on Lyttelton volcano rocks, Christchurch, New Zealand. Geophysical Research Abstracts, EGU General Assembly.

Boulton C, Barth NC, Carpenter BM, Toy VG 2011. Significant along-strike variations in fault gouge thickness, friction coefficient and mineralogy, Alpine Fault, New Zealand. EOS Transactions AGU Fall Meeting Supplement: Abstract T41C-04.

Boulton C, Davies T 2009. Creating Coseismic Fault Rocks. Geosciences Annual Conference, Geological Society of New Zealand Misc. Publication 128A.

Table of Contents

List of Figures

List of Tables

Chapter I

Introduction

1.1 Seismicity and Society

The South Island of New Zealand sits astride the Australian-Pacific plate boundary and comprises a small portion of the circum-Pacific seismic belt (Figure 1.1). The most populous city on the South Island, Christchurch (pop. 350,000), lies approximately 100 km south and east of the fast-moving (20-30 mm/yr) Alpine and Hope Faults, which link two subduction zones of opposite polarity (Figure 1.2). Between 1990 and 2010, field mapping and paleoseismicity studies identified seismically active structures in the Canterbury province encompassing Christchurch (e.g., Van Dissen & Yeats 1991; Barnes 1996; Pettinga et al. 2001; Langride & Berryman 2005; Forsyth et al. 2008; Dorn et al. 2010). The average strain rate within Canterbury was determined geodetically to be nearly uniaxial contraction of c. 10×10^{-9} per year, corresponding to c. 2 mm/yr on structure(s) east of the foothills-bounding Porters Pass Fault (Wallace et al. 2007). Stirling et al. (2002) calculated a very low probability (10% in 50 years) of peak ground acceleration > 0.3 g in Christchurch. Despite these studies, the devastating 2010-2011 Canterbury earthquake sequence, a protracted series of shallow crustal earthquakes that began with the M_w 7.1 Darfield earthquake (3 September 2010 UTC) and included the M_w 6.2 Christchurch earthquake (21 February 2011 UTC), occurred on multiple unmapped structures, produced peak ground accelerations over 0.7 g in the central city, and resulted in 185 fatalities and over NZ$15 billion in remediation costs (e.g., Quigley et al. 2012; Kaiser et al. 2012; Elliott et al. 2012).

Shortly after the M_w 6.2 Christchurch earthquake, the great M_w 9.0 Tohoku earthquake (11 March 2011 UTC) produced a tsunami, and together

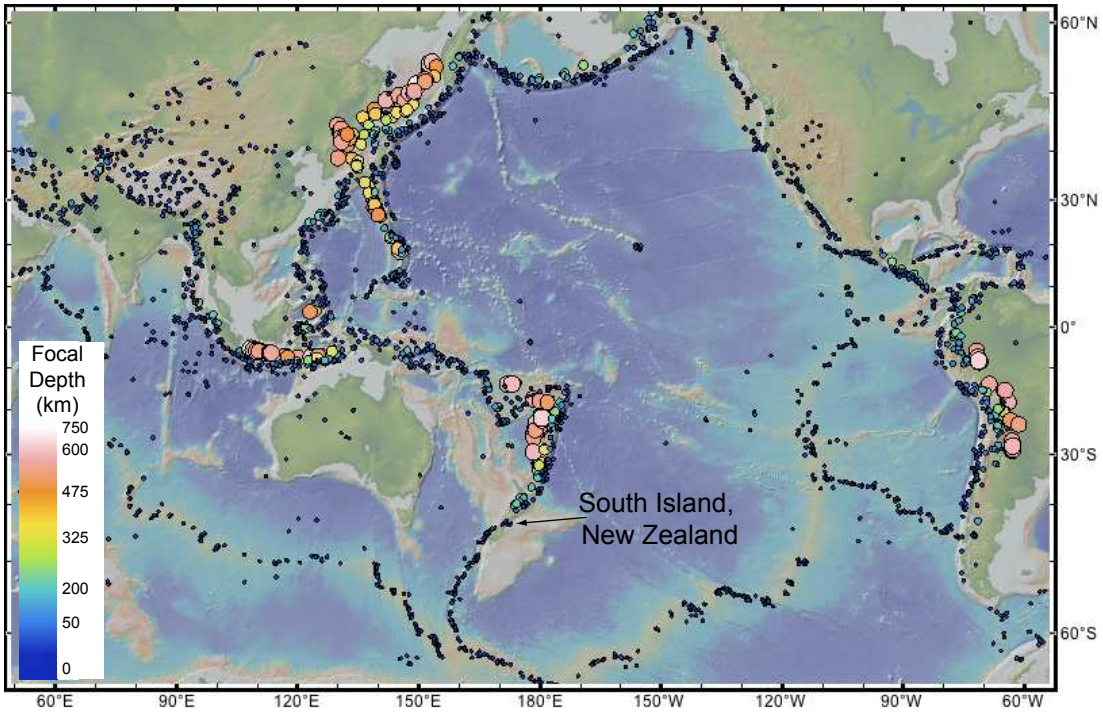

Figure 1.1: New Zealand lies along the circum-Pacific seismic belt, a narrow region of the crust responsible for c. 90% of the world's earthquakes. The location and focal depths of all earthquakes $M_w \geq 5.5$ between 1973 and 2013 are also pictured. Map constructed using GeoMapApp 3.3.8 software and the Advanced National Seismic System (ANSS) composite earthquake catalog.

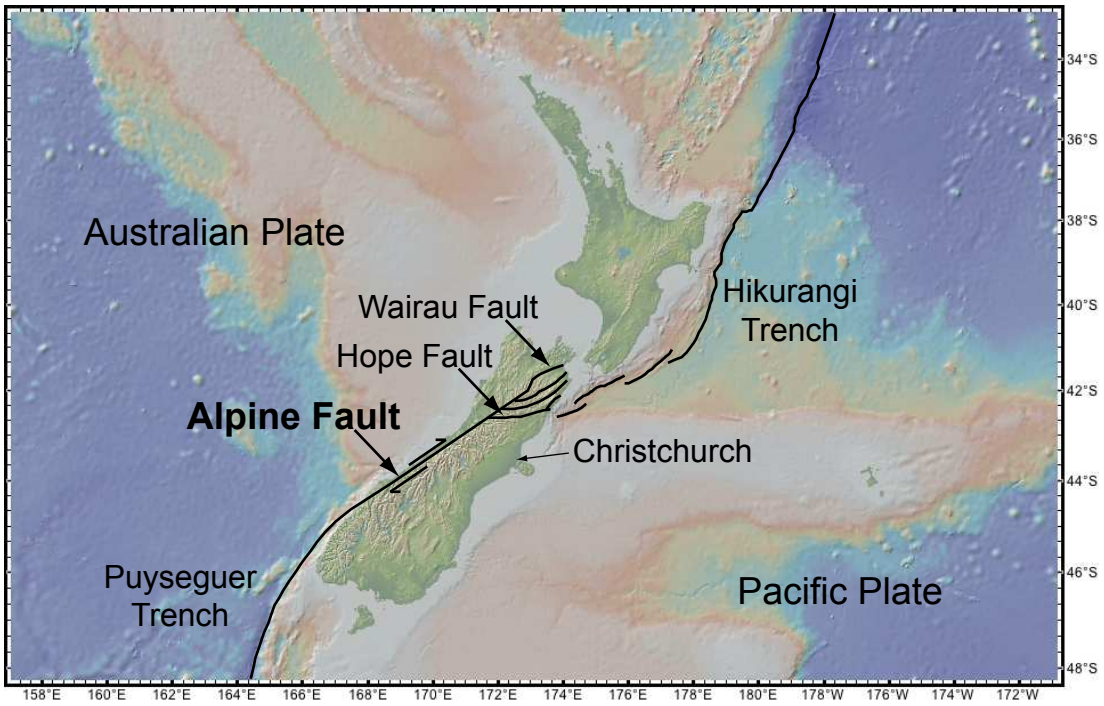

Figure 1.2: The New Zealand plate boundary setting.

these catastrophes caused 22,626 fatalities in Japan (Holzer & Savage 2013). The first decade of the 21st century was characterized by the occurrence of multiple large-magnitude earthquakes in densely populated, poorly prepared areas worldwide. Some 700,000 lives have been lost since AD 2000 due to earthquakes and associated natural disasters. Large-magnitude earthquakes caused thousands of fatalities in India (M_w 7.6 Bhuj, 26 January 2001 UTC), Iran (M_w 6.6 Bam, 26 December 2003 UTC), Southeast Asia (M_w 9.1 Sumatra-Adaman, 26 December 2004 UTC), Pakistan (M_w 7.6 Kashmir, 08 October 2005 UTC), China (M_w 7.9 Wenchuan, 12 May 2008 UTC), and Haiti (M_w 7.0 Haiti, 12 January 2010 UTC). In the 21st century, earthquakes and their effects are estimated to cause at least 1.76±0.33 million more fatalities (Holzer & Savage 2013). Although technological advances continue to improve our ability to monitor earthquakes, document their effects, and engineer infrastructure able to withstand strong ground motion, assessing the hazard associated with earthquakes still involves multiple uncertainties (e.g., Stein et al. 2011; Hanks et al. 2012; Stein & Stein 2013). Moreover, technical advances in the fossil fuel industry are inducing, not mitigating, seismicity in the quest to extract new resources and sequester CO_2 (e.g., Keranen et al. 2013; Ellsworth 2013). As the earth becomes increasingly more populated and urbanized (see Bilham 2009), the need to understand the physical processes that drive earthquake rupture nucleation and propagation remains ever-present.

1.2 Faults: the Seismic Source

Following the 1906 San Francisco Earthquake, California, USA, Reid (1910) formulated the elastic rebound theory. Reid (1910) documented right-lateral displacement along strike of the San Andreas Fault; he posited that the fault is a frictional surface that usually remains locked, allowing regions either side of it to accumulate elastic strain. When the frictional contact slips, Reid (1910) said, this stored elastic strain is suddenly released, causing displacement and generating an earthquake. Globally, the vast majority of earthquakes occur on pre-existing faults (Scholz 1998, 2002). Faults can be defined as lithologically heteterogeneous, anisotropic, discontinuous tabular

bodies across which displacement has occurred. Faults commonly vary in thickness between 10 m and 10^3 m and are partitioned into zones of high strain (often called the fault core) and low strain (often called the damage zone) (Sibson 1986; Caine et al. 1996; Faulkner et al. 2010) (Figure 1.3). Theoretically, faults have been variably treated as granular materials, fractal objects, and tabular Euclidean zones in continuum solids (Ben-Zion & Sammis 2003 and references therein). The common geological observation that most displacement during an earthquake occurs on narrow (< 1 cm-thick) principal slip zones in mature faults (> 1 km cumulative displacement) supports the view that faults can be treated as tabular Euclidean zones in continuum solids (Chester & Logan 1986; Chester & Chester 1998; Sibson 2003; Ben-Zion & Sammis 2003). This treatment allows constitutive friction equations derived from laboratory experiments to be used in numerical models of frictional slip on natural seismogenic faults.

1.3 Friction Theory

1.3.1 Static friction

An object on a frictional surface will resist a tangential force and remain at rest, provided that the magnitude of the tangential force parallel to the surface is less than the product of a static friction coefficient and the normal force (Coulomb 1776; Bowden & Tabor 1986) (Figure 1.4). For a large enough tangential force relative to the normal force, frictional sliding (or failure in a granular material) occurs. This failure criterion, Amonton's Law, is:

$$F_s = \mu_s F_n \tag{1.1}$$

where F_n is the normal force acting on the frictional surface, F_s is the shear (or tangential) force acting on the object at rest, and μ_s is the coefficient of static friction, equal to $\tan\phi$, where ϕ is known as the "angle of friction". In granular materials, the normal and tangential forces are replaced by corresponding normal (σ_n) and shear stresses (τ), and the surface of interaction is replaced by a plane within the material (e.g., Dieterich 1979; Sammis & King 1987; Biegel et al. 1989; Marone 1998; Blanpied et al. 1995, 1998). Coulomb

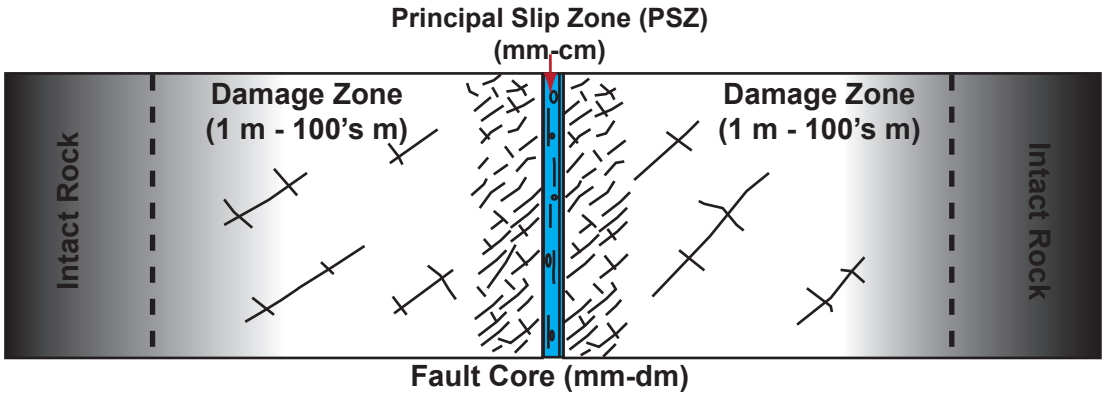

Figure 1.3: A conceptual model for fault zone structure (Caine et al. 1996; Wibberley et al. 2008; Faulkner et al. 2010). Strain is localized in a fault core containing granular fault rocks (gouge, cataclasite, or ultracataclasite; Sibson 1977a). Within the fault core, strain may be homogeneously distributed or localized onto a principal slip zone (PSZ), sometimes termed principal slip surface (PSS). The damage zone, a tabular region containing a greater number of discontinuities (faults or fractures) than is present in the protolith rocks, flanks the fault core.

also discovered that static frictional force increases logarithmically with the amount of time an object is at rest. For metals, the real contact area between two incompletely smooth surfaces increases with time due to creep processes operating at the asperity contacts (also known as contact junctions or micro-contacts). As the contact area increases and normal stress at the contact decreases, this process of asperity (or contact junction) welding slows, leading to a logarithmic dependence of the static frictional force on the time two surfaces are held in contact (Bowden & Tabor 1986). When the real contact area is comparable to the apparent contact area, the shear force is no longer proportional to the normal force, so the coefficient of friction is no longer the proportionality constant. For soft metals, polymers and elastomers, the real contact area is commonly equal to the apparent contact area (Papov 2010).

1.3.2 Rock friction

The static friction theory that developed largely from observations of metallic contacts and adhesion theory was then tested using laboratory experiments on intact and granular rocks (Figure 1.5). Byerlee (1978) measured the initial, maximum and residual coefficient of friction for a wide range of rock types at room temperature and normal stresses up to 2 GPa (Figure 1.6). Following Amonton's Law, the coefficient of friction, μ, was taken as the ratio τ/σ_n. At normal stresses greater than 200 MPa, Byerlee (1978) found that the maximum coefficient of friction had a linear normal stress dependence, following the equation:

$$\tau = 5 + 0.6\sigma_n \tag{1.2}$$

That is, under high normal stress, rocks have 5 MPa of cohesion and a maximum friction coefficient (μ) of 0.6 largely irrespective of rock type. Byerlee (1978) found the following linear relationship at normal stresses less than 200 MPa:

$$\tau = 0.85\sigma_n \tag{1.3}$$

That is, under lower normal stress, rocks are cohesionless, and most have maximum friction coefficients (μ) of 0.85. These observations of the max-

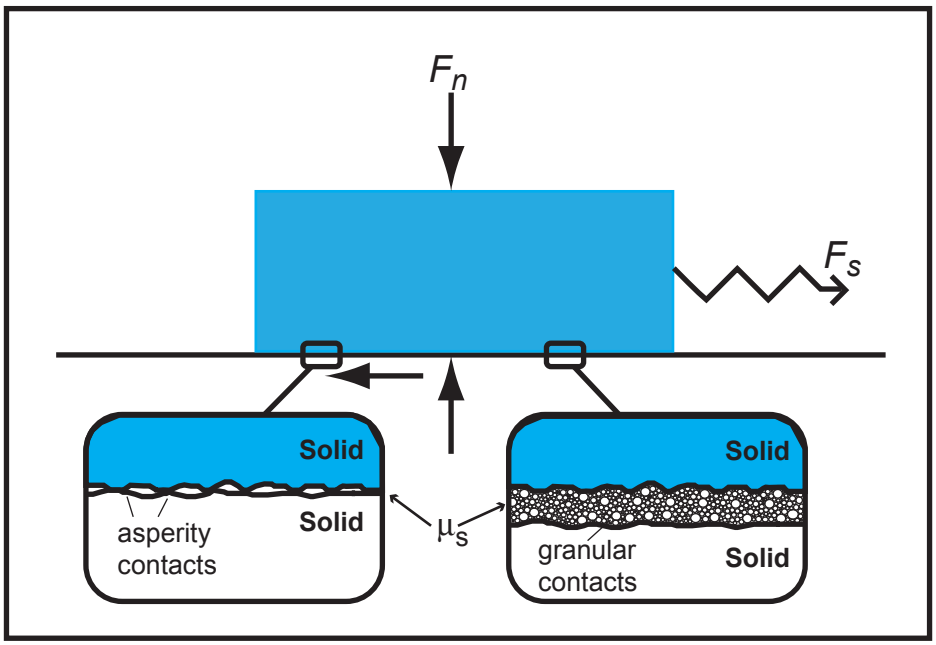

Figure 1.4: Spring-block slider model. An object at rest with a given mass exerts a normal force (F_N) across an interface. The interface has a coefficient of friction (μ_s) governed by both the normal force and the physical properties of the contacts along the interface (enlarged boxes). In a typical friction experiment, a tangential force (F_s) is applied via an elastic spring or elastic-spring analog. Sliding occurs when the magnitude of applied tangential force is equal to or greater than the product of the normal force and coefficient of friction ($F_s = \mu_s F_N$).

imum coefficient of friction (μ) became known as Byerlee's law. The law appears to remain valid for most types of granular and intact rocks at temperatures up to 350°C (Blanpied et al. 1995), but minerals with lower friction coefficients include talc, chrysotile, graphite, muscovite/illite, biotite, and varieties of smectite (e.g., Moore et al. 2004; Moore & Lockner 2004, 2007, 2011; Ikari et al. 2011a; Carpenter et al. 2011; Behnsen & Faulkner 2013). If fluid is present in pores, Terzhagi & Peck (1948) illustrated that pore fluid pressure (P_p) acts to reduce the effective normal stress (σ_n'):

$$\sigma_n' = \sigma_n - \alpha P_p \tag{1.4}$$

The parameter α incorporates physical properties of the rocks, and was determined empirically to be 1 for most rock types (Brace 1972; Paterson 1978; Morrow et al. 1992). Note that if the pores are incompletely saturated, P_p is negative and the σ_n' increases. Then, the effective normal stress-dependent frictional strength of a fault can be calculated following:

$$\tau = C_0 + \mu_s \sigma_n' \tag{1.5}$$

where the static coefficient of friction, μ_s, is generally assumed to be equal to Byerlee's maximum friction coefficient, $0.6 < \mu < 0.85$, σ_n' is the resolved normal stress acting on the fault less the pore fluid pressure, and C_0, cohesion, is generally assumed to be negligible (e.g., Brace & Kohlstedt 1980; Sibson 1982; Townend & Zoback 2000) (Figure 1.7). As with early friction studies, laboratory measurements of fault surfaces comprising both intact and granular rock showed that the static friction coefficient, μ_s, increases linearly with the log of stationary contact time, t_{hold}:

$$\mu_s\left(t_{hold}\right) = \alpha_s + \beta_s \log_{10}\left(t_{hold}\right) \tag{1.6}$$

where α_s is the fault strength at time $t_{hold} = 1$ s and β_s is the healing rate (Dieterich 1972; Dieterich & Kilgore 1994; Scholz 2002).

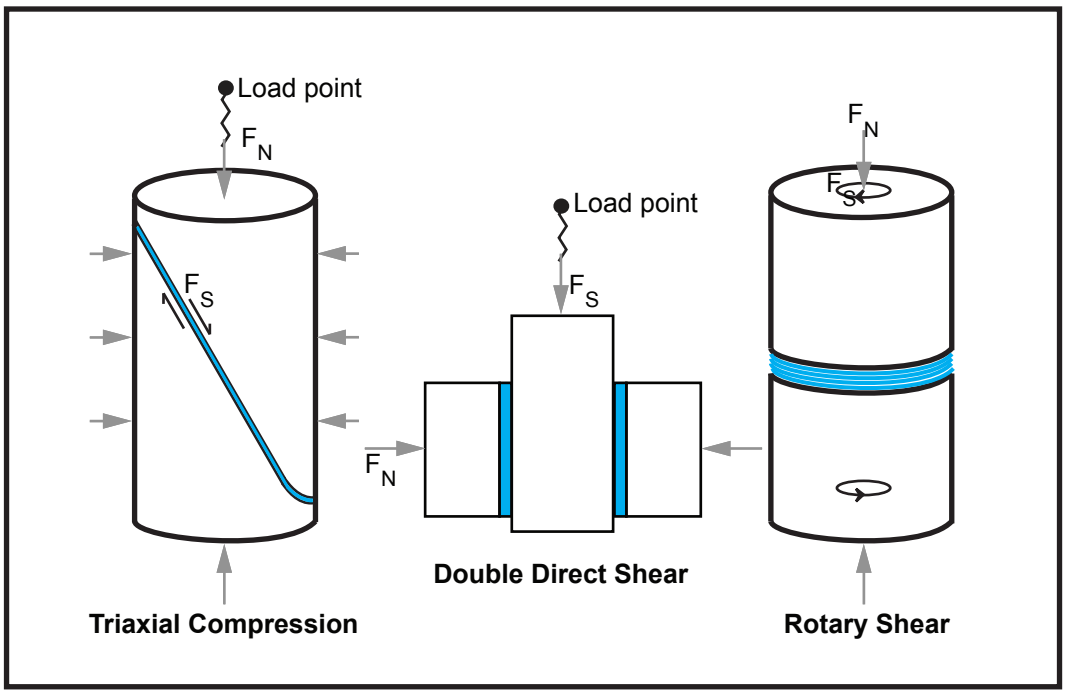

Figure 1.5: Configurations typically used in friction experiments; all three are employed in this thesis. The triaxial compression configuration is best suited to high temperature, high pressure friction experiments wherein the experimental fault (blue) contains a pressurized pore fluid (e.g., Byerlee 1978; Chapter 5). Total displacement on the experimental fault is limited to a few millimetres in triaxial compression experiments. Higher displacements (up to 20 mm) can be achieved in the double direct shear configuration (Chapters 3 and 4). Very high displacements (metres) can be achieved using the rotary shear configuration (Chapter 6).

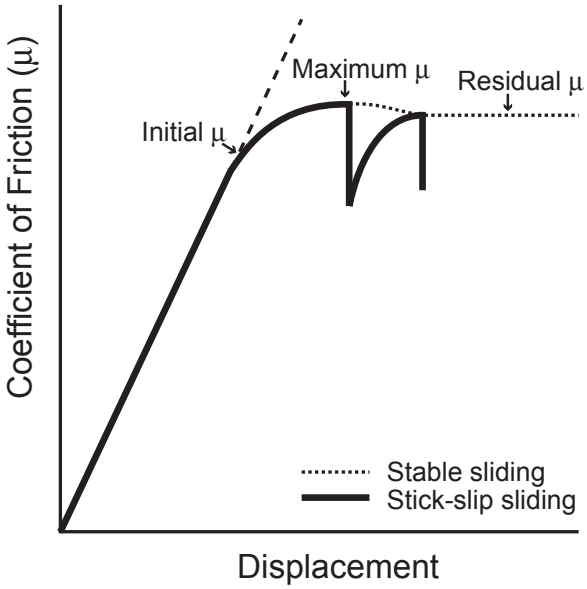

Figure 1.6: A typical plot of coefficient of friction (μ) vs. displacement produced in a friction experiment. This example, modified from triaxial compression experiments conducted by Byerlee (1978), is used to illustrate the definition of the terms initial μ, maximum μ, and residual (or steady-state) μ. The difference between stick-slip (unstable or potentially seismic) sliding (solid line) and steady state (stable or aseismic) sliding (dotted line) is also illustrated. See text for a discussion.

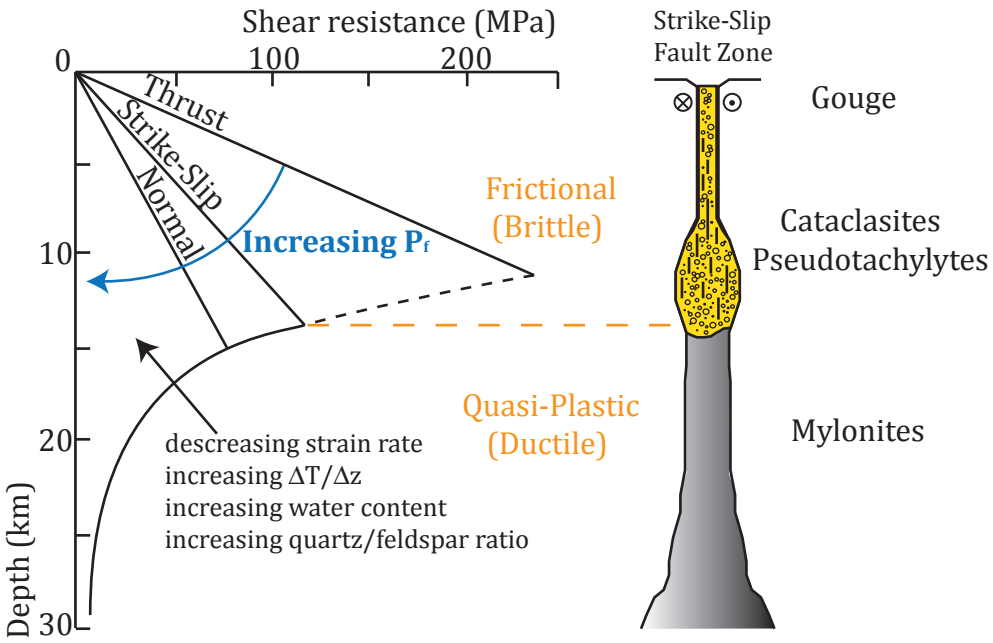

Figure 1.7: Simplified profile of variations in shear resistance with depth for the three faulting regimes: thrust, strike-slip, and normal. Profiles are constructed assuming: the fault is optimally oriented with respect to the maximum compressive stress (e.g., 'Andersonian' faulting); the static coefficient of friction lies intermediate between the range of values reported by Byerlee (1978) ($\mu_s = 0.75$); pore fluid pressure is hydrostatic ($\lambda_v = 0.4$) crustal density is typical of quartzofeldspathic rocks ($\rho = 2650 kg/m^3$) the geothermal gradient is typical for continental crust (dT/dz =25°C/km); and the lower crust is governed by a Westerly Granite flow law (strain rate $10^{-11} s^{-1}$). The variables that affect shear resistance are listed. Also listed is assumed fault zone rheology, the profile of a typical strike-slip fault zone (it remains unclear whether frictional (or brittle) fault zone thickness remains planar, widens, or narrows with increasing depth), and typical variations in fault rock lithology with depth (Figure and caption modified from Sibson 1986).

1.3.3 Kinetic friction

Once the static coefficient of friction is overcome, the shear stress needed to maintain sliding at constant velocity is proportional to the kinetic coefficient of friction (μ_k) (Coulomb 1776). Rabinowicz (1951) discussed the observation that the force needed to set two surfaces at rest into motion is often greater than the force to maintain motion. Rabinowicz (1951) showed that the transition from the static coefficient of friction (μ_s) to the kinetic coefficient of friction (μ_k) is not instantaneous. Instead, the transition occurs over a distance (S_k), and he correlated both the shape of the friction-displacement curve, and the distance needed to reach the steady-state kinetic friction value, with: initial size of metallic asperities ('junctions'); the way in which the asperities break; and the formation of new, perhaps cracked or weaker, asperities as displacement occurs.

As soon as sliding commences the breaking of the original metallic junctions is to some extent compensated for by the formation of new ones. These new junctions are not as strong as the original ones and hence the kinetic coefficient is less than the static, but, since it is not zero, the friction-displacement curve does not go down to the abscissa - Rabinowicz (1951), p. 1377

Following Rabinowicz (1951, 1958), two classes of constitutive equations were developed to describe the evolution of frictional strength (taken to be the product of μ and σ_n') on a fault during a slip event. According to the first class, single-variable displacement-dependent or velocity-dependent constitutive equations, frictional strength (and thus shear stress) weakens according to a fixed function of displacement or displacement velocity (e.g., the linear slip-weakening law of Ida (1972) and Andrews (1976b,a)). In linear slip-weakening models, a fault is locked. Shear stress increases to a yield stress and the static frictional strength is overcome. Over some distance, as the fault slips, shear stress weakens linearly to a residual value equivalent to the final shear stress on the fault (Orowan 1960). Because the final shear stress is constant, a fault cannot regain strength once it ruptures. These constitutive equations incorporate only a few parameters, ignore complicated processes such as dynamic re-strengthening and slip rate dependence, and are only first

order approximations of the range of possible slip and strength behaviors (Beeler 2006). Alternatively, the second class, the Dieterich-Ruina rate and state friction equations (DR friction equations), includes the experimentally observed time- and displacement- dependence of frictional strength. With one or more state variables, the DR friction equations also include healing, defined as the increase in frictional strength with time and/or displacement.

1.3.4 Rate and state friction equations

The constitutive equations know as the Dieterich-Ruina rate and state friction equations (Dieterich 1979; Ruina 1983) were empirically derived to describe the experimental behavior of sliding intact rock surfaces or granular gouges. In these friction experiments, the simulated fault does not have a static coefficient of friction; rather, the kinetic coefficient of friction evolves over a characteristic slip distance from an initial value to a new steady state value following a quasi-instantaneous change in load point velocity between 10^{-3} and $10^{4} \mu m/s$. As such, the DR friction equations cannot explain the time- and displacement-dependent changes in friction that accompany the transition from the static coefficient of friction to the kinetic coefficient of friction (Marone 1998). The underlying assumption is that the frictional surfaces that comprise faults are always loaded by tectonic shear stress, and therefore are sliding at velocities that vary with time in the seismic cycle (e.g., Brace & Byerlee 1966; Brace 1972). Small time- and displacement-dependent alterations in frictional strength, then, describe the gradual transition between "static" and "kinetic" friction, terms that are rather loosely used in fault mechanics literature (cf. the derivation and subsequent use of Byerlee's law described above) (Rice et al. 2001).

In developing the constitutive equations, Dieterich (1979) focused on deriving equations that accounted for the propensity of some rocks surfaces or granular rocks to slide stably while others undergo stick-slip sliding (correlated with earthquake-generating frictional instabilities by Brace & Byerlee 1966) (e.g., Figure 1.6). Dieterich (1979) presumed that stability could be correlated with contact time; that is, he used the previously observed relationship between the static coefficient of friction and hold time (Dieterich

1972) and the relationship between kinetic coefficient of friction and sliding velocity (Dieterich 1978), to underpin the constitutive equations, which are written, following Marone (1998), to be:

$$\mu_{ss} = \mu_0 + a \ln \left(\frac{V}{V_0} \right) + b \ln \left(\frac{V_0 \theta}{d_c} \right) \tag{1.7}$$

where V_0 and V are the initial and final load point velocities, respectively, μ_0 and μ_{ss} are the initial and final, steady state, coefficients of friction, a and b are empirical constants, d_c is the critical slip distance necessary to renew the population of surface contacts (Dieterich 1979), and θ is a state variable introduced by Ruina (1983) (Figure 1.8).

Equation (1.7) is combined with one of two evolution equations (sometimes referred to as 'laws') to capture the history dependence of the friction coefficient. The following differential equation (Marone 1998), termed the 'slowness law' or 'Dieterich law' (Scholz 2002), specifies the rate of change of the state variable with respect to time:

$$\frac{d\theta}{dt} = 1 - \left(\frac{V\theta}{d_c} \right) \tag{1.8}$$

Alternatively, Ruina (1983) considered the rate of change of the state variable to scale with velocity and slip and proposed the following differential equation, known as the 'slip law' or 'Ruina law' (Scholz 2002):

$$\frac{d\theta}{dt} = - \left(\frac{V\theta}{d_c} \right) \ln \left(\frac{V\theta}{d_c} \right) \tag{1.9}$$

For steady state sliding, each of the evolution equations yields $\frac{d\theta}{dt} = 0$, and the parameters a and b can be calculated following:

$$a - b = \frac{\Delta \mu_{ss}}{\ln \left(\frac{V}{V_0} \right)} \tag{1.10}$$

Figure 1.8 illustrates a velocity step increase conducted during a rate and state friction experiment, along with the parameters described above. The DR friction equations are empirically derived, and the micromechanical processes underpinning them are poorly understood. In terms of the parameter a, $a \ln \left(\frac{V}{V_0} \right)$ is the direct effect, quantifying the friction increase for an

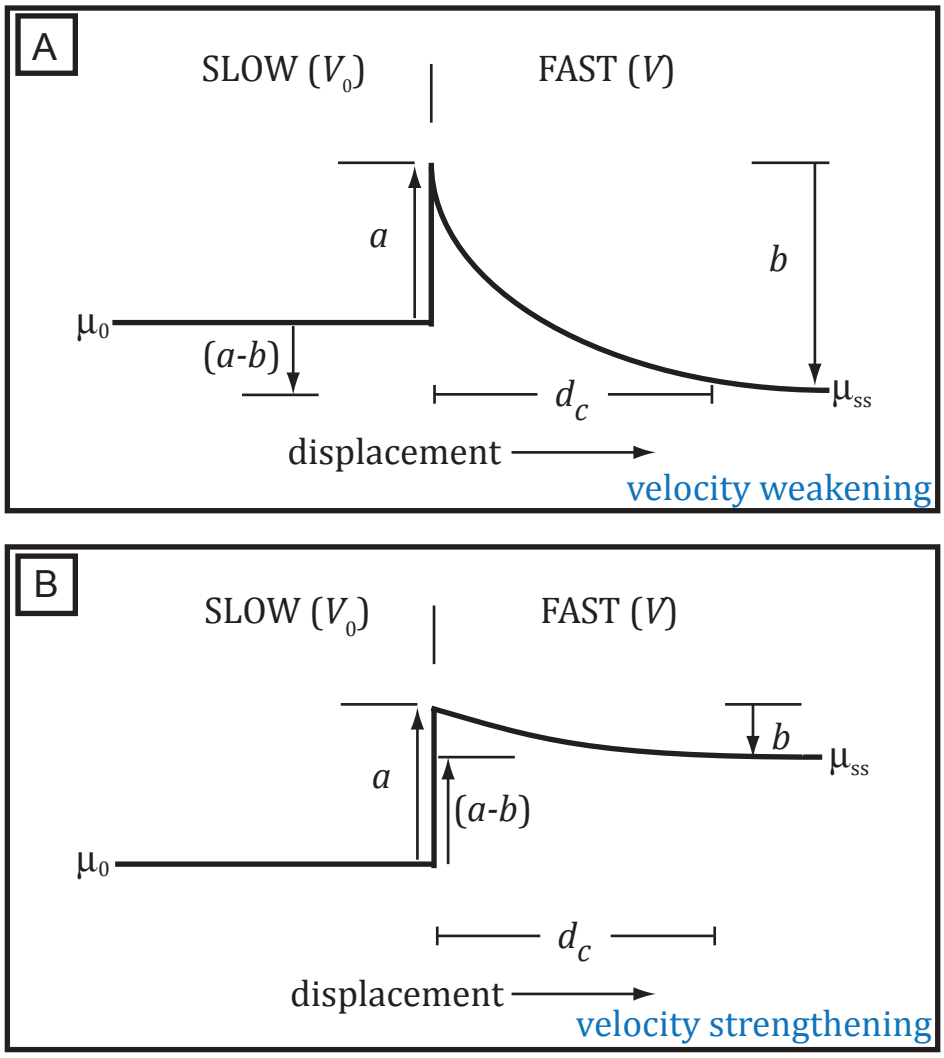

Figure 1.8: Diagrams of changes in the coefficient of friction (μ) following an instantaneous increase in sliding velocity (a velocity step). **A,** Typical response of velocity-weakening material, where the friction rate parameter (a–b) is negative. **B,** Typical response of velocity-strengthening material, where the friction rate parameter (a–b) is positive. See text for a definition of all the variables depicted.

increase in load point velocity and decrease for a decrease in load point velocity (Dieterich 1979). Ruina (1983), Nakatani (2001), and many others have considered a to represent the strain rate dependent shear strength of contacting asperities. For granular materials, dilatancy commonly accompanies a change in velocity, so the magnitude of a also incorporates some amount of volumetric work done against normal stress (e.g., Marone 1998; Niemeijer & Spiers 2005, 2007).

The evolution effect, $b \ln \left(\frac{V_0 \theta}{d_c} \right)$, is interpreted to be related to the change in total contact area and/or the change in contact strength following a change in velocity. For nominally dry, critically stressed (e.g., contact size determined by material yield strength and resolved normal stress), contacts, b may be correlated with the redistribution of energy stored in breaking grains (by extrapolation from Nguyen & Einav 2009) or the sliding strength of stressed asperities deforming by dislocation glide (e.g., Reinen et al. 1994; Sammis & Ben-Zion 2008). Realistically, fluids are likely to be present along sliding fault surfaces or within granular fault materials. In such case, b may be related to solution-assisted mass transfer processes (e.g., Blanpied et al. 1995, 1998; Niemeijer & Spiers 2007). In both nominally dry and fluid-saturated granular materials, some proportion of the magnitude of b is probably associated with a change in volume, i.e., dilation or compaction (e.g., Sammis & Steacy 1994; Niemeijer & Spiers 2007; Niemeijer et al. 2010).

The evolution effect is also a function of the critical slip distance, d_c, which is defined as the characteristic distance of the exponential decay or increase in the coefficient of friction (μ_{ss}) following a change in sliding velocity (up or down) (Marone 1998). The original definition of the critical slip distance by Ruina (1983) was for two contacts sliding over each other. It was later shown that the critical slip distance for granular fault materials depends on many parameters, such as gouge thickness, the degree of localization of deformation, and the grain size (e.g., Marone & Kilgore 1993; Rathbun & Marone 2010). In laboratory friction experiments, d_c is a strongly scale-dependent paramater (cf. Ohnaka 2003); scaling this value up to field-scale earthquakes remains an outstanding problem in fault mechanics and earthquake physics (e.g., Tullis 1988; Spudich & Guatteri 2004; Tinti et al. 2009; Cruz-Atienza et al. 2009; Marone et al. 2009). Although values of d_c should be deter-

mined strictly from velocity stepping experiments, the term has been used to described the distance over which peak friction decays to some residual "steady state" value, in the sense of Rabinowicz (1951) term S_k. Values of d_c (also termed the breakdown distance or slip-weakening distance) reported in the literature range from microns to several microns in lab experiments with bare surfaces (e.g., Marone 1998; Ohnaka 2003) to millimeters for shear fracture of intact granite (Ohnaka 2003) to metre(s) in high velocity friction experiments (e.g., Tsutsumi & Shimamoto 1997; Di Toro et al. 2004, 2011; Mizoguchi et al. 2007; Kitajima et al. 2010).

Another limitation of the DR friction equations is the empirical manner by which healing, defined as time-dependent fault strengthening, is brought into the equation through the state variable(s), θ (see Beeler et al. 1994; Marone 1998; Scholz 2002). For example, if the evolution effect follows the Dieterich law (equation 1.8), μ is assumed to increase in proportion to the natural log of θ, where θ is interpreted as contact lifetime (or at least as its average value). As discussed above, fluids affect time-dependent strengthening at room temperature through subcritical stress corrosion cracking and perhaps also chemically-assisted contact junction growth (Dieterich & Conrad 1984; Frye & Marone 2002). At higher temperatures, fluids affect time-dependent strengthening through both stress corrosion cracking and solution transfer processes; dislocation glide may also occur at contact junctions (e.g., Bos et al. 2000; Kanagawa et al. 2000; Yasuhara & Elsworth 2008; Tenthorey & Cox 2006; Niemeijer et al. 2008). Sealing, the reduction of permeability and porosity by time-dependent compaction and/or mineralization, can result in either time-dependent weakening via pore fluid pressurization (e.g., Sleep & Blanpied 1992), or time-dependent strengthening (e.g., Renard et al. 2000; Tenthorey & Cox 2006; see also chemico-mechanical compaction, Zheng & Elsworth 2013). In turn, the evolution of frictional strength over very long time scales (years to thousands of years) is poorly known (Tse & Rice 1986; Lapusta & Rice 2003; see also Lyakhovsky et al. 2005).

Despite these limitations, DR rate and state friction equations (sometimes termed 'laws') have been used in many numerical simulations to qualitatively and quantitatively predict and reproduce earthquake-source observations (e.g., Scholz 1998; Lapusta & Rice 2003; Hillers et al. 2006, 2007;

Perfettini & Ampuero 2008; Rubin 2008; Gabriel et al. 2012; Scarbek et al. 2012; Noda & Lapusta 2013 and many others). A recent criticism of DR friction equations came from the large number of high velocity friction studies, conducted at coseismic velocities on the order of 1 m/s, that showed reductions in the coefficient of friction much greater ($\sim$ 3-fold), over much larger distances (see above), than previously observed in low velocity experiments ($\leq$ 0.01 m/s) (e.g., Marone 1998; Mizoguchi 2005; Di Toro et al. 2004, 2011). Innovative experiments by Sone & Shimamoto (2009), where granular fault gouges were sheared at the variable slip rates experienced during the 1999 M_w 7.6 Chi-Chi earthquake, showed that even at high velocities, the coefficient of friction still depends on slip rate and an evolving state variable. Lapusta (2009) argued that the constitutive equations derived by Sone & Shimamoto (2009) to explain the exponential velocity-weakening trend could not be generalized in numerical models without additional experiments conducted at a range of conditions experienced in the brittle seismogenic crust (e.g., higher normal stresses, different velocity histories, with fluid(s)). Therefore, in the absence of unifying fault friction constitutive equations, this thesis investigates the low velocity frictional properties of granular rocks (fault gouges and cataclasites; Sibson 1977a) on New Zealand's Alpine Fault using the DR rate and state friction equations described in this section. Further complexities in the micromechanics of fault friction are outlined briefly below.

1.3.5 Earthquakes and frictional instabilities

If defined as a frictional instability, the nucleation of an earthquake requires that a fault weaken during the early portion of its slip at a faster rate than the release of stress driving fault motion. The critical weakening rate depends on the normal stress and elastic properties of the fault region (e.g., Scholz 2002; Beeler 2007). In the context of the DR rate and state friction laws, linear stability analyses for a single degree of freedom elastic system show that frictional sliding will be unstable, or potentially unstable, when the friction rate parameter, $a - b \leq 0$. Frictional sliding will be stable, or aseismic, when the friction rate parameter $a - b > 0$. The stability criterion also requires that the elastic stiffness of the loading system k be smaller than

a critical stiffness k_c, which is defined by the frictional properties of the slipping fault (Ruina 1983; Gu et al. 1984). For simple systems, inertia is ignored and elastic stiffness k is assumed to be inversely proportional to the characteristic dimension of the portion of the fault that is slipping (Beeler 2007). The stability criterion can be written:

$$k < k_c = \frac{-(a-b)\,\sigma_n'}{d_c} \tag{1.11}$$

If the rate of weakening, that is the change in μ with displacement, exceeds a critical value, elastic strain is released from the surrounding materials, causing elastic wave radiation. During an earthquake (seismic slip), the rate of weakening, and the amount of energy consumed by fracture energy and dissipated as heat, is thought to be related to the amount of energy radiated as damaging seismic waves (e.g., Savage & Wood 1971; Sibson 1977b, 1980; Beeler 2006; McGarr 2012) (Figure 1.9). Within this framework (termed the 'earthquake energy budget'), models of the earthquake source are complicated by uncertainties involving the stress level on earthquake faults (e.g., Hanks 1977; Sibson 1986; Townend 2006).

Accumulated evidence indicates that faults slip at a range of rates, from slow slip to rapid coseismic slip (e.g., Ide et al. 2007; Peng & Gomberg 2010). This spectrum of fault slip varies with the frictional properties of faults, and these properties are influenced by numerous variables, including, but not limited to: surface topography (e.g., Sagy & Brodsky 2009; Candela et al. 2012), elastic and plastic deformations at the surface of the contacting bodies (e.g., Brown & Scholz 1985, 1986; Ben-David & Rubinstein 2010a); interactions with wear particles (e.g., Goldsby & Tullis 2002; Anthony & Marone 2005; Guo & Morgan 2006, 2008); microfractures (e.g., Menendez et al. 1996; Hamiel et al. 2005); the nature and extent of damage zone formation (e.g., Ben-Zion 2001, 2008; Dor et al. 2006, 2008); chemical reactions (e.g.,Janecke & Evans 1988; Han et al. 2007; De Paola et al. 2011; Brantut et al. 2011b); temperature (e.g., Lachenbruch 1980; Chester & Higgs 1992; Rice 2006; Hirose & Bystricky 2007; Niemeijer et al. 2008, 2011; Tanikawa & Shimamoto 2009; den Hartog et al. 2012; Yuan & Prakash 2012); variations in the ratio of shear stress to normal stress on the sliding surface (Ben-David et al. 2010;

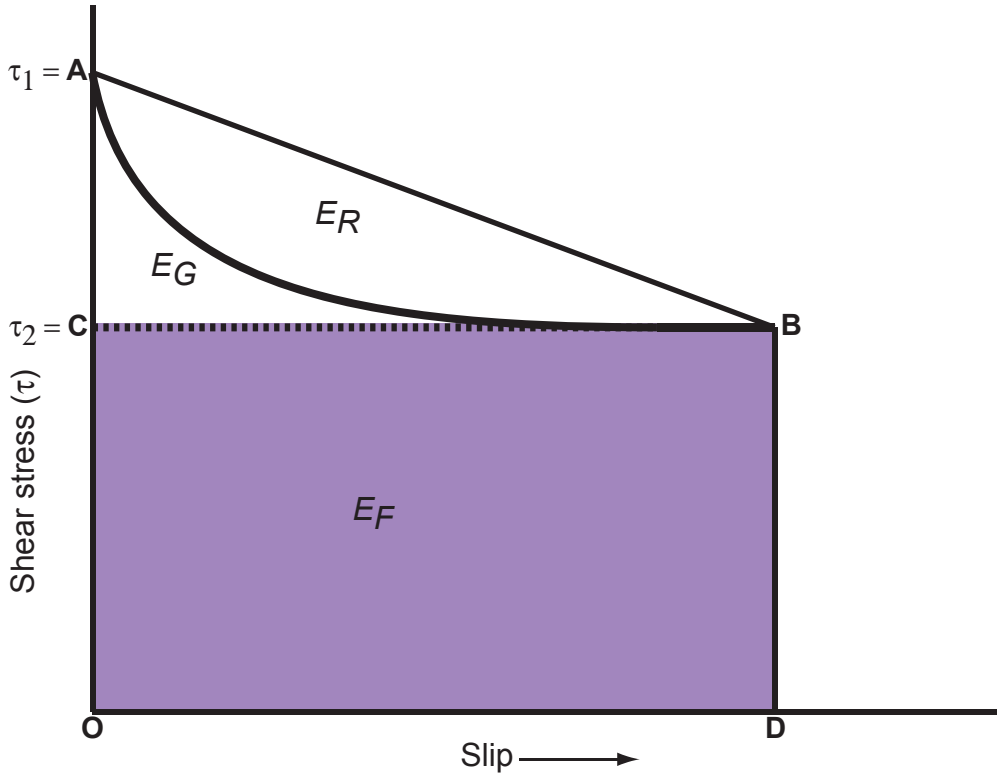

Figure 1.9: Simplified model illustrating the change in shear stress (τ) with slip at a point on a fault during an earthquake. During an earthquake, the total potential energy change (E_T) is given by the trapezoidal area AODB. According to the 'earthquake energy budget', this potential energy is partitioned into: E_F, frictional energy (assumed to be heat); E_G, fracture energy (all energy expended during slip on the fault); and E_R, radiated energy. Assuming the residual strength on the fault is equal to the final stress (τ_2), and that the initial stress (τ_1) is equal to the yield stress, the line AB can be constructed from seismological data (for a complete discussion about these assumptions, see Beeler 2006). However, the exponential decay function (bold) bounding E_G and E_R, which describes the evolution of shear traction on the fault, is poorly constrained using seismological data. Figure after Kanamori & Rivera (2006).

Ben-David & Fineberg 2011); dilatancy (e.g., Segall & Rice 1995; Samuelson et al. 2009, 2011; Segall et al. 2010); acoustic waves (e.g., Melosh 1979, 1996; Johnson et al. 2008; Davies et al. 2012; Xia et al. 2013); slip velocity (e.g., Dieterich 1978, 1979; Marone 1998; Sone & Shimamoto 2009; Di Toro et al. 2011; Chang et al. 2012); slip displacement (e.g., Ikari et al. 2013); and lithological heterogeneity (e.g., Fagereng & Sibson 2010; Fagereng 2011; McLaskey et al. 2012). Furthermore, a number of different instabilities may result in earthquake nucleation, including, but not limited to: fracture formation and/or strain localization (Reid 1910; Reches 1999; Han et al. 2007; Brantut et al. 2011c), stick-slip sliding (Brace & Byerlee 1966; Brace 1972), shear melting (Griggs 1954), thermo-mechanical instability (Regenauer-Lieb & Yuen 2008), creep instability (Orowan 1960), and pore fluid overpressures (Sibson 1992; Sleep & Blanpied 1992; Segall & Rice 1995; Brantut et al. 2011a). To add to this, Boulton et al. (2009) and Davies et al. (2012) considered the theoretical possibility that fragmentation, i.e., the rapid brittle failure of an intact piece of rock under load (Grady & Kipp 1987), of a single elastic grain in a dense granular fault gouge could initiate a frictional instability.

1.3.6 Fragmentation and frictional instabilities

Boulton et al. (2009) and Davies et al. (2012) defined a fault zone as a heterogeneous granular mass composed of densely packed, variably healed, (primarily) quartz grains. They then subdivided an earthquake rupture into two generalized stages: a static failure stage followed by a dynamic slip stage. To explore the relationship between static strength and the remotely (tectonically) applied shear stress resolved on the fault, Boulton et al. (2009) argued that the distribution of static local stresses varies statistically following the probability density distribution (R_f) of normalized grain contact forces in a static three-dimensional granular material under uniform load (Løvoll et al. 1999; see also Behringer et al. 2008) (Figure 1.10). The steeply-dipping tail in Figure 1.10 indicates the presence of local contact forces that greatly exceed the mean, and the relationship between probability, R_f, and contact force f (normalized against the mean) in this region is:

$$R_f = \exp\left(-f\right)^{\beta} \tag{1.12}$$

where β is $\sim 5/3$ (Ngan 2003; Van Eerd et al. 2007). If the grain size distribution and mineralogy of granular material comprising a fault is everywhere equal, then the number of grain contacts varies with the volume of the granular mass. It follows that the probability of occurrence, R_{max}, of the maximum force, f_{max}, normalized to the mean, is inversely related to the number of grain contacts.

In a critically stressed granular mass, f_{max} is limited by the brittle elastic limit of the grain, which is on the order of 100 MPa for unconfined crustal rocks (Prakash & Clifton 1992; see also Sammis et al. 1999). Ignoring temperature and lithological variations, the brittle elastic limit varies with loading rate (Yuan & Prakash 2013) and confining pressure (Yuan et al. 2011). For a granular mass comprising a crustal scale fault zone with a fixed width and thickness, grain volume increases linearly, and:

$$R_{max} = k_2 L_*^{-1} \tag{1.13}$$

where k_2 is a constant and normalized fault length, L_*, is the ratio of fault lengths (L_1/L_2). Thus, given the assumptions made, the maximum normalized compressive force acting on the most highly stressed individual grain increases as the fault gets longer according to:

$$f_{max} \sim -\left(\ln R_{max}\right)^{\beta} = \left(\ln L_*\right)^{\beta} \tag{1.14}$$

Following equation 14, the probability that, under a given applied stress, the local stress will exceed the brittle elastic limit of a grain is greater for longer faults. In a tightly-packed granular mass, when an intact grain breaks via fragmentation, it releases stored elastic strain energy in the form of elastic body waves that radiate from the broken grain and change the ratio of grain-contact normal and shear stresses in the surrounding material (see also Johnson & Jia 2005; Johnson et al. 2008; Savage & Marone 2007). Wherever and whenever the failure criterion for reshear of granular materials (equation 1.5) is met, slip will occur. This argument addresses a paradox in fault

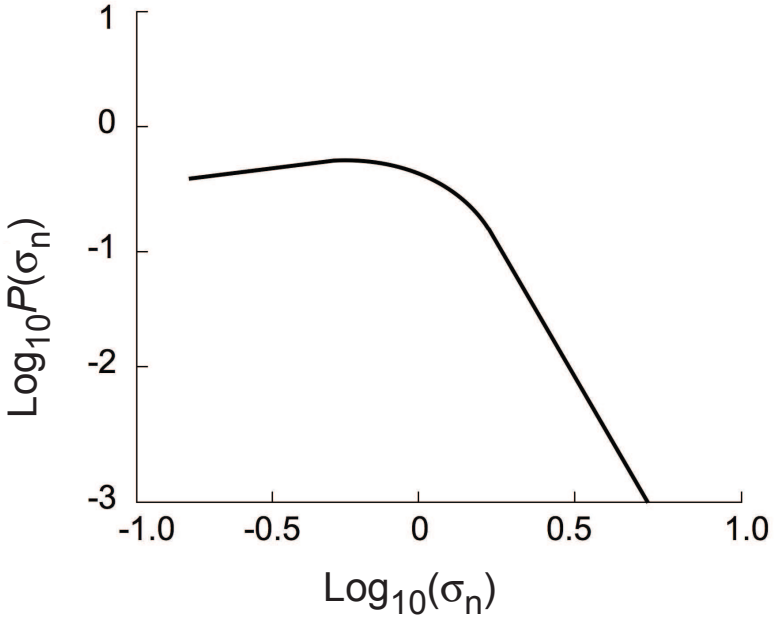

Figure 1.10: Probability distribution $P(\sigma_n)$ of normal stress (σ_n) normalized with respect to the mean stress (i.e., local stress divided by mean stress) (after Løvoll et al. 1999) (Figure and caption from Boulton et al. 2009).

mechanics: the San Andreas Fault is oriented at a high angle to the maximum compressive normal stress, and the resolved shear stress on it is very low ($\tau \sim 10$ MPa; Townend & Zoback 2001). Either frictionally weak materials along the San Andreas Fault act to reduce its strength (e.g., Janecke & Evans 1988; Moore & Rymer 2007; Lockner et al. 2011; Carpenter et al. 2011), or local, highly stressed grains (of some limited volume) control its overall strength and seismic behavior (Boulton et al. 2009; Davies et al. 2012; see also Carpinteri & Paggi 2005) (see also Appendix A).

1.4 The Range of Size Scales and Seismicity

Davies et al. (2012) also emphasized that geometrical and lithological homogeneity promote self-sustaining system-scale earthquake rupture nucleation and propagation (see also Mogi 1967; He et al. 1990). Natural fault zones, however, are lithologically (e.g., Sibson 1977a; Wibberley & Shimamoto 2003; Jefferies et al. 2006 and many others) and geometrically (e.g., Nur 1978; Aki 1979; King 1983; Andrews 1989; Faulkner et al. 2010) complex structures with spatial variations in temperature and effective normal stress. Using observations from seismology, fault mechanics, structural geology, and earthquake physics, Ben-Zion (1996, 2008) proposed that two end-member evolutionary states describe fault zone behavior. Immature fault zones, with low cumulative displacements, are characterized by heterogeneity with a wide range of size scales (ROSS). A narrow ROSS characterizes mature fault zones with large cumulative displacements (e.g., > 1 km, Sibson 2003). Underlying reasons for this distinction include the mode of formation of the fault (e.g., Duebendorfer & Simpson 1994; Govers & Wortel 2005) as well as the gradual elimination of discontinuities with increasing displacement (e.g., Segall & Pollard 1980; Wesnousky 1988; Childs et al. 2008; Frost et al. 2009).

According to this framework, the range of size scales (ROSS), which characterizes the assumed brittle properties, acts as a tuning parameter that governs the frequency-magnitude statistical mode of earthquake behavior (Ben-Zion 1996, 2008). Immature fault zones, with a wide ROSS, have Guttenberg-Richter power law frequency-size earthquake statistics (Gutenberg & Richter 1949). Mature fault zones with a narrow ROSS, on the other hand, have

quasi-periodic characteristic earthquake events (e.g., Wesnousky 1994). An important difference between these two end-member fault zones is that large events (M> 6) appear to occur quasi-periodically on mature faults, whereas large events appear to occur approximately randomly on immature faults Ben-Zion 2008). Delineating which faults exhibit characteristic behavior, and which do not, and determining the first order geological processes that affect this, will ultimately improve our seismic hazard models and probabilistic seismic hazard analyses (e.g., Hanks et al. 2012).

1.5 Integrated Seismological, Field, and Laboratory research

New Zealand's Alpine Fault ruptures quasi-periodically in large magnitude ($M_w \sim 8$) earthquakes Sutherland et al. 2007; Berryman et al. 2012a). Active since c. 25 Ma, the Alpine Fault has accommodated at least 460 km of lateral displacement, and its modern surface trace is continuous for over 800 km if the Wairau Fault represents the northernmost extension of the structure (Wellman & Willett 1942; Wellman 1953; Sutherland et al. 2000, 2007). Therefore, it should (and does) follow a pattern of seismicity consistent with that expected for a mature, evolved fault characterized by a narrow range of size scales (Ben-Zion 2008). By studying the geological processes (e.g., mode of origin of the crustal scale fault zone, fault rock protolith, fault zone geometry, frictional and hydrological changes during the seismic cycle, and the extent of off fault damage accumulation) that produce spatio-temporal variations in Alpine Fault frictional strength and stability, we can observe and quantify the parameters that are likely to govern its earthquake behavior.

A primary objective of this PhD project is to identify the operating microphysical processes in exhumed fault rocks of the Alpine Fault and characterize the conditions under which these rocks were formed and deformed. Furthermore, I aim to characterize the lithological and geometrical heterogeneity of exposed rocks that form the surface trace of the Alpine Fault. Another important question to be answered is how the frictional properties of the various components that comprise the Alpine Fault core vary with pressure, temperature, and sliding velocity and how this could affect earthquake nucleation depth. Several analytical techniques are used to investigate

the lithological, structural, geochemical, hydrological, and frictional properties of granular fault rocks that comprise the Alpine Fault. Original research results are presented in 5 chapters that cover:

- the lithological, geophysical, and geochemical properties of the Alpine Fault at Gaunt Creek (Chapter 2)

- field work and experiments that quantify the structural, mineralogical, hydrological, and low temperature frictional properties of fault gouges and cataclasites collected from central Alpine Fault outcrops (Chapter 3)

- field work and experiments that quantify the structural, mineralogical, hydrological, and low temperature frictional properties of fault gouges and cataclasites collected from southern Alpine Fault outcrops (Chapter 4)

- hydrothermal friction experiments that quantify the high temperature and high pressure frictional properties of Alpine Fault gouges recovered during the first phase of the Deep Fault Drilling Project (Chapter 5)

- high velocity friction experiments that quantify the frictional properties of Alpine Fault gouges and cataclasites at coseismic slip rates (Chapter 6)

Finally, Chapter 7 presents a summary and general conclusions as well as a synthesis and suggestions for future research.

Chapter II

Alpine Fault Architecture at Gaunt Creek: Integrated Field, Drilling, and Laboratory Results

Abstract

Oblique dextral motion on the central Alpine Fault in the last 5-8 Myr has exhumed garnet-oligoclase facies mylonitic fault rocks from depths of c. 35 km. During exhumation, brittle deformation of these mylonites, accompanied by fluid infiltration, has resulted in complex mineralogical and lithological variations in fault rocks retrieved during Deep Fault Drilling Project (DFDP-1) drilling at Gaunt Creek. Preliminary petrophysical, geochemical, and lithological results reveal that the fault comprises a fault core of highly comminuted cataclasites and fault gouges bounded by a damage zone comprising cataclasites, protocataclasites, and fractured mylonites, which are formally described herein. Variations in spontaneous potential, electrical resistivity, and major element geochemistry suggest that phyllosilicate alteration and calcite mineralization has occurred preferentially in hanging wall lithologies comprising the fault core-alteration zone. The mineralogy and major element geochemistry of brown smectite-bearing PSZ gouges suggests that these ultrafine-grained units are the most highly altered rocks recovered. Warr & Cox (2001) constrained the temperatures at which alteration reactions observed in Alpine Fault gouges and cataclasites occur. Their data suggest that at least two stages of chemical alteration have occurred. At temperatures at or near the brittle-to-ductile transition, metasomatic alteration reactions resulted in plagiocase or feldspar replacement by muscovite, sericite or sausserite, and biotite (phlogopite) replacement by chlorite (clinochlore). Abundant chlorite within alteration zone cataclasites indicates that hydrous chloritization of epidote and hornblende (actinolite) also occurred. At lower

temperatures, depending on local redox conditions, primary minerals were altered to kaolinite, smectite and/or pyrite or smectite, kaolinite, Fe-hydroxide (goethite) and/or carbonate. The interplay between fluid-induced changes in fault zone chemistry, mineralogy, (micro)structure and seismogenesis warrants further study.

2.1 Introduction

New Zealand's Alpine Fault ruptures quasi-periodically in large magnitude ($M_w \sim 8$) earthquakes (Berryman et al. 2012a); as such, it represents the largest onshore seismic hazard in the country of 4.4 million people. Earthquakes are frictional instabilities, and their nucleation, propagation, and arrest are governed by fault zone properties (e.g., Sibson 1977a, 1982, 1992; King 1986; Scholz 2002; Ben-Zion 2008). Architecturally, a fault zone consists of a fault core, often containing at least one principal slip zone (PSZ), of fine-grained granular materials (gouge, cataclasite, or pseudotachylyte) where most coseismic displacement occurs (Caine et al. 1996; Chester & Chester 1998; Sibson 2003). Within the fault core, gouges, cataclasites and breccias evidence particle size reduction via fragmentation and abrasion accompanied by translation and rotation (Sibson 1977a). Fault cores are commonly flanked by damage zones, tabular rock bodies with micro- to macro-scale fractures that form as a result of inelastic off-fault deformation (e.g., Chester & Logan 1986; Caine et al. 1996). Characterizing three-dimensional variations in fault zone properties, and taking into account time-dependent changes in these properties, is essential to understanding the physical processes that drive seismicity. The first phase of Deep Fault Drilling Project (DFDP-1) drilling in January-February 2011 retrieved a full sequence of Alpine Fault hanging wall-fault core-footwall fault rocks, enabling detailed examination of fault zone elements on the 0.01-100 m scale. This study reports the integrated results of field, drilling, and laboratory data on the lithology, mineralogy, major element geochemistry, petrophysical properties, and permeability of the Alpine Fault thrust segment at Gaunt Creek, a tributary of the Waitangitaona River.

2.2 Geological Setting

2.2.1 Tectonic history

The New Zealand continental landmass, Zealandia, underwent multiple phases of tectonic deformation as part of the Gondwana supercontinent (Landis & Coombs 1966; Carter & Norris 1976; Mortimer 2004). Zealandia rifted away from the Australia-Antarctica landmass between 80 and 60 Ma (late Cretaceous to Paleocene), forming the north Tasman Sea. Prior to 45 Ma (Eocene), no active plate boundary existed in Zealandia (Sutherland et al. 2000). Sutherland et al. (2000) proposed that the Alpine Fault exploited an existing lithospheric discontinuity, and strike-slip motion began on the proto-Alpine Fault c. 25 Ma (see also Furlong & Kamp 2009). Reyners (2013) used more detailed reconstructions to propose a Subduction-Transform Edge Propagator (STEP fault) origin for the Alpine Fault c. 23 Ma. Present day oblique convergence along the Alpine Fault initiated 5-8 Ma as a result of a major shift in the instantaneous Euler pole for Australian-Pacific plate motion (Walcott 1984; Batt et al. 2004).

2.2.2 Regional structure

The Alpine Fault is a crustal-scale transpressive transform fault that links Pacific (PAC) Plate subduction in the north (Hikurangi margin) to Australian (AUS) Plate subduction in the south (Puyseguer margin) (Figure 2.1). In total, the Alpine Fault has accommodated at least 460 km of cumulative displacement (Wellman 1953). Following Berryman et al. (1992), Barth et al. (2013) subdivided the c. 890 km-long Alpine Fault into 5 sections with distinct kinematic, structural, and/or seismological characteristics (see Chapter 4 for details). The focus of this study is the Alpine Fault at Gaunt Creek, a catchment on the central section of the Alpine Fault; this section extends for 250 km from the Toaroha River to the Martyr River. Along this section, the fault has a strike-slip rate of 27-29 mm/yr and a dip-slip rate of 2-8 mm/yr (Barth et al. 2013). Norris & Cooper (1995, 1997, 2001, 2003) and Cooper & Norris (1994) established the regional structure and geology of the central Alpine Fault. Barth et al. (2012)) used airborne light detection and

ranging (LiDAR) data collected between Franz Josef township and Whataroa River to refine the models summarized in Norris & Cooper (2007). According to these researchers, the orientation of the Alpine Fault at depth parallels the foliation of exhumed mylonites and ultramylonites (055°/45°SE). In the near surface (< 2 km depth, Norris & Cooper 1995, 1997; Townend et al. 2009) the central Alpine Fault exhibits sequences of north-northeast striking oblique thrust faults and linking east-northeast striking dextral faults (Figure 2.2).

Norris & Cooper (1995, 1997) used transpressional sandbox experiments along with field mapping to demonstrate that erosional processes at the range front control the structural expression of the shallowest (< 2 km) portion of the central Alpine Fault. Barth et al. (2012) argued that multiple processes control the orientation and expression of faulting, and that the first-order structure ($<10^6$ to 10^4m) is governed by an inherited discontinuity (Sutherland et al. 2000), transient brittle failure in the upper 8-12 km (Toy et al. 2010; Boese et al. 2012), ongoing ductile deformation that occurs in a shear zone present from 8-12 km depth to the base of the quartzofeldspathic crust at about 35 km depth (Little et al. 2005), thermal-weakening from uplifted hanging wall mylonites (Koons 1987; Koons et al. 2003), and stress concentrations at the base of the brittle seismogenic zone (Ellis et al. 2006). Second-order structural controls (10^4 to 10^3 m) include stress perturbations from hanging wall topography, river incision, and thickness of unconsolidated sediments in the footwall. At shallow depths < 600 m, third order (10^3 to 10^0 m) controls on fault zone structure include footwall sediment thickness, fault damage zone width, changes in stress orientation near the free surface, fault plane orientation, basal gouge frictional strength, and glacial-interglacial cycles.

2.2.3 Gaunt Creek structure

At Gaunt Creek, the focus of this study, there are two natural exposures of the Alpine Fault basal thrust, defined by Norris & Cooper (2007) as the de facto plate boundary oblique thrust contact between hanging wall PAC plate cataclasites and footwall AUS plate gravels, intrusives, or metasediments.

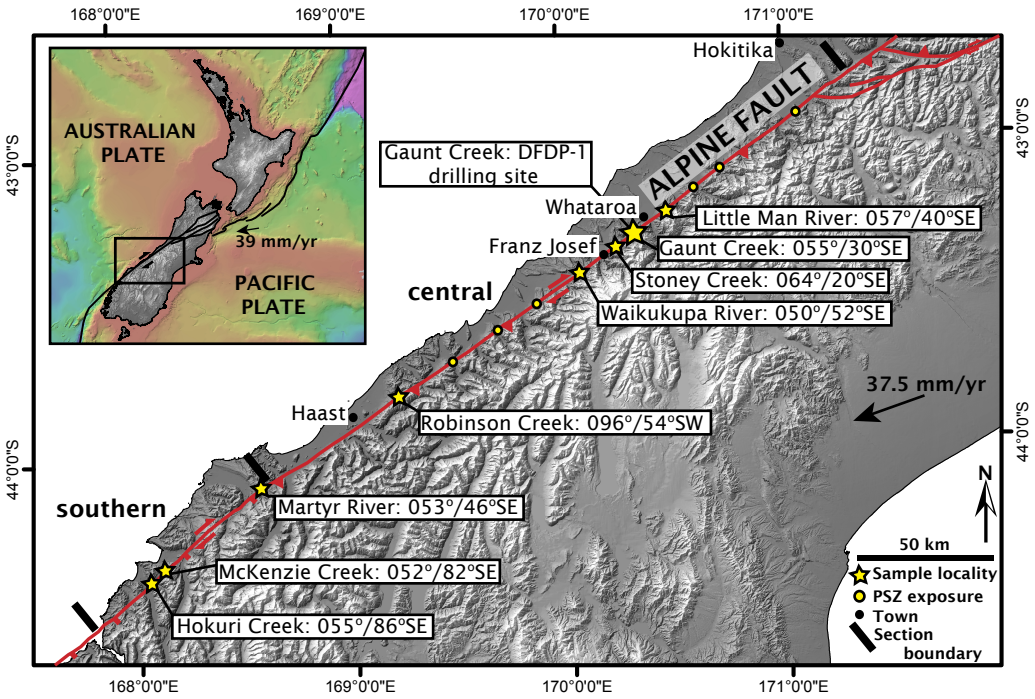

Figure 2.1: Location map, Alpine Fault, South Island, New Zealand. The Alpine Fault forms the spine of the Southern Alps and marks the boundary between the Pacific and Australian plates. The angular velocity describing the relative motion of the Pacific and Australian plates can be resolved into $\sim$ Fault and 6-9 mm/yr perpendicular to it (Beavan et al. 2010) (inset). A DEM image of the central South Island showing the location and strike of the Alpine Fault, which is subdivided into its central and southern sections (Barth et al. 2013). Locations where fault gouge and/or cataclasite samples were collected are starred in the figure, and fault orientation is given. At Gaunt Creek, the local Australian-Pacific plate motion vector is 37.5 mm/yr towards 251.4° (NUVEL-1A; DeMets et al. 1994). Additional exposures of thrust segment fault gouge not analyzed are shown as yellow circles; descriptions of these exposures were given by Reed (1964), Wright (1998), Simpson (1992) and McClintock (1999). Alpine Fault cataclasites were also described by Sibson et al. (1979), Simpson et al. (1994), Norris & Cooper (2007), Toy (2007), Easterbrook (2010), Toy et al. (2011), and Scott (2012).

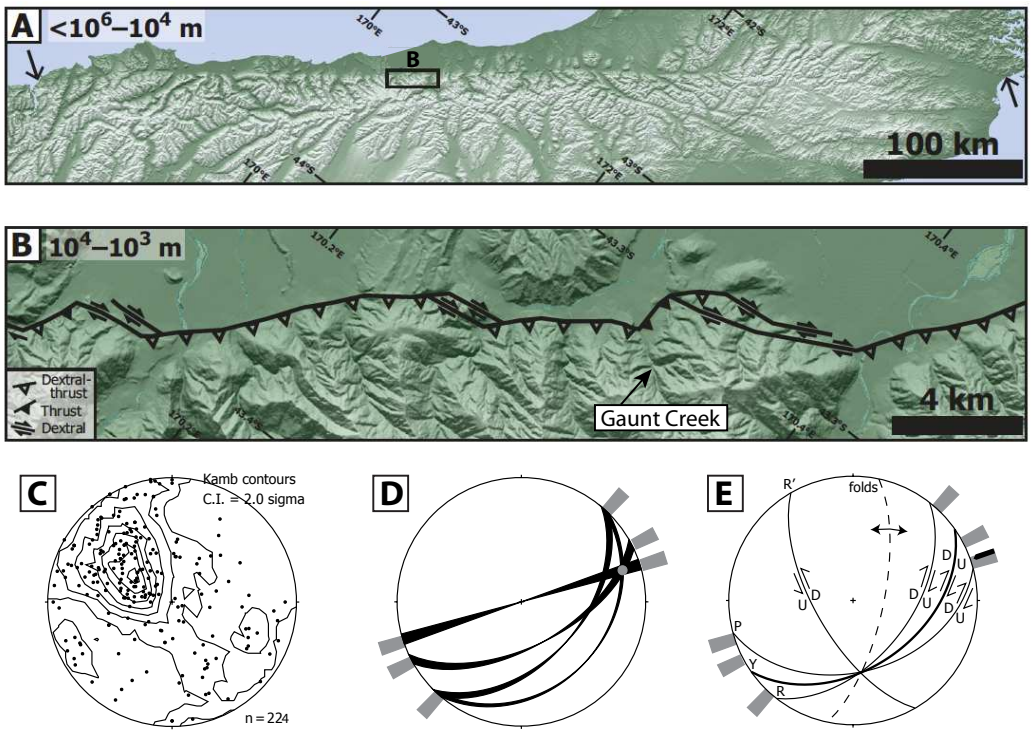

Figure 2.2: Detailed structure of the central Alpine Fault. **A,** The onshore trace of the Alpine Fault, striking between the bold arrows, appears remarkably straight in the Land Information New Zealand 100 m digital elevation model. Figure scaled to highlight the $< 10^6$–10^4 structure. **B,** In detail, oblique dextral motion on the central Alpine Fault is accommodated by shallow (< 2km depth) oblique thrust and dextral faults. Figure scaled to highlight the 10^4–10^3 m structure. **C,** An equal-area lower-hemisphere projection of poles to central Alpine Fault gouge zones reveals considerable variation in near-surface fault plane orientation, with a mean orientation of 030/40°SE. Few measurements of near-vertical strike-slip segments are plotted because the segments are poorly exposed along-strike (data in Norris & Cooper 2007). **D,** Using LiDAR data (grey bars outside circle) and field data (black great circles), the mean orientation of central Alpine Fault dextral thrust, reverse and strike-slip segments is plotted with the slip vector indicated by the grey dot. **E,** A summary equal-area lower-hemisphere projection of the expected orientation of faults in a Riedel shear system (solid great circles) and associated folds (dashed great circle) developed around the central Alpine Fault, which is drawn as the Y-shear great circle assuming an orientation at depth parallel to the mean mylonitic foliation (055/45°SE). Shear sense is given by arrows and U/D labels. Grey bars outside circle indicate orientation of faults measured using LiDAR data. The bold arrow is the trend of the plate-motion vector (Figures and text modified from Barth et al. 2012).

The first natural exposure occurs in a well-studied scarp on the south side of Gaunt Creek (Cooper & Norris 1994; Toy 2007; Boulton et al. 2012), and the second is a terrace on the north side of Gaunt Creek (De Pascale & Langridge 2012; Boulton et al. 2012) (Figure 2.3). Hanging wall cataclasites and mylonites derived from metabasic and quartzofeldspathic schist protoliths crop out in both localities (Cooper & Norris 1994; Toy 2007). Cooper & Norris 1994 determined the postglacial tectonic-, geometric-, and geomorphic-evolution of the fault zone at Gaunt Creek over the past 14 kyr (timing based on a ^{14}C-dated piece of wood collected from overthrust talus breccia). The basal thrust at Gaunt Creek has accommodated over 180 m of overthrusting, deformed internally to form duplex structures, been retrogressively veined and altered by hydrothermal fluid flow, and changed from a moderately southeast-dipping, oblique reverse fault to a shallowly dipping thrust. Noting that the dip of the basal thrust shallows near the toe of the thrust sheet, Cooper & Norris (1994) reported a mean basal fault plane orientation of 060°/39°SE and mean slickenline striations oriented 24/086 for the scarp on the south side of Gaunt Creek. At the same exposure, Boulton et al. (2012) reported a similar basal fault plane orientation of 059°/42°SE with a prominent set of 00/059 slickenline striations overprinted by a faint 36/114 set (Chapter 3). The fault plane exposed in the terrace on the north side of Gaunt Creek is more shallowly dipping, with an average orientation of 005°/28°SE. No slickenline striations were found along the contact between the terrace fault gouge and footwall gravel contact. Drillcore retrieved during DFDP-1A and 1B was not oriented, and estimates of fault dip based on basal gouge contacts have an estimated margin of error of ±5°. The fault plane in DFDP-1A dips approximately 25°-35°, and the primary fault plane in DFDP-1B dips approximately 45°-55°.

2.3 Methods

2.3.1 Drilling operation

In Phase 1 of drilling, the DFDP project completed two vertical boreholes at Gaunt Creek in January and February 2011. DFDP-1A drilled to 100.6 m depth and DFDP-1B drilled to 151.4 m depth. Percussion drilling techniques

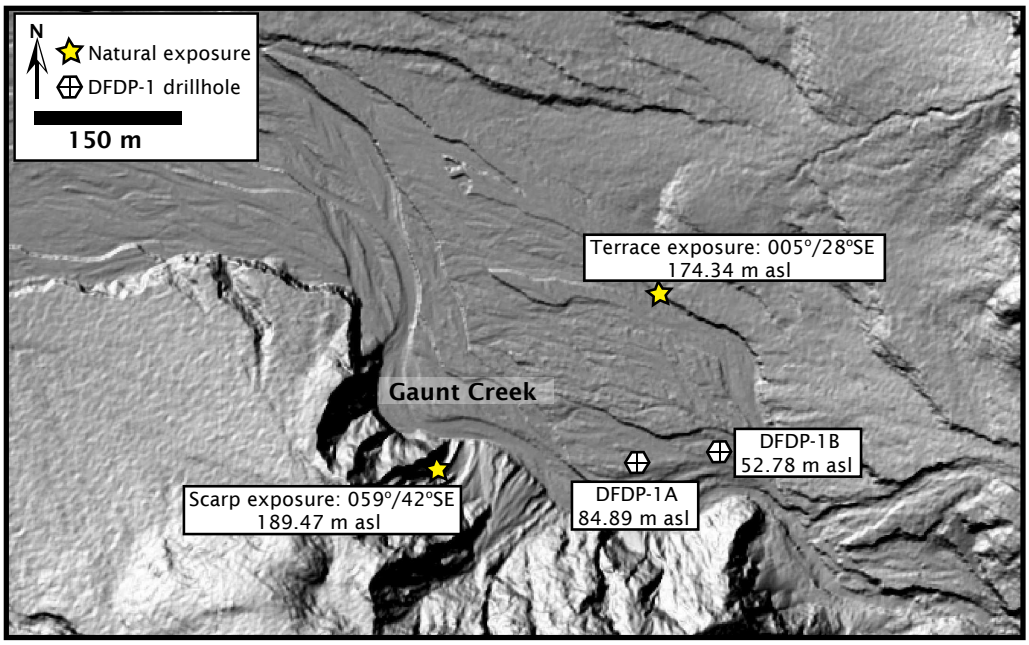

Figure 2.3: Hillshade view of the Gaunt Creek catchment derived from LiDAR data. The location of natural exposures of the faulted contact between (primarily) PAC-plate derived cataclasites and AUS-plate derived cataclasites are shown with stars and the location of DFDP-1 drillholes are shown with crossed hexagons. Elevation of the contact is given in meters above seal level (asl). The Gaunt Creek catchment lies at the junction between dextral thrust and thrust segments of the fault (Barth et al. 2012), the strike of the fault changes from southwest-northeast to southeast-northwest across the creek (see also De Pascale & Langridge 2012), and the slip vector for the fault in the region depicted remains uncertain (S. Cox, *pers.comm.* 2013). A 3-point solution constructed using the strike between the scarp and terrace exposures and the contact elevations yields an average fault dip of 28-30°.

were used in the uppermost portions of the drillholes, followed by wireline coring and some rotary drilling when hole instability precluded wireline coring. Hanging wall, fault core, and footwall sections of fault rocks were recovered, wireline logs were completed, hydraulic observations were made, and downhole observatories for the long-term monitoring of temperatures, fluid pressures and chemistry, and seismicity were established (Sutherland et al. 2012). Drilling methods are described elsewhere in a detailed operational report (Sutherland et al. 2011). DFDP-1 project is a team-based scientific investigation. During the drilling operation, I spent 2 weeks on site doing basic core processing and core logging. I subsequently spent 6 weeks at the University of Otago producing detailed lithological and structural logs of DFDP core and preparing initial samples for geochemical and mineralogical analyses. I also contributed data, text, and comments at every stage of the first two publications on DFDP-1 results (Sutherland et al. 2012; Townend et al. 2013). My contributions to DFDP-1, and the initial publications about it, comprise a majority of the results presented in this chapter. Importantly, the discussion and conclusions reflect my own understanding of the data.

2.3.2 Core logging

Detailed core logs were made from 148 m of near-complete PQ (83 mm) diameter cores. Initial geological logs completed on site recorded lithology, colour, location, styles and orientations of structures, including drilling and handling-induced fractures, and engineering rock quality. Following careful wrapping, labeling, and transport back to the University of Otago, I, along with University of Otago staff (V. Toy and D. Prior) and students, conducted more detailed imaging, defect logging, and lithological descriptions of the core (for methods, see Sutherland et al. 2011).

2.3.3 Thin section preparation

V. Toy and I selected representative samples of the characteristic lithologies, and Brent Pooley, University of Otago, made petrographic thin sections of these samples. Petrographic thin sections of delicate fault gouges and cataclasites were prepared dry and polished using 1 μm diamond paste. Less

friable drillcore materials were prepared following standard petrographic thin section making techniques.

2.3.4 X-ray diffraction

Qualitative X-ray diffaction (XRD) analyses were conducted on 34 clean characteristic lithology samples collected from DFDP-1A and DFDP-1B drillcore. Samples were first ground for 10 minutes in a McCrone micronizing mill under ethanol and dried overnight at 60°C. Approximately 3 g of milled and dried sample powder was then lightly ground with a mortar and pestle and lightly back pressed into stainless steel sample holders. Powder XRD measurements were performed on a PANalytical X'Pert PRO MPD PW 3040/60 X-ray diffractometer in the Department of Geology, University of Otago. Measurement conditions were 40 kV, 30 mA, Cu K_α radiation with 0.125° divergence slit size. XRD patterns were recorded in steps of 0.0080°2θ using X'Pert Data Collector version 2.0e and processed with X'Pert HighScore version 2.2b.

Quantitative XRD analyses were conducted on 6 principal slip zone gouges and cataclasites in DFDP-1B by Mark Raven, CSIRO Land and Water, Urrbrae, South Australia, Australia. For these analyses, approximately 1.5 g of each sample was ground for 10 minutes in a McCrone micronizing mill under ethanol. The resulting slurries were oven-dried at 60°C, thoroughly mixed with mortar and pestle, and lightly back pressed into stainless steel sample holders. XRD patterns were recorded in steps of 0.017°2θ on a PANalytical X'Pert Pro Multipurpose Diffractometer using Fe-filtered Co K_α radiation, variable divergence slit, 1° antiscatter slit and fast X'Celerator Si strip detector. Smectite identification was done using XRD patterns obtained from oriented slides of magnesium-saturated, glycerolated < 2 μm clay separates. Since variable hydration of interlayer water causes problems with quantification, smectite-bearing samples were saturated with calcium and re-analyzed. Quantitative analysis was performed using SIROQUANT, a commercially available software package from Sietronics Pty Ltd. Results are normalized to 100%, and amorphous phases (e.g., goethite) were not identified.

To document some along-strike variations in the mineralogy of principal slip zone gouges and cataclasites, 17 additional quantitative whole rock XRD analyses were conducted on surface-outcrop fault gouges and cataclasites collected from localities pictured in Figure 2.1. Analyses conducted on 9 < 2 μm-diameter clay-fraction separates obtained by centrifugation were also done. Additional quantitative XRD results were obtained for 150 μm-diameter sieved separates of DFDP-1A and DFDP-1B samples that were studied in hydrothermal friction experiments (Chapter 5) and high velocity friction experiments (Chapter 6). Those results are presented in the relevant chapters. Methods are described further in Appendix B; all XRD data files are located in Appendix G.

2.3.5 ICP-AES and X-ray fluorescence analyses

A subset of characteristic lithology DFDP-1 samples, together with fault core samples from natural exposures at Gaunt Creek, were analysed for major element geochemistry using inductively coupled plasma atomic emission spectroscopy (ICP-AES) and X-ray fluorescence (XRF) techniques. 39 clean samples from DFDP-1A and DFDP-1B, weighing between 10 g and 30 g, were selected for ICP-AES analysis. Because material was limited, samples were first ground for 10 minutes in a McCrone micronizing mill under ethanol, dried overnight at 60°C, and subsampled for random powder x-ray diffraction (Section 2.3.4).

The remaining powders were sent to ALS Minerals, ALS Canada Ltd., North Vancouver, British Columbia, Canada, in sterile plastic sample jars for analysis of major element oxides by Inductively Coupled Plasma – Atomic Emission Spectroscopy (ICP-AES). There, a prepared sample (0.200 g) was added to lithium metaborate/lithium tetraborate flux (0.90 g), mixed well, and fused in a furnace at 1000°C. The resulting melt was then cooled and dissolved in 100 mL of 4% nitric acid/2% hydrochloric acid. The solution was then analyzed by ICP-AES and the results were corrected for spectral inter-element interferences. Oxide concentration was calculated from the determined elemental concentration and the results are reported in that format.

Major element oxide analysis of 6 DFDP-1A samples was performed using XRF at the Department of Geology, University of Otago. Clean samples were oven dried at 60°C overnight, crushed with a hydraulic rock splitter, and ground to a powder in a TEMA tungsten carbide mill. To minimize cross-contamination, the mill was thoroughly cleaned with hot water, ethanol and compressed air between samples. Powdered samples were stored at 105ºC for at least 6 hours before being transferred to a desiccator to cool for 1 hour. Lithium borate fusion discs were made by combining 0.64000 ± 0.0005g of sample, 6.80000 ± 0.0001g of lithium borate flux and about 1.000g of ammonium nitrate. A Phoenix 4000 automatic fusion machine, Pt/5% Au crucibles, and casting moulds were used to create major element discs. These 6 DFDP-1A samples were prepared by Richard Wing, University of Otago. All XRF analyses were performed by Damian Walls, University of Otago, on a Philips PW2400 X-ray fluorescence spectrometer.

To constrain along-strike applicability of DFDP-1 results, 23 additional major element analyses were conducted on ultramylonite (1), hanging wall cataclasites (8), fault core gouges (12), and footwall gravel cataclasites (2) using a combination of the above methods. Sample collection localities span 234 km along-strike of the Alpine Fault and are indicated in Figure 2.1. Location co-ordinates and lithology details are listed in Table 2.2. Where samples were used for friction experiments in Chapters 3-6, the information is given in Table 2.3. Data files for all major element geochemistry analyses are located in Appendix G. A detailed analysis of along-strike variations in fault gouge, cataclasite, and footwall gravel major element geochemistry is outside the scope of this research, and the following results, discussion, and conclusions sections focus on DFDP-1 samples.

2.3.6 Loss on Ignition (LOI) determination

To determine loss on ignition (LOI), 1.0 g of prepared sample was placed in an oven at 1000°C for 1 hour, cooled, and then re-weighed by ALS Minerals. At the Department of Geology, University of Otago, 2.0 g of rock powder was placed in an oven at 1100°C for 2 hours, cooled, and then re-weighed.

The percent loss on ignition is reported as the percent difference in sample weight.

2.3.7 Downhole geophysics

Downhole measurements of the in situ petrophysical properties of DFDP-1A and DFDP-1B were conducted during DFDP drilling operations. John Townend (Victoria University of Wellington) and Jennifer Eccles (University of Auckland) supervised data gathering and carried out data processing. Wireline core logging with multiple tools was successful for the interval 31.21-92.47 m in DFDP-1A and the interval 60.0-140.0 m in DFDP-1B. Seven parameters were measured: (1) natural gamma radioactivity (γ), which measures the total intensity of the gamma ray flux (usually from the radioactive elements ^{40}K, ^{232}Th, ^{235,238}U); (2) neutron porosity (ϕ_N), a measure of the flux of neutrons through the rock mass and interpreted to measure interstitial water content and/or mineral bound water (Ellis & Singer 2007); (3) rock compensated density (ρ_c); (4) P-wave velocity (V_p) and impendence ($Z_p = V_{pX}\rho c$); (5) electrical resistivity using short-guard resistivity (ϱ_E) and single-point resistance (R_E); (6) spontaneous potential (SP), a measure of electrical effects produced by the interaction of borehole fluids and wall rocks that is interpreted to reflect both liquid junction potential arising from ionic concentration gradients between the local wall rocks and fluids and membrane potential arising from negatively charged phyllosilicates (the membrane potential signal is 4 times stronger; Ellis & Singer 2007), and (7) borehole diameter (D). Details of data collection and processing are presented in Townend et al. (2013).

2.4 Results

2.4.1 Fault zone structure

Sutherland et al. (2012) identified four main fault-rock units in the DFDP-1 boreholes: hanging wall ultramylonite, hanging wall cataclasite, principal slip zone fault gouge (PSZ), and footwall cataclasite. Within DFDP-1B, two PSZ gouges were identified: one between hanging wall cataclasite and the foot-

wall cataclasite (PSZ-1), and another entirely within footwall cataclasites (PSZ-2) (Figure 2.4). Using initial borehole lithology and petrophysical logs (i.e., electrical conductivity and natural gamma), Sutherland et al. (2012) identified clay-filled zones within 50 m of the PSZ, and enhanced calcite and phyllosilicate mineralization within c. 20 m of the PSZ. The PSZ fault gouge that marks the boundary between hanging wall (primarily) Alpine Schist-derived cataclasites and footwall gravel was intercepted at 90.5 m depth in DFDP-1A. The PSZ-1 fault gouge that marks the boundary between hanging wall (primarily) Alpine Schist-derived cataclasites and footwall granitoid or metasediment-derived cataclasites was intercepted at 128.3 m in DFDP-1B (DFDP-1B depths given in this chapter are corrected by +0.20 m following Townend et al. 2013). Slug tests were performed in both boreholes. Whereas hanging wall mylonites were found to be highly permeable, permeability decreased through the cataclasites and reached a minimum at the PSZ fault gouges, which were found to have very low permeability. Sutherland et al. (2012) attributed the decreasing permeability to the presence of alteration minerals, and identified an alteration zone c. 20 m-thick around the PSZ gouges (Figure 2.4).

2.4.2 Characteristic lithologies

Using detailed imaging, defect logging, lithological descriptions, and thin section analysis, a refined model of hanging wall, fault core, and footwall lithologies was developed (Toy et al. 2012; Townend et al. 2013). Fault rocks were described following the scheme proposed by Sibson (1977a) and modified to include the presence of foliated cataclasites with an interconnected network of phyllosilicate minerals (Chester et al. 1993; Holdsworth 2004; Jefferies et al. 2006). These lithologies are:

Unit1: Grey-green ultramylonites — medium to dark grey (quartzofeldspathic) or dark green (metabasic) mylonite to ultramylonite. This is the dominant lithology present in the >1 km-thick outcrops of shear zone rocks at most locations along the central Alpine Fault zone (Toy et al. 2008). The mineralogy is quartz + oligoclase + biotite + muscovite ± calcite ± hornblende + accessory minerals.

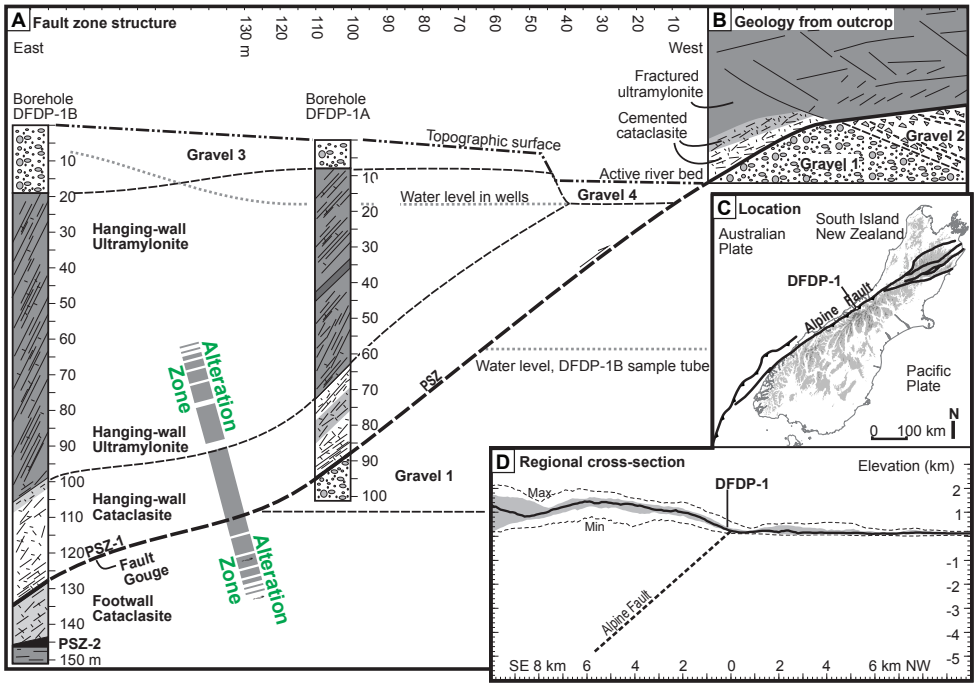

Figure 2.4: Summary of initial results from phase 1 of the Deep Fault Drilling Project. **A,** A cross section of fault rocks logged in DFDP-1A and DFDP-1B. The PSZ gouge in DFDP-1A was correlated with the PSZ-1 in DFDP-1B based on similarity of the hanging wall-fault core sequence in both drillholes, which resembled the same sequence exposed in the nearby scarp exposure. At Gaunt Creek, cataclasites derived from footwall granitoid and metasediment protoliths were described for the first time from rocks retrieved in DFDP-1B. The extent of the alteration zone is also indicated by the shaded grey boxes. Relative water levels in the hanging wall and footwall were determined using fluid sample tubes and piezometers in DFDP-1B. Results revealed a perched water table above the PSZ-1 fault gouge, as indicated by the dotted lines (see Sutherland et al., 2012). **B,** Simplified cross section of Gaunt Creek scarp outcrop geology. De Pascale and Langridge (2012) documented similar lithologies and contacts in the terrace exposure. **C,** Location map for Gaunt Creek. **D,** Cross section showing median topography ± 10 km perpendicular to the strike of the Alpine Fault. Fault dip inferred from mean orientation of hanging wall mylonite foliation. Figure and caption modified from Sutherland et al. (2012).

Unit2: Brown–green–black ultramylonites — brown, olive green and locally black, very fine-grained, planar foliated or millimeter-diameter feldspar augen-bearing ultramylonite. The mineralogy is quartz + plagioclase + chlorite + epidote + accessory minerals.

Unit3: Unfoliated cataclasites — brecciated or more highly comminuted schist-derived ultramylonite (Unit 1) and brown–green–black ultramylonite (Unit 2). The extent to which original intact rock has been fractured and sheared varies so they span the spectrum from 'fractured protolith' to 'ultracataclasite' in a strict sense (Sibson 1977a). Carbonate forms a pervasive cement, so the rock mass is cohesive despite extensive fractures.

Unit4: Foliated cataclasite — cataclasites similar to those of Unit 3, but with planar to locally anastomosing fabrics defined by mm-spaced solution seams of aligned phyllosilicates. The extent of tectonic comminution increases with proximity to the principal slip surface; the most highly comminuted materials are barely cohesive, clay-rich, and equate to ultracataclasite in a strict sense (Sibson 1977a).

Unit5: Gouges — medium brown or grey, clay-rich ultrafine-grained gouge containing clasts of Units 1–4, as well as recycled laminated gouges, and rare fragments of footwall lithologies.

Unit6: Granitoid-gneissic cataclasites — varying proportion mixtures of fragmented, quartz-rich granitoids and metabasites, both foliated and unfoliated. The mineralogy is quartz + potassium feldspar + plagioclase ± biotite ± chlorite ± muscovite + accessory minerals.

Unit7: Breccias — cemented protocataclasite to breccia composed of clasts of quartz + potassium feldspar + amphibole and their retrograde equivalents. This unit is only present in DFDP-1B and borehole instability prevented wireline logging of its petrophysical properties.

Unit8: Fluvio-glacial gravels composed primarily of Alpine Schist clasts. This unit is only present at the base of DFDP-1A as well as in the Gaunt Creek scarp and terrace exposures.

The distribution of each lithology in DFDP-1 core is given in Figure 2.5. Core-scale examples of each characteristic lithology are given in Figure 2.6. In the figure, each unit is further subdivided based on inferred protolith (Unit 1) or the presence/absence of phyllosilicate fabric (Unit 6). Details are given in the caption. Figure 2.7 depicts optical microscope (OM) images of characteristic lithology Units 1 (Figures 2.7A, 2.7B), 2 (Figures 2.7C, 2.7D), 3 (Figure 2.7E), and 4 (Figures 2.7F, 2.7G, 2.7H). Figure 2.8 depicts OM and scanning eletron microscope (SEM) images of characteristic lithology Units 4 (transition to Unit 5, Figure 2.8A), 5 (Figures 2.8B, 2.8C, 2.8D, 2.8F), 6 (Figures 2.8E, 2.8G, 2.9A-D), and 7 (Figure 2.8H). As the focus of much of this thesis is the PSZ gouges, it should be noted that the ultrafine-grained DFDP-1 Unit 5 PSZ gouges have two different mineral assemblages. Blue Unit 5 gouges (e.g., DFDP-1A c. 90.50 - c. 90.70 m depth) contain quartz ± potassium feldspar + plagioclase + calcite + white mica (muscovite and/or illite) + clinochlore + ± pyrite + accessory minerals (Figure 2.8B). Brown Unit 5 gouges (e.g., DFDP1A c. 90.70 -90.80 m, DFDP-1B 128.3 -128.5 m, and DFDP-1B 144.02 - 144.14 m depth) contain quartz + potassium feldspar + plagioclase + smectite + kaolinite ± clinochlore ± actinolite ± pyrite ± anatase + accessory minerals (Figures 2.8C, 2.8D, 2.8F).

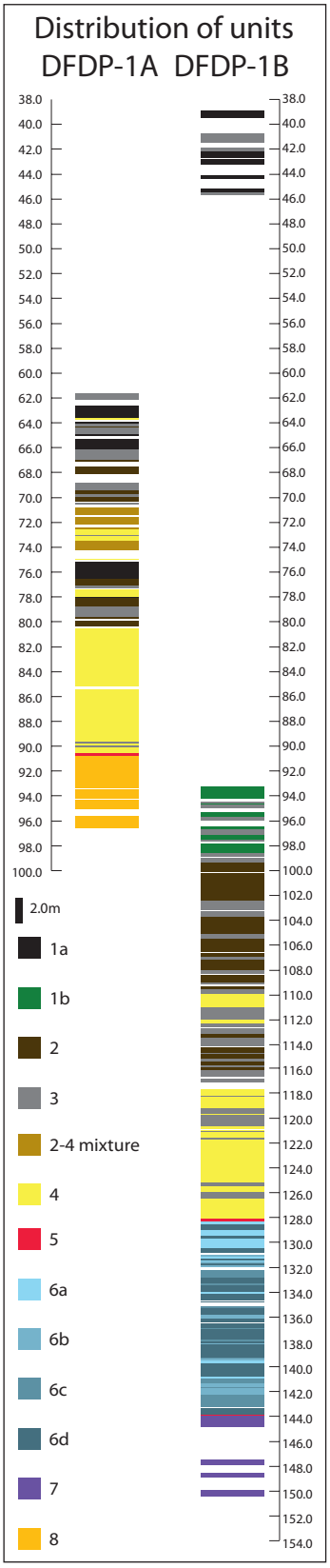

Figure 2.5: Distribution of representative lithologies identified in DFDP-1A and DFDP-1B using samples and descriptions defined by the first author and V. Toy. Logs compiled by V. Toy. Unit descriptions are given in the text.

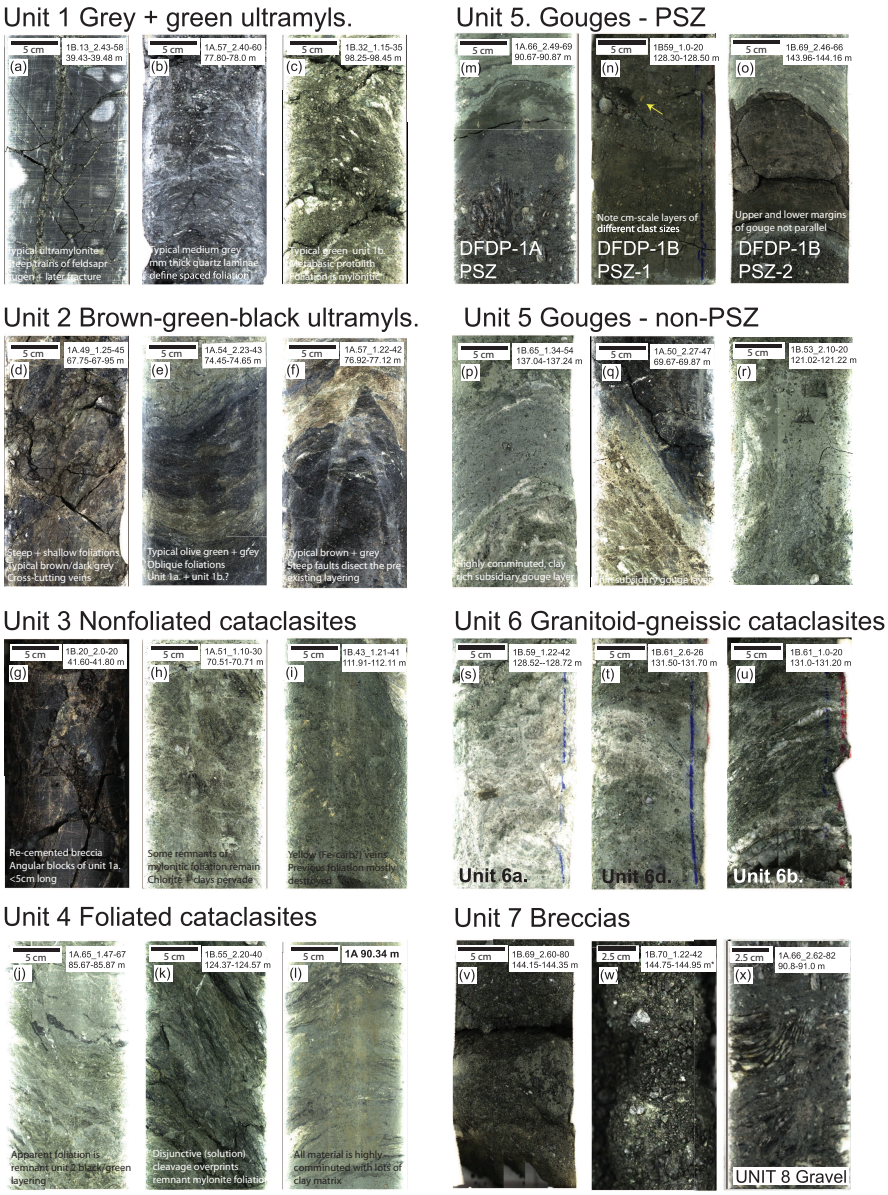

Figure 2.6: Core-scale examples of major lithological units identified in DFDP-1A and DFDP-1B. Unit 1 Alpine Schist-derived mylonites are subdivided into: (1a) medium grey quartzofeldspathic mylonites, and (1b) dark green amphibolite facies metabasite mylonities. Unit 6 footwall cataclasite is subdivided into: (6a) white quartz and feldspar-rich granular cataclasite, (6b) green-grey-black foliated protocataclasite to cataclasite, (6c) unfoliated cataclasite to ultracataclasite, and (6d) a mixture of 6a and 6b. Each picture is a 180° core scan, except for 1B 144.75 m*, which is a flat core scan. On each interval pictured, the drill hole (1A or 1B) and interval top depth is given. Note: in Toy et al. (submitted), Unit 3 nonfoliated cataclasites and Unit 4 foliated cataclasites have been formally named Unit 3 upper nonfoliated cataclasites and Unit 4 upper foliated catclasites, respectively. Unit 6 granitoid-gneissic cataclasites have been renamed Unit 6 lower cataclasites in the same manuscript. This study adopts the terminology of Townend et al. (2013), as stated in the text.

Figure 2.7 (Over) Optical microscope images of characteristic hanging wall lithologies. Abbreviations used in labelling all images: quartz = qtz, biotite = bt, muscovite = mv, hornblende = hbl, plagioclase = plag, illmenite = il, garnet = gt. PPL = plane polarised light; XPL = cross-polarised light. **A,** Unit 1 grey ultramylonite. Major phases are well mixed and foliation is defined mostly by individual mineral long axes; these are deflected into C'-type shear bands and around competent plagioclase porphyroclasts. Quartz grains have undulose extinction and interlobate grain boundaries (arrowed grains at lower L) indicative of dislocation creep. **B,** Unit 1 dark green (metabasite) mylonite. The rock has a spaced foliation of amphibole + biotite + garnet vs. plagioclase + minor quartz. Individual mineral long axes parallel foliation except where deflected into C'-type shear bands (delineated by dashed red line; top-down-to-right indicates overall top-to-W sense of shear in this oriented sample). Spaced foliation is more typical of mylonites and protomylonites that accommodated lower strains than ultramylonites, primarily by dislocation creep (Toy et al. 2011). **C,** Unit 2 black ultramylonite, DFDP-1A 79.72 m depth comprises an aggregate of fine (<50mm)-grained quartz + feldspar + epidote + chlorite + calcite. There are rare larger (<200mm) feldspar porphyroclasts. A spaced foliation is defined by dark, hairline seams of opaques and parallel large grains of mica (sericite?). A few dark seams are at high angle to the dominant foliation. No systematic cross-cutting relationship is observed between these and the main seams; they were presumably coeval. **D,** Transitional Unit 2 black ultramylonite to Unit 4 foliated cataclasite, DFDP-1A 74.50 m depth. mm-thick bands of fine-grained quartz-feldspar-epidote-chlorite alternate with mm-thick bands higher in opaques and clay minerals, commonly concentrated in anastomosing seams that wrap porphyroclasts and their pressure shadows, and define a foliation (horizontal in this photomicrograph). These latter bands contain lensoidal porphyroclasts of the fine-grained mixture and comparatively equant subangular feldspars. **E,** Unit 3 upper unfoliated cataclasite, DFDP-1A 79.35 m depth. Similar fine-grained matrix to Unit 2 but with patches of much finer-grained cryptocrystalline material (labelled as 'clays?'). Although macroscopically unfoliated, a weak foliation with trace in this thin

section trending top L to bottom R, is defined at this scale of observation by anastomosing, dark, hairline inferred solution seams spaced <0.2mm. **F,** Unit 4 upper foliated cataclasite, DFDP-1A 80.50 m depth. Elongate, fractured clasts of feldspar or quartz + epidote + chlorite are dispersed among prominent anastomosing dark seams that define a foliation with trace in this section trending top R to bottom L. Some feldspars (e.g. at '1') have pressure shadows containing finer-grained mixtures of feldspar + quartz + epidote + chlorite. **G,** Unit 4 upper foliated cataclasite, DFDP-1B 128.04 m. Lense-shaped, subangular feldspar and angular calcite porphyroclasts reside in a matrix dominated by phyllosilicates (clays + chlorite). Sparse dark seems are still present but much less common than in (F). The phyllosilicate bands link in an anastomosing network with asymmetric geometry similar to an S-C' fabric, suggesting they accommodated shear. **H,** Unit 4 upper foliated cataclasite, DFDP-1B 128.04 m. <100μm diameter feldspar porphyroclasts reside in a very fine-grained matrix. Three different domains within which grain size and proportion of opaques varies are numbered 1-3 in order of decreasing clast sizes and increasing proportion of clays in matrix. Quartz-feldspar rich bodies (e.g. area 1) do not contain prominent internal foliations (figure and caption in Toy et al. submitted)

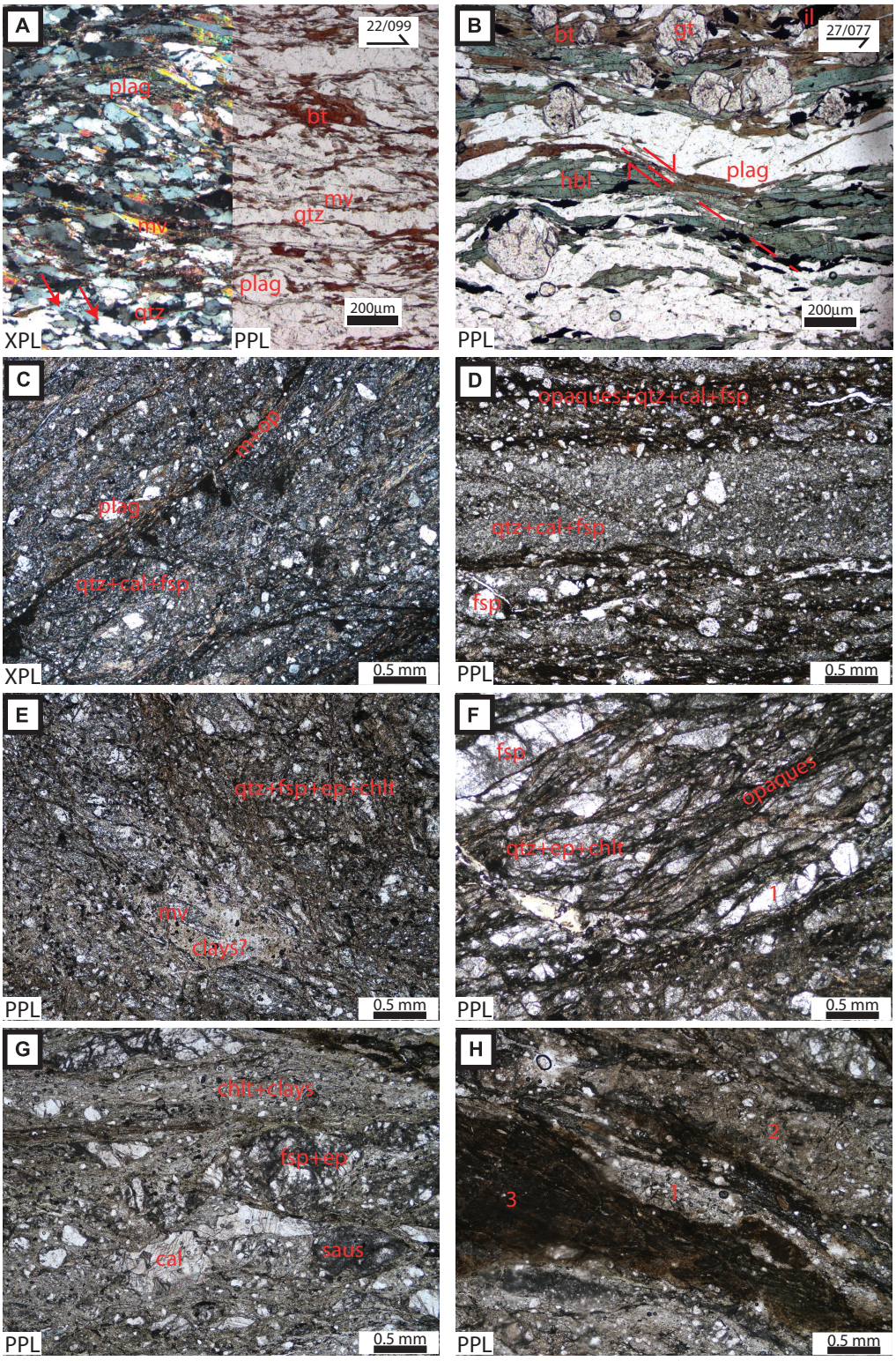
A
plag
mv
qtz
XPL
22/099
bt
mv
qtz
plag
200µm
PPL
B
bt
gt
il
27/077
bbt
plag
200µm
PPL
C
mv+op
plag
qtz+cal+fsp
XPL
0.5 mm
D
opaques+qtz+cal+fsp
qtz+cal+fsp
fsp
PPL
0.5 mm
E
qtz+fsp+ep+chlt
mv
clays?
PPL
0.5 mm
F
fsp
opaques
qtz+ep+chlt
1
PPL
0.5 mm
G
chlt+clays
fsp+ep
cal
saus
PPL
0.5 mm
H
2
3
1
PPL
0.5 mm

Figure 2.7:

Figure 2.8 (Over) Optical microscope (OM) and scanning electron microscope (SEM) images of selected fault core and footwall lithologies. Abbreviations used in labeling all images: qtz = quartz, fsp = feldspar, cal = calcite, ep = epidote, mv = muscovite, chlt = chlorite, u-ccl ultracataclasite (>90% of the rock volume < 0.1 mm in size), ccl= cataclasite (50-90% of the rock volume < 0.1 mm in size), m = gouge matrix, PPL = plane polarized light, XPL = cross polarized light, BSE = backscattered electron SEM image. **A,** Unit 4 foliated cataclasite – Unit 5 blue gouge transition interval in DFDP-1A, 90.36 m depth. Note disaggregated veins and clasts of calcite with narrow, planar e-twins, fractured feldspar clasts with intragranular calcite, and fractured ultracataclasite clasts. These reside in a very fine grained (<0.1 mm) matrix of comminuted feldspar, quartz, chlorite, white mica, and calcite. Matrix foliation, particularly evident toward the top of the image, is defined by anastomosing seams of opaques (solution seams) and apparent elongation of smaller feldspar clasts by overgrowths (arrowed). Manganese and iron oxide-hydroxide staining is evident. **B,** Unit 5 blue gouge in DFDP-1A, 90.62 m depth. Calcite is mostly disseminated in the matrix; disaggregated veins of calcite are relatively rare. Most clasts are rounded K-feldspar or plagioclase with rare epidote. Dynamically recrystallized quartz clasts with embayed margins and subrounded to hexagonal ultracataclasite clasts are also present. The matrix is finer-grained quartz-epidote-feldspar-clay mixture **C,** PSZ Unit 5 brown gouge in DFDP-1A, 90.70 m depth. Angular to subrounded clasts of calcite with narrow e-twins and fine-grained aggregates of calcite with altered (to sericite and saussaurite) feldspar reside in a very fine grained (<0.1 mm) matrix within which a foliation with trace trending top L to bottom R in this section is delineated by patches of opaques, probably goethite. **D,** PSZ-1 Unit 5 brown gouge in DFDP-1B, 128.44 m depth. The prominent pale lozenge-shaped clast is a composite of quartz with fine- grained calcite, plagioclase, and K feldspar. A second clast (labelled pst) contains stretched calcite amygdules; it may have a friction melt origin. The fine-grained matrix is rich in phyllosilicates which wrap clast rims ('snowball' fabric of Warr and Cox, 2001). Cracks cross-cutting the image formed during thin-section preparation. **E,** Unit 6d mixed cataclasite immediately above an undulating contact with PSZ-2 Unit 5 gouge, DFDP-

1B 144.01 m. Subangular to subrounded quartz + feldspar clasts cross-cut by calcite veins are in places fragmented with little clast rotation or translation (e.g., labelled ccl). Elsewhere, there is a matrix of comminuted K feldspar + plagioclase + clinochlore + calcite + apatite + pyrite that must have formed by fragmentation and shear. **F,** PSZ-2 Unit 5 gouge, DFDP-1B 144.02 m. Subangular clasts of quartz, albite, and rare K feldspar are contained in a very fine grained matrix. There are also numerous large clasts of calcite-cemented ultracataclasite. **G,** Unit 6d mixed catalasite with chlorite, feldspar, epidote, muscovite, quartz and opaques. OM, plane polarized light. The main foliation is defined by alignment of long axes of grains in a gneissic texture. In a zone trending from top R to lower L of the image these grains are more fragmented and pervasively sericitised. **H,** Unit 7 breccia, DFDP-1B 146.25 m. Spaced foliation of quartz bands wrapping feldspar porphyroclasts. Phyllosilicates occur on porphyroclast margins. Quartz bands are subdivided into polygonal aggregates and subgrains in elongate patches with similar extinction reminiscent of stretched larger grains and rare elongate grains with undulose extinction but no distinct subgrains (Figure and caption in Toy et al. submitted)

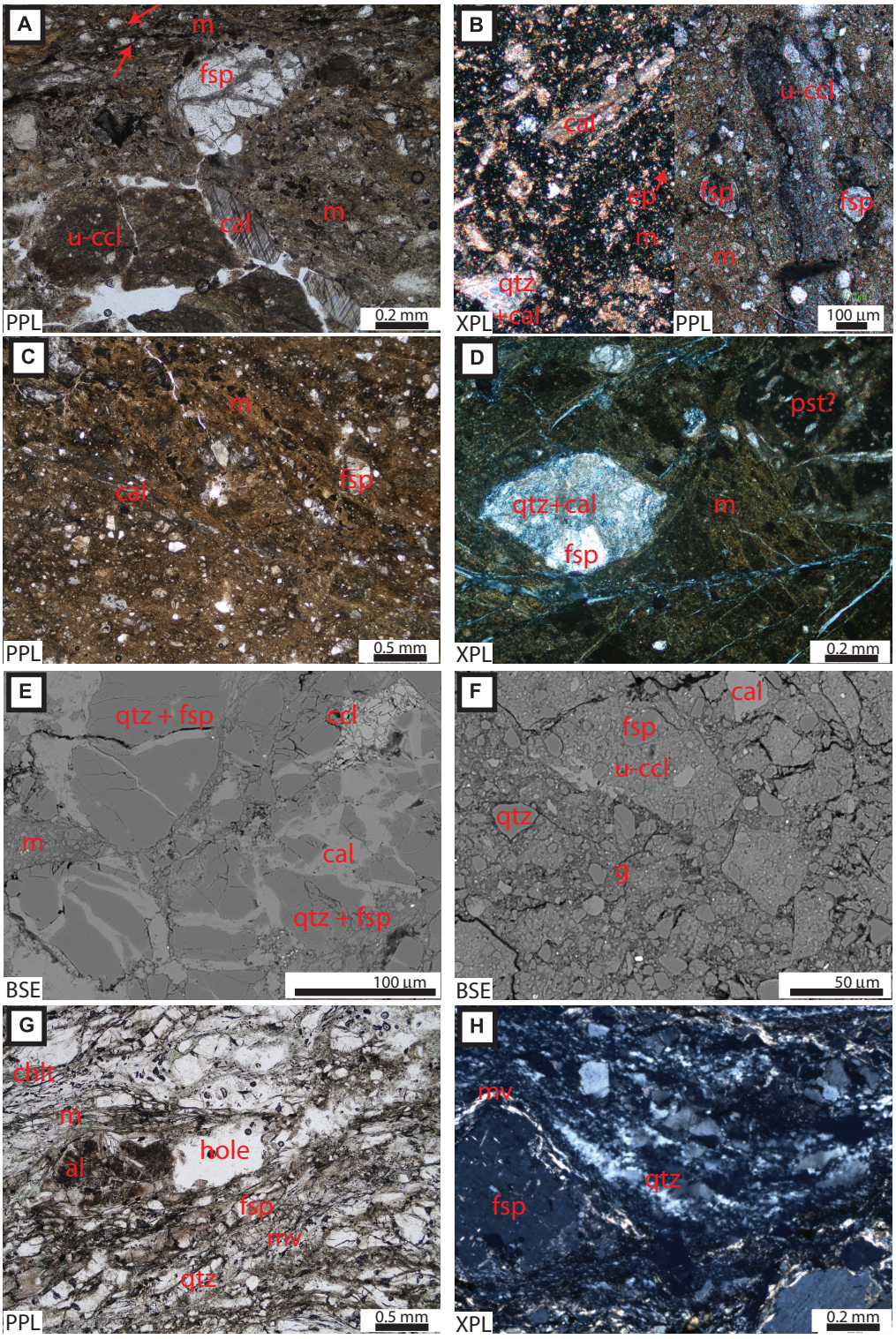
A
m
fsp
u-ccl
cal
m
PPL
0.2 mm
B
cal
ep
m
qtz
+cal
XPL
u-ccl
fsp
fsp
m
PPL
100 µm
C
m
cal
fsp
PPL
0.5 mm
D
pst?
qtz+cal
m
fsp
XPL
0.2 mm
E
qtz + fsp
ccl
m
cal
qtz + fsp
BSE
100 µm
F
cal
fsp
u-ccl
qtz
g
BSE
50 µm
G
chlt
m
al
hole
fsp
mv
qtz
PPL
0.5 mm
H
mv
qtz
fsp
XPL
0.2 mm

Figure 2.8:

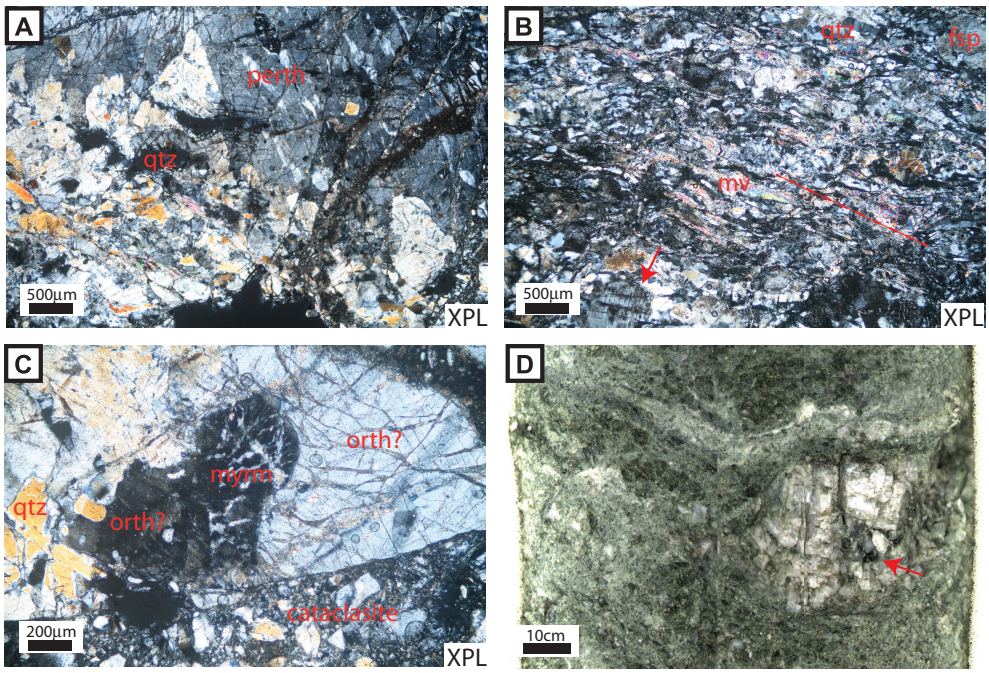

Figure 2.9: Photomicrographs and core-scale examples granitoid-gneissic textures in the Unit 6 granitoid-gneissic cataclasites. **A,** DFDP-1B 131.68 m depth, Unit 6a white quartz and feldspar-rich granular cataclasite. Flame perthite ("perth") results from strain-enhanced exsolution of trace Na from K-feldspar (Pryer & Robin, 1995). **B,** DFDP-1B 138.2 m depth, Unit 6b green-grey-black foliated protocataclasite to cataclasite with a gneissic texture comprising a continuous foliation (dashed line) defined by elongate muscovite and quartz ribbons composed of numerous blocky, moderately equant grains. Arrow points to a feldspar porphyroclast with cross-hatched twins. **C,** DFDP-1B 131.68 m depth, Unit 6a white quartz and feldspar-rich granular cataclasite. Mymekite ("myrm", an intergrowth of quartz and anorthite, is seen here intergrown with K-feldspar (arrow) (Castle & Lindsley, 1993). **D,** DFDP-1B 139.25 m depth, a lensoidal Unit 6a quartz-feldspar-biotite clast within Unit 6d. The Unit 6a clast has an interlocking texture of biotite-quartz-feldspar typical of granitoid rocks (Figure and caption in Toy et al. submitted).

2.4.3 Mineralogy

The mineralogical composition of 23 DFDP-1 core samples was determined using X-ray diffraction (XRD) analysis of random powder disc mounts. These analyses provide an indication of the minerals present in abundances greater than c. 5%. All the samples analyzed contain quartz, plagioclase, white mica (muscovite and/or illite) and chlorite (clinochlore). Carbonates (calcite + ankerite) are most prevalent in hanging-wall samples (Units 1–5) and are only sporadically present in Units 6 and 7 beneath the 128.3 – 128.5 m PSZ in DFDP-1B. Potassium feldspar (K-feldspar) is only found in the hanging wall within 5 m of the PSZ in DFDP-1A and beneath PSZ-1 in DFDP-1B (Table 2.1). At the time of investigation, 6 whole rock samples from the DFDP-1B principal slip zone intervals (PSZ-1 and PSZ-2) were available for quantitative XRD analysis. According to the results, the modal abundance of phyllosilicates in Units 5 (PSZ-1, 128.3 m; PSZ-2, 144.02 m; PSZ-2, 144.14 m depth), Unit 6 (143.9 m depth), and Unit 7 (144.28 m depth) does not vary significantly, being 35-36% for Units 5 and 6, and 27% for Unit 7. The primary difference between the samples lies in the presence of dioctahedral smectite (montmorillonite) in the Unit 5 brown gouges (Table 2.2). Smectite-bearing Unit 5 gouges were also found on basal thrusts on a tributary of Little Man River, Waikukupa River, and Robinson Creek, an along-strike distance of 120 km on the central Alpine Fault (Figure 2.1) (Table 2.3).

Sample	Hole depth	Lithology	Quartz	K Feldspar	Plagioclase	Muscovite	Biotite	Chlorite	Calcite	Ankerite	Spinel	Epidote
1A_63_6	63.60 m	1	X		X	X		X	X			
1A_66_7	66.70 m	2	X		X		X	X	X			
1A_70_6	70.60 m	3	X		X	X		X				
1A_74_5	74.50 m	4	X		X	X		X	X			
1A_82_7	82.70 m	4	X		X	X		X	X			
1A_86_35	86.35 m	4	X	X	X	X		X	X			
1A_88_4	88.40 m	4	X		X	X		X	X			
1A_89_34	89.34 m	4	X	X	X	X		X	X			
1A_90_32	90.32 m	4	X	X	X	X		X	X			
1A_90_62	90.62 m	5	X	X	X	X		X	X			
1A_91_30	91.30 m	8	X		X	X	X	X				
1B_112.12	112.12 m	3	X		X	X		X	X	X		
1B_113.81	113.81 m	3	X		X	X		X				
1B_116.72	116.72 m	3	X		X	X		X	X			
1B_128.04	128.04 m	5	X			X		X	X		X	
1B_128.09	128.09 m	5	X		X	X		X	X			
1B_128.22	128.22 m	5	X		X	X		X	X			
1B_128.50	128.50 m	6	X	X	X	X		X				
1B_128.53	128.53 m	6	X	X	X	X		X				
1B_128.80w	128.80 m	6	X	X	X	X		X				
1B_128.80wg	128.80 m	6	X	X	X	X		X				
1B_128.81	128.81 m	6	X	X	X	X		X				
1B_130.88	130.88 m	6	X	X	X	X		X	X			
1B_131.68	131.68 m	6	X	X	X	X		X				X
1B_132.7	132.70 m	6	X	X	X	X		X				X
1B_133.75	133.75 m	6	X	X	X	X		X				
1B_140.96	140.96 m	6	X		X	X		X	X		X	
1B_141.07	141.07 m	6	X	X	X	X		X				
1B_141.77	141.77 m	6	X	X	X	X		X				X
1B_141.90	141.90 m	6	X		X	X		X			X	
1B_143.90	143.90 m	6	X		X	X		X	X			
1B_144.02	144.02 m	7	X	X	X	X		X	X			
1B_144.145	144.145 m	7	X	X	X	X		X				
1B_144.28	144.28 m	7	X		X	X	X	X				

Table 2.1: Qualitative X-ray diffraction data for selected samples recovered from DFDP-1A and DFDP-1B core. Mineralogy of plagioclase and feldspar could not be discerned. (*) denotes that sample 1a_66_5 may contain both chlorite and biotite. For DFDP-1B 128.80m, "w" and "gw" stand for white and green-white, the colour of the specific sample.

2.4.4 Major element geochemistry

Major element geochemistry results for DFDP-1A fault rocks are presented in Table 2.4; results for DFDP-1B fault rocks are presented in Table 2.5. Additional results obtained for cataclasites and fault gouges collected at other localities along strike of the central Alpine Fault, as well as two analyses from the southern Alpine Fault, are presented in Table 2.6. In addition to major element oxides, the loss on ignition (LOI) and Chemical Index of Alteration (CIA) values are listed. LOI, listed at weight %, is a measure

Sample	Hole Depth	Lithology	Quartz	K feldspar	Plagioclase	Calcite	Kaolin	Smectite	White mica	Chlorite	Amphibole	Pyrite	Total
36184	128.3 m	5 (PSZ1)	25	4	25	9	6	18	12		1	<1	99
36185	143.9 m	6/5 transition	41	<1	14	10			30	5		<1	100
36186	144.02 m	5 (PSZ2)	29	3	24	8		18	17	1		<1	100
36187	144.14 m	5 (PSZ2)	36	4	23	5		15	15	2		<1	100
36188	144.15 m	5/7 transition	33	2	36				26	3		<1	100
36189	144.28 m	7	34	2	35	2			23	4		<1	100

Table 2.2: Quantitative X-ray diffraction data for selected samples recovered from DFDP-1B core. Mineralogy of plagioclase and feldspar could not be discerned. The dioctahedral smectite present is montmorillonite-15Å. White mica denotes muscovite-2M1, but illite-2M1 may also be present. Chlorite is clinochlore-1MIIB, and the amphibole is actinolite. Amorphous phases were not identified and results are normalized to 100%. All samples from the DFDP-1B borehole, latitude/longitude co-ordinates 43.3141°S/170.3259°E.

of the volatile content of the samples, and this measurement includes the weight loss due to both dehydration and decarbonation reactions. CIA is a proxy for the weathering of silicate rocks through hydrolysis reactions that lead to an exchange of the cations Na^+, K^+, and Ca_2^+ for H^+ (Nesbitt & Young 1982, 1989). Mg_2^+ and Si_4^+ may also be lost during these reactions. CIA is calculated using the following equation

$$\mathrm{CIA} = \left[\frac{\mathrm{Al_2O_3}}{\mathrm{Al_2O_3} + \mathrm{Na_2} + \mathrm{K_2O} + \mathrm{CaO}}\right] \times 100 \tag{2.1}$$

where the major element oxides are given in molecular proportions (wt. %). According to the equation, CaO is only present in silicate minerals, so its application to rocks containing carbonates is limited. Metasomatic alteration that results in K_2O addition also lowers the CIA and masks its ability to proxy weathering (Fedo et al. 1995).

Major element oxide data are presented on 2 ternary plots in Figure 2.10, along with average Otago Schist (n=38), Alpine Schist (n=25), Caples Schist (n=20) and metabasite (n=18) protolith compositions determined by Pitcairn (2004). The average compositions of Karamea suite granitoids (n=52), Greenland Group greywackes (n=53), and Greenland Group argillites (n = 93) are also plotted (results downloaded from PETLAB http://pet.gns.cri.nz; original sources are cited in figure caption). In Figure 2.10A, the quartzofeldspathic schist, metabasite, and Karamea suite and Greenland Group protoliths define a trend line along which a majority of DFDP-1 hanging wall and footwall fault rocks lie. The Unit 7 breccia, derived from an augen-

Sample	Friction Exp.	Location	Lithology	Fraction	Quartz	K feldspar	Plagioclase	Calcite	Mg-Calcite	Ankerite	Kaolin	Smectite	White mica	Chlorite	Serpentine	Talc	Amphibole	Pyrite	Laumontite	Total
36959		Little Man R.	5	WR	18	3	33	10			6	20	10							100
34103	p3370, p3673	Gaunt Ck Terrace	5	WR	35	<1	17	6					32	9						99
34103_2		Gaunt Ck Terrace	5	< 2 mm	5		3						50	42						100
35067	p2863	Gaunt Ck Scarp	3	WR	49	10	19	2		12	8				<1					100
34113	p2799, p2863	Gaunt Ck Scarp	3	< 2 mm	<1								68	32						100
34112	p3151	Gaunt Ck Scarp	4fol	< 2 mm	9	3	27	2			4	36	16	2						99
34104	p2798, p2862	Gaunt Ck Scarp	5	WR	30	6	26	7	1		6	7	17							100
34119*		Gaunt Ck Scarp	5	< 2 mm	8		16					29	17	29						99
34105	LHV277, LHV278	Gaunt Ck Scarp	5uccl	WR	25	5	20	5			7	14	16		8					100
34117		Stoney Ck	3	< 2 mm	4	<1	7	8					41	40						100
35363	p2828	Waikukupa R	4	WR	35	33	6			1			6	19				<1	<1	100
34114		Waikukupa R	4	< 2 mm	4		19	2					21	51					2	99
34106	p2830	Waikukupa R	5	WR	28		26	25		<1			14	5			2	<1		100
34118		Waikukupa R	5	< 2 mm	8	<1	10	10				24	26	22						100
34107		Waikukupa R	5uccl	WR	27	1	19	17				16	17	2				<1		99
34108		Waikukupa R	5#	WR	27	<1	20	16				13	20	4				<1		100
36962		Robinson Ck	4	WR	40	14	21	4					17	5						101
36961		Robinson Ck	5	WR	32	6	32					19	7	2			3			101
36960		Robinson Ck	8	WR	35	2	41						16	2			5			101
34109	p3152	Martyr R	5fol	WR	8	4	15	<1					35	39				<1		101
34958	p2861	Martyr R	5	WR	37	4	7	1					36	15						100
34115		Martyr R	5	< 2 mm	2								70	28						100
34111	p3373	McKenzie Ck	5	WR	8	1	1	5				61		11	13					100
34110		Hokuri Ck	4rim	WR	<1			2						5	93					100
34959	p3372, LHV262, LHV270, LHV271, LHV289	Hokuri Ck	5	WR	2			5				74		3	12	2	2			100
34116		Hokuri Ck	5	< 2 mm								78			21	1				100

Table 2.3: Quantitative X-ray diffraction data for cataclasites and fault gouges collected at localities along strike of the central and southern Alpine Fault. (*) Sample 34119 was from a weathered block and was not a separate from sample 34104. Lithologies are described in the text. Abbreviations are: fol, foliations present; uccl, the most highly comminuted, striated gouge that marks the HW/FW contact; rim, a foliated cataclasite present on the rim of a serpentinite pod (see Chapter (4) for details). WR denotes whole rock, and < 2 μm denotes clay-sized fraction. Composition of plagioclase and feldspar could not be discerned. The dioctahedral smectite present is montmorillonite-15Å. White mica denotes muscovite-2M1, but illite-2M1 may also be present. Chlorite is clinochlore-1MIIB, the serpentine is lizardite-1M, and the amphibole is actinolite. Amorphous phases were not identified and results are normalized to 100%. Friction experiments are described in Chapters (3), (4) and (6). Location latitude/longitude co-ordinates are: Little Man River 43.1400°S/170.2818°E; Gaunt Creek Terrace and Gaunt Creek Scarp 43.3141°S/170.3259°E; Stoney Creek 43.2290°S/170.1239°E; Waikukupa River 43.2622°S/170.0490°E; Robinson Creek 43.4956°S/169.1350°E; Martyr River 44.1326°S/168.5536°E; McKenzie Creek 44.3599°S/168.1390°E; Hokuri Creek 44.4062°S/168.0648°E.

Sample	Hole depth	Lithology	SiO_2	TiO_2	Al_2O_3	Fe_2O_3t	MnO	MgO	CaO	Na_2O	K_2O	P_2O_5	Cr_2O_3	SrO	BaO	LOI	Total	CIA
DFDP1	63.6	1	63	0.64	15.05	4.8	0.1	1.62	2.87	3.19	2.78	0.16	0.01	0.04	0.08	4.12	98.46	52.76
DFDP2	66.7	2	63.1	0.83	14.85	4.77	0.09	2.48	4.12	3.19	2.76	0.2	0.01	0.05	0.09	4.92	101.46	48.57
DFDP3	70.4	3	65.9	0.57	13.75	4.65	0.07	2.34	2.17	1.87	3.69	0.15	0.01	0.03	0.06	4.2	99.46	55.52
DFDP4	74.5	4	61.7	0.88	15.8	6.22	0.1	2.69	2.69	3.15	2.59	0.19	0.01	0.04	0.08	4.2	100.34	55.10
RW_XRF	78	2	67.38	0.65	15.37	4.95	0.07	1.64	1.91	2.57	2.74	0.15	NA	NA	NA	3.05	100.48	59.03
RW_XRF	80.5	4	63.40	0.91	14.75	5.36	0.07	3.03	4.01	2.36	2.88	0.19	NA	NA	NA	3.59	100.55	50.79
DFDP5	82.7	4	61.1	0.61	12.5	4.89	0.11	3.36	4.7	1.14	3.2	0.17	0.01	0.03	0.04	6.94	98.8	47.38
RW_XRF	83.7	4	62.53	0.59	13.87	5.05	0.11	3.18	4.84	1.02	3.66	0.15	NA	NA	NA	5.99	100.99	48.99
RW_XRF	85.15	4	66.14	0.66	13.99	5.08	0.07	2.92	2.83	0.86	3.45	0.13	NA	NA	NA	4.65	100.78	57.61
DFDP6	86.35	4	65.5	0.27	12.8	2.22	0.09	1.24	4.68	2.95	3.84	0.07	0.01	0.03	0.05	5.38	99.13	42.22
RW_XRF	87.54	4	61.39	0.87	15.12	5.73	0.10	3.07	3.63	2.19	3.56	0.18	NA	NA	NA	4.68	100.52	51.82
DFDP7	88.4	4	62.2	0.7	13.9	4.7	0.1	3.05	4.93	1.95	3.12	0.19	0.01	0.03	0.04	6.59	101.51	47.20
DFDP8	89.34	4	61.1	0.83	14.4	5.2	0.09	3.09	4.87	2.45	3.58	0.21	0.01	0.05	0.11	5.95	101.94	46.21
RW_XRF	89.8	4	65.47	0.64	14.02	4.77	0.07	2.99	3.34	0.56	3.84	0.15	NA	NA	NA	5.14	100.99	55.70
DFDP9	90.32	4	45	0.67	11	5.52	0.24	4.89	14.75	0.87	2.43	0.19	0.01	0.05	0.04	15.55	101.21	26.27
DFDP10	90.62	5	56.7	0.68	13.1	5.47	0.14	3.35	6.83	0.74	5.52	0.18	0.01	0.04	0.13	8.64	101.53	40.05
DFDP11	91.3	8	70.5	0.56	14.35	4.14	0.06	1.37	1.36	3.32	2.43	0.14	0.01	0.03	0.06	1.93	100.26	57.60

Table 2.4: Major element geochemistry of DFDP-1A samples from XRF and ICP-AES analysis. All values are in wt. %. Fe_2O_3t denotes total Fe_2O_3. NA denotes not analyzed. All DFDP samples analyzed with ICP-AES; instrument precision for this method is ±0.02 wt.%. Analytical error for this method varies with major element oxide and sample abundance of major element oxide. Repeat standard analyses yield the following maximum analytical errors: SiO_2 ±2.20%; TiO_2 ±1.55%; Al_2O_3 ±2.68%; Fe_2O_3 ±2.52%; MnO ±0.01%; MgO ±1.60%; CaO ±5.44%; Na_2O ±9.00%; K_2O ±2.53%. Other oxide abundances (wt. %) were within instrument precision with analytical errors up to 100%. RW_XRF samples were analyzed with XRF; instrument precision for this method was not available. Repeat standard analyses yield the following maximum analytical errors: SiO_2 ±0.20%; TiO_2 ±0.44%; Al_2O_3 ±0.34%; Fe_2O_3 ±0.21%; MnO ±10.88%; MgO ±2.32%; CaO ±0.44%; Na_2O ±8.32%; K_2O ±0.60%. A maximum LOI analytical error ±11.55% was calculated from repeat standard analyses provided by ALS Minerals.

Sample	Hole depth	Lithology	SiO_2	TiO_2	Al_2O_3	Fe_2O_3t	MnO	MgO	CaO	Na_2O	K_2O	P_2O_5	Cr_2O_3	SrO	BaO	LOI	Total	CIA
DFDP12	112.04	4	62.7	0.75	15.05	4.43	0.06	2.78	2.87	1.6	4.23	0.2	0.01	0.03	0.06	6.06	100.83	54.77
DFDP13	112.12	3	60.8	0.81	14	4.31	0.11	2.54	4.2	1.2	4.26	0.21	0.01	0.03	0.05	6.97	99.5	49.61
DFDP14	113.05	3	59.8	1.07	13.95	5.98	0.06	3.43	3.36	2.97	2.83	0.29	0.02	0.05	0.09	4.45	98.35	49.81
DFDP15	113.81	3	52.7	1.31	15.95	8.8	0.07	4.9	2.79	2.12	2.59	0.31	0.03	0.03	0.04	6.41	98.05	58.40
DFDP16	116.72	3	55.1	0.73	13.75	6.61	0.12	4.03	5.24	1.46	2.91	0.22	0.01	0.04	0.04	8.6	98.86	47.70
DFDP17	128.04	4	57.3	0.66	12.75	4.45	0.12	3.15	5.42	0.18	3.86	0.15	0.02	0.02	0.03	8.45	96.56	47.09
DFDP18	128.09	4	57.7	0.55	12.3	4.69	0.13	2.88	6.36	0.85	3.21	0.15	0.01	0.02	0.02	8.6	97.47	42.80
DFDP19	128.22	4	56.3	0.65	12.05	5.06	0.12	3.49	6.72	1.71	2.66	0.18	0.01	0.04	0.04	8.84	97.87	40.22
DFDP20	128.3	5	59.2	0.65	12.75	4.89	0.11	2.84	5.32	2.32	2.72	0.18	0.01	0.06	0.07	8.07	99.19	43.69
DFDP21	128.5	6	70.7	0.44	15.2	2.92	0.02	1.39	0.58	3.45	4.09	0.15	0.01	0.04	0.08	2.16	101.23	57.67
DFDP22	128.53	6	73.6	0.14	13.6	1.31	0.01	0.59	0.46	3.86	4.19	0.1	<0.01	0.03	0.08	1.45	99.42	53.71
DFDP23	128.8	6	71.7	0.18	13.45	1.61	0.02	0.69	1.12	3.03	4.43	0.12	<0.01	0.03	0.07	2.12	98.57	53.23
DFDP24	128.8	6	70.7	0.19	13.25	1.94	0.02	0.92	0.51	3.83	3.46	0.06	0.01	0.03	0.07	1.95	96.94	54.70
DFDP25	130.88	6	63.2	0.88	13.9	6.61	0.08	3.31	2.58	2.01	3.36	0.29	0.03	0.03	0.07	4.84	101.19	54.44
DFDP26	131.68	6	74.6	0.1	13.55	0.79	0.01	0.29	1.1	3.29	4.59	0.16	<0.01	0.03	0.07	NSS	NSS	52.26
DFDP27	132.7	6	68.1	0.47	14.25	3.71	0.03	1.61	0.97	2.2	3.99	0.19	0.01	0.03	0.07	2.65	98.28	59.50
DFDP28	133.75	6	61.4	0.87	15.2	7.01	0.06	3.28	1.28	1	3.41	0.17	0.02	0.02	0.06	4.57	98.35	66.48
DFDP29	138.17	6	62.7	0.66	16.7	4.62	0.04	2.09	1.28	2.35	4.35	0.26	0.01	0.02	0.06	3.3	98.44	60.50
DFDP30	140.96	6	57.3	0.58	16.65	7.48	0.08	3.98	2.37	1.21	4.51	0.14	0.03	0.02	0.06	6.17	100.58	59.83
DFDP31	141.07	6	63.7	0.24	18.1	2.61	0.03	1.34	1.4	1.64	7.83	0.25	<0.01	0.02	0.1	3.44	100.7	56.89
DFDP32	141.35	6	62	0.64	15.1	6.11	0.06	3.36	1.96	1.57	3.61	0.17	0.02	0.02	0.07	5.73	100.42	60.03
DFDP33	141.77	6	65	0.67	14.05	5.38	0.06	2.93	0.89	1.19	3.93	0.11	0.02	0.02	0.1	3.94	98.29	64.22
DFDP34	141.9	6	NSS	NSS	NSS	NSS	NSS	NSS	NSS	NSS	NSS	NSS	NSS	NSS	NSS	4.73	NSS	NSS
DFDP35	143.9	6	63	0.53	12.55	3.81	0.1	2.1	5.17	1.53	3.03	0.16	0.01	0.02	0.03	7.08	99.12	45.23
DFDP36	144.02	5	59.8	0.73	13.95	5.59	0.1	3.4	5.03	1.95	2.43	0.2	0.02	0.08	0.09	8.53	101.9	48.21
DFDP37	144.15	5	68	0.66	14.95	4.73	0.04	2.46	1.34	2.63	3.41	0.25	0.01	0.04	0.07	3.25	101.84	58.85
DFDP38	144.28	7	60.3	0.95	14.8	6.51	0.07	3.37	2.78	1.68	3.52	0.14	0.02	0.03	0.14	3.88	98.19	56.00
DFDP39	146.25	7	59.7	1.07	16.35	6.21	0.06	2.55	4.78	3.43	2.31	0.44	0.03	0.09	0.11	1.81	98.94	49.27

Table 2.5: Major element geochemistry of DFDP-1B samples from ICP-AES analysis. All values are in wt. %. Fe_2O_3t denotes total Fe_2O_3. NSS denotes not sufficient sample. Instrument precision and analytical error as reported in the Table 2.4 caption.

Sample	Location	Lithology	SiO_2	TiO_2	Al_2O_3	Fe_2O_3t	MnO	MgO	CaO	Na_2O	K_2O	P_2O_5	Cr_2O_3	SrO	BaO	LOI	Total	CIA
DFDP48	Little Man R	4	52.8	0.83	14.55	6.4	0.13	3.57	6.24	2.38	2.93	0.17	0.03	0.03	0.05	7.9	98.01	44.12
DFDP47	Little Man R	5	54	0.9	14.55	6.29	0.12	2.83	7.69	2.07	1.85	0.21	0.02	0.09	0.07	9.51	100.2	42.87
AFUC11	Gaunt Ck Terrace	5	59.90	0.79	13.93	6.16	0.10	3.44	4.73	1.01	2.87	0.15	NA	NA	NA	6.48	99.56	51.03
AFUC18	Gaunt Ck Scarp	5	53.99	0.79	14.03	5.79	0.11	3.84	8.85	1.29	3.25	0.18	NA	NA	NA	8.44	100.56	39.23
AFUC19	Gaunt Ck Scarp	5	59.16	0.80	14.57	5.97	0.10	3.43	5.69	1.43	2.71	0.17	NA	NA	NA	6.22	100.25	48.24
AFUC17	Gaunt Ck Scarp	5	59.47	0.81	14.77	6.18	0.11	3.65	5.40	1.44	2.69	0.17	NA	NA	NA	5.52	100.21	49.45
AFUC23	Gaunt Ck Scarp	5	60.48	0.77	14.30	6.02	0.12	3.03	4.33	1.37	3.13	0.16	NA	NA	NA	5.50	99.21	51.41
AFUC24	Gaunt Ck Scarp	8	66.15	0.76	15.27	5.83	0.07	2.84	1.57	1.34	3.84	0.16	NA	NA	NA	3.03	100.86	62.36
AFUC29	Waikikupa R	4	59.51	1.08	14.60	8.86	0.15	4.41	5.68	2.48	0.24	0.11	NA	NA	NA	3.19	100.31	49.89
AFUC30	Waikikupa R	4	66.73	0.40	13.79	5.56	0.11	3.21	5.36	1.97	0.19	0.06	NA	NA	NA	2.95	100.33	51.11
AFUC34	Waikikupa R	4	54.59	0.89	15.21	9.94	0.19	6.25	7.65	2.84	0.21	0.08	NA	NA	NA	3.09	100.94	44.71
AFUC36	Waikikupa R	4	64.08	0.44	13.87	5.62	0.12	3.51	6.05	2.11	0.43	0.07	NA	NA	NA	4.35	100.65	48.15
AFUC37	Waikikupa R	5	50.09	0.69	12.59	6.01	0.15	2.99	12.81	1.42	1.99	0.14	NA	NA	NA	11.85	100.73	31.19
AFUC39	Waikikupa R	5	45.40	0.66	11.79	5.71	0.22	2.58	15.86	1.27	2.01	0.13	NA	NA	NA	14.39	100.02	26.26
DFDP40	Robinson Ck	2	63.8	0.83	15.65	6.41	0.16	1.87	2.47	2.6	2.88	0.19	0.01	0.03	0.08	3.55	100.53	56.84
DFDP41	Robinson Ck	3	43.4	3.14	13.4	13.25	0.19	5.41	10.85	2.83	1.05	0.37	0.02	0.04	0.02	7.78	101.75	34.43
DFDP46	Robinson Ck	4	44.4	2.17	13.1	12.65	0.2	5.54	11.05	2.76	1.01	0.3	0.03	0.03	0.01	7.22	100.47	33.74
DFDP45	Robinson Ck	4	64.6	0.63	14.35	4.44	0.06	2.25	3.31	2.5	2.8	0.15	0.01	0.03	0.05	4.34	99.52	52.16
DFDP44	Robinson Ck	5	57.2	0.79	14.3	6.07	0.1	3.63	5.52	2.42	2.55	0.24	0.02	0.05	0.06	6.12	99.07	46.01
DFDP43	Robinson Ck	5	59.3	0.78	14.45	6.21	0.09	3.3	3.92	2.28	2.18	0.2	0.02	0.07	0.05	7.09	99.94	52.19
DFDP42	Robinson Ck	8	65	0.85	15.1	5.79	0.15	1.96	2.64	3.01	2.22	0.18	0.01	0.04	0.06	2.35	99.36	55.40
AFUC49	McKenzie Ck	5	45.17	0.53	8.04	7.84	0.12	22.55	5.14	0.46	0.15	0.13	NA	NA	NA	10.29	100.42	43.92
AFUC56	Hokuri Ck	5	43.44	0.47	6.81	8.02	0.12	25.21	5.32	0.54	0.12	0.12	NA	NA	NA	10.38	100.55	38.91

Table 2.6: Major element geochemistry of samples from ICP-AES and XRF analysis. All values are in wt. %. Fe_2O_3t denotes total Fe_2O_3. NA denotes not analyzed. DFDP samples analyzed by ICP-AES and AFUC samples analyzed by XRF. Analytical error as reported in the Table 2.4 caption. Sample location latitude/longitude co-ordinates are listed in the Table 2.3 caption.

bearing mylonite (Figure 2.8H) lies at the $MgO + Fe_2O_3$ axis of the footwall trend line in both ternary plots. Unit 6 granitiod-gneissic cataclasites are enriched in K_2O, Na_2O and Al_2O_3 and trend towards the average Karamea suite protolith composition. In Figure 2.10B, data display more scatter. A trend towards CaO enrichment is exhibited by Unit 4 foliated cataclasites and Unit 5 gouges, with the DFDP-1B PSZ-2 gouge at the lower contact between Unit 5 gouge and Unit 7 breccia (e.g., 144.15 m depth) being depleted in CaO relative to the DFDP-1B PSZ-1 gouge and DFDP-1A PSZ gouge.

Figure 2.10(Over) Ternary plots of variations in major element geochemistry for samples analyzed from DFDP-1A and DFDP-1B. All units are wt. %. Hanging wall lithologies are grouped: Units 1 and 2 mylonites (green down triangles), and Units 3 and 4 cataclasites (yellow up triangles). Unit 5 gouges (DFDP-1A PSZ, DFDP-1B PSZ-1 and PSZ-2) are grouped together (red diamonds). Footwall lithologies are: Unit 6 footwall cataclasites (green squares), Unit 7 footwall breccia (grey squares), and Unit 8 footwall gravels (orange squares). Also plotted are average hanging wall protolith, Otago Schist, Alpine Schist, Caples Schist, and metabasite, compositions from Pitcairn (2004). Average footwall protolith, Karamea Suite granitoids, Greenland Group greywacke and argillite, compositions were calculated from data in PETLAB, most of which were published in Nathan (1976, 1998), Roser et al. (1995), Tulloch & Palmer (1990), and Tulloch et al. (2009). Purple shaded regions around each footwall protolith composition represent $\pm 1\sigma$. **A,** A ternary plot of $Al_2O_3 - Na_2O + K_2O - MgO + Fe_2O_3$ variations. Hanging wall lithologies follow a trend between Otago Schist/Alpine Schist and metabasite protolith compositions; the hanging wall cataclasites are relatively more enriched in $MgO + Fe_2O_3$. Footwall lithologies follow a trend between Unit 7 footwall breccia and Karamea Suite protolith, but some Unit 6 cataclasites are relatively enriched in $Al_2O_3 - Na_2O + K_2O$. **B,** A ternary plot of $Al_2O_3 - CaO - MgO + Fe_2O_3$ variations. Hanging wall lithlogies do not follow a trend between protolith compositions, but rather follow a trend from Otago Schist/Alpine Schist protolith composition towards relative CaO-enrichment. A single footwall catclasite, from DFDP-1B 143.9 m immediate above PSZ-2, is relatively enriched in CaO. Footwall lithologies follow a trend between Unit 7 footwall breccia/Greenland Group argillite and Karamea Suite protolith, but some Unit 6 cataclasites are relatively enriched in Al_2O_3.

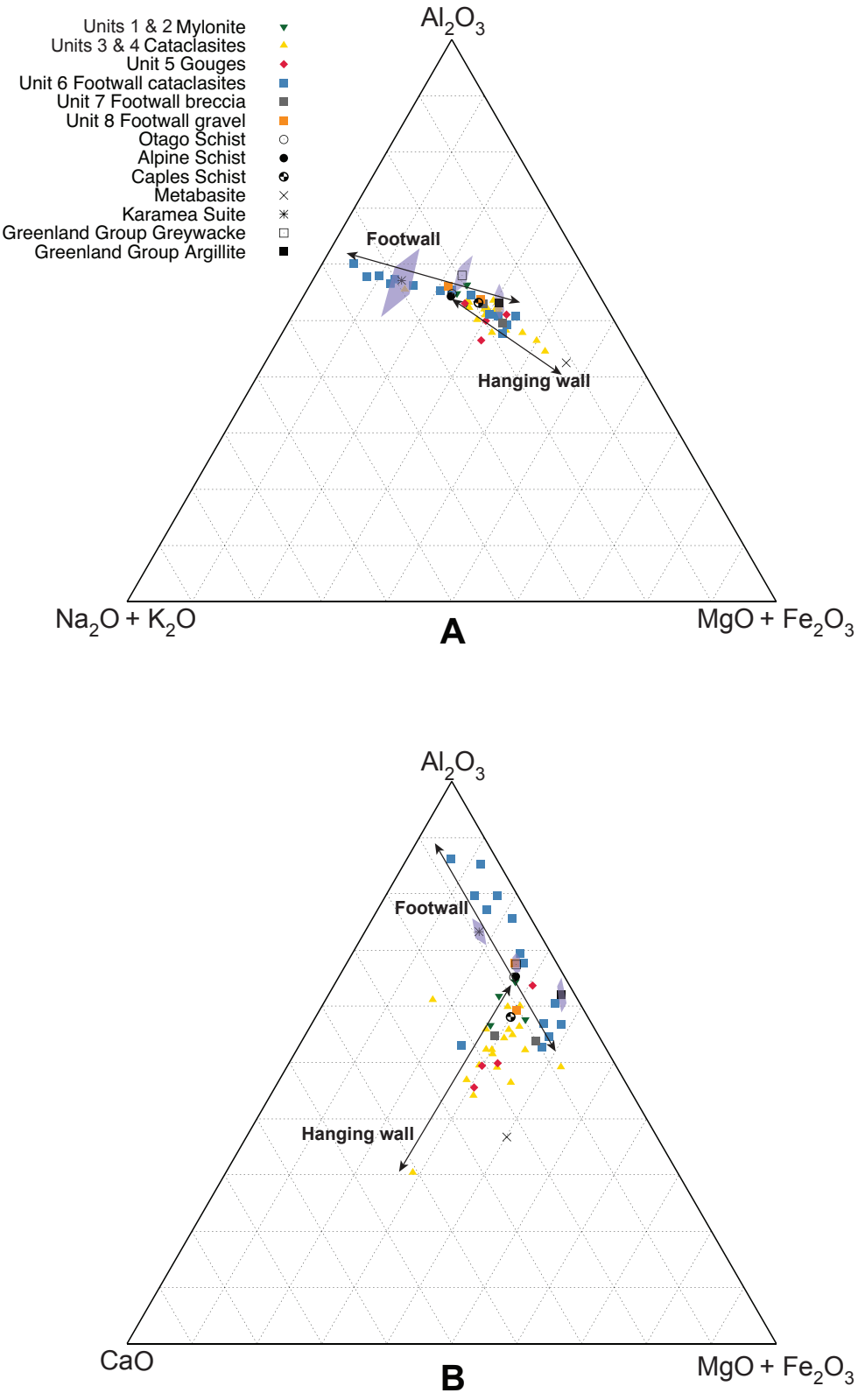
Units 1 & 2 Mylonite
Units 3 & 4 Cataclasites
Unit 5 Gouges
Unit 6 Footwall cataclasites
Unit 7 Footwall breccia
Unit 8 Footwall gravel
Otago Schist
Alpine Schist
Caples Schist
Metabasite
Karamea Suite
Greenland Group Greywacke
Greenland Group Argillite
Al2O3
Footwall
Hanging wall
Na2O + K2O
MgO + Fe2O3
A
Al2O3
Footwall
Hanging wall
CaO
MgO + Fe2O3
B

Figure 2.10:

Variations in relative major element oxide abundance, given as wt. %, with depth in DFDP-1A are plotted in Figure 2.11. All hanging wall fault rocks have between 61.1 and 67.38 wt.% SiO_2; the Unit 4 foliated cataclasite (90.32 m depth) and Unit 5 fault gouge (90.62 m depth) immediately above and within the PSZ are relatively depleted in SiO_2, and the unit 8 footwall gravel (91.3 m depth) is relatively enriched in SiO_2. The Unit 4 foliated cataclasite at 90.32 m depth is also relatively depleted in Al_2O_3 (11 wt.%) compared to other fault rocks in DFDP-1A (12.5 – 15.8 wt.%). The Unit 4 cataclasite at 86.35 m depth is relatively depleted in Fe_2O_3 and MgO (2.22 and 1.24 wt.%, respectively). Relative MnO enrichment occurs within the Unit 4 foliated cataclasite at 90.32 m depth (0.24 wt.%) and within the Unit 5 gouge at 90.62 m depth (0.14 wt.%). The Unit 4 foliated cataclasite (90.32 m depth) and Unit 5 fault gouge (90.62 m depth) are relatively enriched in CaO (14.75 and 6.83 wt.%, respectively), and the Unit 8 footwall gravel (91.3 m depth) is relatively depleted in CaO (1.36 wt.%). Na_2O is relatively depleted in Unit 4 cataclasites between 82.7 and 85.15 m depth (0.86 – 1.14 wt.%) and in the Unit 4 foliated cataclasites and the Unit 5 fault gouge between 89.8 and 90.62 m depth (0.56 – 0.87 wt.%). The Unit 5 fault gouge (90.62 m) is relatively enriched in K_2O (5.52 wt.%). The Unit 4 foliated cataclasite at 86.35 m depth is relatively depleted in P_2O_5 (0.07 wt.%). In the PSZ interval analyzed (90.32 – 90.62 m), the Unit 4 foliated cataclasite and Unit 5 fault gouge have a low CIA and high LOI.

Relative major element oxide variations in hanging wall and footwall protolith rocks recovered in DFDP-1B are plotted in Figure 2.11. The relative abundance of SiO_2 in hanging wall and footwall rocks overlaps, but Unit 6 granitoid-gneissic cataclasites between 128.04 and 128.22 m depth are relatively enriched in SiO_2 (70.7 – 73.6 wt.%). The Unit 6 cataclasite at 131.68 m is also relatively enriched in SiO_2 (74.6 wt.%). PSZ-1 Unit 5 gouges between 128.04 and 128.3 m are relatively depleted in Al_2O_3 (12.05-12.75 wt.%), as is the PSZ-2 Unit 5 gouge at 143.9 m depth (12.55 wt.%). Unit 6 cataclasites between 138.17 and 141.07 m are relatively enriched in Al_2O_3 (16.65 – 18.1 wt.%). Unit 6 cataclasites immediately below PSZ-1 are relatively depleted in Fe_2O_3 and MgO (1.31-2.92 wt.% and 0.59-1.39 wt.%, respectively), but considerable scatter exists within the hanging wall and footwall units.

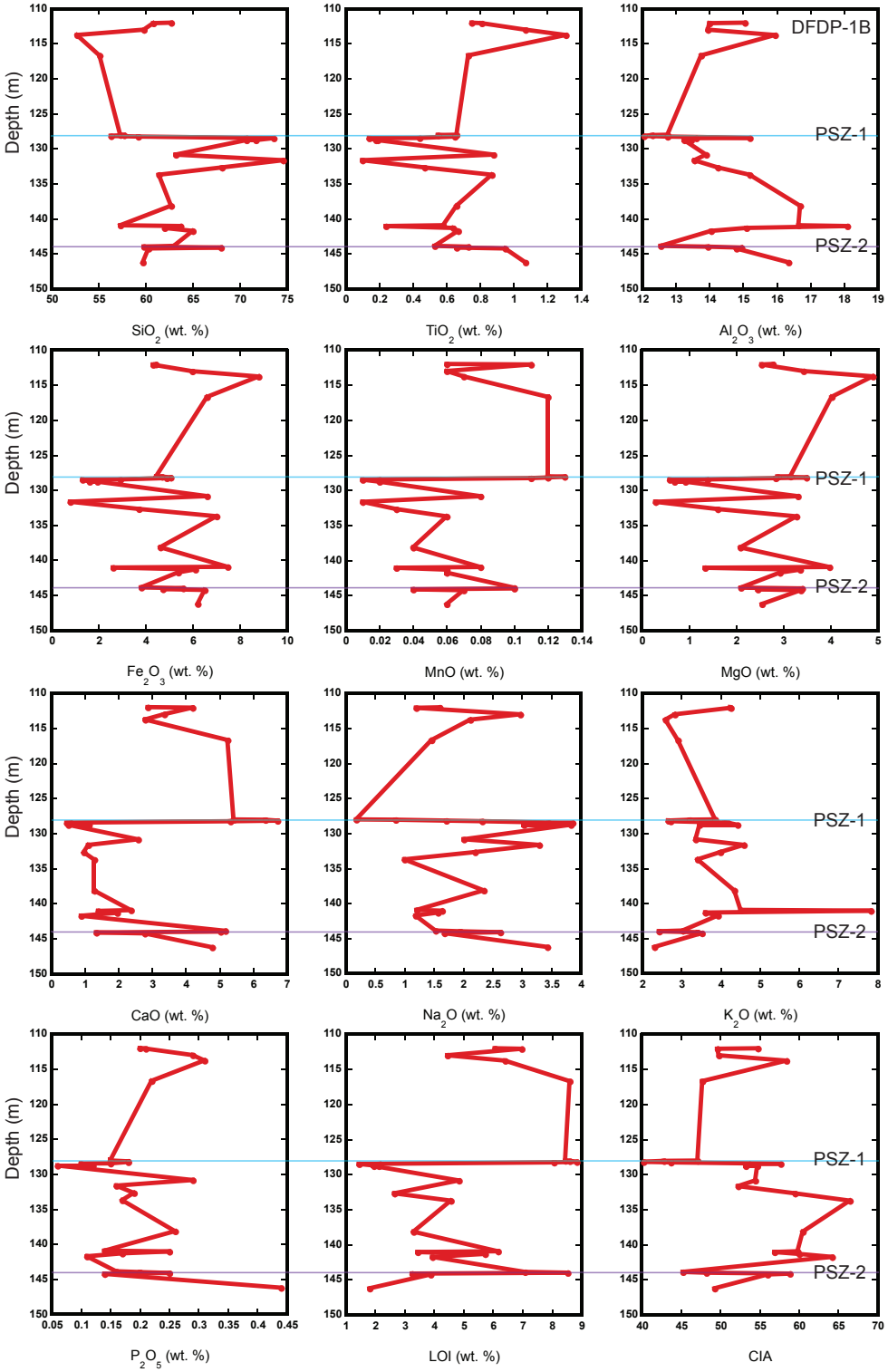

Figure 2.11: Variations in relative major element oxide abundance, given as wt. %, with depth in DFDP-1A. A yellow line marks the depth of the Unit 5 PSZ gouge (labeled PSZ), which is the contact between hanging wall lithologies (Units 1-5) and footwall gravels (Unit 8). See text for details.

The Unit 3 unfoliated cataclasite at 116.72 m and the PSZ-1 Unit 5 gouges between 128.04 and 128.3 m have relatively higher amounts of MnO (0.11-0.13 wt.%) with respect to the Unit 6 cataclasites (0.01-0.08 wt.%). The Unit 3 unfoliated cataclasites at 113.81 m and 116.72 m and Unit 5 PSZ-1 gouges between 128.04 and 128.3 m depths are relatively enriched in CaO (5.32-6.72 wt.%) compared to the Unit 6 cataclasites below PSZ-1 (0.58-2.58 wt.%). The PSZ-2 Unit 5 gouges are also relatively enriched in CaO (5.03-5.17 wt.%). In general, Unit 6 cataclasites are relatively enriched in K_2O (> 3.21 wt.%) compared to other footwall and hanging wall units. Unit 6 cataclasite at 141.07 m depth is particularly enriched (7.83 wt.%) relative to other units analyzed. Na_2O shows less discernible trends, but is, in general, relatively enriched in Unit 6 cataclasites. The Unit 7 breccia at 146.25 m depth is relatively enriched in P_2O_5 (0.44 wt.%) (cf. Figure 2.8H). As observed in DFDP-1A samples, the Unit 5 gouges and adjacent Unit 4 foliated cataclasites haves low CIA and high LOI.

2.4.5 Integrated petrophysical, lithological, and geochemical results

Townend et al. (2013) used wireline data collected from DFDP-1A below 30 m depth, and DFDP-1B below 48 m depth, along with lithological and geochemical results presented above, to identify key petrophysical characteristics of lithologies comprising the fault. Wireline data were collected on the scale of c. 0.1-100 m, but borehole instabilities prevented data collection through the fault core interval in DFDP-1A and through the lower PSZ-2 in DFDP-1B. Therefore, results presented in Townend et al. (2013), and summarized here, focus on the logged interval 60-140 m, including PSZ-1, in DFDP-1B. Figure 2.13 summarizes the correlation between characteristic lithology and natural gamma radioactivity (γ), borehole diameter (D), neutron porosity (ϕ_N), rock compensated density (ϱ_C), P-wave velocity (V_P) and impendence (Z_P), short-guard resistivity (ϱ_E), and spontaneous potential (SP). Using acoustic images of the borehole, Townend et al. (2013) also documented variations in damage zone fracture density and orientation. I was not directly involved in obtaining or interpreting fracture density results, so they are not presented here.

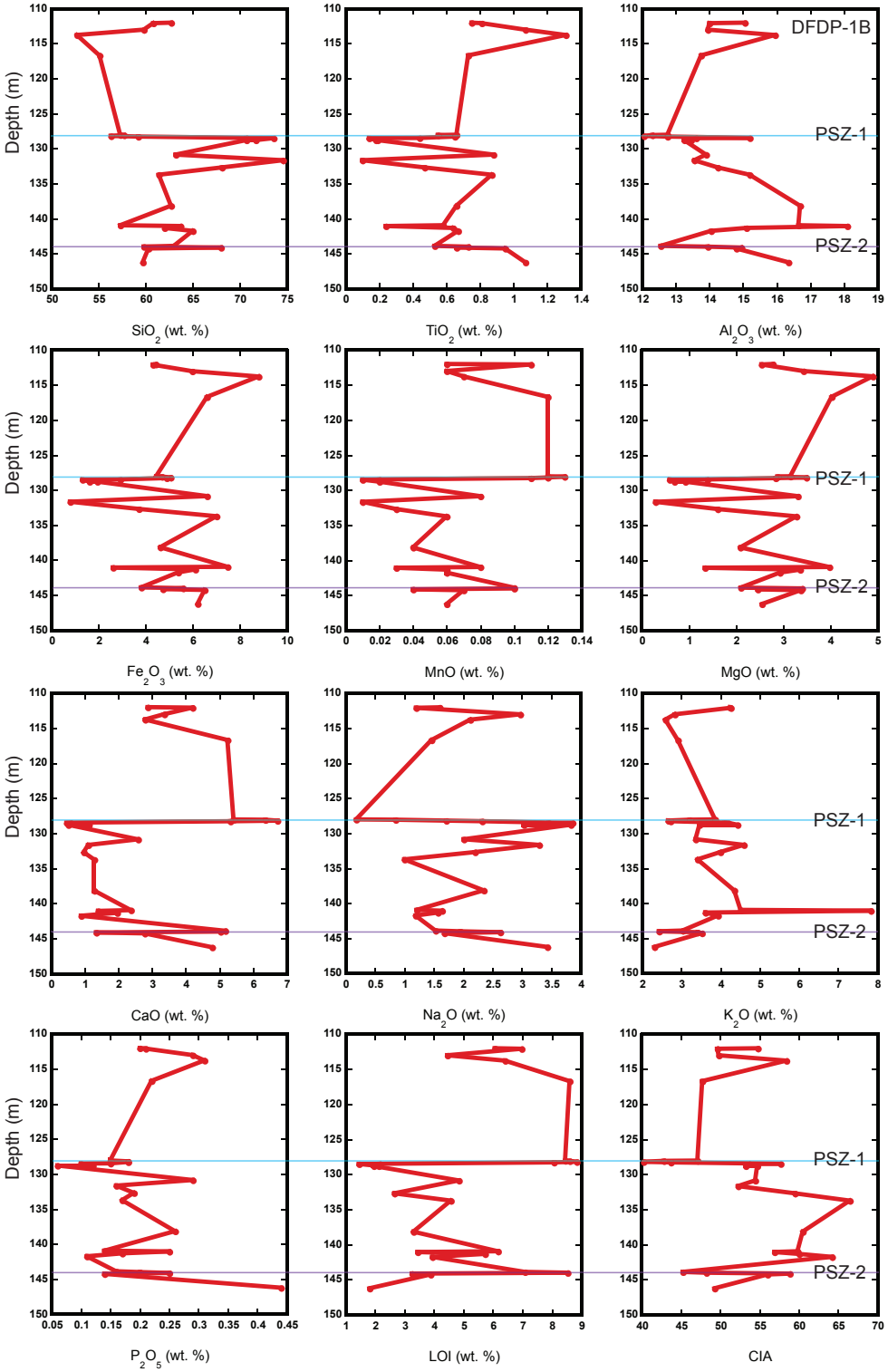

Figure 2.12: Variations in relative major element oxide abundance, given as wt. %, with depth in DFDP-1B. A yellow line marks the depth of the Unit 5 PSZ-1 gouge (labeled PSZ-1), which is the contact between hanging wall lithologies (Units 1-5) and footwall lithologies (Units 6 and 7). A blue line marks the depth of the Unit 5 PSZ-2 gouge (labeled PSZ-2), which is the contact between Unit 6 footwall cataclasites and Unit 7 footwall breccia. See text for details.

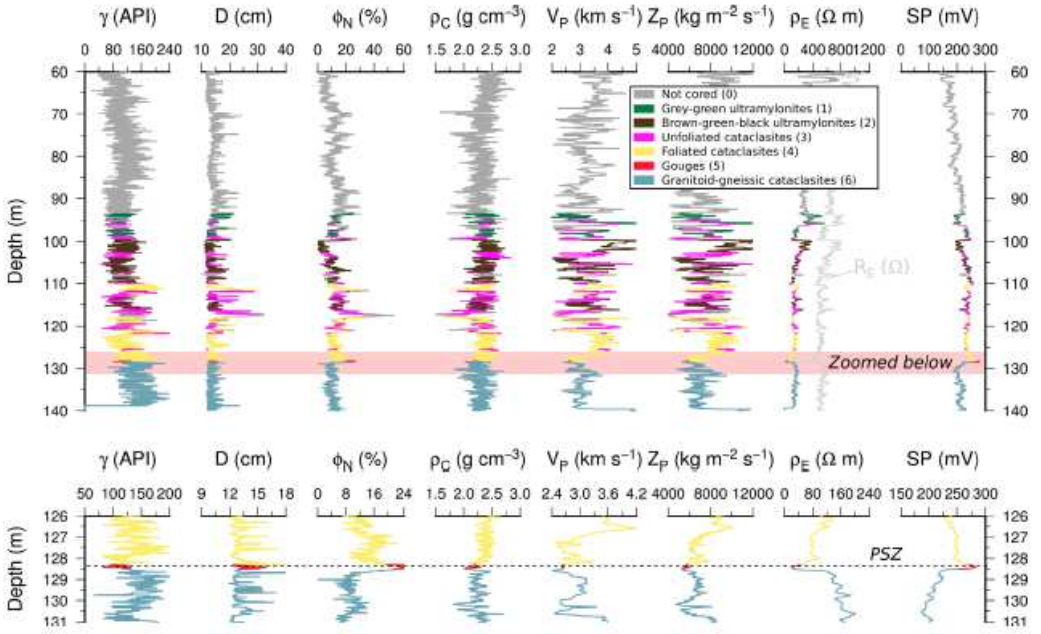

Figure 2.13: A summary of the correlation between characteristic lithology and natural gamma radioactivity (γ), borehole diameter (D), neutron porosity (ϕ_n), rock compensated density (ρ_c), P-wave velocity (V_P) and impendence (Z_P), short-guard resistivity (ρ_E), and spontaneous potential (SP) for the interval 60-140 m depth in DFDP-1B. Figure from Townend et al. (2013).

Unit 1 grey-green ultramylonites have the lowest measured natural gamma radioactivity values of all lithologies (90 API), as well as the smallest interquartile range (20 API). Overall, natural gamma radioactivity values are similar for hanging wall Units 1 through 3. Although the highest values of median electrical resistivity (180 Ωm) and single-point resistance (580 Ω) were obtained from Unit 2 brown-green-black ultramylonites, they cannot be distinguished by their average electrical properties from the Unit 3 and Unit 4 cataclasites, which are intercalated. At 128.3 m depth, the petrophysical properties of the Unit 5 gouge are distinct from all other units in the borehole. The Unit 5 gouge has a rock compensated density $\sim$ 0.3 g/cc less than other units, neutron porosity almost two times higher than other units, extremely low resistivity (23 Ωm at 128.4 m), high spontaneous potential (280 mV at 128.4 m), and a P-wave velocity $\sim$ 1000 m/s lower than other cored lithologies (Figures 2.13 and 2.14).

Combined with Figures 2.11 and 2.12 results, Figures 2.13 and 2.14 show that the peak in spontaneous potential, coinciding with the Unit 5 gouges, correlates with the minimum CIA and maximum LOI. Minimum values of electrical resistivity also coincide with minimum CIA and maximum LOI. Unit 6 granitoid-gneissic cataclasites have the highest median natural gamma value (150 API) of all the units. Apart from the Unit 5 gouge, Unit 6 cataclasites also have the lowest median seismic velocity (3000 m/s) and lowest median density (2.3 g/cm^3). The DFDP-1B logs exhibit an overall increase with depth in natural gamma radioactivity, from c. 80 API at 60 m depth to c. 160 API at 138 m (Figure 2.13). Figure 2.15 summarizes the variation in electrical resistivity and spontaneous potential as a function of borehole depth and lithology. From 60 m depth to c. 138 m depth, resistivity decreases from more than 400 Ωm to c.120 Ωm, and SP increases from c. 165 mV to 260 mV. Within Unit 6 cataclasites, however, the trend reverses, with a systematic increase in electrical resistivity from c. 25 Ωm to c. 200 Ωm and decrease in spontaneous potential from c. 240 mV to c. 195 mV with depth.

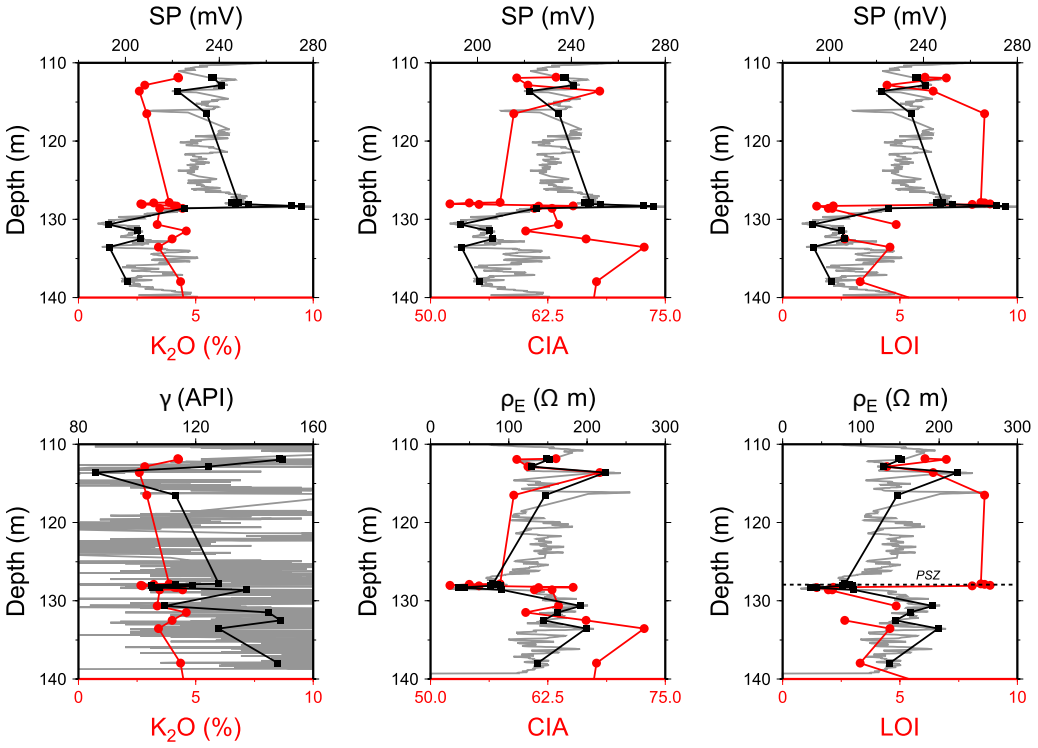

Figure 2.14: Plots of wireline logging data (black) against geochemical data (red) for the same depth interval in DFDP-1B near the 128.1 m PSZ-1. Grey curves are continuously recorded wireline data, black curves are wireline data averaged over 10 cm intervals at the depth of each geochemical measurement. Figure from Townend et al. (2013); caption modified from the same source.

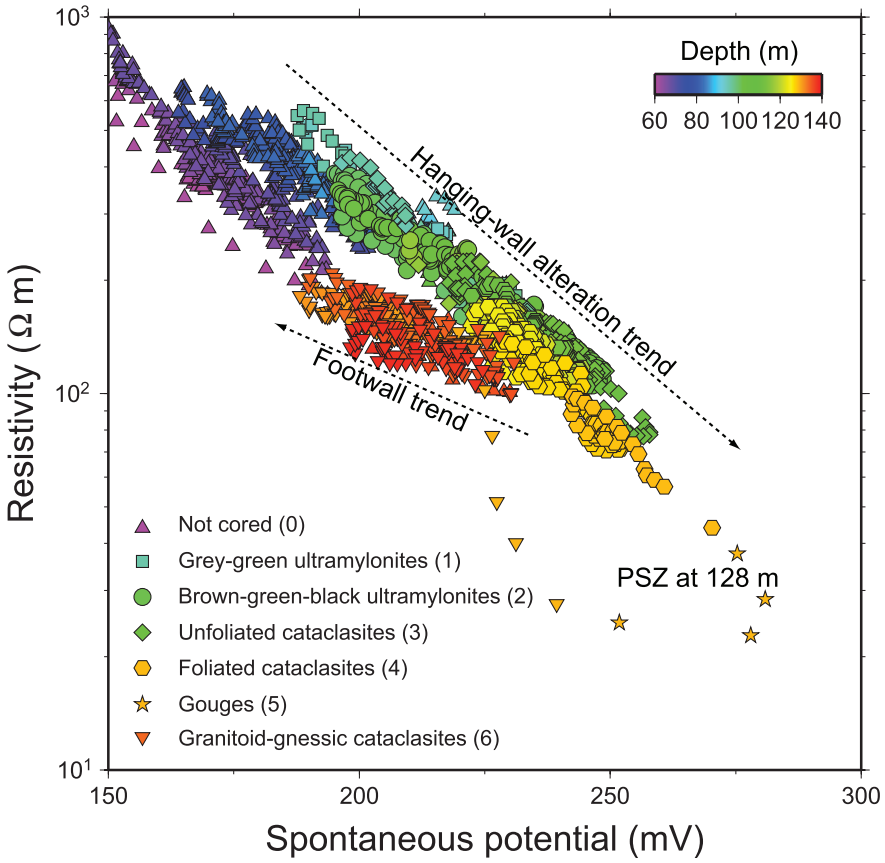

Figure 2.15: A plot of short-guard resistivity (ρ_E) versus spontaneous potential (SP) for the interval 60-140 m depth in DFDP-1B. Different lithlogies are designated by differently shaped symbols, with units given in parentheses. Data are coloured by down-hole depth. Figure from Townend et al. (2013), and caption modified from the same source.

2.5 Discussion

2.5.1 Alteration zone processes

Oblique dextral motion on the central Alpine Fault in the last 5-8 Myr has exhumed garnet-oligoclase facies mylonitic fault rocks from depths of c. 35 km. During exhumation, brittle deformation of these mylonites, accompanied by fluid infiltration, has resulted in complex mineralogical and lithological variations in fault rocks retrieved during DFDP-1 drilling at Gaunt Creek. Preliminary petrophysical, geochemical, and lithological results reveal that fault comprises a fault core of protocataclasites, cataclasites, and fault gouges bounded by a damage zone containing fractured and brecciated ultramylonites and mylonites. These results are consistent with previous descriptions of Alpine Fault rocks (e.g., Reed 1964; Sibson et al. 1979; Norris & Cooper 2007; Toy et al. 2008).

Caine et al. (1996) defined the fault core as the structural, lithologic, and morphologic portion of a fault zone where a majority of displacement has occurred. According to that definition, fault cores have various widths and contain comminuted slip surfaces, clay-rich gouges, geochemically altered zones, and/or cataclasites. Thus the fault core of Caine et al. (1996) correlates directly with the alteration zone of Sutherland et al. (2012). In the DFDP-1 drillcore, the fault core-alteration zone extends c. 20-30 m into the hanging wall if the first documented occurrence of retrogressed mineral assemblages in the Unit 2 brown–green–black ultramylonites (quartz + plagioclase + chlorite + epidote + accessory minerals) represents the maximum width of alteration zone processes. Below PSZ-1 in DFDP-1B, the c. 16 m-thick Unit 6 granitoid-gneissic cataclasites also comprise a portion of the fault core-alteration zone.

Whereas nonfoliated and foliated cataclasites in the hanging wall and footwall contain the phyllosilicates chlorite and white mica, Unit 5 fault core gouges contain kaolinite, smectite, white mica, and rare chlorite (Table 2.7). X-ray diffraction is unable to distinguish the white micas muscovite and illite, as both minerals have the same d-spacing (10Å). Using the ratios of Si to Al and Si to K in white mica (illite or muscovite), Farmer (2010) only found illite in the 10-12 cm thick (Unit 5) brown gouge exposed in the Gaunt Creek scarp

outcrop. Taken together, these results suggest that additional alteration reactions resulting in the formation of low temperature phyllosilicates are occurring preferentially in the geochemically and geophysically distinct Unit 5 gouges.

Using temperature constraints obtained by Warr & Cox (2001) along with reactions documented by Chamberlain et al. (1999) and Wintsch & Yeh (2013), alteration reactions observed in Alpine Fault gouges and cataclasites are outlined in Figure 2.16. These results suggest that at least two stages of chemical alteration have occurred. At temperatures at or near the brittle-to-ductile transition, metasomatic alteration reactions resulted in albite or K-feldspar replacement by muscovite, and biotite (phlogopite) replacement by chlorite (clinochlore). Abundant chlorite within alteration zone cataclasites indicates that hydrous chloritization of epidote and hornblende (actinolite) also occurred. At lower temperatures, alteration reactions occurred in the presence or absence of free electrons. That is, depending on local redox conditions, primary minerals were altered to kaolinite, smectite and/or pyrite or smectite, kaolinite, Fe-hydroxide (goethite) and/or carbonate.

For standard metasomatic alteration reactions involving K-feldspar, plagioclase, muscovite, biotite (phlogopite), and chlorite (clinochlore) (e.g., Figure 2.16), volume loss or gain, and corresponding variations in porosity and permeability, are governed by fluid:rock ratios and $\frac{Mg_2^+}{H^+}$, $\frac{K^+}{H^+}$, and $\frac{Na^+}{H^+}$ activity ratios (Wintsch et al. 1995; Wintsch & Yeh 2013). Hydrolysis reactions involving the reactants K-feldspar, muscovite, biotite (phlogopite), muscovite, chlorite (clinochlore), and albite usually result in volume loss. Notably, a volume gain occurs during the alteration of clinochlore to montmorillonite and during the alteration of muscovite to illite (Table2.7). Precipitation of calcite and goethite also results in a volume gain of 36.9 cm^3 per mol of calcite precipitated and 21.5 cm^3 per mol of goethite precipated. More detailed microstructural observations are needed to document the reaction sequences, their associated microstructures, and the effects these reactions might have had on porosity, permeability, and pore fluids pressures within the fault core-alteration zone (e.g., Hacker 1997).

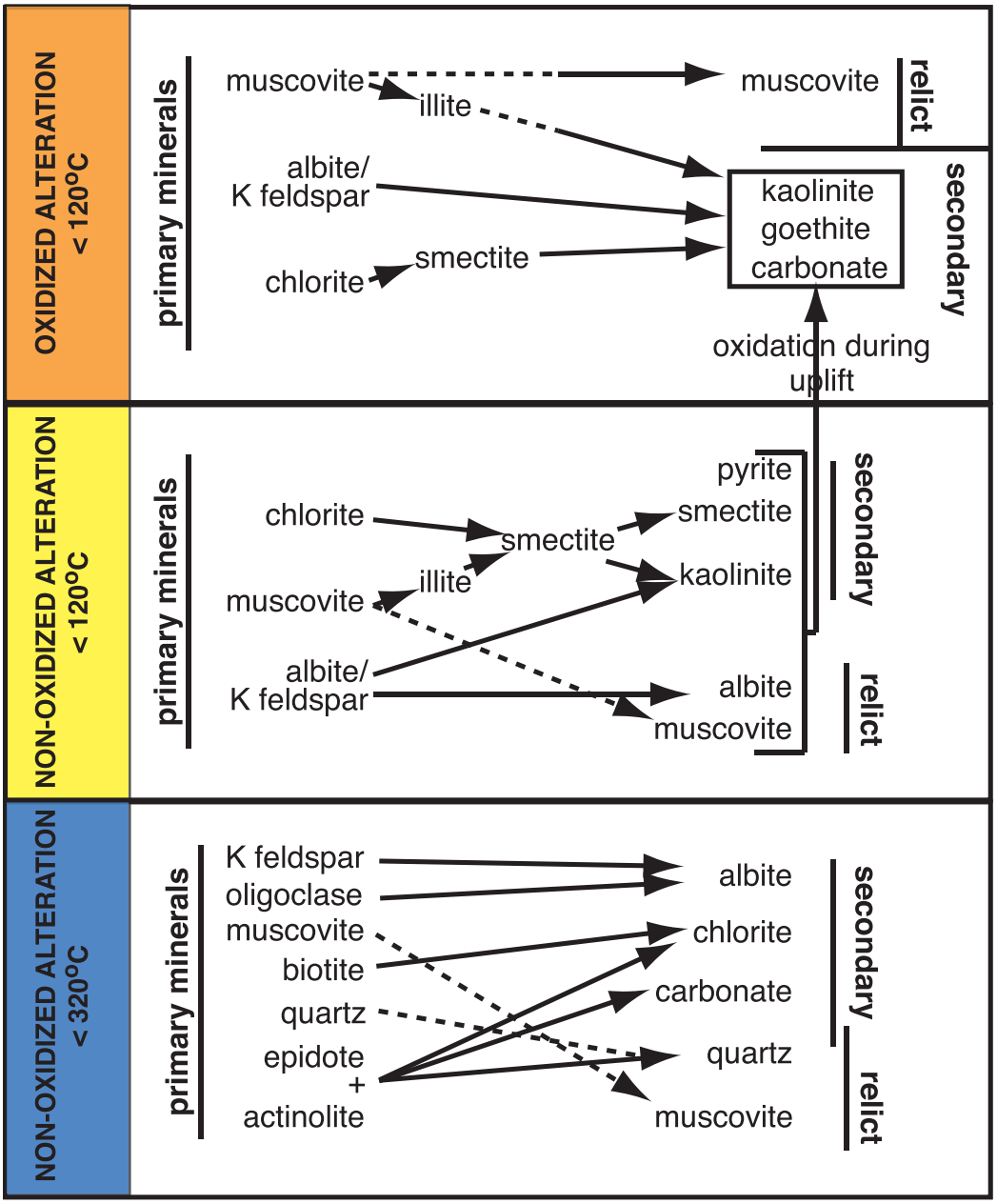

Figure 2.16: During exhumation from subgreenschist facies temperatures and pressures, Alpine Fault cataclasites and gouges have undergone multiple phases of alteration. Following Warr & Cox (2001) and Chamberlain et al. (1999), primary non-oxidized and oxidized alteration reactions are outlined in the figure. K-feldspar is not present in Alpine or Otago Schist protoliths, but it is observed in DFDP-1A and DFDP-1B lithologies, particularly below PSZ-2 in DFDP-1B.

Reaction	$\Delta V_{solid}(\mathrm{cm}^3)$	ΔV_{solid} (%)
1. $\mathrm{K{-}feldspar + Na^+ = Albite + K^+}$	-9	-8
2. $\mathrm{3\,albite + 2\,H^+ + K^+ = muscovite + 6\,SiO_2 + 3\,Na^+}$	-23	-8
3. $\mathrm{3\,K{-}feldspar + 2\,H^+ = muscovite + 6\,SiO_2 + 2\,K^+}$	-49	-15
4. $\mathrm{2\,phlogopite + 4\,H^+ + H_2O = clinochlore + 2\,SiO_2 + Mg^{2+} + 2\,K^+}$	-25	-8
5. $\mathrm{phlogopite + 6\,H^+ = K{-}feldspar + 3\,Mg^{2+} + 4\,H_2O}$	-41	-27
6. $\mathrm{2\,K{-}feldspar + 5\,Mg^{2+} + 8\,H_2O = clinochlore + 3\,SiO_2 + 2\,K^+ + 8\,H^+}$	61	30
7. $\mathrm{3\,clinochlore + 2\,K^+ + 28\,H^+ = 2\,muscovite + 3\,SiO_2 + 15\,Mg^{2+} + 24\,H_2O}$	-272	-44
8. $\mathrm{3\,muscovite + 5\,biotite + 9\,SiO_2 + 4\,H_2O = 8\,K{-}feldspar + 3\,clinochlore}$	-41	-2.7
9. $\mathrm{2\,K{-}feldspar + 6\,H^+ = kaolinite + 2\,K^+ + 4\,SiO_2 + 3\,H_2O}$	-30	-13.7
10. $\mathrm{2\,albite + 6\,H^+ = kaolinite + 2\,Na^+ + 4\,SiO_2 + 3\,H_2O}$	-12.5	-6.2
11. $\mathrm{5 \cdot 5\,muscovite + H^+ = 3\,illite + K^+ + 3\,SiO_2}$	12.5	6.9
12. $\mathrm{clinochlore + 3\,K{-}feldspar + H_2O + 9\,H^+ = 3\,montmorillonite + 3\,Mg^{2+} + 3\,K^+}$	41.8	8.1

Table 2.7: Balanced alteration reactions and solid volume changes associated with each reaction. All reactions balanced assuming simplified end-member mineral formula. Calculated solid volume changes assume the product SiO_2 precipitates as quartz; however, SiO_2 can leave the reaction site as an aqueous species. Iron may be present in clinochlore and montmorillonite minerals, but reactions are balanced assuming only octahedral magnesium cations. Reactions 1-8 from Wintsch & Yeh (2013). End member formulas from Deer et al. (1992); end member illite formula from Deer et al. (1992). Note the density of phyllosilicate minerals can vary with cation ratio and interlayer hydration state (e.g., Totten et al. (2002)).

2.5.2 Major element geochemistry variations

Major element geochemistry results presented in Figures 2.10, 2.11, and 2.12 are not normalized to account for changes in relative element abundance based on silica mobility in the fault zone (e.g., Ague 1994). TiO_2 is commonly assumed to be immobile in fault zones (e.g., Schleicher et al. 2009), but normalizing major element oxides to TiO_2 requires assuming a value for a single unaltered protolith. Moreover, Vry et al. (2001) documented neometamorphic titanite that postdates chloritization of Alpine Fault mylonites at high temperatures (c. 425-500°C). Major element geochemistry results show that within Unit 5 fault core gouges, SiO_2 and Al_2O_3 are relatively depleted and CaO is relatively enriched compared to hanging wall and footwall lithologies. K_2O is relatively enriched in the DFDP-1A Unit 5 gouge at 90.62 m as well as Unit 6 granitoid-gneissic cataclasites. Na_2O and K_2O are relatively enriched in Unit 6 cataclasites, and Fe_2O_3 and MgO are relatively depleted. Unit 6 cataclasites were derived in part from granitoid protoliths rich in

quartz, plagioclase, and K-feldspar, and thus reflect the chemistry of these minerals.

The major element geochemistry of fault rocks retrieved from the DFDP drillholes and collected from nearby natural exposures reflects the composition of the sedimentary, volcanic, or plutonic protolith (Roser et al. 1993; Roser & Korsch 1999; Pitcairn 2004). During burial and metamorphism, secondary changes to the protolith geochemistry occurred. These include solution transfer processes such as vein selvedge formation, removal of silica during cleavage development, and metamorphic recrystallization (Cox 1993; Pitcairn 2004). Finally, exhumation and alteration accompanying Alpine Fault deformation overprinted previous events (e.g., Craw & Campbell 2004; Vry et al. 2001, 2009; Farmer 2010). In addition to exhumation from c. 35 km depth (Little et al. 2005), fault rocks have experienced 100-110 km of dextral translation and brittle deformation (Cooper & Norris 2011).

Farmer (2010) both found that hanging wall cataclasites and quartz-feldspar segregations in the Gaunt Creek scarp outcrop are enriched in radiogenic $^{87}Sr/^{86}Sr$, which could have been derived from in situ dissolution of feldspars, advective transport of $^{87}Sr/^{86}Sr$ enriched fluids into the hanging wall from more radiogenic footwall granitoid protoliths, or incorporation of footwall granitoid protoliths into the hanging wall at some point in the fault's history. Because fault rocks within the fault core and damage zone are derived from multiple protoliths and have experienced multiple phases of deformation, it is difficult to ascertain the original composition of the fault rocks, the nature of fluid mobility through time, and the amount of mass gained and lost (e.g., O'Hara 1988; Ague 1994; Evans & Chester 1995).

2.5.3 Fault zone fluid sources

Abundant evidence exists for the presence of vigorous hydrothermal system and advective fluid flow at depth east of the Alpine Fault beneath the Southern Alps (Craw 1988; Koons & Craw 1991; Koons et al. 1998). Multiple factors drive the Southern Alps hydrothermal system, including elevated isotherms, steep topography, abundant rainfall (Barnes et al. 1978; Koons 1987; Koons & Craw 1991), production of overpressured metamorphic fluids

at depth (Craw & Campbell 2004; Vry et al. 2001, 2009), changes in permeability at the brittle-ductile transition (Upton et al. 1995; Vry et al. 2009), and perhaps coseismic increases in fault rock permeability accompanied by overpressured metamorphic fluid migration (Sibson 1992).

Within this system, rising rock-exchanged fluids mix with descending meteoric waters (Jenkin et al. 1994; Templeton et al. 1998; Upton et al. 1995, 2002). Meteoric waters are topographically driven downward and emerge in the fault's hanging wall as warm springs (Barnes et al. 1978; Allis & Shi 1995). Horton et al. (2003) combined stable isotope (C, O) data with radiogenic $^{87}Sr/^{86}Sr$ isotope data to suggest that young calcite veins within the high grade garnet zone adjacent to the Alpine Fault appear to have formed from meteoric fluids and/or the dissolution of plagioclase and/or feldspar. $\delta^{18}O$ stable isotope values of foliation parallel quartz veins in Alpine Fault mylonites indicate that meteoric fluids are also present in rocks at or below the brittle-to-ductile transition (Upton et al. 1995).

Horton et al. (2003) also found that low grade Alpine Schist veins were derived, at least in part, from deep metamorphic fluids released during prograde dehydration reactions. Magnetotelluric evidence for a low-resistivity anomaly at $\sim$ beneath the Southern Alps was interpreted by Wannamaker et al. (2002) to result from interconnected, overpressured, saline metamorphic fluids. Stern et al. (2007) correlated the low-resistivity anomaly with a zone of low seismic velocity (high P-wave attenuation), providing further evidence for the presence of fluids in the lower crust. More recently, Wech et al. (2012) observed tectonic tremor, often correlated with high fluid pressure (e.g., Audet et al. 2009; Peng & Gomberg 2010), along the downdip projection of the Alpine Fault at 25-45 km depth. This region coincides with the low resistivity anomaly of Wannamaker et al. (2002) and high attenuation region of Stern et al. (2007).

Overpressured, saline fluids are able to rise buoyantly through interlinked fault-fracture meshes (Sibson & Scott 1998), and geological evidence for advective fluid flow exists in horizontal veins, fractures, and vertical backshears in Alpine Schist east of the Alpine Fault (Craw 1997; Wightman & Little 2007). Within the brittle seismogenic crust, Alpine Schist is resistive and electrically isolated from lower crustal conductive fluids, which deflect sur-

faceward 5-10 km east of the Alpine Fault at about 10 km depth. However, localized fluid zones exist within the brittle schist, particularly within the hanging wall at shallow depths (< 4km) (Wannamaker et al. 2002; Menzies 2012). The extent to which fluids influence the rheology and geochemistry of the fault at depths between about 4 km and 10 km remains unknown.

Vry et al. (2001) examined altered hanging wall quartzofeldspathic mylonite exposed on an 18 km-long, thrust-dominated segment of the Alpine Fault east of Hokitika (Figure 2.1). Using C, H, and O stable isotopes together with field and petrographic observations, they showed that the fluid/rock interaction associated with chloritization occurred in the presence of schist-derived metamorphic fluid at temperatures near 450-500°C. Vry et al. (2001) correlated their results with geophysical data that suggest that fluids are concentrated below the brittle-to-ductile transition on the Alpine Fault (e.g., Wannamaker et al. 2002). The authors further suggested that since fluids responsible for chloritization are deflected towards the surface east of the fault trace, the Alpine Schist is dry and little retrogressive alteration occurs within the upper, brittle seismogenic crust. Craw & Campbell (2004) noted that amphibolite-facies Alpine Schist along strike of the central Alpine Fault are variably retrogressed under greenschist-facies conditions along fractures and foliations, yielding albite-epidote-chlorite-actinolite alteration.

The model of Alpine Fault clay alteration developed by Warr & Cox (2001) using samples collected from the Gaunt Creek scarp outcrop contrasts slightly with the results described above. Detailed XRD and Transmission Electron Microscopy (TEM) examination of clay mineralogy revealed that, in Mg-rich metabasic mylonites, cataclastic deformation at temperatures exceeding 350°C was largely anhydrous. Hydrous chloritization occurred at temperatures less than c. 320°C, followed by the formation of smectite within ultra-fine grained gouge at temperatures lower than c. 120°C (cf. Figure 2.16). Depending on the nature and timing of chloritization, as well as the local geothermal gradient, these results do not negate observations of limited fluid flow between 2-4 km and 8-10 km depth (c.f., Shi et al. 1996; Craw 1997; Toy et al. 2010; Sutherland et al. 2012). Along the central Alpine Fault, clay alteration by low temperature (30-100°C) meteoric fluids was also

documented by Johnstone et al. (1990) and Craw & Campbell (2004). X-ray diffraction data obtained in this study reveal that low temperature alteration has occurred in the ultra-fine grained Unit 5 gouges that comprise the principal slip zone(s), and these chemical reactions were governed by local redox conditions.

2.5.4 Rheological implications of fault zone fluid flow

Marking the transition from the damage zone to alteration zone, Unit 1 and 2 ultramylonites exhibit microstructures indicative of deformation by dislocation creep; retrogressed mineral assemblages in Unit 2 indicate some alteration took place in this lithology (e.g., Prior 1988; Norris & Cooper 2003, 2007; Toy et al. 2008, in prep). Within the alteration zone, brittle deformation involving cataclasis has formed Unit 3 nonfoliated cataclasites, some of which show evidence of sealing via multiple generations of carbonates, which are comparatively sparse in the Alpine Fault mylonite sequence (A. Cooper, *pers.comm.* 2012). Authigenic precipitation of clay minerals, particularly chlorite and white mica, and their subsequent shear deformation, has also resulted in the formation of networks of anastomosing phyllosilicates (Unit 4 foliated cataclasites). However, in the Unit 5 fault gouges, these foliations have been disrupted by cataclasis. Furthermore, chlorite has been altered to dioctahedral smectite in these gouges. These mineralogical and structural variations have rheological implications best understood in the context of similar natural and analog fault rocks.

Using observations of natural fault zones containing foliated gouges and cataclasites, and theoretical models of fault zone weakening by solution transfer processes, Holdsworth (2004), Jefferies et al. (2006), Imber et al. (2008) and others have argued that mature fault zones containing foliated gouges and cataclasites, similar to the Alpine Fault, have undergone both reaction- and strain-weakening, leading to faults that accommodate slip largely, but not exclusively, by aseismic creep. Fault gouges (or ultracataclasite) bounded by foliated cataclasites have been described from many inactive fault zones, including the Geesaman fault zone, Arizona, USA, exhumed from < 13 km depth (Janecke & Evans 1988), the Punchbowl Fault, California, USA, ex-

humed from 2-4 km depth (Chester et al. 1993), the Median Tectonic Line, Japan, exhumed from 5-10 km depth (Jefferies et al. 2006), and the Zuccale Fault, exhumed from < 8 km depth (Collettini & Holdsworth 2004; Smith et al. 2011). From detailed microstructural observations, these authors determined that brecciation and/or cataclasis of fault zone protolith(s) created fluid migration pathways. Fluid-assisted hydration reactions then formed phyllosilicate minerals (cf. Janecke & Evans 1988 Figure 1). When the phyllosilicate minerals form an interconnected matrix or fabric with a preferred orientation of (001) parallel to the shearing direction, frictional sliding can occur at low resolved shear stresses because of weak (001) interlayer bond strengths and/or adsorbed water films (e.g., Moore & Lockner 2004; Collettini et al. 2009; Tembe et al. 2009; Niemeijer et al. 2011).

At higher temperatures and pressures, at depths of 3 to 15 km including the brittle-to-ductile transition, strain-rate and grain-size dependent diffusion-assisted pressure solution creep (also termed "grain size sensitive creep") may also operate in foliated fault rocks containing an insoluble (e.g., phyllosilicate) and soluble (e.g., quartz) mineral phase (e.g., Sibson 1977a; Chester & Higgs 1992; Bos & Spiers 2002; Hickman & Evans 1995). Microphysical models of this mechanism predict the shear strength of foliated fault rocks, such as the Unit 4 foliated cataclasites, is governed by: resistance to shear along phyllosilicate foliations; solution transfer in rigid mineral grains; or dilation as sliding foliae are forced to overcome geometrical incompatibilities (cf. Bos & Spiers 2002 Figures 4 and 5).

Analog experiments conducted to high-strain on initially homogeneous halite-kaolinite and halite-muscovite mixtures showed that the development of a through-going phyllosilicate foliation coupled with diffusive pressure solution creep can reduce fault zone strength by 50-70% below Byerlee values ($\mu \approx 0.85$) (Bos & Spiers 2000, 2002; Niemeijer & Spiers 2005). However, this mechanism will only operate in foliated gouges and/or cataclasites at low sliding velocity when the phyllosilicate foliation is interconnected and the rate of mass removal by solution transfer (pressure solution) is fast enough to accommodate shear. Phyllosilicate foliations are disrupted at experimental sliding velocities $>$0.3-1 μm/s (equivalent strain rates $>$0.3-1 s^{-1}) (Bos & Spiers 2001; Niemeijer & Spiers 2005). At higher velocities, pressure solu-

tion of the soluble phase is too slow to accommodate volume/space changes induced by frictional sliding on the insoluble foliae, so dilation (work against normal stress) occurs and the foliation is disrupted (cf. Niemeijer & Spiers 2005 Figure 10).

The frequent juxtaposition of Unit 3 nonfoliated cataclasites and Unit 4 foliated cataclasites within DFDP drillcore may reflect deformation accommodated at various sliding velocities within these materials (Figure 2.5). However, the occurrence of recycled fault gouge clasts, relict pseudotachylyte, and enhanced alteration in the smectite-bearing Unit 5 PSZ gouges suggest that repeated slip events occurred preferentially in these materials (Figure 2.8D). Therefore, understanding the frictional properties of the Unit 5 PSZ gouges remains a primary research objective. Although there is currently no evidence aseismic creep occurs on the Alpine Fault, observations are limited to the past 50 years, a time span covering the late interseismic phase of the seismic cycle (Evison 1971; Sutherland et al. 2007; Beavan et al. 1999, 2010; Lamb & Smith 2013). It is probable that temporal variations in pore pressure, effective normal stress, shear stress, sliding velocity, and pore fluid chemistry promote the operation of mechanically diverse deformation mechanisms (e.g., Smith et al. 2011; Rowe et al. 2011).

Carpenter et al. (accepted) demonstrated that the fault-normal permeability of hanging wall materials decreases with increasing proximity to the highly impermeable Unit 5 PSZ gouges (k decreases from around 10^{-15} m^2 to 10^{-20} m^2). This appears to reflect a decrease in grain size, increase in abundance of fault parallel (or subparallel) fine-grained foliations, and/or increase in pore-infilling, fracture-sealing authigenic clay minerals and carbonate with proximity to the PSZ gouges (Sutherland et al. 2012; Townend et al. 2013; Carpenter et al. accepted; this study). Within alteration zone-fault core lithological units (Units 3-6), solution-assisted compaction might also lead to significant porosity reduction, further decreasing permeability and promoting pore fluid pressurization, which is another viable weakening mechanism (e.g., Sibson 1991; Sleep & Blanpied 1992; Wibberley & Shimamoto 2003). A time-dependent increase in pore fluid pressure within frictionally strong fault material is compatible with repeating seismic failure without the operation of intervening aseismic creep.

Temporal variations in pore fluid pressure can be visualized in the context of an earthquake cycle-model similar to the one proposed for the Alpine Fault by Warr & Cox (2001) (Figure 2.17). The creation of fractures within hanging wall and footwall lithologies during an earthquake increases permeability and promotes fluid migration within the alterations zone. While permeability is likely to increase within alteration zone and damage zone lithologies during a seismic event, high velocity sliding likely decreases PSZ gouge permeability through shear-induced compaction (Tanikawa et al. 2012). Within the alteration zone, migration of carbonate-saturated meteoric fluids in chemical disequilibrium with the rock would promote the precipitation of carbonate, phyllosilicate, and perhaps zeolite minerals, resulting in a time-dependent decrease in permeability and sealing. Coseismic increases in permeability may also facilitate down temperature (up-dip) migration of hotter fault zone fluids into the alteration zone. The net effect of enhanced fluid migration within the alteration zone is the gradual reduction in porosity and permeability within these materials through a combination of grain-scale healing and fracture sealing through precipitation (which requires advective fluid flow and infiltration) (e.g., Warr & Cox 2001; Townend et al. 2013). Thus, fault strength increases, and permeability decreases, during the interseismic phase of the earthquake cycle (Figure 2.17B).

2.5.5 Mechano-chemical lithification processes

A limitation of this model, derived from data on surface-outcrop fault rocks and supported by results from the shallow DFDP-1 boreholes, is that it does not address lithological, spatial, and temporal variations in fault zone healing rates (i.e., mechano-chemical lithification processes in Figure 2.17B). Within framework silicate-rich fault core gouges, compaction and frictional strengthening via solution-assisted mass transfer processes occurs most rapidly at temperatures ≥ 150°C on short time scales (days to weeks or months) (Renard et al. 2000; Niemeijer et al. 2002; Tenthorey & Cox 2006; Gratier et al. 2009, 2011). However, the healing mechanism in phyllosilicate-rich gouges, such as those described here in DFDP-1A and 1B, is poorly understood. In the San Andreas Fault Observatory at Depth (SAFOD), trioctahedral

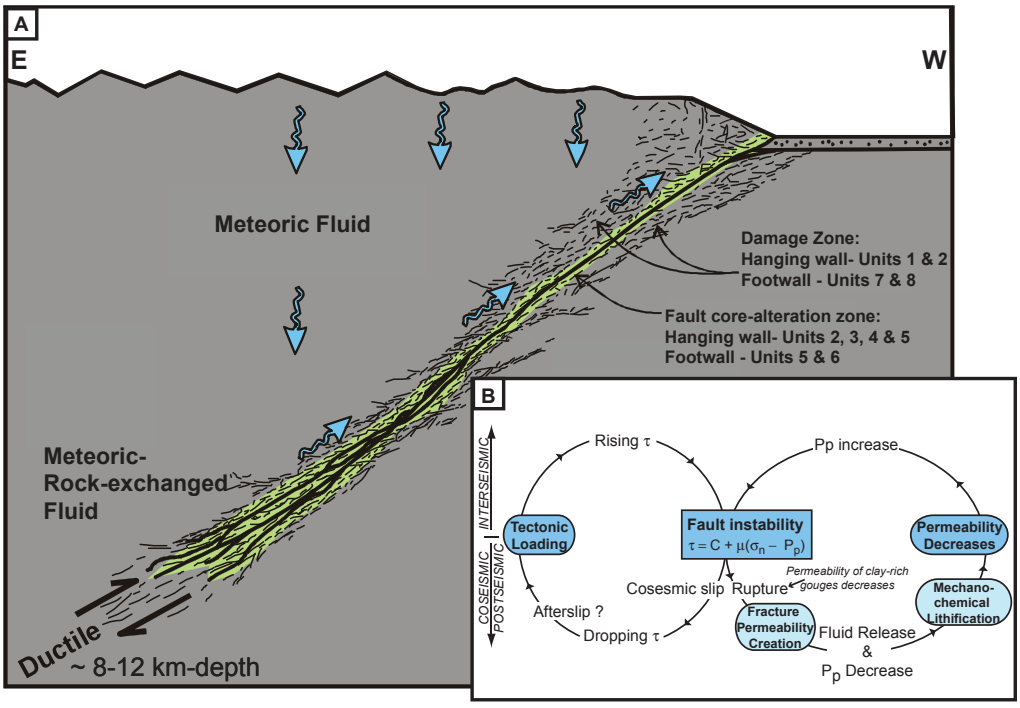

Figure 2.17: Schematic model of earthquake cycle processes occurring on the Alpine Fault at Gaunt Creek. **A,** A cross-section of Alpine Fault architecture modified from Sutherland et al. (2012) and Townend et al. (2013). There are multiple possible sources of fluid within the alteration zone, but previously published stable isotope studies suggest the dominance of meteoric and rock-exchanged fluids (see text for discussion). Lithological units comprising each portion of the fault (fault core, alteration zone, and damage zone) are given. **B,** Schematic diagram illustrating temporal changes in shear stress and pore fluid pressure during an earthquake cycle on the Alpine Fault. See text for a discussion. Diagram modified from Sibson (1992).

smectite (saponite)-rich gouges are actively creeping (Holdsworth et al. 2011; Lockner et al. 2011; Carpenter et al. 2011). Laboratory experiments on fault gouge analogues indicate that other phyllosilicate-rich gouges do not heal via solid-state (e.g., contact junction growth) or solution-assisted mass transfer (e.g., Dieterich 1978; Marone 1998; Bos & Spiers 2000; Niemeijer & Spiers 2006; Boulton et al. 2012). The products of alteration reactions observed in the cohesive smectite-bearing Unit 5 gouges present in DFDP-1A and 1B, as well as other localities along strike of the fault, are calcite and iron hydroxide. Porosity reduction via precipitation of these minerals as cement may be influential in sealing the fault core gouges in the upper c. 2-3 km of the fault.

In the highly fractured hanging wall and/or footwall rocks, healing processes also vary with depth. As with fault core gouges, fine and ultrafine grained (c. 1–10 μm-diameter) framework silicate-rich cataclasites heal rapidly via solution-transfer at temperatures $\geq$ 150°C on short time scales (e.g., Cox & Paterson 1991; Gratier et al. 2009). Larger scale (c. 0.1 – 1 mm) microfracture sealing likely only occurs at temperatures above $\sim$ 100°C (Renard et al. 1999, 2000) due to dissolution at asperity contacts, diffusion, and precipitation (Polak et al. 2003; Mizoguchi & Ueta 2013). Gratier et al. (2003) and Gratier & Gueydan (2007) modeled permeability changes in strike-slip fault zones as a function of gouge compaction, crack sealing, and fluid flow from depth (see also Faulkner & Rutter 2001; Fulton et al. 2009). Late interseismic lithostatic pore fluid overpressures occur most quickly at two different depth intervals: in the upper crust (30°C$<T<$90°C) where calcite is available for mass transfer and relatively fast sealing of veins, and at depth (150°C$<T<$300°C) due to increased quartz solubility combined with inflow of fluids from the lower crust. These models of porosity-, permeability-, and depth-dependent variations in mineralization predict lithostatic pore fluid pressure development within 270 years following an earthquake; this value is within the recurrence interval of Alpine Fault earthquakes (329$\pm$68 years) (Berryman et al. 2012a) Notably, these models depend critically on the kinetics of the involved dissolution and precipitation reactions as well as on diffusion rates which are poorly constrained under hydrothermal conditions. Depth-dependent variations in mineralization and fluid flow rates on the Alpine Fault are supported by geological, geophysical, and geochem-

ical observations (e.g., Upton et al. 1995; Wannamaker et al. 2002; Craw & Campbell 2004).

Abundant evidence exists for persistent 100 m to 1 km-thick damage zones in the shallow crust (< 3 km) (e.g., Li et al. 1990, 2000, 2004; Mitchell & Faulkner 2009; Yang et al. 2011). However, within the fault core-alteration zone at Gaunt Creek, fractures have been sealed by authigenic precipitation of calcite and phyllosilicates (Sutherland et al. 2012; Townend et al. 2013; this study). This sealing has decreased fault normal permeability, increased rock mass competency, and prompted interseismic strain buildup. Further research aimed towards understanding mass transfer processes within the fault zone is integral to underpinning the mechanisms responsible for variations in late interseismic fault zone strength (e.g., Finzi et al. 2011). To quantify the physical processes driving the seismic cycle on the Alpine Fault (e.g., Figure 2.17B), better constraints on mineral reactions, reaction rates, diffusion rates, compaction, and healing rates in the lab and in naturally deformed fault rocks are needed. In addition, geophysical and geochemical observations of fluid flux during interseismic, coseismic, and postseismic periods, are needed for numerical models that quantify how fluid migration, porosity, permeability, and rock strength evolve at depth. Incorporating permeability and fluid pressure evolution variables into empirical rate- and state-dependent constitutive laws will ultimately better constrain how fluid-rock interactions influence fault strength evolution, strain accumulation, and the timing and mode of earthquake rupture nucleation (e.g., Sibson 1992; Segall & Rice 1995; Sibson & Rowland 2003; Hillers & Miller 2007; Ben-Zion 2008; Samuelson et al. 2009).

2.6 Conclusions

1. Two shallow (100.6 m and 151.4 m) boreholes were drilled into a moderately dipping thrust segment of the Alpine Fault at Gaunt Creek, a tributary to the Waitangi-taona River.

2. A damage zone, characterized by higher than background levels of fracturing, extends from the PSZ to at least 50 m into hanging wall Unit

2 brown-green-black ultramylonites, and Unit 1 grey-green ultramylonites.

3. The true thickness of the damage zone cannot be quantified using only the interval of core recovered from the shallow boreholes (i.e., continuous core recovery in DFDP-1A and DFDP-1B only occurred across an interval < 35 m either side of the PSZ and PSZ-1, respectively).

4. The fault core-alteration zone, characterized by alteration of primary phases to phyllosilicate minerals and multiple episodes of calcite mineralization and cataclasis, extends from the PSZ up to c. 20-30 m into the hanging wall if the first documented occurrence of retrogressed mineral assemblages in the Unit 2 brown–green–black ultramylonites (quartz + plagioclase + chlorite + epidote + accessory minerals) represents the maximum extent of alteration zone processes within the fault core. In a strict sense, the Unit 6 granitoid-gneissic cataclasites also evidence cataclasis and alteration associated with fluid migration and frictional slip within the fault core-alteration zone.

5. The mineralogy and major element geochemistry of brown smectite-bearing Unit 5 PSZ gouges suggests that these units are the most highly altered rocks recovered. Alteration reactions in the Unit 5 gouges have resulted in relative enrichment in CaO and a corresponding relative depletion in SiO_2 and Al_2O_3. Major element geochemistry results largely reflect the presence of variably comminuted vein calcite and secondary calcite cement in these units.

6. Similar smectite-bearing Unit 5 PSZ gouges were collected from thrust segments of the central Alpine Fault at Little Man River, Waikukupa River, and Robinson Creek, an along-strike distance of 120 km.

7. Hanging wall Unit 3 and Unit 4 cataclasites appear to have formed from (primarily) Alpine Schist-derived metabasite and quartzofeldspathic ultramylonites (Units 1 and 2) (Cooper & Norris 1994; Toy 2007).

8. Footwall Unit 6 cataclasites formed from feldspar-plagioclase-quartz-rich granitoids and metasediments (Greenland Group and Karamea Suite protoliths; Nathan et al. 2002; Mortimer et al. 2013).

9. The origin of the Unit 7 augen-bearing mylonite breccia remains unknown; it likely correlates with Fraser Complex mylonites that crop out west of the Alpine Fault (Sibson et al. 1979; Rattenbury 1987).

10. Mass transfer processes, including local dissolution-precipitation reactions, as well as reactions driven by the infiltration of meteoric and (potentially) metamorphic or rock-exchanged hydrothermal fluids, play an important role in the observed variations in fault zone mineralogy, lithology, major element geochemistry, and petrophysical properties.

Chapter III

Physical Properties of Surface-Outcrop Cataclastic Fault Rocks, Alpine Fault, New Zealand

C. Boulton[1], B. M. Carpenter[2], V. Toy[3] and C. Marone[2]

[1] University of Canterbury, Christchurch, New Zealand

[2] Pennsylvania State University, University Park, Pennsylvania, USA

[3] University of Otago, Dunedin, New Zealand

3.1 Abstract

We present a unified analysis of physical properties of cataclastic fault rocks collected from surface exposures of the central Alpine Fault at Gaunt Creek and Waikukupa River, New Zealand. Friction experiments on fault gouge and intact samples of cataclasite were conducted at 30-33 MPa effective normal stress (σ_η') using a double-direct shear configuration and controlled pore fluid pressure in a true triaxial pressure vessel. Samples from a scarp outcrop on the southwest bank of Gaunt Creek display (1) an increase in fault normal permeability ($k = 7.45 \times 10^{-20}$ m^2 to $k = 1.15 \times 10^{-16}$ m^2), (2) a transition from frictionally weak ($\mu = 0.44$) fault gouge to frictionally strong ($\mu =$ 0.50-0.55) cataclasite, (3) a change in friction rate dependence ($a - b$) from solely velocity strengthening, to velocity strengthening and weakening, and (4) an increase in the rate of frictional healing with increasing distance from the footwall fluvioglacial gravels contact. At Gaunt Creek, alteration of the primary clay minerals chlorite and illite/muscovite to smectite, kaolinite and goethite accompanies an increase in the friction coefficient ($\mu = 0.31$ to

$\mu = 0.44$) and fault perpendicular permeability ($k = 3.10 \times 10^{-20}$ m^2 to $k = 7.45 \times 10^{-20}$ m^2). Comminution of frictionally strong ($\mu = 0.51$–0.57) cataclasites forms weaker ($\mu = 0.31 - 0.50$) foliated cataclasites and fault gouges with behaviors associated with aseismic creep at low strain rates. Combined with previously published evidence for large magnitude ($M_w \sim 8$) surface rupture events, petrological observations indicate that shear failure involved frictional sliding within previously formed, velocity-strengthening fault gouge.

3.2 Introduction

The Alpine Fault accommodates Pacific-Australian plate boundary convergence on a single northeast-southwest striking structure with a surface trace at least 800 km long and a cumulative offset of $\sim$ 460 km Wellman 1953). The central segment of the Alpine Fault, between Haast River and Toaroha River accommodates $\sim$ 70% of the 37$\pm$2 mm/yr relative motion between the plate boundaries (Sutherland et al. 2007) (Figure 3.1). Detailed field mapping within this segment shows that, in the near surface, the Alpine Fault is serially partitioned into alternating oblique thrust and strike-slip segments with average strikes ranging from 010° to 050° and 070° to 090°, respectively (Norris & Cooper 2007). Along-strike dimensions of the segments (typically $\leq$3 km) correspond to the spacing of major rivers (Norris & Cooper 1997), and the segmented structures likely merge into a single oblique structure at a depth comparable to the topographic relief ($\sim$ 1000-1500 m) (Townend et al. 2009).

Multiple lines of geological, seismological and paleoseismological evidence indicate that accumulated elastic strain on the central segment is released every few hundred years in M_w 7.5-8 earthquakes with horizontal displacements up to 8-9 m and vertical displacements up to 1.5 m (e.g., Sutherland et al. 2007 and references therein). Geodetic studies further indicate that strain release is entirely coseismic, with interseismic creep at or near zero from the surface to 13-18 km depth (Beavan et al. 2010). Extremely rapid ($\sim$ 5-10 mm/yr) exhumation along the central segment has exposed a sequence of mylonites, ultramylonites and cataclastic (brittle frictional) fault

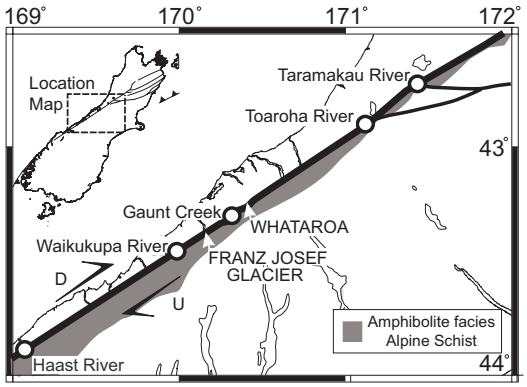

Figure 3.1: Location map for places mentioned and outcrops sampled in this study of the central segment of the Alpine Fault

rocks in the uplifted hanging wall (Little et al. 2005). Displacement on the shallowest part of this section of the Alpine Fault (< 1 km depth) is localized in a narrow zone of fault gouge and cataclasite. Outcrops of shattered, hydrothermally altered mylonites that have been thrust over Quaternary gravels yield estimates of strike-slip displacement rates of $\sim$ 25 mm/yr and dip-slip displacement rates of <10 mm/yr (Norris & Cooper 2007).

Our study combines new petrological observations with the first laboratory measurements of hydrological and frictional properties of cataclastic fault rocks exposed on oblique thrust segments of the Alpine Fault at Gaunt Creek and Waikukupa River, South Island, New Zealand (Figure 3.1). X-ray diffraction results quantify in situ and along strike changes in the mineralogy of fault gouges. Numerical constraints on the frictional and hydrological properties of the fault gouges and cataclasites also inform a discussion of the mechanisms governing earthquake rupture nucleation and propagation on this seismically active crustal-scale structure.

3.3 Surface Exposure Fault Rocks

Over the last 5-8 Myr, oblique slip on the Alpine Fault has exhumed deformed rocks from depths up to 35 km (Figure 3.1) (Little et al. 2005). Along strike, brittle-ductile fault rocks form in a near-homogeneous quartzofeldspathic Alpine Schist protolith containing small amounts of metabasite and metachert. The 1 km-thick mylonite sequence becomes progressively deformed with increasing proximity to a 10 to 50 m-thick damage zone containing fault rocks in sharp, striated, faulted contact with crushed fluvioglacial gravels (Norris & Cooper 2007). In the hanging wall, pseudotachylytes (solidified friction melts) are preserved in several settings within the mylonite-cataclasite sequence (Toy et al. 2011). The widespread occurrence of pseudotachylyte indicates that earthquakes nucleate and propagate dynamically within these rocks in the upper crustal seismogenic zone (Sibson & Toy 2006). Exposures in outcrop, trench, and borehole sections provide further evidence that earthquake ruptures propagate to the Earth's surface within a thin (< 60 cm), moderately dipping (38°-45°) plane of fine-grained fault rocks (Figure 3.2).

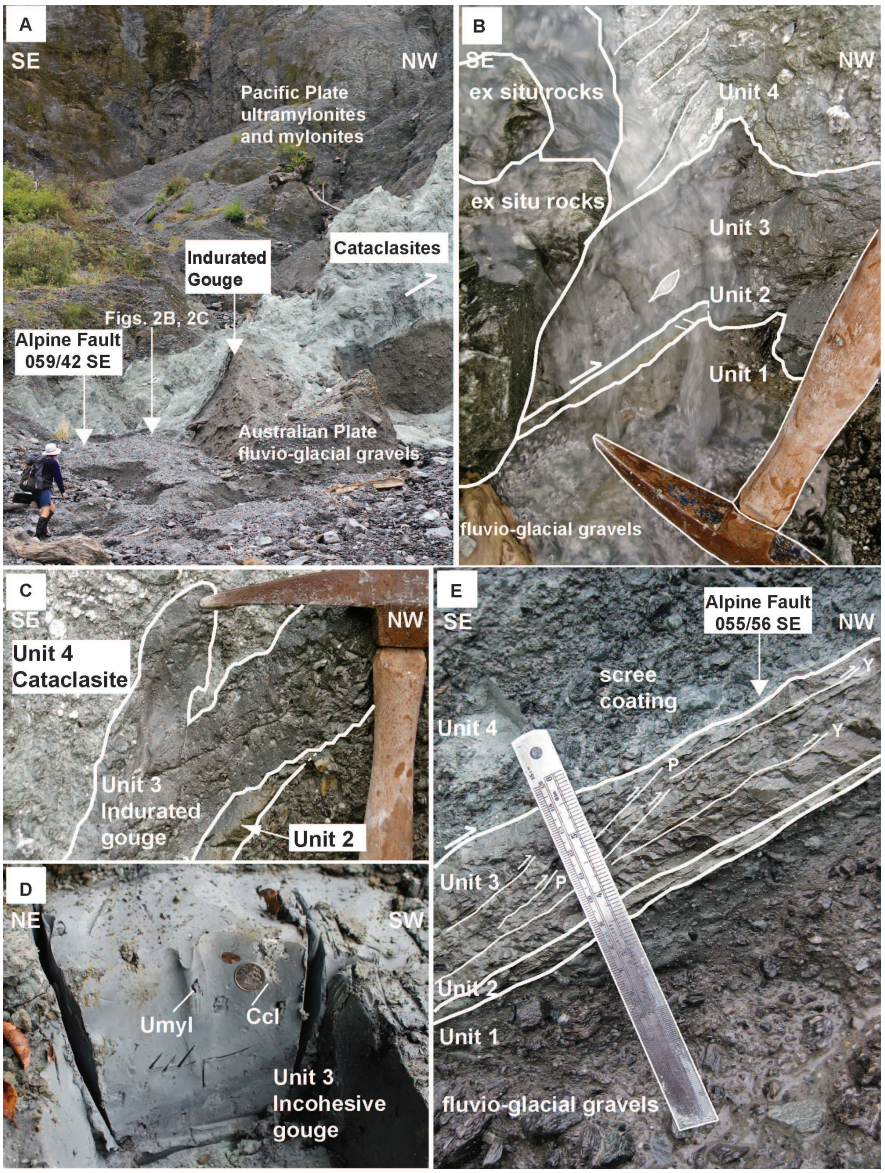

Figure 3.2: Field photographs of Alpine Fault sampling localities. **A,** At the Gaunt Creek scarp exposure, the Alpine Fault emplaces Pacific Plate mylonites over Australian Plate fluvioglacial gravels as indicated by the white arrow. Scree obscures much of the detailed structure of the outcrop. **B,** Line drawing on a photograph of a freshly scoured cataclastic fault rocks at the GC scarp exposure. The continuation of Unit 2 is obscured by an aspect change in Unit 3. Detailed descriptions of Units 1-4 are given in the text. **C,** Line drawing on a photograph of an irregular contact between Unit 3 fault gouge and into Unit 4 cataclasite, GC scarp exposure. Here, Unit 2 is truncated by Unit 3. **D,** Incohesive fault gouge with rounded black clasts of ultramylonite (Umyl) and angular, crushed clasts of pale green cataclasite (Ccl), GC terrace exposure 360 m NE of the GC scarp exposure illustrated in Figures 3.2A-3.2C. **E,** Line drawing on a photograph of the fault rock sequence exposed on the Waikukupa Thrust. Scree obscures the Unit 4 cataclasite. Y and P shears in Unit 3 are labeled. The contact between Unit 1 and the fluvioglacial gravels is gradational.

In this study, we systematically sampled rocks forming the fault core and hanging wall of a prominent, well-documented surface outcrop of the Alpine Fault on the south bank of Gaunt Creek (hereafter referred to as the GC scarp exposure) (Figure 3.2A-3.2C) (Cooper & Norris 1994; Warr & Cox 2001). We also collected fault gouge from a new exposure of the Alpine Fault located in an excavation adjacent to a terrace riser 360 m northeast of the GC scarp exposure (hereafter referred to as the GC terrace exposure) (Figure 3.2D).

At Gaunt Creek, quartzofeldspathic mylonites are thrust over fluvioglacial gravels ^{14}C dated at c. 12,650 years BP (Cooper & Norris 1994). Four general types of fault rock are found adjacent to and within the fault core; each rock type sampled contains microstructural evidence for strain localization and cataclasis sensu stricto (Figure 3.2B) (Sibson 1977a). These cataclastic fault rocks are described below, following the fault rock nomenclature of Sibson (1977a). Unit 1 is a grey-brown cataclasite derived from Quaternary alluvial gravels deposited on the Australian plate. Unit 1 varies in thickness from 0 to 40 mm, forms a gradational contact with the underlying clast-supported gravels, and contains $\geq$ 60% matrix grains (matrix grains are by definition $<$ 0.1 mm in diameter). Unit 1 is absent where cobbles or boulders form the contact with Units 2 or 3.

Unit 2 is a discontinuous gray-brown, fine-grained fault gouge that overlies and forms a sharp contact with Unit 1. In the GC scarp exposure, the contact is oriented 059°/42°SE with a prominent set of 0/059 striations overprinted by a faint 36/114 set. Unit 2 varies in thickness and color; where present, it is always less than 2 cm thick and contains $\geq$90% matrix grains. Visible grains include quartz, feldspar, carbonate, opaques and phyllosilicates set in a fine-grained matrix cemented with cryptocrystalline carbonate and amorphous iron oxide. Rare clasts include subrounded reworked fault gouge, metamorphic quartz and vein quartz. Unweathered Unit 2 gouge has a foliation defined by phyllosilicates, with uniform extinction and color viewed through the sensitive tint plate, indicating that this mineral aggregate has a crystallographic preferred orientation (Figure 3.2E). Unit 2 weathers rapidly in outcrop, becoming indurated, stained with iron oxides, and fractured by

numerous empty tension cracks. This alteration makes sampling intact wafers impractical.

Unit 3 is a grey incohesive fault gouge that weathers to a brown indurated material; it forms a sharp undulating contact with either Unit 1 or Unit 2 (Figure 3.2A-3.2D). Hand specimens and thin sections of Unit 3 display variations in grain size, with some samples containing >30% visible clasts >1mm (Figure 3.3C-3.3D). Clast long axes are tilted towards the SE with respect to the fault plane, indicating a top-to-the-northwest shear sense (Figure 3.2B). In the GC scarp exposure, Unit 3 varies in thickness between 6 cm and 8 cm and occasionally forms irregular contacts with Unit 4 (Figure 3.2C). In the terrace exposure, Unit 3 reaches a maximum thickness of 60 cm (Figure 3.2D). Because it appears continuous along strike, Unit 3 is the fault core lithology sampled and tested for permeability and frictional properties in this study.

Unit 4 is a pale green cataclasite that is foliated in places. Unit 4 cataclasite contains fractured, sometimes sericitized, feldspars and recrystallized quartz aggregates with undulose extinction and finely sutured grain boundaries, separated by a faint anastamosing foliation defined by chlorite, illite-muscovite and calcite (Figure 3.3A). The cataclasite commonly contains altered pseudotachylyte and/or ultracataclasite (e.g., Toy et al. 2011).

Near the contact with Unit 3, the lower 4-8 cm of Unit 4 contains fault plane-parallel layers of finely comminuted incohesive cataclasite up to 1 cm thick oriented 059°/50°SE with striations plunging 44/117; this lithology is referred to as the Unit 4 foliated cataclasite (Figure 3.3B). Microstructures in Unit 4 provide evidence of multiple deformation mechanisms; each deformation mechanism would have dominated at different conditions of strain rate, temperature and pressure. Unit 4 is the hanging wall damage zone lithology sampled for permeability and frictional properties in this study.

For comparison, we sampled Unit 3 fault gouge and Unit 4 cataclasite from a surface exposure of the Waikukupa Thrust located 25 km to the southeast of Gaunt Creek along strike (Figure 3.1). The Waikukupa Thrust emplaces Pacific Plate mylonites and cataclasites over Australian Plate fluvioglacial gravels older than 40,000 years BP. The Waikukupa Thrust was abandoned approximately 20,000 BP when slip was transferred to the Hare

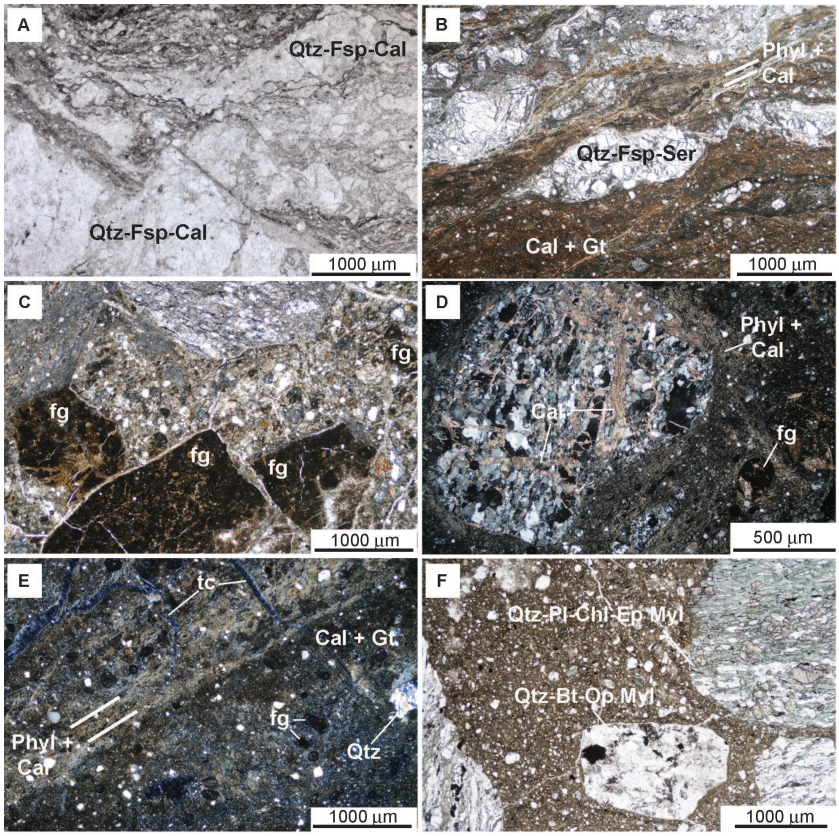

Figure 3.3: Photomicrographs of cataclastic fault rocks collected from Alpine Fault thrust segments. **A,** Unit 4 cataclasite comprising boudinaged, microcracked feldspar (Fsp)-quartz (Qtz) porphyroclasts in a matrix of comminuted quartz-feldspar plagioclase-calcite. Concentrations of opaques define a spaced but discontinuous foliation. GC scarp exposure; plane polarized light = PPL. **B,** Unit 4 foliated cataclasite with boudinaged, microcracked, sericitized feldspar porphyroclast pods (Fsp+Ser) in a matrix comprising anastomosing layers of phyllosilicates (Phyl) and fine grained gouge cemented with goethite (Gt) and calcite (Cal). Alignment of layered phyllosilicates indicated by bold white lines. GC scarp exposure; cross polarized light = XPL. **C,** Unit 3 fault gouge showing angular to rounded clasts of reworked fault gouge (dark brown material, labeled 'fg'). Other clasts are calcite-cemented mylonite fragments. GC scarp exposure; PPL. **D,** Unit 3 fault gouge with phyllosilicates mantling a clast of quartzose mylonite cut by calcite veins. Reworked fault gouge clasts are also apparent. GC terrace exposure; XPL. **E,** Incipiently altered Unit 2 fault gouge containing empty tension cracks (labeled 'tc') that cross-cut aligned phyllosilicate-rich layers oriented subparallel to the fault plane. GC scarp exposure; XPL. **F,** Unit 3 fault gouge containing clasts of weakly foliated quartz-biotite (Bt)-opaque (Op) mylonite and metabasic mylonite with a continuous foliation defined by elongate chlorite (Chl) and epidote (Ep). Waikukupa River; PPL.

Experiment	Lithology	Mineralogy[a]
n/a	Gaunt Creek Scarp U2 Gouge	Quartz 25%, Orthoclase 5%, Albite 20%, Calcite 5%, Illite-Muscovite 16%, Smectite 14%, Kaolinite 7%, Lizardite 9%
p2798, p2862	Gaunt Creek Scarp U3 Gouge	Quartz 30%, Orthoclase 6%, Albite 26%, Calcite 7%, Mg-Calcite 1%, Illite-Muscovite 17%, Smectite 7%, Kaolinite 6%
p3151	Gaunt Creek Scarp U4 Fol. Cataclasite[b]	Quartz 9%, Orthoclase 3%, Albite 27%, Calcite 2%, Illite-Muscovite 16%, Smectite 36%, Chlorite 2%, Kaolinite 4%
p2799, p2863	Gaunt Creek Scarp U4 Cataclasite	Quartz 49%, Orthoclase 10%, Albite 19%, Calcite 2%, Illite-Muscovite 10%, Chlorite 8%
p3370	Gaunt Creek Terrace U3 Gouge	Quartz 35%, Orthoclase <1%, Albite 17%, Calcite 6%, Illite-Muscovite 32%, Chlorite 9%
n/a	Waikukupa River U2 Gouge	Quartz 27%, Orthoclase 1%, Albite 19%, Calcite 17%, Illite-Muscovite 17%, Smectite 16%, Chlorite 2%, Pyrite <1%
p2830	Waikukupa River U3 Gouge	Quartz 28%, Albite 26%, Calcite 25%, Illite-Muscovite 14%, Chlorite 5%, Actinolite 2%, Pyrite <1%
p2828	Waikukupa River U4 Cataclasite	Quartz 35%, Albite 33%, Calcite 6%, Mg-Calcite 1%, Illite-Muscovite 6%, Chlorite 19%, Pyrite <1%, Laumontite <1%

Table 3.1: Summary of surface-outcrop Alpine Fault rock mineralogy. Superscripts denote: ([a]) results are normalized to 100% and do not include estimates of unidentified or amorphous materials; ([b]) data are from the <2 μm fraction only.

Mare imbricate thrust (Norris & Cooper 1997). Where sampled, Waikukupa Thrust Unit 3 is an 8-cm thick, reverse graded fault gouge oriented 055°/56°SE; the fault gouge forms a sharp contact with underlying footwall gravels with striations plunging 15/066 and (Figure 3.2E). Clasts within the Unit 3 fault gouge include unaltered to retrogressed quartzofeldspathic and metabasic mylonite set in a fine-grained matrix if quartz, feldspar, albite, chloritized biotite and amphibole, sericitized feldspar, epidote, titanite, and calcite (Figure 3.3F). Unit 4 is a cataclasite with mylonite clasts that have been subject to in situ fragmentation, translation and rotation in a matrix of comminuted quartz, feldspar, illite-muscovite, chlorite, calcite and pyrite.

3.4 Analytical Methods

For quantitative X-ray diffraction (XRD), approximately 1.5g of each oven-dried sample was ground for 10 minutes in a McCrone micronizing mill under ethanol. The resulting slurries were oven dried at 60°C, thoroughly mixed with an agate mortar and pestle, and lightly back pressed into stainless steel sample holders. XRD patterns were recorded in steps of 0.017° 2θ on a PANalytical X'Pert Pro Multi-purpose Diffractometer using Fe-filtered Co Kα radiation, variable divergence slit, 1° anti-scatter slit and fast X'Celerator Si strip detector. Quantitative analysis was performed using the commercial package SIROQUANT from Sietronics Pty Ltd. Smectite identification was done using XRD patterns obtained from oriented slides of Mg-saturated, glycerolated < 2 μm clay separates. Results are listed in Table 3.2.

Experiment	Lithology	σ_n' (MPa)	P_c (MPa)	P_p (MPa)	k m^2	μ
p2798	Gaunt Creek Scarp U3 Gouge	31	25	10	7.45 E-20	0.44
p2862	Gaunt Creek Scarp U3 Gouge[a]	33	25	10	n/a	0.57
p3151	Gaunt Creek U4 Scarp Fol. Cataclasite	31	25	10	1.41 E-18	0.50
p2799	Gaunt Creek Scarp U4 Cataclasite	30	25	10	1.15 E-16	0.51
p2863	Gaunt Creek Scarp U4 Cataclasite	30	25	10	n/a	0.55
p3370	Gaunt Creek Terrace U3 Gouge	31	25	10	3.10 E-20	0.31
p2800	Waikukupa River U3 Gouge	31	25	10	1.71 E-20	0.39
p2830	Waikukupa River U3 Gouge	31	25	10	1.16 E-20	0.41
p2801	Waikukupa River U4 Cataclasite	30	25	10	1.45 E-17	0.54
p2828	Waikukupa River U4 Cataclasite	30	25	10	1.23 E-16	0.57

Table 3.2: Summary of experiment details and results. Symbols are: (σ_n') effective normal stress in MPa, calculated from the combined effects of applied normal load, confining pressure, and pore pressure; (P_c) confining pressure in MPa; (P_p) pore pressure in MPa; (k) permeability in m^2; (μ) steady-state coefficient of friction. Superscripts denote: ([a]) Experiment p2862 was done on a powdered sample.

3.5 Experimental Methods

Large blocks of fault core gouges (Unit 3) and adjacent hanging wall cataclasites (Unit 4) were collected from the outcrop using a portable rock saw. These blocks were cut into wafers 6-8 mm thick, 54 mm wide, and 61 mm long; the wafer long axis was cut parallel to the fault shear direction as indicated by striation measurements. A total of 10 double-direct shear friction experiments were conducted on Gaunt Creek and Waikukupa Thrust fault rocks (Figure 3.1) (Table 3.2).

We deformed fault rock samples in a servo-hydraulic controlled biaxial testing apparatus fitted with a pressure vessel (Samuelson et al. 2009; Ikari et al. 2011b). We sheared all samples under saturated, drained conditions at room temperature. We held effective normal stress (σ_n'), confining pressure (P_c), and pore pressure (P_p) constant at $\sim$ 31 MPa, 25 MPa, and 10 MPa, respectively (Table 3.2). These variables are geologically reasonable if we assume hydrostatic pore fluid pressure, an effective normal stress appropriate for 1 km depth on an oblique thrust fault striking NW-SE, and a stress tensor with $\sigma_1 = 45$ MPa, $\sigma_v = \sigma_2 = \sigma_3 = 25$ MPa. Along the Alpine Fault, the maximum compressive stress (σ_1) is subhorizontal trending 120° and the least principal stress (σ_3) is subhorizontal trending 030°, with some local variance

between $\sigma_v = \sigma_2$ and $\sigma_v = \sigma_3$ expected for a combination of strike-slip and reverse faulting (Leitner et al. 2001).

Flow-through permeability tests were conducted prior to shearing intact wafers of fault rock. In each experiment, two wafers were placed between a three-piece steel block assembly fitted with porous, stainless steel frits and then jacketed (see Samuelson et al. 2009) for a complete description of the experimental apparatus and methods). In the pressure vessel, normal (σ_n), confining (P_c), and pore fluid (P_p) pressures were applied to the sample, resulting in a true triaxial stress state. Pore fluid (University Park, Pennsylvania, USA tapwater with pH = 7 and total cation concentration $\left(\mathrm{Ca}_2^+ + \mathrm{Mg}_2^+\right)$= 2-4 mmol/L) was plumbed directly into the fault rock samples and allowed to equilibrate until steady state boundary conditions were reached. We imposed a differential fluid pressure to induce flow normal to the shear direction of the intact wafers. When flow rate reached steady state, permeability was calculated using Darcy's law.

In the double-direct shear configuration, fault rock samples are sheared by driving the center block with a servo controlled vertical piston at a constant displacement rate to attain steady state frictional behavior (Figure 3.4A). At steady state, the coefficient of sliding friction μ was determined from the ratio of shear stress τ to effective normal stress σ_n' assuming cohesion of zero. We then performed velocity step tests (Figure 3.4B) to determine the rate and state dependence of friction. Load point velocity was varied between 1 and 100 µm/s, and in some cases 300 µm/s, to measure the friction rate parameter $(a - b) = \frac{\Delta\mu}{\Delta \ln V}$ where a is the direct effect, b is the evolution effect, $\Delta\mu$ is the change in steady state sliding friction and V is the sliding velocity (e.g., Marone 1998) (Figure 3.4b). We also carried out a series of slide-hold-slide tests to measure the frictional healing rate. In these tests, the load point was driven at 10 μm/s, held motionless for a prescribed time, t, between 1 and 300s and then driven at 10 μm/s again. Frictional healing $\Delta\mu$ is the difference in peak friction, following a hold, relative to the steady-state sliding friction prior to the hold. The healing rate is the change in $\Delta\mu$ per factor of 10 change in hold time measured in seconds (Figure 3.4C).

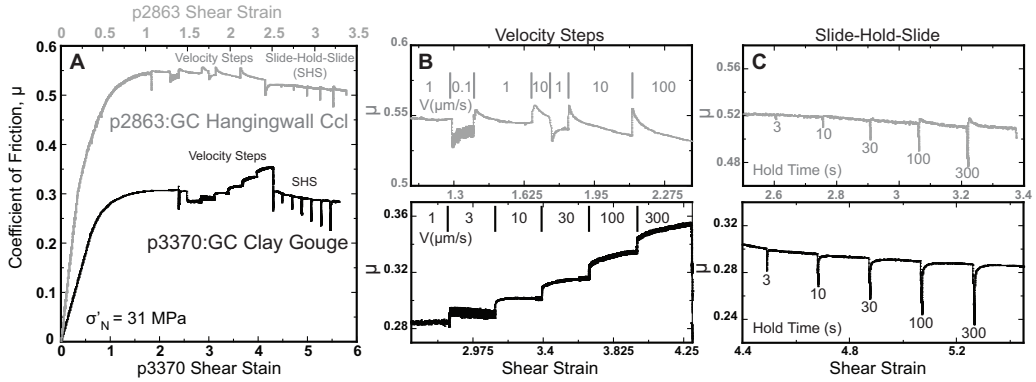

Figure 3.4: **A,** Plot of coefficient of friction ($\mu = \frac{\tau}{\sigma_{n'}}$) vs. strain for a double direct shear experiments on GC scarp exposure Unit 4 hangingwall cataclasite (ccl) and GC terrace exposure Unit 3 fault gouge. After measuring the friction coefficient at steady-state sliding, **B,** velocity step tests were performed and **C,** slide-hold-slide tests were performed. Measurement accuracy is ± 0.002 MPa for load and ± 0.1 μm for displacement.

3.6 Results

3.6.1 Permeability

All permeability measurements were made on intact wafers of cataclastic fault rocks at effective normal stresses between 30 and 31 MPa. The fault perpendicular permeability of Unit 3 fault gouges varies between $k = 1.16 \times 10^{-20}$ m^2 and $k = 7.45 \times 10^{-20}$ m^2 (Table 3.2); these values are typical value for natural and experimental fault gouges (e.g., Faulkner & Rutter 2000, 2001). The fault perpendicular permeability of Unit 4 is almost 3 orders of magnitude greater than Unit 3, increasing from from $k = 1.41 \times 10^{-18}$ m^2 in the Gaunt Creek Unit 4 foliated cataclasite to $k = 1.15 \times 10^{-17}$ m^2 in Gaunt Creek Unit 4 cataclasite and $k = 1.23 \times 10^{-16}$ m^2 and $k = 1.45 \times 10^{-17}$ m^2 in Waikukupa Thrust Unit 4 cataclasites. This increase in permeability corresponds with a decreasing abundance of phyllosilicate layers and an overall increase in mean grain size (Figures 3.2 and 3.3). These results are consistent with measurements on similar fault rocks collected from the Nojima Fault Zone (Lockner et al. 2000) and Median Tectonic Line in Japan (Wibberley & Shimamoto 2003).

3.6.2 Friction

Values of steady-state sliding friction coefficients for fault core (Unit 3) and hanging wall cataclasites (Unit 4) range from $\mu = 0.31$ to 0.57 (Table 3.2 and Figure 3.5A). The Unit 3 fault gouges are the weakest, with μ =0.31 and μ =0.44 for intact wafers of fault gouge collected from the GC terrace and GC scarp exposures, respectively. The measured friction coefficients of Waikukupa Thrust fault gouge, μ =0.39 and μ =0.41, lie within this range. Hanging wall cataclasites are stronger, with intact wafers of Unit 4 foliated cataclasite having a μ =0.50. Intact wafers of Gaunt Creek and Waikukupa Thrust cataclasites have friction coefficients of μ =0.51 - 0.55 and μ =0.54 - 0.57, respectively. The powdered sample of Gaunt Creek Unit 3 has a higher friction coefficient, μ =0.57, than its wafer equivalent, which is consistent with recent experiments showing that phyllosilicate-rich rocks are generally stronger in powder form (Collettini et al. 2009; Ikari et al. 2011b).

3.6.3 Friction rate dependence

We performed velocity step tests in six experiments to determine rate/state friction constitutive parameters (Figure 3.4B). This parameterization is useful for inferring whether shear will be stable or unstable under conditions of tectonic faulting (e.g., Marone 1998). The friction rate parameter, a–b, describes the variation in steady sliding friction with slip velocity. Materials are said to be velocity strengthening if a–$b > 0$; these materials tend to slide stably, accommodating strain aseismically. Materials exhibiting negative a–b values are termed velocity-weakening; these materials may undergo a frictional instability that results in earthquake nucleation and seismic rupture propagation (Scholz 2002).

Results from velocity step tests are summarized in Figure 3.5B. Jacket failure precluded measuring the friction rate parameters and frictional healing rates of intact wafers of Unit 3 from the GC scarp exposure; a powdered sample of Unit 3 from that locality exhibited velocity-strengthening behavior (a–b = 0.00012–0.0016). Unit 3 fault gouges collected from the GC terrace exposure and Waikukupa Thrust displayed clear velocity-strengthening behavior (a–$b = 0.0052 - 0.018$) (Figures 3.4B and 3.5B). Gaunt Creek Unit

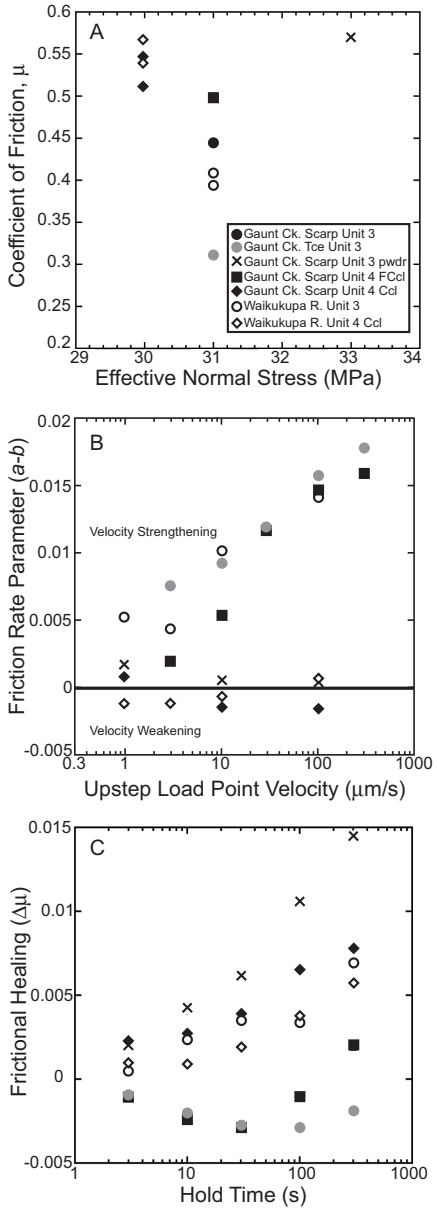

Figure 3.5: Summary plots of the frictional properties of Alpine Fault cataclastic fault rocks. **A,** A plot of coefficient of friction ($\mu = \frac{\tau}{\sigma_n'}$) against effective normal stress σ_n'. **B,** Friction rate parameter (a–b) is plotted against the upstep load point velocity V (μm/s). **C,** Frictional healing rates are plotted as the change in the coefficient of friction ($\Delta\mu$) as a function of hold time (t). Symbols given in the legend of Figure 3.4A are valid for all plots. Abbreviations are: foliated cataclasite (Fccl), cataclasite (Ccl), powder (pwdr), GC terrace exposure (Tce), GC scarp exposure (Scarp), R (River).

4 foliated cataclasite also exhibited velocity-strengthening behavior (a–b = $0.0019 - 0.016$). These units also show strong positive $a - b$ rate dependence, a behavior observed in other clay gouges (e.g., Ikari et al. 2011a).

Intact wafers of Unit 4 cataclasites displayed a range of $a - b$ values, depending on the magnitude of the velocity perturbation. Values of a–b for the cataclasites range between -0.0016 and 0.00082. We observe no systematic relationship between the size of the velocity perturbation and the value of a–b in the cataclasites (Figure 3.5B). Other frictionally strong gouges ($\mu \geq 0.50$) commonly exhibit both velocity-strengthening and velocity-weakening behavior in velocity step experiments (e.g., Ikari et al. 2011a).

3.6.4 Frictional healing

Frictional strength varies with the real area of contact. Under stationary conditions, asperity contacts can heal with time, increasing the likelihood of unstable frictional sliding in some materials (Marone 1998; Scholz 2002). Slide-hold-slide tests were performed to measure the rate of frictional healing (Figure 3.4C). As in the velocity step experiments, data on GC scarp exposure Unit 3 are from gouge powder, which healed at a faster rate than intact wafers of all lithologies (Figure 3.5C).

Intact wafers of GC terrace exposure Unit 3 and GC scarp exposure Unit 4 foliated cataclasite weakened with hold time for all hold times between $t = 3$ s and $t = 100$ s (Figures 3.4C and 3.5C). The gouge layers have very low permeabilities, and consolidation during hold time may have resulted in elevated pore fluid pressures and thus lower friction coefficients (e.g., Byerlee 1993; Faulkner & Rutter 2001). However, we observe no systematic correlation between hold time and frictional healing across the range of hold times imposed. The results of the GC terrace exposure Unit 3 experiment are discussed futher below.

GC scarp exposure Unit 4 nonfoliated cataclasite, Waikukupa Thrust Unit 3 fault gouge, and Waikukupa Thrust Unit 4 cataclasite all showed a positive correlation between hold time and $\Delta\mu$ (Figure 3.5C). This behavior is consistent with mechanistic interpretations of healing in rocks composed of framework silicates, where the real area of contact increases with time

because of contact junction growth and/or strengthening (Dieterich 1978; Marone 1998).

3.7 Discussion

Along thrust segments at Gaunt Creek and Waikukupa River, the east dipping Alpine Fault plane is overlain by 10–50 m of cataclasite comprising comminuted clasts of quartzofeldspathic and metabasic mylonites in a finely comminuted clay-rich chloritized matrix. Near the striated basal contact with footwall fluvioglacial gravels, strain localization in the hangingwall has resulted in further grain size reduction and fault gouge formation. In places, mechanically aligned phyllosilicates form a planar fabric oriented subparallel to the fault plane (e.g., Figure 3.3E).

Quantitative X-ray diffraction analyses indicate that strain localization and grain size reduction was accompanied by changes in the nature and abundance of phyllosilicate phases at the Gaunt Creek localities (Table 3.1). At the GC scarp exposure, fault gouges comprising Units 2 and 3 contain a high percentage of clay minerals (57-60%) relative to Unit 4 cataclasite (20%). Unit 4 cataclasite contains higher temperature clay minerals chlorite (clinochlore-1MIIb) and muscovite (2M1). Unit 3, however, contains the lower temperature clay minerals smectite (montmorillonite) and kaolinite as well as chlorite (clinochlore-1MIIb) (e.g., Moore & Reynolds 1997). Based on mineralogy, microstructures and grain size, the Unit 4 foliated cataclasite contains components of both the cataclasite and fault gouge (Table 3.1) (Figure 3.3B). Basal Unit 2 gouges contain predominantly lower temperature phyllosilicates, with the exception of lizardite (1M) at the GC scarp exposure (Table 3.1). The origin of lizardite (1M) is unknown; it is possible this mineral was derived from footwall gravels or a protolith present downdip or along-strike.

Hand specimen and thin section identification of relict clasts in the fault gouges and cataclasites, along with X-ray diffraction analysis, indicate that comminution of hanging wall mylonites and protocataclasites formed the granulated cataclasites and gouges analysed in this study. By an analysis of garnet fragments in cataclasites, (Cooper & Norris 1994) reached the same

conclusion, but they could not discount a contribution from footwall granitoids at depth. Most mylonite hanging wall rocks are quartzofeldspathic, composed of the primary minerals: quartz, plagioclase, muscovite, and biotite with minor amounts of garnet, ilmenite and calcite. Metabasic mylonites contain amphibole, as reflected in the mineralogy of the Waikukupa Thrust samples (Toy et al. 2010).

In addition to primary minerals, GC exposure fault gouges and foliated cataclasite fault gouges contain kaolinite and the weak dioctahedral clay mineral smectite ($\mu = 0.15-0.32$) (Saffer & Marone 2003). Warr & Cox (2001) found that smectite forms from low temperature alteration in Alpine Fault mylonite-derived cataclasites and gouges. Smectite can form from low temperature alteration (< 120°C) of the primary minerals illite/muscovite and chlorite. In our samples, smectite occurrence coincides with chlorite depletion relative to adjacent hangingwall cataclasites. Oxidized alteration of chlorite forms smectite, which further alters into kaolinite and amorphous iron oxide (goethite) (e.g., Craw 1984; Chamberlain et al. 1999); these minerals are all present in Units 2, 3 and 4 on the GC scarp exposure. Warr & Cox (2001) suggested that the growth of smectite leads to mechanical weakening in Alpine Fault gouges, but its association with secondary cement strengthens the GC scarp exposure fault gouge ($\mu = 0.44$) relative to the GC terrace exposure fault gouge ($\mu = 0.31$).

GC terrace exposure Unit 3, GC scarp exposure Unit 4 cataclasite, Waikukupa Thrust Unit 3 fault gouge and Waikukupa Thrust Unit 4 cataclasite contain the primary mineral phases quartz, albite $\pm$ orthoclase, calcite, illite-muscovite (2M1), and chlorite (clinochlore 1MIIB). These minerals are likely to remain stable to sub-greenschist conditions (< 320°C) near the base of the brittle seismogenic zone (Warr & Cox 2001). Using a geothermal gradient of 40°C/km, this equates to a depth of 8 km on the Alpine Fault (Toy et al. 2010). At effective normal stresses > 60 MPa, however, clay-rich gouge behavior becomes increasingly nonlinear, and pressure solution creep may compete with friction to accommodate grain sliding in clay-rich gouges containing a soluble mineral phase such as quartz or calcite (e.g., Rutter 1983; Bos & Spiers 2002; Niemeijer & Spiers 2007; Gratier et al. 2009). Whether deformation is accommodated in the gouges via frictional sliding and cataclasis

or pressure solution creep depends on many factors, foremost temperature and magnitude of differential stress resolved on the Alpine Fault (Rutter 1976; Cox & Etheridge 1989; Gratier et al. 2009).

Our experiments were conducted at room temperature on saturated fault gouges loaded at effective normal stresses $\sim$ 30 MPa and loading rates between 1 and 300 µm/s. At these conditions, clay-rich Unit 3 fault gouges are frictionally weak, exhibit velocity-strengthening frictional behavior, and do not undergo frictional healing. The weak ($\mu = 0.31$), velocity-strengthening (a–$b = 0.0075 - 0.016$), nonhealing ($\Delta\mu$ = -0.003 after t =100 s) properties of the GC terrace exposure Unit 3 gouge (illite-muscovite 32%; chlorite 9%) best represents the frictional behavior of clay-rich fault gouges at depth.

Figure 3.4A illustrates that the GC terrace exposure Unit 3 fault gouge did not display peak friction. Experimental observations indicate that aligned layers of chlorite (chlinochlore-1MIIb) and illite-muscovite (2M1) facilitated strain accommodation during the early stages of shearing, suppressing peak strength (Saffer & Marone 2003). At higher strains during the slide-hold-slide tests, little or no contact strengthening occurred in these aligned clay grains, and we observed no frictional healing with hold time (e.g., Bos & Spiers 2000).

An additional factor influencing peak strength and frictional healing is dilation. Dilation is a physical response to shear-induced strain localization observed in many granular materials. By increasing the thickness of the shearing granular layer, dilation increases effective normal stress, decreases pore fluid pressures, and suppresses frictional instabilities. The lack of frictional healing in the GC terrace exposure and Waikukupa Thrust Unit 3 fault gouges suggest that aligned clay layers do not exhibit classical healing behavior governed by a combination of frictional strengthening during the hold and dilatancy-strengthening upon reshear. These units have very low permeabilities, and time-dependent compaction may result in high pore fluid pressures and undrained loading (Lockner & Byerlee 1994; Garagash & Rudnicki 2003; Faulkner et al. 2011; Schmitt et al. 2011).

Unit 3 fault gouges exhibit velocity-strengthening behavior, a frictional property that promotes stable (aseismic) sliding, inhibits earthquake rupture nucleation, and may contribute to earthquake rupture arrest at shallow

depths (3 km) (Marone 1998). However, paleoseismological, geomorphological and geodetic evidence suggests that the Alpine Fault fails coseismically in large earthquakes, forming surface ruptures with an average slip per event of $\sim$ 8 m dextrally and $\sim$ 1 m vertically (Sutherland et al. 2007).

Along the Alpine Fault, the upper stability transition, which defines the updip-limit of the seismogenic zone, is either too shallow to arrest seismic rupture propagating from below, or the upper, stable region is not sufficiently velocity-strengthening to arrest rupture (Marone 1998). Alternatively, theoretical considerations, numerical modeling and high velocity rock friction experiments show that rapid undrained loading in low-permeability fault gouge results in thermal pressurization of pore fluids at slip rates greater than 0.1 m/s and displacements on the order of a few microns (e.g., Sibson 1973; Lachenbruch 1980; Rice 2006).

Sufficient shear heating can induce thermal pressurization, a weakening mechanism that operates before seismic slip speeds are obtained (Schmitt et al. 2011). Faulkner et al. (2011) presented experimental data on saturated clay-rich gouges sheared in a high-velocity rotary apparatus at low normal stress (1.63 MPa) and high slip velocity (1.3 m/s). They attributed the immediate frictional weakening to rapid thermal pressurization of the pore fluid, which resulted in a negligible critical slip weakening distance and fracture energy. A rapid loss of strength at the tip of an earthquake rupture may make propagation through clay-rich gouges energetically favorable (e.g., Tinti et al. 2005; Bizarri & Cocco 2006a,b). As slip speeds grow to within a few orders of magnitude of elastic wave speeds, however, additional factors contribute to the physics of earthquake propagation through velocity-strengthening material, including elastically radiated energy, fracture energy, and poromechanical effects (Rice 1993; Lapusta et al. 2000; Perfettini & Ampuero 2008).

The inclusion of reworked clasts of fault gouge and hangin wall cataclasites in Unit 3 fault gouges indicates that large magnitude surface ruptures on the Alpine Fault have occurred repeatedly within the same fault core (Figure 3.3). Local pore fluid overpressures are indicated by the irregular contacts between Unit 3 fault gouge and Unit 4 cataclasite at the GC scarp exposure (Figure 3.2c). Questions remain, however, about whether these

irregular contacts formed interseismically by creep, compaction, and pore fluid pressurization in the impermeable, clay-rich gouge or coseismically as gouge injection structures formed by shear-induced thermal pressurization (e.g., Cowan 1999; Meneghini et al. 2010; Lin 2011).

3.8 Conclusions

Oblique thrust fault segments of the Alpine Fault form surface outcrops at Gaunt Creek and Waikukupa River. Samples of cataclastic fault rocks were collected and investigated using a double-direct shear friction configuration under controlled pore pressure. At effective normal stresses between 30 and 31 MPa, fault core gouges have fault normal permeabilities up to 3 orders of magnitude lower than hanging wall cataclasites (Table 3.2). Fault core gouges are velocity strengthening and have lower friction coefficients ($\mu = 0.31-0.44$) than hanging wall cataclasites. Cataclasites are frictionally strong ($\mu = 0.50 - 0.57$), exhibit normal to high rates of frictional healing, and display both velocity-strengthening and velocity-weakening behaviors. These results support general models of mature fault cores as weak with respect to the surrounding crust (e.g., Rice & Cocco 2006; Carpenter et al. 2011).

Current geodetic estimates indicate that the Alpine Fault is locked to a depth of 13-18 km, and total elastic strain accumulation is released in large magnitude (M_w 7.5-8) earthquakes that propagate along-strike distances between 300 and 600 km (Beavan et al. 2010; Sutherland et al. 2007). Petrological observations of clasts of reworked fault gouge in fault core rocks sampled in this study reveal that earthquake ruptures preferentially propagate through velocity-strengthening fault gouges exposed in surface outcrops at Gaunt Creek and Waikukupa River. Understanding the mechanisms facilitating earthquake rupture propagation through clay-rich gouges remains an important goal in rock mechanics and earthquake physics.

3.9 Acknowledgements

The first author received support for this research from the Claude McCarthy Foundation and the University of Canterbury Roper Scholarship. We would like to thank to Sam Haines for doing preliminary X-ray diffraction analyses

and Mark Raven, CSIRO, Australia for doing more detailed, quantitative analyses. Greg De Pascale discovered the Alpine Fault terrace exposure at Gaunt Creek. The laboratory work was supported by by NSF grants OCE-0648331, EAR-0746192, and EAR-0950517 to C. Marone. Reviews by Dan Faulkner and an anonymous reviewer greatly improved the quality of this manuscript.

Chapter IV

Slip Localization on the Southern Alpine Fault, New Zealand

N.C. Barth[1], C. Boulton[2], B.M. Carpenter[3], G.E. Batt[4], and V.G. Toy[1]

[1] University of Otago, Dunedin, New Zealand

[2] University of Canterbury, Christchurch, New Zealand

[3] Pennsylvania State University, University Park, Pennsylvania, USA

[4] The University of Western Australia, Western Australia, Australia

4.1 Abstract

Results of a detailed field study of the southern onshore portion of New Zealand's Alpine Fault reveal that for 75 km along-strike, dextral-normal slip on this long-lived structure is highly localized in phyllosilicate-rich fault core gouges and along their contact with more competent rocks. At three localities (Martyr River, McKenzie Creek, Hokuri Creek), we document complete cross sections through the fault. New $^{40}Ar/^{39}Ar$ dates on mylonites, combined with microstructural and mechanical data on phyllosilicate-rich fault core gouges show that modern slip is localized onto a single, steeply-dipping 1 to 12 m-thick fault core composed of impermeable ($k = 10^{-20}$ to 10^{-22} m^2), frictionally weak ($\mu = 0.12 - 0.37$), velocity-strengthening, illite-chlorite and saponite-chlorite-lizardite fault gouges. Fault core materials are (1) comparable to those of other major weak-cored faults (e.g., San Andreas Fault), and (2) most compatible with fault creep, despite paleoseismic evidence of

quasi-periodic large magnitude earthquakes ($M_w > 7$) on this portion of the Alpine Fault. We conclude that frictional properties of gouges at the surface do not characterize the overall seismogenic behavior of the southern Alpine Fault.

4.2 Introduction

A primary objective of earthquake science research remains understanding the factors that influence variations in seismological behavior, and achieving this objective requires integrating data on the structure and mechanical behavior of faults (e.g., Segall 2012; Noda & Lapusta 2013). Because of their relatively large fault plane area and geometrical simplicity, large-displacement, crustal-scale faults represent globally significant seismic hazards. On these structures, strain is thought to localize as quasi-static and/or dynamic wear processes in the brittle crust gradually eliminate structural complexity with increasing displacement (Segall & Pollard 1983; Wesnousky 1988; Ben-Zion & Sammis 2003; Biegel & Sammis 2004). At all crustal depths, including below the brittle-ductile transition, these processes are accompanied by strain softening through grain size reduction, recrystallization, reaction softening, alignment of weak material components forming a pervasive fabric, shear zone coalescence and shear heating (Wintsch et al. 1995; Goodwin & Wenk 1995; Handy & Brun 2004; Holdsworth 2004; Jefferies et al. 2006).

With a remarkably straight surface trace striking northeast-southwest for over 800 km, and a cumulative displacement of > 460km, the Alpine Fault is a continental transform fault that accommodates about 70 percent of the relative motion between the Australian (AUS) and Pacific (PAC) plates in the central South Island of New Zealand (Cooper & Kostro 2006). It represents both a mature crustal-scale plate boundary fault and the largest onshore seismic hazard in New Zealand (Sutherland et al. 2007). Since c. 45 Ma, relative plate boundary motion has resulted in various modes of deformation accommodated by faulting through the New Zealand continent (i.e., Zealandia), beginning with asymmetric rifting in the late Eocene (c. 45-35 Ma), followed by transtension from the late Eocene to Oligocene (c. 35-25 Ma), wrench faulting from the early to late Miocene (c. 25-6 Ma),

and oblique strike-slip motion since the late Miocene (c. 6 Ma) (Kamp 1996; Cooper et al. 1987; Walcott 1998).

With a last known surface rupturing earthquake that occurred in 1717 AD (Wells et al. 1999), an estimated mean recurrence interval of 329 ± 68 years (Berryman et al. 2012a), and average slip rates between 20 and 30 mm/yr , the Alpine Fault is late in its seismic cycle. Since 2004, the San Andreas Fault Observatory at Depth (SAFOD) project has greatly advanced our understanding of fundamental processes of rock deformation in fault zones and earthquake physics (e.g., Zoback et al. 2010). A similar project, the Deep Fault Drilling Project (DFDP), located on the central Alpine Fault, is now underway with the goal of sampling and monitoring the fault to a few kilometers depth (Townend et al. 2009). Results from the first phase of drilling (Sutherland et al. 2012), together with recent light detection and ranging (LiDAR) data (Barth et al. 2012) , paleoseismicity studies (e.g., De Pascale & Langridge 2012; Howarth et al. 2012), laboratory measurements of fault rock frictional and hydrologic properties (Boulton et al. 2012), and seismicity catalogs from the Southern Alps Microearthquake Borehole Array (SAMBA) (Boese et al. 2012; Wech et al. 2012), are now rapidly augmenting our knowledge of the central Alpine Fault.

Comparatively, the southern onshore Alpine Fault (hereafter termed the southern Alpine Fault) is much less studied. Seismicity catalogs, geological mapping, and tectonic reconstructions indicate that the southern Alpine Fault has structural, seismological and lithological properties distinct from the central section (e.g., Berryman et al. 1992; Sutherland et al. 2000; GNS 2010; Norris & Cooper 2007; Reyners et al. 2011; Geo 2012) . In this paper, using $^{40}Ar/^{39}Ar$ dating, we provide new ages for formation of mylonites in both the footwall and hanging wall, which show the southern Alpine Fault exploits a Cretaceous zone of shear and that the Alpine Fault accommodated displacement in the modern plate boundary configuration since at least the Early Micoene. We also document the first three complete cross sections through the fault, which in places is composed of the Mg-rich phyllosilicate mineral saponite, a weak mineral widely cited as the cause of fault creep on the San Andreas Fault (Carpenter et al. 2011; Holdsworth et al. 2011; Lockner et al. 2011; Moore & Rymer 2012).

4.3 Tectonic Setting

4.3.1 Geologic history

New Zealand comprises the emergent portion of a mostly submerged continental landmass, Zealandia. No Precambrian cratonic core is exposed in New Zealand (GNS 2010), and basement rocks consist of nine Cambrian to Early Cretaceous volcani-sedimentary tectonostratigraphic terranes accreted to Zealandia when it comprised the convergent margin of the Gondwana supercontinent (e.g., Mortimer 2004 and references therein). Three regional batholiths (e.g., Median Batholith) and three regional metamorphic belts (e.g., Haast Schist) overprint the terranes Mortimer 2004). In the South Island, the basement terranes are classified into the Cambrian-Devonian Western Province and the Permian-Cretaceous Eastern Province stitched together by the Carboniferous-Early Cretaceous Median Batholith (e.g., Bishop et al. 1985; Storey et al. 1999).

Late Cretaceous sea floor spreading rifted Zealandia from the landmasses of Australia and Antarctica to open the Tasman Sea (e.g., Gaina et al. 1998; Sutherland 1999). A distinctive belt of ultramafic rocks (a portion of the Dun Mountain-Maitai terrane) exposed both in the Nelson area (northeast South Island) and in the study area (South Westland) has been offset 460 km by the Alpine Fault (Figure 4.1A); this along-strike distance is now widely accepted as the minimum Neogene offset accomplished by the Alpine Fault (e.g., Sutherland 1999). While spatially much of the South Island is dominated by pelitic greyschist/greenschist and its sedimentary protoliths (purple on Figure 4.1), there is a high lithologic diversity represented by the terranes overall (Figure 4.1). This lithologic diversity is highest in the study area.

Figure 4.1 (Over): Geologic Setting. **A,** Simplified basement lithology map of the South Island of New Zealand with major plate boundary structures. Alpine Fault sections are those defined in Table 4.1. Geological mapping after GNS Science 1:1 000 000 geological map [2010]. Plate motion vectors from NUVEL-1A [DeMets et al. 1994]. Dotted line denotes the continuation of the Permian Dun Mountain Ophiolite Belt (DMOB), which has been dextrally offset 460 km across the Alpine Fault Wellman 1955]. **B,** Simplified basement lithology map of the study area showing relative heterogeneity of rock types adjacent to the Alpine Fault overlain on LINZ 15m DEM. We present a basement lithology map rather than a more traditional basement terrane map to emphasize the diversity of rock types adjacent to the southern Alpine Fault and to point out likely correlations of rock types across major structures (e.g., the Glade-Darrans Fault). Lithologies correspond roughly to Permo-Triassic basement terranes. Active and inactive structures are shown. Geological mapping after Rattenbury et al. (2010), Turnbull et al. (2010), Barnes et al. (2005), Turnbull (2000), and this study. Abbreviations and correlations: MA (Martyr River), MC (McKenzie Creek), H (Hokuri Creek), SS (Sutherland Sound), ASZ (Anita Shear Zone), BSVG (Brook Street Volcanic Group; Brook Street terrane), DMUG (Dun Mountain Ultramafics Group; Dun Mountain-Maitai terrane, synonymous with the Dun Mountain Ophiolite Belt), Greenland Group (Buller terrane), Haast Schist (Torlesse composite terrane, Rakaia terrane), LVG (Livingstone Volcanics Group; Dun Mountain-Maitai terrane), MWG (Mt Webb Gneiss; correlation uncertain, likely Paleozoic protolith of an Anita Shear Zone lithology),

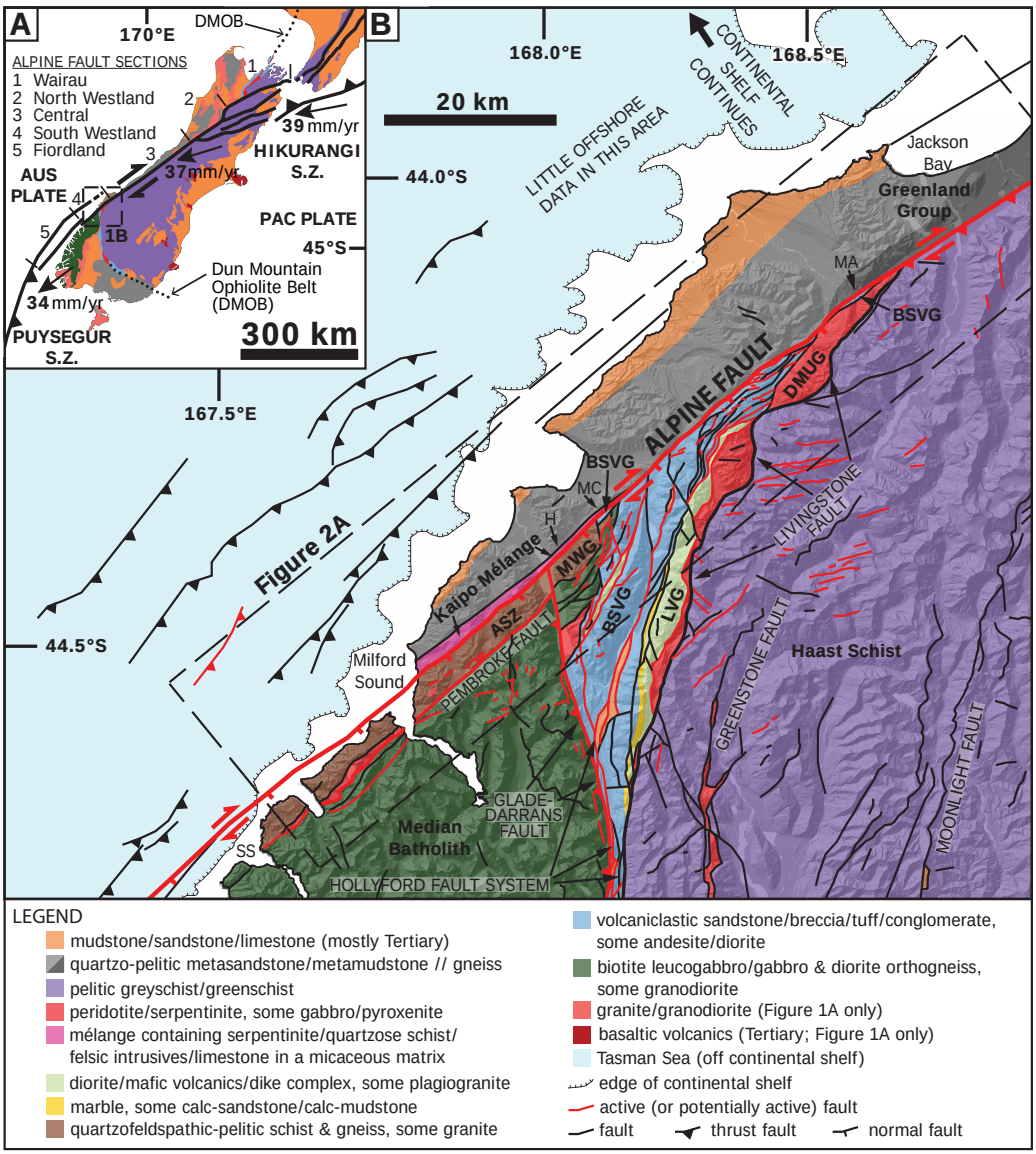
A
170°E
DMOB
ALPINE FAULT SECTIONS
1 Wairau
2 North Westland
3 Central
4 South Westland
5 Fiordland
39 mm/yr
HIKURANGI S.Z.
37 mm/yr
AUS PLATE
PAC PLATE
45°S
1B
Dun Mountain Ophiolite Belt (DMOB)
34 mm/yr
PUYSEGUR S.Z.
300 km
B
168.0°E
168.5°E
20 km
CONTINENTAL SHELF CONTINUES
LITTLE OFFSHORE DATA IN THIS AREA
44.0°S
Jackson Bay
Greenland Group
MA
BSVG
DMUG
ALPINE FAULT
167.5°E
Figure 2A
MC
H
LIVINGSTONE FAULT
Kaipo Mélange
MWG
ASZ
PEMBROKE FAULT
LVG
44.5°S
Milford Sound
Haast Schist
GREENSTONE FAULT
MOONLIGHT FAULT
GLADE-DARRANS FAULT
Median Batholith
SS
HOLLYFORD FAULT SYSTEM
LEGEND
mudstone/sandstone/limestone (mostly Tertiary)
quartzo-pelitic metasandstone/metamudstone // gneiss
pelitic greyschist/greenschist
peridotite/serpentinite, some gabbro/pyroxenite
mélange containing serpentinite/quartzose schist/ felsic intrusives/limestone in a micaceous matrix
diorite/mafic volcanics/dike complex, some plagiogranite
marble, some calc-sandstone/calc-mudstone
quartzofeldspathic-pelitic schist & gneiss, some granite
volcaniclastic sandstone/breccia/tuff/conglomerate, some andesite/diorite
biotite leucogabbro/gabbro & diorite orthogneiss, some granodiorite
granite/granodiorite (Figure 1A only)
basaltic volcanics (Tertiary; Figure 1A only)
Tasman Sea (off continental shelf)
edge of continental shelf
active (or potentially active) fault
fault
thrust fault
normal fault

Figure 4.1:

4.3.2 Along-strike variations in fault structure

We focus on improving our understanding of the southern Alpine Fault, formally named the South Westland section. There are distinct along strike differences in fault properties which allow subdivision into sections, as proposed by Evison (1971), Berryman et al. (1992), Bull (1996), Barnes et al. (2005), and Sutherland et al. (2007). Distinguishing structural, seismic and geomorphic features of these major sections of the fault are summarized in Table 4.1. We place the northern boundary of the southern Alpine Fault, the focus of this contribution, at the Martyr River where there is an abrupt change in uplift polarity (discussed below) and the southern boundary at Caswell Sound where there is a 4 km-wide step-over in the fault plane (Figure 4.1A). The Central section of the Alpine Fault has long been recognized as having low background seismicity to as far south as $\sim$ 25 km north of the Martyr River (e.g., Evison 1971). In contrast, the southern Alpine Fault has higher rates of post-1940 recorded seismicity Evison 1971; Anderson & Webb 1994; Wallace et al. 2007; Boese et al. 2012; Geo 2012).

Offshore Jackson Bay marks the transition from a continental/continental transpressive margin to a continental/oceanic transpressive margin in the south; this is the only such transition on the fault (Figure 4.1b) (Berryman et al. 1992). Outboard of the continental shelf southwest of Jackson Bay, a youthful, north propagating subduction zone subducts the AUS plate obliquely beneath the Alpine Fault Barnes et al. 2002). The associated Wadati-Benioff zone extends as far north as Hokuri Creek in the Hollyford Valley (Figure 4.1B) (Geo 2012). An unfaulted onshore AUS plate block provides a stark contrast to lithologically diverse Paleozoic-Mesozoic basement terranes on the PAC plate where both inherited and newly formed structures are present (Figure 4.1b). In addition to the Alpine Fault, major faults in the area include the Pembroke, Glade-Darrans, Hollyford, Livingstone, Greenstone and Moonlight fault systems (Figure 4.1b). While the geology in this region is generally well-mapped, large uncertainties persist about the extent to which structures have recently been active (c.f. Cox et al. 2012).

Previous studies of the southern Alpine Fault have largely been at the regional scale and reconnaissance level (Wellman & Willett 1942; Clark &

Section name	Wairau	North Westland	Central	South Westland	Fiordland
Informal name	Wairau Fault	northern Alpine Fault	central Alpine Fault	southern Alpine Fault	Resolution section
Length (km)	200	150	250	160	130
Northeastern extent	Cook Strait	Matakitaki River	Toaroha River	Martyr River	Caswell Sound
Southwestern extent	Matakitaki River	Toaroha River	Martyr River	Caswell Sound	Dusky Sound
Strike-slip rate (mm/yr)	3–6.7	10–13.6 (-2/+1.8)	27–29 (-5/+6)	23–27.2 (-2/+1.8)	31.4 (-3.5/+1.8)
NUVEL-1A plate vector (mm/yr→°)	39.6 → 258°	38.4 → 255°	37.5 → 251°	36.6 → 247°	35.9 → 244°
Current % of plate boundary motion	8–17%	26–35%	72–77%	63–74%	87%
Regional fault strike (>10 km lengths)	056°–081°	006°–055°	052°–060°	040°–059°	036°–056°
Section average fault strike/dip	067°/90	055°/55°SE	055°/45°SE	052°/82°SE	040°/75°SE
Dip-slip rate (mm/yr)	~0	3.4–6 (-0.6/+2)	2.25–8 (-0.5/+1)	0.6 (-0.2/+0.3)	~0
Net uplifted side	x	SE	SE	NW	NW
Along-strike lithological variation	Low	Generally low	Low	High	Low
Single event strike-slip displacement (m)	5–7	~6	8–9	7.5–9 (-0.5)	Unknown
Single event dip-slip displacement (m)	0	≤3	1–<4	~1	Unknown
Background seismicity	Very Low	Low	Low	High	High
Intersections with other faults	Few	Many	Few	Many	Moderate
Tectonic Complexities	MFS rotation	MFS interaction	SP (<2km depth)	DS at CR	AW, Rooted into OM SZ
Major transitions	NIFS	MFS	OM FR	TF to SZ, CC to OC	Large SO
Large scale fault bends	RSB & LSB OFF	20 km wide LSB	None	10° B ON, 20° B OFF	3 major LSBs

Table 4.1: Alpine Fault Sections. Sections define the largest changes in fault character. Section names are largely after Berryman et al. (1992), although we propose slightly different extents to most of the sections and add the Fiordland section. Refer to Figure 4.1a for geographic extents. Strike-slip and dip-slip rates are bracketed by the highest and lowest published rates on the section followed by the uncertainty of the lowest and highest published values (where given). Measurements of single event displacement are presented similarly. Net uplifted side is considered based on geomorphology and seismic reflection data. Regional fault strike values are averaged over fault lengths >10 km. Section averaged fault strike/dip is characteristic of the majority of the length of the fault section at upper crustal levels. Fault dip from Wairau and Fiordland sections are estimated from offshore seismic reflection data. Background seismicity considered is within 15 km of the Alpine Fault trace. Intersections with active and potentially active faults are both considered. We emphasize the sections we propose do not necessarily correlate with segments affected by individual earthquake ruptures, but based on this compilation, these section boundaries represent the largest changes in observable fault behavior. Note that with the exception of the South Westland- Fiordland boundary, all other section boundaries are not defined by breaks in the fault plane. Compiled using data from Anderson & Webb (1994), Arabasz & Robinson (1976), Barnes (2009), Barnes & Pondard (2010), Barnes et al. (2001), Barnes et al. (2005), Beavan et al. (2010), Berryman et al. (1992), Berryman et al. (2012a,b), Bourne et al. (1998), Cooper & Kostro (2006), DeMets et al. (1994), Evison (1971), Grapes & Wellman (1986), Leitner et al. (2001), Lensen (1976), Norris & Cooper (2001), Pearson et al. (1995), Pearson et al. (2000), Reyners et al. (2011), Sutherland & Norris (1995), Sutherland et al. (2006), Zachariasen et al. (2006), N.C. Barth unpublished data, and this study. AW: accretionary wedge; B: bend (in fault strike); CC: continental crust; DS: duplex structure; FR: fault ramping; LSB: left stepping bend; MFS: Marlborough Fault System; NIFS: North Island Fault System; OC: oceanic crust; OFF: offshore; OM: oblique motion; ON: onshore; RSB: right-stepping bend; SP: serial partitioning; SZ: subduction zone; TF: transform fault.

Wellman 1959; Hull & Berryman 1986; Berryman et al. 1992; Campbell 2005; Wellman & Wilson 1964). Sutherland & Norris (1995) focused on slip rates and tectonic geomorphology, but included observations of the structure of the Alpine Fault zone at Hokuri Creek where they noted altered ultramafic blocks within a wide zone of clay-rich fault gouge. Also at Hokuri Creek, Berryman et al. (2012a) used an exposed sequence of silt/peat cycles ponded against the Alpine Fault scarp to obtain a quasi-periodic record of earthquake events over the last 8000 years. Berryman et al. (2012a) infer that the event record at this site reflects the fault's geometrically simple structure, high slip-rate, and tendency to work in isolation from other faults. In this paper, we use field observations and lab-based analytical techniques to describe and quantify the architecture, mechanical behavior, and tectonic history of the southern Alpine Fault.

4.4 Field Observations

4.4.1 Plate boundary structure & kinematics

We mapped surface outcrops of the southern Alpine Fault at 10 major locations along strike. In this remote, rainforest-covered region, the fault core is well-exposed at five locations. An abrupt change in kinematics and geomorphic expression occurs immediately southwest of the Martyr River without a major change in fault strike, fault dip or side-stepping of the outcropping fault plane (Figure 4.2). To the northeast on the central Alpine Fault, fault kinematic data indicate oblique motion is accommodated on a 055°-striking, $\sim$ 045° southeast dipping dextral-reverse fault plane causing net uplift of the PAC plate (Figure 4.2). To the southwest on the southern Alpine Fault, the fault plane maintains a $\sim$ 052° stike, but its dip steepens to 80-90° southeast. Though the motion resolved on the southern Alpine Fault is almost purely strike-slip, a ubiquitous normal component is associated with net uplift of the AUS plate. This relationship appears to continue for at least 75 km offshore to Caswell Sound (Barnes et al. 2005).

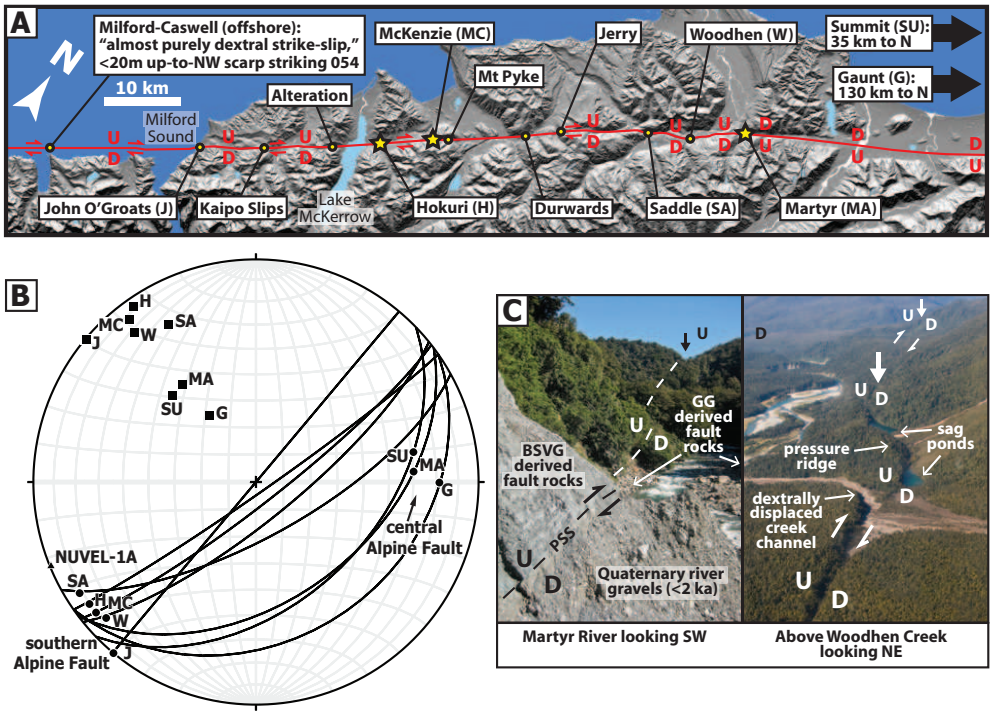

Figure 4.2: Alpine Fault Kinematics. **A,** Strip map of the South Westland section of the Alpine Fault (area shown in Figure 4.1). Location names refer to creeks or rivers labeled. Up/Down (U/D) and strike-slip motion is constrained by geomorphology. Offshore description is from Barnes et al. (2005). Stars denote localities shown in Figure 4.5. **B,** Equal area lower hemisphere stereonet with best representative measurements of slickenlines (circles) on Australian-Pacific principal slip surface (great circles and poles to planes as squares) at locations shown in A. Variability of strike, dip, trend, and plunge at each location is typically $<$ 5-10° and all measurements are taken at or close to where the fault juxtaposes bedrock on bedrock. John O'Groats measurements are from Clark & Wellman (1959); all others are from this study. Triangle denotes NUVEL-1A plate vector calculated for Hokuri Creek (DeMets et al. 1994). Notice the distinct dips and slip vectors of the southern and central Alpine Fault. **C,** Field photos showing examples of fault rocks overthrusting Quaternary sediments and geomorphic expression of fault motion. Up/Down (U/D) denotes sense of dip-slip fault motion and paired arrows denote sense of strike-slip motion. PSS stands for principal slip surface. GG stands for Greenland Group. BSVG stands for Brook Street Volcanic Group. Geomorphic observations are everywhere compatible with fault plane slickenline data.

4.4.2 Fault zone architecture

In this study, fault zone architecture is described using the simple fault core zone and damage zone model proposed by Caine et al. (1996), which Sutherland et al. (2012) adopted for the central Alpine Fault. We define the damage zone as the tabular zone in which minor faults, folds, veins and fractures have formed because of deformation associated with faulting. Within this damage zone, there is a fault core that contains fault rocks formed by particle size-reduction in the brittle regime and dynamic recrystallization of highly strained grains in the ductile regime (Reed 1964; Sibson 1977a; Sibson et al. 1981; Norris & Cooper 2007). The fault core (or cores) may contain one or more principal slip surfaces (PSSs) which accommodated a significant portion of the total offset across the fault zone (Sibson 2003). We also use alteration zone to describe the region where fluid-rock interactions alter the physical, chemical and hydrological properties of the fault zone Sutherland et al. 2012). On the Alpine Fault, fluid-rock interaction within the alteration zone occurred primarily at greenschist facies temperatures and pressures, as indicated by the modally dominant chlorite and epidote alteration minerals (e.g., Warr & Cox 2001; Sutherland et al. 2012). Within this zone, carbonate vein abundance is also above regional levels Warr & Cox 2001; Vry et al. 2001; Norris & Cooper 2007).

While fault cores commonly comprise thin (mm to cm-wide) planes (Ben-Zion & Sammis 2003; Sibson 2003), wider, branching, anastomosing fault cores are also common worldwide Faulkner et al. 2003, 2010). The evolution of fault strength during coseismic slip depends critically on the width of the actively slipping portion of the fault core Marone & Kilgore 1993), and field observations of active fault cores provide information necessary for numerical modeling of earthquake processes (e.g., Rice & Cocco 2006; Niemeijer et al. 2012).

We present detailed cross sections of the Alpine Fault core and damage zone at three localities. Fault rocks described are classified into protoliths, damaged rocks including protocataclasites, and fault core rocks including random fabric cataclasites, foliated cataclasites, and fault gouges. Fault rocks are classified based on the scheme proposed by Sibson (1977a) and modified

to include the presence of foliated cataclasites with an interconnected network of phyllosilicate minerals (Holdsworth 2004; Jefferies et al. 2006). A separate type of fault rock, pulverized rock, characterized by a fracture-induced reduction in grain size with minimal distortion of the primary rock structure **?**Dor et al. 2009; Wilson et al. 2005), was not observed in the study area.

4.4.3 Protoliths

The Greenland Group is a widespread and voluminous metasedimentary unit of the Buller terrane which comprises a portion of the AUS plate. The Greenland Group is the principal lithology outcropping west of the southern and central portions of Alpine Fault as far south as McKenzie Creek (Figure 4.1B). The unit consists predominantly of interbedded quartzose metasandstone and metamudstone, variably metamorphosed to quartz-muscovite-biotite schist and amphibolite-facies gneiss (e.g., Rattenbury et al. 2010). Pelitic layers in the gneiss often exhibit coarsely-crystalline, boudinaged quartz-feldspar-muscovite leucosomes. Local granite intrusions have created hornfels textures. In the vicinity of the Martyr River and Jackson Bay, there is a regional increase in metamorphic grade from chlorite zone to sillimanite-microcline zone to the southeast towards the Alpine Fault (e.g., Mortimer et al. 2012). Within 160 m of the Alpine Fault at the Martyr River, the sillimanite grade gneiss is overprinted by a mylonitic fabric associated with chlorite alteration and an absence of biotite. Transposed leucosomes are still identifiable within the mylonitic fabric, and the age of this mylonitization is discussed in Section 4.7.

4.4.3.1 Greenland Group

The Greenland Group is a widespread and voluminous metasedimentary unit of the Buller terrane which comprises a portion of the AUS plate. The Greenland Group is the principal lithology outcropping west of the southern and central portions of Alpine Fault as far south as McKenzie Creek (Figure 4.1B). The unit consists predominantly of interbedded quartzose metasandstone and metamudstone, variably metamorphosed to quartz-muscovite-biotite schist and amphibolite-facies gneiss (e.g., Rattenbury et al.

2010). Pelitic layers in the gneiss often exhibit coarsely-crystalline, boudinaged quartz-feldspar-muscovite leucosomes. Local granite intrusions have created hornfels textures. In the vicinity of the Martyr River and Jackson Bay, there is a regional increase in metamorphic grade from chlorite zone to sillimanite-microcline zone to the southeast towards the Alpine Fault (e.g., Mortimer et al. 2012). Within 160 m of the Alpine Fault at the Martyr River, the sillimanite grade gneiss is overprinted by a mylonitic fabric associated with chlorite alteration and an absence of biotite. Transposed leucosomes are still identifiable within the mylonitic fabric, and the age of this mylonitization is discussed in Section 4.7.

4.4.3.2 Brook Street Volcanic Group

The Brook Street Volcanic Group of the Brook Street terrane, occurs on the Pacific Plate in fault-bounded slivers adjacent to the Alpine Fault at the Martyr River and McKenzie Creek (Figure 4.1B). At McKenzie Creek, the unit is chloritically altered and dominated by andesite-derived metasandstone, metatuff, metaconglomerate and metabreccia (e.g., Rattenbury et al. 2010). In places it has a well-developed foliation, while in others the unit can be chert-like and completely lack any obvious anisotropy. At the Martyr River, the Brook Street Volcanic Group has a mylonitic fabric. Here the rock consists solely of fine-grained chlorite-epidote with occasional quartz segregations. Epidote-rich horizons are boudinaged. It contains rare 1.5 m-wide by 6 m-long foliation-parallel pods of a mylonitized diorite with large hornblende porphyroclasts. The age of this mylonitization is discussed in Section 4.7.

4.4.3.3 Mt Webb Gneiss

The Mt Webb Gneiss is an enigmatic unit consisting of biotite garnet gneiss, mylonitic amphibolite, gneissic biotite granite and lenses of marble outcropping in the vicinity of Hokuri and McKenzie creeks (Figure 4.1B) (e.g., Turnbull 2000). It is characterized by low regional abundance of faults and fractures (<5 through-going fractures per 1 meter length of outcrop). Textural and metamorphic facies distinctions led Ballard (1989) to propose a new unit

despite lithologic similarities to the Thurso Formation of the Anita Shear Zone (Wood 1962). However, based on our textural and lithologic observations, we concur with Wood's original correlation. Although not exposed adjacent to the Alpine Fault at Hokuri Creek due to Quaternary sediment cover, the Mt Webb Gneiss is exposed in creeks to the southwest of the McKenzie Creek locality where it appears relatively unfractured and unaltered.

4.4.3.4 Kaipo Mélange

In this study, we identify, describe and formally name the Kaipo Mélange, an AUS plate-hosted tectonic mélange which crops out adjacent to the Alpine Fault for $\sim$ 40 km from the Pyke River to Milford Sound (Figure 4.1B). Because this unit forms the immediate footwall at two key study sites and has a genetic relationship to fault core rocks, we briefly describe it here based on reconnaissance mapping done at six sites between the Kaipo Slips and McKenzie Creek.

Outcrops of this mélange had previously been examined by Wellman & Wilson (1964) who introduced the stratigraphic name "Kaipo Formation" and did not recognize it as a mélange. At their type section, the Kaipo Slips, the section includes sequences of granite between fault-bounded sedimentary units without any evidence for stratigraphic continuity or contact metamorphism. Here, we use the name "Kaipo Mélange" because we observe the sequence everywhere along strike to be strictly a tectonic mixture including exotic blocks (as per Raymond 1984).

In southern exposures (e.g., Kaipo Slips, Alteration Creek), large (up to 70 m-across) fault-bounded blocks of chlorite-altered felsic intrusives, deformed Middle Eocene-Late Oligocene limestone (Nathan 1978; Sutherland et al. 1996), calc-silicate, and rare serpentinite occur in a scaly calcareous mudstone matrix (Figure 4.3A, 4.3B, and 4.3C). Northeastern exposures (e.g., Hokuri Creek, McKenzie Creek) contain smaller ($< \sim$ 5 m-across) tabular blocks of serpentine (common), felsic intrusives, quartzose schist, marble, and limestone (rare) in a sheared phyllosilicate matrix (Figure 4.3D and 4.3F). Pervasive alteration of blocks after incorporation in the mélange

makes a direct comparison to source rocks difficult; provenance of the felsic intrusives, schist and serpentinite remains unknown.

From northeast to southwest, the mélange increases in width, reaching a maximum horizontal width of over 1.5 km. From northeast to southwest, average block size increases and block aspect ratio decreases. Southwestern exposures tend have a higher percentage of incompetent matrix to competent blocks; in addition, the incompetent phyllosilicate matrix is more chaotically folded (cf., Figure 4.3C to 4.3D and 4.3F). Southwestern exposures also lack the boudinaged blocks, brittle fractures, and through-going shear surfaces recorded in the northeastern outcrops (cf. Figure 4.3A, 4.3B, and 4.3C to 4.3D, 4.3E and 4.3F); these observations indicate that the deformation history of the mélange varies along strike. We note that Sutherland & Norris (1995) incorrectly attributed basement rocks exposed northwest of the fault core at Hokuri Creek as cataclastically deformed upper greenschist or amphibolite grade Greenland Group; these footwall basement rocks are a part of the Kaipo Mélange (e.g., Figure 4.3D). Tectonic implications of this mélange are explored in Section 4.6.

4.4.4 Damage zone

On the southern Alpine Fault, steep northwest-draining creeks cut orthogonally to the Alpine Fault, and provide the best outcrops of both sides of the plate boundary structure through the entire width of the damage zone. These outcrops were documented with photographs, structural measurements and sampling. We find that the extent and nature of the damage zone vary significantly along strike.

4.4.4.1 Martyr River

At the Martyr River, the damage zone width is asymmetric: $\sim$ 160 m-wide within the AUS plate and $\sim$ 80 m-wide within the PAC plate (Figure 4.4). Foliations in the Greenland Group gneiss and mylonite both tend to strike parallel to the Alpine Fault, but dip 60-80° to both the northwest and southeast (Figure 4.4A, 4.4B, and 4.4C). The mylonitic fabric tends to dip more steeply than the orientation of the gneiss fabric and has a weak chlorite al-

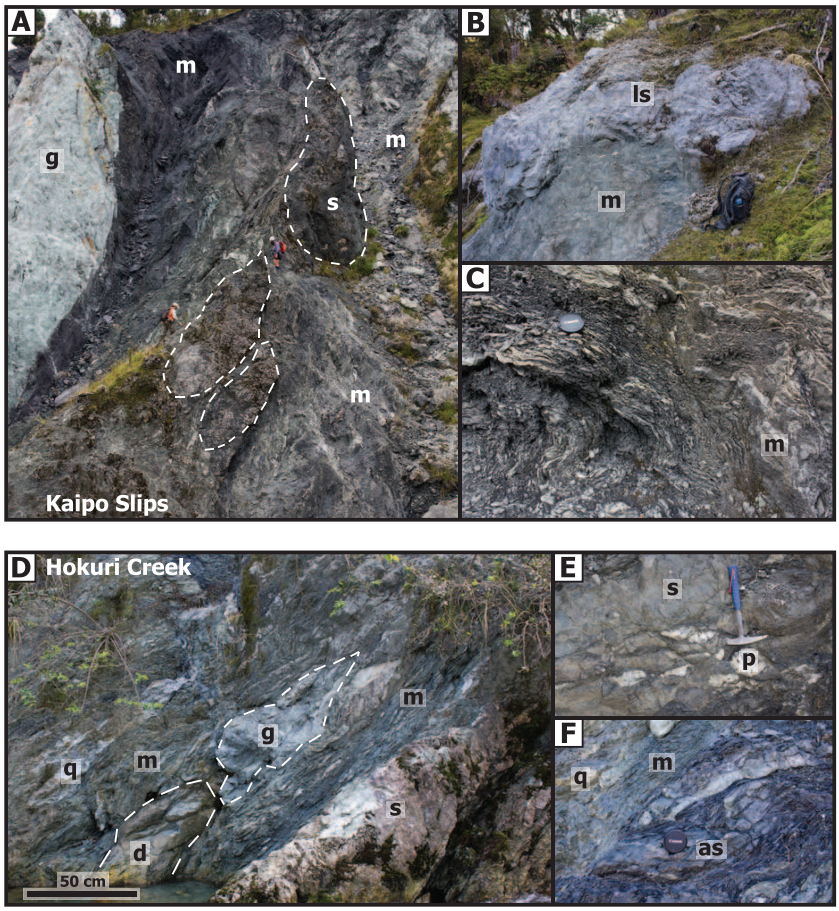

Figure 4.3: Kaipo Mélange. Field photographs contrasting Kaipo Mélange textures at the Kaipo Slips **(A-C)** in the southwest and Hokuri Creek **(D-F)** in the northeast. Key along-strike changes towards the southwest include: a decrease in block size, increase in block aspect ratio, less sedimentary and plutonic blocks, more serpentinite blocks, and a more planar phyllosilicate matrix (in contrast to folded, fissile, calcareous mudstone matrix to the southwest). Some blocks have been outlined for clarity. Abbreviations used: g (granite), m (calcareous mudstone or phyllosilicate mélange matrix), s (serpentinite), ls (limestone), q (quartz), d (diorite), p (pegmatite), as (altered schist).

teration overprinting it. Secondary faults containing phyllosilicate gouge can usually be constrained to have < 1 m of offset; most occur within about 40 m of the Alpine Fault core. Late-stage tensile fractures up to 1 m in length commonly form orthogonal to the mylonitic foliation (Figure 4.4B).

Figure 4.4 (Over): Key features of the Alpine Fault damage zone at the Martyr River. Planar structures are represented as poles to planes on equal area lower hemisphere stereonets. The subscripts AUS and PAC are used to denote Australian and Pacific plate structures. Foliations are denoted with an S, planes of shear are denoted with a C, and tensile fractures are denoted with a F. Black bars above the schematic cross section denote areas where there is no outcrop. Greenland Group (GG) gneiss **A,** is overprinted by a Cretaceous mylonitic fabric **(B),** which is then overprinted by minor faults and fractures of the Alpine Fault zone, including a strong S-C cataclastic fabric within 4 m of the fault core **(C**). Note transposed leucosomes are still identifiable within the mylonitic fabric (cf. **B**). The pre-existing mylonitic foliation tends to form the long axis of the clasts within the S-C cataclastic fabric, parallel to the S planes. Brook Street Volcanic Group (BSVG) rocks have an Early Miocene mylonitic fabric overprinted by a chlorite-epidote alteration zone, which is then overprinted by minor faults and fractures of the Alpine Fault zone **(D)**, especially protocataclasite **(E)**, and cataclasite **(F)** within $\sim$ 30 cm of the principal slip zone (PSS). Discontinuous open fractures in the PAC plate (e.g., e) were not mapped in detail due to their short lengths, but are generally oriented perpendicular to the foliation. Stars denote locations of $^{40}Ar/^{39}Ar$ geochronology samples discussed in the text; see Section 4.7 for discussion of the ages of mylonitization.

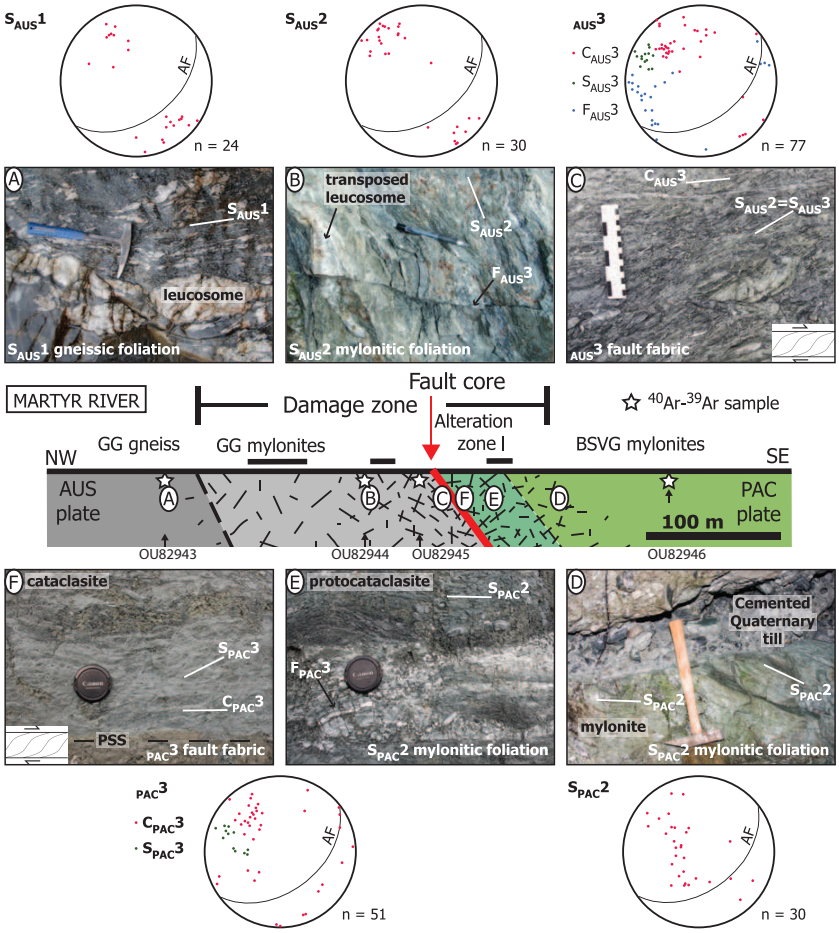

Figure 4.4:

Within 3-10 m of the fault core on the AUS plate, Greenland Group mylonites are overprinted by a foliated cataclasite exhibiting a strong S-C fabric defined by phyllosilicate-rich S shear planes parallel to the Alpine Fault, inclined phyllosilicate-rich C planes and fractured, sigmoidal clasts of the quartz-rich portions of the Greenland Group mylonite (Figure 4.4C). This S-C relationship indicates dextral-normal motion consistent with expected Alpine Fault kinematics. Calcite veins only occur crosscutting the mylonite clasts, indicating that they pre-date the S-C fabric. Rare gouge zones cross-cut the S-C fabric at a high angle suggesting the S-C fabric is no longer active. A $\sim$ 2 ka iron-cemented fluvial gravel unit deposited on a portion of this outcrop does not show any signs of deformation. Above this iron cemented

fluvial gravel unit, <2 ka fluvial gravels have been passively overridden by ∼ 10 m by the principal slip surface of the Alpine Fault (Figure 4.2C).

On the PAC plate, Brook Street Volcanic Group mylonites are openly folded on a cm-dm scale (Figure 4.4D). These mylonites have a pervasive chlorite alteration within 40 m of the fault core; this alteration frequently obscures the mylonitic fabric except where quartz-rich mylonitic segregations occur. Calcite, quartz and chlorite coat many of the fracture and fault surfaces. Though fractures and minor faults are abundant throughout the PAC plate alteration zone, remnant foliations are continuous for over 5 m, indicating that chemically altered damage zone fault rocks are best described as protocataclasites (Figure 4.4E). Cataclasite, which contains fragmented particles that have been translated and rotated, occurs only within ∼ 1 m of the fault core. Foliated cataclasite, with a network of phyllosilicate-rich shear bands that form an S-C fabric consistent with dextral shear, occurs within ∼ 30 cm of the fault core (Figure 4.4F).

On both sides of the fault at the Martyr River, we observe that fractures are most pervasive in the most altered rocks. In the vicinity of the Martyr River, a well-indurated, iron-oxide cemented glacial till (inferred to be ∼ 10 ka) overlies many fault-damaged outcrops; this till acts as a deformation marker that delimits the extent of fault damage at the surface (e.g., Figure 4.4D). Fractures and small offset faults in the bedrock nowhere affect the cemented till above the bedrock. This glacial till is not offset across foliated cataclasites adjacent to the fault core on the AUS plate, suggesting they are not actively deforming. The small faults and fractures crosscutting the PAC mylonites at a distance of 60 m from the fault core are similarly inactive. A <18 ka glacial silt unit occurs on the PAC plate at the Martyr River within 20 m of the fault core; it exhibits folds resulting from soft sediment deformation which have been later cut by hairline reverse faults with cm-scale offset. The active damage zone at the surface at the Martyr River appears to be highly localized (potentially <40 m-wide).

4.4.4.2 McKenzie Creek and Hokuri Creek

At McKenzie Creek and Hokuri Creek, the damage zone is considerably harder to define as it is unclear to what extent alteration and fracturing in the Kaipo Mélange can (and should) be directly attributed to the Alpine Fault. During reconnaissance mapping, detailed studies were mostly focused on the fault core. Nevertheless, the width of the zone appears to be much less than at the Martyr River and we define the damage zone as being $\sim$ 90 m-wide within the AUS plate and 50 m-wide within the PAC plate).

The PAC plate damage zone at McKenzie Creek is pervasively fractured. Here, tensile fractures break the isotropic chert-like Brook Street Volcanic Group metatuff into <1-2 cm-sized cubes within 2 m of the PSZ (Figure 4.5B). These fracture sets are everywhere unmineralized. The PAC plate basement (Mt Webb Gneiss) is not exposed adjacent to the Alpine Fault at Hokuri Creek, but Mt Webb Gneiss is exposed adjacent to the fault at an unnamed tributary southwest of McKenzie Creek. Here Mt Webb Gneiss displays 2-5 cm-spaced tensile fractures that are orthogonal to the foliation, few faults, and little chloritic alteration. Chlorite alteration is strongest in the PAC plate Brook Street Volcanic Group lithologies within 20 m of the fault core at Mckenzie Creek; overall, chloritic assemblages are less pervasive at McKenzie and Hokuri Creeks. Friction melt (pseudotachylyte) is not observed at any of the three sites in the study.

At both Hokuri and McKenzie creeks, secondary faults within 200 m of the fault core exhibit little evidence of brittle cataclasis and accompanying grain size reduction. These secondary faults typically have displacements $\leq$1 m and do not offset capping Quaternary sediments. Hokuri Creek, in particular, contains a record of Quaternary glacial, fluvial, and lacustrine sediments that have been studied in detail by Sutherland & Norris (1995) and Berryman et al. (2012a). Sutherland & Norris (1995) describe flat-lying 15 ka glacial lake silts which coat AUS plate outcrop along the Hokuri River for a distance of about 60 m from the fault core; these silts are unfaulted, indicating the secondary faults exposed within the underlying Kaipo Mélange have been inactive over this time. The post $\sim$ 10 ka peat and silt on the PAC plate at Hokuri Creek are undisturbed and unfaulted, except where they

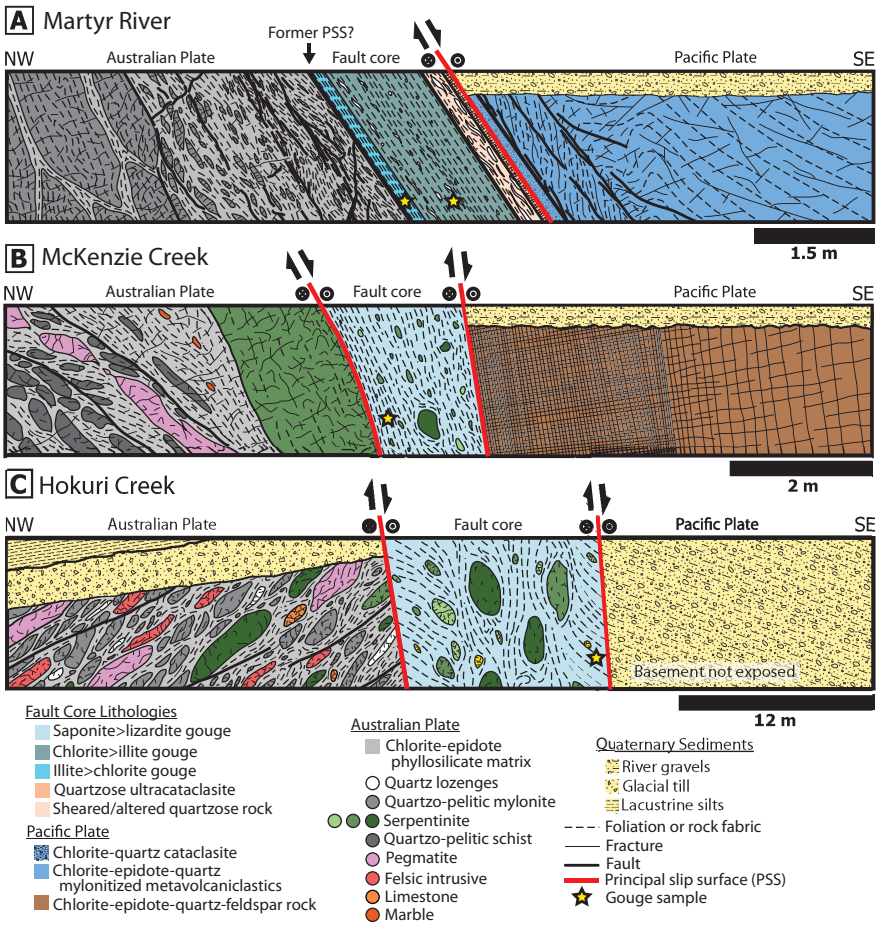

Figure 4.5: Fault Core Cross Sections. Complete composite cross sections through the Alpine Fault core at **A,** the Martyr River, **B,** McKenzie Creek and **C,** Hokuri Creek, compiled from field measurements, measured sections and by tracing structures from high-resolution orthorectified field photos (e.g., Figure 4.6a, 4.6b, and 4.6c). Horizontal and vertical scale are the same. At all localities, no other major fault cores outcrop northwest or southeast of the section indicated. Quaternary sedimentary units can be used to constrain what fault slip and fault damage has occurred since their deposition as outlined in the text.

were close enough to the fault scarp to have interfingering colluvial wedges (Berryman et al. 2012a). It is worth noting that Sutherland & Norris (1995) describe glacial silts dipping 20° both on the AUS plate and PAC plate at Hokuri Creek; these glacial silts were folded into an anticline-syncline pair at some time during the last 100 kyr.

Because we do not observe secondary faults in the damage zone with significant offset or evidence of brittle grain size reduction, and because no secondary faults disturb capping Quaternary sediments (apart from those within the immediate hanging wall at the Marytr River), we argue that the vast majority of slip on the Alpine Fault at the surface must be accommodated within a single fault core or on its margins. At all three locations mapped in detail, we observe Quaternary sediments juxtaposed in fault contact against at least one margin of the fault core. Since the primary concern of this paper is characterizing slip on the southern Alpine Fault, we now focus on a detailed examination of fault core exposures.

4.4.5 Fault Core

We present the first complete composite cross sections through the fault core of the southern Alpine Fault from exposures at three locations (Figures 4.5A-4.5C) compiled from field measurements, measured sections and high-resolution orthorectified field photo tracings (e.g., Figures 4.6A-4.6C). At all three locations, the fault core is a single, well-defined, $>$ 1 m wide tabular zone containing only AUS plate derived materials, indicating that the geologically defined sensu stricto plate boundary is the striated southeastern margin of the fault core.

Figure 4.6 (Over): Fault Core Observations. Field photographs of the Alpine Fault core at Martyr **(A)**, McKenzie **(B)** and Hokuri **(C)** sites (hammer, hammer, and backpack for scale respectively). PSS stands for principal slip surface. **(D, E, F)** Hand-sample-scale photos of clast textures suspended in phyllosilicate-rich gouge matrix. Srp stands for serpentine and Qtz stands for quartz. Single-headed white arrows in **C** and **F** point out serpentine block boundaries, which commonly are composed of a reaction halo

of lizardite-chlorite gouge. **(G, H, I)** Petrographic thin section photomicrographs of phyllosilicate-rich fault gouges seen in cross polarized light. Dark areas are where phyllosilicate matrix is missing due to sample preparation. **(J, K, L)** Scanning electron microscope (SEM) images of phyllosilicate-rich fault gouges taken with an angle selective backscatter (AsB) detector. Black voids are desiccation cracks due to sample preparation.

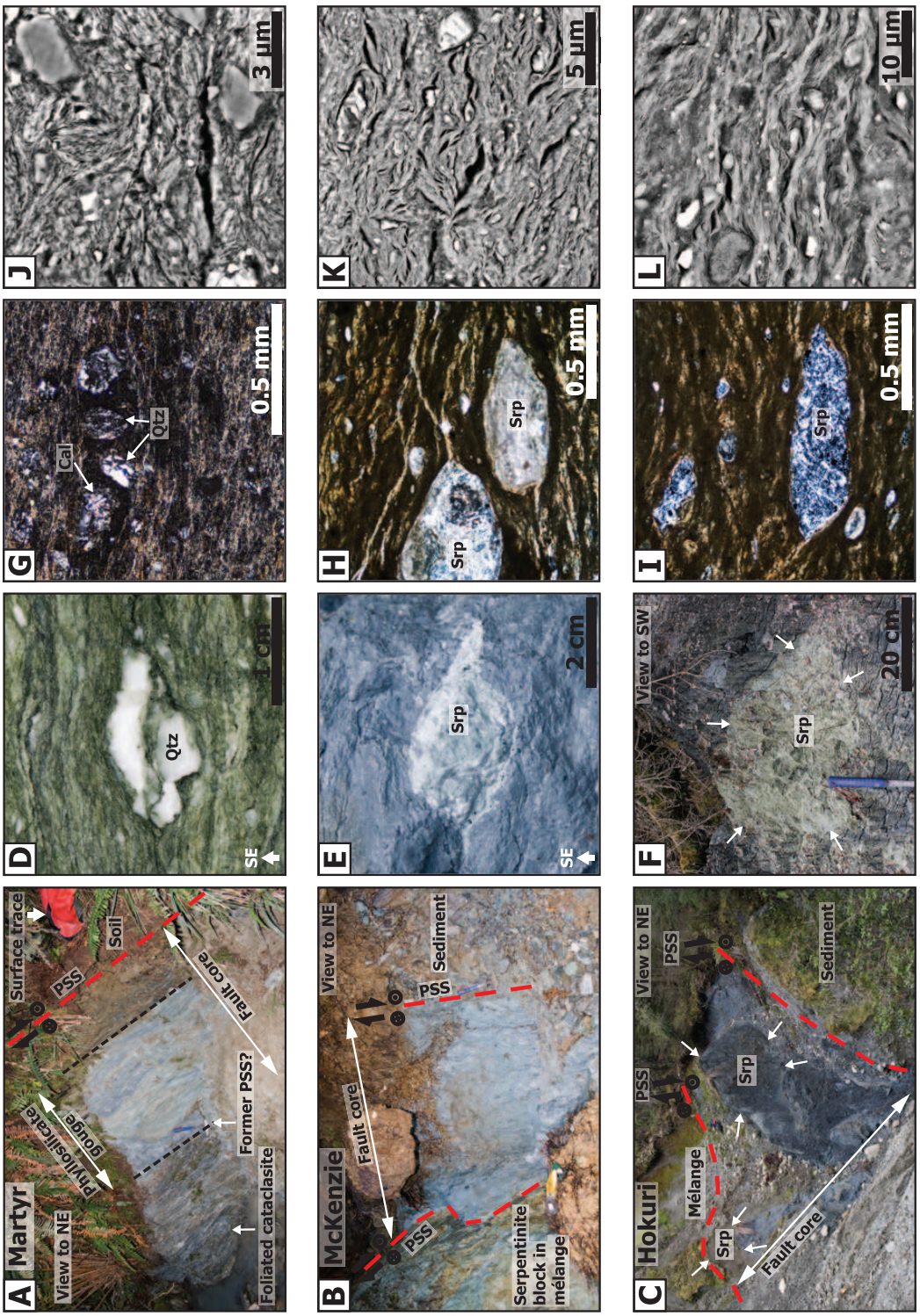
A Martyr
View to NE
Surface trace
Soil
PSS
Phyllosilicate gouge
Former PSS?
Fault core
Foliated cataclasite
B McKenzie
View to NE
Fault core
PSS
Sediment
PSS
Serpentinite block in mélange
C Hokuri
View to NE
PSS
PSS
Mélange
Srp
Srp
Sediment
Fault core
D
Qtz
1 cm
SE
E
Srp
2 cm
SE
F
View to SW
Srp
20 cm
G
Cal
Qtz
0.5 mm
H
Srp
Srp
0.5 mm
I
Srp
0.5 mm
J
3 µm
K
5 µm
L
10 µm

Figure 4.6:

At the Martyr River, a 1.5 m-wide fault core is composed primarily of blue-grey and white foliated chlorite-illite gouge (according to XRD analyses presented in Table 4.2) with $<$ 4 cm-long clasts of quartz + calcite (Figure 4.6A). Microfolded mylonitic textures with cross-cutting calcite present in many of the clasts with diameters larger than 3 mm are identical to those of quartzopelitic mylonites on the adjacent AUS plate. Cataclastically deformed sigmoidally shaped clasts indicate a dextral-normal shear sense (Figure 4.6D). Chlorite-illite gouge foliation is sub-parallel to the fault core margins.

At the southeast margin of the fault core, AUS plate quartz-pelite-derived ultracataclasite, sheared rock and phyllosilicate gouge are juxtaposed against altered chloritic PAC plate cataclasite; this principal slip surface coincides with a prominent surface trace of the fault and is inferred to be the active PSS. Intense surface weathering precluded collection of this material for further analysis. On the northwest margin of the fault core, we mapped a 15 cm-thick blue illite-chlorite gouge with fine 2 mm-wide laminations and an average quartz + calcite clast size of $<$ 1 mm; this gouge is interpreted to represent a former PSS and was collected for friction and permeability experiments (described below). Few other outcrops of this quartz-pelite-derived gouge were observed, but its Greenland Group parent lithology is widespread along the fault to the northeast and southwest, and it may be extensive along strike.

Between McKenzie Creek and Hokuri Creek, deformation is strongly localized in a 1.1 to 12 m-wide fault core containing pods of completely serpentinized peridotites (serpentinites) suspended in trioctahedral smectite (saponite)-rich foliated fault gouge. Surface outcrops of these serpentinite-derived gouges can be traced for 10 km along strike. Uncommon cataclased sigmoidal clasts always indicate dextral movement (Figure 4.6E). Clast size, clast aspect ratio and fault core thickness consistently increase to the southwest. The largest clasts or pods (sometimes $>$ 5 m across) tend to occur in the center of the fault core and commonly are surrounded by a reaction halo of lizardite-chlorite gouge (Figure 4.6C and 4.6F). These pods typically have oblate shapes (e.g., dimensions of 2.5 m x 2.5 m x 1.5m) with their long axes parallel to the fault core margins. While clast concentrations vary

throughout the fault core, the regions surrounding large serpentinite pods tend to be more clast-rich. We did not observe saponite gouge outside the fault core. Outcrops where the fault core is less than 2 m wide exhibit gouge foliations concordant to the fault core margins, but foliations within wider cores are discordant to the margins. Saponite gouge foliation anastomoses around the rigid serpentinite clasts. Within the gouge there are no obvious through-going zones or planes on which slip may have been localized.

4.5 Mineralogical & Microstructural Observations

4.5.1 Analytical methods

Bulk rock quantitative x-ray diffraction (XRD) was used to determine the matrix mineralogy of each fault core gouge (see Boulton et al. 2012 for detailed analytical methods). Petrographic thin sections of fault gouges were prepared dry and polished using 1 μm diamond paste. Thin sections were imaged in a Zeiss Sigma field emission scanning electron microscope (SEM), mostly using an angle-selective backscatter (AsB) detector to highlight compositional and topographical variations. Energy-dispersive X-ray (EDS) was used to identify minerals and create element variation maps. EDS was particularly useful for distinguishing between minerals that could not be isolated by XRD, like muscovite and illite. Thin section petrography aided determination of the variety of serpentine present (lizardite).

4.5.2 Martyr River

The bulk of the exposed AUS plate fault core at the Martyr River is composed of macroscopically-foliated gouge with a chlorite-illite matrix. The softest gouge in the fault core, most readily malleable by fingertips, is interpreted to be a former PSS or perhaps secondary PSS; this gouge is illite-chlorite-rich, with illite being more abundant than chlorite (Table 4.2). Microstructurally, the main textural difference between the foliated chlorite-illite and illite-chlorite gouges is that clasts are relatively abundant within the stronger foliated gouge; these clasts inhibit the formation of interconnected phyllosilicate layers. Although some common extinction (and therefore preferred

CSIRO ID	Sample	Quartz	Orthoclase/Microcline	Albite	Calcite	Smectitea	Mica/Illite	Chlorite	Serpentine (Lizardite)	Talc	Amphibole (Actinolite)	Pyrite	Total
34103	Gaunt Creek gouge	35	<1	17	6		32	9					99
34958	Martyr River gouge	37	4	7	1		36	15					100
34109	Martyr River foliated gouge	8	4	15	<1		35	39				<1	101
34111	McKenzie Creek gouge	8	1	1	5	61		11	13				100
34959	Hokuri Creek gouge	2			5	74		3	12	2	2		100
34110	Hokuri Creek pod rim gouge	<1			2			5	93				100

Table 4.2: Bulk Rock Quantitative XRD.

orientation) of phyllosilicate grains is indicated in photomicrographs (Figure 4.6G), SEM images (Figure 4.6J) reveal that that individual phyllosilicate grains are seldom particularly continuous. Instead, the phyllosilicates form packages a few microns across, bounded by discrete, anastomosing surfaces. Phyllosilicates within individual packages have common orientations, but these orientations are not parallel in adjacent packages.

Both Martyr River fault core gouges contain clasts of polycrystalline quartz ± illite ± albite ± cross-cutting calcite, and monomineralic clasts of titanite and rare pyrite (Figure 4.7A). This is the same assemblage found in the AUS plate quartzopelitic mylonites immediately northwest of the fault core (with the exception that in the AUS plate mylonites muscovite occurs in place of illite). Some clasts have lobate (i.e., embayed) boundaries. Mylonitic textures are visible in some of the larger clasts, and cross-cutting calcite veins within the clasts are truncated by the phyllosilicate foliation at clast boundaries. These veins are similar to those pervasively present in the adjacent AUS plate quartzopelitic rocks. No calcite veins or disseminated grains are observed within the gouge matrix. Clasts 1-2 cm across commonly have sigmoidal tails of comminuted clast material, while clasts smaller than 1 mm tend to be more equant with sub-angular to sub-rounded shapes (Figure 4.6D, 4.6G, and 4.6J).

4.5.3 McKenzie Creek & Hokuri Creek

McKenzie Creek and Hokuri Creek gouges have a saponite-lizardite-chlorite matrix (Figure 4.7B and 4.7C). Both gouges contain over 60% trioctahedral smectite (saponite). McKenzie Creek and Hokuri Creek gouges are petrographically similar, but differ in minor proportions of saponite, chlorite, quartz and talc (Table 4.2). In thin section, individual phyllosilicate layers are commonly traceable for several millimeters (Figure 4.6H and 4.6I). Gouge

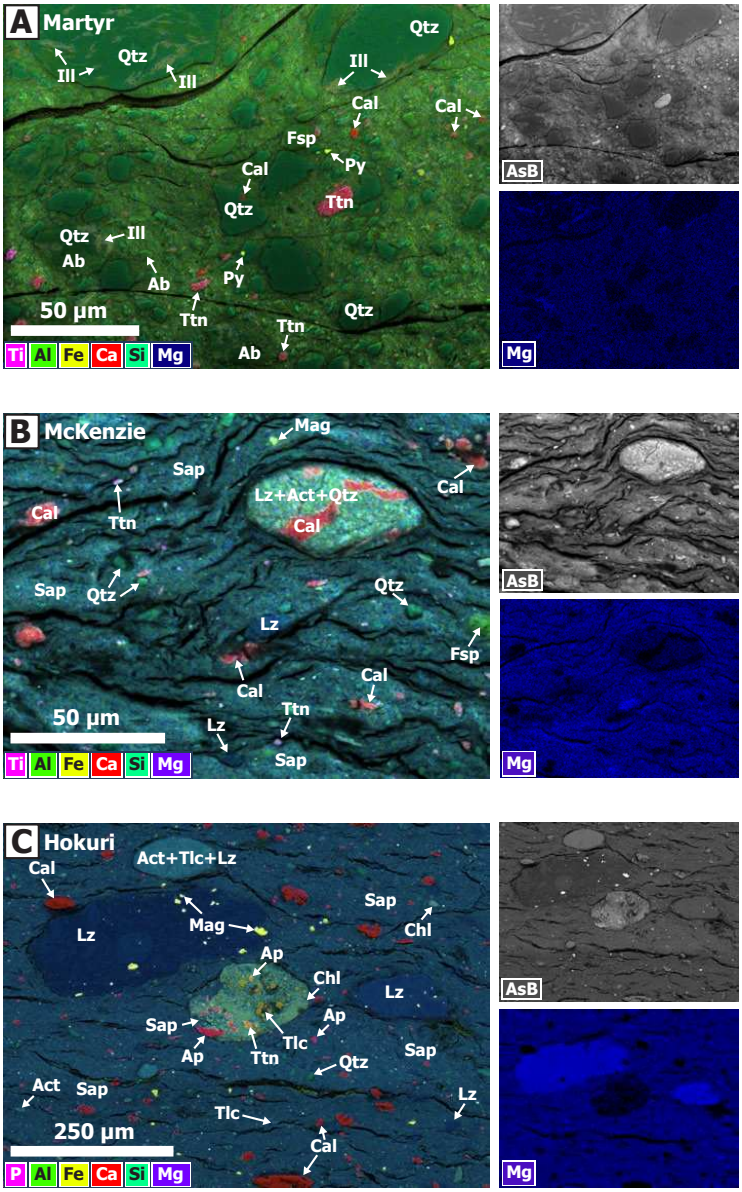

Figure 4.7: Fault Core Mineralogy. Energy-dispersive X-ray spectroscopy (EDS) element maps (least-squares averaged) and angle-selective backscatter (AsB) SEM images of phyllosilicate-rich gouges from **A,** Martyr, **B,** McKenzie, and **C,** Hokuri creeks. Colors denote concentrations of key elements: pink (Ti), green (Al), yellow (Fe), red (Ca), teal (Si), blue (Mg). The field of view for all three images of a sample is the same. Black voids are desiccation cracks due to sample preparation. Mineral abbreviations used: Ab (albite), Act (actinolite), Ap (apatite), Cal (calcite), Fsp (feldspar), Ill (illite), Lz (lizardite), Mag (magnetite), Py (pyrite), Qtz (quartz), Sap (saponite), Tlc (talc), Ttn (titanite).

foliation can be planar or tightly folded. Individual phyllosilicate sheets are $\sim$ 5 μm-long. Unlike the Martyr gouges, at the SEM scale, we do not observe an interconnected network of discrete surfaces (Figure 4.6K and 4.6L). EDS mapping down to a few micron spot size show no detectable variations in Mg (or other elements) across foliation (Figure 4.7B and 4.7C), although we observe varying grayscale intensities indicating either compositional or topographic variations in extreme close-up AsB images (e.g., Figure 4.6L).

Clasts are typically ellipsoidal in shape with the long axis parallel to the gouge foliation and have sub-rounded to rounded surfaces (Figures 4.6K, 4.6L, 4.7B and 4.7C). Serpentinite clasts occasionally preserve original peridotite texture, but typically these are obscured by serpentinization textures (Figure 4.6I). We observe scale dependence in clast mineralogy in the Hokuri and McKenzie Creek fault cores. Outcrop to thin section scale clasts are dominated by serpentine minerals, with rare quartzopelitic and quartzofeldspathic lithogies present. In contrast, at the SEM scale (about <50 μm) calcite and quartz are the most abundant clast phases (although not volumetrically dominant). Many of the larger serpentinite pods seen in outcrop are surrounded by a <10 cm-wide reaction rind dominated by lizardite with associated chlorite (Table 4.2; Figure 4.6C and 4.6F). In thin section, a highly birefringent rim similar to the macroscale rind can be found around serpentinite clasts; rim-forming minerals have been dragged into tails consistent with a dextral shear sense (Figure 4.6H and 4.6I). Lizardite-rich gouge clasts with a diameter less than 1 mm have sometimes been incorporated into the saponite-rich gouge, but never vice versa.

The clast population and mineral assemblage is diverse, reflecting the diversity of lithologies present in the protolith Kaipo Mélange. Clast mineralogies include: serpentinite ± actinolite ± talc ± quartz ± pyrite ± magnetite ± calcite; calcite; quartz ± calcite; titanite; epidote; chlorite; magnetite; pyrite; chromite ± magnetite; chalcopyrite; and rare apatite + titanite + talc + chlorite + saponite; and quartz-feldspar-muscovite-biotite schist lithics. We observe clasts of chromite with rims and internal cracks of magnetite, similar to those observed by Moore & Rymer (2012) in saponite-rich gouge from SAFOD and a nearby surface outcrop. The presence of remnant apatite and titanite in some clasts associated with talc and saponite suggests

the clasts are former mafic rocks that have been severely metasomatically altered; these otherwise low-Mg clasts are the only clasts we have identified saponite within (Figure 4.7C).

4.6 Frictional & Hydrological Properties

4.6.1 Experimental methods

Friction and permeability experiments were undertaken on intact wafers of fault core gouges. Wafer long-axis orientations were cut parallel to fault shear direction and had final dimensions of 5-8 mm thick, 54 mm wide and 61 mm long. In each experiment, two fault rock wafers were placed between a three-piece steel block assembly, jacketed, and deformed at room temperature in a servo-controlled biaxial testing apparatus fitted with pressure vessel (see Samuelson et al. 2009 for deformation apparatus and experimental method details) (Figure 4.8 inset). A total of four friction experiments were conducted on fault gouges collected from the Martyr River, McKenzie Creek and Hokuri Creek sites. An additional experiment was done on fault gouge collected from a fresh exposure at Gaunt Creek on the central section of the Alpine Fault, to allow a more direct comparison between fault gouges exposed on the central and southern Alpine Fault (Table 4.2).

At the start of each experiment, wafers were saturated with pore fluid (University Park, Pennsylvania, USA tapwater), loaded to a constant effective normal stress between 6 MPa and 31 MPa and left under load until compacted thickness remained unchanged. Wafers were then sheared by driving the center block at a constant displacement rate to attain steady state frictional behavior. The steady state coefficient of friction (μ) was calculated as the ratio of shear stress (τ) to effective normal stress (σ_n') assuming zero cohesion.

In the second part of each experiment, velocity step tests were conducted by varying the load point velocity between 1 and 300 μm/s; velocity was increased incrementally and the frictional response to each velocity step was recorded. We used empirical rate-and-state friction (RSF) equations to describe velocity step results, where

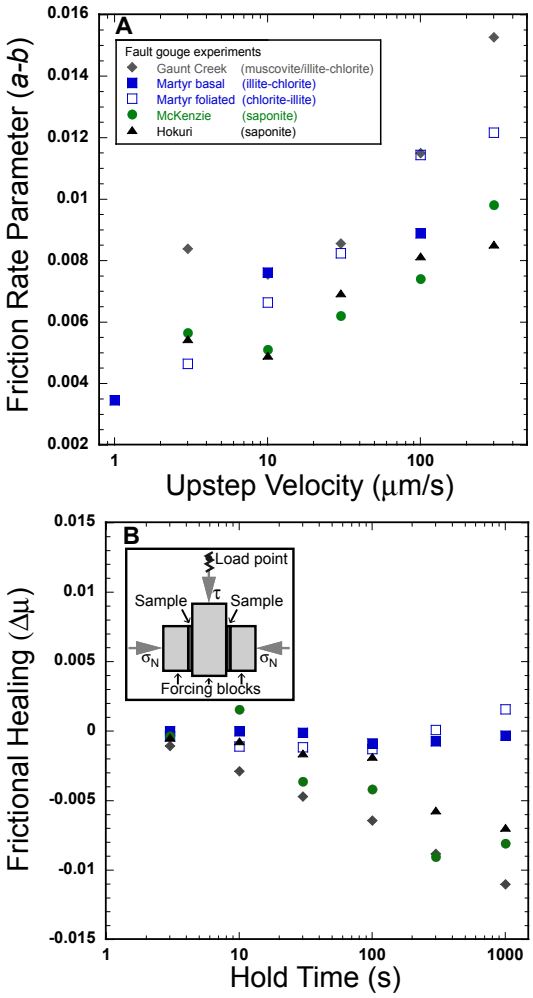

Figure 4.8: Fault Core Friction Parameters. **A,** Plot of friction rate parameter $(a-b)$ versus upstep velocity (μm/s) for intact wafers of phyllosilicate-rich fault gouges. See text for definitions. Experiment names: Gaunt Creek muscovite/illite-chlorite gouge (GC_Gp3673), Martyr River illite-chlorite basal gouge (MR_Gp2861), Martyr River chlorite-illite foliated gouge (MR_FGp3152), McKenzie Creek saponite gouge (MK_CGp3373), and Hokuri Creek saponite gouge (HK_CGp3372). **B,** Plot of frictional healing ($\Delta\mu$) versus hold time (s). Inset shows double direct shear apparatus configuration used for these experiments.

$$\mu_{ss} = \mu_0 + a \ln \left(\frac{V}{V_0} \right) + b \ln \left(\frac{V_0 \theta}{d_c} \right) \tag{4.1}$$

and μ_0 and μ_{ss} are the initial and final, steady state, friction coefficient at the reference sliding velocities V_0 and V is the sliding velocity, a is a parameter that describes the direct effect, b is the parameter that describes the evolution effect, d_c is the critical slip distance, and θ is the state parameter, given by

$$\frac{d\theta}{d\tau} = 1 - \frac{V\theta}{d_c} \tag{4.2}$$

in the Dieterich formulation of the law (Dieterich 1978). The friction rate parameter (a–b) describes the effect of changes in slip velocity on steady state friction, and from (4.1) and (4.2), $(a - b) = \frac{\Delta\mu}{\Delta \ln \nu}$. We determined the friction rate parameter for each velocity step by iteratively solving equations (4.1) and (4.2) to find least squares best fit to our data (e.g., Marone 1998).

At the end of each experiment, a series of slide-hold-slide tests were done to measure the frictional healing. Frictional healing ($\Delta\mu$) is the difference in peak friction following a hold relative to the steady-state sliding friction prior to the hold. In these tests, wafers were sheared at 10 μm/s, held motionless for a prescribed time (t_h) between 1 and 1000 s and then driven at 10 μm/s again.

Separate flow-through permeability measurements were made on wafers of each fault rock at 31 MPa effective normal stress using the same experimental configuration. In the pressure vessel, normal and confining pressures were applied and maintained via hydraulic servo-controllers. Fault rock wafers were then saturated with pore fluid and allowed to equilibrate until steady state boundary conditions were reached. A differential fluid pressure was imposed to induce flow normal to the shear direction of the intact wafers, and permeability was calculated at steady state flow rate using Darcy's law.

4.6.2 Frictional properties

All fault core rocks tested have low friction coefficients (μ = 0.12 to 0.37) and positive values of a–b between 0.0035 and 0.015 (see Figure 4.5 for locations of samples; Table 4.3; Figure 4.8A). The weakest fault gouges, collected

Experiment	Sample	σ'_n (MPa)	P_c (MPa)	P_p (MPa)	k m2	ms
p3673	Gaunt Creek gouge	6	4	1	3.1 e-20	0.28
p2861	Martyr River gouge	30.9	25	10	1.88 e-20	0.32
p3152	Martyr River foliated gouge	31	15	10	1.16 e-19	0.37
p3373	McKenzie Creek gouge	6	4	1	1.5 e-22	0.13
p3372	Hokuri Creek gouge	6	4	1	3.6 e-21	0.12

Table 4.3: Friction / Permeability Experiment Details and Results.

from McKenzie and Hokuri Creeks, are composed primarily of saponite, chlorite and lizardite (Figure 4.7 and Table 4.2). The very low friction coefficients of these gouges ($\mu = 0.13$ and 0.12 respectively) lie within the range measured on saturated saponite-rich gouges collected from the Gokasho-Arashima Tectonic Line, Japan ($\mu = 0.06 - 0.12$) (Sone et al., 2012) and the San Andreas Fault ($\mu = 0.09 - 0.25$) (Lockner et al. 2011; Carpenter et al. 2011, 2012). Saponite-rich fault core rocks also exhibit velocity-strengthening behavior, with positive values of the friction rate parameter (a–$b = 0.0049 - 0.0098$) that fall within the range reported for fault gouge comprising the actively creeping central deforming zone (CDZ) of the San Andreas Fault (a–$b = 0.0040 - 0.019$) (Carpenter et al. 2012).

Phyllosilicate-rich muscovite/illite-chlorite fault gouge from Gaunt Creek and saponite-chlorite fault gouges from McKenzie and Hokuri Creeks exhibited frictional healing of zero or below, even over the longest hold times (t_h =1000 s) (Figure 4.8b). The healing behavior of illite-chlorite gouge and chlorite-illite foliated gouge from the Martyr River varied. The illite-chlorite gouge sometimes strengthened with hold time, while the foliated gouge weakened over short hold times (t_h =3, 10, and 30 s) and strengthened over longer hold times (t_h =300 and 1000 s). A lack of frictional healing with hold time was observed in muscovite/illite-chlorite gouges on the central section of the Alpine Fault (Boulton et al. 2012), and saponite-chlorite-rich fault gouges on the San Andreas Fault (Carpenter et al. 2011, 2012). Fault gouges that do not undergo frictional healing are requisite for aseismic creep, but there currently exists no detailed microphysical understanding of this behavior (e.g., Scholz 2002).

4.6.3 Fault gouge hydrological properties

Fault core rocks had very low fault normal permeability (Table 4.3). The saponite-rich fault core gouges from McKenzie and Hokuri Creeks were less permeable ($k = 1.5 \times 10^{-22}$ m^2 and $k = 3.6 \times 10^{-21}$ m^2, respectively) than the illite-rich gouge ($k = 1.88 \times 10^{-20}$ m^2) and chlorite-illite foliated gouge ($k = 1.16 \times 10^{-19}$ m^2) collected from the Martyr River. SEM observations show greater interconnectedness of phyllosilicate sheets in the saponite-rich McKenzie and Hokuri Creek gouges than in Martyr River gouges, which is consistent with their lower permeability. These permeability values are of the same order of magnitude as or lower than those published on central Alpine Fault gouges (Boulton et al. 2012), San Andreas Fault gouges (Morrow et al. 2011), Median Tectonic Line gouges (Wibberley & Shimamoto 2003), and Nojima Fault Zone gouges (Lockner et al. 2000). Low fault core permeability may weaken the Alpine Fault interseismically and coseismically because it allows for the pressurization of pore fluids (Lachenbruch 1980; Sleep & Blanpied 1992; Faulkner & Rutter 2001; Rice 2006; Garagash 2012).

4.7 ^{40}Ar/^{39}Ar Age Constraints on Fault Zone History

^{40}Ar/^{39}Ar step heating analysis was undertaken on individual muscovite crystals from four Greenland Group (AUS plate) samples from the Martyr river area (Table 4.4). Directly equivalent analyses could not be obtained from the PAC plate side of the Alpine Fault in this area due to the absence of appropriate mica phases, but comparable data were derived from step heating of a 30 mg multi-grain aliquot of hornblende separated from a sheared diorite hosted within Brook Street Volcanic Group (PAC plate) mylonites. More detailed analytical methods, petrology and results are provided in the supporting information.

Within the AUS plate domain, all four mica age spectra express a common general form. Young initial ages increase to older ages over the bulk of gas release, defining an irregular plateau or exhibiting mild dispersal about a general attractor (Figure 4.9A). These results are consistent with the deformed character of the sampled materials. Deformed materials are typically partially disturbed systems with a thermal and/or mineralogical overprint

Sample Name	Analysis	Locality	Unit	Unit type	Latitude (°S)	Longitude (°E)	Elevation (m)
p3673	Friction/XRD	Gaunt Creek	fault core	gouge	43.3141	170.3259	180
p2861	Friction/XRD	Martyr River	fault core	gouge	44.1326	168.5536	240
p3152	Friction/XRD	Martyr River	fault core	foliated gouge	44.1326	168.5536	240
p3373	Friction/XRD	McKenzie Creek	fault core	gouge	44.3599	168.1390	580
p3372	Friction/XRD	Hokuri Creek	fault core	gouge	44.4062	168.0648	40
N102801A	40Ar/39Ar	Spoon Slip	AUS - Greenland Group	leucosome	44.1964	168.4301	190
N090610A	40Ar/39Ar	Monkey Puzzle Gorge	AUS - Greenland Group	gneiss	44.1238	168.5523	100
N100102M	40Ar/39Ar	Martyr River	AUS - Greenland Group	mylonite	44.1314	168.5560	170
N091503B1	40Ar/39Ar	Martyr River	AUS - Greenland Group	mylonite	44.1285	168.5594	120
N110603H	40Ar/39Ar	Martyr River	PAC - Maitai Group	mylonite	44.1269	168.5724	270

Table 4.4: Summary of analyzed samples.

that resets the argon systematics of exterior and less retentive sites within the crystal lattice (Batt et al. 2004; Beltrando et al. 2009; Forster & Lister 2009). In such systems, the young initial ages in particular can provide significant geological meaning by dating the nominal episode of disturbance. Although rendered imprecise by diffusional mobility of ^{40}Ar during the disturbance episode, the older age attractor can also provide a qualitative guide to the inherited age upon which the disturbance was imposed (Beltrando et al. 2009; McDougall & Kilgore 1999).

The AUS plate sample fabrics identified and dated in this study are all older than 70 Ma. These results indicate that mylonites on the AUS plate adjacent to the southern Alpine Fault appear to have been unaffected by Alpine Fault-related mylonitization beginning $\sim$ 25 Ma (Kamp 1996; Cooper et al. 1987; Sutherland et al. 2000). Characterization of the isotope systematics using inverse isochron plots could not be applied to the four AUS plate muscovite samples, as data from these tend to cluster near the radiogenic axis and exhibit a poor spread along nominal mixing lines, preventing the robust distinction of isotopic trends.

An Alpine Fault-related signal is apparent, however, in the age signature of PAC plate amphibole sample OU82946. The inverse isochron plot (^{39}Ar/^{40}Ar ratio against ^{36}Ar/^{40}Ar ratio) in Figure 4.9b characterizes the isotope systematics and provides additional confidence in these ages. Fitting reverse isochrons through the hornblende data produces refined model ages of 18 $\pm$ 4 Ma for the initial plateau of the PAC plate mylonite, which we infer results from resetting during Alpine Fault-related mylonitization under greenschist facies conditions (Figure 4.9B). The older 294 $\pm$ 10 Ma age obtained from this sample is interpreted as a Permian crystallization age for

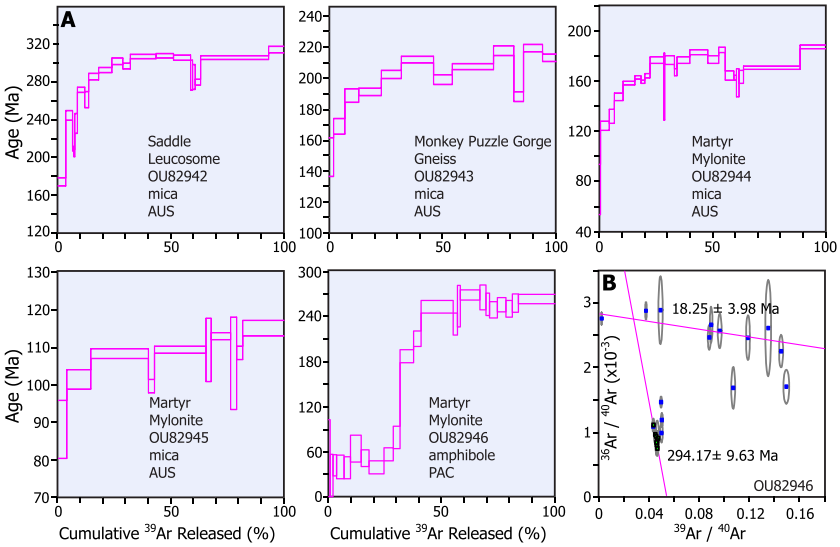

Figure 4.9: $^{40}Ar/^{39}Ar$ Age Plots. **A,** Age spectra plotting variation in the nominal age (Ma) for each heating step against cumulative release of ^{39}Ar (%) as a proxy for experimental progress towards complete outgassing. **B,** Inverse isochron plot ($^{39}Ar/^{40}Ar$ ratio against $^{36}Ar/^{40}Ar$ ratio) for sample OU82946 (PAC plate mylonite).

the hornblende diorite. Thus, the PAC plate amphibole sample records a Miocene disturbance age and an inherited Permian age.

4.8 Discussion

4.8.1 Timing of slip

4.8.1.1 Martyr River

Thermochronological constraints from $^{40}Ar/^{39}Ar$ dating of muscovite separated from AUS mylonites on the southern Alpine Fault reveal that ductile mylonitic fabrics identified in AUS plate rocks west of the Alpine Fault at Martyr Creek are older than 70 Ma. These results corroborate previous geophysical, geological, and geochronological data that indicate that the Alpine Fault exploits, at least locally, a pre-existing continental fault zone active during the Cretaceous (continental because it affects Greenland Group continental sediments) (e.g., Batt et al. 2004; Rattenbury 1987; Sutherland et al. 2000). Although younger AUS plate mylonites that post-date the inception of the modern Alpine Fault at $\sim$ 25 Ma (Sutherland et al. 2000) may be present at depth, our results demonstrate that Miocene-Recent exhumation has not been sufficient to expose such rocks along the southern Alpine Fault.

In contrast, hornblende $^{40}Ar/^{39}Ar$ ages from mylonitized PAC plate diorite sample OU82946 collected 1 km northeast of the Martyr River indicate the ductile fabrics at this site were imposed at 18 $\pm$ 4 Ma – within the known period of Alpine Fault activity. These PAC mylonites were most likely a product of dextral-reverse shear on the central Alpine Fault. The reverse component of shear further north exhumed them at that location, and they were then dextrally translated to their present position in South Westland, where dominantly strike-slip fault motion could not accomplish this exhumation. PAC plate mylonites of comparable age on the central Alpine Fault have been removed due to high exhumation and erosion rates rates (e.g., Batt et al. 2004; Little et al. 2005). PAC plate mylonites from near the Martyr River are thus some of the oldest exhumed mylonites with fabrics formed during activity on the Miocene-Recent Alpine Fault. The alteration

and brittle deformation of the PAC plate mylonites at the Martyr River must also be related to Miocene-Recent Alpine Fault activity.

4.8.1.2 McKenzie Creek & Hokuri Creek

We only observe serpentinite pods hosted within Mg-rich Alpine Fault gouges in the vicinity of McKenzie and Hokuri Creeks, where the immediately adjacent AUS plate Kaipo Mélange contains the greatest abundance of serpentinized ultramafic lithologies. This observation, together with the textural similarities between fault-hosted and mélange-hosted serpentinites, indicates that the Kaipo Mélange is the source of the fault core lithologies. Thus, the serpentine-bearing fault core gouges must be younger than the mélange. At the Kaipo Slips, fold geometry and extent of re-crystallization in the Middle Eocene-Late Oligocene limestone blocks in the mélange is comparable to their counterparts exposed in stratigraphic succession 5 km to the northwest, indicating the Kaipo Mélange formed after limestone re-crystallization.

Nathan (1978) suggested that the thin-bedded mudstone and calcareous sandstone abundant at the Kaipo Slips is similar to Middle Miocene units exposed in a nearby coastal section (Kaipo Member of the Tititira Formation), which could place a further constraint on the maximum age of the Kaipo Mélange. We suggest that the mélange may represent subduction-related accretionary wedge material translated into the Alpine Fault from the southern extent of AUS plate continental crust. If the mélange formation was not a time-transgressive event along strike, the block provenance indicates that slip was localized into the current fault core here after the Late Oligocene ($\sim$ 24 Ma) and possibly after the Middle Miocene (13-8 Ma). A young age for the mélange is consistent with the youthful nature of the Alpine Fault offshore, which is characterized by fault segmentations and step-overs, changes in fault strike, and pull-apart basins. These structural features appear to have formed as a result of inherited Eocene rift structures entering the subducting AUS plate, probably since 6-3 Ma (Barnes et al. 2005). Sutherland et al. (2000) proposed that the Eocene rift boundary may be inherited from Cretaceous oceanic transform faults and an additional older discontinuity

within continental Zealandia. Our AUS mylonite data suggest this exploited discontinuity may be a crustal-scale, Cretaceous-active continental fault zone.

4.8.2 Nature of slip

4.8.2.1 Saponite-rich gouges

Previous studies on the San Andreas Fault correlated creeping sections of the fault in central and northern California with serpentine-bearing rocks of the Franciscan Mélange (Allen 1968; Hanna et al. 1972; Moore & Rymer 2007), and the San Andreas Fault Observatory at Depth (SAFOD) drilling program demonstrated a direct correlation between active fault creep in two active fault cores at $\sim$ 3200 m depth (the CDZ and SDZ) and saponite-bearing fault gouges (Bradbury et al. 2011; Carpenter et al. 2011, 2012; Holdsworth et al. 2011; Lockner et al. 2011). The trioctahedral smectite saponite is thought to form by metasomatic reactions between quartzofeldspathic sedimentary rocks and serpentinite (e.g., Moore & Rymer 2012 and references therein).

Within the Hokuri Creek fault gouge, clasts with relict apatite and titanite associated with talc and saponite may formerly have been mafic rocks; these otherwise low-Mg clasts are the only clasts we have identified saponite within. The relatively low abundance of serpentinite clasts smaller than $\sim$ 1 mm in the Mg-rich gouges may indicate these clast sizes preferentially react to form the saponite matrix. This would suggest that the saponite-forming reactions occur within the gouge zone itself. The thickness of the saponite-rich fault core at Hokuri Creek and McKenzie Creek, and the presence of lizardite-chlorite reaction rims surrounding some serpentinite pods, support a focused fluid flow origin for the saponite, as Holdsworth et al. (2011) proposed for the saponite-bearing SAFOD gouges.

4.8.2.2 Mechanisms of slip

In all the examined gouges, the dominant through-going fabrics are associated with phyllosilicate minerals. Calcite veins are preserved only within clasts. This is dissimilar to observations in SAFOD fault gouge, which have been interpreted to indicate deformation accommodation by solution-transfer processes (Hadizadeh et al. 2012). Furthermore, there is no evidence of clast

indentation, and only a few embayed clast boundaries. The latter could have formed by dissolution during contact with other clasts, but these contacting grains have since been translated away by shear within the surrounding matrix. Based on these observations, we infer that solution-transfer was not important during the most recent deformation of these materials.

The illite-chlorite gouges from the Martyr River are composed of spaced phyllosilicate grains between an anastomosing network of discrete surfaces. On the other hand, the saponite-lizardite-chlorite gouges are composed of continuous phyllosilicates sheets. We infer that the most recent increment of deformation within the illite-chlorite gouges occurred on the anastomosing surfaces and that the phyllosilicate packages were mostly passively rotated between these. Conversely, we infer that a more distributed deformation was relatively evenly accommodated by glide on weak phyllosilicate basal planes in the saponite-rich gouges. This is consistent with observations of experimental and natural serpentine gouge textures, where gouges produced by stable fault creep exhibited a strong alignment of phyllosilicates and lack of strain localization structures (Reinen 2000). In addition to mineralogy, we find that clast abundance and the presence of discrete surfaces likely exerts an important control on frictional properties, with the more clast-rich foliated gouge at the Martyr River exhibiting a higher friction coefficient and positive frictional healing over longer hold times.

On the central Alpine Fault, coseismic slip is inferred to have been focused within cm-thick layers of ultracomminuted material (e.g., ultracataclasite) forming the PSS at the footwall-hanging wall contact (Boulton et al. 2012; Sutherland et al. 2012). We infer similar behavior at the Martyr River where cm-thick layers of ultracataclasite separate PAC and AUS plate lithologies; the ultracataclasite is frequently cemented, exhibits a single striated surface, and in places is juxtaposed against Quaternary sediments by fault motion. At the Martyr River, we can also clearly correlate surface traces of the fault with outcrops of the ultracomminuted material separating PAC and AUS plate lithologies.

In contrast, there are no planar layers of ultracomminuted material within the wide saponite-rich fault core at McKenzie Creek or Hokuri Creek. We consider it unlikely that a single event coseismic displacement of ~ 8 m could

be accommodated within the fault core gouge without leaving evidence of slip localization. Therefore, we suggest that coseismic slip propagates along the slickenlined fault core margins at the contact between phyllosilicate-rich gouge and more competent lithologies. Ikari & Kopf (2011) noted that fault core boundary interfaces have less cohesion than phyllosilicate-rich gouges, and results from field observations, laboratory experiments, and numerical models all indicate that strain localization mostly commonly occurs between materials with different mechanical properties (competencies) (e.g., Goodwin & Tikoff 2002 and references therein).

4.8.2.3 Extent of weak gouges

The extent to which the weak fault gouges accommodate displacement via fault creep and affect rupture propagation depends on the extent to which they are present along-strike and down-dip. Our geological mapping indicates that exceptionally weak saponite-rich gouges derived from the Kaipo Mélange are present for at least 10 km along strike north of Lake McKerrow, but the mélange itself outcrops adjacent to the Alpine Fault for $\sim$ 40 km onshore and may extend an additional 30 km offshore to Sutherland Sound where the continental shelf terminates against the Alpine Fault. Along-strike observations of the mélange indicate that the greatest abundance of ultramafic constituents occurs in the northeast where the tectonic fabric is more ductile in nature and marble is present instead of Tertiary limestone. We thus interpret the northeastern portion of the mélange to have been exhumed from a deeper structural level, and propose that the along-fault distribution of ultramafics (and thus saponite-rich gouges) may be greater than exposed at the surface. We have no direct constraints on the down dip extent of these gouges, except to note that pure smectite is unstable at temperatures above $\sim$ 100°C, and is therefore unlikely to be present at depths greater than $\sim$ 4 km assuming a normal geothermal gradient of 25°C/km (Huang et al. 1993). Below this depth, the distribution of illite/muscovite, chlorite, mixed-layer chlorite-smectite, and serpentinite minerals, with correspondingly higher coefficients of friction, likely controls fault core strength (e.g., Moore & Lockner 2011; Moore et al. 1996; Reinen et al. 1991, 1994; Schleicher et al. 2012).

4.8.3 Linking Fault Outcrops to Fault Behavior

Our results highlight a conundrum: weak fault rocks with textures and frictional properties suggestive of slow aseismic slip are exposed in surface outcrops of the Alpine Fault, despite abundant paleoseismic evidence that large magnitude earthquakes occur here (Cooper & Norris 1990; Wells et al. 1999; Wells & Goff 2007; Berryman et al. 2012a). Although GPS, InSAR and survey data quality remain poor on the southern Alpine Fault, we have found no direct evidence of active fault creep in our study area, supporting previous observations made on the Alpine Fault overall by Evison (1971), Wood & Blick (1986), Wallace et al. (2007), Sutherland et al. (2007) and others. Phyllosilicate-rich fault core rocks examined in this study are frictionally weak ($\mu < 0.37$) and velocity strengthening ($a - b > 0$). In addition, all fault gouges exhibited healing rates of zero or below, reflecting static values of friction at or below sliding values of friction. Theoretically, velocity weakening frictional behavior and positive healing rates are required for earthquake rupture nucleation and propagation (e.g., Marone 1998; Scholz 2002). Combined with previously published results, our experiments indicate that wherever studied, fault core gouges exposed on the surface on the Alpine Fault should creep aseismically (e.g., Boulton et al. 2012).

Adjacent to the locus of the widest (12 m-wide), frictionally weakest ($\mu = 0.12$) saponite-bearing fault core at Hokuri Creek, an 8000 yr off-fault paleoseismological record suggests remarkably time-dependent rupture behavior involving large magnitude earthquakes (Berryman et al. 2012a). Thus our fault core observations are in direct conflict with the known seismogenic behavior of the fault at the same location, which leads us to caution workers attempting to characterize the overall behavior of a fault based on surface outcrops. Where weak and strong materials are present in varying distributions (e.g., Handy et al. 2006; Perfettini & Ampuero 2008; Fagereng & Sibson 2010), fault roughness causes variations in normal stress (e.g., Dieterich & Smith 2009), fluctuations in pore fluid pressure occur (e.g., Sibson 1992; Hillers & Miller 2007), or temperature, strain rate and grain-size sensitive deformation mechanisms compete with frictional sliding within the fault core (e.g., Sibson 1977a; Rutter 1983; Bos & Spiers 2000; Gratier et al. 2009,

2011), the Alpine Fault may display rheological behavior that varies spatially and temporally.

In particular, pressure- and temperature-dependent variations in fault rock rheology probably play an important role in the observed lack of aseismic creep. Experimental studies on a variety of fault gouge and fault gouge analogues reveal that temperature strongly influences a given material's friction rate parameters, that is, whether it is velocity strengthening or velocity weakening in response to an instantaneous change in sliding velocity. Using different experimental apparatuses, confining pressures, pore fluid pressures, and sliding velocities between 0.01 and 100 μm/s, each of the following studies found that at elevated temperatures, velocity-strengthening gouges become velocity-weakening: wet quartz gouges (100°C to 300°C) (Chester & Higgs 1992; Kanagawa et al. 2000), wet quartz-illite gouges (250°C to 400°C) (den Hartog & Spiers 2012; den Hartog et al. 2012), wet granite gouges (100°C to 350°C, except at 250°C) (Blanpied et al. 1995), and wet San Andreas Fault gouges (266°C to 349°C) (Tembe et al. 2009). Above the critical temperature necessary for the activation of intracrystalline plastic deformation, c. 300±50°C (Tullis & Yund 1977), quartz-rich gouges in turn becomes velocity strengthening, a process thought to be responsible for the down-dip seismogenic limit (e.g., Sibson 1982; Scholz 2002). Given the high shallow geothermal gradient of 60-70°C/km on the central Alpine Fault (Allis & Shi 1995; Sutherland et al. 2012), and the unknown, but probably lower geothermal gradient on the southern Alpine Fault, additional experiments are needed to quantify the frictional strength, rate and state friction parameters, and healing behavior of Alpine Fault PSS gouges at conditions experienced by the fault from the surface to the brittle-ductile transition. Our observations highlight the importance of considering the cooperative behavior of all parts of an upper crustal fault zone.

4.9 Conclusions

1. Slip on the southern Alpine Fault is localized to a single 1-12 m-thick zone of impermeable, frictionally weak, velocity-strengthening, saponite-lizardite and illite-chlorite-rich foliated gouges. At the sur-

face, coseismic slip appears to propagate along slickensided fault core margins.

2. Australian plate rocks were mylonitized before 70 Ma; thus while the southern Alpine Fault follows a pre-existing locus of deep-seated continental shear, its motion since $\sim$ from the (strike-slip predominant) southern portion of the fault. In contrast, $\sim$ 18 Ma Pacific plate mylonites that outcrop here are some of the oldest and southernmost Alpine Fault-related mylonites exhumed by the dextral-reverse central Alpine Fault and subsequently translated to the south by strike-slip motion. All fault-related damage overprinting Pacific plate mylonites here is thus attributed to Neogene slip on the Alpine Fault.

3. The frictionally weakest, velocity-strengthening fault core material is associated with a serpentine-bearing mélange that is no older than $\sim$ 24 Ma (i.e. is Alpine Fault-related), but possibly younger than $\sim$ 13-8 Ma.

4. While our mineralogical and frictional data of Alpine Fault core gouges are comparable to those of other major weak-cored faults (e.g., San Andreas Fault, Gokasho-Arashima Tectonic Line), they are incompatible with abundant evidence indicating that the southern Alpine Fault fails in large magnitude quasi-periodic earthquakes. Our study highlights the limitations of using surficial outcrop materials and shallow surface, low velocity (below coseismic slip rates of c. 1 m/s) experimental conditions to understand spatio-temporal variations in fault properties.

4.10 Acknowledgements

We wish to thank Brent Pooley for assistance with thin sectioning phyllosilicate-rich gouges, Richard Norris for structural measurements from Summit Creek and helpful discussions, Dave Prior for SEM/EDS use, Alan Cooper for help with thin section petrography, Dave Craw (all above at U. of Otago) for help identifying opaque minerals, Cristiano Collettini for a helpful review an early version of the manuscript, Mark Raven (CSIRO) for quantitative XRD

analyses, John Ristau (GNS Science) for providing focal mechanism data, John Beavan (GNS Science) for details on the Lake McKerrow triangulation/trilateration survey, and Francesca Ghisetti and Rick Sibson for useful discussions. This work was supported by funding from the New Zealand Foundation for Research, Science and Technology (FRST) and the National Geographic Society. This manuscript was greatly improved by reviews from Bob Holdsworth and Tim Little, and by editorial assistance from Onno Oncken.

4.A Appendix

4.A.1 $^{40}Ar/^{39}Ar$ Analytical Procedures

Samples were prepared for $^{40}Ar/^{39}Ar$ dating at the Western Australian Argon Isotope Facility at Curtin University of Technology (Australia), operated by a consortium consisting of Curtin University and the University of Western Australia. Hornblende separates were pretreated by leaching in dilute HF for one minute, and both hornblende and mica grains were thoroughly rinsed with distilled water in an ultrasonic cleaner. Samples were then loaded into individual wells in an aluminum disc for irradiation, bracketed by Fish Canyon sanidine (FCs) as a neutron fluence monitor, for which an age of 28.03 $\pm$ 0.08 Ma was adopted (Jourdan & Renne 2007). The discs were Cd-shielded to minimize undesirable nuclear interference reactions and irradiated for 25 hours in the Hamilton McMaster University nuclear reactor (Canada) in position 5C. Mica samples were analysed by step-heating individual c. 0.5mm diameter grains with a 110 W Spectron Laser Systems continuous Nd-YAG (I1064 nm) laser, rastering the beam over the sample for approximately 1 minute for each heating step to ensure homogenous distribution of temperature. Approximately 30 mg of hornblende sample OU82946 was packaged in zero-blank niobium foil and step-heated in a double vacuum high frequency Pond Engineering furnace. Gas was purified in a stainless steel extraction line using three SAES AP10 getters and a liquid nitrogen condensation trap. Ar isotopes were measured across 10 cycles of peak hopping using a MAP 215-50 mass spectrometer operated in static mode with a Balzers SEV 217 electron multiplier. Data acquisition was performed in a LabView environ-

ment with the Argus program written by M. O. McWilliams. Raw data were processed using ArArCALC software [Koppers, 2002], and the ages quoted have been calculated using the decay constants recommended by Steiger & Jager (1977). Laser blanks were monitored every 3 to 4 steps and typical ^{40}Ar blanks range from 1×10^{-16} to 2×10^{-16} mol. Furnace blanks were monitored every 3 samples and range from 3 to 10 times the laser blanks.

4.A.2 Sample Petrology

Sample OU82942 is a weakly mylonitized foliation-parallel quartzfeldspar leucosome hosted in calcic plagioclase (hornfels facies) metamorphic zone Greenland Group metasandstone and metapelite from Spoon Slip, 12 km southwest of the Martyr River, and about 150 m northwest of the Alpine Fault (metamorphic zones after Rattenbury et al. 2010). OU82943 is a sillimanite (amphibolites facies) metamorphic zone Greenland Group gneiss (the highest metamorphic grade this unit reaches) from Monkey Puzzle Gorge, about 1 km northwest of the Alpine Fault at the Martyr River. OU82944 is a low grade quartzo-pelitic mylonite with anatomosing foliation and a semi-brittle overprint about 90 m northwest of the Alpine Fault in a tributary of the Martyr Rvier. OU82945 is a well-foliated quartzo-pelitic mylonite from 50 m northwest of the Alpine Fault at the Martyr River. Outcrops clearly show the low grade mylonitization in OU82944 and OU82945 overprints the sillimanite grade gneissic fabric in OU82943. OU82946 is a rare 2 m by 5 m lozenge of L $>$ S fabric hornblende dioritic mylonite hosted within a 400 m wide section of fine-grained chlorite-epidote-quartz metavolcaniclastic mylonite on the PAC plate. Thin section observations indicate the chlorite-epidote alteration occurred at a similar time to the mylonitization (and likely at the same time as the host Brook Street terrane-derived volcaniclastic mylonites). Ductile folding in both AUS and PAC mylonites appears to post-date shear fabrics.

4.A.3 Expanded Results

Results from ^{40}Ar-^{39}Ar analyses are summarised in Figure 4.7A as age spectra plotting variation in the nominal age for each heating step against progressive release of ^{39}Ar as a proxy for experimental progress towards complete out-

gassing. Additional isotopic characterisation is provided for hornblende sample OU82946 by an inverse isochron plot ($^{39}Ar/^{40}Ar$ ratio against $^{36}Ar/^{40}Ar$ ratio) (Figure 4.9B). Such interrogation was not considered relevant for the mica samples, as data from these tend to cluster near the radiogenic axis and exhibit a poor spread along nominal mixing lines, preventing the robust distinction of isotopic trends.

With the possible exception of OU82943, the age spectra express a common general form, with young initial ages increasing to older levels over the bulk of gas release defining an irregular plateau (mica OU82945 and hornblende OU82946) or exhibiting mild dispersal about a general attractor (OU82944 and OU82942). Such patterns are typical of partially disturbed systems, where a thermal and/or mineralogical overprint has reset the argon systematics of exterior and less retentive sites within the crystal lattice. In such systems, significant geological meaning can be derived from the young initial ages – which date the nominal episode of disturbance – and to a lesser degree, the older age attractor. Although rendered imprecise by diffusional mobility of ^{40}Ar during the disturbance episode, the older age attractor provides at least a qualitative guide to the inherited age on which the disturbance was imposed.

This breakdown is best defined for hornblende sample OU82946, for which the initial lower age defines an extended plateau rather than a simple asymptotic limit. $^{39}Ar/^{40}Ar$-$^{36}Ar/^{40}Ar$ isotope ratio trends demonstrate equilibration of this sample with non-atmospheric argon reservoirs, such that elementary correction for non-radiogenic argon misestimates sample ages. Fitting reverse isochrons through relevant data points to more appropriately correct for this mixing produces model ages of 18 $\pm$ 4 Ma for the initial plateau and 294 $\pm$ 10 Ma for the older heating steps later in the experiment. Although less precisely defined and not individually compelling, the initial disturbance ages for mica samples OU82945, OU82944 and OU82942 are all consistent with the Early Miocene episode postulated for OU82946, supporting the attribution of wider geological significance to this age. The older ages for these samples are more varied, with imprecisely defined attractors at approximately 260 Ma for OU82942 and 210 Ma for OU82944, and a rigorous plateau age (comprising sequential steps with statistically indistinguishable

apparent ages) of 142.9 ± 2.4 Ma across the last 47% of argon release for sample OU82945. Although limited to a largely qualitative definition, the two-fold variation in these older signals indicates that this probably reflects real variation in the pre-Miocene fabric ages of these samples. Mica sample OU82943 departs from this general behavior, with progressive age release dominated by mild dispersal about an attractor at c. 235 Ma throughout the bulk of gas release. Although exhibiting slightly reduced and variable initial ages, no clear evidence of a specific disturbance episode can be resolved for this sample.

Chapter V

Frictional Properties of Exhumed Fault Gouges in DFDP-1 Cores, Alpine Fault, New Zealand

Carolyn Boulton[1], Diane E. Moore[2], David A. Lockner[2], Virginia G. Toy[3], John Townend[4], Rupert Sutherland[5]

[1]Department of Geological Sciences, University of Canterbury, Private Bag 4800, Christchurch 8140, New Zealand

[2]U.S. Geological Survey, Menlo Park, California, USA, 94025

[3]Department of Geology, University of Otago, PO Box 56, Dunedin 9054, New Zealand

[4]School of Geography, Environment, and Earth Sciences, Victoria University of Wellington, PO Box 600, Wellington 6012, New Zealand

[5]GNS Science, PO Box 30368, Lower Hutt 5010, New Zealand

Abstract

Principal slip zone gouges recovered during the Deep Fault Drilling Project (DFDP-1), Alpine Fault, New Zealand, were deformed in triaxial friction experiments at temperatures, T, of up to 350°C, effective normal stresses, σ_n' , of up to 156 MPa, and velocities between 0.01 and 3 μm/s. Chlorite/white mica-bearing DFDP-1A blue gouge, 90.62 m sample depth, is frictionally strong (friction coefficient, μ, 0.61–0.76) across all experimental conditions tested (T = 70–350°C, σ_n' = 31.2–156 MPa); it undergoes a transition from

positive to negative rate dependence as T increases past 210°C. The friction coefficient of smectite-bearing DFDP-1B brown gouge, 128.42 m sample depth, increases from 0.49 to 0.74 with increasing temperature and pressure (T = 70–210°C, σ_n' = 31.2–93.6 MPa); the positive to negative rate dependence transition occurs as T increases past 140°C. These measurements indicate that, in the absence of elevated pore fluid pressures, DFDP-1 gouges are frictionally strong under conditions representative of the seismogenic crust.

5.1 Introduction

Damaging shallow crustal earthquakes have long been interpreted in terms of stick-slip frictional instabilities on laboratory faults (Brace & Byerlee 1966; Byerlee 1978), and an outstanding goal in fault mechanics remains determining the primary factors governing the frictional strength and stability of fault zone materials (Scholz 1998; Beeler 2007). Numerous room temperature experiments, covering a range of sliding velocities spanning eight orders of magnitude (10^{-3} to 10^4 μm/s), have quantified the frictional properties of bare rock surfaces and granular fault gouge (e.g., Marone 1998; Moore & Lockner 2007; Tembe et al. 2010; Saffer et al. 2012; Boulton et al. 2012). Relatively fewer experiments have been conducted at hydrothermal conditions that better represent the brittle seismogenic crust ($T \sim$ 100°C to 400°C) (e.g., Blanpied et al. 1995; Moore & Lockner 2008, 2011; Niemeijer et al. 2008; Tembe et al. 2009; den Hartog et al. 2012).

The Alpine Fault represents the largest onshore seismic hazard in New Zealand, accommodates 65–75% of the total relative Australia-Pacific plate boundary motion, ruptures episodically in large magnitude (Mw ~ 8) earthquakes, and is late in its seismic cycle (last event 1717 AD; recurrence interval 329 ± 68 years) (Sutherland et al. 2007; Berryman et al. 2012a). On the central Alpine Fault, between the Wanganui and Waiho (Franz Josef) Rivers, rapid exhumation of amphibolite-facies mylonites from c. 35 km depth in the past 5-8 Myr has resulted in a high shallow geothermal gradient of 62.6±2.1°C/km (e.g., Norris & Cooper 2007; Sutherland et al. 2007, 2012). Because the central Alpine Fault exhumes its hanging wall, the mineralogical,

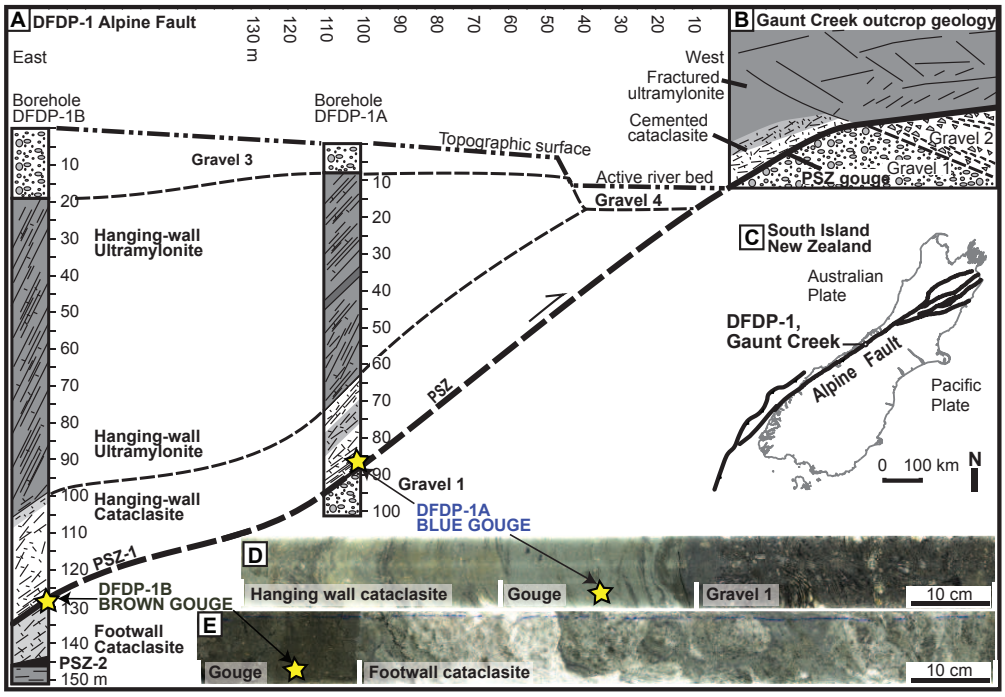

Figure 5.1: Location map and materials used in hydrothermal friction experiments. **A,** Lithological cross-sections of the two boreholes drilled during Phase 1 of the Deep Fault Drilling Project (DFDP-1), Alpine Fault, at Gaunt Creek. Samples were collected from the depths designated with stars. **B,** A schematic cross-section of prominent fault scarp outcrop geology on the south side of Gaunt Creek. **C,** The Australia–Pacific plate boundary in the South Island of New Zealand. **D,** 180° scan of DFDP-1A Run 66, Section 1, from which 1A blue gouge was sampled. **E,** 180° scan of DFDP-1B Run 59, Section 1, from which 1B brown gouge was sampled. Figure modified from Sutherland et al. (2012).

microstructural, and frictional properties of PSZ materials may be diagnostic of similar materials currently deforming at depth (Townend et al. 2009).

Understanding the geological, geophysical, hydrological, and seismological properties of the Alpine Fault are aims of the Deep Fault Drilling Project (DFDP). The first phase of the Deep Fault Drilling Project (DFDP-1) successfully constructed two shallow boreholes intersecting the fault (DFDP-1A, 96.6 m and DFDP-1B, 150.4 m) at Gaunt Creek and collected rock cores, wireline logging data, and hydraulic measurements spanning the fault zone (Figure 5.1). Initial DFDP publications have highlighted the important role

fluid-rock interactions, which result in phyllosilicate precipitation and calcite mineralization, may play in modulating the mechanical properties of the Alpine Fault (Sutherland et al. 2012; Townend et al. 2013).

Norris and Cooper (2007) found that central Alpine Fault gouges and cataclasites form from mechano-chemical alteration of primarily Pacific-plate Alpine Schist-derived mylonites, which are continuous for ~150 km along-strike. Warr and Cox (2001) documented two main phases of alteration in Gaunt Creek surface-outcrop fault gouges and cataclasites: (1) hydrous chloritization at temperatures less than 320°C, and (2) growth of swelling clays, particularly smectite, at temperatures less than 120°C. The extent to which alteration processes affect the frictional strength and frictional stability of central Alpine Fault gouges remains incompletely understood. Here, we report the results of low-velocity hydrothermal friction experiments designed to investigate the conditions requisite for earthquake rupture nucleation. Experiments were conducted on two fault gouges comprising the principal slip zone (PSZ) intersected in DFDP-1A and DFDP-1B. Because each PSZ gouge has a distinct mineral assemblage representative of high or low temperature alteration, experimental results quantify how frictional properties vary with mineralogy, temperature, and pressure.

5.2 Methods

5.2.1 Material characterization

Two fault gouges (incohesive fault rock with >90% matrix grains <0.1 mm in size) were selected from DFDP-1A and DFDP-1B cores for investigation. Gouge samples were vacuum dried overnight at 40ºC to remove moisture and then gently disaggregated using a mortar and pestle. Sieved separates (<150 μm) were made by passing each gouge powder through a 100# sieve. Quantitative X-ray diffraction (XRD) was done on the sieved gouge separates used in friction experiments following methods described by Boulton et al. (2012) (Chapters 2 and 3). Particle size analysis of each separate was undertaken with a Saturn Digisizer 5205 following the method of Storti & Balsamo (2010) (for detailed methods, see Appendix E).

5.2.2 Material description

DFDP-1 principal slip zone (PSZ) materials occur within a wider (c. 20–30 m) fault core-alteration zone characterized by products of cataclasis, authigenic clay mineralization, and carbonate alteration (Sutherland et al. 2012; Townend et al. 2013) (Figure 5.1). Hydrothermal experiments were conducted on two PSZ fault gouges: (1) a blue fault gouge from DFDP-1A (Run 66, Section 1, 0.44 m below top of core, 90.62 m adjusted hole depth; hereafter "1A blue gouge"); and (2) a brown fault gouge from DFDP-1B (Run 59, Section 1, 0.12 m below top of core, 128.42 m adjusted hole depth; hereafter "1B brown gouge"). Field observations indicate that gouges with similar contact relationships and mineralogy occur in fault exposures that span at least 120 km along strike (Boulton et al. 2012; Barth et al. 2013).

The c. 18 cm-thick 1A blue gouge forms a gradational upper contact with foliated cataclasite and a sharp, but undulating (cm- to mm-scale) lower contact with c. 2 cm-thick brown gouge. It contains calcite vein fragments and clasts of ultramylonite, cataclasites, and the underlying brown gouge. The sieved separate contains the following minerals: quartz (29%), K feldspar (42%), plagioclase (6%), calcite (7%), muscovite/illite (9%), clinochlore (7%), anatase (<1%), and rare pyrite. Median grain size is c. 4 μm, with 90% of analyzed grains having diameters <65 μm.

The upper contact of the c. 20 cm-thick 1B brown gouge was not retrieved but this material is compositionally similar to the brown gouge that occurs below the 1A blue gouge. Compared to the 1A blue gouge, 1B brown gouge has a higher proportion of brown gouge clasts, fewer cataclasite and ultramylonite clasts, fewer calcite vein fragments, and Fe oxide-hydroxide cement. The sieved separate contains the following minerals: quartz (22%), K feldspar (15%), plagioclase (21%), calcite (10%), muscovite/illite (5%), montmorillonite (26%), clinochlore (1%), and rare pyrite. The 1B brown gouge median grain size is c. 3 μm, with 90% of analyzed grains having diameters <41 μm; thus, it is finer grained than the 1A blue gouge.

5.3 Hydrothermal Friction Experiments

5.3.1 Experimental procedure

Eighteen shearing experiments were conducted using a triaxial deformation apparatus: ten experiments following a lithostatic confining pressure gradient consistent with crustal density of 2650 kg/m^3, hydrostatic pore fluid pressure, and a 35°C/km geothermal gradient; six at equivalent stresses with elevated temperatures; and two at room temperature and σ_n' = 31.2 MPa (Table 5.1). Minerals comprising the 1A blue gouge are thermodynamically stable to temperatures of c. 320-350°C. Montmorillonite in the 1B brown gouge is thermodynamically unstable above temperatures of c. 120-140°C (Pytte & Reynolds 1988; Moore & Reynolds 1997; Warr & Cox 2001). Thus, the 1A blue gouge was tested across a wider range of temperatures and pressures. Experiments were conducted using an inclined (30° plane) sawcut configuration, furnace assembly, and methods described in Moore & Lockner (2011).

For each experiment, the test sample, a 1 mm-thick layer of gouge, was applied to a 30° inclined plane cut in a 19.1 mm-diameter by 41 mm-long Westerly Granite cylinder. Sawcut surfaces were roughened with 120 grit SiC to avoid boundary slippage. Deionized water was used as pore fluid and maintained at constant pressure with access to the fault by a 2.4 mm-diameter hole. Servo-controlled confining pressure was adjusted once per second in response to changes in axial load to maintain constant normal stress on the inclined sawcut. Furnace heating took 30 minutes, and temperature varied less than 2°C during each experiment. To determine the friction rate parameter (a–b), velocity steps between 0.01 and 3 mm/s were imposed according to predefined scripts. Total axial displacement varied between 2.41 and 3.63 mm (Figure 5.2). For a 30° inclined sawcut, fault-parallel displacement is approximately 15% larger.

Corrections were made for seal friction, the pressure- and velocity-dependence of seal friction, changes in contact area of the sawcut surfaces, elastic deformation of the loading system, copper and lead jacket shear resistance, and Teflon® shim friction (see Tembe et al. 2010; Moore & Lockner 2008, 2011; Appendix E). Below 250°C, shear stress corrections for Cu jackets are 6 to 10

Experiment	Material	Temp (°C)	σ'_n (MPa)	P_p (MPa)	μ^*	$(a-b)^\#$
AFHT07	1A blue gouge	350	156.0	104.0	0.76	-0.0089
AFHT23	1A blue gouge	350	93.6	93.6	0.76	-0.0079
AFHT24	1A blue gouge	350	62.4	41.6	0.76	-0.017
AFHT05	1A blue gouge	280	125.0	83.0	0.71	-0.0053
AFHT16	1A blue gouge	280	93.6	93.6	0.70	-0.013
AFHT18	1A blue gouge	280	62.4	41.6	0.70	-0.0089
AFHT06	1A blue gouge	210	93.6	93.6	0.63	-0.0035
AFHT15	1A blue gouge	210	93.6	93.6	0.62	-0.0059
AFHT19	1A blue gouge	210	62.4	41.6	0.65	-0.0051
AFHT20	1A blue gouge	210	31.2	20.8	0.67	-0.012
AFHT08	1A blue gouge	140	62.4	41.6	0.60	0.00077
AFHT09	1A blue gouge	70	31.2	20.8	0.61	0.0050
AFHT10	1A blue gouge	23	31.2	20.8	0.63	0.0076
AFHT13	1B brown gouge	210	93.6	93.6	0.74	-0.011
AFHT25	1B brown gouge	175	78.0	52.0	0.67	-0.0084
AFHT12	1B brown gouge	140	62.4	41.6	0.65	-0.0061
AFHT14	1B brown gouge	70	31.2	20.8	0.49	0.0031
AFHT11	1B brown gouge	23	31.2	20.8	0.43	0.0043

Table 5.1: Experiment conditions and materials with results summary. Columns are experiment number, matieral, temperature in °C, effective normal stress (σ'_n) in MPa, pore fluid pressure (P_p) in MPa, coefficient of friction, and friction rate parameter (a–b). (*) indicates that the coefficient of friction listed is the residual coefficient of friction at 2.70 mm axial displacement. The coefficient of friction in AFHT16 and AFHT23 was taken at 2.39 mm axial displacement. ($^\#$) indicates that the friction rate parameter (a–b) listed was determined from the 1 μm/s to 0.1 μm/s velocity step at 2.30 mm axial displacement.

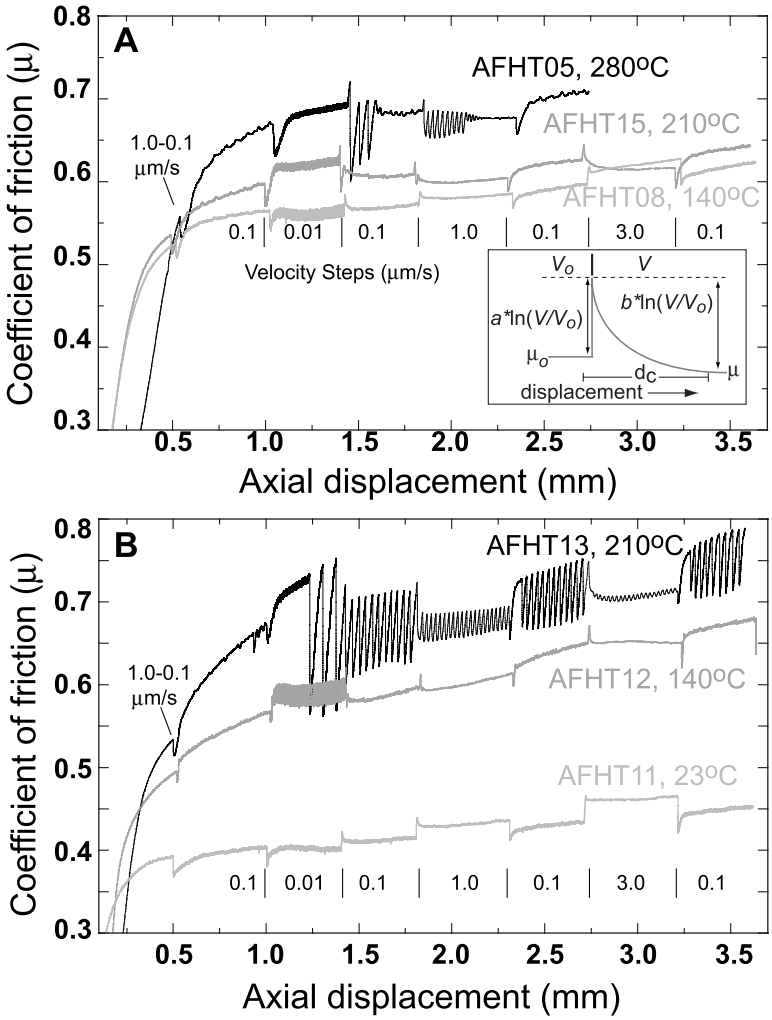

Figure 5.2: Plots of coefficient of friction vs. axial displacement for triaxial experiments conducted on Alpine Fault gouges. For a 30° inclined sawcut, fault-parallel displacement is approximately 15% larger than axial displacement **A,** Representative DFDP-1A blue gouge experiments conducted following depth-dependent increases in temperature and effective normal stress. Velocity steps are demarcated. Rate and state friction parameters are depicted graphically in the inset figure. **B,** Representative DFDP-1B brown gouge experiments conducted following the same method. All run plots are located in Appendix E.

MPa; therefore, tests in this temperature range are performed with Pb jackets (corrections are less than 2 MPa). Typical uncertainties in μ for tests from room temperature to 210° (using Pb jackets) are ± 0.02 while uncertainties at higher temperatures (with Cu jackets) are ± 0.03. A repeat experiment conducted on DFDP-1A gouge at 210°C, σ_n' = 93.6 MPa, revealed a difference in μ for copper and lead jackets of 0.01. Cu jackets exhibit rate-dependent strength variations in the range of (a–b) = 0.01. Lead jackets do not have measureable velocity sensitivity.

5.3.2 Data analysis

Strength results are presented in terms of the coefficient of friction $\mu = \frac{\tau}{\sigma_n'}$ where τ is the resolved shear stress, $\sigma_n' = \sigma_n - P_p$ is the effective normal stress, and σ_n and P_p are the resolve normal stress and the pore pressure, respectively. To minimize the effects of strain hardening that varies from test to test, representative strengths are reported at a velocity of 0.1 μm/s and 2.70 mm axial displacement (nominal fault-parallel slip of 3.1 mm). Two samples (AFHT16 and AFHT23) underwent early jacket failure; in those cases, μ was measured near the beginning of the velocity step (2.39 mm slip).

In terms of rate and state friction laws, linear stability analyses show that the mechanical conditions and constitutive properties that distinguish stable (aseismic) from unstable (seismic) sliding can be quantified by the friction rate parameters (a–b) and the critical slip distance d_c (Dieterich 1979; Ruina 1983; Scholz 1998). We estimated (a–b) and other constitutive parameters using an iterative least squares method incorporating the Dieterich (1979) constitutive friction equation:

$$\mu_{ss} = \mu_0 + a \ln\left(\frac{V}{V_0}\right) + b_1 \ln\left(\frac{V_0\theta_1}{d_{c1}}\right) + b_2 \ln\left(\frac{V_0\theta_2}{d_{c2}}\right) \tag{5.1}$$

$$\frac{d\theta_i}{dt} = 1 - \frac{V\theta_i}{d_{ci}}, (i = 1, 2) \tag{5.2}$$

where V_0 and V are the initial and final load point velocities, respectively, μ_0 and μ_{ss} are the initial and final, steady state, coefficients of friction, and a,

b_1, b_2, and the critical slip distances d_{c1} and d_{c2} are empirically derived constants. The state variables θ_1 and θ_2 evolve with time according to equation (5.1). For many velocity steps, data are well fit using a single state variable, and $\theta_2 = 0$ (equation 5.1). In the two state variable models, a–b was determined by letting $b = b_1 + b_2$. Even with the inclusion of two state variables, equations 5.1 and 5.2 are unlikely to represent all of the physicochemical processes that occur under hydrothermal conditions in these experiments. It was necessary to add an additional term, proportional to displacement, to correct for displacement-strengthening or -weakening (Blanpied et al. 1998). Additional effects, such as permanent time-dependent strengthening, were not modeled. Only stable fault slip is possible if (a–b) is positive. If (a–b) is negative, fault slip is unstable when stiffness (k) is less than a critical positive stiffness (k_{crit}) and oscillatory in the vicinity of k_{crit} (Scholz 1998). In a single degree of freedom spring-slider model, k_{crit} is given by:

$$k_{crit} = \frac{-(a-b)\,\sigma_n'}{d_c} \tag{5.3}$$

(Beeler 2007). Constitutive parameters for the least-squares fit of all modeled velocity steps are tabulated in the auxiliary material, Table 5.2.

5.3.3 Frictional strength

The frictional strength of the 1A blue gouge increased from $\mu = 0.61$ at low effective normal stress and temperature (σ_n' = 31.2 MPa and T = 70°C) to $\mu = 0.76$ at higher effective normal stress and temperature conditions (σ_n' = 156 MPa and T = 350°C). As seen in Figure 5.3, 1A blue gouge strength depends primarily on temperature and has little sensitivity to σ_n', especially above 250°C. 1B brown gouge frictional strength rapidly increased from μ = 0.49 at low effective normal stress and temperature (σ_n' = 31.2 MPa and T = 70°C) to μ = 0.74 at higher effective normal stress and temperature conditions (σ_n' = 93.6 MPa and T = 210°C; Figures 5.2, 5.3).

5.3.4 Frictional stability

1A blue gouge exhibited near zero or positive (a–b) for all velocity steps conducted at T = 23°C to 140°C, σ_n' = 31.2 MPa to 62.4 MPa (Figures 5.2A

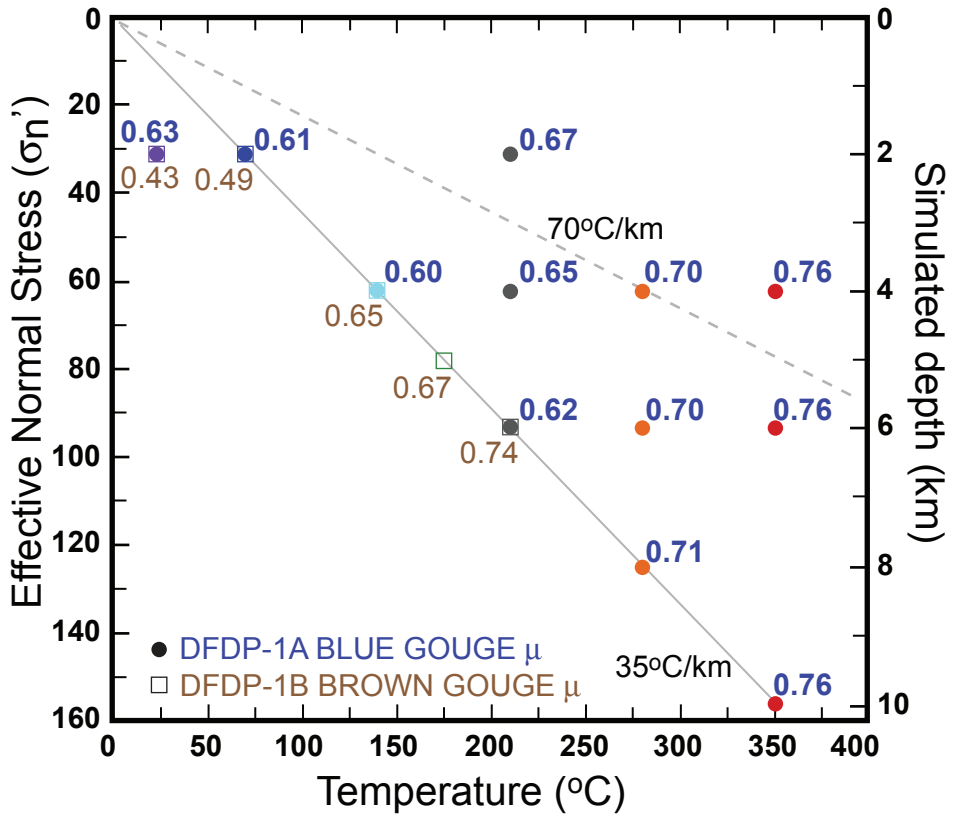

Figure 5.3: Frictional strength as a function of gouge lithology, temperature, and effective normal stress. Plotted for reference are 35°C/km and 70°C/km geothermal gradients. DFDP-1A blue gouge μ values are in blue font, and DFDP-1B brown gouge μ values are in brown font. 1A blue gouge symbols (circles) and 1B brown gouge symbols (open squares) are color-coded to match temperature in Figure 5.3.

and 5.4A). In experiments conducted at temperatures $\geq$ 210°C, values of (a–b) were negative for all velocities and all effective normal stresses (Figures 5.4A and 5.4B). An exception occurred at 210°C, σ_n' = 62.4 MPa, v = 3 μm/s, where (a–b) was positive (Figure 5.4B).

In 1A blue gouge experiments conducted at different effective normal stresses (σ_n' = 31.2 to 156 MPa) and constant temperatures of 350°C (3 experiments), 280°C (3 experiments), and 210°C (3 experiments), a positive correlation between temperature and magnitude of the individual parameters a and b was observed. There was also a velocity dependence; the magnitude of a and b magnitude decreased with increasing velocity. With the available data, the correlation between effective normal stress and the magnitude of a and b is less clear (Figure 5.5) (Table 5.2).

While 1B brown gouge frictional strength increased markedly with temperature and pressure, frictional stability, as measured by the friction rate parameter (a–b), became increasingly negative (Figures 5.2B and 5.4C). 1B brown gouge (a–b) was near zero or positive at 23°C and 70°C. At 140°C, σ_n' = 62.4 MPa, values of (a–b) were negative for every velocity step size, becoming less negative with increasing velocity. At 175°C, σ_n' = 78.0 MPa, and at 210°C, σ_n' = 93.6 MPa, values of (a–b) were also negative for every velocity step size (Figure 5.4C).

5.4 Discussion

The Alpine Fault exhumes its hanging wall, and minerals in the 1A blue gouge are stable to c. 350°C (Warr & Cox 2001). Therefore, mineralogical, microstructural, and frictional properties of PSZ materials recovered in DFDP-1 may be diagnostic of similar materials currently deforming at depth (Townend et al. 2009). Because the incohesive, ultrafine-grained 1A blue gouge contains clasts of ultramylonite, cataclasite, and underlying 1A brown gouge, it comprises part of a <50 cm-thick principal slip zone that includes the 1A brown gouge (Sutherland et al. 2012) (Figure 5.1). For the hydrothermal friction experiments, brown PSZ gouge could only be sampled from DFDP-1B. The 1B brown gouge, like its 1A corollary, formed from mechanical comminution of hanging wall material and low-temperature alter-

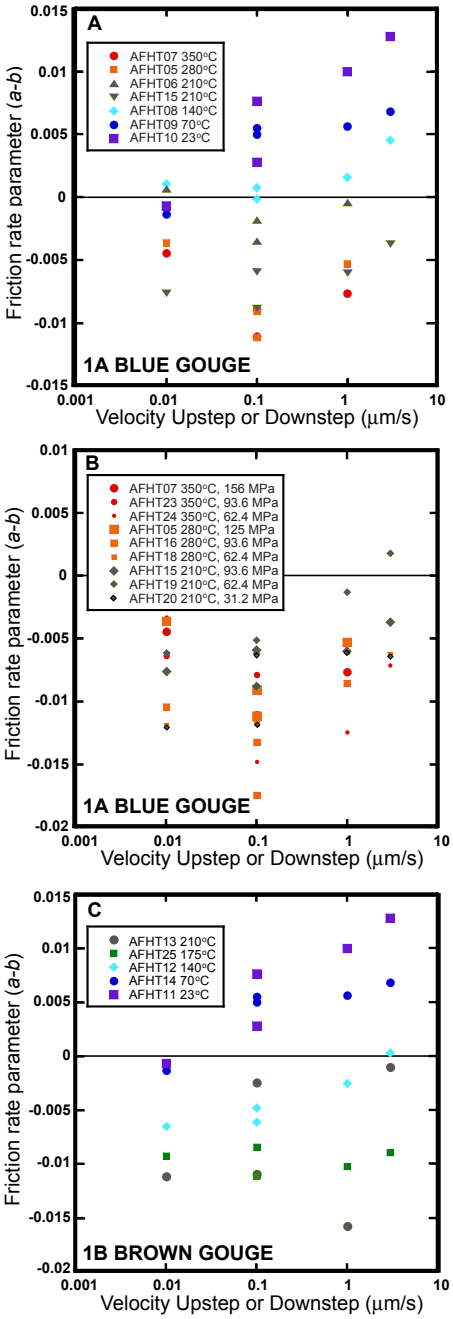

Figure 5.4: Rate and state friction parameters obtained from velocity steps conducted in hydrothermal friction experiments. **A,** DFDP-1A blue gouge friction rate parameters from experiments obtained following simulated depth-dependent increases in temperature and pressure. Also plotted are results from a room temperature experiment. **B,** Results from more detailed experiments on 1A blue gouge investigating the competing effects of temperature and pressure on frictional stability. At all temperatures above 210°C, (a–b) is negative; (a–b) minima occur during the 0.1 μm/s step. **C,** DFDP-1B brown gouge friction rate parameters obtained from experiments conducted following simulated depth-dependent increases in temperature and pressure. Also plotted are room temperature results. The standard deviation in a, $b1$, $b2$ and (a–b) is on the order of 10^{-4}.

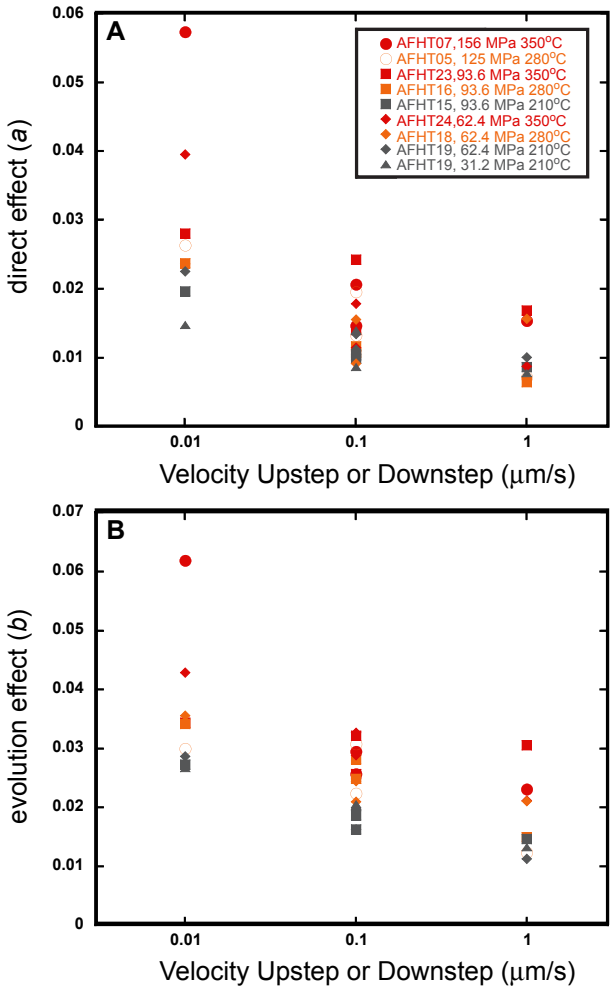

Figure 5.5: Results of 9 experiments on 1A blue gouge at various effective normal stresses (σ_n' = 31.2 to 156 MPa) and temperatures of 210°C, 280°C, and 350°C. Symbols are colour-coded by temperature to match Figures 5.2 and 5.3. Symbols correspond to effective normal stress: 156 MPa (closed circle); 125 MPa (open circle); 93.6 MPa (close squares); 62.4 MPa (closed diamonds); 31.2 MPa (triangle). **(a)** Values of the rate parameter a are larger at higher temperatures and slower velocities. **(b)** Values of the rate parameter b are also larger at higher temperatures and slower velocities.

ation of clinochlore to form montmorillonite (dioctahedral smectite) (Section 5.2) (Boulton et al. 2012). Hydrothermal friction experiments conducted on both types of fault gouge reveal that thermally activated mechanisms influenced frictional strength and stability.

In hydrothermal experiments conducted following a 35°C/km geothermal gradient to a simulated depth of 10 km, 1A blue gouge μ increased from 0.61 to 0.76 (Figure 5.3). These results correspond to those obtained from experiments performed using compositionally similar granite gouges (μ = 0.65 − 0.75, T = 23°C-350°C, σ_n' = 400 MPa) (Blanpied et al. 1995). In addition, the 1A blue gouge underwent a transition from positive to negative (a–b) at c. 210°C (Figure 5.4a). The transition from positive to negative (a–b) at elevated temperatures has also been observed in low velocity hydrothermal friction experiments on granite gouges (T = 100°C-350°C) (Blanpied et al. 1995), San Andreas Fault gouges (T = 266°C-349°C) (Tembe et al. 2009), and quartz-illite gouges (T = 250°C-400°C) (den Hartog et al. 2012).

The transition from positive to negative (a–b) observed in the 1A blue gouge at c. 210°C can be interpreted in the context of microphysical models proposed by Niemeijer & Spiers (2005, 2007) (see den Hartog et al. 2012 for clay-rich gouge models). According to these models, shear deformation in the gouge is accommodated by granular flow with interchanging framework silicate contacts and frictional slip on phyllosilicates. For slip to occur on inclined contacts, the shearing grains must dilate along a vector determined by the dilatancy angle (Figure 5.6). The dilatancy angle depends on the local geometry of the fault gouge, which in turn is determined by factors such as grain size distribution and grain shape and can be altered during shear due to dilation and compaction. These processes are in turn governed by shearing velocity, normal stress, and time-dependent, thermally activated processes such as intergranular pressure solution and stress corrosion cracking as well as plastic processes such as dislocation and diffusion creep.

At lower sliding velocities and/or higher temperatures, the time-dependent, thermally activated processes dominate over shear-induced dilation, thus promoting porosity reduction, an increase in grain contact area, and an increase in the average dilatancy angle. In turn, steady state dense microstructures

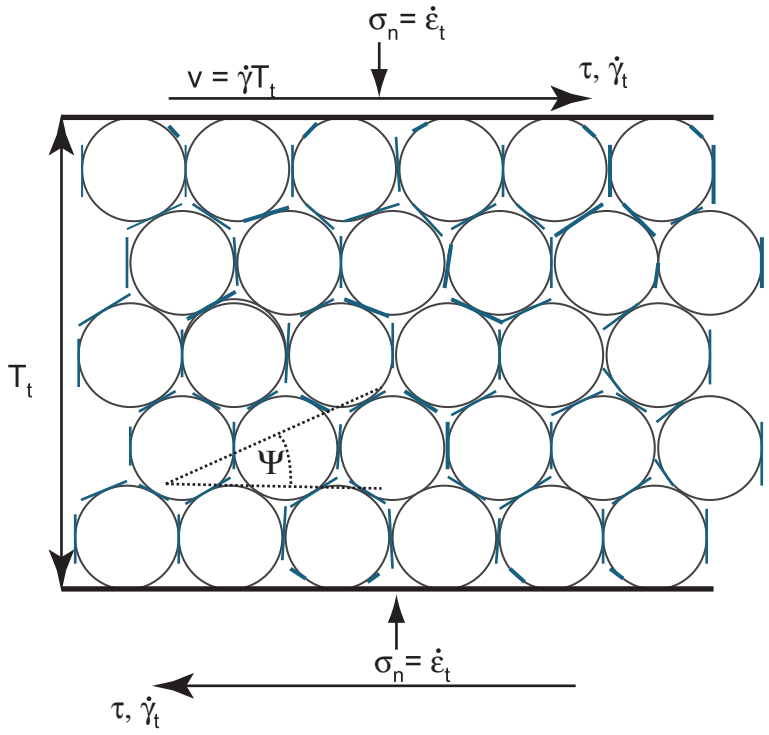

Figure 5.6: Geometry of an ideal gouge deforming by granular flow, in two dimensions. The velocity of deforming gouge is given by v and the thickness of the gouge layer is TT. Framework silicates (e.g., quartz) are open circles, framework silicates (e.g., chlorite and white mica) are blue lines, and the dilatancy angle is ψ Normal stress (σ_n), normal strain rate ($\dot{\epsilon}$), shear stress (τ), and shear strain rate ($\dot{\gamma}$) are given. According to this model, the deforming gouge is fully drained and changes in pore fluid pressure (and thus effective normal stress) are neglected; changes in grain shape are also neglected. Figure and caption after Niemeijer & Spiers (2007).

develop, grain contact shear strength increases, and frictional strength increases according to the relation

$$\tau = \frac{\tilde{\mu} + \tan\psi}{1 - \tilde{\mu}\tan\psi} \times \sigma_n' \tag{5.4}$$

where the tilde denotes grain contact forces, ψ is dilatancy angle, and σ_n' is effective normal stress (Figure 5.6) (Niemeijer & Spiers 2007). At steady state, dilation is balanced by solution-assisted compaction and gouge porosity remains low. During an instantaneous velocity step, dilation accompanying frictional slip along the grain contacts overwhelms solution-assisted compaction. Materials with lower porosities and higher strengths at steady state will exhibit higher dilatancy angles during a velocity step (Beeler 2007; Niemeijer & Spiers 2007 and references therein). Since dilation requires work to be done against normal stress, this results in larger values of the rate parameter a, the direct effect, which agrees with our results (Figure 5.5A).

The evolution effect (b) similarly co-varies with temperature and sliding velocity (Figure 5.5B). As mentioned above, an instantaneous increase in velocity causes dilation, thus increasing porosity and decreasing the dilatancy angle. Following equation 5.4, gouge strength decreases at steady state if the dilation (increase in porosity) that accompanies a velocity increase is greater than the compaction (decrease in porosity) that accompanies sliding at the higher velocity. Thus, larger values of the rate parameter b result, and velocity-weakening behaviour is observed. The microphysical models suggest that negative (a–b) is linked to temperature-, grain size-, effective normal stress-, and time-dependent solution-transfer processes at temperatures greater than c. 150-250°C and less than c. 350-450°C, depending on the ratio of quartz to phyllosilicates (neglecting feldspars). At lower temperatures and/or higher sliding velocities, increases in grain contact area associated with solution-assisted compaction are presumably too slow to be observed; shear deformation is accommodated primarily by dilational frictional sliding along grain contacts. According to the 1A blue gouge frictional stability data, velocity-weakening behaviour correlates more strongly with temperature than with effective normal stress.

The frictional strength of the 1B brown gouge increased with increasing temperature and effective normal stress from $\mu = 0.49$ to $\mu = 0.74$; the increase in frictional strength was accompanied by a transition from positive to negative (a–b) at 140°C (Figures 5.3 and 5.4C). This transition has not previously been observed in room temperature smectite-bearing gouge experiments (e.g., Saffer et al. 2012 and references therein). The observation of increased frictional strength coincident with velocity-weakening behavior agrees with previous findings correlating conditionally unstable or unstable (seismic) slip with frictionally strong materials (Beeler 2007; Ikari et al. 2011a). The change from velocity-strengthening to velocity-weakening behaviour in the 1B brown gouge occurred in the temperature range associated with the thermally driven dehydration of smectite to illite ($T = 120$–$150°C$) (Pytte & Reynolds 1988). Smectite dehydration releases interlayer water, which may accelerate compaction via intergranular pressure solution and/or promote strain localization, both of which are associated with unstable behavior (e.g., Marone 1998; Niemeijer & Spiers 2007; Niemeijer et al. 2008; Saffer et al. 2012; den Hartog et al. 2012). In addition, increasing either temperature or normal stress can drive off films of adsorbed water that lubricate phyllosilicates and reduce frictional resistance (Morrow et al. 2000; Moore & Lockner 2004, 2007).

Knowledge of the frictional strength of the Alpine Fault at seismogenic depths is integral to analysis of its favorability for reactivation (Barth et al. 2012; Boese et al. 2012), as well as the potential stress drop that will accompany coseismic slip (Beeler 2007). Hydrothermal friction experiments on the 1A blue gouge reveal relatively high frictional strength. This could be reduced if interconnected networks of weak phyllosilicates form (Bos & Spiers 2001, 2002), but PSZ fault gouges retrieved during DFDP-1 have random fabrics. High pore fluid pressures could reduce brittle fault strength despite the high frictional strength of the gouge by lowering the effective normal stress. However, the brittle seismogenic crust comprising the Alpine Fault at depth (c. 4-10 km) is resistive and electrically isolated from lower crustal conductive fluids (Wannamaker et al. 2002). If, as the hydrothermal friction results indicate, earthquake rupture nucleation occurs in frictionally strong, velocity-weakening Alpine Fault PSZ gouges, determining the stress

field and fault geometry at depth is critically important to understanding earthquake rupture nucleation (Sibson 1985; Leclère & Fabbri 2013). Based on our measurements, we suggest that a majority of the seismic moment release will accompany failure of rate-weakening material comprising the fault plane over the depth range of c. 3–10 km. In turn, this will govern earthquake rupture propagation rate, the mode of rupture propagation, the frequency and amplitude of radiated energy, and ground motion (e.g., Noda et al. 2009).

5.5 Conclusions

The coefficient of friction of DFDP-1A blue gouge increases with temperature and pressure from $\mu = 0.61$ to $\mu = 0.76$. The stability transition in 1A blue gouge from positive to negative (a–b) occurs at 210°C, irrespective of effective normal stress in the range tested (σ_n' = 31.2 to 93.6 MPa). The frictional strength of DFDP-1B brown gouge increases markedly from $\mu = 0.49$ at room temperature to $\mu = 0.65$ at $T = 140°C$ and σ_n' = 62.4 MPa, coincident with the transition from positive to negative (a–b). Montmorillonite in the 1B brown gouge is thermodynamically unstable. Thus, wherever present on the fault plane, 1A blue gouge frictional properties would govern the Alpine Fault's frictional strength and stability at depths greater than c. 2-3 km given the high shallow geothermal gradient.

Acknowledgements

The first author thanks Mark Raven, Brent Pooley, Rob Spiers, and Lee-Gray Boze for expert technical assistance. Rate and state friction models were done with XLook. The drilling operation was made possible by Horizon Drilling, Alex Pyne, Rupert Sutherland, the New Zealand Department of Conservation, the Whataroa Community, GNS Science, the Victoria University of Wellington, the Universities of Otago, Auckland, Canterbury, Bremen, and Liverpool, the Marsden Fund, Deutsche Forschungsgemeinschaft, and National Environment Research Council grant NE/H012486/1. This manuscript benefited from discussions with Carolin Boese, Dave Craw, Tim Davies, André Niemeijer, and Marléne Villeneuve and reviews by N. Beeler, B. Kilgore, Åke Fagereng, and an anonymous reviewer. Laboratory research

was supported by Marsden Grant UOO0919 to V. Toy and the U.S. Geological Survey, Department of the Interior.

5.A Appendix

Table 5.2: The constitutive friction parameters for least-squares fit of the Dieterich constitutive friction equations for all modeled velocity steps. Friction rate parameter (a–b) and other constitutive parameters were determined using an inverse modeling technique with an iterative least squares method in the XLook program, developed by C. Marone at Pennsylvania State University and described theoretically in Blanpied et al. (1998). The standard deviation in a, b_1, and b_2 is on the order of 10^{-4}. Data were used to calculate the friction rate parameter (a–b) presented graphically in Figures 5.4 and 5.5.

Experiment	Temp (°C)	σ_n' (MPa)	V step	a	b_1	d_{c1}	b_2	d_{c2}	$a-b$
AFHT05	280	125	0.1-0.01	0.0264	0.0300	0.0700	-	-	-0.0036
AFHT05	280	125	0.01-0.1	0.0196	0.0308	0.0040	-	-	-0.0111
AFHT05	280	125	0.1-1	0.0072	0.0124	0.0030	-	-	-0.0053
AFHT05	280	125	1-0.1	0.0133	0.0224	0.0630	-	-	-0.0091
AFHT06	210	93.6	0.1-0.01	0.0233	0.0226	0.0250	-	-	0.0007
AFHT06	210	93.6	0.01-0.1	0.0099	0.0117	0.0020	-	-	-0.0018
AFHT06	210	93.6	0.1-1	0.0094	0.0098	0.0020	0.0018	0.0590	-0.0004
AFHT06	210	93.6	1-0.1	0.0083	0.0118	0.0800	-	-	-0.0035
AFHT07	350	156	0.1-0.01	0.0574	0.0339	0.0060	0.0280	0.1000	-0.0044
AFHT07	350	156	0.01-0.1	0.0147	0.0257	0.0060	-	-	-0.0111
AFHT07	350	156	0.1-1	0.0154	0.0040	0.0240	0.0191	0.0030	-0.0076
AFHT07	350	156	1-0.1	0.0207	0.0295	0.0490	-	-	-0.0089
AFHT08	140	62.4	0.1-0.01	0.0217	0.0103	0.0010	0.0102	0.0140	0.0011
AFHT08	140	62.4	0.01-0.1	0.0098	0.0035	0.0230	0.0064	0.0030	-0.0001
AFHT08	140	62.4	0.1-1	0.0072	0.0034	0.0040	0.0022	0.0560	0.0016

Experiment	Temp (°C)	σ_n' (MPa)	V step	a	b_1	d_{c1}	b_2	d_{c2}	$a-b$
AFHT08	140	62.4	1-0.1	0.0130	0.0054	0.0520	0.0068	0.0030	0.0008
AFHT08	140	62.4	0.1-3	0.0070	0.0015	0.0020	0.0010	0.0020	0.0045
AFHT08	140	62.4	3-0.1	0.0098	0.0042	0.0440	-	-	0.0055
AFHT09	70	31.2	0.1-0.01	0.0157	0.0082	0.0010	0.0088	0.0730	-0.0013
AFHT09	70	31.2	0.01-0.1	0.0114	0.0044	0.0020	0.0015	0.0110	0.0055
AFHT09	70	31.2	0.1-1	0.0069	0.0012	0.0050	-	-	0.0056
AFHT09	70	31.2	1-0.1	0.0120	0.0030	0.0300	0.0040	0.0100	0.0050
AFHT09	70	31.2	0.1-3	0.0089	0.0021	0.0010	-	-	0.0068
AFHT09	70	31.2	3-0.1	0.0127	0.0032	0.0080	-	-	0.0095
AFHT10	25	31.2	0.1-0.01	0.0074	0.0081	0.0860	-	-	-0.0007
AFHT10	25	31.2	0.01-0.1	0.0094	0.0031	0.0020	0.0035	0.0390	0.0028
AFHT10	25	31.2	0.1-1	0.0124	0.0024	0.0010	-	-	0.0100
AFHT10	25	31.2	1-0.1	0.0105	0.0029	0.1860	-	-	0.0076
AFHT10	25	31.2	0.1-3	0.0088	-0.0040	0.0180	-	-	0.0128
AFHT10	25	31.2	3-0.1	0.0135	-0.0030	0.1220	-	-	0.0165
AFHT11	25	31.2	0.1-0.01	0.0097	0.0072	0.0460	0.0031	0.0470	-0.0006
AFHT11	25	31.2	0.01-0.1	0.0097	0.0050	0.0030	0.0020	0.0270	0.0028
AFHT11	25	31.2	0.1-1	0.0121	0.0050	0.0030	0.0020	0.0330	0.0051
AFHT11	25	31.2	1-0.1	0.0129	0.0037	0.0740	0.0049	0.0090	0.0043
AFHT11	25	31.2	0.1-3	0.0101	0.0059	0.0410	0.0019	0.0020	0.0076
AFHT11	25	31.2	3-0.1	0.0179	0.0118	0.0180	-	-	0.0061
AFHT12	140	62.4	0.1-0.01	0.0077	0.0142	0.0080	-	-	-0.0065
AFHT12	140	62.4	0.01-0.1	0.0243	0.0238	0.0010	0.0053	0.0240	-0.0048
AFHT12	140	62.4	0.1-1	0.0096	0.0098	0.0020	0.0023	0.0260	-0.0025
AFHT12	140	62.4	1-0.1	0.0158	0.0169	0.0040	0.0050	0.1220	-0.0061
AFHT12	140	62.4	0.1-3	0.0094	0.0056	0.0010	0.0035	0.0040	0.0003
AFHT12	140	62.4	3-0.1	0.0269	0.0211	0.0010	0.0093	0.0300	-0.0035
AFHT13	210	93.6	0.1-0.01	0.0152	0.0263	0.0450	-	-	-0.0111
AFHT13	210	93.6	0.01-0.1	0.0735	0.0759	0.0020	-	-	-0.0025
AFHT13	210	93.6	0.1-1	0.0106	0.0263	0.0060	0.0000	0.0000	-0.0157
AFHT13	210	93.6	1-0.1	0.0271	0.0380	0.0030	0.0000	0.0000	-0.0109
AFHT13	210	93.6	0.1-3	0.0186	0.0070	0.0310	0.0126	0.0030	-0.0010

Experiment	Temp (°C)	σ'_n (MPa)	V step	a	b_1	d_{c1}	b_2	d_{c2}	$a-b$
AFHT13	210	93.6	3-0.1	0.0147	0.0221	0.0110	-	-	-0.0074
AFHT14	70	31.2	0.1-0.01	0.0045	0.0122	0.0290	0.0120	0.1020	-0.0197
AFHT14	70	31.2	0.01-0.1	0.0122	0.0080	0.0010	0.0039	0.0060	0.0003
AFHT14	70	31.2	0.1-1	0.0107	0.0051	0.0020	0.0038	0.0510	0.0018
AFHT14	70	31.2	1-0.1	0.0112	0.0051	0.0060	0.0029	0.0060	0.0031
AFHT14	70	31.2	0.1-3	0.0087	0.0020	0.0020	0.0023	0.0290	0.0044
AFHT14	70	31.2	3-0.1	0.0132	0.0018	0.0080	0.0068	0.0080	0.0046
AFHT15	210	93.6	0.1-0.01	0.0197	0.0139	0.0350	0.0134	0.0350	-0.0076
AFHT15	210	93.6	0.01-0.1	0.0099	0.0154	0.0030	0.0033	0.0780	-0.0088
AFHT15	210	93.6	0.1-1	0.0087	0.0104	0.0020	0.0043	0.0480	-0.0060
AFHT15	210	93.6	1-0.1	0.0104	0.0110	0.0730	0.0053	0.0090	-0.0059
AFHT15	210	93.6	0.1-3	0.0063	0.0055	0.0040	0.0045	0.0320	-0.0037
AFHT15	210	93.6	3-0.1	0.0104	0.0099	0.0520	0.0044	0.0044	-0.0039
AFHT16	280	93.6	0.1-0.01	0.0238	0.0342	0.0650	-	-	-0.0104
AFHT16	280	93.6	0.01-0.1	0.0108	0.0202	0.0050	0.0081	0.0050	-0.0174
AFHT16	280	93.6	0.1-1	0.0065	0.0075	0.0040	0.0075	0.0040	-0.0085
AFHT16	280	93.6	1-0.1	0.0117	0.0249	0.0340	-	-	-0.0132
AFHT18	350	62.4	0.1-0.01	0.0237	0.0356	0.0670	-	-	-0.0119
AFHT18	350	62.4	0.01-0.1	0.0092	0.0106	0.0030	0.0104	0.0020	-0.0117
AFHT18	350	62.4	0.1-1	0.0157	0.0211	0.0050	-	-	-0.0055
AFHT18	350	62.4	1-0.1	0.0156	0.0245	0.0240	-	-	-0.0089
AFHT18	350	62.4	0.1-3	0.0027	0.0027	0.0380	0.0088	0.0020	-0.0062
AFHT19	210	62.4	0.1-0.01	0.0226	0.0287	0.0130	na	na	-0.0061
AFHT19	210	62.4	0.01-0.1	0.0135	0.0151	0.0010	0.0045	0.0330	-0.0062
AFHT19	210	62.4	0.1-1	0.0101	0.0094	0.0010	0.0020	0.0410	-0.0013
AFHT19	210	62.4	1-0.1	0.0112	0.0118	0.0830	0.0045	0.0020	-0.0051
AFHT19	210	62.4	0.1-3	0.0072	0.0054	0.0010	-	-	0.0018
AFHT19	210	62.4	3-0.1	0.0113	0.0097	0.1350	-	-	0.0016
AFHT20	210	31.2	0.1-0.01	0.0148	0.0267	0.0270	-	-	-0.0120
AFHT20	210	31.2	0.01-0.1	0.0140	0.0165	0.0010	0.0038	0.0520	-0.0063
AFHT20	210	31.2	0.1-1	0.0078	0.0103	0.0010	0.0030	0.0360	-0.0061
AFHT20	210	31.2	1-0.1	0.0087	0.0128	0.0100	0.0077	0.0730	-0.0118

Experiment	Temp (°C)	σ_n' (MPa)	V step	a	b_1	d_{c1}	b_2	d_{c2}	$a-b$
AFHT20	210	31.2	0.1-3	0.0050	0.0081	0.0020	0.0032	0.0320	-0.0064
AFHT20	210	31.2	3-0.1	0.0059	0.0151	0.0610	-	-	-0.0092
AFHT23	350	93.6	0.1-0.01	0.0281	0.0344	0.0580	-	-	-0.0063
AFHT23	350	93.6	0.01-0.1	0.0141	0.0257	0.0050	-	-	-0.0115
AFHT23	350	93.6	0.1-1	0.0169	0.0285	0.0030	0.0021	0.0030	-0.0060
AFHT23	350	93.6	1-0.1	0.0243	0.0322	0.0240	-	-	-0.0079
AFHT24	350	62.4	0.1-0.01	0.0396	0.0325	0.0860	0.0104	0.0900	-0.0033
AFHT24	350	62.4	0.01-0.1	0.0179	0.0204	0.0050	0.0123	0.0050	-0.0148
AFHT24	350	62.4	0.1-1	0.0088	0.0155	0.0050	0.0056	0.0050	-0.0124
AFHT24	350	62.4	1-0.1	0.0115	0.0289	0.0190	-	-	-0.0174
AFHT24	350	62.4	0.1-3	0.0083	0.0154	0.0030	-	-	-0.0071
AFHT25	175	78	0.1-0.01	0.0069	0.0161	0.0090	-	-	-0.0093
AFHT25	175	78	0.01-0.1	0.0119	0.0167	0.0020	0.0063	0.0100	-0.0110
AFHT25	175	78	0.1-1	0.0082	0.0040	0.0730	0.0144	0.0040	-0.0102
AFHT25	175	78	1-0.1	0.0110	0.0194	0.0080	-	-	-0.0084
AFHT25	175	78	0.1-3	0.0070	0.0131	0.0070	0.0028	0.0620	-0.0089
AFHT25	175	78	3-0.1	0.0118	0.0186	0.0190	-	-	-0.0069

Chapter VI

High-velocity Frictional Properties of Cataclastic Fault Rocks, Alpine Fault, New Zealand

Abstract

To investigate the high-velocity frictional behaviour of Alpine Fault gouges and cataclasites, 15 rotary shear experiments were conducted at 1 MPa normal stress and 1 m/s equivalent velocity. Experiments were first conducted on room-dry fault rocks, and then repeated with the addition of 25 wt.% deionized water to simulate fluid-saturated conditions. In the room-dry experiments, the peak coefficient of friction of Alpine Fault cataclasites and fault gouges was consistently high (mean $\mu_p = 0.69 \pm 0.06$). Variations in mineralogy and permeability were more apparent in the wet experiments, wherein the peak coefficient of friction of the cataclasites (mean $\mu_p = 0.64 \pm 0.04$) was higher than the fault gouges (mean $\mu_p = 0.24 \pm 0.16$). All fault rocks exhibited very low steady state coefficients of friction (μ_{ss}) (room-dry experiments mean $\mu_{ss} = 0.18 \pm 0.04$; wet experiments mean $\mu_{ss} = 0.10 \pm 0.04$). The three experiments conducted on wet smectite-bearing principal slip zone (PSZ) fault gouges had the lowest peak friction coefficients ($\mu_p = 0.13-0.18$), lowest steady state friction coefficients ($\mu_{ss} = 0.02-0.10$), and lowest breakdown work values ($W_B = 0.07 - 0.11$ MJ/m^2) of all the experiments performed. Microstructural interpretations, combined with axial displacement data, indicate that thermal pressurization of ambient pore fluid, dehydrated adsorbed water and/or dehydrated smectite interlayer water was the primary dynamic-weakening mechanism responsible for low friction in the high velocity experiments. Given sufficient acceleration, earthquake rupture propagation through the smectite-bearing PSZ fault gouges is energetically favourable over the cataclasites.

6.1 Introduction

The Alpine Fault, South Island, New Zealand is a long-lived crustal-scale continental transform fault that has accommodated at least 460 km of cumulative displacement in the past c. 25 Myr (Wellman 1953; Sutherland et al. 2000). Paleoseismological records indicate that the Alpine Fault produces quasi-periodic large-magnitude ($M_w \sim 8$) Wells & Goff 2007; Sutherland et al. 2007; Berryman et al. 2012a). Single-event strike-slip and dip-slip surface displacements on the central and southern Alpine Fault are 7.5-9 m and c. 1 m, respectively (Barth et al. 2013, Table 1). Boulton et al. (2012) and Barth et al. (2013) measured the frictional strength and stability of principal slip zone (PSZ) gouges from well-studied localities distributed c. 220 km along strike of the central and southern Alpine Fault. They concluded that the velocity-strengthening frictional properties of surface-outcrop PSZ gouges tested fluid-saturated at room temperature and low sliding velocities (v <100-300 μm/s) are incompatible with paleoseismological and geomorphological evidence for surface-rupturing earthquakes (Chapter 3, Chapter 4). Subsequent hydrothermal experiments at close to in situ conditions showed that central Alpine Fault gouges do have the velocity-weakening properties required for earthquake nucleation at approximately 3-4 km depth, depending on material and geothermal gradient (Chapter 5).

Boulton et al. (2012) hypothesized that, once nucleated, thermal pressurization of pore fluids may facilitate rupture propagation through the velocity-strengthening, low-permeability Alpine Fault gouges (e.g., Noda et al. 2009; Schmitt et al. 2011; Noda & Lapusta 2013). Theoretically, thermal pressurization occurs at slip rates greater than 0.1 m/s when frictional heating generates excess fluid pressure and reduces fault strength by lowering effective normal stress (e.g., Sibson 1973; Lachenbruch 1980). The present study reports results room-dry and water-saturated high velocity, low normal stress (v = 1 m/s, σ_n = 1 MPa) friction experiments conducted on Alpine Fault gouge and cataclasite samples collected at Gaunt Creek and Hokuri Creek (Figure 6.1). A focus of these experiments is to quantify the peak coefficient of friction (μ_p), as this value represents the yield strength and thus the primary barrier to rupture propagation. An additional aim is to quantify the

steady state coefficient of friction (μ_{ss}) at high velocity as well as the slip weakening distance (d_w) required to establish μ_{ss} (Figure 6.2). The possible occurrence of thermal pressurization is considered and implications for the seismic behavior of the Alpine Fault are discussed.

6.2 Fault Rock Descriptions

Samples for high velocity friction experiments were collected from drillcore retrieved during phase 1 of the Deep Fault Drilling Project (DFDP-1), Gaunt Creek, South Island, New Zealand (Figure 6.1). Only a small amount of brown PSZ-2 gouge from DFDP-1B was available, so an additional sample was collected from a nearby outcrop (Gaunt Creek scarp outcrop, Chapter 2). Samples are described using the table of characteristic fault rock lithologies developed by Toy et al. (2012), published in Townend et al. (2013), and presented in Chapter 2. All sample depths reported from DFDP-1B are adjusted by +0.20 m from borehole lithological logs following Townend et al. (2013). Saponite-rich gouge collected from a 12 m-wide PSZ at Hokuri Creek (HcK PSZ) on the southern Alpine Fault was also tested; gouge mineralogy, microstructure, and low velocity frictional and hydrological properties were described in detail by Barth et al. (2013) (Chapter 4). Apart from the DFDP-1B brown gouge, all samples were gently disaggregated using mortar and pestle, and the powdered material was passed through a 100# sieve to obtain a <150 μm separate. Following the methods documented in Chapter 2, quantitative X-ray diffraction (XRD) analyses were done to determine the mineralogy of each sieved DFDP separate and the bulk rock mineralogy of DFDP-1B PSZ-2 brown gouge, which was tested unsieved.

6.2.1 Fault rock occurrence, nomenclature, and mineralogy

Brief descriptions of the seven fault rock samples used in high velocity friction experiments are presented here, and core-scale images of the DFDP-1 samples are portrayed in Figure 6.1. Figures of thin-section photomicrographs of the same or similar fault rocks in Chapters 2 and 3 are also referenced. High velocity friction experiments were performed on two Unit 4 foliated cataclasites (DFDP-1A 86.41 m and DFDP-1A 90.32m), one Unit 6

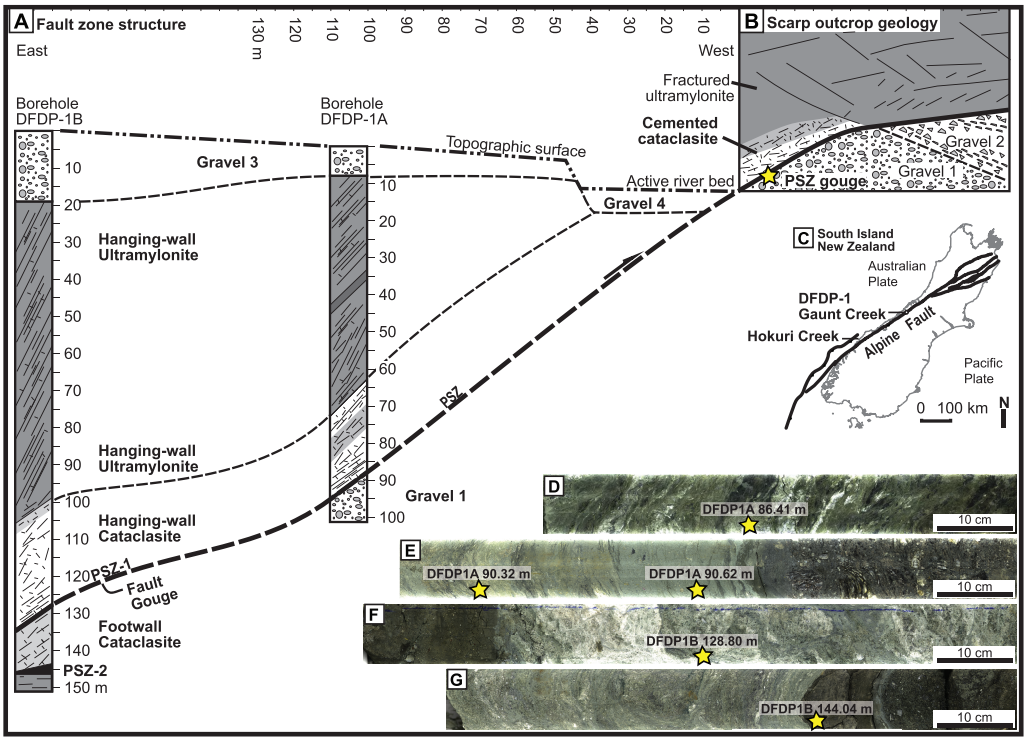

Figure 6.1: **A,** Schematic cross-section of Alpine Fault geology in boreholes DFDP-1A and DFDP-1B, drilled at Gaunt Creek in January and February 2011. PSZ denotes principal slip zone. In DFDP-1A, one smectite-bearing PSZ fault gouge was intersected, and two smectite-bearing PSZ fault gouges were intersected in DFDP-1B. **B,** Schematic cross-section of Alpine Fault geology in a scarp outcrop on the southern side of Gaunt Creek. Experimental sample GC Scarp PSZ gouge was collected from this locality (star). **C,** Location map of Alpine Fault sample localities discussion in the text (Figs. 6.2A, 6.2B, and 6.2C modified from Sutherland et al. 2012). **D,** 180° core scan of DFDP-1A Run 63_2, from which DFDP1A 86.41 m foliated cataclasite was collected. **E,** 180° core scan of DFDP-1A Run 66_2, from which DFDP1A 90.32 m foliated cataclasite and DFDP1A 90.62 m fault gouge were collected. **F,** 180° core scan of DFDP-1B Run 59_1, from which DFDP1B 128.80 m cataclasite was collected. **G,** 180° core scan of DFDP-1B Run 69_2, from which DFDP1B 144.04 gouge was collected. Detailed descriptions of the Hokuri Creek (HkC) PSZ gouge were given in Chapter 4.

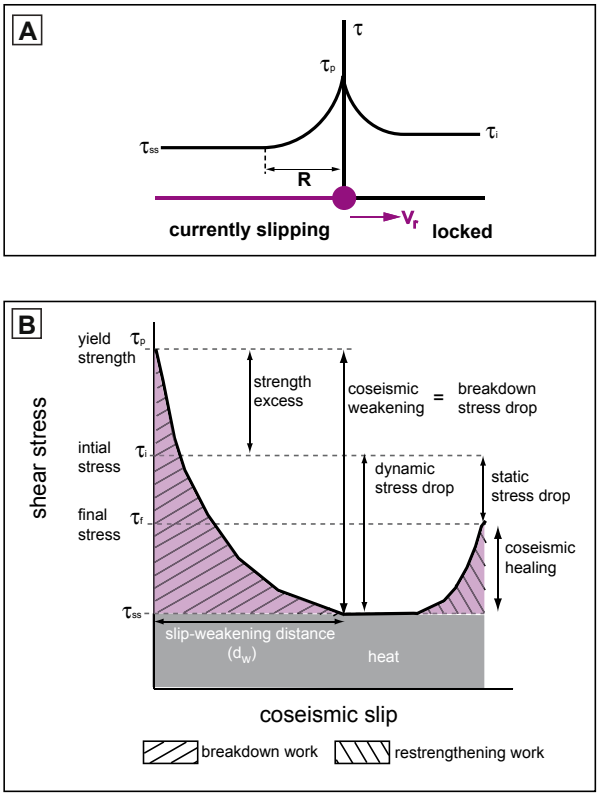

Figure 6.2: **A,** Schematic diagram showing the evolution of shear stress (i.e., traction) around a propagating rupture tip, ahead of part of the fault that is currently slipping. As the rupture tip approaches a locked portion of the fault, shear stress increases from a residual shear stress (τ_{ss}) to the peak shear stress (τ_p). Before the initiation of sliding, the work done ahead of the rupture tip (R) involves both elastic (recoverable) and inelastic (irrecoverable) deformation. Rupture velocity (V_r) is prescribed by the initial shear stress (τ_i) of the locked portion of the fault, breakdown work, and the slope of the slip-weakening curve, the values of which are a source of considerable epistemic uncertainty (Andrews 2005; Noda et al. 2009; Schmedes et al. 2010) (Figure 6.2A and caption after Faulkner et al. 2011). **B,** A more detailed schematic diagram of the earthquake energy budget at a single point on a fault. As in Figure 6.2(a), once the yield strength (τ_p) is reached, shear stress on the fault corresponds with coseismic fault strength, and shear stress decays exponentially to the residual shear stress (τ_{ss}) over a slip-weakening distance (d_w) (Abercrombie & Rice 2005). The residual shear stress may or may not be equal to the final shear stress (τ_f), and therefore the dynamic stress drop ($\tau_p - \tau_{ss}$) may or may not be equal to the static stress drop ($\tau_p - \tau_f$). In this figure, τ_f is higher than τ_{ss}, indicative of undershoot. Undershoot is expected for faults on which thermal pressurization or frictional melting occurs (Beeler 2006). Breakdown work, the integral of the experimental shear stress curve, is the seismological equivalent of fracture energy, the energy spent per unit fault area for the advancement of rupture. Breakdown work does not include the area shaded below the residual shear stress, which is most often identified with heat (see Cocco & Tinti 2008 for a discussion). In the high velocity friction experiments conducted in this study a constant sliding velocity is imposed, and traction on the fault plane, including a coseismic healing phase, is not allowed to evolve naturally (e.g., Sone & Shimamoto 2009; Chang et al. 2012). Thus, the work done prior to slip (R) and during coseismic healing (restrengthening work) was not simulated and could not be quantified (Figure 6.2B and caption after Niemeijer et al. 2012).

granitoid-gneissic cataclasite (DFDP-1B 128.80 m), and three Unit 5 gouges (DFDP-1A 90.62 m, DFDP-1B 144.04 m, and GC Scarp PSZ) (Figure 6.2A, 6.2B, 6.2D-G). Hokuri Creek fault gouge was also deformed (cf. Chapter 4). Henceforth, DFDP-1 samples will be referred to by hole (1A or 1B), depth below top of the hole (m), and fault rock lithology (foliated cataclasite, gouge, or cataclasite).

The Unit 4 foliated cataclasites formed from brittle fragmentation, translation, and rotation (e.g., cataclasis) of ultramylonite; these samples contain irregularly spaced planar to locally anastomosing seams of aligned phyllosilicates (cf. Figure 2.6F) (Figure 6.1D, 6.1E). The Unit 6 cataclasite comprises comminuted white quartz-plagioclase-potassium feldspar (cf. Figure 2.7G) (Figure 6.1F). The Unit 5 gouges are incohesive fault rocks with >90% matrix grains <0.1 mm in size. Unit 5 gouges can be differentiated by phyllosilicate mineralogy (described below) and the nature and abundance of protolith clasts. 1A 90.62 m blue gouge contains ultramylonite and cataclasite clasts, calcite vein fragments, and rare clasts of underlying brown gouge (Figure 2.7B) (Figure 6.1E). 1B 144.04 m (PSZ-2) brown gouge contains grains of quartz, plagioclase, rare potassium feldspar, calcite, apatite, and opaques, as well as foliated gneiss, ultramylonite, brown gouge and quartz-feldspar-plagioclase composite clasts (Figure 2.7F) (Figure 6.1G). Visible grains in GC Scarp PSZ gouge include quartz, plagioclase, carbonate, opaques and locally aligned phyllosilicates. GC Scarp PSZ clasts include reworked fault gouge, metamorphic quartz and vein quartz (Figure 3.3E).

Table 6.1 lists the mineralogy of each fault rock < 150 μm separate; note the 1B 144.04 m gouge was not sieved. All fault rocks analysed are polymineralic, and it is known that the presence of phyllosilicate minerals influences the frictional strength (e.g., Byerlee 1978; Shimamoto & Logan 1981; Tembe et al. 2009; Ikari et al. 2009). The fault rocks studied are classified as phyllosilicate-rich ($\geq$ 20% phyllosilicates) or phyllosilicate-poor ($<$ 20% phyllosilicates) following the observations of Shimamoto & Logan (1981). 1A 86.41 m foliated cataclasite (18% white mica and chlorite) and 1B128.80 m cataclasite (16% white mica and chlorite) are phyllosilicate-poor. 1A 90.32 m foliated cataclasite (34% white mica and chlorite), 1A 90.62m gouge (20% white mica and chlorite), 1B 144.04 m gouge (32% montmorillonite, white

CSIRO ID	Hole Depth/Sample	Lithology	Quartz	K Feldspar	Plagioclase	Calcite	Kaolinite	Smectite[a]	Smectite[b]	White mica	Chlorite	Serpentine[c]	Amphibole[d]	Talc	Anatase	Pyrite
37924	1A 86.41 m	4	31	22	28	5	1			12	5					
37925	1A 90.32 m	4	44	6	9	4				30	4					
37926	1A 90.62 m	5	28	40	6	12				8	12				<1	
37927	1B 128.80 m	6	31	20	30	1				15	1					
36187	1B 144.04 m*	5	36	4	23	5		15		15	2					<1
37928	GC Scarp PSZ	5	29	21	20	5		14		10	5					
34959	HkC PSZ WR	5	2						74		3	12	2	2		
34116	HkC PSZ < 2μm	5				5			75			21	1			

Table 6.1: Quantitative X-ray diffraction data for high velocity friction experiment materials. Lithologies are the lithological units defined in Chapter 2. Superscripts denote: (*) due to small sample size, 1B 144.04 m gouge was not sieved to <150 μm; ([a]) the smectite mineral present is dioctahedral smectite (montmorillonite); ([b]) the smectite mineral present is trioctahedral smectite (saponite); ([c]) the serpentine mineral present is lizardite; ([d]) the amphibole mineral present is actinolite.

mica, and chlorite), GC Scarp PSZ gouge (29% montmorillonite, white mica, and chlorite), and HkC PSZ gouge are phyllosilicate-rich. Quantitative XRD analysis of the HkC PSZ gouge 150 μm separate was not done because whole rock and 2 μm separate XRD analyses of the gouge revealed that mineralogy did not vary considerably (Table 6.1). Phyllosilicates (saponite+trace chlorite) comprise 77% of the whole rock and 78% of the 2 μm separate; thus, the 150 μm separate likely contains $74 - 78\%$ saponite.

6.3 High Velocity Friction Experiments

6.3.1 Experimental procedure

High velocity friction experiments were conducted on all Alpine Fault materials using the low to high velocity (LHV) friction apparatus at the State Key Laboratory of Earthquake Dynamics, Institute of Geology, China Earthquake Administration, Beijing, China (cf. Hou et al. 2012 Figure 9) (Appendix F). Experimental procedures followed the method outlined in Mizoguchi et al. (2007). In every experiment, an air actuator applied an axial force of 1.25 kN to a solid cylindrical sample 40 mm in diameter, yielding an applied normal stress (σ_n) of 0.995 MPa which was kept constant to $\pm$0.004 MPa (inset Figure 6.2A). In Table 6.2, normal stress for each experiment is reported to be 1.0 MPa. The effect of pre-compacting HkC PSZ gouge at σ_n=2.0 MPa was tested in room dry experiment LHV262. Prior to imposing shear, samples

Experiment	Material	Lithology	Dry/Wet	σ_n (MPa)	v_{eq}(m/s)	d_{eq}(m)	μ_p	μ_{ss}	d_w(m)	W_B(MJ/m^2)*
LHV281	1A 86.41 m	4	Dry	1.0	1.0	20.40	0.74	0.21	5.25	0.98
LHV284	1A 86.41 m	4	Wet	1.0	1.0	20.96	0.59	0.12	9.10	0.25
LHV282	1A 90.32 m	4	Dry	1.0	1.0	20.50	0.65	0.25	6.54	0.88
LHV285	1A 90.32 m	4	Wet	1.0	1.0	20.50	0.65	0.13	7.23	0.33
LHV279	1A 90.62 m	5	Dry	1.0	1.0	20.00	0.68	0.20	7.50	1.18
LHV286	1A 90.62 m	5	Wet	1.0	1.0	20.71	0.47	0.12	4.57	0.03
LHV277	GC Scarp PSZ	5	Dry	1.0	1.0	21.00	0.78	0.20	4.70	0.87
LHV278	GC Scarp PSZ	5	Wet	1.0	1.0	20.09	0.13	0.06	16.33	0.10
LHV280	1B 128.80 m	6	Dry	1.0	1.0	17.50	0.67	0.18	7.40	1.21
LHV287	1B 128.80 m	6	Wet	1.0	1.0	20.62	0.67	0.14	3.01	0.07
LHV283	1B 144.04 m	5	Dry	1.0	1.0	20.50	0.58	0.15	4.42	0.77
LHV288	1B 144.04 m	5	Wet	1.0	1.0	20.00	0.18	0.10	16.23	0.11
LHV262a	Hok Ck PSZ	5	Dry	1.0	1.0	14.50	0.72	0.15	3.47	0.66
LHV272	Hok Ck PSZ	5	Dry	1.0	1.0	15.50	0.71	0.14	3.33	0.62
LHV289	Hok Ck PSZ	5	Wet	1.0	1.0	20.12	0.16	0.02	13.03	0.07

Table 6.2: Summary of high velocity friction experiments and results. Symbols are: (σ_n), normal stress in MPa; (v_{eq}) equivalent slip velocity in m/s; (d_{eq}) total equivalent slip distance in m; (μ_p) peak coefficient of friction; (μ_{ss}) steady state coefficient of friction; (d_w) total slip-weakening distance in m, and for wet experiments fit with two slip-weakening curves, the value listed is the second slip-weakening distance, ($d_{w2}*$) in Table 6.2; (W_B) breakdown work in MJ/m^2. Superscripts denote: (a) LHV262 was pre-compacted at 2 MPa normal stress; (*) to account for the two peak friction values observed in wet experiments, breakdown work (W_B) for the wet experiments is the sum of the integrals of the two fitted curves.

were left under load until the displacement transducer recorded steady state thickness, typically less than 1 hour.

To establish shear, a 22 kW servo-motor rotated one side of the sample assembly while the other side was kept stationary. Velocity varies with position on solid cylindrical samples, and the equivalent slip velocity (veq) is calculated following:

$$v_{eq} = \frac{4\pi R r_o}{3} \tag{6.1}$$

where r_o is the outer radius and R is the revolution speed in revolutions per second. Equivalent slip velocity was defined such that the rate of frictional work is $\tau v_{eq} S$ if the shear stress is assumed to be constant over the sliding surface of area S (Tsutsumi & Shimamoto 1997; Hirose & Shimamoto 2005a; Mizoguchi et al. 2007). For a full analysis of the assumption that normal stress and shear stress acting on the sample is uniform, i.e., that the coefficient of friction is independent of position in the sample, see Kitajima et al.

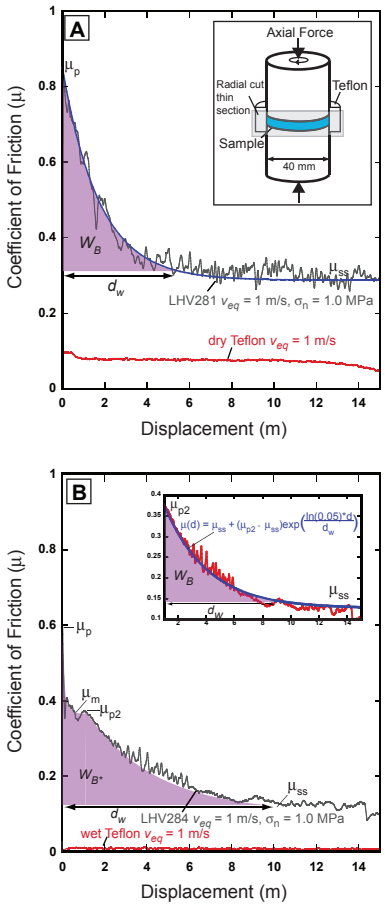

Figure 6.3: **A,** Enlarged plot of the uncorrected coefficient of friction (μ) vs. displacement (d) for the room-dry high velocity friction test conducted on 1A 86.41 m foliated cataclasite (LHV281). The peak coefficient of friction (μ_p) and steady state coefficient of friction (μ_{ss}) were calculated from the ratio of recorded shear stress (τ) to recorded normal stress (σ_n). Breakdown work (W_B) and slip-weakening distance (d_w) were determined by fitting equation (6.2) to the raw data. Also plotted is the frictional strength of dry Teflon® (red line). Inset figure depicts the sample assembly and location of the radially cut thin section. **B,** Enlarged plot of the uncorrected coefficient of friction (μ) vs. displacement (d) for the wet high velocity friction test conducted on 1A 86.41 m foliated cataclasite (LHV284). The peak coefficient of friction (μ_p) and steady state coefficient of friction (μ_{ss}) were calculated from the ratio of recorded shear stress (τ) to recorded normal stress (σ_n). It should be assumed that the effective normal stress ($\sigma'_n = \sigma_n - P_p$) in the sample is lower because of some amount of pore pressure, which could not be measured experimentally. Equation (6.2) was fit to the raw data twice, in order to capture the first (μ_p) and second (μ_{p2}) peak friction coefficients, as well as the evolution of traction to a minimum coefficient of friction (μ_m) and steady state coefficient of friction (μ_m). In the wet experiments, breakdown work (W_B) was calculated as the sum of the integrated areas under the 2 slip-weakening curves (see text for details). Also plotted is the frictional strength of wet Teflon® (red line). Inset figure depicts the second peak friction coefficient of friction, slip-weakening curve, and equation (6.2).

(2010). Experiments were conducted at a v_{eq} of 1.0 m/s. After the initial acceleration to 1.0 m/s, which occurred within 0.20±0.12 seconds ($n = 15$), v_{eq} varied by ±0.0004 m/s during an experiment. Torque, axial force, axial displacement, and rotary motion data were recorded at a sampling rate of 200 Hz.

Each sample assembly comprised two cylinders of Indian gabbro, a Teflon sleeve, and 2.5 g of air-dry (dry) 150 μm fault rock separate (the 1B 144.04 m gouge was not sieved). Relative humidity in the laboratory ranged between 40% and 60%. Initial sample thickness ranged between 1.0 mm and 1.3 mm. For the water-saturated (wet) experiments, 0.625 mL (25 wt.%) of de-ionized water was added to the fault rock powder. To allow the water to permeate the sample, it was sheared 1 full rotation in 3 minutes under 0.477 MPa normal stress. The normal stress was then increased to 1.0 MPa prior to the high velocity experiment. Fault rock powders were placed between two 39.980-39.990 mm-diameter Indian gabbro cylinders (permeability $<10^{-22}$ m^2) with sliding surfaces ground on a 150# (100 μm) diamond-grinding wheel to make them planar. Sliding surfaces were also roughened with 80# SiC (180 μm) to inhibit slippage. Each fault rock powder was contained by a Teflon® sleeve with an inner diameter 135-180 μm smaller than the gabbro cylinders (inset Figure 6.3A). It remains impossible to directly measure the pore fluid pressure during high velocity water-saturated experiments. Chen et al. (2013) used numerical modeling to estimate the initial pore fluid pressure to be between 0.10 and 0.65 MPa.

Using Teflon® sleeves is undesirable because they contribute to the total torque measurement, fluctuate in torque because of sample assembly misalignment, decomposition to release a highly reactive fluorine gas, and wear to produce small particles that mix with the sample. To minimize torque fluctuations, upper and lower portions of the sample assembly were aligned to within 1 μm prior to each experiment. A pungent odour and black grooves in the Teflon® sleeves indicates that decomposition occurred when temperatures $\geq$ 260°C were reached during the dry experiments (`http://www2.dupont.com/Teflon_Industrial/en_US/tech_info/prodinfo_ptfe.html`). Teflon® sleeves used in wet experiments, however, showed no visible signs of wear or decomposition. Kitajima et al. (2010) found that Teflon® parti-

Experiment	Material	Lithology	Dry/Wet	μ_p	μ_{ss}or μ_m*	μ_{p2}*	μ_{ss}*	d_w	d_{w2}*	R^2	R^{2}*
LHV281	1A 86.41 m	4	Dry	0.84	0.29	-	-	5.58		0.9497	
LHV284	1A 86.41 m	4	Wet	0.60	0.36	0.37	0.13	0.16	9.10	0.9193	0.9047
LHV282	1A 90.32 m	4	Dry	0.75	0.32			6.55		0.9626	
LHV285	1A 90.32 m	4	Wet	0.48	0.37	0.25	0.14	0.10	7.23	0.9762	0.8160
LHV279	1A 90.62 m	5	Dry	0.77	0.28			7.51		0.7576	
LHV286	1A 90.62 m	5	Wet	0.48	0.11	0.16	0.13	0.25	4.57	0.9866	0.8847
LHV277	GC Scarp PSZ	5	Dry	0.87	0.27			4.70		0.7793	
LHV278	GC Scarp PSZ	5	Wet	0.14	0.12	0.15	0.07	0.72	16.33	0.4799	0.8543
LHV280	1B 128.80 m	6	Dry	0.77	0.25			7.40		0.9620	
LHV287	1B 128.80 m	6	Wet	0.68	0.27	0.32	0.15	0.30	3.01	0.9247	0.8747
LHV283	1B 144.04 m	5	Dry	0.78	0.23			4.43		0.9198	
LHV288	1B 144.04 m	5	Wet	0.18	0.14	0.18	0.10	0.27	16.23	0.9331	0.7907
LHV262^	Hok Ck PSZ	5	Dry	0.82	0.22			3.48		0.7198	
LHV272	Hok Ck PSZ	5	Dry	0.81	0.22			3.33		0.6581	
LHV289	Hok Ck PSZ	5	Wet	0.17	0.05	0.08	0.03	0.14	13.03	0.9549	0.9480

Table 6.3: Summary of curve fitting parameters. Symbols are: (μ_p) peak coefficient of friction; (μ_{ss}) steady state coefficient of friction; (μ_m*) friction minimum in wet experiments; (μ_{p2}) second peak friction in wet experiments; (μ_{ss}*) is the final steady state friction achieved in wet experiments; (d_w) total slip-weakening distance for dry experiments or initial slip-weakening distance for wet experiments; ($d_{w2}*$) second slip-weakening distance for wet experiments; (R^2) coefficient of correlation for the single curve fit to dry experiments or first curve fit to wet experiments; (R^2*) coefficient of correlation for the second curve fit to the second peak friction in wet experiments. All values of μ are uncorrected for Teflon® friction.

cles are unlikely to affect the coefficient of friction because they are usually present in insignificant amounts.

To account for the contribution of the room dry and water-saturated Teflon® to the total torque, two experiments were conducted where the sample assembly, without gouge, was sheared at v_{eq}=1.0 m/s without the gabbro cylinders touching. Dry Teflon® had a peak shear stress of 0.097 MPa, which decayed exponentially to a steady-state shear stress of 0.077 MPa; wet Teflon® displayed a constant shear stress of 0.007 MPa (Figure 6.3A, 6.3B). Values of the peak coefficient of friction (μ_p) and steady state coefficient of friction (μ_{ss}) reported in Table 6.2 have been corrected for Teflon® friction. Subtracting the contribution of Teflon® to total torque nowhere results in a negative friction coefficient. In Figures 6.4 and 6.6A, slip-weakening curves from the dry experiments were corrected following the method of Togo et al. (2011). For a more detailed discussion about Teflon® friction, see the appendix in Sawai et al. (2012).

6.3.2 Data analysis

Published results confirm that, for dry high velocity friction experiments in the absence of melt, the relationship between shear stress and normal stress follows Amonton's Law (e.g., Ujiie & Tsutsumi 2010; Di Toro et al. 2011; Sawai et al. 2012; Smith et al. 2011; Yao et al. 2013). Therefore, the coefficient of friction (μ) is taken to equal the ratio of shear stress (τ) to normal stress (σ_n). To describe the relationship between displacement and the coefficient of friction, slip weakening curves for raw dry and wet data were fit with the following negative exponential equation:

$$\mu(d) = \mu_{ss} + (\mu_p - \mu_{ss}) \exp\left(\frac{\ln(0.05)d}{d_w}\right) \tag{6.2}$$

where μ is the coefficient of friction, μ_{ss} is the steady state coefficient of friction, μ_p is the peak coefficient of friction, d is displacement after the peak friction coefficient, and d_w is the displacement at which (μ_p–μ_{ss}) reduces to 5% of (μ_p–μ_{ss}) (Mizoguchi et al. 2007) (inset, Figure 6.3B). To avoid confusion with d_c in the rate and state friction equations, d_w rather than D_c is used to denote the slip-weakening distance in high velocity experiments (Niemeijer et al. 2012). In fitting equation (6.2), values of μ_p and μ_{ss} were fixed manually, displacement was zeroed at μ_p, and d_w was determined using an inverse least-squares method. From ten repeat room dry LHV experiments (v_{eq} = 1.4 m/s, σ_n = 0.8 MPa) conducted on gray-blackish Pingxi fault zone gouge, the analytical error for each parameter is: μ_p= ±0.058, μ_{ss}= ±0.035, d_w= ±4.43 m (Yao, *pers comm* 2013).

Relative to dry high velocity friction experiments (see Di Toro et al. 2011 for a review), few papers have been published on wet materials deformed at high velocity. Treatment of data obtained on wet experiments has been inconsistent, with researchers focusing primarily on peak friction (Faulkner et al. 2011) or microstructures and slip-weakening mechanisms (Boutareaud et al. 2008, 2010; Ujiie & Tsutsumi 2010; Kitajima et al. 2010; Ferri et al. 2011; Han & Hirose 2012). Each wet experiment conducted on fault rocks collected from the Alpine Fault exhibited two slip-weakening episodes. As Figure 6.3B depicts, an initial, sharp peak (μ_p) followed by an exponential decrease in the friction coefficient to a minimum value (μ_m) was followed

by a second peak friction (μ_{p2}), which also decays exponentially to a steady state coefficient of friction (μ_{ss}). In the wet experiments, equation (6.2) was fit to each slip-weakening curve separately. The value of peak friction (μ_p) reported in Table 6.2 is the initial, higher peak friction. The slip-weakening distance (d_w) reported in Table 6.2 is the distance required to reach the final steady state coefficient of friction (μ_{ss}). For the wet experiments, the value of d_w reported in Table 6.2 is the slip-weakening distance obtained for the second modeled curve. For both dry and wet experiments, the parameters of each curve fit using equation 6.2, and the coefficient of determination (R^2), are listed in Table 6.3.

Quantifying energy partitioning during high velocity friction experiments, conducted at coseismic rates >0.1 m/s, may allow extrapolation of laboratory results to natural seismogenic faults (e.g.,Beeler 2006; Niemeijer et al. 2012; see also Cocco & Tinti 2008). To that end, many researchers have correlated the integral of equation (6.2) with seismological breakdown work (W_B), the work done at a point on a fault to propagate an earthquake rupture (e.g., Cocco & Tinti 2008; Niemeijer et al. 2012) (Figure 6.2B). Breakdown work is also termed "fracture energy" (e.g., Beeler 2006; Faulkner et al. 2010; Hirono & Hamada 2010; Brantut & Rice 2011) or "normalized fracture energy" (Togo et al. 2011; Yao et al. 2013). In this study, breakdown work was calculated as the integral of equation (6.2) fit to a single peak for the dry experiments and the sum of the integrals of equation (6.2) fit to the two peaks exhibited by the wet experiments (Figure 6.3A, 6.3B). Equation (6.2) was fit to data uncorrected for Teflon® friction, so the value of breakdown work reported for dry experiments includes a small amount attributable to Teflon® (c. 0.01 MJ/m^2). This definition of breakdown work does not include frictional work done below μ_{ss} (Figure 6.3). For the wet experiments, this definition also does not include the small amount of re-strengthening work done prior to the second peak friction (μ_{p2}) (Figure 6.3B).

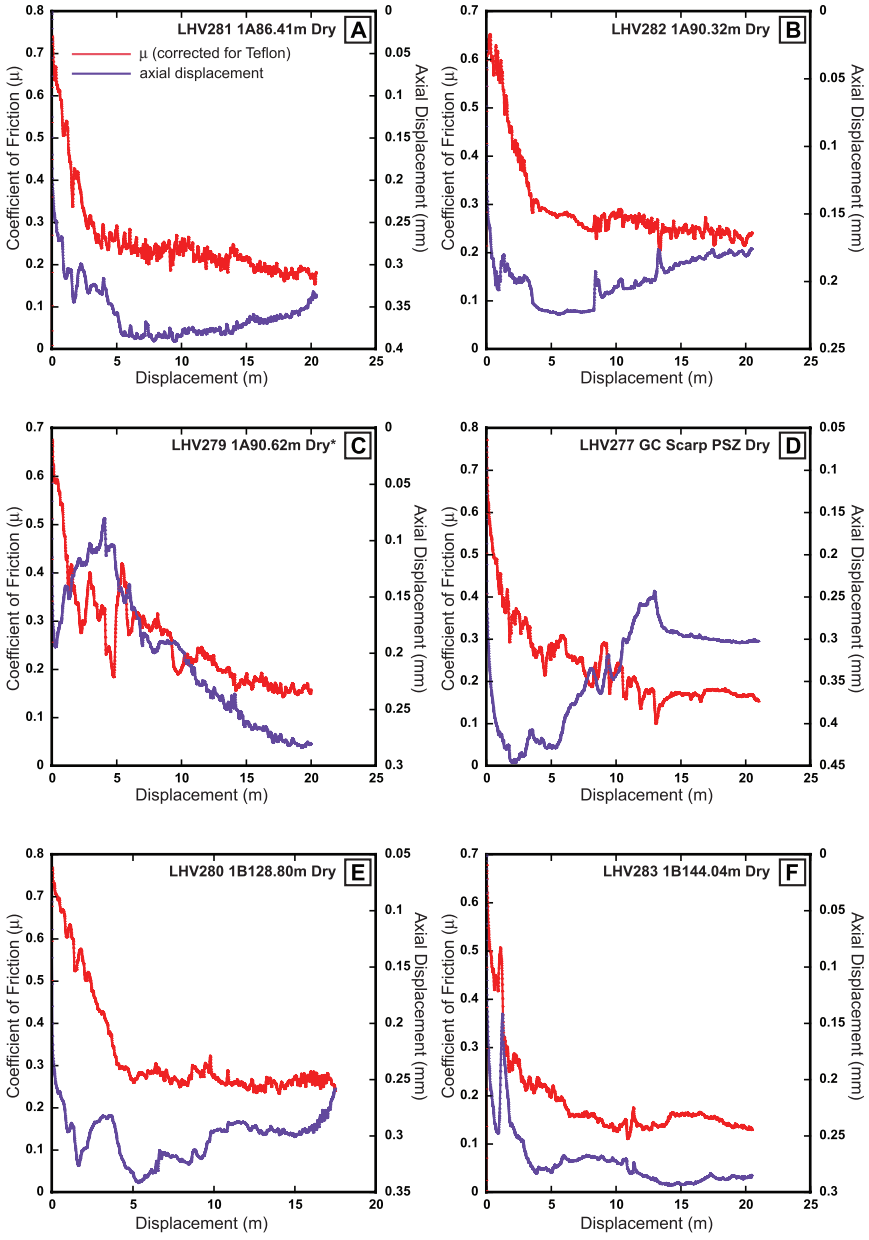

Figure 6.4: Run plots of corrected coefficient of friction (red line) and axial displacement (purple line) vs. displacement for the room-dry high velocity experiments on: **A,** LHV281, 1A 86.41 m foliated cataclasite; **B,** LHV282, 1A 90.32 m foliated cataclasite; **C,** LHV279 1A 90.62 m gouge (* denotes severe gouge loss occurred at c. 4 m displacement, despite repeated efforts to contain sample); **D,** LHV277, GC Scarp PSZ; **E,** LHV280, 1B 128.80 m cataclasite; **F,** LHV283, 1B 144.04 m gouge. Note positive values of axial displacement indicate compaction, and negative values indicate dilation relative to an initial value of 0 mm.

6.4 High Velocity Friction Results

6.4.1 Room-dry high velocity friction experiments

In Figures 6.4, 6.5 and 6.6, coefficient of friction (the ratio between shear stress and normal stress) and axial displacement (the vertical movement of the loading column measured from the stationary, non-rotating side) are plotted as a function of equivalent displacement. Positive values of axial displacement correspond to compaction and negative values correspond to dilation with respect to a value of 0 mm at the start of the experiment. Inflection points in the axial displacement curves correspond to a change from compaction to dilation or vice versa. Total equivalent displacement (measured at $2r_0/3$), peak coefficient of friction (μ_p), steady state coefficient of friction (μ_{ss}), slip-weakening distance (d_w), and breakdown work (W_B) results are listed in Table6.2.

In all 8 dry experiments, central and southern Alpine Fault foliated cataclasite, cataclasite, and gouge powders exhibited a dramatic ($>$ 2.6-fold) reduction in the coefficients of friction from peak values (μ_p=0.58-0.78; mean μ_p=0.69±0.06) to steady state values (μ_{ss}=0.14-0.25; mean μ_{ss}=0.185±0.037) (Figures 6.4, 6.6). The slip weakening distance (d_w) necessary to achieve steady state friction was 5.32±1.65 m. T-tests show that there is no statistically significant difference in the μ_p, μ_{ss}, and d_w determined for dry phyllosilicate-poor and phyllosilicate-rich materials. Smectite-bearing PSZ gouges collected from the DFDP-1 drillcore (1B 144.04 m), the Gaunt Creek scarp outcrop (GC Scarp PSZ), and the southern Alpine Fault (HkC PSZ) did exhibit the largest relative difference between peak and steady state coefficient of friction values (Figure 6.4D, 6.4F, 6.6A, 6.6B; Table 6.2).

Peak friction was reached within 0.031 m displacement in all but one experiment, LHV282 on 1A 90.32 m foliated cataclasite, where peak friction occurred at 0.27 m displacement. Peak friction always occurred simultaneously with ongoing compaction (Figure 6.7). Apart from experiment LHV279, where gouge loss occurred at 4.02 m displacement, dilation occurred prior to and/or during steady state frictional sliding (Figure 6.4, 6.6). Changes in loading column length associated with dilation ranged from minima of

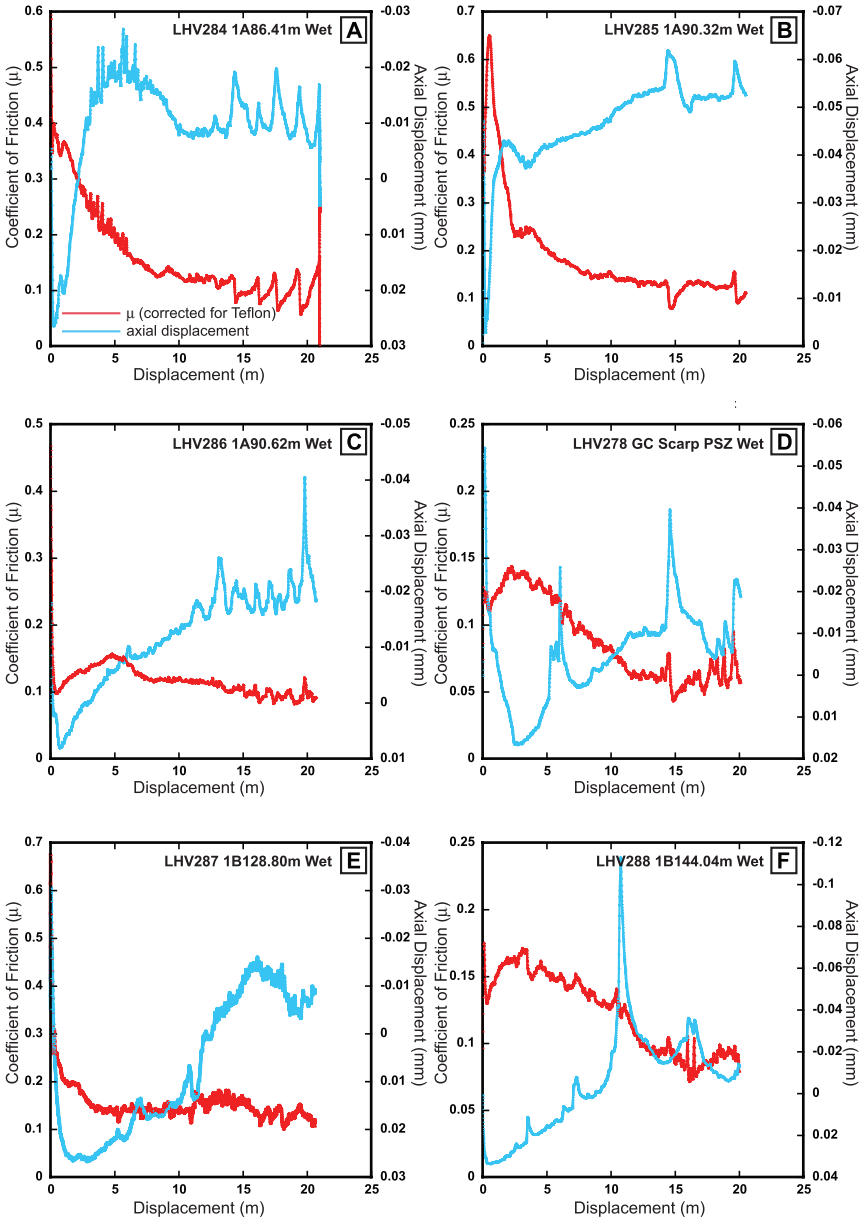

Figure 6.5: Run plots of corrected coefficient of friction (red line) and axial displacement (blue line) vs. displacement for the wet high velocity experiments on: **A,** LHV284, 1A 86.41 m foliated cataclasite; **B,** LHV285, 1A 90.32 m foliated cataclasite; **C,** LHV86 1A 90.62 m gouge; **D,** LHV278, GC Scarp PSZ; **E,** LHV287, 1B 128.80 m cataclasite; **F,** LHV288, 1B 144.04 m gouge. Note positive values of axial displacement indicate compaction, and negative values indicate dilation relative to an initial value of 0 mm.

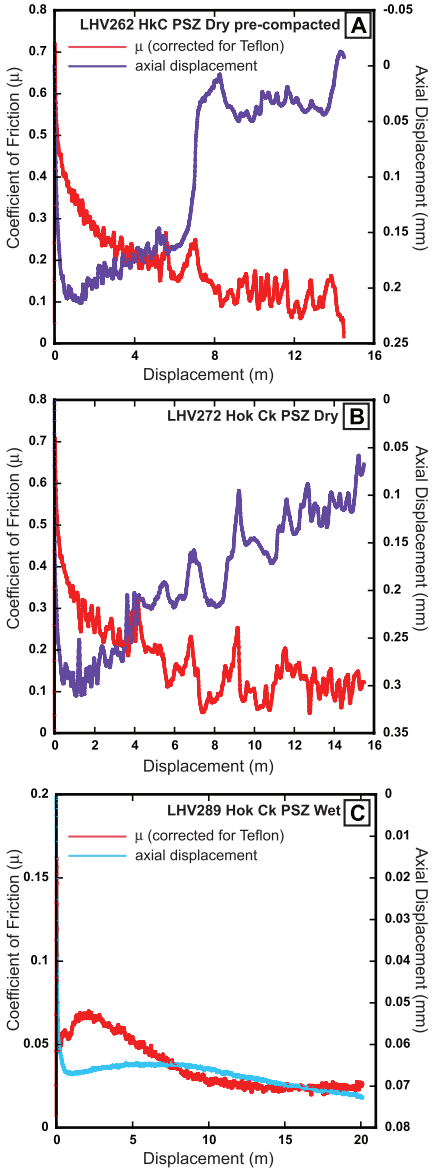

Figure 6.6: Run plots of corrected coefficient of friction (red line) and axial displacement (purple line) vs. displacement for room-dry high velocity experiments on: **A,** LHV 262, Hokuri Creek principal slip zone (HkC PSZ) gouge pre-compacted at 2 MPa normal stress; **B,** LHV272, HkC PSZ gouge prepared normally. Note little difference in the high velocity frictional behaviour of the materials. In **C,** the coefficient of friction (red line) and axial displacement (blue line) vs. displacement recorded during the wet high velocity experiment LHV289 on HkC PSZ gouge. Note positive values of axial displacement indicate compaction, and negative values indicate dilation relative to an initial value of 0 mm.

c. 0.04 mm in the foliated cataclasites to maxima of 0.10-0.25 mm in the smectite-bearing PSZ gouges (Figures 6.4, 6.6A, 6.6B).

6.4.2 Wet high velocity friction experiments

Relative to the dry experiments conducted on the same materials, 7 wet experiments on central and southern Alpine Fault foliated cataclasite, cataclasite, and gouge powders exhibited a wider range of peak coefficients of friction ($\mu_p = 0.13 - 0.67$; mean $\mu_p = 0.41 \pm 0.24$) and steady state coefficient of friction ($\mu_{ss} = 0.02 - 0.14$; mean $\mu_{ss} = 0.099 \pm 0.043$) values. The slip weakening distance necessary to achieve steady state friction was 9.93±5.40 m (Figures 6.5, 6.6C; Table 6.2). T-tests show that of the three values determined, only μ_p was significantly different between phyllosilicate-poor and phyllosilicate-rich materials; mean μ_p was lower for phyllosilicate-rich material ($\mu_p = 0.32 \pm 0.23$). The wet saponite-bearing HcK PSZ gouge exhibited the most dramatic relative reduction in the coefficient of friction measured (6.7-fold), decreasing from 0.16 to 0.02 over a slip-weakening distance of 13.03 m (Figure 6.6C).

Peak friction was reached within 0.015 m displacement in all but one experiment, LHV285 on 1A 90.32 m foliated cataclasite, where peak friction occurred at 0.52 m displacement. Peak friction often, but not always, occurred simultaneously with dilation (Figure 6.7). From either the start of the experiment (LHV288, LHV289) or following peak friction (LHV284, LHV285, LHV286, LHV278, LHV287), compaction occurred to equivalent displacements between 0.22 m and 2.50 m. Coincident with or following maximum compaction, all wet experiments exhibited a second, smaller, peak friction ($\mu_{p2} = 0.07 - 0.36$; mean $\mu_{p2} = 0.21 \pm 0.10$). Dilation accompanied steady state frictional sliding in the wet high velocity experiments. Changes in loading column thickness associated with dilation are irregular and range from a minimum of c. 0.001 mm in the HkC PSZ gouge to a maximum of 0.14 mm in the smectite-bearing 1B 144.04m gouge (Figures 6.5, 6.6C).

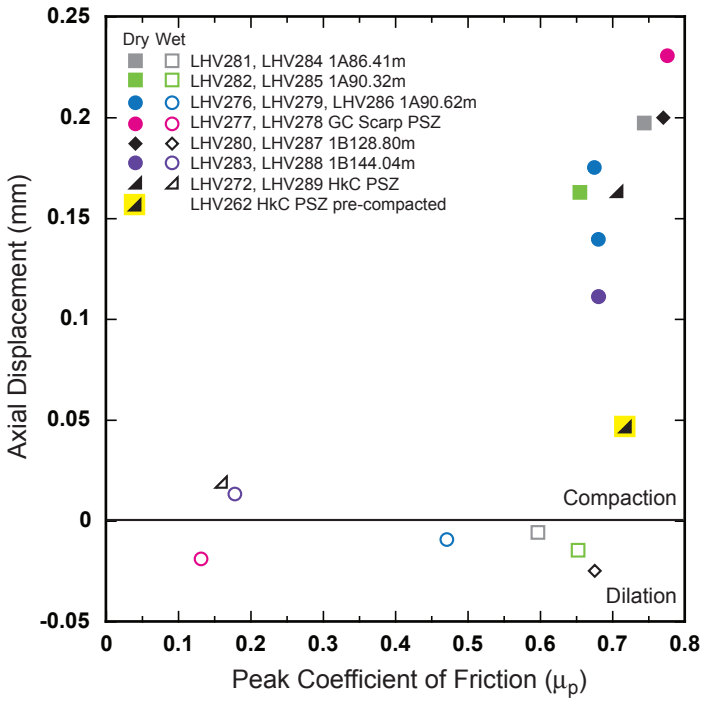

Figure 6.7: A plot of axial displacement recorded at the peak coefficient of friction vs. the value of the peak coefficient of friction for all high velocity experiments. Solid symbols denote room-dry experiments, and open symbols denote wet experiments. Positive values of axial displacement indicate compaction, and negative values indicate dilation relative to an initial value of 0 mm. For all dry experiments, compaction coincides with peak friction. The HkC PSZ gouge sample pre-compacted at $\sigma_n = 2$ MPa exhibited less compaction at peak friction. Wet experiments, in contrast, exhibited either lower amounts of compaction or dilation coincident with peak friction. See text for a discussion.

6.4.3 Breakdown work in dry and wet high velocity friction experiments

Breakdown work values are given in Table 6.3. Relative to dry experiments conducted on the same materials (mean $W_B = 0.90 \pm 0.22$ MJ/m^2), lower values of breakdown work are associated with wet high velocity friction experiments (mean $W_B = 0.14 \pm 0.11$ MJ/m^2). Dry experiments conducted on 1A 86.41 m and 1A 90.32 m foliated cataclasites, 1A 90.62 m gouge, and 1B 128.80 m cataclasite exhibited the highest values of breakdown work ($W_B = 0.88 - 1.18$ MJ/m^2). Wet experiments conducted on all phyllosilicate-rich fault gouges exhibited the lowest values of breakdown work ($W_B = 0.03 - 0.11$ MJ/m^2).

6.5 Microstructures Produced During Dry High Velocity Experiments

6.5.1 Analytical methods

Experimentally deformed fault rock and host rock samples were impregnated with LR White resin, a low viscosity epoxy resin, and vacuum dried overnight at 60°C. The epoxy resin set poorly in the samples deformed wet, and microstructures formed during these experiments were destroyed during transport from Beijing, China to Christchurch, New Zealand. Thin sections of microstructures produced during dry experiments were cut through the axis of the sample cylinder, prepared dry, and polished using 1 μm diamond paste (inset Figure 6.3A). Microstructures were imaged using a Zeiss Sigma field emission scanning electron microscope (SEM) with an angle-selective backscatter (AsB) detector, 20 kV accelerating voltage and 8.0-8.1 mm working distance, 145x magnification.

Microstructures in composite 1.0 mm-scale images are described using the four structural units proposed by Kitajima et al. (2010). The four structural units are numbered in order of increasing displacement and velocity and are distinguished by maximum grain size, grain shape, fabric, clay foliation, and presence of localized slip surfaces. The prefix SU is used to distinguish the microstructural units from the lithological units defined by Townend et al. (2013) (Chapter 2; Section 6.2.2). Particle rounding and sphericity

are described using the scheme devised by Waddell (1932). Structural unit 1 (SU-1) is somewhat compacted granular fault rock resembling the starting material and is defined by the absence of flattened grains, clay foliation, reduced particle sizes, and particle rounding. Even at the axes of rotation, all deformed materials examined in this study contain flattened grains and variable grain sizes. Since reliable criteria for distinguishing SU-1 from SU-2 could not be established, SU-1 is not identified in the LHV thin sections (cf. Kitajima et al. 2010 Figure 9).

Structural unit 2 (SU-2) is a foliated fault rock containing rounded clasts of the starting material, flattened grains, reduced particles sizes, variable porosity, and clay-lined microshears that form two sets inclined symmetrical to the axis of rotation. This original definition of SU-2 has been modified to account for variations in protolith material; for phyllolicate-poor fault rocks, the degree of particle rounding in SU-2 varies, and foliations, as well as microshears, may be absent. Structural unit 3 (SU-3) has a very fine-grained matrix containing angular to well rounded, mineral grains with or without intragranular fractures, rounded to well-rounded clasts of SU-2 and SU-4, and clay-clast aggregates (CCAs), defined by Boutareaud et al. (2008, 2010) as central mineral or aggregate grains surrounded by a cortex of concentric clay layers commonly including very fine (<5 μm) mineral fragments. In addition, matrix grains in SU-3 are isotropic, and SU-3 can be distinguished from SU-2 using reflected light microscopy.

SU-4 forms thin, highly comminuted, foliated or nonfoliated, sometimes folded layers that may be isotropic, weakly isotropic, or anisotropic when viewed in reflected light. SU-4 has been interpreted by many researchers to be the primary slipping zone in high velocity experiments on materials containing phyllosilicates (e.g., Brantut et al. 2008; Boutareaud et al. 2008; Boullier et al. 2009; Mizoguchi et al. 2009; Kitajima et al. 2010; Ferri et al. 2011; Shimamoto & Togo 2012; Tanikawa et al. 2012). SU-4, which is best developed in phyllosilicate-rich fault gouge, is most often located along the boundary of the rotating wall rock. In dry experiments conducted on phyllosililcate-poor materials, the boundary of the rotating wall rock is commonly the observed (or inferred) locus of nanoparticles with diameters finer than 0.1 μm (e.g.,

De Paola et al. 2011; Brantut et al. 2010; Han et al. 2010; Reches & Lockner 2010).

6.5.2 Microstructure descriptions

Microstructures formed during dry experiments conducted on 6 fault rocks from the central Alpine Fault at Gaunt Creek are depicted in Figures 6.8 through 6.13, with additional higher magnification images presented in Figure 6.14. Because of poor thin section quality, a composite image of LHV272 on HkC PSZ gouge could not be constructed. High magnification images from LHV272 are presented in Figure 6.14. Structural units are described relative to radial distance from the axis of rotation. Defromed central Alpine Fault samples are described in order of occurrence in the DFDP-1 boreholes, from the hanging wall to the footwall. A short description of the deformed saponite-bearing HkC PSZ gouge is then provided.

Figure 6.8(Over): Angle-selective backscatter (AsB) scanning electron microscope (SEM) image of 1A 86.41 m foliated cataclasite microstructures formed during high velocity experiment LHV281. In all microstructure figures, the upper gabbro wall rock rotates clockwise during an experiment. In the scale bars below each SEM image, variations in velocity are given with respect to radial distance from the axis of rotation. All thin sections were cut radially through the axis of rotation, so the sense of shear is in and out of the plane of the page. For all microstructure figures, SU-2 denotes structural unit 2, SU-3 denotes structural unit 3, and SU-4 denotes structural unit 4. The distribution of SU-2 and SU-3, as labeled in all images, was confirmed using reflected light microscopy. In this figure, the thickness of SU-3 tapers inward, and the lateral transition between SU-2 and SU-3 is gradational between r=10 mm and r=13.33 mm. Although SU-4 appears restricted to the sample/upper wall rock contact, foliated fine-grained layers in the labeled clast at r=19.5 mm resemble SU-4 microstructures. Detailed descriptions of the structural units are given in the text.

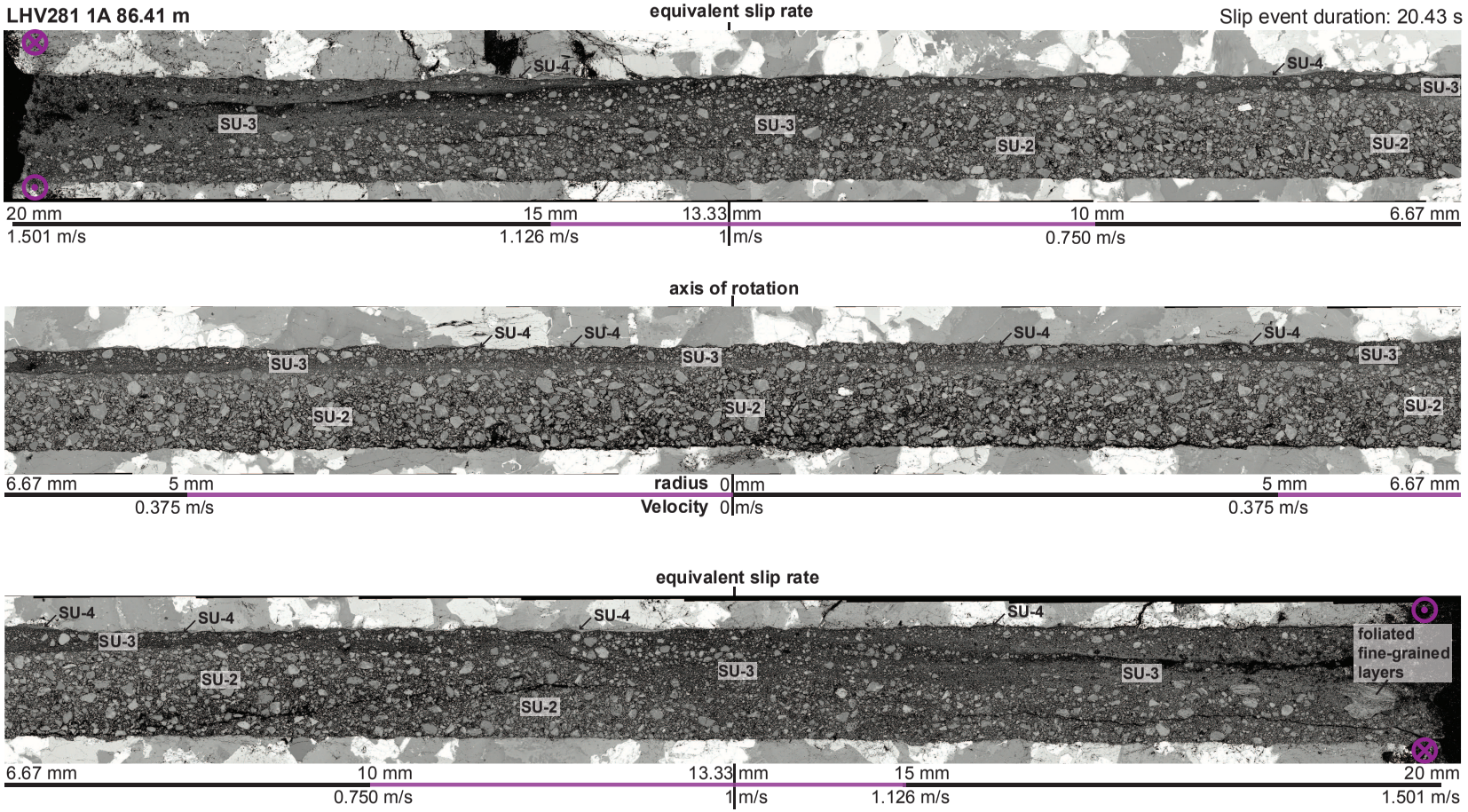

Figure 6.8: 203

Figure 6.9 (Over): AsB SEM image of 1A 90.32 m foliated cataclasite microstructures formed during high velocity experiment LHV282. The upper, left-hand portion of the thin section broke during preparation. CCA denotes clay-clast aggregates, which are well-rounded, high sphericity clasts that are mantled with small mineral fragments. Not all CCA's are labeled. Note that the foliated fine-grained layers that occur between SU-2 and SU-3 microstructurally resemble SU-4. Detailed descriptions of the structural units are given in the text.

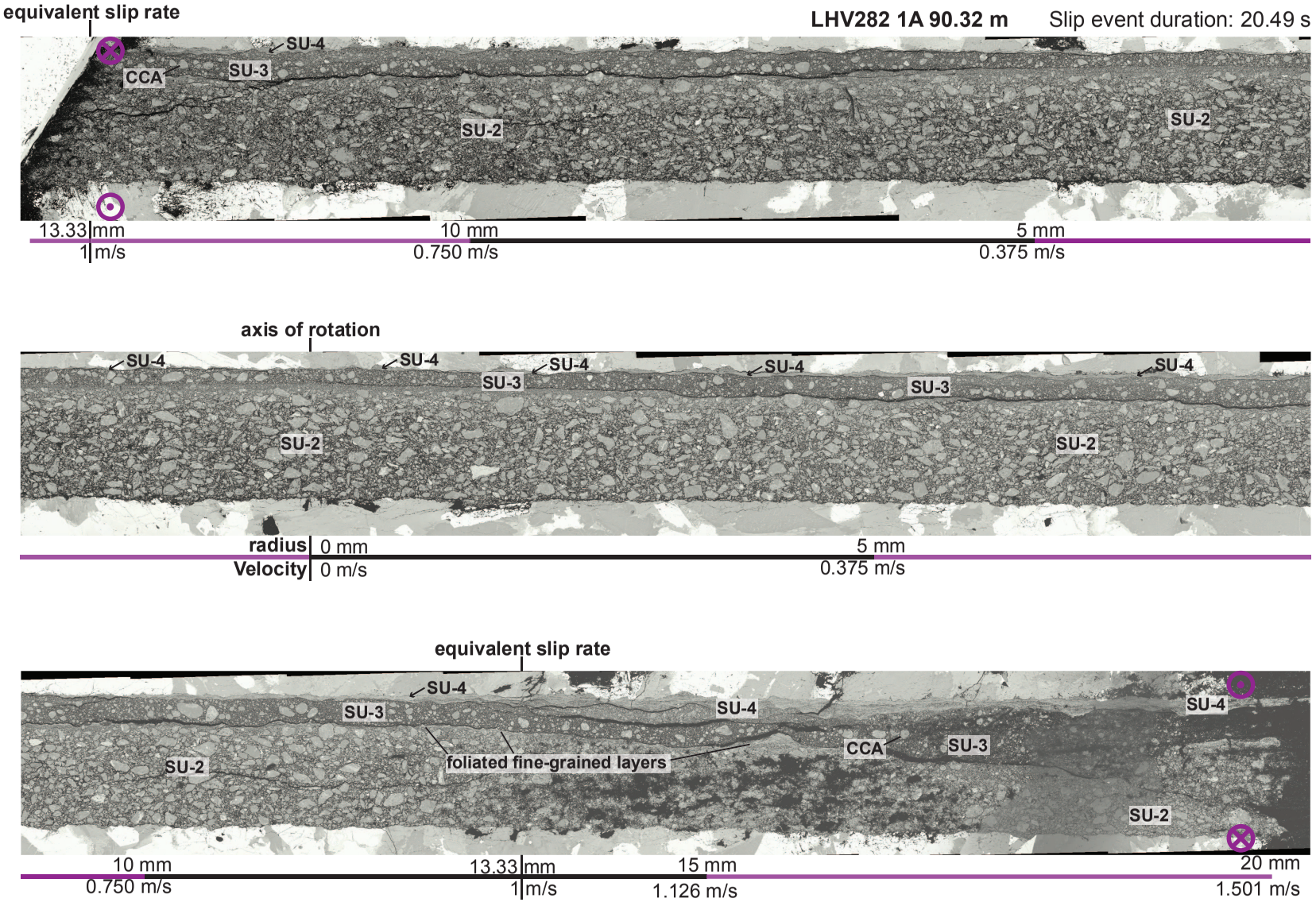

Figure 6.9:
205

Figure 6.10 (Over): AsB SEM image of 1A 90.62 m gouge microstructures formed during high velocity experiment LHV279. CCA denotes clay-clast aggregate(s). Detailed descriptions of the structural units are given in the text.

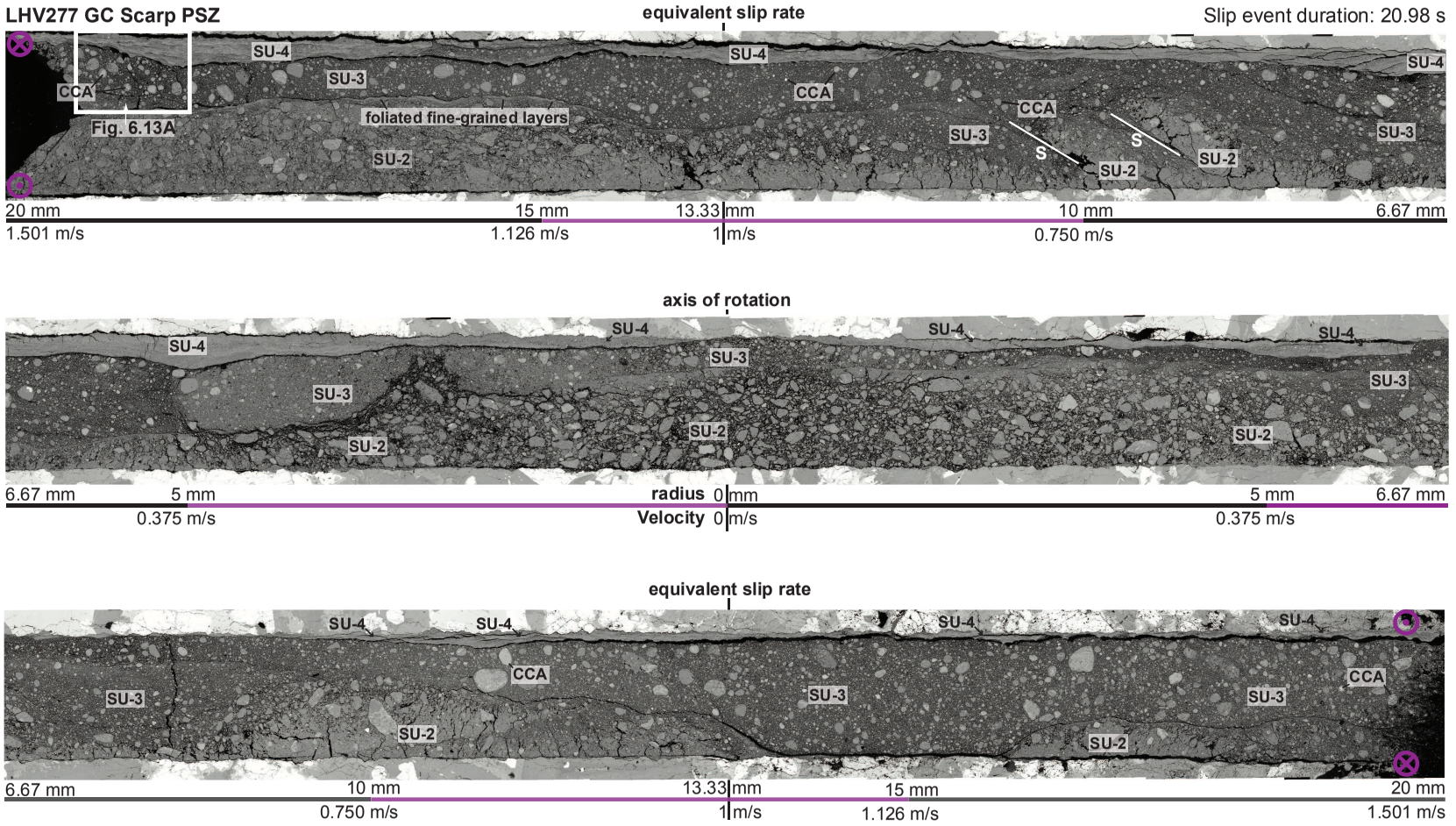

Figure 6.10:
207

Figure 6.11 (Over): AsB SEM image of GC Scarp PSZ gouge microstructures formed during high velocity experiment LHV277. CCA denotes clay-clast aggregate(s). The foliated fine-grained layers that occur between SU-2 and SU-3 microstructurally resemble SU-4. SU-2 is being translated, comminuted, and incorporated into SU-3 along oblique shears (S). The white box indicates the location of Figure 6.13A. Detailed descriptions of the structural units are given in the text.

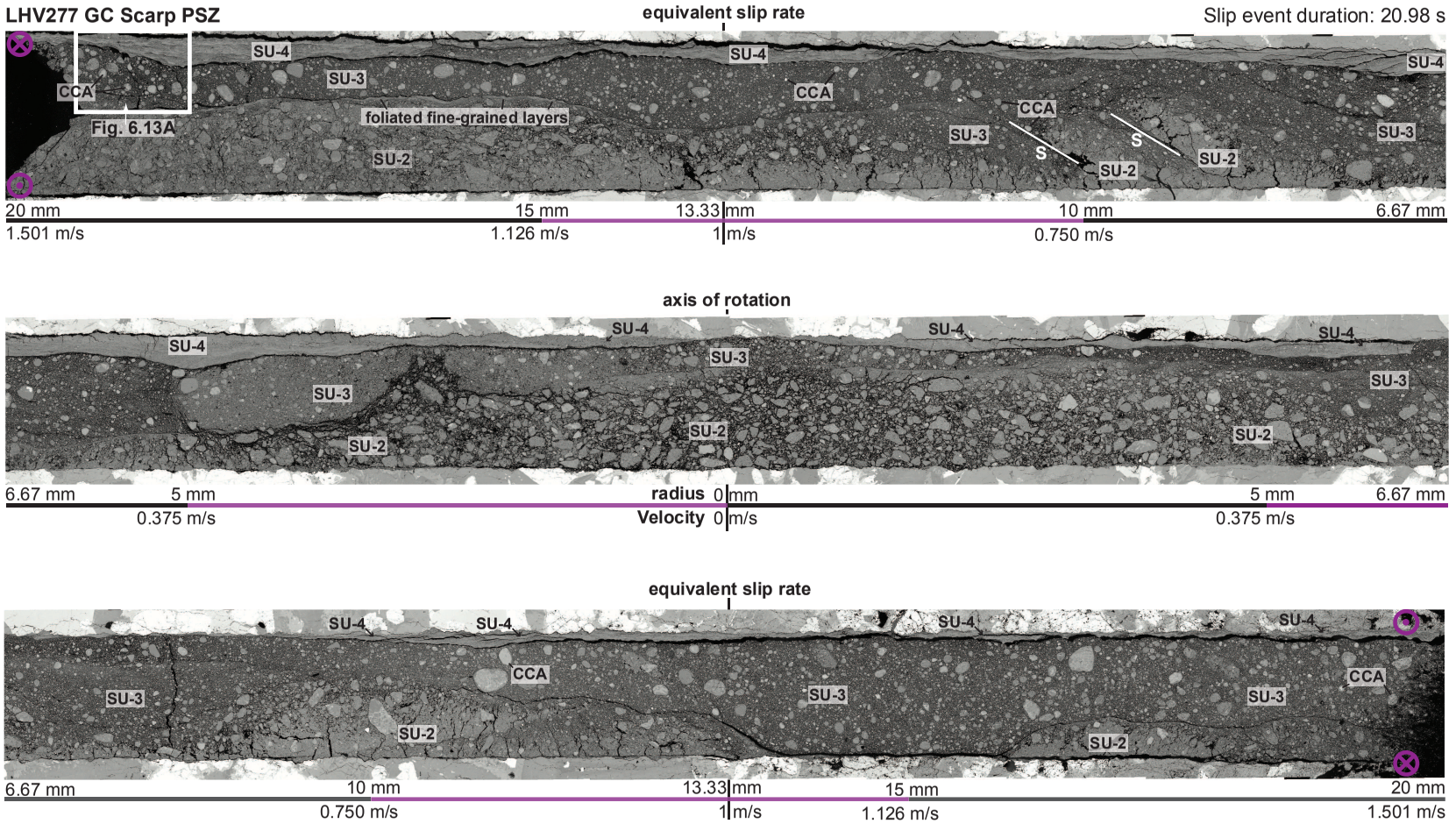

Figure 6.11:
209

Figure 6.12 (Over): AsB SEM image of 1B 144.04 m gouge microstructures formed during high velocity experiment LHV283. CCA denotes clay-clast aggregate(s). The foliated fine-grained layers that occur between SU-2 and SU-3 microstructurally resemble SU-4. The white box indicates the location of Figure 6.13B. Detailed descriptions of the structural units are given in the text.

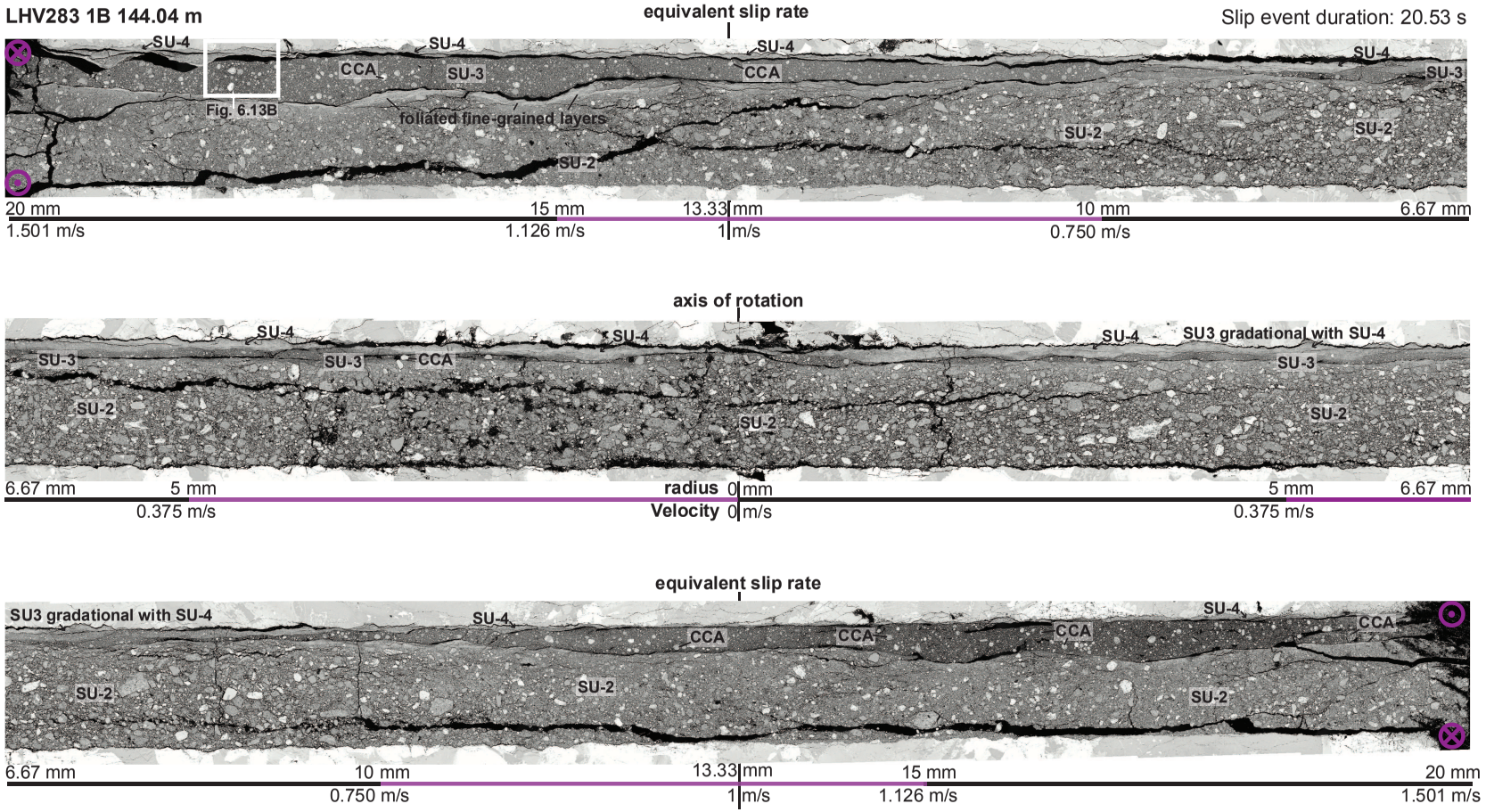

Figure 6.12:
211

Figure 6.13 (Over): AsB SEM image of 1B 128.80 m cataclasite microstructures formed during high velocity experiment LHV280. The white box indicates the location of Figure 6.13C. Detailed descriptions of the structural units are given in the text.

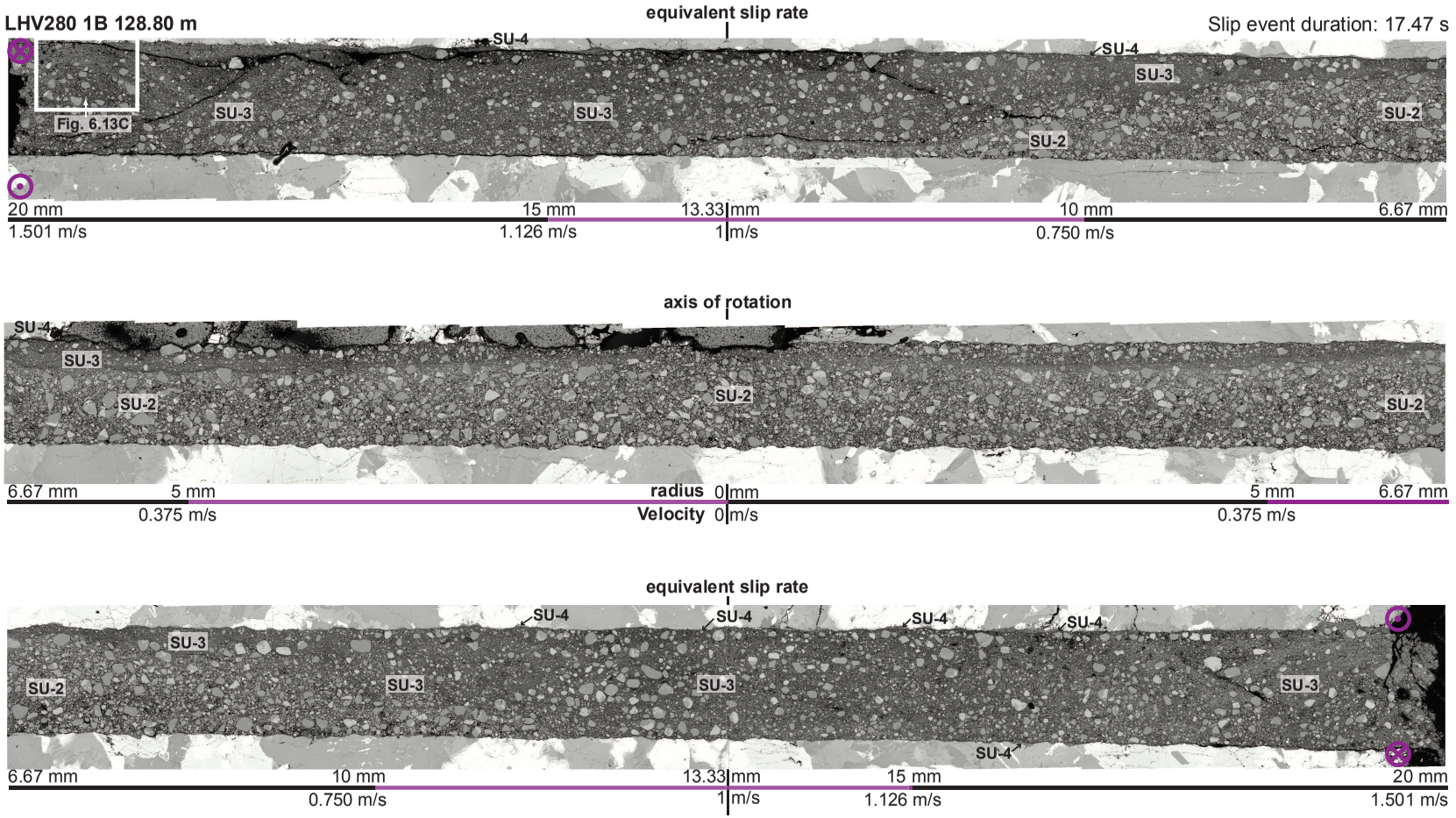

Figure 6.13:
213

Figure 6.14(Over): **A,** AsB SEM image of structural unit 3 and 4 microstructures formed during high velocity experiment LHV277 on GC Scarp PSZ gouge. Abundant clay-clast aggregates (CCA) up to 100 μm in diameter occur in SU-3. CCA's range in size, and not all CCA's are labeled. SU-4 is foliated, with foliations defined by very fine-grained, folded layers of phyllosilicates anastomosing around coarser grained layers. **B,** AsB SEM image of structural unit 3 and 4 microstructures formed during high velocity experiment LHV283 on 1B 144.04 m gouge. Two types of CCA are visible in SU-3. One type contains a central clast of quartz, calcite, or feldspar surrounded by a cortex of very fine-grained material. Another comprises foliated, very fine-grained SU-4 material (f. CCA). Not all CCA's and f. CCA's are labeled. The contact between SU-4 and SU-3 is sharp and lacks fluidal peaks. **C,** AsB SEM image of structural unit 3 and 4 microstructures formed during high velocity experiment LHV280. Relative to the phyllosilicate-rich gouges, SU-3 and SU-4 are coarser-grained. In particular, SU-4 is thin and discontinuous. SU-3 lacks CCA's, although quartz grains are subrounded to well-rounded, have medium to high sphericity, and maybe be partially mantled by phyllosilicates (phyll) or other fine-grained material. In all images, open, black cracks are epoxy-filled and formed during thin section preparation. **D,** AsB SEM image of structural units 2 and 3 formed during high velocity experiment LHV272. Image was taken at a radial distance of c. 2.3 mm, and total displacement at this point on the experimental fault was c. 2.3 m. Note the abundance of tensile (desiccation) cracks formed during the thin section-making process. **E,** AsB SEM image of structural units 3 and 4 formed during high velocity experiment LHV272. Image was taken at a radial distance of c. 15 mm, and total displacement at this point on the experimental fault was c. 17.5 m. Note that the contacts between SU-3 and SU-4 are laminar. CCA's are also present in SU-3. **F,** AsB SEM image of a clay-clast aggregate comprising a metasomatically altered mafic clast surrounded by concentric rinds of phyllosilicates (presumably saponite). Extremely fine-grained CCA's are also present.

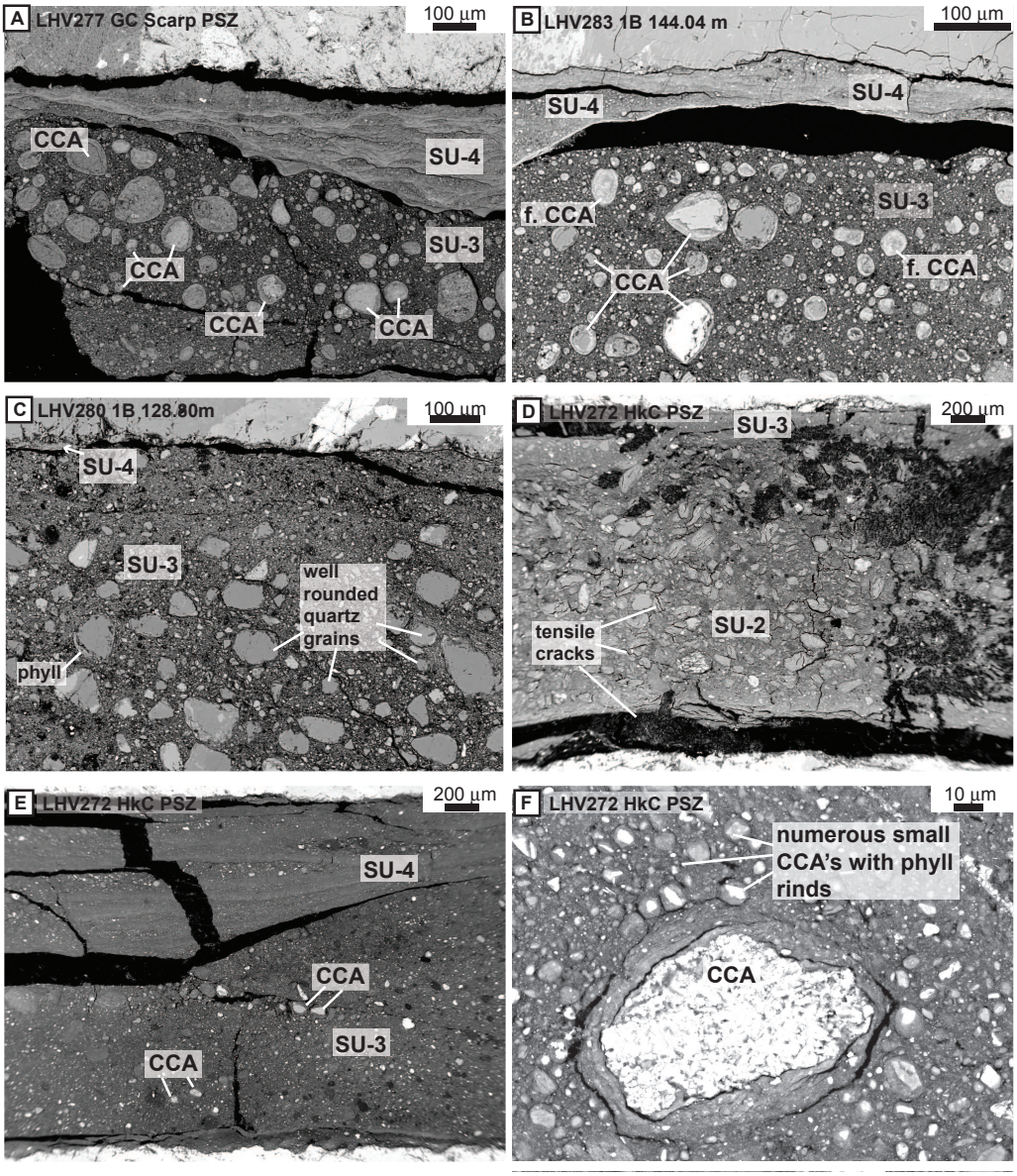

Figure 6.14:

LHV281, phyllosilicate-poor 1A 86.41 m foliated catalcasite, contains structural units (SU) 2 and 3 at the axis of rotation. A zone of enhanced cataclasis <100 μm-thick separates angular to sub-rounded, flattened grains of protolith cataclasite in SU-2 from very fine-grained, rarely foliated particles including subrounded to rounded, high sphericity clay-clast aggregates in SU-3. Near the axis of rotation, very fine-grained particles comprising SU-

4 are present in pockets <10 μm-thick on the lee side of topographic highs in the upper, rotating boundary gabbro cylinder. A semi-continuous layer of SU-4 particles is present at radial distances greater than c. 4 mm (total displacment $\geq$ 6 m). The thickness of SU-3 is greatest at the outer radius and tapers inwards. The boundaries between structural units 2, and 3 are gradational, rather than sharp as described by Kitajima et al. (2010) (Figure 6.8).

LHV282, phyllosilicate-rich 1A 90.32 m foliated cataclasite, contains structural units 2, 3 and 4 at the axis of rotation. As in LHV281, SU-3 is distinguished from SU-2 by its finer grain size, increased proportion of matrix particles, more rounded particles and the presence of clay-clast aggregates (Figure 6.9). In LHV 282, the contact between SU-2 and SU-3 is sharp, often comprising foliated fine-grained layers of very fine-grained, presumably phyllosilicate-rich, material with fluidal peaks. SU-4 forms a continuous layer along the upper rotating gabbro wall rock from the axis of rotation to the outer radius of the cylindrical sample. SU-4 is ultra-fine grained, displays internal layering, and reaches a maximum thickness of c. 150 μm. The contact between SU-4 and the underlying SU-3 is sharp and comprises numerous fluidal peaks similar to those observed at the contact between SU-2 and SU-3. The thickness of structural units 3 and 4 is greatest at the outer radius of the cylinder and tapers inwards.

The phyllosilicate-rich fault gouges, 1A 90.62 m (LHV279), GC Scarp PSZ (LHV277), and 1B 144.04 m (LHV283) contain similar microstructures (Figures 6.10, 6.11, 6.12). Relative to the foliated cataclasites described above, SU-2 in the fault gouges is finer-grained and contains more rounded clasts of both quartz-calcite-feldspar-rich cataclasite and fault gouge. The contact between SU-2 and SU-3 is gradational in the fault gouges, and the units are distinguishable by the occurrence of clay-clast aggregates and/or layers or fragments of SU-4 in SU-3. CCAs are greatest in abundance in montmorillonite-bearing brown GC Scarp PSZ and 1B 144.04 m (Figure 6.14A, 6.14B). Non-foliated and foliated layers of very fine-grained material comprise SU-4 in the three fault gouges. In 1A 90.62 m (LHV279, Figure 6.10), SU-4 is discontinuous, ranges in thickness from <1 μm to c. 100 μm, and occurs either against the upper rotating gabbro wall rock or entirely

within SU-3. In GC Scarp PSZ (LHV277), SU-4 forms a continuous layer along the upper rotating gabbro wall rock (Figure 6.11). In 1B 144.04 m (LHV283), the transition between SU-3 and SU-4 is gradational, and SU-4 is not ubiquitous (Figure 6.12). In the fault gouges, SU-4 ranges in thickness from <1 μm to c. 200 μm and displays complex internal structures, including folding, fluidal peaks, and interlayering with sharp or gradational contacts with coarser-grained SU-3 (Figure 6.14A, 6.14B). GC Scarp PSZ (LHV277) also contains oblique shears along which SU-2 is being translated and incorporated into SU-3. In addition, late-stage tensile fractures cross-cut SU-2 and SU-3 (Figure 6.11).

LHV280, phyllosilicate-poor 1B 128.80 m cataclasite, contains few internal microstructures (Figure 6.13). In this granular, quartz-feldspar-plagioclase-rich cataclasite, SU-3 cannot be distinguished from SU-2 based on the occurrence of CCA's, or clasts and/or layers of SU-4. The units can be delimited based on grain size, percent matrix, and degree of particle rounding. SU-3 contains finer particles and subrounded to well rounded, high sphericity quartz and composite grains up to c. 90 μm in diameter (Figure 6.14C). Noting damage to the upper wall rock in the thin section making process, SU-2 is the only structural unit present at the axis of rotation. At radial distances greater than 10-13 mm, SU-3 comprises a majority of the deformed sample. At the scale observed, ultra-fined grained SU-4 occasionally infills topographic lows in both gabbro wall rocks and rarely mantles topographic highs (Figures 6.13, 6.14C).

LHV272, phyllosilicate-rich HcK PSZ gouge, contains microstructures similar to those described in the montmorillonite-bearing brown GC Scarp PSZ and 1B 144.04 m (Figure 6.14A, 6.14B). SU-2 is the dominant unit at the axis of rotation, and it comprises predominantly subangular to subrounded clasts of saponite-rich gouge along with serpentine minerals and rare quartzopelitic and quartzofeldspathic lithologies. Gouge foliation within individual saponite clasts is randomly oriented and desiccation cracks formed in the thin section making process cross-cut individual clast- and matrix-fabrics (Figure 6.14D). A prominent set of open tensile cracks forms parallel to the upper and lower gouge-wall rock contacts, where SU-3 is present wherever the slide is not worn away. The contact between SU-2 and finer-grained, CCA-bearing

SU-3 is everywhere gradational, and the relative proportion of SU-3 to SU-2 increases with distance from the axis of rotation. At radial distances greater than c. 10 mm (total displacements $\geq$11.6 m), SU-2 is not observed. Instead, SU-3 is the dominant structural unit present; SU-3 is very fine-grained, has an isotropic matrix, and contains clay-clast aggregates mantled by rinds of saponite gouge (Figure 6.14E, 6.14F). At radial distances greater than c. 13 mm, SU-3 forms an inclined, gradational contact with a unit that comprises interlayered SU-3 and SU-4; this unit reaches a maximum thickness of c. 700 μm near the outermost portion of the deformed gouge. Whereas SU-3 has an isotropic matrix, SU-4 has laminar foliations that show uniform extinction when viewed with a sensitive tint plate, indicating that the extremely fine-grained material comprising the foliations has a crystallographic preferred orientation.

6.6 Discussion

6.6.1 Yield strength during high velocity friction experiments

It is commonly assumed that earthquake nucleation occurs at very low sliding velocities (Marone 1998). However, once an earthquake nucleates, acceleration to coseismic slip rates at a rupture front may result in a peak friction (equal to $\frac{\tau_p}{\sigma_n'}$) that differs from the steady state coefficient of friction measured in low velocity sliding experiments (e.g., Beeler 2006; Ben-Zion 2008). Quantifying the effect acceleration to coseismic slip rates (e.g., $v \sim 1$ m/s) might have on the peak coefficient of friction is important, because this represents the yield strength and primary barrier to rupture propagation (Figure 6.2). On average, all wet experiments had lower values of peak friction (mean $\mu_p = 0.407 \pm 0.243$) compared to the dry experiments on the same material (mean $\mu_p = 0.691 \pm 0.061$). Notably, the peak coefficient of friction for 1A 90.32 m foliated cataclasite was the same in the dry and wet experiments ($\mu_p = 0.65$) (Table 6.2).

Only the wet smectite-bearing fault gouges, GC Scarp PSZ, 1B 144.04 m, and HcK PSZ, exhibited extremely low values of peak friction ($\mu_p = 0.13 - 0.18$) (Table 6.2). Ferri et al. (2011) conducted wet high velocity ($v_{eq} = 1.3$ m/s) friction experiments on smectite-bearing (60-70% smectite;

30-40% calcite and minor quartz) Vaiont landslide gouge under the same normal stress ($\sigma_n = 1$ MPa). The reported peak friction values ($\mu_p = 0.10-0.19$) are consistent with those obtained here on Alpine Fault PSZ gouges. The extremely low yield strength of the wet smectite-bearing Alpine Fault gouges would make earthquake rupture propagation through these materials energetically favourable (e.g., Faulkner et al. 2011). These results are consistent with microstructural observations of reworked smectite-bearing gouge clasts in Alpine Fault PSZ gouges, which were interpreted to indicate multiple episodes of frictional sliding in the same material (Chapter 2, Chapter 3).

6.6.2 Evolution of friction during high velocity sliding

In the dry high velocity experiments, evolution of fault strength to steady state values followed an exponential decay function similar to the rate and state friction experiments. However, there are three important differences: (1) all materials, even smectite-bearing fault gouges that were velocity-strengthening in low velocity ($v = 0.01 - 300$ μm/s) room temperature experiments (cf. Chapters 3-5), are slip-weakening at coseismic slip rates $v = 1$ m/s, (2) weakening following smaller magnitude velocity perturbations in rate and state friction experiments occurs over at least 5 orders of magnitude smaller distances (cf. Table 5.2, mean $d_c = 41 \pm 39$ μm; $n = 96$) than that observed in the high velocity experiments (mean $d_w = 5.32 \pm 1.65$ m; n=8), and (3) the weakening is about an order of magnitude greater in high velocity experiments (mean $\Delta\mu = 0.51 \pm 0.07$; $n = 8$) (cf. Figures 3.4, 5.2) (Figures 6.4, 6.6A).

During low displacement ($d<$ 20 mm), low sliding velocity ($v \leq 300$ μm/s) experiments, measured changes in temperature for gouges materials are low ($\Delta T \leq$2.5°C), the degree of mechanical wear is typically low, the critical slip distance (d_c) needed to renew a population of contacts is short ($d_c < 100$ μm), and the corresponding change in the coefficient of friction is relatively small ($\Delta\mu < |0.03|$) (e.g., Fulton & Rathbun 2011; Marone 1998; Noda & Shimamoto 2009). At high sliding velocity ($v \geq 0.1$ m/s) and high displacement ($d > 0.1$ m), rapid comminution and frictional heating ($\Delta T \approx$100-900°C) in granular materials result in complex rate-dependent thermomechanical pro-

cesses (e.g., Sone & Shimamoto 2009; Boutareaud et al. 2008, 2010; Brantut et al. 2010; Kitajima et al. 2010; Ferri et al. 2011; Di Toro et al. 2011; Smith et al. 2013). These thermomechanical processes are not included in the empirically-derived rate and state friction equations (Dieterich 1979; Ruina 1983; Marone 1998), result in strong slip-weakening in high velocity experiments, and are discussed further in Section 6.6.3.

In the wet high velocity experiments, slip-weakening curves exhibited considerable complexity (Figures 6.5, 6.6B). Initial attempts to fit a single slip-weakening curve (equation 6.2) to the data resulted in low coefficient of determination values (e.g., $R^2 = 0.4445 - 0.7556$). By identifying two values of peak friction and modeling two slip-weakening curves, improved coefficient of determination values were obtained (e.g., $R^2 = 0.7907 - 0.9866$) (Table 6.3). In papers published on wet experiments, researchers either did not fit an equation to the experimental results (Boutareaud et al. 2008; Ujiie & Tsutsumi 2010; Faulkner et al. 2011; Ferri et al. 2011; Han & Hirose 2012; Tanikawa et al. 2012), fit a single peak and did not report R^2 values (Chen et al. 2013), or reported an inability to obtain a reasonable fit (Boutareaud et al. 2012). Published descriptions of slip-weakening curves commonly cite the first slip-weakening distance (d_w in Table 6.3) as the experimental slip-weakening distance (e.g., Ujiie & Tsutsumi 2010; Ferri et al. 2011; Tanikawa et al. 2012; Chen et al. 2013), but this neglects the complexities inherent in the wet experiments, which resulted in two values of peak friction, as well as values of $d_w + d_{w2}$ for the phyllosilicate-rich fault gouges than are larger that those observed in the dry experiments (Table 6.3) (Section 6.6.3).

Two or more values of peak friction are commonly seen in high velocity experiments involving frictional melting of intact rocks (e.g., Hirose & Shimamoto 2005a,b; Ujiie et al. 2009; Niemeijer et al. 2011). Experimentally and theoretically, the evolution of frictional strength is well-explained by the growth of a viscous melt layer whose properties result from four coupled equations involving viscous shear, temperature-dependent viscosity, and the thermal balance of shear heating, diffusion, latent heat, and extrusion of melt under and applied normal stress (e.g., a Stefan problem) (Nielsen et al. 2008, 2010). Because granular materials do not melt during high velocity sliding (e.g., Di Toro et al. 2011; Niemeijer et al. 2012), it is possible that

the very low values of steady state coefficient of friction ($\mu_{ss} = 0.02 - 0.14$) obtained in the wet experiments reflect the effective viscosity of a thin film of viscous fluid (Brodske & Kanamori 2001; Ferri et al. 2011) or granular fluid (Manzawa & Otsuki 2003; Brodsky et al. 2009; Ujiie & Tsutsumi 2010; Chen et al. 2013). In the absence of pore fluid pressure measurements, data from experiments conducted at the same velocity under a wide range of normal stresses and corresponding microstructures are required for a definitive identification of the processes responsible for the evolution of frictional strength recorded, which is beyond the scope of this research. Nevertheless, a discussion of the thermomechanical processes that may be responsible for the dynamic weakening is warranted.

6.6.3 Evidence for dynamic weakening mechanisms

A large ($\geq$ 3-fold) reduction in the coefficient of friction of both intact and granular rocks during high velocity sliding has been observed repeatedly since the seminal rotary shear experiments by Tsutsumi & Shimamoto (1997) (for reviews, see Wibberley et al. 2008; Boulton et al. 2009; Di Toro et al. 2011; Niemeijer et al. 2012). At low normal stress (1 MPa) and high sliding velocity (1 m/s), Alpine Fault gouges and cataclasites, like all other rocks studied under similar conditions, underwent dramatic slip-weakening (Table 6.3; Figures 6.4, 6.5, 6.6). A wide range of dynamic weakening mechanisms has been proposed to explain this effect, including: melt lubrication (e.g., Hirose & Shimamoto 2005a; Nielsen et al. 2008; Niemeijer et al. 2011), silica gel lubrication (Goldsby & Tullis 2002; Di Toro et al. 2004), flash heating (Rice 2006; Beeler et al. 2008), powder lubrication (e.g., Han et al. 2010; Reches & Lockner 2010; Chang et al. 2012), fluid film lubrication (Brodske & Kanamori 2001; Ferri et al. 2011), and thermal pressurization (e.g., Sibson 1973; Lachenbruch 1980; Wibberley & Shimamoto 2005; Rice 2006; Sulem et al. 2007; Tanikawa & Shimamoto 2009; Faulkner et al. 2011) or thermochemical pressurization (Brantut et al. 2010; Chen et al. 2013). Since many weakening mechanisms can occur contemporaneously, distinguishing one from another remains challenging (De Paola et al. 2011). However, microstuctural observations provide

some indication of the mechanism(s) operating in the dry high velocity experiments conducted on Alpine Fault cataclasites and gouges.

In the high velocity experiments conducted on dry phyllosilicate-rich cataclasites and gouges ($\geq$ 20% phyllosilicates), microstructures formed include clay clast aggregates (CCA's) and nonfoliated or foliated gouge layer(s). These microstructures formed at the contact between the sample and wall rock in 2 distinct units (SU-3 and SU-4) that overlie less deformed and less comminuted material (SU-2) (Figures 6.9, 6.10, 6.11, 6.12, 6.14A, 6.14B, 6.14E). Fluidal contacts within the foliated gouge layer (SU-4), random-fabric in SU-3, and the presence of well-rounded, high-sphericity CCA's have been interpreted to indicate gouge fluidization (e.g., Mizoguchi et al. 2009; Boutareaud et al. 2008, 2010; Kitajima et al. 2010; Ferri et al. 2011; Sawai et al. 2012). In dry high velocity experiments on Punchbowl Fault, California, USA gouge and Usukidani Fault, Japan gouge, Kitajima et al. (2010) and Boutareaud et al. (2008, 2010) found that CCA's formed when frictional heating in the gouges was sufficient to cause water vaporization (c. 180°C at 0.6-1.0 MPa) (Lide 2008). Boutareaud et al. (2008, 2010) argued that water vaporization creates sufficient pressure to balance or exceed the normal load, allow the gouge to dilate and fluidize. These processes facilitate the formation of CCA's through particle rolling. As the central clast particles in CCA's roll, electostatic forces attract fine-grained material to the clast, and capillary forces bind the fragments to the core of the growing aggregate. Ferri et al. (2011) observed CCA's in microstructures formed during dry high velocity experiments on another smecite-bearing gouge from the Vaiont landslide; they emphasized the importance of smectite dehydration at T =120°C-150°C, which releases interlayer water (e.g., Inoue & Utada 1991; Saffer et al. 2012).

Direct temperature measurements, and results from thermomechanical FEM models, indicate that temperature increases of 150-200°C are achieved at the edge of a dry gouge layer shearing at v_{eq} = 1.3 m/s, σ_n = 0.6 MPa within 1 to 5 m of displacement (Kitajima et al. 2010). In all four dry smectite-bearing Alpine Fault gouge experiments, the steady state friction was reached within a slip-weakening distance of 3.33 m to 4.70 m, within the range needed for the gouges to reach the critical temperature necessary

to dehydrate smectite, release interlayer water, and induce the fluid-vapor phase change (Table 6.2). Compared to the smectite-bearing fault gouges tested, CCA's are qualitatively less common in the chlorite-illite/muscovite-bearing 1A 90.32 m foliated cataclasite and 1A 90.62 m gouge (Figures 6.9, 6.10). In addition, larger displacements were required to reach the steady state coefficient of friction in these materials. Much higher temperatures, above c. 500°C, are required to cause kaolinite, illite/muscovite, and chlorite dehydration reactions (Moore & Reynolds 1997; Brantut et al. 2010), and the temperature rise in shearing natural clay-bearing fault gouges appears to be limited to $\leq$ 380°C for large displacement (up to 40 m) experiments conducted at $v_{eq} = 0.7 - 1.3$ m/s, $\sigma_n = 0.6 - 1.3$ MPa (Mizoguchi et al. 2007, 2009; Boutareaud et al. 2010; Kitajima et al. 2010; Ferri et al. 2011).

More recently, Han & Hirose (2012) formed quartz clasts with rims of ultrafine bentonite grains similar to CCA's during lower displacement ($d < 3.72$ m), lower velocity ($v_{eq} = 0.0005$ m/s and 0.08 m/s) dry rotary shear experiments. The authors argued that CCA's form at subseismic velocities and low temperatures (<c. 50°C) and therefore are only diagnostic of particle rolling, not frictional sliding at coseismic slip rates. However, the CCA's formed in the low velocity experiments lack the high sphericity, sub-rounded to well-rounded attributes of those formed in high velocity experiments on smectite-bearing PSZ gouge (Figure 6.14A, 6.14B) (cf. Han & Hirose 2012 Figure 3). Moreover, the extremely fine-grained structural unit 4 gouges formed in the low velocity experiments lacked the fluidal contacts described above in Section 6.5.2, and dramatic slip-weakening did not occur (Han & Hirose 2012). Warr & Cox (2001) described well-rounded quartz clasts formed within relict friction melts becoming "snowballed" by smectite during low temperature cataclastic deformation of Alpine Fault gouge at Gaunt Creek (Warr & Cox 2001 Figure 5). Subsequent authors have cited the "snowballed" smectite clasts as natural examples of CCA's (e.g., Boullier et al. 2009; Han & Hirose 2012), but there is an ongoing debate about whether CCA's form during high velocity sliding in water-saturated gouges (Boullier et al. 2009; Ferri et al. 2011; Han & Hirose 2012).

In the 2 high velocity experiments conducted on dry phyllosilicate-poor 1A 86.41 m foliated cataclasite and 1B 128.80 m cataclasite, CCA's and flu-

idized localization structures are absent. Instead, these materials have undergone grain size reduction and particle rounding along the upper gouge/wall rock contact (SU-3). Potential dynamic weakening mechanisms include silica gel or powder lubrication (Goldsby & Tullis 2002; Di Toro et al. 2004; Reches & Lockner 2010; Han et al. 2010 2013), but silica gel and/or nanoparticles (microscopic particles with at least one dimension <100 nm) were not observed at the scale examined (c. 100 μm) (Figures 6.8, 6.13, 6.14C). Alternatively, flash heating at highly stressed frictional micro-contacts may have occurred (Rice 2006; Beeler et al. 2008; Noda et al. 2009). Flash heating induces weakening by catalyzing phase changes at the micro-contacts (sometimes called "thermal softening"). This mechanism requires that slip be fully localized onto a fault slip surface, and slip weakening is predicted to occur over distances comparable to the maximum micro-contact size (e.g., a few tens of micrometers). This theoretically predicted slip-weakening distance is orders of magnitude smaller than that recorded in the dry experiments. Thus, extrapolating results from numerical models of flash weakening to thick gouge-filled shear zones remains difficult because of a number of poorly quantified variables that evolve with displacement (e.g., contact dimension, thermal diffusivity, volumetric heat capacity) (e.g., Beeler et al. 2008).

Axial displacement measurements provide additional information about weakening mechanisms that may have operated during dry and wet high velocity experiments. In all dry experiments, the peak coefficient of friction occurred contemporaneously with compaction (Figure 6.7). In most experiments, dilation occurred near d_w and usually continued during steady sliding (Figures 6.4, 6.7A, 6.6B). Axial displacement recorded in experiment LHV279 on 1A 90.62m gouge, was affected by gouge escaping from the Teflon sleeve at about 4 m displacement (Figure 6.4C). The magnitude of the dilation observed in experiments on the 1A 86.41 m, 1A 90.32 m foliated cataclasites, and 1B 128.80 m cataclasite ($\Delta h = 0.04 - 0.08$ mm), may reflect thermal expansion of the gabbro wall rock(s). Assuming a linear thermal expansion coefficient of gabbro to equal c. 8.51 x 10^{-6}/°C (Richter & Simmons 1974) and a temperature rise of 380°C in two 10 mm-thick layers of gabbro, thermal expansion would produce c. 0.06 mm of dilation. Dilation recorded in dry experiments on the smectite-bearing PSZ gouges, $\Delta h = 0.10 - 0.25$ mm,

exceeds that possible via thermal expansion of the gabbro wall rock(s) alone, indicating fault gouge dilation due to high pore fluid pressures (Figures 6.4D, 6.4F, 6.6A, 6.6B).

Microstructural interpretations suggest that smectite minerals in the GC Scarp PSZ, 1B 144.04 m, and HkC PSZ gouges underwent dehydration reactions and released interlayer water, which underwent further heating, thermal expansion, pressurization and/or volatilization (e.g., thermochemical pressurization; Brantut et al. 2010). Dilation resulted when pore fluid (and/or water vapor) pressures exceeded the applied normal stress (e.g., Boutareaud et al. 2008, 2010; Ferri et al. 2011; Tanikawa et al. 2012). To test if smectite dehydration reactions occurred in the dry tests, X-ray diffraction data should be obtained from the sheared smectite-bearing samples to prove that an illite-type clay replaced montmorillonite in the GC Scarp PSZ and 1B 144.04 m gouges and that chlorite, mixed-layered chlorite-smectite, or corrensite replaced saponite in the HkC PSZ gouge (Ferri et al. 2011; Schleicher et al. 2012). An alternative explanation, which is not mutually exclusive with smectite dehydration, is that frictional heating caused water adsorbed onto the room-dry fault rocks to volatilize (e.g., Mizoguchi et al. 2006; Brantut et al. 2008). This water vapor, like the dehydrated interlayer water formed in the clay dehydration reactions, could only have created an internal pressure if it did not escape past the Teflon® sleeve as a fluid, vapor, or fluid-vapor mixture (De Paola et al. 2011; Chen et al. 2013).

In the wet high velocity experiments, peak friction values were lower than those recorded in the dry experiments; in addition, μ_p occurred contemporaneously with either dilation or a smaller amount of compaction (Figure 6.7). Even in the dry experiments, at higher shear stresses, insufficient heat was generated in the first $<$0.50 m displacement to cause dilation via the volatilization of adsorbed water, the pressurization of structurally bound water, or the thermal expansion of gabbro wall rocks. Therefore, a separate dynamic weakening mechanism(s) must have operated in the saturated gouges and cataclasites. In natural shallow crustal fault zones comprising fluid-saturated granular material, thermal pressurization of pore fluid is widely considered to be the dominant weakening mechanism at coseismic slip rates greater than c. 0.1 m/s (e.g., Sibson 1973; Lachenbruch 1980; Andrews 2002;

Wibberley & Shimamoto 2005; Bizarri & Cocco 2006a; Rice 2006; Noda et al. 2009; Schmitt et al. 2011; Garagash 2012 and many others). Thermal pressurization occurs because the thermal expansibility of pore fluid is greater than the thermal expansibility of pore space (Sibson 1973; Lachenbruch 1980). As a result, fluid pressure increases with cumulative slip unless fluid diffusion and/or dilatancy dissipate the pressure increase (e.g., Garagash & Rudnicki 2003; Rice 2006; Segall et al. 2010). During rapid coseismic slip, the rate of frictional heating greatly exceeds the rate of fluid diffusion, and strongly localized slip surfaces less than $\sim$ 10 mm-thick can undergo undrained adiabatic shearing (e.g., Lachenbruch 1980; Rice 2006; Garagash and Germanovich 2012).

In the original one-dimensional mathematical model of thermal pressurization, Lachenbruch (1980) identified the material properties requisite for undrained adiabatic shearing to occur, namely: the heat production rate, which is governed by frictional heat generation, temperature rise, bulk density, specific heat, thermal conductivity, and deformation zone width; and the rate of pore pressure change, which is governed by water expansibility, specific storage, permeability, porosity, fluid density, fluid viscosity, and deformation zone width (see also Wibberley & Shimamoto 2005; Tanikawa & Shimamoto 2009). Quantifying the thermal and hydraulic transport properties of all of the Alpine Fault materials tested, and how these properties change with effective pressure and displacement at coseismic slip rates, is outside the scope of this research (cf. Chen et al. 2013). However, theoretical considerations proposed by Andrews (2003) and Mizoguchi (2005) suggest that, as a proxy for the other poorly quantified variables, materials with a permeability of $k \leq 10^{-17}$ m^2 are likely to undergo thermal pressurization during high velocity shearing on a localized slip surface. Tanikawa & Shimamoto (2009) further demonstrated the necessity of impermeable wall rocks ($k \leq 10^{-16}$ m^2). Although the gabbro wall rocks used were impermeable ($k < 10^{-22}$ m^2), water on the outside of the sample assembly after each wet test indicates that the Teflon® sleeves had a poor sealing capacity.

The permeability of surface outcrop PSZ gouges at Gaunt Creek is on the order of $k = 10^{-20}$ m^2, with hanging wall cataclasites having higher permeabilities, $k = 10^{-18}$ m^2 to 10^{-16} m^2 (Chapter 3). Carpenter et al. (accepted)

reported similar permeabilities for DFDP-1A hanging wall cataclasites (i.e., $k = 10^{-17}$–10^{-18} m^2) and DFDP-1B gouge ($k = 10^{-19}$–10^{-20} m^2). A DFDP-1B footwall cataclasite was slightly more permeable ($k = 10^{-16} - 10^{-17}$ m^2) (Carpenter et al. accepted). The HkC PSZ gouge permeability was $k = 10^{-21}$ m^2 (Chapter 4). All permeability measurements were made on static materials; high velocity sliding has been shown to further decrease the permeability of phyllosilicate-rich fault gouge (Tanikawa et al. 2012). These permeability measurements indicate that thermal pressurization may occur in any of the fault rocks tested, although perhaps not at low confining pressures in hanging wall and footwall cataclasites.

Assuming the lower peak friction values in the wet experiments resulted from thermal pressurization of pore fluid, lower permeability smectite-bearing PSZ gouges exhibit the lowest μ_p values compared to dry experiments on the same gouges. Smaller differences between dry and wet μ_p values were observed in the 1A 90.62 m gouge and 1A 86.41 m foliated cataclasite; no difference was observed in the 1A 90.32 m foliated cataclasite and 1B 128.80 m cataclasite (Table 6.2) (Figure 6.7). Chen et al. (2013) numerically modeled the difference between peak friction values in wet and dry high velocity experiments on gouges from the Longmenshan fault system. They determined that in addition to thermal pressurization, a component of compaction-related pore fluid pressure was needed to explain the dramatically lower μ_p values observed (Chen et al. 2013 Figure 15).

Another distinguishing feature of the wet experiments is the very short initial slip-weakening distance (Table 6.3). Comparably short slip-weakening distances observed in wet experiments by Ujiie et al. (2011) and Chen et al. (2013) were interpreted to reflect thermal pressurization of pore fluid. Garagash and Germanovich (2012) theoretically calculated the slip-weakening distance characteristic of thermal pressurization to be $\sim 5h$ where h is the thickness of the localized slip surface, yielding a maximum $d_w \sim 0.005$ m in experiments conducted on 1 mm-thick gouge layers. This slip-weakening distance is at least an order of magnitude smaller than that observed experimentally. It is possible that, in most experiments, the initial dilation event decreased the pore fluid pressure generated by thermal pressurization, leading to a longer slip-weakening distance (Garagash & Rudnicki 2003). A

larger total slip-weakening distance, and steady state sliding punctuated by oscillations in friction and axial displacement, indicates that the interplay between dilation and compaction-related frictional heating, pore fluid pressure generation, and variable fluid loss through the Teflon® sleeve resulted in a complex evolution of frictional strength involving two values of peak friction (Table 6.2) (Figures 6.5, 6.5C). Multiple processes are responsible for the measurements made, including, but not limited to: thermal pressurization, dilation, compaction-induced pore fluid pressurization, displacement-, effective pressure-, and material-dependent variations in fluid and heat transport properties, fluid mass liberation from dehydrated smectite minerals, the temperature-buffering effect of endothermic dehydration reactions and water phase change(s), and/or the variable sealing efficiency of the Teflon® sleeve (Han & Hirose 2012; Chen et al. 2013).

6.6.4 Implications for earthquake rupture nucleation and propagation

In the room-dry and wet high velocity experiments, the slip-weakening curves describe the evolution of shear stress (or frictional strength) at a point on the Alpine Fault during sliding at coseismic slip rates. Therefore, the integral of the slip-weakening curve, less the residual stress, is the breakdown work (Figures 6.1, 6.2). Breakdown work defined in this way is the energy density associated with the breakdown phase in the experiment, and it has been correlated with the seismological "fracture energy", which is the energy density needed to propagate a rupture at a determined velocity (Beeler 2006; Cocco & Tinti 2008). Values of breakdown work were higher in granular, dry framework-silicate rich materials as opposed to dry phyllosilicate-rich materials. Smaller values of breakdown work were measured in experiments conducted on water saturated cataclasites and gouges. Wet smectite-rich gouges had the smallest breakdown work, indicating that it is energetically favorable for earthquake ruptures to propagate through these materials (e.g., Faulkner et al. 2011). There are limitations, however, in extrapolating the breakdown work measured experimentally to a natural fault composed of the same materials.

The slip-weakening distance, a key variable used in calculations of breakdown work, is poorly constrained in laboratory experiments conducted on granular materials at low normal stresses (e.g., Mizoguchi et al. 2007; Han et al. 2010; Togo et al. 2011; Di Toro et al. 2011; Chang et al. 2012). Togo et al. (2011) proposed normalizing breakdown work by normal stress using the following empirical equation:

$$\frac{W_b}{\sigma_n} \sim 0.334\,(\mu_p - \mu_{ss})\,d_w \tag{6.3}$$

where all of the terms have been previously defined. Kato (2012) theoretically derived the same equation with a constant of 0.5. Thus, the ratio of breakdown work (W_B) to normal stress (σ_n) is linearly proportional to the slip-weakening distance (d_w), with a slope depending on ($\mu_p - \mu_{ss}$). Using equation 6.3, normalizing the experimentally determined breakdown work by a reasonable shallow crustal normal stress ($\sigma_n = 30$ MPa) would yield extremely small values of equivalent breakdown work on the order of $0.001-0.04$ MJ/m^2 (Table 6.2).

Values of breakdown work obtained from seismological estimates range between 0.15 and 41 MJ/m^2 for natural earthquakes (e.g., Rice 2006; Cocco & Tinti 2008; see also theoretical estimates of 0.2 kJ/m^2 for thermal pressurization in Noda et al. 2009). There are at least two possible reasons for this discrepancy. First, it is unclear why breakdown work should be scaled only by normal stress. Where thermally driven processes are activated at high sliding velocities, d_w depends nonlinearly on slip-rate history as well as pressure-, temperature-, and material-dependent thermal (and hydraulic) transport properties of the fault zone (e.g., Wibberley & Shimamoto 2005; Noda et al. 2009; Noda & Shimamoto 2009; Di Toro et al. 2011). Second, breakdown work in the high velocity experiments includes energy used to create new surfaces ($\leq 1-3\%$ of W_B) (Pittarello et al. 2008; Togo et al. 2012), energy consumed in dehydration reactions and water phase changes ($< 1-50\%$ of W_B) (Brantut et al. 2008, 2011a), and energy consumed as frictional heat ($> 90\%$ of W_B) (Pittarello et al. 2008; Brantut et al. 2008; Fulton & Rathbun 2011; Togo et al. 2011). On a natural fault with realistic variations in surface roughness and geometry, breakdown work also includes

energy consumed by inelastic off-fault damage (e.g., Andrews 2005; Cocco & Tinti 2008). Imposing a constant velocity during each high velocity experiment is also an oversimplification, because variations in acceleration and deceleration affect the evolution of frictional strength (e.g., Sone & Shimamoto 2009; Chang et al. 2012).

Despite uncertainties involved in extrapolating experimentally determined slip-weakening distance and breakdown work values to natural faults, the high velocity experiments conducted did validate the hypothesis made in Chapter 3: velocity-strengthening PSZ gouges can become velocity-weakening at coseismic slip rates of 1 m/s. This dramatic weakening at high velocity reveals that, as long as rupture energy is sufficient to overcome the low-slip-rate-barrier, Alpine Fault PSZ gouges do not hinder rupture propagation, as was earlier proposed (e.g., Marone 1998; Scholz 1998, 2002). Whether the propagating rupture tip can provide the acceleration needed to activate dynamic weakening mechanisms in the PSZ gouges depends on its velocity before entering the velocity-strengthening material. This is governed by the size of the seismic moment up to that point on the fault, which is given by the stress drop and area of velocity-weakening material that nucleated the rupture (and/or failed dynamically) (e.g., Noda et al. 2009; Kozdon & Dunham 2013). Other key variables include the magnitude and velocity-dependence of $(a-b)$ in the velocity-strengthening gouges (e.g., Marone 1998; Perfettini & Ampuero 2008), the areal distribution of velocity-strengthening and velocity-weakening materials (e.g., Hillers et al. 2006; Noda & Lapusta 2013), and the dampening effects of dilatancy strengthening (e.g., Segall & Rice 1995; Samuelson et al. 2009; Segall et al. 2010). Indeed, frictional failure of the Alpine Fault requires the presence of velocity-weakening material in a nucleation patch as well as sufficient resolved shear stress to overcome its frictional strength. Once nucleated, the complex interplay between resolved shear stress, peak strength, dynamic strength loss, slip weakening distance, and dynamic strength recovery in lithologically heterogeneous materials governs rupture propagation rate, the mode of rupture propagation, the frequency and amplitude of radiated energy, and ground motion (e.g., Cocco and Rice 2007; Beeler 2006; Ben-Zion 2008; Noda et al. 2009; Noda & Lapusta 2013).

6.7 Conclusions

1. In room-dry high velocity friction experiments, the peak coefficient of friction (μ_p) of phyllosilicate-poor cataclasites (mean $\mu_p = 0.70 \pm 0.05$; $n = 3$) and phyllosilicate-rich gouges and cataclasites (mean $\mu_p = 0.69 \pm 0.07$; $n = 6$), was consistently high regardless of sample grain size and mineralogy.

2. In wet high velocity friction experiments, the peak coefficients of friction of the phyllosilicate-poor cataclasites (mean $\mu_p = 0.63 \pm 0.06$; $n = 2$) was higher than the phyllosilicate-rich gouges and cataclasites (mean $\mu_p = 0.32 \pm 0.23$; $n = 5$).

3. All Alpine Fault rocks tested in room-dry and wet conditions exhibited very low steady state coefficients of friction (μ_{ss}) at high sliding velocity. Dry materials had higher steady state friction coefficients (mean $\mu_{ss} = 0.18 \pm 0.04$; $n = 8$) than wet materials (mean $\mu_{ss} = 0.10 \pm 0.04$; $n = 7$).

4. The three experiments conducted on wet smectite-bearing PSZ fault gouges had the lowest peak friction coefficients ($\mu_p = 0.13 - 0.18$), lowest steady state friction coefficients ($\mu_{ss} = 0.02 - 0.10$), and lowest breakdown work values ($W_B = 0.07 - 0.11$ MJ/m^2) of all the experiments performed.

5. Given sufficient acceleration, rupture propagation through the smectite-bearing PSZ fault gouges is energetically favourable compared with other fault gouges and cataclasites tested.

6. Microstructural interpretations, combined with axial displacement data, indicate that thermal pressurization of ambient pore fluid, dehydrated adsorbed water and/or dehydrated smectite interlayer water was the primary dynamic-weakening mechanism responsible for low friction in the high velocity experiments. Flash heating at asperity contacts may have also occurred.

7. Understanding the role of fluids in modulating peak friction, slip-weakening distance, and steady state friction requires better experimental methods and equipment.

Chapter VII

Conclusions, Synthesis, and Suggestions for Future Research

7.1 Conclusions

7.1.1 Fault zone architecture

- Two boreholes (100.6 m and 151.4 m deep) were drilled into a moderately dipping (35°-45°) thrust segment of the Alpine Fault at Gaunt Creek, a tributary to the Waitangi-taona River, during the Deep Fault Drilling Project (DFDP-1). A ^{14}C-dated wood fragment collected from a footwall breccia formed from uplifted fault rocks indicates that the Gaunt Creek thrust segment has been active for c. 14 kyr (Cooper & Norris 1994).

- A damage zone, characterized by higher than background levels of fracturing, extends from the principal slip zone (PSZ) to at least 50 m into Unit 2 brown-green-black ultramylonites and Unit 1 grey-green ultramylonites (see also Townend et al. 2013).

- The true thickness of the damage zone cannot be quantified using only the interval of core recovered from the shallow boreholes (i.e., continuous core recovery in DFDP-1A and DFDP-1B only occurred across an interval <35 m either side of the PSZ and PSZ-1, respectively).

- The fault core-alteration zone, characterized by alteration of primary phases to phyllosilicate minerals and multiple episodes of calcite mineralization and cataclasis, extends from the PSZ up to c. 20-30 m into the hanging wall if the first documented occurrence of retrogressed mineral

assemblages in the Unit 2 brown–green–black ultramylonites (quartz + plagioclase + chlorite + epidote + accessory minerals) represents the maximum extent of alteration zone processes within the fault core. In a strict sense, the Unit 6 granitoid-gneissic cataclasites also evidence cataclasis and alteration associated with fluid migration and frictional slip within the fault core-alteration zone.

- Unit 3 nonfoliated cataclasites, Unit 4 foliated cataclasites, and Unit 6 granitoid-gneissic cataclasites in the hanging wall and footwall contain the phyllosilicates chlorite and white mica. Unit 5 fault core gouges are mineralogically distinct and contain white mica and rare chlorite as well as the low temperature phyllosilicates kaolinite and dioctahedral smectite (montmorillonite).

- The mineralogy of brown Unit 5 PSZ gouges suggests that these ultrafine-grained units are the most highly altered rocks recovered from DFDP-1 and surface outcrop samples. Low temperature ($T < 120$°C) oxidized alteration of white mica, plagioclase, K-feldspar, and chlorite occurred preferentially in these ultrafine-grained gouges and resulted in the precipitation of kaolinite and smectite, as well as goethite cement.

- Mineralogically similar brown Unit 5 PSZ gouges were collected from thrust segments of the central Alpine Fault at Little Man River, Waikukupa River, and Robinson Creek, localities distributed 120 km along the strike of the fault.

- Major element geochemistry results from the Unit 5 PSZ gouges largely reflect the presence of variably comminuted vein calcite and secondary calcite cement, as CaO has been enriched relative to SiO_2 and Al_2O_3.

- Major element geochemistry trends, and petrographic observations, indicate that hanging wall Unit 3 and Unit 4 cataclasites formed from (primarily) Alpine Schist-derived metabasite and quartzofeldspathic ultramylonites (Units 1 and 2) (Cooper & Norris 1994; Toy 2007). Footwall Unit 6 cataclasites formed from feldspar-plagioclase-quartz-rich

granitoids and metasediments (Greenland Group and Karamea suite protoliths; Nathan et al. 2002; Mortimer et al. 2013). The origin of the Unit 7 augen-bearing mylonite breccia remains unknown; it likely correlates with Fraser Complex mylonites that crop out west of the Alpine Fault (Sibson et al. 1979; Rattenbury 1987).

- Mass transfer processes, including local dissolution-precipitation reactions, as well as reactions driven by the infiltration of meteoric and (potentially) metamorphic or rock-exchanged hydrothermal fluids have influenced fault zone mineralogy, lithology, major element geochemistry, and petrophysical properties.

- The presence of recycled gouge clasts and relict pseudotachylyte within the Unit 5 PSZ gouges, which juxtapose footwall gravels (outcrops, DFDP-1A borehole) and Unit 6 granitoid-gneissic cataclasites (DFDP-1B borehole) along sharp, striated contacts, suggests that coseismic slip occurs repeatedly in these units.

- A change in fault kinematics and geomorphic expression occurs on the southern Alpine Fault southwest of the Martyr River. From the Martyr River to Caswell Sound (an along-strike distance of c. 75 km), the Alpine Fault maintains an $\sim 052^{\circ}$ strike, but its dip steepens to 80°-90° SW and a component of normal displacement results in net uplift of the Australian plate.

- Three complete cross-sections through the southern Alpine Fault at the Martyr River, McKenzie Creek, and Hokuri Creek show that slip is localized to a single 1-12 m thick zone of illite-chlorite and saponite-lizardite foliated fault gouges. At the surface, coseismic slip appears to propagate along slickensided fault core margins.

- At the Martyr River, McKenzie Creek, and Hokuri Creek, Quaternary sediments juxtapose at least one margin of the fault core. At the Martyr River, fractures and faults in Australian and Pacific plate bedrock do not propagate into overlying cemented glacial tills. A single <18

ka Pacific plate glacial silt within 20 m of the fault core at the Martyr River has folds resulting from soft sediment deformation which are later cut by small hairline reverse faults with cm-scale offsets. If theses structures formed as a result of active faulting, the damage zone at the Martyr River is very narrow (<40 m) and structures within it currently accommodate small displacements. Strain appears to have been localized in the fault core at the Martyr River for the past ≤18 kyr.

- At McKenzie Creek and Hokuri Creek, defining the nature and extent of the damage zone is complicated by the presence of the highly deformed Kaipo Mélange, a subduction-related wedge of accreted material translated alongside, and into, the Alpine Fault from the southern extent of Australian plate continental crust. The age of the Kaipo Mélange is thought to be late Oligocene (∼ 24 Ma) to post-middle Miocene (13-8 Ma).

- Nevertheless, secondary faults within 200 m of the fault core at McKenzie and Hokuri Creeks typically have displacements ≤1 m, show little evidence of cataclasis, and do not offset overlying Quaternary sediments.

- On the Australian plate at Hokuri Creek, 15 ka glacial lake silts described by Sutherland & Norris (1995) have not been internally faulted. On the Pacific plate at Hokuri Creek, a ∼ 10 ka sequence of peat and silt is unfaulted, even though wedges of colluvium interfinger the peats and silts adjacent to the active fault scarp (e.g., Berryman et al. 2012a). Strain appears to have been localized in the fault core at Hokuri Creek for the past ≤15 kyr.

- The Kaipo Mélange is the inferred source of serpentinite pods and clasts within the fault core at McKenzie Creek and Hokuri Creek.

- Scanning-electron microscrope observations, and correlation of these observations with results from the San Andreas Fault Observatory at

Depth (SAFOD) (e.g., Holdsworth et al. 2011; Moore & Rymer 2012), indicate that the saponite-rich fault gouges at McKenzie Creek and Hokuri Creek formed as a result of metasomatic reactions between serpentinite and quartzo-feldspathic lithologies.

7.1.2 Fault zone permeability

- The fault-normal permeability of oriented, intact samples of selected surface outcrop Alpine Fault cataclasites and gouges was measured inside a pressure vessel fitted to the double-direct shear apparatus. Permeability was tested at 30 or 31 MPa effective normal stress. Results are as follows.

- Fault rock samples collected from outcrops at Gaunt Creek and Waikukupa River show an increase in fault normal permeability with distance from PSZ gouges. The permeability of smectite-bearing gouges ranged from $k = 1.16 \times 10^{-20}$ m^2 to 7.45×10^{-20} m^2 in the fault gouges (Unit 3 gouges in Boulton et al. 2012, Chapter 3, correspond to Unit 5 gouges in Chapter 2).

- An chlorite and white mica gouge collected from a terrace exposure at Gaunt Creek also had low permeability, $k = 3.10 \times 10^{-20}$ m^2.

- At Gaunt Creek, the permeability of a foliated cataclasite collected from the hanging wall immediately adjacent to the smectite-bearing gouge was $k = 1.41 \times 10^{-18}$m^2 (Unit 4 foliated cataclasite in Boulton et al. 2012, Chapter 3, corresponds to Unit 4 foliated cataclasite in Chapter 2).

- At Gaunt Creek and Waikukupa River, the permeabilities of hanging wall cataclasites ranged from $k = 1.15 \times 10^{-16}$ m^2 to 1.45×10^{-17} m^2 (Unit 4 cataclasites in Boulton et al. 2012, Chapter 3, can be broadly classified as Unit 3 cataclasites in Chapter 2, although the Gaunt Creek samples, p2799 and p2863, have dissolution seams that define a faint foliation oblique to the fault plane).

- The permeabilities of southern Alpine Fault gouges were uniformly low. Chlorite-white mica gouges collected from the Martyr River had permeabilities of 1.88×10^{-20} m^2 and 1.16×10^{-19} m^2. Trioctahedral smectite (saponite)-chlorite gouges collected from McKenzie Creek and Hokuri Creek had permeabilities of 1.50×10^{-22} m^2 and 3.60×10^{-21} m^2, respectively.

- These results indicate that wherever similar fault gouges are present on the Alpine Fault, they would act as barriers to cross-fault fluid flow. On the field scale, the Deep Fault Drilling Project (DFDP-1) found a perched water table above impermeable PSZ gouges at Gaunt Creek (Sutherland et al. 2012). On a regional scale, the absence of footwall warm springs indicates that topographically driven meteoric waters form warm springs only in the hanging wall because of impermeable barrier(s) on or near the Alpine Fault (e.g., Barnes et al. 1978; Reyes et al. 2010; Menzies 2012).

- On the central and southern Alpine Fault, highly impermeable fault core gouges are bounded by variably fractured, relatively more permeable, damage zone protoliths containing discrete phyllosilicate-rich seams and cataclasites. This permeability structure conforms to the combined barrier-conduit model of fault zone architecture (see Caine et al. 1996, Table 1). According to this model, cataclasites and clay-rich gouges in the fault core act as barriers to fault-normal fluid flow, and open fractures in the damage zone act as conduits for fault-parallel fluid flow.

7.1.3 Fault zone frictional properties

- Friction experiments were conducted on saturated, oriented wafers of surface outcrop fault gouges and cataclasites using the double direct shear configuration. Experiments were done at room temperature (c. 23°C), effective normal stresses (σ_n') of 6 MPa, 30 MPa, 31 MPa or 33 MPa, and load point velocities of 1 μm/s to 300 μm/s. Frictional healing properties were also measured with a series of slide-hold-slide

experiments. All calculated coefficients of friction are the ratio of τ to σ_n' assuming no cohesion. Results are as follows.

- In the double direct shear experiments, the steady-state friction coefficients (μ) of intact samples of central Alpine Fault PSZ gouges were measured at load point velocities of 1 μm/s and 31 MPa effective normal stress. The chlorite-white mica Gaunt Creek terrace gouge had a lower friction coefficient ($\mu = 0.31$) than the dioctahedral smectite (montmorillonite)-bearing Gaunt Creek scarp and Waikukupa Thrust gouges ($\mu = 0.39 - 0.44$). Hanging wall cataclasites had higher friction coefficients ($\mu = 0.50 - 0.57$).

- In the double direct shear experiments, the steady-state friction coefficients (μ) of intact samples of southern Alpine Fault gouges were measured at load point velocities of 10 μm/s and 6 MPa effective normal stress. To allow direct comparison of southern Alpine Fault gouges with a central Alpine Fault gouge, the Gaunt Creek terrace gouge was sheared at $\sigma_n' = 6$ MPa. Chlorite-white mica fault gouges collected from the Martyr River had friction coefficients ($\mu = 0.32$ and $\mu = 0.37$) comparable to the chlorite-white mica Gaunt Creek terrace gouge ($\mu = 0.28$). Trioctahedral smectite (saponite)-chlorite gouges collected from McKenzie Creek and Hokuri Creek had extremely low friction coefficients ($\mu = 0.13$ and $\mu = 0.12$, respectively) comparable to saponite-bearing gouges recovered from the creeping segment of the San Andreas Fault (Lockner et al. 2011; Carpenter et al. 2011).

- Velocity step experiments, where the load point velocity is instantaneously increased to determine the rate dependency of the coefficient of friction, were conducted in the double direct shear configuration. From the record of coefficient of friction vs. displacement, the friction rate parameters (a–b) of central Alpine Fault materials (Chapter 3) were calculated using $(a - b) = \frac{\Delta\mu}{\Delta \ln V}$, where a is the direct effect, b is the evolution effect, $\Delta\mu$ is the change in steady state sliding friction, and V is the sliding velocity (Marone 1998) (Chapter 3). The friction rate parameters (a–b) of southern Alpine Fault gouges were modeled using

an iterative, least-squares method to solve the Dieterich formulation of the rate and state friction equations (Chapter 4). The results obtained using the steady state method in Chapter 3 were checked against models of the same steps, and the difference between the values of (a–b) obtained is insignificant.

- Central Alpine Fault cataclasites had rate-weakening (negative values of (a–b), rate-neutral (near 0 values of a–b), and rate-strengthening (positive values of a–b) behaviour, depending on the size of the velocity perturbation. There was no correlation between the size of the velocity step and the magnitude of (a–b). Friction experiments were not conducted on southern Alpine Fault cataclasites.

- Slide-hold-slide tests were conducted on all surface outcrop gouge and cataclasite samples. In these tests, the load point was driven at 10 μm/s, held motionless for a prescribed time, t, between 1 and 300s and then driven at 10 μm/s again. All fault gouges, except for the Waikukupa Thrust gouge, weakened with hold time. The Gaunt Creek scarp outcrop foliated cataclasite also weakened with hold time. Along with the Waikukupa Thrust gouge, all cataclasite samples strengthened with hold.

- Taken together, the room temperature frictional properties of central and southern Alpine Fault gouges are compatible with aseismic creep, although there is no observational or geodetic evidence for creep on the plate boundary structure (e.g., Evison 1971; Sutherland et al. 2007; Beavan et al. 1999; Lamb & Smith 2013).

- In Chapter 4, it was concluded that there are limitations to using surface outcrop materials and shallow subsurface, low velocity (below coseismic slip rates of approximately 1 m/s) experimental conditions to understand spatio-temporal variations in fault properties. Thus, Chapters 5 and 6 documented the results of experiments that explored the effects of high temperatures and pressures (Chapter 5) and high veloci-

ties (Chapter 6) on the frictional properties of cataclasites and/or fault gouges.

- Hydrothermal friction experiments were conducted on two PSZ fault gouges: (1) a blue fault gouge from DFDP-1A (Run 66, Section 1, 0.44 m below top of core, 90.62 m adjusted hole depth, the "1A blue gouge"); and (2) a brown fault gouge from DFDP-1B (Run 59, Section 1, 0.12 m below top of core, 128.42 m adjusted hole depth, the "1B brown gouge"). Eighteen experiments were conducted using a triaxial deformation apparatus. Sieved gouge powders were applied to an inclined (30° plane) sawcut surface and tested using the furnace assembly and methods described in Moore and Lockner et al. (2011). All reported coefficients of friction are the ratio of τ to σ_n' assuming no cohesion. To determine the rate dependence of friction, velocity steps of 0.01–3 μm/s were imposed. The friction rate parameters (a–b) of DFDP-1 fault gouges were modeled using an iterative, least-squares method to solve the Dieterich formulation of the rate and state friction equations.

- The chlorite/white mica-bearing DFDP-1A blue gouge was frictionally strong ($\mu = 0.61$–0.76) across a range of experimental conditions ($T =$ 23–350°C, σ_n' = 31.2–156 MPa) and underwent a stability transition from velocity strengthening to velocity weakening (positive to negative $a - b$) at $T = 210$°C.

- The coefficient of friction of montmorillonite-bearing DFDP-1B brown gouge increased from $\mu = 0.49$ to $\mu = 0.74$ with increasing temperature and pressure ($T =$ 70–210°C, σ_n' = 31.2–93.6 MPa), and it underwent a transition from velocity strengthening to velocity weakening at $T =$ 140°C, σ_n' = 62.4 MPa.

- The observation of increased frictional strength coincident with rate-weakening behavior agrees with previous findings correlating conditionally unstable or unstable (seismic) slip with frictionally strong materials (Beeler 2007; Ikari et al. 2011a).

- Hydrothermal frictional strength and stability results indicate that a majority of the seismic moment release will accompany failure of rate-weakening material comprising the fault plane over the depth range of c. 3–10 km.

- High velocity, low normal stress ($v = 1$ m/s, $\sigma_n = 1$ MPa) rotary shear friction experiments were conducted on central and southern Alpine Fault gouge and cataclasite samples. Samples tested included: two Unit 4 foliated cataclasites (DFDP-1A 86.41 m and DFDP-1A 90.32m), one Unit 6 granitoid-gneissic cataclasite (DFDP-1B 128.80 m), three Unit 5 gouges (DFDP-1A 90.62 m, DFDP-1B 144.04 m, and GC Scarp PSZ), and Hokuri Creek fault gouge.

- A focus of the high velocity experiments was quantifying the peak coefficient of friction (μ_p), as this value represents the yield strength and thus the primary barrier to rupture propagation. An additional aim was to quantify the steady state coefficient of friction (μ_{ss}) at high velocity, the slip weakening distance (d_w) required to establish μ_{ss}, and breakdown work (W_B). Finally, the effect of pore fluid on μ_p, μ_{ss}, d_w, and W_B was investigated.

- In room-dry high velocity friction experiments, the peak coefficient of friction (μ_p) of phyllosilicate-poor cataclasites (mean $\mu_p = 0.70 \pm 0.05$; $n = 3$) and phyllosilicate-rich gouges and cataclasites (mean $\mu_p = 0.69 \pm 0.07$; $n = 6$), was consistently high regardless of sample grain size and mineralogy.

- In wet high velocity friction experiments, the peak coefficients of friction of the phyllosilicate-poor cataclasites (mean $\mu_p = 0.63 \pm 0.06$; $n = 2$) was higher than the phyllosilicate-rich gouges and cataclasites (mean $\mu_p = 0.32 \pm 0.23$; $n = 5$).

- All Alpine Fault rocks tested in room-dry and wet conditions exhibited very low steady state coefficients of friction (μ_{ss}) at high sliding velocity.

Dry materials had higher steady state friction coefficients (mean $\mu_{ss} = 0.18 \pm 0.04$; $n = 8$) than wet materials (mean $\mu_{ss} = 0.10 \pm 0.04$; $n = 7$).

- The three experiments conducted on wet smectite-bearing PSZ fault gouges had the lowest peak friction coefficients ($\mu_p = 0.13 - 0.18$), lowest steady state friction coefficients ($\mu_{ss} = 0.02 - 0.10$), and lowest breakdown work values ($W_B = 0.07 - 0.11$ MJ/m^2) of all the experiments performed.

- Given sufficient acceleration, rupture propagation through the smectite-bearing PSZ fault gouges is energetically favourable because it requires lower driving stress (shear force) than rupture propagation through other fault gouges and cataclasites tested.

- Microstructural interpretations were made of the gouges and cataclasites deformed in the dry high velocity experiments. Combined with axial displacement data, these interpretations indicate that thermal pressurization of ambient pore fluid, dehydrated adsorbed water and/or dehydrated smectite interlayer water was the primary dynamic-weakening mechanism responsible for low friction in the high velocity experiments. Flash heating at asperity contacts may have also occurred.

7.2 Synthesis

The rate and state friction equations imply that the seismogenic behaviour of a fault depends purely on frictional stability, not on mechanical strength. If faults represent single degree of freedom elastic systems, linear stability analyses show that frictional sliding will be unstable, or potentially unstable, when the friction rate parameter, a–$b \leq 0$ (velocity weakening). Frictional sliding will be stable, or aseismic, when the friction rate parameter a–$b > 0$ (velocity strengthening). The stability criterion also requires that the elastic stiffness of the loading system k be smaller than a critical stiffness k_c, which is defined by the frictional properties of the slipping fault (Ruina 1983; Gu et al. 1984). However, low velocity friction experiments conducted in Chapters 3, 4, and 5 found a correlation between strength and stability. This correlation

between frictional strength and stability was postulated by Beeler (2007) and Ikari et al. (2011a). In the double direct shear experiments (Chapter 3), hanging wall cataclasites ($\mu = 0.50 - 0.57$) exhibited velocity-weakening behavior during some, but not all, velocity steps. Frictionally weak gouges ($\mu < 0.50$) consistently exhibited velocity-strengthening behaviour. In hydrothermal triaxial compression experiments, consistent rate-weakening behaviour in the 1A blue and 1B brown gouges correlated with friction coefficients (μ) ≥ 0.62.

These measurements indicate that sufficient shear stress must be resolved on the Alpine Fault, or pore fluid pressures must be sufficiently high, to overcome the frictional strength of velocity-weakening material and nucleate an earthquake. Sibson (1985) first introduced a mechanical analysis of the reactivation potential of a fault subjected to stress. The Mohr-Coulomb theory forms the basis of the analysis and states that frictional failure will occur when:

$$\tau = C_0 + \mu_i \, (\sigma_n\text{'}) = C_0 + \mu_i \, (\sigma_n – P_p) \tag{7.1}$$

Here shear stress is equal to cohesion (C_0) plus the product of the internal friction coefficient (μ_i) and the effective normal stress (σ_n'). Effective normal stress is normal stress (σ_n) less pore fluid pressure (P_p). For existing faults, cohesion is considered negligible, and the equation reduced to Amonton's Law:

$$\tau = \mu_s \, (\sigma_n - P_p) \tag{7.2}$$

and (μ_s) is the static coefficient of friction. Knowing then the orientation of the fault plane and the stress tensor ($\sigma_1 > \sigma_2 > \sigma_3$), Sibson (1985) proposed that an effective stress ratio (R'):

$$R\text{'} = \frac{\sigma_1 - P_p}{\sigma_3 - P_p} \tag{7.3}$$

is required to initiate frictional slip on the fault plane. The 2-D analysis stipulates that frictional slip will occur when the fault intersects the Mohr-Coulomb failure envelope (Figure 7.1). Importantly, this analysis presumes that one of the principal stresses is vertical (i.e., 'Andersonian' faulting) and

that the intermediate principal stress is contained within the fault plane. Depending on the angle (θ_r) between the fault plane and the maximum principal stress, a fault may be optimally, favourably, unfavourably, or severely misoriented for reactivation. The optimal angle for reactivation, θ_r^*, is given by:

$$\theta_r^* = 0.5 \tan^{-1} \left(\frac{1}{\mu_s} \right) \tag{7.4}$$

Severely misoriented faults, those lying at $\theta_r > 2\theta_r^*$, require $P_p > \sigma_3$ for frictional slip to occur. Negative values of R' are obtained for severely misoriented faults.

Experimentally, it was shown that for the materials and conditions tested, a $\mu \geq 0.62$ is needed for unstable (potentially seismogenic) behaviour on the Alpine Fault (Figure 5.3). That is, negative values of (a–b) occur for all velocity steps, regardless of step size, when $\mu \geq 0.62$. Following many others, an average $\mu = 0.65$ measured for the 1A blue gouge across a range of normal stresses (σ_n' = 31 − 96 MPa) at T = 210°C is taken to equal the coefficient of static friction (μ_s) in equation 7.2 (e.g., Scholz 2002). The optimal angle for reactivation for a fault with a static friction coefficient of 0.65 is 29.5°. From focal mechanism inversions of Alpine Fault hanging wall microseismicity, Boese et al. (2012) determined that the stress tensor is oriented $\sigma_1 = \sigma_{Hmax} = 0/115°(\pm 10°)$, $\sigma_2 = \sigma_v$, and $\sigma_3 = 0/205°(\pm 10°)$. Boese et al. (2013) refined the stress tensor to be $\sigma_1 = \sigma_{Hmax} = 0/117°$, $\sigma_2 = \sigma_v$, and $\sigma 3 = 0/207°$. Townend et al. (2013) showed that this stress tensor is applicable over most of the South Island. Following Barth et al. (2012, 2013), the mean orientation of the central Alpine Fault is assumed to be parallel to the mylonitic foliation, 055°/45°SE, at depths > c. 2 km. The mean orientation of the southern Alpine Fault at depth is assumed to be parallel to surface measurements of the fault plane, 052°/82°SE (Table4.1). Thus, using the seismologically determined stress tensor and geological constraints on fault orientation, the central Alpine Fault at depth lies at an angle of 51.4° to σ_1. The southern Alpine Fault lies at an angle of 64.8° to σ_1.

The central and southern Alpine Fault do not contain the intermediate principal stress, so the assumptions inherent in the Sibson (1985) reactivation

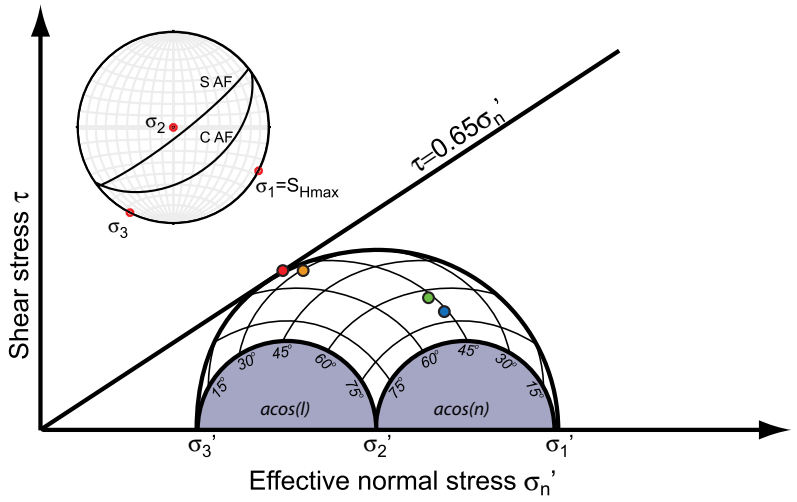

Figure 7.1: A Mohr diagram showing the reshear criterion assumed in the 3-D reactivation analysis, $\tau = 0.65\sigma_n$'. The arbelos are drawn for a stress shape ratio (Φ) of 0.5, equal to the mean seismologically determined stress shape ratio determined from focal mechanism inversions of Alpine Fault hanging wall microseismicity (Boese 2012). In the inner circles, *acos* stands for inverse cosine function. The orientation of four representative fault planes are shown: one optimally oriented (red circle), one favourably oriented (orange circle), one unfavourably oriented (green circle), and one severely misoriented (blue circle). In the inset lower hemisphere equal area stereoplot, the orientation of the central (CAF) and southern (SAF) Alpine Fault planes are plotted along with the seismologically determined orientation of the 3 principal stresses (Barth et al. 2013; Boese 2012; Boese et al. 2012; Townend et al. 2013).

analysis are invalid. Morris et al. (1996) extended the 2-D reactivation analysis to include the full 3-D stress tensor in a slip tendency analysis, but this method fails to identify the faults which can only be reactivated by with $P_p > \sigma_3$. Barth et al. (2012) conducted at slip tendency analysis on the central Alpine Fault and found that shear stress resolved is compatible with a coefficient of friction of c. 0.35 on the fault at depth. They speculated that a rotation of the stress tensor in the vicinity of the fault may allow slip on unfavourably oriented planes, but could not evaluate the role of pore fluid pressure. Using the new 3-D reactivation analysis developed by Leclère & Fabbri (2013), I now evaluate the role pore fluid pressure might play in allowing slip to occur on areas of the central and southern Alpine Fault comprising frictionally strong rate-weakening material. Leclère & Fabbri (2013) derived the method used, and it is summarized briefly below. All analyses were performed in Matlab®.

Jaeger et al. (2007) found that if the magnitudes and orientations of the principal effective stresses (σ_n' $= (\sigma_1 - P_p) > \sigma_2$' $= (\sigma_2 - P_p) > \sigma_3$' $= (\sigma_3 - P_p)$), shear stress and effective normal stress acting on the plane can be calculated following:

$$\tau = (\sigma'_1 - \sigma'_2)^2 l^2 m^2 + (\sigma'_2 - \sigma'_3)^2 m^2 n^2 + (\sigma'_3 - \sigma'_1)^2 l^2 n^2 \tag{7.5}$$

and

$$\sigma'_n = l^2 \sigma'_1 + m^2 \sigma'_2 + n^2 \sigma'_3 \tag{7.6}$$

where l, m, and n are the direction cosines between the pole to the fault plane and the principal stress axes σ_1, σ_2, and σ_3. Where the magnitudes of the principal effective stresses are unknown, the relative magnitudes is expressed by the stress shape ratio Φ:

$$\Phi = \frac{\sigma_2 - \sigma_3}{\sigma_1 - \sigma_3} \tag{7.7}$$

Effective principal stress magnitudes are unknown for the Alpine Fault. Focal mechanism inversions of microseismicity in the fault's hanging wall yield a stress shape ratio of 0.5±0.2 (Boese 2012). Leclère & Fabbri (2013) defined the effective stress ratio, Q, such that:

$$Q = \frac{\sigma_2' - \sigma_3'}{\sigma_1' - \sigma_3'} \tag{7.8}$$

By substituting equation (7.8) into equations (7.1), (7.5) and (7.6), Leclère & Fabbri (2013) found that:

$$\mu_s = \frac{\sqrt{Q^2C - 2QC + C} - \left(\frac{C_0}{\sigma_1'}\right)}{QA + B} \tag{7.9}$$

where

$$A = m^2 + n^2 + \Phi m^2 \tag{7.10}$$

$$B = l^2 + \Phi m^2 \tag{7.11}$$

$$C = (1 - \Phi)\, l^2 m^2 + \Phi^2 n^2 m^2 + l^2 n^2 \tag{7.12}$$

Q can then be expressed as a function of l, m, n, Φ, and C_0/σ_1:

$$Q^2 \left(A^2\mu^2 - C\right) + Q\left(2AD\mu_s + 2C\right) + D^2 - C = 0 \tag{7.13}$$

By letting:

$$D = B\mu_s + \left(\frac{C_0}{\sigma_1'}\right) \tag{7.14}$$

Equation 7.13 can be solved with

$$\Delta = \left(2AD\mu_s + 2C\right)^2 - 4\left(A^2\mu_s^2 - C\right)\left(D^2 - C\right) \tag{7.15}$$

$$Q = \frac{-\left(2AD\mu_s + 2C\right) \pm \sqrt{\Delta}}{A^2\mu_s^2 - C} \tag{7.16}$$

where Q and μ_s are a subset of all real numbers, with $Q \leq 1$ and $\mu_s \geq 1$. If σ_1' = σ_3', $Q = Q_{max} = 1$. Using θ_r^* defined in equation 7.4 and ignoring cohesion, $Q_{optimal}$ is given by:

$$Q_{optimal} = \frac{1 - \mu_s \tan(\theta_r^*)}{1 + \mu_s \cot(\theta_r^*)} \tag{7.17}$$

Figure 7.1 is a Mohr Circle plot depicting the orientation of optimal (red circle), favourable (orange circle), unfavourable (green circle), and severely misoriented (blue circle) planes. Unfavourably oriented fault planes have Q values between 2/3 $Q_{optimal}$ and 0; severely misoriented planes have negative Q values. Frictional slip on severely misoriented fault planes requires $P_p > \sigma_3$.

Using the 3-D reactivation analysis of Leclère & Fabbri (2013), conditions necessary for frictional slip on the central and southern Alpine Fault were explored. Input parameters were: the seismologically determined stress tensor ($\sigma_1 = \sigma_{Hmax} = 0/117°, \sigma_2 = \sigma_v$, and $\sigma_3 = 0/207°$) and stress ratio ($\Phi = 0.5 \pm 0.2$); the orientation of the central (055°/45°SE) and southern (052°/82°SE) Alpine Fault; and the experimentally determined coefficient of friction ($\mu_s = 0.65$). Stereoplots in Figure 7.2 depict results for $\Phi = 0.3$, 0.5 and 0.7. For a stress shape ratio of 0.3, corresponding to a stress tensor with the magnitude of σ_2' close to σ_1', the central Alpine Fault is unfavourably oriented; the southern Alpine Fault is severely misoriented. Results of analyses using all values of μ_s and Φ are shown in Figures 7.3 and 7.4, contour plots of Q values. On the central Alpine Fault, for all values of $\Phi > 0.35$, $P_p > \sigma_3$ is required for frictional slip to occur in velocity-weakening materials ($\mu_s \geq 0.65$). On the southern Alpine Fault, for all values of Φ analysed, $P_p > \sigma_3$ is required for frictional slip to occur in rate-weakening materials ($\mu_s \geq 0.65$).

According to the barrier-conduit model of fault zone architecture proposed by Caine et al. (1996), fault gouges and cataclasites comprising fault cores can create seals such that fault normal permeability is much lower than fault parallel permeability. This condition is requisite for suprahydrostatic and lithostatic pore fluid pressure development (Rice 1992; Faulkner & Rutter 2001). Regional observations of hanging wall warm springs, combined with field and laboratory measurements, indicate that the fault core gouges and cataclasites have very low fault-normal permeabilities (Menzies 2012; Boulton et al. 2012; Sutherland et al. 2012; Barth et al. 2013; Carpenter et al. accepted). For the central Alpine Fault, it is possible that high pore

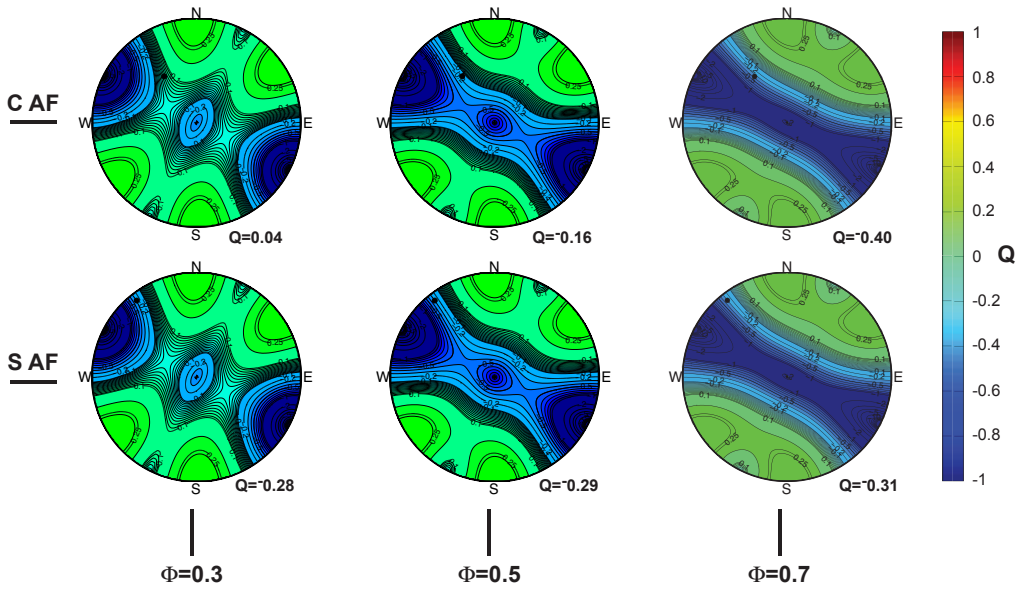

Figure 7.2: Example stereoplots created in the 3-D reactivation analysis conducted on the central (μ_s = 0.65, 055°/45°SE) and southern (μ_s = 0.65, 052°/82°SE) Alpine Fault. The pole to the fault plane is given by a dark solid dot in the stereoplots. Colours are shaded according to the orientation of the representative fault planes in Figure 7.2, with green and blue shades indicating unfavourably and severely misorientated faults. Pictured are results for stress shape ratios (Φ) 0.3, 0.5, and 0.6. Q values for each analysis are listed below the corresponding stereoplot.

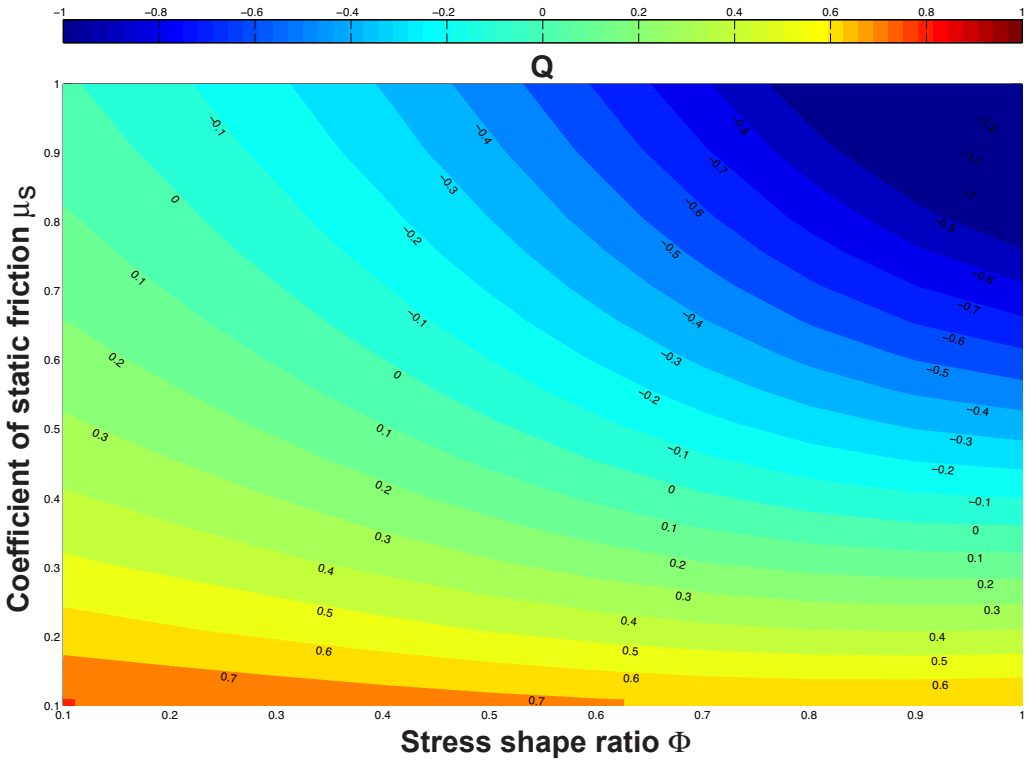

Figure 7.3: A contour plot generated from Q values obtained in the 3-D reactivation analysis of the central Alpine Fault. All stress shape ratios (Φ) between 0.1 and 1.0, and all coefficients of static friction (μ_s) between 0.1 and 1.0 were evaluated.

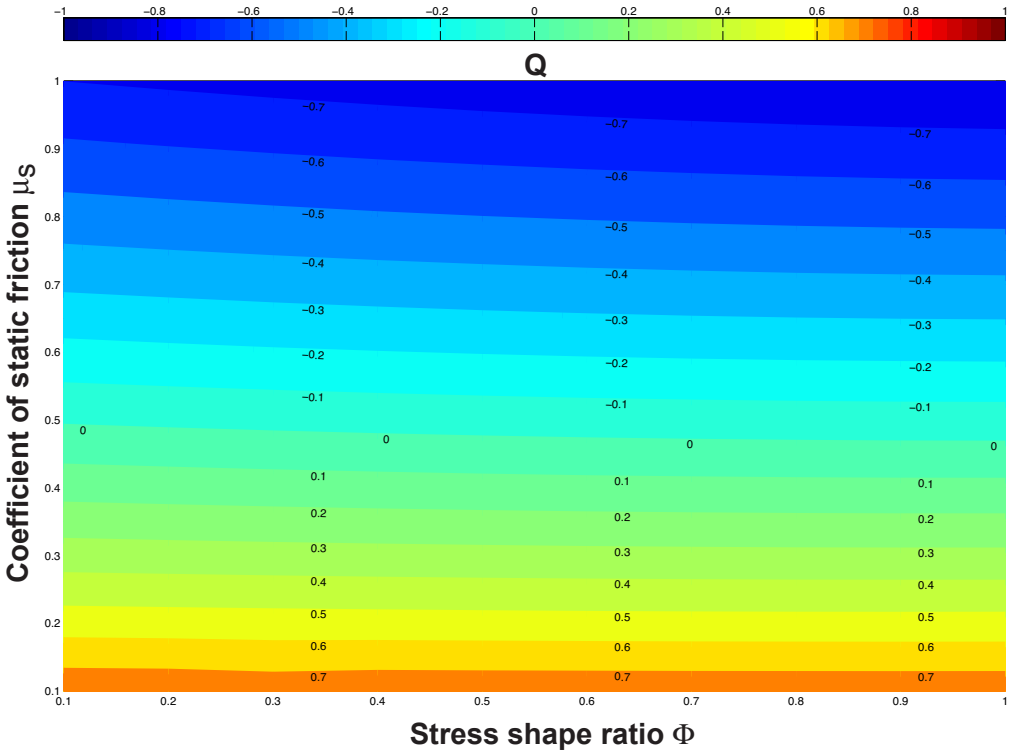

Figure 7.4: A contour plot generated from Q values obtained in the 3-D reactivation analysis of the southern Alpine Fault. All stress shape ratios (Φ) between 0.1 and 1.0, and all coefficients of static friction (μ_s) between 0.1 and 1.0 were evaluated.

fluid pressures are present in low permeability materials comprising the fault core in the upper c. 4 km or at depths greater than c. 10 km where geochemical and geophysical evidence suggests interconnected fluids are present (Wannamaker et al. 2002; Stern et al. 2007; Menzies 2012). To my knowledge, no information on the distribution of pore fluids at depth is available for the southern Alpine Fault.

This 3-D reactivation analysis assumes that interconnected pore fluids are instrumental in reducing fault strength and changing the stress state. In a seismic cycle, time-dependent pore fluid pressurization is aided by intergranular healing, fault zone sealing, interseismic creep and compaction (e.g., Sibson 1992; Sleep & Blanpied 1992; Miller et al. 1996; Hacker 1997; Gratier & Gueydan 2007; Hillers & Miller 2007; Cox 2010). Additional factors may influence the fault's stress state. With increasing time in the seismic cycle, tectonic loading leads to increasing shear stress (e.g., Scholz 2002). Small changes (both increases and decreases) in shear stress may also occur in response to slip on nearby faults (e.g., Stein 1999; King 2007). Fabric anisotropy in the mylonites and foliated cataclasites may result in rotation of the stress tensor in close proximity to the fault plane (e.g., Faulkner et al. 2006; Healy 2008). It is possible that one or more of these processes drive earthquake nucleation on the Alpine Fault, a long-lived fault with a high-strain, thermally-weakened ductile shear zone at depth (Koons 1987; Koons et al. 2003; Norris & Cooper 2003). Once nucleated, the 3-D reactivation analysis indicates that sufficient shear stress is resolved on both sections of the Alpine Fault to overcome the peak friction coefficients of phyllosilicate-rich gouges and cataclasites ($\mu_p = 0.32 \pm 0.23$) measured in the high velocity rotary shear experiments.

7.3 Suggestions for future research

Fault friction is controlled by a complex interplay of various thermo-poro-mechanical and physic-chemical prcoesses. The multi-disciplinary, integrated dataset obtained during the course of this doctoral thesis provides new information about these processes acting in Alpine Fault rocks, but multiple research questions remain. Below, I present suggestions for future research.

Drill deeper. The Deep Fault Drilling Project aims to drill through the Alpine Fault ultimately to depths of $\sim$ 4 km. Key objectives of future drilling operations include a more accurate determination of the geothermal gradient, determination of the orientation and magnitude of the principal stresses, improved measurements of pore fluid pressure and geochemistry, more complete wireline logging of geophysical properties, and recovery of an oriented suite of fault rock lithologies.

Determine the minimum pore fluid pressure requisite for frictional slip to occur on the central and southern Alpine Fault. In section 7.2, a 3-D reactivation analysis showed that high pore fluid pressure is required for reshear to occur on the Alpine Fault. By making some assumptions, this analysis can be extended. Since the magnitudes of the principal stresses acting on the fault are unknown, results from other in situ stress measurements can be extrapolated to the Alpine Fault. Streit (Table 1, 1999) showed that differential stress ($\sigma_1 - \sigma_3$) increases c. 15 MPa per km depth. For strike-slip faults, i.e. the Alpine Fault, $\sigma_v = \sigma_2 = \rho g z$ according to Anderson's faulting theory. In this analysis, quartzofeldsparthic crustal rock density (ρ) is 2650 km/m^3, gravitational acceleration (g) is 9.81 m/s, and z is depth in metres. Letting $\sigma_3 = \sigma_2 - (\Phi * (\sigma_1 - \sigma_3))$, and $\sigma_1 = (\sigma_1 – \sigma_3) + \sigma_3$, pore fluid pressure ($P_p$) can be calculated using the Q values obtained in section 7.2 following:

$$P_p = (Q\sigma_1) - \frac{\sigma_3}{Q - 1} \tag{7.18}$$

It was found that frictional strength and stability are strongly correlated with temperature. DFDP-1A blue gouge was rate-weakening regardless of velocity step size at c. 210°C. At this temperature, across a range of effective normal stresses, the average coefficient of friction was 0.65.

If I assume c. 210°C is the critical temperature for the onset of rate-weakening behaviour and a moderate geothermal gradient of 35°C, earthquake nucleation will occur at depths of 6 km and deeper. Using the above-mentioned gradient in differential stress of 15 MPa/km, I obtain a differential stress of 90 MPa. For the mean seismologically determined stress shape ratio, $\Phi = 0.5$ and $\mu_s = 0.65$, the Q value is equal to -0.1631. Using these numbers, I calculate that a pore fluid pressure of c. 125 MPa is required

to satisfy the reshear failure criterion for the central Alpine Fault (equation 7.2). Taking the pore fluid factor (λ_v) as being equal to P_p divided by σ_v, this value corresponds to a suprahydrostatic pore fluid factor of 0.8 (Hubbert & Rubey 1959).

This analysis should be extended to the southern Alpine Fault, and it should be used to construct failure mode diagrams following Cox (2010). By doing so, the competition between conditions required for reshear of a severely misoriented fault and the formation of a new, optimally oriented fault in intact rock, can be explored. The relationships between differential stress, tensile strength, stress state, and failure mode (e.g., extensional failure, hybrid extensional-shear failure, and shear failure) can also be explored. Finally, the effect of time-dependent increases in cohesion, as a result of crack sealing, recrystallization, porosity reduction, and intergranular healing (e.g., Muhuri et al. 2003; Gratier & Gueydan 2007), can be explored by including cohesion in the 3-D reactivation analysis (equations 1 and 10). Analyses using all of these variables would be better constrained by field and laboratory measurements of their values under in-situ conditions of pressure and temperature.

Establish a microphysical understanding of weak friction. Where phyllosilicates are present in sufficient amounts to form an interconnected matrix (e.g., Tembe et al. 2009), or comprise interconnected foliations (e.g., Bos & Spiers 2002; Collettini et al. 2009), frictional sliding can occur along the (001) layers. For dry room-temperature experiments, the coefficient of friction for phyllosilicates corresponds approximately to the mineral's (001) interlayer bond strength, and the relative strength is: kaolinite > lizardite > chlorite illite/muscovite > biotite > talc ≈ dioctahedral smectite (montmorillonite) > trioctahedreal smectite (saponite) (e.g., Byerlee 1978; Moore & Lockner 2004; Moore & Rymer 2007). Extrapolation of frictional strength values obtained in these experiments, however, remains difficult because of the lubricating effects of adsorbed water layers in water-saturated phyllosilicates (e.g., Moore & Lockner 2004), the activation of dislocation glide at elevated temperatures (e.g., Mariani et al. 2006), the common occurrence of phyllosilicate mixtures and dissolution-assisted pressure solution creep (e.g., Bos & Spiers 2002; Ikari et al. 2007, 2011a; Niemeijer & Spiers 2005, 2007), and the

effects of pore fluid chemistry (e.g., Behnsen & Faulkner 2013). Evaluating the effects of these variables experimentally and numerically would contribute to a better understanding of the microphysical basis for weak friction, and, by extension, the propensity for some faults to creep aseismically (e.g.,Imber et al. 2008; Lockner et al. 2011; Carpenter et al. 2011).

Establish a microphysical understanding of velocity-weakening and velocity-strengthening behaviours. The rate and state friction equations are empirical equations derived from laboratory observations of a rock or rock-analogue material's frictional response to sudden changes in velocity (velocity steps) and stationary hold time (slide-hold-slide tests). Numerous published papers report values of (a–b), a key variable in the stability criterion, but as yet there exists no microphysical understanding of variations in (a–b), and perhaps more importantly d_c, as a function of temperature, pressure, sliding velocity, and porosity (layer thickness) (e.g., Marone & Kilgore 1993; Blanpied et al. 1995, 1998; Chester et al. 1993; Marone 1998; Scholz 1998; Nakatani 2001; Scholz 2002; Niemeijer & Spiers 2007; Marone et al. 2009; Ikari et al. 2011a2010, 2011). Thus, there is considerable epistemic uncertainty regarding the microphysical processes responsible for frictional (in-)stability. Given the utility of the rate and state friction equations in explaining numerous seismic phenomena (e.g., Marone 1998), it seems apposite to systematically study the evolution of frictional stability at a range of strains, strain rates, temperatures, normal stresses, and pore fluid pressures (including a range of appropriate pore fluid chemistries) (e.g., Beeler 2007).

Combining measurements of layer thickness (to account for dilatancy and compaction), pore fluid pressure, shear stress, normal stress, pore fluid pressure, temperature, and acoustic emissions, with, ideally, real-time imaging of microstructural evolution in mineralogically disparate materials, should improve our understanding of the physical processes responsible for rate-strengthening and rate-weakening behaviour. Of particular interest to this research, the evolution of frictional strength and stability of DFDP-1A blue gouge and DFDP-1B brown gouge (Chapter 5) at high strains under hydrothermal condition should be investigated. These experiments, in a high temperature-high pressure rotary shear apparatus, might reveal whether fabric formation at strains greater than c. 8-10 results in lower frictional strength

and positive values of (a–b) (e.g., Bos & Spiers 2001, 2002; Niemeijer & Spiers 2005, 2007). With a sound understanding of the physical processes underpinning frictional stability, upscaling of laboratory results to crustal fault zones, i.e. the Alpine Fault, should become possible with numerical models (e.g., Perfettini & Ampuero 2008; Rubin & Ampuero 2009). Moreover, experimentally produced microstructures can be linked with naturally occurring microstructures to understand their origin and rheological significance.

Understand mass transfer processes occurring within the fault zone. To quantify the physical processes driving the seismic cycle on the Alpine Fault, better laboratory constraints on mineral reactions, reaction rates, diffusion rates, compaction rates, and healing rates in the lab and in naturally deformed fault rocks are needed. This research would greatly benefit from experiments targeting the quantification of diffusion rates in grain contacts in phyllosilicate-quartz mixtures and feldspar-quartz mixtures. Diffusion is commonly assumed to be the rate-limiting step in pressure solution, the process that drives intergranular healing in the upper crust, but it is possible that the rate-limiting step varies with porosity, pore fluid chemistry and grain size (e.g., Gratier et al. 2003; Niemeijer et al. 2002, 2009; Yasuhara et al. 2003). It would also benefit from more careful observations of exhumed Alpine Fault rocks using scanning electron microscopy (SEM) and transmission electron microscopy (TEM) combined with energy-dispersive spectroscopy (EDS) to identify mineral chemistry and crack-seal textures and electron backscatter diffraction (EBSD) to measure crystallographic preferred orientation (particularly in the foliated cataclasites). X-ray computed tomography (x-ray CT) could be used to image and quantify the number and orientation of fractures within larger scale drillcore samples, as well as the structural relationships between fractures and fabrics.

Identify all the mineralogical constituents of the characteristic lithologies, the paragenetic sequence(s), and the textural relationships between characteristic microstructures and open fractures. This information would improve our understanding of the seismological implications of mass transfer and damage zone processes (e.g., Hacker 1997; Gratier & Gueydan 2007; Beeler 2007; Mitchell & Faulkner 2009; Faulkner et al. 2010). With better measurements of the orientation of fabrics and fractures within the fault core-

alteration zone, for example, models predicting a rotation of the maximum principal stress (σ_1) within the fault core could be tested (e.g., Faulkner et al. 2006; Healy 2008). In addition, geophysical and geochemical observations of fluid flux during interseismic, coseismic, and postseismic periods are needed for numerical models that quantify how fluid migration, porosity, permeability, and rock strength evolve at depth. Incorporating permeability and fluid pressure evolution variables into empirical rate- and state-dependent constitutive laws would better constrain how fluid-rock interactions influence fault strength evolution, strain accumulation, and the timing and mode of earthquake rupture nucleation (e.g., Sibson 1992; Segall & Rice 1995; Sibson & Rowland 2003; Hillers & Miller 2007; Ben-Zion 2008; Samuelson et al. 2009).

Improve methods used in high velocity friction experiments. Obtaining thin sections from high velocity rotary shear experiments under saturated conditions would facilitate better interpretation of the dynamic weakening mechanism(s) that occurred in these experiments. Better identification of the dynamic weakening mechanism(s) could also be made with measurements of (1) humidity in a sample chamber during the experiments, (2) local pore fluid pressure and (3) temperature in deforming gouges and cataclasites, (4) changes in fault gouge clay mineralogy as a result of frictional heating, (5) identification of minerals and particles comprising structural unit 4. To avoid rapid pore fluid fluctuations and fluid loss through the Teflon® sleeve, a better sample sealing mechanism could be devised. The effect of wall rock permeability on the efficiency of thermal pressurization could be investigated by using a range of wall rocks with different permeabilities, but it should be noted that these rocks may have different thermal conductivies (e.g., Tanikawa & Shimamoto 2009). Conducting the high velocity experiments across a wider range of normal stresses would reveal to what extent saturated samples behave as viscous fluids. Programming slip functions that more accurately simulate an earthquake-like slip event (i.e., a Yoffe function) would yield traction curves that strengthen during the decelerating phase of the slip event, more akin to seismic undershoot (Tinti et al. 2005; Sone & Shimamoto 2009; Beeler 2006; Chang et al. 2012). Comparing microstructures formed during earthquake-like slip events with those formed during constant velocity experiments and along natural seismogenic faults would al-

low experimental methods to be refined to simulate more realistic conditions. Linking experimentally produced and naturally formed microstructures will also enable extrapolation of laboratory results to the field.

Longstanding issues with experiments on the low to high velocity rotary shear apparatus used in the experiments documented in Chapter 6 include Teflon® sleeve wear and decomposition as well as radial variations in shear stress, normal stress, velocity, and temperature (e.g., Kitajima et al. 2010; Sawai et al. 2012; Niemeijer et al. 2012). I built a new high velocity rotary shear apparatus at the University of Canterbury over the course of this doctoral research (frontispiece). In this apparatus, the Teflon® seal is not in contact with the experimental fault, higher normal stresses ($\leq$ 4.3 MPa) are achievable, there is a small radial difference between the outer (50 mm) and inner (45 mm) walls of the sample chamber, and the effect of acceleration and deceleration on fault strength can be explored by inputting custom slip functions. With a maximum motor speed of 1455 rpm and a maximum gear box speed of 427 rpm, 5 mm-thick layers of granular gouge can be sheared at sliding velocities between 2 mm/s and 420 mm/s. The theoretical resolution of each sensor is: linear variable differential transformer (LVDT), for measuring axial displacement, 0.0001$\pm$0.00005 mm; shear stress load cells 0.015$\pm$0.073 N; normal stress load cells 0.038$\pm$0.012 N; rotary encoder, for measuring angular displacement, 0.17 mm. In practice, experimental error is higher and varies with sample preparation, normal load, motor performance, machine eccentricity, and wear of the sealing rings. This apparatus has been built, tested, calibrated, and used to gather reproducible data on the frictional strength of crushed limestone. It should be used in future high velocity friction experiments on a range of fault gouge and fault gouge analog materials.

References

2010. 1:1 000 000 Geological Map of New Zealand. Institute of Geological & Nuclear Sciences.
URL `http://portal.onegeology.org`

2012. GeoNet.
URL `http://www.geonet.org.nz/earthquake/resources`

Abercrombie R & Rice J, 2005. Can observations of earthquake scaling constrain slip weakening? Geophysical Journal International, 162:406–424.

Ague J, 1994. Mass transfer during Barrovian metamorphism of pelites, south-central Conneticut. I: Evidence for changes in composition and volume. American Journal of Science, 294:989–1057.

Aki K, 1979. Characterization of barriers on an earthquake fault. Journal of Geophysical Research, 84:6140–6148.

Allen CR, 1968. The tectonic environments of seismically active and inactive areas along the San Andreas fault system. In Dickinson W & Grantz A, editors, Proceedings of Conference on Geologic Problems of San Andreas Fault System, volume 11, pages 70–80. Stanford University Publications in the Geological Sciences.

Allis R & Shi Y, 1995. New insights into temperature and pressure beneath the central Southern Alps, New Zealand. New Zealand Journal of Geology and Geophysics, 38:585–592.

Anderson H & Webb T, 1994. New Zealand seismicity: patterns revealed by the upgraded National Seismograph Network. New Zealand Journal of Geology and Geophysics, 37:477–493.

Andrews D, 1976a. Rupture propagations with finite stress in antiplane strain. Journal of Geophysical Research, 81:5679–5687.

Andrews D, 1976b. Rupture velocity of plane strain shear cracks. Journal of Geophysical Research, 81:5679–5687.

Andrews D, 1989. Mechanics of fault junctions. Journal of Geophysical Research, 94:9389–9397.

Andrews D, 2002. A fault constitutive relation accounting for thermal pressurization of pore fluid. Journal of Geophysical Research, 107(B12):2363. doi:10.1029/2002JB001942.

Andrews D, 2005. Rupture dynamics with energy loss outside the slip zone. Journal of Geophysical Research, 110(B01307). doi:10.1029/2004JB003191.

Anthony J & Marone C, 2005. Influence of particles characteristic on granular friction. Journal of Geophysical Research, 110(B08409). doi:10.1029/2004JB003399.

Arabasz W & Robinson R, 1976. Microseismicity and geologic structure in the northern South Island, New Zealand. New Zealand Journal of Geology and Geophysics, 9:407–25.

Audet P, Bostock M, Christensen N, & Peacock S, 2009. Seismic evidence for overpressured subducted oceanic crust and megathrust fault sealing. Nature, 457:76–78.

Ballard H, 1989. Permian Arc Volcanism and aspects of the general geology of the Skippers Range, NW Otago. Ph.D. thesis, Dep. of Geology, University of Otago, Dunedin, New Zealand.

Barnes I, Downes C, & Hurlston J, 1978. Warm springs, South Island New Zealand and their potentials to yield laumontite. American Journal of Science, 278(10):1412–1427. doi:10.2475/ajs.278.10.1412.

Barnes P & Pondard N, 2010. Derivation of direct on-fault submarine paleoearthquake records from high-resolution seismic reflection profiles: Wairau Fault, New Zealand. Geochemistry Geophysics Geosystems, 11(11). doi:10.1029/2010GC003254.

Barnes P, Sutherland R, Davy B, & Delteil J, 2001. Rapid creation and destruction of sedimentary basins on mature strike-slip faults: An example from the offshore Alpine Fault, New Zealand. Journal of Structural Geology, 23:1727–1739. doi:10.1016/S0191-8141(01)00044-X.

Barnes P, Davy B, Sutherland R, & Delteil J, 2002. Frontal accretion and thrust wedge evolution under very oblique plate convergence: Fiordland basin, New Zealand. Basin Research, 14:439–466. doi:10.1046/J.1365-2117.2002.00178.X.

Barnes P, Sutherland R, & Delteil J, 2005. Strike-slip structure and sedimentary basins of the southern Alpine Fault, Fiordland, New Zealand. Geological Society of America Bulletin, 117(3/4). doi:10.1130/B25458.

Barnes PM, 1996. Active folding of Pleistocene unconformities on the edge of the Autralian-Pacific plate boundary zone, offshore North Canterbury, New Zealand. Tectonics, 15:623–640.

Barnes PM, 2009. Postglacial (after 20 ka) dextral slip rate of the offshore Alpine fault, New Zealand. Geology, 37:3–6. doi:10.1130/G24764A.1.

Barth N, 2013. A Tectono-Geomorphic Study of the Alpine Fault, New Zealand. Ph.D. thesis, University of Otago, Dunedin, New Zealand.

Barth N, Toy V, Langridge R, & Norris R, 2012. Scale dependence of oblique plate-boundary partitioning: New insights from LiDAR, central Alpine fault, New Zealand. Lithosphere. doi:10.1130/L201.1.

Barth N, Boulton C, Carpenter B, Batt G, & Toy V, 2013. Slip localization on the southern Alpine Fault, New Zealand. Tectonics, 32:1–21.

Batt G, Baldwin S, Cottam M, Fitzgerald P, Brandon M, & Spell T, 2004. Cenozoic plate boundary evolution in the South Island of New Zealand: New thermochronological constraints. Tectonics, 23:TC4001. doi:10.1029/2003TC001527.

Beavan J, Moore M, Pearson C, Henderson M, Parsons B, Bourne S, England P, Walcott D, Blick G, Darby D, & Hodgkinson K, 1999. Crustal deformation during 1994-1998, due to oblique continental collision in the central Southern Alps, New Zealand, and implications for seismic potential of the Alpine fault. Journal of Geophysical Research, 104(B11):25233–25255. doi:10.1029/1999JB900198.

Beavan J, Denys P, Denham M, Hager B, Herring T, & Molnar P, 2010. Distribution of present-day vertical deformation across the Southern Alps, New Zealand, from 10 years of GPS data. Geophysical Research Letters, 37:L16305. doi:10.1029/2010GL044165.

Beeler N, 2006. Inferring earthquake source properties from laboratory observations and the scope of lab contributions to source physics. In Abercrombie R, McGarr A, Kanamori H, & Di Toro G, editors, Earthquakes: Radiated Energy and the Physics of Faulting, volume 170, pages 99–119. American Geophysical Union. doi:10.1029/170GM12.

Beeler N, 2007. Laboratory-observed faulting in intrinsically and apparently weak materials. In Dixon TH & Moore JC, editors, The Seismogenic Zone of Subduction Thrust Faults, pages 370–449. Columbia University Press.

Beeler N, Tullis T, & Weeks J, 1994. The roles of time and displacement in the evolution effect in rock friction. Geophysical Research Letters, 21(18):1987–1990.

Beeler N, Tullis T, & Goldsby D, 2008. Constitutive relationships and physical basis of fault strength due to flash heating. Journal of Geophysical Research, 113(B01401). doi:10.1029/2007JB004988.

Behnsen J & Faulkner D, 2013. Permeability and frictional strength of cation-exchanged montmorillonite. Journal of Geophysical Research, 118:1–11. doi:10.1002/jgrb.50226.

Behringer R, Daniels K, Majmudar T, & Sperl M, 2008. Fluctuations, correlations and transitions in granular materials: statistical mechanics and non-conventional systems. Philosophical Transactions of the Royal Society, A366:493–504.

Beltrando M, Lister G, Forster M, Dunlap W, Fraser G, & Hermann J, 2009. Dating microstructures by the $^{40}Ar/^{39}Ar$ step heating technique: Deformation-pressure-temperature-time history of the Penninic Units of the Western Alps. Lithos, 113(3-4):801–819. doi:10.1016/j.lithos.2009.07.006.

Ben-David O & Fineberg J, 2011. Static friction coefficient is not a material constant. Physical Review Letters, 106:254301.

Ben-David O & Rubinstein S, 2010. Slip-stick and the evolution of frictional strength. Nature, 463:76–79.

Ben-David O, Cohen G, & Fineberg J, 2010. The dynamics of the onset of frictional slip. Science, 330:211–214.

Ben-Zion Y, 1996. Stress, slip, and earthquakes in models of complex single-fault systems incorporating brittle and creep deformations. Journal of Geophysical Research, 101(B3):5677–5706.

Ben-Zion Y, 2001. Dynamic ruptures in recent models of earthquake faults. Journal of the Mechanics and Physics of Solids, 49:2209–2244.

Ben-Zion Y, 2008. Collective behavior of earthquakes and faults: continuum-discrete transitions, progressive evolutionary changes, and different dynamic regimes. Reviews of Geophysics, 46(RG4006).

Ben-Zion Y & Sammis C, 2003. Characterization of Fault Zones. Pure and Applied Geophysics, 160:677–715.

Berryman K, Beanland S, Cooper A, Cutten H, Norris R, & Wood P, 1992. The Alpine Fault, New Zealand: variation in Quaternary structural style and geomorphic expression. Annales Tectonicae IV, pages 126–163.

Berryman K, Cochran U, Clark K, Biasi G, Langridge R, & Villamor P, 2012a. Major earthquakes occur regularly on an isolated plate boundary fault. Science, 336(6089):1690–1693. doi:10.1126/science.1218959.

Berryman K, Cooper A, Norris R, Villamor P, Sutherland R, Wright T, Schermer E, Langridge R, & Biasi G, 2012b. Late Holocene Rupture History of the Alpine Fault in South Westland, New Zealand. Bulletin of the Seismological Society of America, 102(2):620–638.

Biegel R & Sammis C, 2004. Relating fault mechanics to fault zone structure. Advances in Geophysics, 47:65–111.

Biegel R, Sammis C, & Dieterich J, 1989. Frictional properties of simulated debris. Journal of Structural Geology, 11:827–846.

Bilham R, 2009. The seismic future of cities. Bulletin of Earthquake Engineering, 7(4):839–887. doi:10.1007/s10518-009-9147-0.

Bishop D, Bradshaw J, & Landis C, 1985. Provisional terrane map of South Island, New Zealand. pages 515–521.

Bizarri A & Cocco M, 2006a. A thermal pressurization model for the spontaneous dynamic rupture propagation on a three-dimensional fault: 1. Methodological approach. Journal of Geophysical Research, 111:B05303. doi:10.1029/2005JB003862.

Bizarri A & Cocco M, 2006b. A thermal pressurization model for the spontaneous dynamic rupture propagation on a three-dimensional fault: 2. Traction evolution and dynamic parameters. Journal of Geophysical Research, 111:B05304. doi:10.1029/2005JB003864.

Blanpied M, Lockner D, & Byerlee J, 1995. Frictional slip of granite at hydrothermal conditions. Journal of Geophysical Research, 100(B7):13045–13064. doi:10.1029/95JB00862.

Blanpied M, Marone C, Lockner D, Byerlee J, & King D, 1998. Quatitative measure of the variation in fault rheology due to fluid-rock interactions. Journal of Geophysical Research, 103(B5):9691–9712.

Boese C, 2012. Microseismicity in the central Southern Alps, Westland, New Zealand. Ph.D. thesis, Victoria University of Wellington, Wellingon, New Zealand.

Boese C, Townend J, Smith E, & Stern T, 2012. Microseismicity and stress in the vicinity of the Alpine Fault, central Southern Alps, New Zealand. Journal of Geophysical Research, 117:B02302. doi:10.1029/2011JB008460.

Boese C, Stern T, Townend J, Bourguignon S, Sheehan A, & Smith E, 2013. Sub-crustal earthquakes within the Australia-Pacific plate boundary zone beneath the Southern Alps, New Zealand. Earth and Planetary Science Letters, 376:212–219. doi:10.1016/j.epsl.2013.06.030.

Bos B & Spiers C, 2000. Effect of phyllosilicates on fluid-assisted healing of gouge-bearing faults. Earth and Planetary Science Letters, 184:199–210.

Bos B & Spiers C, 2001. Experimental investigation into the microstructural and mechanical evolution of phyllosilicate-bearing fault rock under conditions favouring pressure solution. Journal of Structural Geology, 23:1187–1202.

Bos B & Spiers C, 2002. Frictional-viscous flow of phyllosilicate-bearing fault rock: Microphysical model and implications for crustal strength profiles. Journal of Geophysical Researc, 107(B2). doi:10.1029/2001JB000301.

Bos B, Peach C, & Spiers C, 2000. Slip behavior of simulated gouge-bearing faults under conditions favoring pressure solution. Journal of Geophysical Research, 105(B7):16699–16717. doi:10.1029/2000JB900089.

Boullier A, Yeh E, Boutareaud S, Song S, & Tsai C, 2009. Microscale anatomy of the 1999 Chi-Chi earthquake fault zone. Geochemistry, Geophysics, Geosystems, 10(3):Q03016. doi:10.1029/2008GC002252.

Boulton C, Davies T, & McSaveney M, 2009. The frictional strength of granular fault gouge: application of theory to the mechanics of low-angle normal faults. Geological Society Special Publications, 321:9–31.

Boulton C, Carpenter B, Toy V, & Marone C, 2012. Physical properties of surface outcrop cataclastic fault rocks, Alpine Fault, New Zealand. Geochemistry Geophysics Geosystems, 13(Q01018). doi:10.1029/2011GC003872.

Boulton C, Moore D, Lockner D, Toy V, Townend J, & Sutherland R, 2014. Frictional strength and stability of exhumed fault gouges in DFDP-1 cores, Alpine Fault, New Zealand. Geophysical Research Letters. doi:10.1002/2013GL058236.

Bourne S, Arnadottir T, Beavan J, Darby D, England P, Parsons B, Walcott R, & Wood P, 1998. Crustal deformation of the Marlborought fault zone in the South island of New Zealand: Geodetic constraints over the interval 1982-1994. Journal of Geophysical Research, 103:30147–30165.

Boutareaud S, Calugaru D, Han R, Fabbri O, Mizoguchi K, Tsutsumi A, & Shi Y, 2008. Clay-clast aggregates: a new textural evidence for seismic fault sliding? Geophysical Research Letters, 35(L05302). doi:10.1029/2007GL032554.

Boutareaud S, Boullier A, Andreani M, Calugaru D, Beck P, Song S, & Shimamoto T, 2010. Clay-clast aggregates in gouges: a new textural evidence for seismic faulting. Journal of Geophysical Research, 115(B02408). doi:10.1029/2008JB006254.

Boutareaud S, Hirose T, Andreani M, Pec M, Calugaru D, Boullier A, & Doan ML, 2012. On the role of phyllosilicates on fault lubrication: Insight from

micro- and nanostructural investigations on talc friction experiments. Journal of Geophysical Research, 117(B08408). doi:10.1029/2011JB009006.

Bowden F & Tabor D, 1986. The Friction and Lubrication of Solids. Clarendon Press.

Brace W & Byerlee J, 1966. Stick-slip as a mechanism for earthquakes. Science, 153:990.

Brace W & Kohlstedt D, 1980. Limits on lithospheric stress imposed by laboratory measurements. Journal of Geophysical Research, 85:6248–6252.

Brace WF, 1972. Laboratory studies of stick-slip and their application to earthquakes. In Savarensky E & Rikitake T, editors, Forerunners of Strong Earthquakes, volume 14, pages 189–200.

Bradbury K, Evans J, Chester J, Chester F, & Kirschner D, 2011. Lithology and internal structure of the San Andreas fault at depth based on characterization of Phase 3 whole-rock core in the San Andreas Fault Observatory at Depth (SAFOD) borehole. Earth and Planetary Science Letters, 100:131–144.

Brantut N & Rice J, 2011. How pore fluid pressurization influences crack tip processes during dynamic rupture. Geophysical Research Letters, 38(L24314). doi:10.1029/2011GL050044.

Brantut N, Schubnel A, Rouzaud J, Brunet F, & Shimamoto T, 2008. High-velocity frictional properties of a clay-bearing fault gouge and implications for earthquake mechanics. Journal of Geophysical Research, 113(B10401). doi:10.1029/2007JB005551.

Brantut N, Schubnel A, Corvisier J, & Sorout J, 2010. Thermochemical pressurization of faults during coseismic slip. Journal of Geophysical Research, 115:B05314. doi:10.1029/2009JB006533.

Brantut N, Han R, Shimamoto T, Findling N, & Schubnel A, 2011a. Fast slip inhibited temperature rise due to mineral dehydration: Evidence from experiments on gypsum. Geology, 39:59–62. doi:10.1130/G31424.1.

Brantut N, Schubnel A, & Gueguen Y, 2011b. Damage and rupture dynamics at the brittle-ductile transition: The case of gypsum. Journal of Geophysical Research, 116(B01404). doi:10.1029/2010JB007675.

Brantut N, Sulem J, & Schubnel A, 2011c. Effect of dehydration reactions on earthquake nucleation: Stable sliding, slow transients, and unstable slip. Journal of Geophysical Research, 116(B05304). doi:10.1029/2010JB007876.

Brodske E & Kanamori H, 2001. Elastohydrodynamic lubrication of faults. Journal of Geophysical Research, 106(B8):16357–16374. doi:10.1029/2001JB000430.

Brodsky E, Rowe C, Meneghini F, & Moore J, 2009. A geological fingerprint of low-viscosity fault fluids mobilized during an earthquake. Journal of Geophysical Research, 114(B01303). doi:10.1029/2008JB005633.

Brown S & Scholz C, 1985. Closure of random elastic surfaces in contact. Journal of Geophysical Research, 90:5531–5545.

Brown S & Scholz C, 1986. Closure of rock joints. Journal of Geophysical Research, 91:4939–4948.

Bull W, 1996. Prehistorical earthquakes on the Alpine fault, New Zealand. Journal of Geophysical Research, 10(B3):6037–6050.

Byerlee J, 1978. Friction of rocks. Pure and Applied Geophysics, 116:615–626.

Byerlee J, 1993. Model for episodic flow of high pressure water in fault zones before earthquake. Geology, 21:303–306.

Caine J, Evans J, & Forster C, 1996. Fault zone architecture and permeability structure. Geology, 24(11):1025–1028.

Campbell H, 2005. Partitioning of Plate Boundary Deformation in South Westland, New Zealand: controls from reactivated structures. Ph.D. thesis, Dep. of Geology, University of Otago, Dunedin, New Zealand.

Candela T, Rendard F, Klinger Y, Mair K, Schmittbuhl J, & Brodsky E, 2012. Roughness of fault surfaces over nine decades of length scales. Journal of Geophysical Research, 117(B08409). doi:10.1029/2011JB009041.

Carpenter B, Marone C, & Saffer D, 2011. Weakness of the San Andreas Fault revealed by samples from the active fault zone. Nature Geoscience, 4(4):251–254. doi:10.1038/NGEO1089.

Carpenter B, Saffer D, & Marone C, 2012. Frictional properties and sliding stability of the San Andreas fault from deep drill core. Geology, 40(8):759–762. doi:10.1130/G33007.

Carpenter B, Kitajima H, & Saffer D, accepted. Permeability and elastic properties of the active Alpine Fault, New Zealand: Laboratory measurements on shallow drill core. Earth and Planetary Science Letters.

Carpinteri A & Paggi M, 2005. Size-scale effects on the friction coefficient. International Journal of Solids and Structures, 42:2901–2910.

Carter R & Norris R, 1976. Cainozoic history of southern New Zealand: An accord between geological observations and plate tectonic predictions. Earth and Planetary Science Letters, 31:85–94.

Chamberlain C, Poage M, Craw D, & Reynolds R, 1999. Topographic development of the Southern Alps recorded by the isotopic composition of authigenic clay minerals, South Island, New Zealand. Chemical Geology, 155:279–294.

Chang J, Lockner D, & Reches Z, 2012. Rapid acceleration leads to rapid weakening in earthquake-like laboratory experiments. Science, 338(6103):101–105.

Chen J, Yang X, Duan Q, Shimamoto T, & Spiers C, 2013. Importance of thermochemical pressurization in the dynamic weakening of the Longmenshan Fault during the 2008 Wenchuan earthquake: Inferences from experiments and modeling. Journal of Geophysical Research Solid Earth, 118:1–25. doi:10.1002/jgrb.50260.

Chester F & Chester J, 1998. Ultracataclasite structure and friction processes of the Punchbowl fault, San Andreas system, California. Tectonophysics, 295:199–221.

Chester F & Higgs N, 1992. Multimechanism friction constitutive model for ultrafine quartz gouge at hypocentral conditions. Journal of Geophysical Research, 97(B2):1859–1870.

Chester F & Logan J, 1986. Implications for mechanical properties of brittle faults from observations of the Punchbowl fault zone, California. Pure and Applied Geophysics, 124:79–106.

Chester F, Evans J, & Biegal R, 1993. Internal structure and weakening mechanisms of the San Andreas fault. Journal of Geophysical Research, 98:771–786.

Clark R & Wellman H, 1959. The Alpine Fault from lake McKerrow to Milford Sound. New Zealand Journal of Geology and Geophysics, 23:590–601.

Cocco M & Tinti E, 2008. Scale dependence in the dynamics of earthquake propagation: Evidence from seismological and geological observations. Earth and Planetary Science Letters, 273:123–131. doi:10.1016/j.epsl.2008.06.025.

Collettini C & Holdsworth R, 2004. Fault zone weakening and character of slip along low-angle normal faults: insights from the Zuccale fault, Elba, Italy. Journal of the Geological Society London, 161:1039–1051.

Collettini C, Niemeijer A, Viti C, & Marone C, 2009. Fault zone fabric and fault weakness. Nature, 462:907–910. doi:10.1038/nature08585.

Cooper A & Kostro F, 2006. A tectonically uplifted marine shoreline deposit, Knights Point, Westland, New Zealand. New Zealand Journal of Geology and Geophysics, 49:203–216.

Cooper A & Norris R, 1990. Estimates for the timing of the last coseismic displacement on the Alpine Fault, northern Fiordland, New Zealand. New Zealand Journal of Geology and Geophysics, 336:303–307. doi:10.1080/00288306.1990.10425688.

Cooper A & Norris R, 1994. Anatomy, structural evolution and slip rate of a plate-boundary thrust: The Alpine fault at Gaunt Creek, Westland, New Zealand. Geological Society of America Bulletin, 106:627–633.

Cooper A & Norris R, 2011. Inverted metamorphic sequences in Alpine fault mylonites produced by oblique shear within a plate boundary fault zone, New Zealand. Geology, 39(11):1023–1026. doi:10.1130/G32273.

Cooper A, Barreiro B, Kimbrough D, & Mattinson J, 1987. Lamprophyre dike intrusion and the age of the Alpine fault, New Zealand. Geology, 15(10):941–944. doi:10.1130/0091-7613(1987)15<941:LDIATA>2.0.CO;2.

Coulomb A, 1776. Memoires de Mathematiques et de Physique. Paris, L'Imprimerie Royal.

Cowan D, 1999. Do faults preserve a record of seismic slip? A field geologist's opinion. Journal of Structural Geology, 21:995–1001.

Cox S, 1993. Veins, Fluid, Fractals, Scale and Schist: an investigation of fluid rock interaction during deformation of the Torlesse Terrane, New Zealand. Ph.D. thesis, University of Otago, Dunedin, New Zealand.

Cox S, 2010. The application of failure mode diagrams for exploring the roles of fluid pressure and stress states in controlling styles of fracture-controlled permeability enhancement in faults and shear zones. Geofluids, 10:217–233. doi:10.1111/j/1468-8123.2010.00281.x.

Cox S & Etheridge M, 1989. Coupled grain-scale dilatancy and mass transfer during deformation at high fluid pressures: Examples from Mount Lyell, Tasmania. Journal of Structural Geology, 11:147–162. doi:10.1016/091-8141(89)90040-0.

Cox S & Paterson M, 1991. Experimental dissolution-precipitation creep in quartz aggregates at high temperatures. Geophysical Research Letters, 18:1401–1404.

Cox S, Stirling M, Herman F, Gerstenberger M, & Ristau J, 2012. Potentially active faults in the rapidly eroding landscape adjacent to the Alpine Fault, central Southern Alps, New Zealand. Tectonics, 31(2):TC2011. doi:10.1029/2011TC003038.

Craw D, 1984. Ferrous-iron-bearing vermiculite-smectite series formed during alteration of chlorite to kaolinite, Otago Schist, New Zealand. Clay Minerals, 19:509–520.

Craw D, 1988. Shallow level penetration of metamorphic fluids in a high uplift rate mountain belt, Southern Alps, New Zealand. Journal of Metamorphic Geology, 6:1–16.

Craw D, 1997. Fluid inclusion evidence for geothermal structure beneath the Southern Alps, New Zealand. New Zealand Journal of Geology and Geophysics, 40(1):43–52.

Craw D & Campbell J, 2004. Tectonic and structural setting for active mesothermal gold vein systems, Southern Alps, New Zealand. Journal of Structural Geology, 26:995–1005.

Cruz-Atienza V, Olsen K, & Dalguer L, 2009. Estimation of the breakdown slip from strong-motion seismograms: insights from numerical experiments. Bulletin of the Seismological Society of America, 99(6):3454–3469. doi:10.1785/0120080330.

Davies T, McSaveney M, & Boulton C, 2012. Elastic strain energy release from fragmenting grains: Effects on fault rupture. Journal of Structural Geology, 38:265–277.

De Paola N, Hirose T, Mitchell M, Di Toro G, Viti C, & Shimamoto T, 2011. Fault lubrication and earthquake propagation in thermally unstable rocks. Geology, 39:35–38. doi:10.1130/G31398.1.

De Pascale G & Langridge R, 2012. New off-fault evidence for a great earthquake in A.D. 1717, central Alpine fault, New Zealand. Geology, 40(9):791–794. doi:10.1130/G33363.1.

Deer W, Howie R, & Zussman J, 1992. An Introduction to Rock-Forming Minerals, 2nd edition. Longman Group UK Limited.

DeMets C, Gordon G, Argus D, & Stein S, 1994. Effect of revision to the geomagnetic reversal time scale on estimates of current plate motions. Geophysical Research Letters, 21:2191–2194.

den Hartog S, Niemeijer A, & Spiers C, 2012. New constraints on megathrust slip stability under subduction zone P-T conditions. Earth and Planetary Science Letters, pages 353–354, 240–252.

den Hartog SAM & Spiers CJ, 2012. Influence of subduction zone conditions and gouge composition on frictional slip stability of megathrust faults. Tectonophysics, 600:75–90. ISSN 0040-1951. doi:10.1016/j.tecto.2012.11.006.

Di Toro G, Goldsby D, & Tullis T, 2004. Friction falls towards zero in quartz rock as slip velocity approaches seismic rates. Nature, 427:436–439. doi:10.1038/Nature02249.

Di Toro G, Han R, Hirose T, De Paola N, Nielsen S, Mizoguchi K, Ferri F, Cocco M, & Shimamoto T, 2011. Fault lubrication during earthquakes. Nature, 471:494–498. doi:10.1038/nature09838.

Dieterich J, 1972. Time-dependent friction in rocks. Journal of Geophysical Research, 77:3690–3697.

Dieterich J, 1978. Time-dependent friction and the mechanics of stick-slip. Pure and Applied Geophysics, 116:790–805.

Dieterich J, 1979. Modeling of rock friction 1. Experimental results and constitutive equations. Journal of Geophysical Research, 84(B5):2162–2168. doi:10.1029/JB084iB05p02151.

Dieterich J & Conrad G, 1984. Effect of humidity on time and velocity-dependent friction in rocks. Journal of Geophysical Research, 89:4196–4202.

Dieterich J & Kilgore B, 1994. Direct observations of friction contacts-new insights for state-dependent properties. Pure and Applied Geophysics, 143:283–302.

Dieterich J & Smith D, 2009. Nonplanar Faults: Mechanics of Slip and Off-fault Damage. Pure and Applied Geophysics, 166:1799–1815.

Dor O, Rockwell T, & Ben-Zion Y, 2006. Geological observations of damage asymmetry in the structure of the San Jacinto, San Andreas, and Punchbowl Faults in Southern California: A possible indicator for preferred rupture propagation direction. Pure and Applied Geophysics, 163:301–349.

Dor O, Yildirum C, Rockwell T, Ben-Zion Y, Emre O, Sisk M, & Duman T, 2008. Geological and geomorphologic asymmetry across the rupture zones of the 1943 and 1944 earthquakes on the North Anatolian Fault: possible signals for preferred earthquake propagation direction. Geophysical Journal International, 173(2):484–504.

Dor O, Chester J, Ben-Zion Y, Brune J, & Rockwell T, 2009. Characterization of Damage in Sandstones along the Mojave Section of the San Andreas Fault: Implications for the Shallow Extent of Damage Generation. Pure and Applied Geophysics, 166(10-11):1747–1773. ISSN 0033-4553. doi: 10.1007/s00024-009-0516-z.

Dorn C, Green A, Jongens R, Carpentier S, Kaiser A, Campbell F, Horstmeyer H, Campbell J, Finnemore M, & Pettinga J, 2010. High-resolution seismic images of potentially seismogenic structures beneath the northwest Canterbury Plains, New Zealand. Journal of Geophysical Research, 115(B11303). doi:10.1029/2010JB007459.

Duebendorfer E & Simpson D, 1994. Kinematics and timing of Tertiary extension in the western Lake Mead region, Nevada. Geological Society of America Bulletin, 106:1057–1073.

Easterbrook L, 2010. The Alpine Fault Zone Along the Waitangi-toana River, West Coast, New Zealand. Master's thesis, University of Otago.

Elliott J, Nissen E, England P, Jackson J, Lamb S, Li Z, Oehlers M, & Parsons B, 2012. Slip in the 2010-2011 Canterbury earthquakes, New Zealand. Journal of Geophysical Research, 117(B03401). doi:10.1029/2011JB008868.

Ellis D & Singer J, 2007. Well Logging for Earth Scientists. SpringerLink (Online service).

Ellis S, Beavan J, Eberhart-Phillips D, & Stockhert B, 2006. Simplified models of the Alpine Fault seismic cycle: stress transfer in the mid-crust. Geophysical Journal International, 166:386–402.

Ellsworth W, 2013. Injection-induced earthquakes. Science, 341. doi:10.1126/science.1225942.

Evans J & Chester F, 1995. Fluid-rock interaction in faults of the San Andreas system: Inferences from San Gabriel fault rock geochemistry and microstructures. Journal of Geophysical Research, 100:13007–13020.

Evison F, 1971. Seismicity of the Alpine Fault, New Zealand. Recent Crustal Movements, Royal Society of New Zealand Bulletin, 9:161–165.

Fagereng Å, 2011. Frequency-size distribution of competent lenses in a block-in-matrix mélange: Imposed length scales of brittle deformation? Journal of Geophysical Research, 116(B05302). doi:10.1029/2010JB007775.

Fagereng Å & Sibson RH, 2010. Melange rheology and seismic style,. Geology, 38(*):751–754. doi:10.1130/G30868.1.

Farmer L, 2010. A Study of Clay Mineralogy Along an Active Fault Zone: The Structure, Composition and Origin fault gouge from Gaunt Creek, New Zealand. Master's thesis, University of Southampton.

Faulkner D & Rutter E, 2000. Comparisons of water and argon permeability in natural clay-bearing fault gouge under high pressure at 20 degrees C. Journal of Geophysical Research, 105:16415–16426. doi: 10.1029/2000JB900134.

Faulkner D & Rutter E, 2001. Can the maintenance of overpressured fluids in large strike-slip fault zones explain their apparent weakness? Geology, 29:503–506.

Faulkner D, Lewis A, & Rutter E, 2003. On the internal structure and mechanics of large strike-slip fault zones: field observations of the Carboneras fault in southeastern Spain. Tectonophysics, 367(3-4):235–251.

Faulkner D, Mitchell TM, & Healy D, 2006. Slip on 'weak' faults by the rotation of regional stress in the fracture damage zone. Nature, 444(7121):922–925. doi:10.1038/nature05353.

Faulkner D, Jackson C, Lunn R, Schlische R, Shipton Z, Wibberley C, & Withjack M, 2010. A review of recent developments concerning the structure, mechanics and fluid flow properties of fault zones. Journal of Structural Geology, 32(11):1557–1575. doi:10.1016/j.jsg.2010.06.009.

Faulkner D, Mitchell T, Behnsen J, Hirose T, & Shimamoto T, 2011. Stuck in the mud? Earthquake nucleation and propagation through accretionary forearcs. Geophysical Research Letters, 38. doi:10.1039/2011GL048552.

Fedo C, Nesbitt H, & Young G, 1995. Unraveling the effects of potassium metasomatism in sedimentary rocks and paleosols, with implications for paleoweathering conditions and provenance. Geology, 23:921–924.

Ferri F, Di Toro G, Hirose T, Han R, & Noda H, 2011. Low- to high-velocity frictional properties of the clay-rich gouges from the slipping zone of the 1963 Vaiont slide, nothern Italy. Journal of Geophysical Research, 116(B09208). doi:10.1029/2011JB008338.

Finzi Y, Hearn E, Lyakhovsky V, & Gross L, 2011. Fault-zone healing effectiveness and the structural evolution of strike-slip fault systems. Geophysical Journal International, 186:963–970.

Forster M & Lister G, 2009. Core-complex-related extension of the Aegean lithosphere initiated at the Eocene-Oligocene transition. Journal of Geophysical Research, 114(B2).

Forsyth P, Barrell D, & Jongens R, 2008. Geology of the Christchurch area, scale 1:250000. Institute of Geological & Nuclear Sciences Limited, 1:250000 Geological Map 16, 1 sheet + 67 p. ISBN 978-0-478-19649-8.

Frye K & Marone C, 2002. Effect of humidity on granular friction at room temperature. Journal of Geophysical Research, 107(B11):2309. doi:10.1029/2001JB000654.

Fulton P & Rathbun A, 2011. Experimental constraints on energy partitioning during stick-slip and stable sliding within analog fault gouge. Earth and Planetary Science Letters, 308:185–192. doi:10.1016/j.epsl.2011.05.051.

Fulton P, Saffer D, & Bekins B, 2009. A critical evaluation of crustal dehydration as the cause of an overpressured and weak San Andreas Fault. Earth and Planetary Science Letters, 284:447–454.

Furlong K & Kamp P, 2009. The lithospheric geodynamics of plate boundary transpression in New Zealand: Initiating and emplacing subduction along the Hikurangi margin, and the tectonic evolution of the Alpine Fault system. Tectonophysics, 474:449–462.

Gabriel AA, Ampuero J, Dalguer L, & Mai P, 2012. The transition of dynamic rupture styles in elastic media under velocity-weakening friction. Journal of Geophysical Research, 117(B09311). doi:10.1029/2012JB009468.

Gaina C, Müller D, Royer J, Stock J, Hardebeck J, & Symonds P, 1998. The tectonic history of the Tasman Sea: A puzzle with 13 pieces. Journal of Geophysical Research, 103(B6):12413–12433.

Garagash D, 2012. Seismic and aseismic slip pulses driven by thermal pressurization of pore fluid. Journal of Geophysical Research: Solid Earth (1978–2012), 117(B4). doi:10.1029/2011JB008889.

Garagash D & Rudnicki J, 2003. Shear heating of a fluid-saturated slip-weakening dilatant fault zone 1. Limiting regimes. Journal of Geophysical Research, 108. doi:10.1029/2001JB001653.

Goldsby D & Tullis T, 2002. Low frictional strength of quartz rocks at subseismic slip rates. Geophysical Research Letters, 29(17):1844. doi:10.1029/2002GL015240.

Goodwin L & Tikoff B, 2002. Competency contrast, kinematics, and the development of foliations and lineations in the crust. Journal of Structural Geology, 24:1065–1085.

Goodwin L & Wenk H, 1995. Development of phyllonite from granodiorite: mechanisms of grain-size reduction in the Santa Rosa mylonite zone, California. Journal of Structural Geology, 17:689–707.

Govers R & Wortel M, 2005. Lithosphere tearing at STEP faults: response to edges of subduction zones. Earth and Planetary Science Letters, 236(1-2):505–523.

Grady D & Kipp M, 1987. Dynamic rock fragmentation. In Atkinson B, editor, Fracture Mechanics of Rock., pages 429–475. Academic Press Ltd.

Grapes R & Wellman H, 1986. The north-east end of the Wairau Fault, Marlborough, New Zealand. Journal of the Royal Society of New Zealand, 160:245–250.

Gratier J & Gueydan F, 2007. Fluid processes in deep crustal fault zones. pages 295–318.

Gratier J, Favreau P, & Renard F, 2003. Modeling fluid transfer along California faults when integrating pressure solution crack sealing and compaction processes. Journal of Geophysical Research, 108(B2):2104. doi: 10.1029/2001JB000380.

Gratier J, Guiguet R, Renard F, Jenatton L, & Bernard D, 2009. A pressure solution creep law for quartz from indentation experiments. Journal of Geophysical Research, 114(B3):B03403. doi:10.1029/2008JB005652.

Gratier J, Richard J, Renard F, Mittempergher S, Doan M, Di Toro G, Hadizadeh J, & Boullier M, 2011. Aseismic sliding of active faults by pressure solution creep: Evidence from the San Andreas Fault Observatory at Depth. Geology, 39(12):1131–1134. doi:10.1130/G32073.1.

Griggs D, 1954. High pressure phenomena with application to geophysics. In Ridenour L & Nierenberg W, editors, Modern Physics for the Engineer, pages 272–305. McGraw-Hill.

Gu J, Rice J, Ruina A, & Tse S, 1984. Slip motion and stability of a single degree of freedom elastic system with rate and state dependent friction. ournal of the Mechanics and Physics of Solids, 32(3):167–196.

Guo Y & Morgan J, 2006. The frictional and micromechanical effects of grain comminution in fault gouge from distinct element simulations. Journal of Geophysical Research, 111(B12406). doi:10.1029/2005JB004049.

Guo Y & Morgan J, 2008. Fault gouge evolution and its dependence on normal stress and rock strength- Results of discrete element simulations: Gouge zone micromechanics. Journal of Geophysical Research, 113(B08417). doi:10.1029/2006JB004525.

Gutenberg B & Richter C, 1949. Seismicity of the Earth and Associated Phenomena. Princeton University Press.

Hacker B, 1997. Diagenesis and fault valve seismicity of crustal faults. Journal of Geophysical Research, 102(B11):24459–24467.

Hadizadeh J, Mittempergher S, Gratier J, Renard F, Di Toro G, Richard J, & Babaie H, 2012. A microstructural study of fault rocks from the SAFOD: Implications for the deformation mechanisms and strength of the creeping segment of the San Andreas Fault. Journal of Structural Geology, 42:246–260. doi:10.1016/j.jsg.2012.04.011.

Hamiel Y, Lyakhovsky V, & Agnon A, 2005. Rock dilation, nonlinear deformation, and pore pressure change under shear. Earth and Planetary Science Letters, 237:577–589.

Han R & Hirose E, 2012. Clay-clast aggregates in fault gouge: an unequivocal indicator of seismic faulting at shallow depths? Journal of Structural Geology, 43:92–99. doi:10.1016/j.jsg.2012.07.008.

Han R, Shimamoto T, Ree JH, & Ando J, 2007. Ultralow friction of carbonate faults caused by thermal decomposition. Science, 316:878–881. doi:10.1126/Science.1139763.

Han R, Hirose T, & Shimamoto T, 2010. Strong velocity weakening and powder lubrication of simulated carbonate faults at seismic slip rates. Journal of Geophysical Research, 115(B03412). doi:10.1029/2008JB006136.

Handy M & Brun J, 2004. Seismicity, structure and strength of the continental lithosphere. Earth and Planetary Science Letters, 223:427–441. doi:10.1016/j.epsl.2004.04.021.

Handy M, Hirth G, & Burgmann R, 2006. Continental Fault Structure and Rheology from the Frictional-to-Viscous Transition Downward. In Handy MR, editor, Tetonic Faults: Agents of Change on a Dynamic Earth, pages 132–182. The MIT Press.

Hanks T, 1977. Earthquake stress drops, ambient tectonic stresses, and stresses that drive plate motions. Pure and Applied Geophysics, 115:441–458.

Hanks T, Beroza G, & Toda S, 2012. Have recent earthquakes exposed flaws in or misunderstandings of probabilistic seismic hazard analysis? Seismological Research Letters, 83(5):759–764. doi:10.1785/0220120043.

Hanna W, Brown R, Ross D, & Griscom A, 1972. Aeromagnetic reconnaissance and generalized geologic map of the San Andreas fault between San Francisco and San Bernadino, California. United States Geological Survey Geophysical Investigations Map GP-815.

He C, Okubo S, & Nishimatsu Y, 1990. A study on the Class II behavior of rock. Rock Mechanics and Rock Engineering, 23:261–273.

Healy D, 2008. Damage patterns, stress rotations and pore fluid pressures in strike-slip fault zones. Journal of Geophysical Research, 113(B12407). doi:10.1029/2008JB005655.

Hickman S & Evans B, 1995. Kinetics of pressure solution at halite-silica interfaces and intergranular films. Journal of Geophysical Research, 100(B7):13113–13132.

Hillers G & Miller S, 2007. Dilatancy controlled spatiotemporal slip evolution of a sealed fault with spatial variations of the pore pressure. Geophysical Journal International, 168:431–445. doi:10.1111/j.1365-246X.2006.03167.

Hillers G, Ben-Zion Y, & Mai P, 2006. Seismicity on a fault controlled by rate and state-dependent friction with spatial variations of the critical slip distance. Journal of Geophysical Research, 111(B01403). doi:10.1029/2005JB003859.

Hillers G, Mai P, Ben-Zion Y, & Ampuero J, 2007. Statistical properties of seismicity of fault zones at different evolutionary stages. Geophysical Journal International, 169:515–533.

Hirono T & Hamada Y, 2010. Specific heat capacity and thermal diffusivity and their temperature dependencies in a rock sample from adjacent to the Taiwan Chelungpu fault. Journal of Geophysical Research, 115(B05313). doi:10.1029/2009JB006816.

Hirose T & Bystricky M, 2007. Extreme dynamic weakening of faults during dehydration by coseismic shear heating. Geophysical Research Letters, 34(L14311). doi:10.1029/2007GL030049.

Hirose T & Shimamoto T, 2005a. Growth of molten zone as a mechanism of slip weakening of simulated faults in gabbro during frictional melting. Journal of Geophysical Research, 110(B05202). doi:10.1029/2004JB003207.

Hirose T & Shimamoto T, 2005b. Slip-weakening distance of faults during frictional melting as inferred from experimental and natural pseudotachylytes. Bulletin of the Seismological Society of America, 95(5):1666–1673.

Holdsworth R, 2004. Weak faults-Rotten cores. Science, 303:181–182.

Holdsworth R, van Diggelen E, Spiers C, de Bresser J, Walker W, & Bowen L, 2011. Fault rocks from the SAFOD core samples: implications for weakening at shallow depths along the San Andreas Fault, California. Journal of Structural Geology, 336:132–144.

Holzer T & Savage J, 2013. Global earthquake fatalities and population. Earthquake Spectra, 29(1):155–175.

Horton T, Blum J, Craw D, Koons P, & Chamberlain C, 2003. Oxygen, carbon, and strontium isotopic constraints on timing and sources of crustal fluids in an active orogen: South Island, New Zealand. New Zealand Journal of Geology and Geophysics, 46:457–471.

Hou L, Shimamoto T, Chen J, Yao L, & Okimura Y, 2012. Internal structures and high-velocity frictional properties of a bedding-parallel carbonate fault at Xiajiaqiao outcrop activated by the 2008 Wenchuan earthquake. Earthquake Science, 25:197–217. doi:10.1007/s11589-012-0846-2.

Howarth J, Fitzsimmons S, Norris R, & Jacobsen G, 2012. Lake sediments record cycles of sediment flux driven by large earthquakes on the Alpine Fault, New Zealand. Geology, 40(12):1091–1094. doi:10.1346/CCMN.1993.0410205.

Huang W, Longo J, & Pevear D, 1993. An experimentally derived model for smectite to illite conversion and its use as a geothermometer. Clays and Clay Minerals, 41(2):162–177. doi:10.1346/CCMN.1993.0410205.

Hubbert M & Rubey W, 1959. Role of fluid pressure in the mechanics of overthrust faulting. Geological Society of American Bulletin, 70:115–205.

Hull A & Berryman K, 1986. Holocene tectonism in the region of the Alpine Fault at Lake McKerrow, Fiordland, New Zealand. Royal Society of New Zealand Bulletin, 24:317–331.

Ida Y, 1972. Cohesive force across the tip of a longitudinal-shear crack and Griffith's specific surface energy. Journal of Geophysical Research, 77(20):3796–3805. doi:10.1029/JB077i020p03796.

Ide S, Beroza G, Shelly D, & Uchide T, 2007. A scaling law for slow earthquakes. Nature, 447:76–79. doi:10.1038/nature05780.

Ikari M & Kopf A, 2011. Cohesive strength of clay-rich sediment. Geophysical Research Letters, 38(16). doi:10.1029/2011GL047918.

Ikari M, Saffer D, & Marone C, 2009. Frictional and hydrologic properties of clay-rich fault gouge. Journal of Geophysical Research, 114(B05409). doi:10.1029/2008JB006089.

Ikari M, Marone C, & Saffer D, 2011a. On the relation between fault strength and frictional stability. Geology, 39(1):83–86.

Ikari M, Niemeijer A, & Marone C, 2011b. The Role of Fault Zone Fabric and Lithification State on Frictional Strength, Constitutive Behavior and Deformation Microstructure. Journal of Geophysical Research. doi:10.1029/2011JB008264.

Ikari M, Marone C, Saffer D, & Kopf A, 2013. Slip weakening as a mechanism for slow earthquakes. Nature Geoscience, 6:468–472. doi:10.1038/NGEO1818.

Ikari MJ, Saffer DM, & Marone C, 2007. Effect of hydration state on the frictional properties of montmorillonite-based fault gouge. Journal of Geophysical Research, 112:B06423. doi:10.1029/2006JB004748.

Imber J, Holdsworth R, Smith S, Jefferies S, & Collettini C, 2008. Frictional-viscous flow, seismicity and the geology of weak faults: a review and future directions. In The Internal Structure of Fault Zones: Implications for Mechanical and Fluid-Flow Properties, volume 299, pages 151–173.

Inoue A & Utada M, 1991. Smectite-to-chlorite transformation in thermally metamorphosed volcanoclastic rocks in the Kamikita area, northern Honshu, Japan. American Mineralogist, 76:628–640.

Janecke S & Evans J, 1988. Feldspar-influenced rock rheologies. Geology, 16:1064–1067.

Jefferies S, Holdsworth R, Shimamoto T, Takagi H, Lloyd G, & Spiers C, 2006. Origin and mechanical significance of foliated cataclastic rocks in the cores of crustal-scale faults: Examples from the Median Tectonic Line, Japan. Journal of Geophysical Research: Solid Earth (1978–2012), 111(B12). doi:10.1029/2005JB004205.

Jenkin G, Craw D, & Fallick A, 1994. Stable isotopic and fluid inclusion evidence for meteoric fluid penetration into an active mountain belt, Alpine Schist, New Zealand. Journal of Metamorphic Geology, 12:429–444.

Johnson P & Jia X, 2005. Nonlinear dynamics, granular media and dynamic earthquake triggering. Nature, 437:871–874. doi:10.1038/nature04015.

Johnson P, Savage H, Knuth M, Gomberg J, & Marone C, 2008. Effects of acoustic waves on stick-slip in granular media and implications for earthquakes. Nature, 451:57–60. doi:10.1038/nature06440.

Johnstone R, Craw D, & Rattenbury M, 1990. Southern Alps Cu-Au hydrothermal system, Westland, New Zealand. Mineralium Deposita, 25:118–125.

Jourdan F & Renne P, 2007. Age calibration of the Fish Canyon sanidine 40Ar/39Ar dating standard using primary K-Ar standards. Geochimica et Cosmochimica Acta, 71:387–402.

Kaiser A, Holden C, Beavan JP, Beetham D, Benites R, Celentano A, Collett D, Cousins J, Cubrinovski M, Dellow G, Denys P, Fielding E, Fry B, Gerstenberger M, Langridge RM, Massey C, Motagh M, Pondard N, McVerry G, Ristau J, Stirling MW, Thomas J, Uma S, & Zhao J, 2012. The Mw 6.2 Christchurch earthquake of February 2011: preliminary report. New Zealand Journal of Geology and Geophysics, 55:67–90.

Kamp P, 1996. The mid-Cenozoic Challenger Rift System of western New Zealand and its implications for the age of Alpine fault inception. Geological Society of America Bulletin, 97:255–281. doi:10.1130/0016-7606(1986)97<255:TMCRSO>2.0.CO;2.

Kanagawa K, Cox S, & Zhang S, 2000. Effects of dissolution-precipitation processes on the strength and mechanical behavior of quartz gouge at high-temperature hydrothermal conditions. Journal of Geophysical Research, 105(B5):11115–11126. doi:10.1029/2000JB900038.

Kanamori H & Rivera L, 2006. Energy partitioning during an earthquake. In Abercrombie R, McGarr A, Kanamori H, & Di Toro G, editors, Earthquakes: Radiated Energy and the Physics of Faulting, volume 170, pages 3–13. AGU. ISBN 978-0-87590-435-1. doi:10.1029/GM170.

Kato N, 2012. Dependence of earthquake stress drop on critical slip-weakening distance. Journal of Geophysical Research, 117(B01301). doi:10.1029/2011JB008359.

Keranen K, Savage H, Abers G, & Cochran E, 2013. Potentially induced earthquakes in Oklahoma, USA: Links between wastewater injection and the 2011 Mw 5.7 earthquake sequence. Geology. doi:10.1130/G34045.1.

King G, 1983. The accommodation of large strains in the upper lithosphere of the earth and other solids by self-similar fault systems: The geometrical origin of b-value. Pure and Applied Geophysics, 121:761–814.

King G, 1986. Speculations on the Geometry of the Initiation and Termination Processes of Earthquake Rupture and its Relation to Morphology and Geological Structure. Pure and Applied Geophysics, 124:567–585.

King G, 2007. Fault interaction, earthquake stress changes, and the evolution of seismicity. Treatise on Geophysics, 4:225–255.

Kitajima H, Chester J, Chester F, & Shimamoto T, 2010. High-spreed friction of disaggregated ultracataclasite in rotary shear: Characterization of frictional heating, mechanical behavior, and microstructure evolution. Journal of Geophysical Research, 115(B08408). doi:10.1029/2009JB007038.

Koons P, 1987. Some thermal and mechanical consequences of rapid uplift: an example from the Southern Alps, New Zealand. Earth and Planetary Science Letters, 86:307–319.

Koons P & Craw D, 1991. Evolution of fluid driving forces and composition within collisional orogens. Geophysical Research Letters, 18:935–938.

Koons P, Craw D, Cox S, Upton P, & Chamberlain C, 1998. Fluid flow during active oblique convergence: A Southern Alps model from mechanical and geochemical observations. Geology, 26:159–162.

Koons P, Norris R, Craw D, & Cooper A, 2003. Influence of exhumation on the structural evolution of transpressional plate boundaries: An example from the Southern Alps, New Zealand. Geology, 31:3–6.

Kozdon J & Dunham E, 2013. Rupture to the trench: dynamic rupture simulations of the 11 March 2011 Tohoku Earthquake. Bulletin of the Seismological Society of America, 103(2B):1275–1289. doi:10.1785/0120120136.

Lachenbruch A, 1980. Frictional heating, fluid pressure, and the resistance to fault motion. Journal of Geophysical Research, 85:6097–6112. doi:10.1029/JB085iB11p06097.

Lamb S & Smith E, 2013. The nature of the plate interface and driving force of interseismic deformation in the New Zealand plate-boundary zone, revealed by the continuous GPS velocity field. Journal of Geophysical Research, 118. doi:10.1002/jgrb.50221.

Landis C & Coombs D, 1966. Metamorphic belts and orogenesis in southern New Zealand. Tectonophysics, 4:501–518.

Langride R & Berryman KR, 2005. Morphology and slip rate of the Hurunui section of the Hope Fault, South Island, New Zealand. New Zealand Journal of Geology and Geophysics, 48(1):43–57.

Lapusta N, 2009. The roller coaster of fault friction. Nature Geoscience, 2:676–677.

Lapusta N & Rice JR, 2003. Nucleation and early seismic propagation of small and large events in a crustal earthquake model. Journal of Geophysical Research, 108(B1). doi:10.1029/2001JB001681.

Lapusta N, Rice JR, Ben-Zion Y, & Zheng G, 2000. Elastodynamic analysis for slow tectonic loading with spontaneous rupture episodes on faults with rate- and state- dependent friction. Journal of Geophysical Research, 105(B10). doi:10.1029/2000JB900250.

Leclère H & Fabbri O, 2013. A new three-dimensional method of fault reactivation analysis. Journal of Structural Geology, 48:153–161.

Leitner B, Eberhart-Phillips D, Anderson H, & Nabelek JL, 2001. A focused look at the Alpine Fault, New Zealand; seismicity, focal mechanisms and stress observations. Journal of Geophysical Research, 106(2):2193–2220. doi:10.1029/2000JB900303.

Lensen GJ, 1976. Late Quaternary tectonic map of New Zealand 1:50 000, 2 maps and text (2Opp).

Li Y, Leary P, Aki K, & Malin P, 1990. Seismic trapped modes in the Oroville and San Andreas fault zones. Science, 249:763–766.

Li Y, Vidale J, Aki K, & Xu F, 2000. Depth-dependent structure of the Landers fault zone using fault zone trapped waves generated by aftershocks. Journal of Geophysical Research, 105:6237–6254.

Li Y, Vidale J, & Cochran E, 2004. Low-velocity damaged structure of the San Andreas Fault at Parkfield from fault zone trapped waves. Geophysical Research Letters, 31(L12S06). doi:10.1029/2003GL019044.

Lide D, 2008. CRC Handbook of Chemistry and Physics, 89th Edition. CRC Press, 89th edition. ISBN 142006679X.

Lin A, 2011. Seismic slip recorded by fluidized ultracataclastic veins form in a coseismic shear zone during the 2008 Mw 7.9 Wenchuan earthquake. Geology, 39(6082):547–550.

Little TA, Cox SC, Vry JK, & Batt GE, 2005. Variations in exhumation level and uplift-rate along the oblique-slip Alpine fault, central Southern Alps, New Zealand. Geological Society of America Bulletin, 117(5-6):707–723.

Lockner DA & Byerlee JD, 1994. Dilatancy in hydraulically isolated faults and the suppression of instability. Geophysical Research Letters, 21(22):2353–2356. doi:10.1029/94GL02366.

Lockner DA, Naka H, Ito H, & Ikeda R, 2000. Permeability and strength of core samples from the Nojima fault of the 1995 Kobe earthquake. USGS Open File Report, 129:147–152.

Lockner DA, Morrow C, Moore D, & Hickman S, 2011. Low strength of deep San Andreas fault gouge from SAFOD core. Nature, 472:82–86. doi: 10.1038/nature09927.

Løvoll G, Maloy K, & Flekkoy E, 1999. Force measurements on static granular materials. Physical Review, E(60):5872–5878.

Lyakhovsky V, Ben-Zion Y, & Agnon A, 2005. A viscoelastic damage rheology and rate- and state-dependent friction. Geophysical Journal International, 161:179–190.

Manzawa N & Otsuki K, 2003. Comminution and fluidization of granular fault materials: Implications for fault slip behavior. Tectonophysics, 367(1-2):127–143.

Mariani E, KH B, & Rutter EH, 2006. Experimental deformation of muscovite shear zones at high temperatures under hydrothermal conditions and the strength of phyllosilicate-bearing faults in nature. Journal of Structural Geology, 28:1569–1587.

Marone C, 1998. Laboratory-derived friction laws and their application to seismic faulting. Annual Review of Earth and Planetary Sciences, 26:643–696.

Marone C & Kilgore B, 1993. Scaling of the critical slip distance for seismic faulting with shear strain in fault zones. Nature, 362:618–620.

Marone C, Cocco M, Richardson E, & Tinti E, 2009. The critical slip distance for seismic and aseismic fault zones of finite width. In Fukuyama E, editor, Fault Zone Properties and Earthquake Rupture Dynamics, volume 94, pages 135–162.

McClintock M, 1999. Alpine Fault Zone structure and tectonometamorphic evolution, Makawhio River, South Westland. Master's thesis, University of Otago, Dunedin, New Zealand.

McDougall I & Kilgore B, 1999. Oxford University Press.

McGarr A, 2012. Relating stick-slip friction experiments to earthquake source parameters. Geophysical Research Letters, 39(L05303). doi: 10.1029/2011GL050327.

McLaskey G, Thomas A, Glaser S, & Nadeau R, 2012. Fault healing promotes high-frequency earthquakes in laboratory experiments and on natural faults. Nature, 491:101–104. doi:10.1038/nature11512.

Melosh H, 1979. Acoustic fluidization- new geologic process. Journal of Geophysical Research, 84:7513–7520.

Melosh H, 1996. Dynamical weakening of faults by acoustic fluidization. Nature, 379:601–606.

Meneghini F, Di Toro G, Rowe CD, Moore JC, Tsutsumi A, & Yamaguchi A, 2010. Record of mega-earthquakes in subduction thrusts: the black fault rocks of Pasagshak Point (Kodiak Island, Alaska). Geological Society of America Bulletin, 122(7-8):1280–1297.

Menendez B, Zhu W, & Wong Tf, 1996. Micromechanics of brittle faulting and cataclastic flow in Berea sandstone. Journal of Structural Geology, 18(1):1–16.

Menzies C, 2012. Fluid Flow Associated with the Alpine Fault, South Island, New Zealand. Ph.D. thesis, University of Southampton, Southampton, UK.

Miller SA, Nur A, & DL O, 1996. Earthquakes as a coupled shear stress-high pore pressure dynamical system. Geophysical Research Letters, 23(2):197–200.

Mitchell TM & Faulkner DR, 2009. The nature and origin of off-fault damage surrounding strike-slip fault zones with a wide range of displacements: A field study from the Atacama fault system, northern Chile. Journal of Structural Geology, 31:902–816. doi:10.1016/j.jsg.2009.05.002.

Mizoguchi K, 2005. High-velocity frictional behavior of Nojima fault gouge and its implications for seismogenic fault motion. Ph.D. thesis, Kyoto University, Kyoto, Japan.

Mizoguchi K & Ueta K, 2013. Microfractures within the fault damage zone record the history of fault activity. Geophysical Research Letters, 40:1–5. doi:10.1002/grl50469.

Mizoguchi K, Hirose T, Shimamoto T, & Fukuyama E, 2006. Moisture-related weakening and strengthening of a fault activated at seismic slip rates. Geophysical Research Letters, 33(L16319). doi:10.1029/2006GL026980.

Mizoguchi K, Hirose T, Shimamoto T, & Fukuyama E, 2007. Reconstruction of seismic faulting by high-velocity friction experiments: An example of the 1995 Kobe earthquake. Geophysical Research Letters, 34(L01308). doi:10.1029/2006GL027931.

Mizoguchi K, Hirose T, Shimamoto T, & Fukuyama E, 2009. High-velocity frictional behavior and microstructure evolution of fault gouge obtained from Nojima fault, southwest Japan. Tectonophysics, 471:285–296. doi: 10.1016/j.tecto.2009.02.033.

Mogi K, 1967. Earthquakes and fractures. Tectonophysics, 5(1):35–55.

Moore DE & Lockner DA, 2004. Crystallographic controls on the frictional behavior of dry and water-saturated sheet structure minerals. Journal of Geophysical Research, 109(B03401). doi:10.1029/2003JB002582.

Moore DE & Lockner DA, 2007. Friction of the smectite clay montmorillonite: A review and interpretation of data. pages 317–345.

Moore DE & Lockner DA, 2008. Talc friction in the temperature range 25Â°C-400Â°C: Relevance for fault-zone weakening. Tectonophysics, 449:120–132. doi:10.1016/j.tecto.2007.11.039.

Moore DE & Lockner DA, 2011. Frictional strengths of talc-serpentine and talc-quartz mixtures. Journal of Geophysical Research, 116:B01403. doi: 10.1029/2010JB007881.

Moore DE & Rymer MJ, 2007. Talc-bearing serpentinite and the creeping section of the San Andreas fault. Nature, 448:795–797. doi:10.1038/ nature06064.

Moore DE & Rymer MJ, 2012. Correlation of clayey gouge in a surface exposure of serpentinite in the San Andreas Fault with gouge from the San Andreas Fault Observatory at Depth (SAFOD). Journal of Structural Geology, 38:51–60.

Moore DE, Lockner DA, Summer R, Shengli M, & Byerlee JD, 1996. Strength of chrysotile-serpentinite gouge under hydrothermal conditions: Can it explain a weak San Andreas fault? Geology, 24(11):1041–1044.

Moore DE, Lockner DA, Tanaka H, & Iwata K, 2004. The Coefficient of Friction of Chrysotile Gouge at Seismogenic Depths. International Geology Review, 46:385–398.

Moore DM & Reynolds RC, 1997. X-ray Diffraction and the Identification and Analysis of Clay Minerals (2^{nd}ed.). Oxford University Press.

Morrow C, Radney B, & Byerlee JD, 1992. Frictional strength and the effective pressure law of montmorillonite and illite clays. In Evans B & Wong TF, editors, Fault Mechanisms and Transport Properties of Rocks, pages 69–88. Elsevier.

Morrow C, Moore DE, & Lockner DA, 2000. The effect of mineral bond strength and adsorbed water on fault gouge frictional strength. Geophysical Research Letters, 26(6):815–818.

Morrow C, Lockner D, Moore D, & Hickman S, 2011. Permeability, Electrical Resistivity and Frictional Strength of SAFOD Fault Gouge and Damage Zone Rocks. AGU Fall Meeting Abstracts 2011, pages T23E–2468.

Mortimer N, 2004. New Zealand's geological foundations. Gondwana Research, 7:261–272.

Mortimer N, Nathan S, Kawachi Y, Ryland C, Cooper AF, Stewart M, & Randall S, 2012. Regional metamorphism of the Early Paleozoic Greenland Group, South Westland, New Zealand. New Zealand Journal of Geology and Geophysics, 56:1–15. doi:10.1080/00288306.2012.734830.

Mortimer N, Nathan S, Jongens R, Kawachi Y, Ryland C, Cooper A, Stewart M, & Randall S, 2013. Regional metamorphism of the Early Palaeozoic Greenland Group, South Westland, New Zealand. New Zealand Journal of Geology and Geophysics, 1(56):1–15. doi:10.1080/00288306.2012.734830.

Muhuri S, Dewers T, Scott TJ, & Reches Z, 2003. Interseismic fault strengthening and earthquake-slip instability: friction or cohesion? Geology, 31(10):881–884.

Nakatani M, 2001. Conceptual and physical clarification of rate and state friction: frictional sliding as a thermally activated rheology. Journal of Geophysical Research, 106(B7):13347–13380.

Nathan S, 1976. Geochemistry of the Greenland Group (Early Ordovician), New Zealand. New Zealand Journal of Geology and Geophysics, 19:683–706.

Nathan S, 1978. Upper Cenozoic stratigraphy of South Westland, New Zealand. New Zealand Journal of Geology and Geophysics, 21(3):329–361. doi:10.1080/00288306.1978.10424061.

Nathan S, 1998. Petrographic notes on samples from the Glasgow and Victoria Ranges. Technical report.

Nathan S, Rattenbury M, & Suggate R, 2002. Geology of the Greymouth Area: Scale 1:250000. 12:58.

Nesbitt H & Young G, 1982. Prediction of some weathering trends of plutonic and volcanic rocks based on thermodynamics and kinetic considerations. Geochmica Cosmochima Acta, 44:1659–1666.

Nesbitt H & Young G, 1989. Formation and Diagenesis of Weathering Profiles. The Journal of Geology, 97:129–147.

Ngan A, 2003. Mechanical analog of temperature for the description of force distribution in static granular packings. Physical Review, E(68(011301)):1–10.

Nguyen G & Einav I, 2009. The Energetics of Cataclasis Based on Breakage Mechanics. Pure and Applied Geophysics, 166:1693–1724. doi:10.1007/s00024-009-0518-x.

Nielsen S, Di Toro G, Hirose T, & Shimamoto T, 2008. Frictional melt and seismic slip. Journal of Geophysical Research, 113(B01308). doi:10.1029/2007JB005122.

Nielsen S, Mosca P, Giberti G, Di Toro G, Hirose T, & Shimamoto T, 2010. On the transient behavior of frictional melt during seismic slip. Journal of Geophysical Research, 115(B10301). doi:10.1029/2009JB007020.

Niemeijer A & Spiers C, 2005. Influence of phyllosilicates on fault strength in the brittle-ductile transition: insights from rock analogue experiments. London, Geological Society Special Publications, 245:303–327.

Niemeijer AR & Spiers C, 2006. Velocity dependence of strength and healing behavior in simulated phyllosilicate-bearing fault gouge. Tectonophysics, 427:231–253.

Niemeijer AR & Spiers CJ, 2007. A microphysical model for strong velocity weakening in phyllosilicate-bearing fault gouges. Journal of Geophysical Research, 112. doi:10.1029/2007JB005008.

Niemeijer AR, Spiers CJ, & Bos B, 2002. Compaction creep of quartz sand at 400-600°C: experimental evidence for dissolution-controlled pressure solution. Earth and Planetary Science Letters, 195:261–275.

Niemeijer AR, Spiers CJ, & Peach CJ, 2008. Frictional behaviour of simulated quartz fault gouges under hydrothermal conditions: Results from ultra-high strain rotary shear experiments. Tectonophysics, 460:288–303.

Niemeijer AR, Elsworth D, & Marone C, 2009. Significant effect of grain size distribution on compaction rates in granular aggregates. Earth and Planetary Science Letters, 284:386–391. doi:10.1016/j.epsl.2009.04.041.

Niemeijer AR, Marone C, & Elsworth D, 2010. Frictional strength and strain weakening in simulated fault gouge: competition between geometrical weakening and chemical strengthening. Journal of Geophysical Research, 115(B10207). doi:10.1029/2009JB000838.

Niemeijer AR, Di Toro G, Nielsen S, & Di Felice F, 2011. Frictional melting of gabbro under extreme experimental conditions of normal stress, accel-

eration, and sliding velocity. Journal of Geophysical Research, 116(B7). doi:10.1029/2010JB008181.

Niemeijer AR, Di Toro G, Ashley Griffith W, Bistachhi A, Smith SAF, & Nielsen S, 2012. Inferring earthquake physics and chemistry using an integrated field and laboratory approach. Journal of Structural Geology, 39:2–36.

Noda H & Lapusta N, 2013. Stable creeping fault segments can become destructive as a result of dynamic weakening. Nature, 493(7433):518–521. doi:10.1038/nature11703.

Noda H & Shimamoto T, 2009. Constitutive properties of clayey fault gouge from the Hanaore fault zone, southwest Japan. Journal of Geophysical Research, 114(B04409).

Noda H, Dunham E, & Rice JR, 2009. Earthquake ruptures with thermal weakening and the operation of major faults at low overall stress levels. Journal of Geophysical Research, 114(B07302). doi:10.1029/2008JB006143.

Norris R & Cooper A, 1995. Origin of small-scale segmentation and transpressional thrusting along the Alpine fault, New Zealand. Bulletin of the Geological Society of America, 107:231–240.

Norris RJ & Cooper AF, 1997. Erosional control on the structural evolution of a transpressional thrust complex on the Alpine Fault, New Zealand. Geology, 19:1323–1342.

Norris RJ & Cooper AF, 2001. Late Quaternary slip rates and slip partitioning on the Alpine fault, New Zealand. Journal of Structural Geology, 23(2–3):507–520. doi:10.1016/S0191-8141(00)00122-X.

Norris RJ & Cooper AF, 2003. Very high strains recorded in mylonites along the Alpine Fault, New Zealand: implications for the deep structure of plate boundary faults. Journal of Structural Geology, 25:2141–2157.

Norris RJ & Cooper AF, 2007. The Alpine Fault, New Zealand: Surface geology and field relationships. In Okaya D, Stern T, & Davey F, editors, A Continental Plate Boundary: Tectonics at South Island, New Zealand, volume 175, pages 159–178. American Geophysical Union. doi:10.1029/175GM09.

Nur A, 1978. Nonuniform friction as a physical basis for earthquake mechanisms. Pure and Applied Geophysics, 116:964–989.

O'Hara K, 1988. Fluid flow and volume loss during mylonitization- An origin for phyllonite in an overthrust setting, North Carolina, USA. Tectonophysics, 156:21–36.

Ohnaka M, 2003. A constitutive scaling law and a unified comprehension for frictional slip failure, shear fracture of intact rock, and earthquake rupture. Journal of Geophysical Research, 108:2080.

Orowan E, 1960. The mechanism of seismic faulting. Geological Society of America Memoir, 79:232–245.

Papov V, 2010. Contact Mechanics and Friction. Springer-Verlag.

Paterson M, 1978. Experimental Rock Deformation: The Brittle Field. Springer-Verlag.

Pearson C, Denys P, & Hodgkinson K, 2000. Geodetic constraints on the kinematics of the Alpine Fault in the southern South Island of New Zealand, using results from the Hawea-Haast GPS Transect. Geophysical Research Letters, 27:1319–1322. doi:10.1029/1999GL008412.

Pearson CE, Beavan JP, Darby DJ, Blick GH, & Walcott RI, 1995. Strain Distribution across the Australian-Pacific Plate Boundary in the Central South Island, New Zealand, from 1992 GPS and Earlier Terrestrial Observations. Journal of Geophysical Research, 100:22071–22081.

Peng Z & Gomberg J, 2010. An integrated perspective of the continuum between earthquakes and slow-slip phenomena. Nature Geoscience, 3:599–607. doi:10.1038/NGEO940.

Perfettini H & Ampuero JP, 2008. Dynamics of a velocity strengthening region: implications for slow earthquakes and postseismic slip. Journal of Geophysical Research, 113(B9):B09317. doi:10.1029/2007JB005553.

Pettinga J, Yetton MD, Van Dissen D, & Downes G, 2001. Earthquake source identification and characterization for the Canterbury region, South Island, New Zealand. Bulletin of the New Zealand Society for Earthquake Engineering, 34(4):282–317.

Pitcairn I, 2004. Sources of fluids and metals in orogenic gold deposits: The Otago schist's, New Zealand. Ph.D. thesis, University of Southampton, Southampton, UK.

Polak A, Elsworth D, Yasuhara H, Grader A, & Halleck P, 2003. Permeability reduction of a natural fracture under net dissolution by hydrothermal fluids. Geophysical Research Letters, 30:2020. doi:10.1029/2003GL017575.

Prakash V & Clifton R, 1992. Pressure-induced plate impact measurement of dynamic friction for high speed machining applications. In Proceedings of VII International Congress on Experimental Mechanics, pages 556–564.

Prior D, 1988. Deformation processes in the Alpine Fault Mylonites, South Island, New Zealand. Ph.D. thesis, University of Leeds, Leeds, UK.

Pytte AM & Reynolds RC, 1988. The thermal transformation of smectite to illite. In McCulloh TH & Naeser ND, editors, Thermal Histories of Sedimentary Basins, pages 133–140,. Springer.

Quigley M, Van Dissen R, Litchfield N, Villamor P, Duffy B, Barrell D, Furlong K, Stahl T, Bilderback R, & Noble D, 2012. Surface rupture during the 2010 Mw 7.1 Darfield (Canterbury) earthquake: Implications

for fault rupture dynamics and seismic-hazard analysis. Geology, 40(1):55–58. doi:10.1130/G32528.1.

Rabinowicz E, 1951. The Nature of the Static and Kinetic Coefficients of Friction. Journal of Applied Physics, 22(11):1373–1379.

Rabinowicz E, 1958. The intrinsic variables affecting the stick-slip process. Proceedings of the Physical Society of London, 71:668–675.

Rathbun A & Marone C, 2010. Effect of strain localization on frictional behavior of sheared granular materials. Journal of Geophysical Research, 115(B01204). doi:10.1029/2009JB006466.

Rattenbury MS, 1987. Fraser Complex and Alpine Fault tectonics, central Westland, New Zealand. Ph.D. thesis, University of Otago, Dunedin, New Zealand.

Rattenbury MS, Jongens R, & Cox SC, 2010. Geology of the Haast area: scale 1:250,000. Institute of Geological & Nuclear Sciences 1:250,000 geological map, 14:58.

Raymond L, 1984. Classification of mélanges, Geological Society of America. Geological Society of America, Special Paper 198:7–20.

Read S, 1994. Alpine Fault Segmentation and Range Front Structure between Gaunt Creek and Little Man River, near Whataroa, central Westland, New Zealand. Master's thesis, University of Otago, Dunedin, New Zealand.

Reches Z, 1999. Mechanisms of slip nucleation during earthquakes. Earth and Planetary Science Letters, 170:475–486.

Reches Z & Lockner DA, 2010. Fault weakening and earthquake instability by powder lubrication. Nature, 467:452–456. doi:10.1038/nature09348.

Reed JJ, 1964. Mylonites, cataclasites, and associated rocks along the Alpine Fault, South Island, New Zealand. New Zealand Journal of Geology and Geophysics, 7:645–684.

Regenauer-Lieb K & Yuen D, 2008. Multiscale brittle-ductile coupling and genesis of slow earthquakes. Pure and Applied Geophysics, 165:523–543.

Reid H, 1910. The California earthquake of April 18, 1906; the mechanics of the earthquake. In The California Earthquake of April 18, 1906, Report of the State Earthquake Investigation Commission Vol. 2, pages 1–192. Carnegie Institution.

Reinen LA, 2000. Seismic and aseismic slip indicators in serpentinite gouge. Geology, 28(2):135–138. doi:10.1130/0091-7613(2000)28<135:SAASII>.

Reinen LA, Weeks JD, & Tullis TE, 1991. The frictional behavior of serpentinite: Implications for aseismic creep on shallow crustal faults. Geophysical Research Letters, 18(10):1921–1924. doi:10.1029/91GL02637.

Reinen LA, Weeks JD, & Tullis TE, 1994. The frictional behavior of lizardite and antigorite serpentinites: Experiments, constitutive models, and implications for natural faults. Pure and Applied Geophysics, 143:317–358.

Renard F, Park A, Ortoleva P, & Gratier JP, 1999. An integrated model for transitional pressure solution in sandstones. Tectonophysics, 312:97–115.

Renard F, Gratier J, & Jamtveit B, 2000. Kinetics of crack-sealing, intergranular pressure solution, and compaction around active faults. Journal of Structural Geology, 22:1395–1407.

Reyes A, Christenson B, & Faure K, 2010. Sources of solutes and heat in low-enthalpy mineral waters and their relation to tectonic setting, New Zealand. Journal of Volcanology and Geothermal Research, 192:117–141.

Reyners MD, 2013. The central role of the Hikurangi Plateau in the Cenozoic tectonics of New Zealand and the Southwest Pacific. Earth and Planetary Science Letters, 361:460–468. doi:10.1016/j.epsl.2012.11.010.

Reyners MD, Eberhart-Phillips D, & Bannister S, 2011. Tracking repeated subduction of the Hikurangi Plateau beneath New Zealand. Earth and Planetary Science Letters, 311:165–171. doi:10.1016/j.epsl.2011.09.011.

Rice JR, 1993. Spatio-temporal complexity of slip on a fault. Journal of Geophysical Research, 98(B6). doi:10.1029/93JB00191.

Rice JR, 2006. Heating and weakening of faults during earthquake slip. Journal of Geophysical Research, 111(B5):B05311. doi:10.1029/2005JB004006.

Rice JR & Cocco M, 2006. Seismic Fault Rheology and Earthquake Dynamics. In Handy MR, editor, The Dynamics of Fault Zones, pages 99–137. The MIT Press.

Rice JR, Lapusta N, & Ranjith K, 2001. Rate and state dependent friction and the stability of sliding between elastically deformable solids. Journal of the Mechanics and Physics of Solids, 49:1865–1898.

Richter D & Simmons G, 1974. Thermal expansion behavior of igneous rocks. International Journal of Rock Mechanics and Mining Science and Geomechanics Abstracts, 11:403–411.

Roser B & Korsch R, 1999. Geochemical characterization, evolution and source of a Mesozoic accretionary wedge: the Torlesse terrane, New Zealand. Geological Magazine, 136:493–512.

Roser B, Mortimer N, Turnbull I, & Landis C, 1993. Geology and Geochemistry of the Caples Terrane, Otago, New Zealand: Compositional variations near and Permo-Triassic arc margin.

Roser B, Grapes R, & Palmer K, 1995. XRF analyses of sandstones and argillites from the Torlesse terrane, New Zealand. Wellington Geology Board Studies Publication, 15:40.

Rowe C, Meneghini F, & Casey Moore J, 2011. Textural record of the seismic cycle: strain-rate variation in an ancient subduction thrust. In Geology of the Earthquake Source: A Volume in Honour of Rick Sibson, volume 359, pages 77–95.

Rubin A, 2008. Episodic slow slip events and rate-and-state friction. Journal of Geophysical Research, 113(B11414). doi:10.1029/2008JB005642.

Rubin A & Ampuero JP, 2009. Self-similar slip pulses during rate-and-state earthquake nucleation. Journal of Geophysical Research, 114(B11305). doi:10.1029/2009JB006529.

Ruina AL, 1983. Slip instability and state variable friction laws. Journal of Geophysical Research, 115(B12):10359–10370.

Rutter EH, 1976. The kinetics of rock deformation by pressure solution. Philosophical Transactions of the Royal Society of London, A283:203–219.

Rutter EH, 1983. Pressure solution in nature, theory and experiment. Journal of the Geological Society of London, 140:725–740.

Saffer DM & Marone C, 2003. Comparison of smectite- and illite-rich gouge frictional properties: Application to the updip limit of the seismogenic zone along subduction megathrusts. Earth and Planetary Science Letters, 215:219–235. doi:10.1016/S0012-821X(03)00424-2.

Saffer DM, Lockner DA, & McKiernan A, 2012. Effects of smectite to illite transformation on the frictional strength and sliding stability of intact marine mudstones. Geophysical Research Letters, 39:L11304. doi:10.1029/2012GL051761.

Sagy A & Brodsky E, 2009. Geometric and rheological asperities in an exposed fault zone. Journal of Geophysical Research, 114(B02301). doi:10.1029/2008JB005701.

Sammis C & King R, 1987. The kinematics of gouge deformation. Pure and Applied Geophysics, 125(5):777–812.

Sammis C, Nadeau R, & Johnson L, 1999. How strong is an asperity? Journal of Geophysical Research, 104(B5):10609–10619.

Sammis CG & Ben-Zion Y, 2008. Mechanics of grain-size reduction in fault zones. Journal of Geophysical Research, 113(B02306). doi:10.1029/2006JB004892.

Sammis CG & Steacy S, 1994. The micromechanics of friction in a granular layer. Pure and Applied Geophysics, 142(3/4):778–794.

Samuelson J, Elsworth D, & Marone C, 2009. Shear-induced dilatancy of fluid-saturated faults: Experiment and theory. Journal of Geophysical Research, 114:B12404. doi:10.1029/2008JB006273.

Samuelson J, Elsworth D, & Marone C, 2011. Influence of dilatancy on the frictional constitutive behavior of a saturated fault zone under a variety of drainage conditions. Journal of Geophysical Research, 116. doi:10.1029/2011JB007406.

Savage H & Marone C, 2007. Effects of shear velocity oscillations on stick-slip behavior in laboratory experiments. Journal of Geophysical Research, 112(B02301). doi:10.1029/2005JB004238.

Savage J & Wood M, 1971. The relationship between apparent stress and stress drop. Bulleting of the Seismological Society of America, 61:1381–1388.

Sawai M, Shimamoto T, & Togo T, 2012. Reduction in BET surface area of Nojima fault gouge with seismic slip and its implication for the fracture energy of earthquakes. Journal of Structural Geology, 38:117–138. doi:10.1016/j.jsg.2012.01.002.

Scarbek R, Rempel A, & Schmidt D, 2012. Geologic heterogeneity can produce aseismic slip transients. Geophysical Research Letters, 39(L21306). doi:10.1029/2012GL053762.

Schleicher AM, Tourscher S, van der Pluijm BA, & Warr LN, 2009. Constraints on mineralization, fluid-rock interaction, and mass transfer during

faulting at 2-3 km depth from the SAFOD drill hole. Journal of Geophysical Research, 114(B04202). doi:10.1029/2008JB006092.

Schleicher AM, van der Pluijm BA, & Warr LN, 2012. Chlorite-smectite clay minerals and fault behavior: New evidence from the San Andreas Fault Observatory at Depth (SAFOD) core. Lithosphere, L158. doi:10.1130/L158.1.

Schmedes J, Archuleta R, & Lavallée D, 2010. Correlation of earthquake source parameters inferred from dynamic rupture simulations. Journal of Geophysical Research, 115(B03304). doi:10.1029/2009JB006689.

Schmitt VS, Segall P, & Matsuzawa T, 2011. Shear heating-induced thermal pressurization during earthquake nucleation. Journal of Geophysical Research, 116:B06308. doi:10.1029/2010JB008035.

Scholz CH, 1998. Earthquakes and friction laws. Nature, 391:37–42.

Scholz CH, 2002. The Mechanics of Earthquakes and Faulting, 2^{nd} ed. Cambridge Press.

Scott H, 2012. Cataclastic processes within the Alpine fault zone. Master's thesis, University of Otago, Dunedin, New Zealand.

Segall P, 2012. Understanding Earthquakes. Science, 336(6082):676–677. doi:10.1126/science.1220946.

Segall P & Pollard DD, 1980. Mechanics of discontinuous faults. Journal of Geophysical Research, 85:4337–4350.

Segall P & Pollard DD, 1983. Nucleation and growth of strike-slip faults in granite. Journal of Geophysical Research, 88:555–568. doi:10.1029/JB088iB01p00555.

Segall P & Rice JR, 1995. Dilatancy, compaction, and slip instability of a fluid-infiltrated fault. Journal of Geophysical Research, 100:22155–22171. doi:10.1029/95JB02403.

Segall P, Rubin A, Bradley A, & Rice JR, 2010. Dilatant strengthening as a mechanism for slow slip events. Journal of Geophysical Research, 115(B12305). doi:10.1029/2010JB007449.

Shi Y, Allis R, & Davey F, 1996. Thermal modeling of the Southern Alps. Pure and Applied Geophysics, 146:469–501.

Shimamoto T & Logan J, 1981. Effects of simulated clay gouges on the sliding behavior of tennessee sandstone. Tectonophysics, 75:243–255.

Shimamoto T & Togo T, 2012. Earthquakes in the Lab. Science, 338:54–55.

Sibson RH, 1973. Interactions between temperature and pore-fluid pressure during earthquake faulting and a mechanism for partial or total stress relief. Nature, 243:66–68.

Sibson RH, 1977a. Fault rocks and fault mechanisms. Geological Society of London, 133:191–213.

Sibson RH, 1977b. Kinetic shear resistance, fluid pressure and radiation efficiency during seismic faulting. Pure and Applied Geophysics, 115:387–400.

Sibson RH, 1980. Power dissipation and stress levels on faults in the upper crust. Journal of Geophysical Research, 85(B11):6239–6247.

Sibson RH, 1982. Fault Zone Models, Heat Flow, and the Depth Distribution of Earthquakes in the Continental Crust of the United States. Bulletin of the Seismological Society of America, 72(1):151–163.

Sibson RH, 1985. A note on fault reactivation. Journal of Structural Geology, 7:751–754.

Sibson RH, 1986. Earthquakes and rock deformation in crustal fault zones. Annual Review of Earth and Planetary Sciences, 14:149–175.

Sibson RH, 1991. Loading of faults to failure. Bulletin of the Seismological Society of America, 81(6):2493–2497.

Sibson RH, 1992. Implications of fault-valve behavior for rupture nucleation and recurrenc. Tectonophysics, 211:283–393.

Sibson RH, 2003. Thickness of the seismic slip zone. Bulletin of the Seismological Society of America, 93:1169–1178. doi:10.1785/0120020061.

Sibson RH & Rowland J, 2003. Stress, fluid pressure and structural permeability in seismogenic crust, North Island, New Zealand. Geophysical Journal International, 154:584–594.

Sibson RH & Scott J, 1998. Stress/fault controls on the containment and release of overpressured fluids: Examples from gold-quartz vein systems in Juneau, Alaska; Victoria, Australia and Otago, New Zealand. Ore Geology Reviews, 13:293–306.

Sibson RH & Toy VG, 2006. The habitat of fault-generated pseudotachylyte: presence vs absence of friction melt. In Abercrombie Rea, editor, Radiated Energy and the Physics of Faulting, Geophys. Monogr. Ser, pages 153–166. AGU.

Sibson RH, White SH, & Atkinson BK, 1979. Fault rock distribution and structure within the Alpine Fault Zone: a preliminary account. In Walcott R & Cresswell M, editors, The Origin of the Southern Alps, volume 18, pages 55–65. Bulletin of the Royal Society of New Zealand.

Sibson RH, White SH, & Atkinson BK, 1981. Structure and distribution of fault rocks in the Alpine Fault Zone, New Zealand. In McClay KR & Price NJ, editors, Thrust and Nappe Tectonics, volume 9, pages 197–210. Geological Society of London Special Publication.

Simpson G, 1992. Quaternary evolution of the Alpine Fault Zone, and a mineralogical/microstructural study of the schist-mylonite transition. Master's thesis, University of Otago, Dunedin, New Zealand.

Simpson G, Cooper AF, & Norris RJ, 1994. Late Quaternary evolution of the Alpine Fault Zone at Paringa, South Westland, New Zealand. New Zealand Journal of Geology and Geophysics, 37:49–58.

Sleep NH & Blanpied ML, 1992. Creep, compaction, and the weak rheology of major faults. Nature, 359:687–692.

Smith SAF, Holdsworth RE, Collettini C, & MA P, 2011. The microstructural character and mechanical significance of fault rocks associated with a continental low-angle normal fault: the Zuccale Fault, Elba Island, Italy. In Fagereng A, Toy VG, & Rowland JK, editors, Geology of the Earthquake Source: A Volume in Honour of Rick Sibson. London, volume 359, pages 97–113.

Smith SAF, Di Toro G, Kim S, Ree JH, Nielsen S, Billi A, & Spiess R, 2013. Coseismic recrystallization during shallow earthquake slip. Geology, 41(1):63–66. doi:10.1130/G33488.1.

Sone H & Shimamoto T, 2009. Frictional resistance of faults during accelerating and decelerating earthquake slip. Nature Geoscience, 2:705–708. doi:10.1038/NGEO637.

Spudich P & Guatteri M, 2004. The effect of bandwidth limitations on the inference of earthquake slip-weakening distance from seismograms. Bulletin of the Seismological Society of America, 94(6):2038–2036. doi:10.1785/0120030104.

Steiger R & Jager E, 1977. Subcommission on geochronology: Convention on the use of decay constants in geo- and cosmochronology. Earth and Planetary Science Letters, 36:359–362.

Stein R, 1999. The role of stress transfer in earthquake occurrence. Nature, 402:605–609.

Stein S & Stein J, 2013. Shallow versus deep uncertainties in natural hazard assessments. EOS, Transactions, American Geophysical Union, 94(14):133–140.

Stein S, Geller R, & Liu M, 2011. Bad assumptions or bad luck: Why earthquake hazard maps need objective testing. Seismological Research Letters, 82:623–626.

Stern T, Okaya D, Kleffman S, Scherwath M, Henrys SA, & Davey F, 2007. Geophysical exploration and dynamics of the Alpine Fault Zone. New Zealand. Geophysical Monograph Series, 175:235–251.

Stirling MW, McVerry G, & Berryman KR, 2002. A new seismic hazard model for New Zealand. Bulletin of the Seismological Society of America, 92(5):1878–1903.

Storey BC, Rubridge BS, Cole DI, & de Wit MJ, editors, 1999. Overview of the Median Batholith, New Zealand : a new interpretation of the geology of the Median Tectonic Zone and adjacent rocks, volume 29. Elsevier.

Storti F & Balsamo F, 2010. Particle size distributions by laser diffraction: sensitivity of granular matter strength to analytical operating procedures. Solid Earth, 10:25–48.

Sulem J, Lazar P, & Vardoulakis I, 2007. Thermo-poro-mechanical properties of clayey gouge and application to rapid fault shearing. International Journal for Numerical and Analytical Methods in Geomechanics, 31:523–540.

Sutherland R, 1999. Basement geology and tectonic development of the greater New Zealand region: an interpretation from regional magnetic data. Tectonophysics, 308:341–362.

Sutherland R & Norris RJ, 1995. Late Quaternary displacement rate, paleoseismicity, and geomorphic evolution of the Alpine Fault: evidence from

Hokuri Creek, South Westland, New Zealan. New Zealand Journal of Geology and Geophysics, 38:419–430.

Sutherland R, Hollis CJ, Nathan S, Strong CP, & Wilson GJ, 1996. Age of Jackson Formation proves late Cenozoic allochthony in South Westland, New Zealand. New Zealand Journal of Geology and Geophysics, 39(4):559–563. doi:10.1080/00288306.1996.9514733.

Sutherland R, Davey F, & Beavan JP, 2000. Plate boundary deformation in South Island, New Zealand, is related to inherited lithopheric structure. Earth and Planetary Science Letters, 177:141–151.

Sutherland R, Berryman KR, & Norris RJ, 2006. Quaternary slip rate and geomorphology of the Alpine fault: Implications for the kinematics and seismic hazard in southwest New Zealand. Geological Society of America Bulletin, 118:464–474. doi:10.1130/B25627.1.

Sutherland R, Eberhart-Phillips D, Harris RA, Stern TA, Beavan RJ, Ellis SM, Henrys SA, Cox SC, Norris RJ, Berryman KR, Townend J, Bannister S, Pettinga J, Leitner B, Wallace LM, Little TA, Cooper AF, Yetton M, & Stirling MW, 2007. Do great earthquakes occur on the Alpine fault in central South Island, New Zealand? In Okaya D, Stern T, & Davey F, editors, A Continental Plate Boundary: Tectonics at South Island, New Zealand, volume 175 of *American Geophysical Union Monograph*, pages 235–251.

Sutherland R, Toy VG, Townend J, Eccles JD, Prior DJ, Norris RJ, Mariani E, Faulkner DR, DePascale G, Carpenter BM, Boulton C, Menzies CD, Cox SC, Little TA, Hasting M, Cole-Baker J, Langridge RM, Scott HR, Reid-Lindroos Z, Fleming B, & Wing R, 2011. Operations and well completion report for boreholes DFDP-1A and DFDP-1B, Deep Fault Drilling Project, Alpine Fault, Gaunt Creek, New Zealand. Technical Report 48, Institute of Geological & Nuclear Sciences.

Sutherland R, Toy VG, Townend J, Cox SC, Eccles JD, Faulkner DR, Prior DJ, Norris RJ, Mariani E, Boulton C, Carpenter BM, Menzies CD, Little

TA, Hasting M, De Pascale GP, Langridge RM, Scott HR, Reid-Lindroos Z, & Fleming B, 2012. Drilling reveals fluid control on architecture and rupture of the Alpine Fault. Geology, 40:1143–1146. doi:10.1130/G33614.1.

Tanikawa W & Shimamoto T, 2009. Frictional and transport properties of the Chelungpu fault from shallow borehole data and their correlation with seismic behavior during the 1999 Chi-Chi earthquake. Journal of Geophysical Research, 114(B01402). doi:10.1029/2008JB005750.

Tanikawa W, Mukoyoshi H, Tadai O, Hirose T, Tsutsumi A, & Lin W, 2012. Velocity dependence of shear-induced permeability associated with frictional behavior in fault zones of the Nankai subduction zone. Journal of Geophysical Research, 117(B05405). doi:10.1029/2011JB008956.

Tembe S, Lockner DA, & Wong Tf, 2009. Constraints on the stress state of the San Andreas Fault with analysis based on core and cuttings from San Andreas Fault Observatory at Depth (SAFOD) drilling phases 1 and 2. Journal of Geophysical Research, 114:B11401. doi:10.1029/2008JB005883.

Tembe S, Lockner DA, & Wong Tf, 2010. Effect of clay content and mineraology on frictional sliding behavior of simulated gouges: Binary and ternary mixtures of quartz, illite, and montmorillonite. Journal of Geophysical Research, 115:B03416. doi:10.1029/2009JB006383.

Templeton A, Chamberlain CP, Koons PO, & Craw D, 1998. Stable isotopic evidence for mixing between metamorphic fluids and surface-derived waters during recent uplift of the Southern Alps, New Zealand. Earth and Planetary Science Letters, pages 73–92.

Tenthorey E & Cox S, 2006. Cohesive strengthening of fault zones during the interseismic period: an experimental study. Journal of Geophysical Research, 111(B09202). doi:10.1029/2005JB004122.

Terzhagi K & Peck R, 1948. Soil Mechanics in engineering practice. Wiley.

Tinti E, Spudich P, & Cocco M, 2005. Earthquake fracture energy inferred from kinematic rupture models on extended faultsEarthquake fracture energy inferred from kinematic rupture models on extended faults. Journal of Geophysical Research, 110:B12303. doi:10.1029/2005JB003644.

Tinti E, Cocco M, Fukuyuma E, & Piatanessi A, 2009. Dependence of slip weakening distance (Dc) on final slip during dynamic rupture of earthquakes. Geophysical Journal International, 177:1205–1220.

Togo T, Shimamoto T, MA S, & Hirose T, 2011. High-velocity frictional behavior of Longmenshan fault gouge from Hongkou outcrop and its implications for dynamic weakening of fault during 2008 Wenchuan earthquake. Earthquake Science, 24:267–281.

Totten M, Hanan M, Knight D, & Borgess J, 2002. Characteristics of mixed-layer smectite/illite density separates during burial diagenesis. American Mineralogist, 87:1571–1579.

Townend J, 2006. What do faults feel? Observational constraints on the stresses acting on seismogenic faults. In Abercrombie R, McGarr A, Kanamori H, & Di Toro G, editors, Earthquakes: Radiated Energy and the Physics of Faulting, volume 170, pages 313–327. American Geophysical Union.

Townend J & Zoback MD, 2000. How faulting keeps the crust strong. Geology, 28(5):399–402.

Townend J & Zoback MD, 2001. Implications of earthquake focal mechanisms for the frictional strength of the San Andreas fault system. Geological Society Special Publications, 186:13–21.

Townend J, Sutherland R, & Toy VG, 2009. Deep Fault Drilling Project-Alpine Fault, New Zealand. Scientific Drilling, 85:75–82.

Townend J, Sutherland R, Toy VG, Eccles JD, Boulton C, Cox SC, & McNamara D, 2013. Late-interseismic state of a continental plate-bounding

fault: Petrophysical results from DFDP-1 wireline logging and core analysis, Alpine Fault, New Zealand. Geochemistry, Geophysics, Geosystems. doi:10.1002/ggge.20236.

Toy V, Boulton C, Prior D, RJ N, Mariani E, Faulkner D, Sutherland R, & Townend J, 2012. Lithological Characteristics of the Alpine Fault Zone from DFDP-1 and Outcrop Observations. EOS Transactions AGU Fall Meeting Supplement, (T31C-2612).

Toy V, Boulton C, Sutherland R, Townend J, Norris R, Little T, Prior D, Mariani E, Faulkner D, Menzies C, Scott H, & Carpenter B, in prep. Rock types, deformation mechanisms, and architecture of the Alpine Fault, revealed by DFDP-1 drilling, New Zealand. Earth and Planetary Science Letters.

Toy VG, 2007. Rheology of the Alpine Fault Mylonite Zone: deformation processes at and below the base of the seismogenic zone in a major plate boundary structures. Ph.D. thesis, University of Otago, Dunedin, New Zealand.

Toy VG, Prior D, & Norris RJ, 2008. Quartz textures in the Alpine fault mylonites: influence of pre-existing preferred orientations on fabric development during progressive uplift. Journal of Structural Geology, 30:602–621.

Toy VG, Craw D, Cooper AF, & Norris RJ, 2010. Thermal regime in the central Alpine Fault zone, New Zealand: Constraints from microstructures, biotite chemistry and fluid inclusion data. Tectonophysics, 485:178–192. doi:10.1016/j.tecto.2009.12.013.

Toy VG, Ritchie S, & Sibson RH, 2011. Diverse habitats of pseudotachylytes in the Alpine Fault Zone and relationships to current seismicity. In Fagereng A, Toy VG, & Rowland JK, editors, Geology of the Earthquake Source: a volume in honour of Professor Richard Sibson. Geological Society of London Special Publication.

Tse ST & Rice JR, 1986. Crustal earthquake instability in relation to depth variation of frictional slip properties. Journal of Geophysical Research, 91:9452–9472.

Tsutsumi A & Shimamoto T, 1997. High-velocity frictional properties of gabbro. Geophysical Research Letters, 24:699–702.

Tullis J & Yund RA, 1977. Experimental deformation of dry Westerly granite. Journal of Geophysical Research, 82:5705–5718.

Tullis TE, 1988. Rock Friction Constitutive Behavior from Laboratory Experiments and Its Implications for an Earthquake Prediction Field Monitoring Program. Pure and Applied Geophysics, 126:555–588.

Tulloch AJ & Palmer K, 1990. Tectonic implications of granite cobbles from the mid-Cretaceous Pororari Group, southwest Nelson, New Zealand. New Zealand Journal of Geology and Geophysics, 33(2):205–217.

Tulloch AJ, Ramezani J, Kimbrough DL, Faure K, & Allibone AH, 2009. U-Pb geochronology of mid-Paleozoic plutonism in western New Zealand: implications for S-type granite generation and growth of the east Gondwana margin. Geological Society of America Bulletin, 121:1236–1261.

Turnbull IM, 2000. Geology of the Wakatipu area: scale 1:250,000. Institute of Geological & Nuclear Sciences 1:250,000 geological map, 18:725–740.

Turnbull IM, Allibone AH, & Jongens R, 2010. Geology of the Fiordland area: scale 1:250,000. Institute of Geological & Nuclear Sciences 1:250,000 geological map, 17:97.

Ujiie K & Tsutsumi A, 2010. High-velocity frictional properties of clay-rich fault gouge in a megasplay fault zone, Nakai subduction zone. Geophysical Research Letters, 37(L24310). doi:10.1029/2010GL046002.

Ujiie K, Tsutsumi A, Fialko Y, & Yamaguchi A, 2009. Experimental investigation of frictional melting of argillite at high slip rates: Implications

for seismic slip in subduction-accretion complexes. Journal of Geophysical Research, 114(B04308). doi:10.1029/2008JB006165.

Upton P, Koons PO, & Chamberlain CP, 1995. Penetration of deformation-driven meteoric water into ductile rocks: isotopic and model observations from the Southern Alps, New Zealand. Journal of Geology and Geophysics, 38:535–543.

Upton P, Craw D, Caldwell TG, Koons PO, James Z, Wannamaker PE, Jiracek G, & Chamberlain CP, 2002. Upper crustal fluid flow in the outboard region of the Southern Alps, New Zealand. Geofluids, 1:1–12.

Van Dissen R & Yeats R, 1991. Hope Fault, Jordan Thrust, and uplift of the Seaward Kaikoura Range, New Zealand. Geology, 19(4):393–396.

Van Eerd A, Ellenbroek W, van Hecke M, Snoeijer M, & Vlugt T, 2007. The tail of the contact force distribution in static granular materials. Physical Review, E(060302(R)).

Vry JK, Storkey AC, & Harris C, 2001. Role of fluids in the metamorphism of the Alpine Fault Zone. Journal of Metamophic Geology, 19:21–31.

Vry JK, Powell R, Golden K, & Peterson K, 2009. The role of exhumation in metamorphic dehydration and fluid production. Nature Geoscience, 3:31–35.

Waddell H, 1932. Volume, shape and roundness of rock particles. Journal of Geology, 40:443–451.

Walcott RI, 1984. Reconstructions of the New Zealand region for the Neogene. Palaeogeography, Palaeoclimatology, Palaeoecology, 46:217–231.

Walcott RI, 1998. Modes of oblique compression: Late Cenozoic tectonics of the South Island of New Zealand. Reviews of Geophysics, 362:1–26.

Wallace LM, Beavan JP, McCaffrey R, Berryman KR, & Denys P, 2007. Balancing the plate motion budget in the South Island, New Zealand using GPS, geological and seismological data. Geophysical Journal International, 168:332–252.

Wannamaker PE, Jiracek GR, Stodt JA, Caldwell TG, Gonzalez VM, McKnight JD, & Porter AD, 2002. Fluid generation and pathways beneath an active compressional orogen, the New Zealand Southern Alps, inferred from magnetotelluric data. Journal of Geophysical Research, 107. doi: 10.1029/2001JB000186.

Warr LN & Cox SC, 2001. Clay mineral transformations and weakening mechanisms along the Alpine Fault, New Zealand. In Holdsworth RE, Strachan RA, Magloughlin JF, & Knipe RJ, editors, The Nature and Tectonic Significance of Fault Zone Weakening: Geological Society of London Special Publication, volume 186, pages 85–101. Geol. Soc. London.

Wech AG, Boese CM, Stern TA, & Townend J, 2012. Tectonic tremor and deep slow slip on the Alpine Fault. Geophysical Research Letters, 39(10). doi:10.1029/2012GL051751.

Wellman HW, 1953. Data for the study of Recent and late Pleistocene faulting in the South Island of New Zealand. The New Zealand Journal of Science and Technology, 34B:270–288.

Wellman HW, 1955. New Zealand Quaternary tectonics. Geologische Rundschau, 43:248–257. doi:10.1007/BF01764108.

Wellman HW & Willett RW, 1942. The geology of the West Coast from Abut Head to Milford Sound-Part 1. Transactions of the Royal Society of New Zealand, 71:282–306.

Wellman HW & Wilson AT, 1964. Notes on the geology and archeology of the Martins Bay district. New Zealand Journal of Geology and Geophysics, 7:702–721.

Wells A & Goff J, 2007. Coastal dunes in Westland, New Zealand, provide a record of paleoseismic activity on the Alpine fault. Geology, 35(8):731–734. doi:10.1130/G23554A.1.

Wells A, Yetton MD, Duncan RP, & Stewart GH, 1999. Prehistoric dates of the most recent Alpine fault earthquakes, New Zealand. Geology, 27:995–998. doi:10.1130/0091-7613(1999)027<0995:PDOTMR>2.3.CO;2.

Wesnousky SG, 1988. Seismological and structural evolution of strike-slip faults. Nature, 335:340–342. doi:10.1038/335340a0.

Wesnousky SG, 1994. The Gutenberg-Richter or Characteristic Earthquake Distribution, Which is It? Bulletin of the Seismological Society of America, 84(6):1940–1959.

Wibberley CAJ & Shimamoto T, 2003. Internal structure and permeability of major strike-slip fault zones: The Median Tectonic Line in Mid Prefecture, southwest Japan. Journal of Structural Geology, 25:59–78.

Wibberley CAJ & Shimamoto T, 2005. Earthquake slip weakening and asperities explained by thermal pressurization. Nature, 436:689–692. doi:10.1038/nature03901.

Wibberley CAJ, Yielding G, & Di Toro G, 2008. Structure of Fault Zones: Implications for Mechanical and Fluid-flow Properties. Structure of Fault Zones: Implications for Mechanical and Fluid-flow Properties, 299:5–33.

Wightman R & Little T, 2007. Deformation of the Pacific Plate above the Alpine Fault ramp and its relationship to expulsion of metamorphic fluids: An array of backshears. Geophysical Monograph Series, 175:177–205.

Wilson B, Dewers T, Reches Z, & Brune JN, 2005. Particle size and energetics of gouge from earthquake rupture zones. Nature, 434:749–752.

Wintsch RP & Yeh MW, 2013. Oscillating brittle and viscous behavior through the earthquake cycle in the Red River Shear Zone: Monitoring flips

between reaction and textural softening and hardening. Tectonophysics, 587:46–62.

Wintsch RP, Christoffersen R, & Kronenberg AK, 1995. Fluid-rock weakening of fault zones. Journal of Geophysical Research, 100(B7):13021–13032. doi:10.1029/1994JB02622.

Wood BL, 1962. Sheet 22 – Wakatipu. Geological map of New Zealand 1:250,000. Wellington. page 22.

Wood PR & Blick GH, 1986. Some results of geodetic fault monitoring in South Island, New Zealand. In Reilly WI & Harford BE, editors, Recent Crustal Movements of the Pacific Region, volume 24, pages 39–45. Royal Society New Zealand Bulletin.

Wright C, 1998. Geology and Paleoseismology of the Central Alpine Fault New Zealand. Master's thesis, University of Otago, Dunedin, New Zealand.

Xia K, Huang S, & Marone C, 2013. Laboratory observation of acoustic fluidization in granular fault gouge and implications for dynamic weakening of earthquake faults. Geochemistry Geophysics Geosystems, 14(4):1012–1022. doi:10.1002/ggge.20076.

Yang H, Zhu L, & Cochran E, 2011. Seismic structures of the Calico fault zone inferred from local earthquake travel time modeling. Geophysical Journal International, 186:760–770.

Yao L, Shimamoto T, Togo T, & Ma S, 2013. Structures and high-velocity friction properties of the Pingxi fault zone in the Longmenshan fault system, Sichian, China, activation during the 2008 Wenchuan earthquake. Tectonophysics, 599:135–156. doi:10.1016/j.tecto.2013.04.011.

Yasuhara H & Elsworth D, 2008. Compaction of a rock fracture moderated by competing role of stress corrosion and pressure solution. Pure and Applied Geophysics, 165:1289–1306. doi:10.1007/s00024-008-0356-2.

Yasuhara H, Elsworth D, & Polak A, 2003. A mechanistic model for compaction of granular aggregates moderated by pressure solution. Journal of Geophysical Research, 108. doi:10.1029/2003JB002536.

Yuan F & Prakash V, 2012. Laboratory observations of transient frictional slip in rock-analog materials at co-seismic slip rates and rapid changes in normal stress. Tectonophysics, 558-559:58–69.

Yuan F & Prakash V, 2013. Plate impact experiments to investigate shock-induced inelasticity in Westerly granite. International Journal of Rock Mechanics and Mining Sciences, 60:277–287.

Yuan F, Prakash V, & Tullis TE, 2011. Origin of pulverized rocks during earthquake fault rupture. Journal of Geophysical Research, 116(B06309). doi:10.1029/2010JB007721.

Zachariasen J, Berryman KR, Langridge RM, Prentice C, Rymer MJ, Stirling MW, & Villamor P, 2006. Timing of late Holocene surface rupture of the Wairau fault, Marlborough, New Zealand. New Zealand Journal of Geology and Geophysics, 49:159–174.

Zheng B & Elsworth D, 2013. Strength evolution in heterogeneous granular aggregates during chemo-mechanical compaction. International Journal of Rock Mechanics and Mining Sciences, 60:217–226.

Zoback MD, Hickman S, & Ellsworth B, 2010. Scientific drilling into the San Andreas fault zone. Eos (Transcations, American Geophysical Union), 91(22):197–204. doi:10.1029/2010EO220001.

Appendix A

The frictional strength of granular fault gouge: application of theory to the mechanics of low-angle normal faults

UNIVERSITY OF CANTERBURY
Te Whare Wānanga o Waitaha
CHRISTCHURCH NEW ZEALAND

Deputy Vice-Chancellor's Office
Postgraduate Office

Co-Authorship Form

This form is to accompany the submission of any thesis that contains research reported in co-authored work that has been published, accepted for publication, or submitted for publication. A copy of this form should be included for each co-authored work that is included in the thesis. Completed forms should be included at the front (after the thesis abstract) of each copy of the thesis submitted for examination and library deposit.

Please indicate the chapter/section/pages of this thesis that are extracted from co-authored work and provide details of the publication or submission from the extract comes:

Chapter 1, Introduction, contains material published in the following articles:

***Boulton C**, Davies T, McSaveney M 2009. The frictional strength of granular fault gouge: application of theory to the mechanics of low-angle normal faults. In: Ring U, Wernicke B eds. Extending a Continent: Architecture, Rheology and Heat Budget. London, Geological Society Special Publications 321: 9-31.*

*Davies TRH, McSaveney MJ, **Boulton CJ** 2012. Elastic strain energy release from fragmenting grains: Effects on fault rupture. Journal of Structural Geology 38: 265-277.*

Please detail the nature and extent (%) of contribution by the candidate:

Boulton et al. (2009). This was a review article. The candidate contributed, in total, 75% of the research, manuscript drafting, manuscript writing, and manuscript revision. Details of manuscript reviewers can be found in the acknowledgements section of the publication, reprinted in its entirety in Appendix A.

Davies et al. (2012). The manuscript contained a detailed analysis of the effects of fragmenting grains on fault strength and earthquake rupture. The candidate contributed, in total, 30% of the manuscript research, manuscripting drafting, manuscript writing, and manuscript revision. Details of manuscript reviewers can be found in the acknowledgements section of the publication.

Certification by Co-authors:

If there is more than one co-author then a single co-author can sign on behalf of all

The undersigned certifys that:

- The above statement correctly reflects the nature and extent of the PhD candidate's contribution to this co-authored work

- In cases where the candidate was the lead author of the co-authored work he or she wrote the text

Name: *Tim Davies* Signature: Date: *20 June 2013*

Subject: FW: Permission to include your paper in your PhD
From: Carolyn Boulton <carolyn.boulton@pg.canterbury.ac.nz>
Date: 11/11/13 12:47 PM
To: "cjb205@uclive.ac.nz" <cjb205@uclive.ac.nz>

From: Angharad Hills [angharad.hills@geolsoc.org.uk]
Sent: Tuesday, October 29, 2013 10:46 PM
To: Carolyn Boulton
Subject: Permission to include your paper in your PhD

Dear Carolyn

Thank you for your letter requesting permission to use material from GSL copyright.

Please see our permissions page for information on what you can use without permission and how to obtain permission for other material: www.geolsoc.org.uk/permissions (you don't need permission to include your paper in a PhD thesis).

Best wishes
Angharad

Ms Angharad HILLS
Commissioning Editor

Email: angharad.hills@geolsoc.org.uk
Tel: +44 (0)1225 476402 (direct)
Tel: +44 (0)1225 445046 (switchboard)
Fax: +44 (0)1225 442836
Web: www.geolsoc.org.uk
Online bookshop: www.geolsoc.org.uk/bookshop
Lyell Collection: www.lyellcollection.org

The Geological Society Publishing House
Unit 7 Brassmill Enterprise Centre
Brassmill Lane
Bath BA1 3JN
UK

From: Donna Fitzgerald
Sent: 29 October 2013 09:40
To: Angharad Hills
Subject: FW: New Enquiry at GSL website from Carolyn Boulton

Hi Angharad

One for you!

Donna

From: website@geolsoc.org.uk [mailto:website@geolsoc.org.uk]
Sent: 29 October 2013 00:02
To: enquiries
Subject: New Enquiry at GSL website from Carolyn Boulton

New Enquiry has been added at GSL website:

Name: Carolyn Boulton
Email: carolyn.boulton@pg.canterburya.c.nz
Fellow Number:
Department: enquiries@geolsoc.org.uk
Enquiry: Hello. I would like to request permission to include a paper that I wrote: Boulton, C.J., T.R. Davies, and M.J. McSaveney (2009), The frictional strength of granular fault gouge: application of theory to the mechanics of low-angle normal faults, Journal Geological Society London Special Publications, 321, 9-31. As an appendix in my PhD thesis. Please can you provide me with written permission? Thank you, Carolyn

---

This email is confidential and is intended for the addressee(s) only. If you have received it in error, please do not reproduce or disseminate the contents of this message; please contact us by return email, or by telephone on +44 (0)20 7434 9944, and delete this message and any copies of it from your computer systems. The Society does not accept liability for individuals' opinions, advice or views expressed in this email. The Geological Society of London is a registered charity, number 210161, registered address Burlington House, Piccadilly, London, W1J 0BG.

This e-mail has been scanned for all viruses by Star Internet. The service is powered by MessageLabs. For more information on a proactive anti-virus service working around the clock, around the globe, visit: http://www.star.net.uk

---

The frictional strength of granular fault gouge: application of theory to the mechanics of low-angle normal faults

Carolyn Boulton, Tim Davies, Mauri McSaveney

Boulton C, Davies TRH, McSaveney MJ 2009. The frictional strength of granular fault gouge: application of theory to the mechanics of low-angle normal faults. In: Ring U, Wernicke B eds. Extending a Continent: Architecture, Rheology, and Heat Budget. London, Geological Society Special Publications 321: 9-31, doi:10.1144/SP321.2.

Abstract

There is a persistent body of literature that suggests low-angle normal faults (LANF) form and slip seismically; if true, the effective friction coefficient is much lower (< 0.3) than that found in laboratory tests of rock friction (~ 0.8) and in low displacement faults which lack well-developed fault cores. This paper summarizes and discusses the mechanisms proposed to explain the low apparent friction of crustal-scale faults with low resolved shear stresses. Emphasis is placed on differentiating static weakening mechanisms, operating at strain rates ~ 10^{-12} s^{-1} - 10^{-15} s^{-1}, from dynamic weakening mechanisms, operating at strain rates > 10^{-1} s^{-1}. Previous published explanations for low fault friction do not appear to meet the key requirements of (i) reducing both static and dynamic frictional strength of LANF and (ii) operating only along crustal-scale faults. Fault rock assemblages in quartzo-feldspathic continental crust reveal that grain size reduction, or comminution, plays an fundamental role in fault zone development. As a fault accrues displacement, a fault core forms which contains granular material. We postulate that dynamic rock fragmentation occurs during the shearing of confined granular material; dynamic fragmentation is a volume-dependent mechanism responsible for reducing the static and dynamic frictional strengths of faults.

Introduction

Brittle normal faults accommodate crustal extension and commonly exhibit cumulative slips exceeding 10 km. If normal faulting took place with conventional dips (> 30º), then 10 km of extension on a single fault would necessarily be associated with > 5 km of vertical structural relief. Some normal faults have extensions of 100 km or more, and typical extensions are 10-50 km, implying implausible relief generation (e.g. Ring et al. 2001; Axen 2004). Logically, large-extension normal faults should not occur. However, this problem is at least partly resolved by the fact that large displacement normal faults usually have low inclinations to the horizontal. Fault mechanics theory dictates that normal faults should slip at dips of no less than 30^{o} to the horizontal, so a kinematic conundrum is replaced by a theoretical one (Anderson 1951; Byerlee 1978; Sibson 1983, 1994).

Fundamentally, in theory and in practice, shear failures in triaxially-loaded rocks align at about 30º to the axis of maximum compressive stress in rock types with typical angles of internal friction of ~ 30 - 45º. The vertical lithostatic load is the maximum principal stress in extensional tectonic settings, so normal faults should occur at an angle of ~ 30^{o} to 60^{o} from vertical (Anderson 1951). Nevertheless, numerous examples of low-angle normal faults (LANF) dipping less than 30^{o} occur worldwide: in the Basin and Range province of North American (Lister and Davis 1989; Cowan *et al*. 2003); Greece (Forster and Lister 1999); the East African Rift System (Morley 1999); the Northern Appenines of Italy (Collettini and Barchi 2004; Smith *et al*. 2007) and West Iberia (Dean *et al.* 2008). Thermal, paleomagnetic and structural constraints suggest that LANF initiated and were active at very low dips (e.g. Wernicke 1995). In the field, LANF truncate and post-date high angle normal faults, and these structural relationships suggest a vertical principal compressive stress during the time of LANF formation (Reynolds and Lister 1987; Axen and Selverstone 1994). In order to form LANF, then, the friction coefficient of the rock must be less (and sometimes substantially less) than the laboratory ("Byerlee") value of about 0.6 to 0.85 (Byerlee 1978).

Field investigations consistently measure Byerlee friction values in crustal rocks (e.g. McGarr and Gay 1978; Brudy *et al*. 1997), and historical records of

seismicity have also failed to resolve the problem of LANF. Evidence gathered from the seismological record substantiates fault mechanics tenets, as no clearly resolved large magnitude (M>5.5) earthquake has occurred on a normal fault nodal plane dipping less than 30^{o} (Jackson and White 1989; Colletini and Sibson 2001). Some convincing geological and seismic reflection evidence exists showing that the 1954 Dixie Valley earthquake (M_s=6.8), Dixie Valley, Nevada, ruptured a low-angle normal fault dipping 25 to 30^{o} to a depth of 2.7 km. Fault plane solutions for the Dixie Valley earthquake, however, are obscured by waveforms from the Fairview Peak earthquake (M_s = 7.2), which occurred 4 min and 20 s earlier (Abbott et al. 2001). The lack of recorded, unambiguous, moderate to large ruptures on LANF has led to the deduction that LANF fail aseismically, microseimically, or in large earthquakes with long recurrence intervals (Reitbrock *et al*. 1996; Collettini and Barchi 2004; Wernicke 1995).

Although it appears theoretically unlikely, sufficient seismological and geological evidence exists to justify considering that LANF form at their present inclinations and remain seismically active (e.g. Wenicke 1995; Rigo *et al*. 1996; Abbott et al. 2001; Axen 2004). This is especially true when one considers that a number of other crustal-scale faults also appear to require low friction to explain the stress conditions under which they rupture (e.g. the Cascadia subduction fault, USA, Wang *et al*. 1995; the San Andreas fault, USA, Townend and Zoback 2004; the Marlborough fault zone, New Zealand, Balfour *et al.* 2005). This independent association of large-scale faulting with low friction lends some credibility by association to the suggestion that LANF slip seismically under resolved stresses that necessitate low frictional strength both statically and dynamically.

Geology and Occurrence of LANF

A low-angle normal fault, or detachment fault, is a moderately- to gently-dipping fault that accommodates crustal extension. While gently dipping normal faults often appear in seismic reflection profiling of the upper few kilometres of sedimentary basins, these faults are commonly listric structures that sole into detachment horizons (for a review of the mechanisms generating fault curvature see Vendeville 1991 and White and Yielding 1991). In this paper, the term LANF applies to gently dipping (< 30°) planar fault surfaces of large areal extent (up to 200 km^2) along which large

magnitude slip (typically 10 – 50 km) has taken place. These structures have been described by Coney (1980), Lister and Davis (1989), John and Foster (1993), Wernicke (1995), Axen (2004), and Dean et al. (2008) among others.

Many LANF juxtapose unfaulted crystalline footwall rocks against faulted sedimentary and/or volcanic hangingwall rocks (Lister and Davis 1989; John and Foster 1993) (Fig. 1). Ductile rocks in the footwall of LANF include mylonites and mylonitic gneisses developed under greenschist to amphibolite facies metamorphic conditions. Goodwin (1999) documented intense comminution and pseudotachylyte ("fossil earthquake") formation on narrow shear surfaces in mylonitic LANF rocks, illustrating alternating brittle and ductile behaviour at the base of the seismogenic crust. At lower temperatures in the shallow crust, ductile fault rocks are overprinted by brittle deformation (Coney 1980). Field descriptions of brittle fault rocks commonly highlight the occurrence of finely comminuted cataclasite, fault gouge, and fault breccia on narrow slip zones in the fault core (e.g. John and Forster 1993; Cladouhos 1999; Hayman 2006). The term fault core was defined by Caine et al. (1996) as 'the structural, lithologic, and morphologic portion of the fault zone where most of the displacement is accommodated'.

Low-angle normal faults form in various tectonic settings in the continental crust: in continental rift-related metamorphic core complexes (e.g. Crittenden et al. 1980; Lister and Davis 1989; Wernicke 1995; Axen 2004); in highly extended passive continental margins (e.g. Manatschal *et al*. 2000); in an active propagating oceanic-to-continental rift (Kopf 2001); and in a post-collisional region of extension (Colletini and Holdsworth 2004). Whereas evidence of fluid involvement during faulting is scarce along some LANF (Hayman 2006), other detachment faults are conduits for hydrothermal fluids, meteoric fluids, saline seawater, mantle-derived fluids, or voluminous CO_2 produced from mantle degassing (Spencer and Welty 1986; Morrison 1994; Losh 1997; Kopf 2001; Collettini and Barchi 2004; Miller *et al*. 2004; Smith et al. 2008). LANF appear to have been active structures in a wide variety of crustal rocks with both hydrostatic and lithostatic pore-fluid pressures.

The initiation of low-angle normal faults remains one of the most contentious issues in fault mechanics. Some authors contend that low-angle normal faults form at

a high angle, slip, and rotate to shallow angles as simple tilted fault blocks (e.g. Wong and Gans 2008) or along other normal faults (e.g. Proffett 1977). In a series of widely accepted papers, Wernicke (1981, 1985, 1992) and Wernicke and Axen (1988) detailed a "rolling hinge" model to explain the formation and rotation of low angle normal faults. In the model, a large LANF transects the upper 15-20 km of the crust and undergoes slip, which results in asymmetrical denudation of the hangingwall strata. Isostatic rebound then results in flexure of the LANF footwall and corollary rotation of the initially steep fault into shallow dips. Nevertheless, compelling evidence exists for the initiation of shallowly-dipping LANF (John and Foster 1993; Wernicke 1995); this requires both a static and dynamic low-friction mechanism.

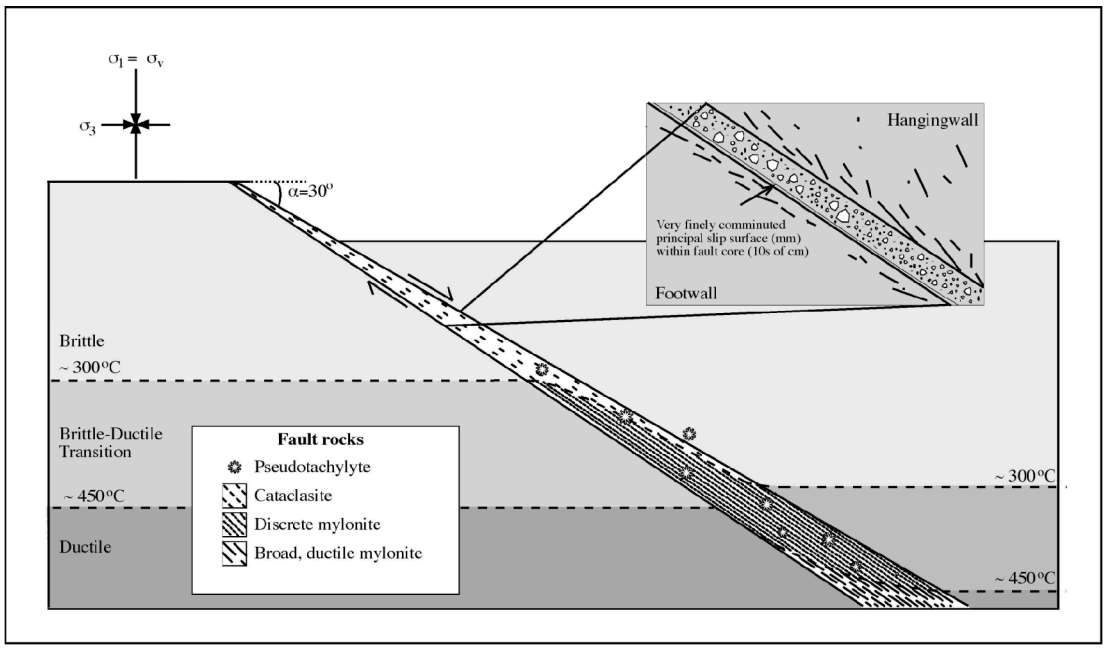

Fig. 1. A diagrammatic representation of a low angle normal fault showing a typical assemblage of ductile and brittle fault rocks. In cross section, LANF fault cores commonly containing a narrow (mm-cm) principal slip zone of highly comminuted ultracataclasite surrounded by finely comminuted cataclasite and gouge fragments (cm-m wide). Fault core rocks have a fractal particle size distribution. Highly damaged and brecciated rock may extend into the hangingwall 10s to 100s of meters away from the slip zone. Footwall rocks are commonly intact and comprise preserved mylonites formed in the ductile lower crust (after Handy et al. 2007).

This paper addresses the question: can the application of granular flow theory, coupled with a consideration of the elastic strain energy released by grains deforming by dynamic fragmentation (Davies et al. 2007), explain the origin and significance of the brittle fault rocks exposed along low-angle normal faults? In light of ongoing debate about the apparent weakness of crustal-scale faults such as the San Andreas Fault, this paper: (1) presents a summary of frictional mechanics; (2) provides an overview of fault weakening mechanisms capable of producing low apparent friction on faults; (3) summarises descriptions of brittle fault rocks exposed along the Chemehuevi and Black Mountain detachment faults, California, USA; and (4) proposes that the widespread occurrence of cataclastic fault rocks in fault cores warrants consideration of how granular flow theory helps to explain the low frictional strength of brittle fault rocks. In conclusion, we suggest that dynamic fragmentation is the most plausible mechanism so far proposed for explaining the low static and dynamic frictional strengths of crustal-scale faults.

Mechanics of friction

At temperatures below about 350^{o}C, corresponding to about 12 km depth in continental crust, quartzo-feldspathic rocks fail by brittle fracturing. The constitutive equations governing brittle failure are based on linear elastic fracture mechanics, and the empirical constitutive equation for the shear failure of intact rock is the Mohr-Coulomb criterion:

$$\tau \geq C_o + \mu_i \sigma_n' \qquad (1)$$

where τ is the shear stress, C_o is the cohesive strength, μ_I is the internal coefficient of friction and σ_n' is the effective normal stress. Terzhagi and Peck (1948) illustrated that the effective normal stress is equal to:

$$\sigma_n' = \sigma_n - P_f \qquad (2)$$

where the pore fluid pressure P_f is given by

$$P_f = \rho_w g z \quad (3)$$

where ρ_w is the density of the pore fluid, g is the acceleration due to gravity and z is the depth below the fluid surface. The formation of new faults occurs at about +/- 30^o to the maximum compressive stress when conditions of the Mohr-Coulomb criterion are met.

Failure of pre-existing cohesionless planes is governed by Amonton's Law:

$$\tau = \mu_s \sigma_n' \quad (4)$$

where μ_s is the coefficient of static friction. Rabinowicz (1951) demonstrated that the coefficient of static friction μ_s, which corresponds to the force needed to start motion, is generally greater than μ_k, the coefficient of kinetic friction, which is operative for moving surfaces. We use the term 'strength' to refer only to the static resistance to shear, and the term 'apparent friction' to refer to either the static or dynamic frictional shear resistance of granular material.

Requirements for reduced friction

Amonton's Law (Eq. 4) shows that apparent friction can be reduced by reducing the coefficient of friction μ_s, or by reducing the effective direct stress σ_n'. During sliding, friction is determined by the morphology and properties of the solids in contact, and can only be altered by altering the profile of the contacts or the deformability of the materials. As with solid sliding, reducing friction in granular flow requires either intrinsically low sliding friction between the solid grains, or a reduction of the effective normal stress between the grains. Maveyraud *et al.* (1999) show that solid sliding friction gives consistent values of μ over a wide range of rock materials and normal pressures, as long as the material remains elastic. Thus, there are three possibilities for varying μ in sliding friction: (1) by altering the properties of the solid material via frictional-adiabatic heating or isothermal heating with depth; (2) by exceeding the elastic limit of the material and altering the micromorphology of the

surfaces via the creation of granular material; or (3) via the chemical alteration of minerals to intrinsically low-friction materials such as graphite or some sheet silicates.

The normal stress σ_n acting between surfaces in contact is the result of the applied stress field, which along faults includes the lithostatic and tectonic stresses; σ_n can be reduced by the presence of an interstitial fluid that resists some of the applied normal stress (Eq. 2) (a fluid by definition cannot resist a shear stress). If a fault core is occupied by water at hydrostatic pressure, P_f is given by Eq. (3) and the pressure gradient in the water resists normal stress. This is equivalent to the hydrostatic uplift reducing the weight of the overlying saturated rock. In the extreme case, if the pore pressure distribution is lithostatic, pore pressure resists the total weight of the overlying rock and the normal stress across the fault reduces to zero; therefore, so does the apparent friction. Any non-hydrostatic pore fluid pressure distribution, however, will tend to cause water to migrate by seepage (unless one of the fault blocks is completely impermeable) and the pressure distribution returns to hydrostatic. The overpressure will dissipate with time at a rate dependent on the permeability of the fault zone and adjacent damage zones. Besides water, other potential pore fluids include molten rock, water vapour from boiling of pore water, and CO_2 from frictional heating of carbonates (e.g. O'Hara et al. 2006; Han et al. 2007).

During shear failure in the brittle crust, seismogenic slip occurs on a fault plane at velocities of 0.1-2 ms^{-1} (Brune 1976). Earthquake rupture is a mixed process between frictional slip failure on a plane or thin zone of weakness (or pre-existing fault) and fracture of intact rock. In turn, the frictional strength of a fault during rupture is likely to be highly heterogeneous, incorporating failure criteria (Eq. 1) and (Eq. 4) as well as the local effects of pore water pressure (P_f) (Eq. 2; Ohnaka 2003; Shipton *et al*. 2006).

Thus, the requirements for reducing apparent friction on faults are that: (1) the friction coefficient μ is reduced, (2) the effective direct stress σ_n' causing frictional resistance is reduced, or (3) both of these. This applies to both static shearing ("failure") and to dynamic shearing (Fig. 2).

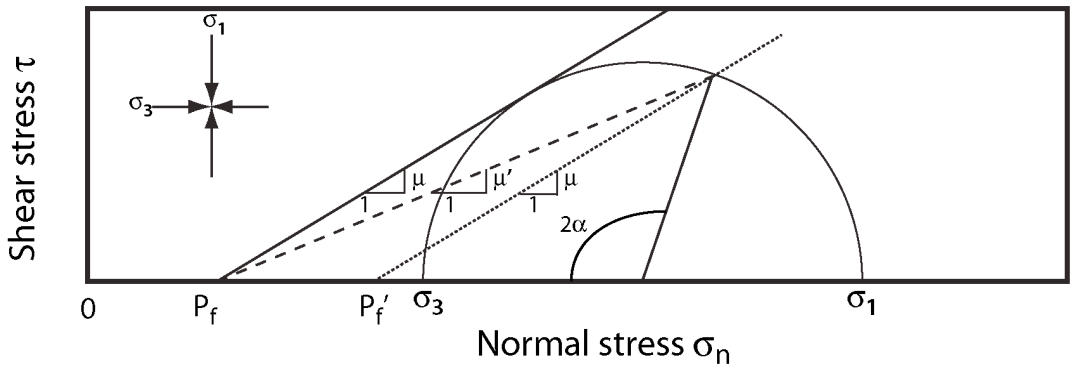

Fig. 2. A Mohr diagram illustrating the failure criteria for frictional sliding (solid line) of a misoriented cohesionless fault with a Byerlee friction coefficient $\mu = 0.6$ at hydrostatic pore fluid pressure P_f. According to Amonton's Law, shear failure will occur with a reduction in the apparent friction coefficient (μ') (dashed line) or with an increase in pore fluid pressure (P_f') (dotted line). Inset figure depicts the Andersonian stress state for normal faulting (after Townend 2006).

Field studies indicate that mature faults with large volumes of granular fault rock commonly exhibit low frictional strength (Sibson 1994; Townend 2006; J. Townend, Victoria University, Wellington, New Zealand, pers. comm. 2007). In addition, laboratory data indicate that low rock-on-rock friction occurs only with high strain rates and high grain contact stresses (e.g. Di Toro et al. 2004). These observations suggest another criterion for assessing proposed low-friction mechanisms: any low-friction mechanisms which could operate in intact rock at low stress and/or strain rate are poorly substantiated and hypothetical.

Thus, our criteria for assessing low-friction mechanisms are: they must be able to reduce apparent friction at both static and dynamic strain rates, *and* they must be only be effective on mature faults with a fault core comprising granular material.

Mechanical explanations for low frictional strength

Recent experiments with intact rocks and natural fault gouges have found that very low frictional resistance to shear can occur at high strain-rates (10^1 s^{-1} to 10^{-2} s^{-1})

under low to moderate normal stresses (0.6 to 100 MPa) (e.g. Di Toro *et al*. 2004, Mizoguchi *et al*. 2007; see also Fig. 7, Wibberly et al. 2008, for a summary of experimental data). The dramatic (more than three-fold) reduction in frictional strength has been attributed to complex thermo-poro-elasto-dynamic processes. However, low-strain-rate (10^{-4} s^{-1} to 10^{-7} s^{-1}) rock-on-rock friction tests invariably show conventional friction coefficients of 0.6 to 0.85 (Byerlee 1978). In the Earth's crust, fault rocks are generally tectonically loaded at very low strain rates ($<<10^{-12}$ s^{-1}) that are impractical to simulate in the laboratory. A number of explanations for low rock friction at very low strain rates have been proposed, mainly in the context of large faults such as the San Andreas (e.g. Townend and Zoback 2001; Scholz and Hanks 2004). Explanations for static and dynamic weak fault friction include:

1. weak materials such as silica gel (Goldsby and Tullis, 2002), talc (Moore and Rymer 2007), clay (Tembe *et al*. 2006; Numelin *et al*. 2007) or melted rock (pseudotachylyte; e.g. Sibson 1975; Sibson and Toy 2006; Hirose and Bystricky 2007) reducing apparent friction
2. flash heating of asperities (Rice 1999, 2006; Hirose and Bystricky 2007);
3. the presence of long-term pore fluid overpressures reducing effective stress (Sleep and Blanpied 1992; Sibson 2001);
4. thermal pressurization of pore fluids during frictional sliding (Sibson 1973; Andrews 2002) or elastohydrodynamic lubrication (Brodsky and Kanamori 2001)
5. Normal interface separation during rupture along a bimaterial interface (Weertman 1980; Ben-Zion 2001).
6. acoustic fluidization (Melosh 1996)

Here we briefly describe the mechanisms proposed for low-strength faulting, and comment on their apparent advantages and drawbacks, before evaluating them against the above criteria.

High pore fluid pressure

Due to the well-known effect of pore water pressure in reducing the effective stress, this is possibly the most commonly-used mechanism (Eq. (2); Terzhagi and Peck 1948; Hubbert and Rubey 1959, Sibson 1973). We discuss the mechanism first in the context of static failure.

Static Failure

Fault strength might be partly controlled by the evolution of fluid pressure in the fault zone. Arrays of mineralized veins surrounding ancient and modern normal faults provide evidence for fluid cycling, and mechanical theory can account for the failure of LANF by pore fluid overpressures (Eq. (2); Parry and Bruhn, 1990; Axen and Selverstone 1994; Sibson 2001). High pore fluid pressures can also be generated interseismically by compaction creep and porosity reduction (Sleep and Blanpied 1992). Scholz (1992) noted that brittle wall rock material cannot resist pore fluid pressure greater than the least principal stress σ_3 without fracturing in response and allowing pore fluid to drain.

Rice (1992) published a classic paper showing that fault cores can sustain high pore pressures due to locally inhomogeneous stress distributions. The Rice (1992) model requires that high pore fluid pressures be maintained within relatively permeable fault cores by either an upwelling of overpressured fluids from depth or by impermeable seals which trap fluids at high pressures (e.g. Byerlee 1990). Axen (1992) applied this model to detachment faults in the Basin and Range, USA; he cited many examples of fluid focusing and seal formation along and near LANF fault cores. Recently, Healy (2008) expanded the model of Faulkner *et al.* (2006) to show that large stress rotations are possible on fault core rocks with an anisotropic fabric; these stress rotations enable elevated pore pressures to develop without hydraulic fracturing in strike-slip faults. Models such as these have not yet been developed for normal faults, but it appears that pore fluid overpressures can develop on LANF given the required low permeability.

A number of researchers have investigated the permeability of fault gouge. Takahashi *et al.* (2007) found that dramatic slip-induced reduction of permeability occurred in quartz gouge with Na-montmorillonite at concentrations between 18 and 24% at a confining pressure of 80 MPa, suggesting that clay material concentrations of this magnitude are needed to cause sealing. At > 1 km depth in the Nojima fault zone, Japan, Lin *et al.* (2007) report that although fracture networks are important fluid conduits, they lose permeability as pore spaces collapse and cementation proceeds. Giger *et al.* (2007) found that quartz gouge could seal hydrothermally by a

combination of dissolution and precipitation creep processes above 700ºC, relevant to the mid-lower crustal regions.

Permeability-reducing processes compete with hydrolytic weakening, stress corrosion, and distributed microcracking which act to increase the permeability of fault-zone rocks (Sornette 1999; Crampin and Chastin 2003). Zoback and Townend (2001) showed that fault zone permeability is high and suggested that frictional failure on faults must dominate (largely aseismic) creep and compaction processes. Zoback *et al.* (2007) found no evidence of either cohesive materials or pore-water overpressures in the 2.7 km deep San Andreas Fault Observatory (SAFOD) drill hole, California, USA. Furthermore, whether pore-water overpressures can initiate a seismic rupture on weak faults remains a topic of ongoing research; models suggest that ruptures preferentially nucleate in regions of low pore fluid pressure (e.g. Hillers and Miller 2007).

Dynamic failure

Sibson (1973) suggested that frictional heating due to slip in an earthquake could raise the pressure of pore fluid in a fluid-saturated fault zone to near-lithostatic values, reducing effective pressure and frictional resistance during slip. Garagash and Rudnicki (2003a) concluded that shear heating might induce the high pore fluid pressures that destabilize slip. However, complicated feedback mechanisms occur because high pore fluid pressures induce fault dilatancy, which subsequently reduces shear heating. The feedback process was analysed further by Garagash and Rudnicki (2003b), who concluded that weakening effects were strongly dependent on whether fault zones are hydraulically and thermally isolated from the surrounding rock mass. Indeed, permeability is unlikely to remain constant during an earthquake and it may become large enough that fluid pressure is limited by the permeability of the surrounding damage zone (Andrews 2002).

A difficulty with thermal pressurization of aqueous fluid is that seismic slip is required to generate sufficient heat to elevate pore fluid pressures. This topic has recently been examined closely by Rice (2006) and Rudnicki and Rice (2006). Consideration of fault rock permeabilities leads to the conclusion that shear heating alone cannot nucleate unstable slip in the absence of independent slip weakening, but

that it can have an effect following strong stress perturbations. If fault rupture is preceded by slow slip (<< mm s^{-1}), thermal pressurisation can occur, but over the critical weakening distance, slip will be at normal friction because there is no low-friction mechanism operating. This means that the overall friction coefficient must be a combination of normal friction in the early phases and low friction during the late phases. Finally, while high pore fluid pressures may develop more readily in the thick gouge of large-displacement (> 1 km) faults, this is offset by the greater difficulty of establishing and maintaining high pressures over sufficiently large areas of the fault.

Brodsky and Kanomori (2001) presented an analysis elastohydrodynamic lubrication. According to this theory, grains in a fault core act like bearings which are lubricated by a thin film of slurry comprising finely comminuted gouge mixed with water. During frictional sliding, the slurry decreases the apparent friction by increasing the pore fluid pressure. In the model, full lubrication pressure is reached after a critical slip distance of ~0.5 m if the permeability of the surrounding rock is sufficiently low to confine the fluid to the slipping fault. A significant advantage of this model over thermal pressurization of pore fluids is that, at most, fluid pressures reach 40% of the lithostatic load; they are therefore unlikely to induce hydraulic fractures. Like thermal pressurisation, however, elastohydrodynamic lubrication depends on impermeable wall rocks bounding the fault core and a critical slip distance in order to act as an effective mechanism for reducing dynamic fault friction.

Weak fault materials

Minerals. Fluids in fault zones induce chemical reactions that alter the rheology of fault rocks. Most of the reactions result in the formation of weaker minerals (e.g. Janecke and Evans 1988, Gratier and Gueydan 2007). Weak materials with low coefficients of friction (μ = 0.2-0.4) include platey minerals such as talc, water-saturated sheet silicates, and graphite (Moore and Lockner 2004). If platelets are aligned parallel to each other, weak interstitial bonds (talc, graphite) or the high-pressure interstitial water (clays) allow the platelets to shear at low applied stress. A shear zone containing these materials can therefore be expected to have low static friction, and also low dynamic friction if the orientation of the platelets is not altered by large strains. Recently, Moore and Rymer (2007) suggested that principal slip

surfaces composed of talc, a low shear strength mineral that accommodates shear displacement by (aseismic) stable sliding, may be responsible for the observed static and dynamic low frictional strength of the San Andreas Fault.

At lower greenschist facies conditions at the base of the seismogenic zone, feldspar breakdown to fine-grained muscovite (or sericite) commonly occurs, and this reaction may be an important reaction-softening step in granitic fault zones. This mechanism has also been invoked to explain the low frictional strength of the San Andreas fault zone (Evans and Chester 1995; Wintsch *et al*. 1995). At high temperatures and pressures, micas deform relatively easily by grain boundary sliding, cleavage plane slip, and dislocation glide; the formation of an aligned mica foliation weakens highly strained fault rocks. Wibberley (1999) pointed out, however, that granitic faults may strengthen or weaken due to feldspar to mica reactions depending on the behaviour of silica released during the reactions; silica cement strengthens faults.

During dynamic fault failure, Sulem *et al*. (2007) showed that shear heating and fluid pressurization are possible mechanisms leading to full fluidization of clay material in a shear band. Hirose and Bystricky (2007) also showed in high velocity laboratory experiments that phyllosilicate dehydration due to frictional heating resulted in a marked decrease in frictional strength after very high strains. Boutareaud *et al.* (2008) tested natural clay-clast (16% clay) aggregates from fault gouge in a shear apparatus at low stresses (0.6 MPa) and found that very high strains (tens of metres) were needed to significantly reduce friction.

Fault rupture zones, however, rarely contain high concentrations of these materials. Usually the low-friction materials are found at low concentrations in the fractal, cohesionless angular rock fragments comprising the gouge. Their ability to reduce the total friction of the gouge depends critically on the material being present in high concentrations or localizing onto very thin principal slip surfaces. Takahashi *et al.* (2007) found that the friction coefficient of quartz gouge fell from 0.7 to 0.4 as the clay (Na-montmorillonite) concentration increased from zero to 50% by volume. Brown *et al.* (2003) found similar behaviour with smectite, illite and chlorite. In addition, the frictional resistance of many sheet silicates varies with depth: pressure

and temperature conditions, as well as slip rate, determine whether the minerals exhibit stick-slip (seismic) or stable (aseismic) frictional sliding (Moore and Lockner 2004). Testing material recovered from the SAFOD drill hole, Carpenter *et al.* (2007) found normal friction coefficients for most materials. Serpentinite melange (which can produce talc) had a friction coefficient of 0.2-0.3, but was found to strengthen with increasing velocity under both dry and saturated conditions.

In summary, if low-friction materials are present at high concentrations or are localized onto thin principal slip surfaces, reduced frictional strength can occur. Numelin *et al*. (2007) highlight the importance of clay fabric development in reducing the frictional strength of LANF in the upper brittle crust (< 5 km depth), and emphasize that clays enable the faults to undergo stable (aseismic) slip. This mechanism for low apparent friction depends strongly on the spatial distribution and interconnectivity of the weak clay fabric. Dynamic (seismic) fault failure involving grain comminution down to nanometre size (Heilbronner and Kuelen 2006) at high strain rates in narrow shear bands (Rice 2006), probably disrupts the low-friction arrangement of parallel platelets.

Silica gel. Frictional sliding on smooth surfaces of rock with silica contents of 70% or greater facilitates the generation of a layer of silica gel that results in a dramatic decrease in shear resistance (Yund *et al*. 1990; Goldsby and Tullis 2002; Di Toro *et al*. 2004). These studies show that the amorphous material formed as a result of grain comminution at lower speeds, 10mm to 100 mm/s, than required for weakening caused by flash heating, but it requires displacements of about 1m to attain steady state. Thus, the weakening distance may be related to the distance necessary to accumulate a thick layer of gouge and/or lubricant. Based on inference and microstructures, Goldsby and Tullis (2002) and Di Toro *et al*. (2004) suggested that shear lubricates the surface through production of a highly comminuted and amorphous material that may be thixotropic silica gel, a near-fluid that becomes less viscous when strained. When shearing ceases the material regains strength with time at a rate controlled by the bond forming chemical reaction.

Heating

Under the stresses experienced by a large fault during rupture, friction inevitably generates heat. Thermal pressurization of pore fluid was discussed previously. This section will focus on melting of rock to generate pseudotachylyte (e.g. Hirose and Shimamoto 2005a) and flash heating at high-stress contact asperities with local melting (e.g. Rice 1999). Clearly, these mechanisms relate only to dynamic friction as ambient temperatures sufficient to develop melt do not occur in the brittle crust.

Rock melting. Pseudotachylyte is a very fine-grained fault rock that is generally thought to form coseismically by frictional melting and comminution. Spray (1995) demonstrated experimentally that comminution is a necessary precursor to frictional melting, and his results have been verified by Di Toro *et al*. (2004) among others. Field evidence suggests that pseudotachylytes may be divided into melt-origin types which preserve glass or glassy material (e.g. Philpotts 1964; Sibson 1975) or crush origin types, which form by mechanical stress during intense grain comminution (e.g. Ozawa and Takizawa 2007).

Pseudotachylyte formed by frictional melting is rarely found in the geological record, suggesting either that it rarely forms or that it is rarely preserved (Sibson and Toy 2006). Documented examples of melt-origin pseudotachylyte formed during coseismic slip indicate that pseudotachylyte first appears as isolated patches of viscous fluid, which *increase* the frictional resistance to shear; frictional resistance decreases significantly only when a continuous molten layer is established (Warr and Van der Pluijm 2005; Hirose and Shimamoto 2005a; Fialko and Khazan 2005).

Pseudotachylyte formed by the comminution of grains to amorphous materials several tens of nanometers in size can behave similarly to melt-origin pseudotachylyte (Ozawa and Takizawa 2007). Pseudotachylyte formed in this way occurs in the field as both fault veins and injection veins, indicating that it flowed under pressure gradients like a viscous fluid. We shall later show that dynamic comminution can allow a granular material to flow under relatively low applied stresses, and this process may also explain the behaviour of crush origin pseudotachylyte without invoking high temperatures.

Flash heating of asperities. During rock-on-rock sliding experiments, flash heating at asperity contacts causes weakening at slip speeds above 100 mm/s in quartzite, gabbro, and granite, which all melt at room pressure, as well as soda lime glass (Goldsby and Tullis 2002; Rempel 2006). Flash heating is velocity-dependent, and above 100 mm/s, the coefficient of kinetic friction drops rapidly to < 0.2 when shear localizes along a thin principal slip zone (Rice 1999, 2006).

Flash heating at asperity contacts does not occur in other rock types. In calcite marble and dolomite, calcite undergoes a phase change and breaks down to CaO and CO_2. Recent reviews reveal that the breakdown of clays in natural fault gouge via dehydration may prevent weakening from flash heating because of pore fluid pressurization. During high velocity shearing, clayey fault gouge becomes fully fluidized, but it remains difficult to determine whether the effect is from shear heating or fluid pressurization (Brantut *et al*. 2007; Sulem *et al*. 2007).

Recent experiments by Goldsby and Tullis (2007) suggest that gouge material behaves differently than intact rocks. In the presence of a thin fault gouge (< 1 mm), a velocity greater than coseismic slip rates (> 1 m/s) is required to initiate flash heating at grain contacts. This suggests that flash heating at asperity contacts does not occur in fault gouge. Given the ubiquity of gouge in real faults, the role of flash heating of asperities in fault weakening appears questionable.

Mechanical processes.

Here we deal with mechanisms that stem from aspects of contact forces between rocks or fragments experiencing shear forces, which do not require the presence of anomalous materials, pore fluids, or heat.

Self-healing slip pulses. The rupture characteristics of a number of recorded earthquakes correspond to the propagation of a coherent slip pulse along the fault, with the fault healing itself again after the passage of the pulse (e.g. Heaton 1990). This makes sense - for example, suppose a fault rupture causes 1 m of horizontal ground motion at a velocity of ~ 1 ms^{-1}, taking 1 second to complete. At a rupture

propagation velocity of 2 km s^{-1}, the rupture will propagate ~ 2 km while the ground at any one point is moving. Thus the passage of the rupture along the fault will be in the form of a 2-km long non-uniform slip pulse propagating at 2 km s^{-1}.

Self-healing slip pulses propagate near the Rayleigh wave speed along bimaterial interfaces (Heaton 1990; Ben-Zion 2001) and generate spatially localized normal interface separation. Small faults, on which the majority of ongoing seismicity occurs, may be considered to be surrounded by nominally homogenous solid rock. However, plate boundaries and other major faults generally resemble bimaterial interfaces because zones of crushed rock, cataclasite and foliated gouge abruptly abut intact rock. In addition, different rock bodies are juxtaposed across large displacement faults. Low angle normal faults, for example, commonly juxtapose high-grade metamorphic and plutonic footwall rocks against poorly consolidated sedimentary and/or volcanic hanging wall rocks (e.g. Coney 1980).

Rupture along a bimaterial interface may differ significantly from a corresponding rupture in a homogeneous solid. The differences arise from the fact that ruptures propagating along a bimaterial interface induce dynamic changes in normal stress near the tip causing normal stress to vary as a function of slip (Weertman 1980; Ben-Zion 2001). The interaction between slip and normal stress along a bimaterial interface can dynamically reduce the friction strength to zero and may lead to local fault opening (Eqs 1 and 4) (Andrews and Ben-Zion 1997; Anooshehpoor and Brune 1999). This makes bimaterial interfaces mechanically favoured surfaces for rupture propagation and may help to help the reactivation of misoriented faults with lower resolved Coulomb stresses rather than the formation of new faults optimally oriented for failure (Fig. 2). However, the degree to which interfaces separate during slip remains poorly understood (Rubinstein *et al*. 2004). In addition, this mechanism requires slip to be present in order to initiate the pulse, so applies only to dynamic shear resistance.

Acoustic fluidisation. This mechanism was first proposed by Melosh (1976) in the context of impact crater formation, and applied by Melosh (1996) to faulting. It involves the effect of vibrations passing through granular materials, in such a way that the interparticle stresses vary significantly with time; in particular, at times the direct

stresses are low so that frictional resistance to sliding is low. The mechanism is thus specifically applicable to granular gouge, but it presumably requires some initial source of vibration so is applicable only to dynamic friction. Sornette (1999) has closely examined acoustic fluidisation in the earthquake context, noting (a) that the mechanism predicts slip velocities far smaller than those observed during earthquakes, suggesting that if acoustic fluidisation is present it is not significant; and (b) that modifying the analysis to address this point by using realistically-varying parameters creates a high degree of non-linearity. Melosh (1996) claims that the theory has been confirmed by experiment, but one of the quoted sources (Zik *et al*, 1992) for example, reports reduced friction on a sphere moving through other spheres that are *vibrating at accelerations greater than that of gravity*; whereas Collins and Melosh (2003) are at pains to point out that in acoustic fluidisation, individual grains are *not* vibrating energetically.

Another significant difficulty with the concept of acoustic fluidisation is that, as presented, it takes no account of grain comminution. As we discuss below, comminution drastically alters the behaviour of shearing grains, so the applicability of acoustic fluidisation to faulting is difficult to assess.

Evaluation of mechanisms

We have five main contenders for causing the low apparent friction exhibited by large-scale faults: (1) pore fluid overpressure and thermal pressurization of pore water; (2) weak material (talc, silica gel, clay); (3) heating (rock melting and flash heating at asperity contact); (4) self-healing slip pulse; (5) acoustic fluidization

We also have two major criteria on which to evaluate them: (a) does this mechanism function equally well in both static and dynamic conditions; (b) does this mechanism only function for large-scale faults?

The result of evaluation on this basis is shown in Table 1. None of the existing mechanisms has the potential to explain the static and dynamic weakness of large-scale faults, together with the high strength of small faults. The high strength of small faults requires only that static or dynamic apparent friction be high, not both. High

pore fluid pressure fails because it also predicts both low static (due to long-term overpressure) and low dynamic (due to heating) apparent friction in small faults. The other mechanisms, being applicable equally to both large and small faults, predict that large and small faults should behave identically, which is not the case.

Table 1 Evaluation of weak fault mechanisms

Mechanism	**Static**	**Dynamic**	**Large-scale only**
Fluid overpressure	√	X	X
Weak material	√	X	X
Heating	X	√	X
Self-healing slip pulse	X	√	X
Acoustic fluidization	X	√	X

In the light of this conclusion, we now review the effects of rock fragmentation on the dynamics of confined granular flow; this mechanism has been outlined in increasing detail in the context of land- and blockslides (Davies *et al*. 1999, 2006, 2007; Davies and McSaveney 2002, 2005, 2008 *a, b*; McSaveney and Davies 2007, 2006, 2005; McSaveney *et al*. 2000; Smith *et al*. 2006). It appears to meet both the above criteria.

Granular friction

The Mohr-Coulomb criterion (Eq. 1) and Amonton's Law (Eq. 4) work very well to describe the macroscopic friction of both solids and granular materials sliding tangentially with respect to another. Detailed experiments conducted by Bowden and Tabor (1986), however, showed that frictional strength correlates strongly with the real area of contact between two sliding surfaces, where real area of contact is the sum

of the contacting spots or asperities on a surface. Very smooth surfaces and very rough surfaces have higher contact areas than intermediate surfaces, and have higher friction coefficients (see Rabinowicz 1995 for a detailed discussion).

In granular materials, the relationship between the frictional strength of the material and contact area is further complicated by the fact that multiple variably-sized and irregularly-shaped particles carry the shear and normal stresses at point contacts. Hence the stresses at the individual contacts are indeterminate (but much higher than the overall mean stress), and the need for large-scale averaging is much more apparent than with solid friction (e.g. Majmudar and Behringer 2005). Moreover, the spatial arrangement of platy grains such as sheet silicates may be initially non-random, causing unusually high or low initial (static) frictional strength.

During compressive shear deformation, granular materials form an inhomogeneous contact network which carries most of the external load along force chains (e.g. Matsuoka 1974; Cundall and Strack, 1979; Cates *et al*. 1999; Morgan and Boettcher 1999; Anthony and Marone 2005). Force chains are quasi-linear structures of highly stressed grains surrounded by less-stressed grains in a weak network. Most of the stress applied to the shearing granular material is transmitted from one shear boundary to the other along force chains. In simple shear these initially assemble parallel to the direction of maximum compressive stress and strain (about 45^{o} to the shear zone walls) and subsequently rotate in the shear strain field to cause both shear zone dilatation and increase in force-chain shear stress (Fig. 3).

Granular flow requires force-chains to fail so that strain can continue, and failure can be by intergranular slip, grain rotation, buckling or grain crushing (Biegel *et al*. 1989; Hooke and Iverson 1995; Fig. 3). Under high lithostatic stresses with angular grains, grains are most likely to fail by buckling, or alternatively by crushing, a process in which force-chain loading causes a particle to fragment (Sammis and King 2007). Following Grady and Kipp (1987), we term particle crushing during shear *dynamic fragmentation*. The strength of grains varies with grain size, temperature, confining pressure, and strain rate; for silicates, grain strength also varies with the presence of absence of water (e.g. Paterson 1978). The way in which force chains fail also varies with these factors.

Force chains continuously form and fail to accommodate shear deformation, and this process causes sheared granular materials to develop self-similar particle-size distributions (PSDs) (Marone and Scholz 1989). In confined flow, force chains are generally ten grains wide and the total width depends on the distribution of particle sizes within the granular material (Francois *et al.* 2002). Sammis and Ben-Zion (2008) showed that during compressive failure, shock loading and subcritical crack growth can form fragments much smaller (< 10 nm) than the theoretical grinding limit (1 μm). This result means that grains will continue to fragment to smaller sizes in granular flow, driving shear localization onto thinner principal slip zones as comminution proceeds. For a fault core containing granular gouge with a mean grain size of 100 μm, slip may occur along a plane 1 mm-wide. Fault cores on large-displacement faults commonly contain mm-thick ultracataclasite along which a majority of fault slip is inferred to have taken place (e.g. Chester and Logan 1987). Results from numerical models of compressional shear fracture initiation in intact crystalline and porous rocks show that force chains comprising individual minerals or grains may form to carry the applied stress in a manner similar to that in noncohesive granular materials (Potyondi and Cundall 2000; Hazzard *et al.* 2000).

Dynamic rock fragmentation.

As outlined above, experimental, numerical and computational studies in granular physics indicate a small proportion of grains in a granular material carry the bulk of the applied shear stress and normal stress. The frictional behavior of dense granular material depends on micro-scale interactions that occur at grain contacts in force chains, and on the interaction between grains in the strong and weak networks (e.g. Garcia and Medina 2008). The physics governing these contacts is complex, and information gathered from models indicates that the macroscopic frictional behavior of granular material depends on: elastic grain-grain interactions; a repulsive nonlinear viscoelastic contact force between grains; grain mass; and the friction coefficient of the material (e.g., Campbell 2002; Zhu *et al*. 2008). Most models simulate grains as intact spheres because simulating particle fracture is very difficult. However, under

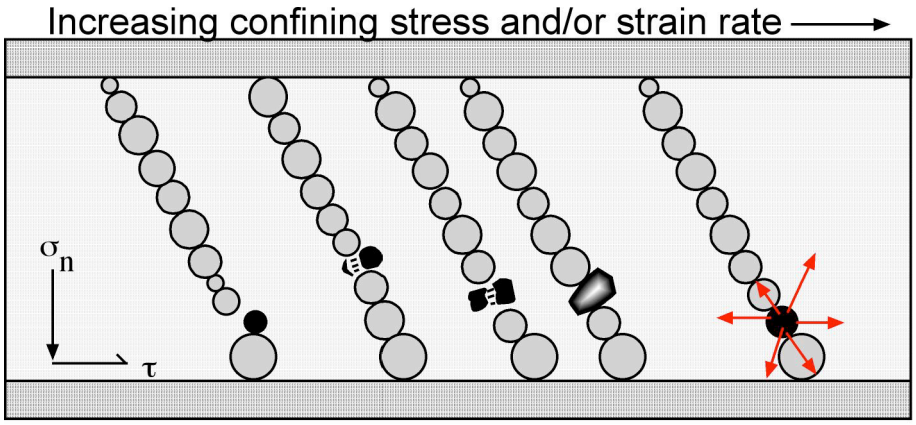

Fig. 3. Force chains are quasilinear structures that support most of the internal stresses in shearing granular material. The frictional strength of granular material is related to the stresses resolved on the force chains within it. Force chains fail by sliding, spalling, fracturing, crushing and fragmentation during cataclastic deformation. In reality, grains within a fault gouge would likely have fractally distributed shapes and sizes (after Rawling and Goodwin 2003; Davies et al. 2007).

high confining pressures and/or strain rates, cataclasis involving particle fragmentation may redistribute energy in grain flows through the process of dynamic rock fragmentation.

Dynamic rock fragmentation (Grady and Kipp 1987) is the mechanism whereby an intact piece of rock fails in a brittle manner (i.e. rapidly or catastrophically) under load, generating fragments that move away from the original centre of their mass at high velocity. This is the same effect as the '…large rapid compressions and decompressions…' associated with asperity failures by O'Hara (2005). That fragmenting grains generate high fragment energies, and hence high local pressures, is widely acknowledged, and demonstrated even under very slow applied strain rates by the phenomenon of rock-bursts in mines. Moreover, it is universally accepted that comminution or fragmentation of rock is a ubiquitous process in shearing of fault gouge in earthquakes (e.g. Sammis and Ben-Zion 2008).

Davies et al. (1999) and Davies and McSaveney (2008) proposed that dynamic fragmentation could explain the extraordinarily long runout distance of large

landslides. McSaveney and Davies (submitted) applied this theory to the static and dynamic strengths of large-scale faults. According to this theory, rock avalanches, shear planes at the base of large blockslides, and fault cores all comprise granular material which accommodates shear displacement by the formation of and failure of force chains (Fig. 3). The failure of force chains by particle fragmentation creates a granular material comprising both intact grains and angular grain fragments; the interaction between these particles likely affects the rheology of the flow (e.g. Guo and Morgan 2006).

Fault rupure involves high strain rates between 0.1 and 2 ms^{-1} (Brune 1976) on thin localized slip zones about 1–5 mm thick (Rice 2006). Spatially averaged strain rates are in the range 20–2000 s^{-1}. This means that the failure of grains is virtually instantaneous; failure conditions overlap with those of shock loading (>100 s^{-1}; Melosh 1993; Sammis and Ben-Zion 2008). Grains within force chains loaded at such high strain rates likely fail by dynamic fragmentation, during which the elastic strain energy stored in a fragmenting grain is converted instantaneously to kinetic energy. In fault gouge at seismic depths, the free travel distance of the fragments is extremely small and their kinetic energy is thus immediately converted into pressure energy exerted on the surrounding grains (Fig. 4). Under these conditions there is evidence that a fragmenting grain behaves as a high-pressure fluid (e.g. Benz and Asphaug 1995). We have shown that the magnitude of this fluid pressure is of the same order as the failure stress of the grain, which at seismic depth at the high strain rates experienced by fault cores during rupture is in the GPa range (Davies *et al*. 2007; Davies and McSaveney, 2008*b*). The thermal effect of fragmenting grains in increasing the temperature of the material on which it impacts *follows* the mechanical effect of exerting pressure (Yuan and Prakash 2007), so the pressure effect is the primary effect.

Dynamic fault friction. During grain failure by dynamic fragmentation, the rapid and different alterations of the grain's elastic and shear moduli during damage transform it into a short-lived high-pressure fluid, able to resist compression but not shear (Fig. 4). In this way, the fragmenting grain becomes part of the fluid phase in the bi-phase fluid-rock fault core. The ability of the force chain to transmit shear across the slip zone vanishes, while the normal stress continues to be transmitted across the slip zone

due to the granular fluid pressure exerted by the fragmenting grain on the grains immediately surrounding it. In effect, the total shear resistance reduces to that of the weakly-stressed force chains in the surrounding gouge. We envisage that at all instants as the rupture propagates along the fault, many force-chains are failing by fragmentation in this way and are dynamically reducing the resistance to shear on the fault.

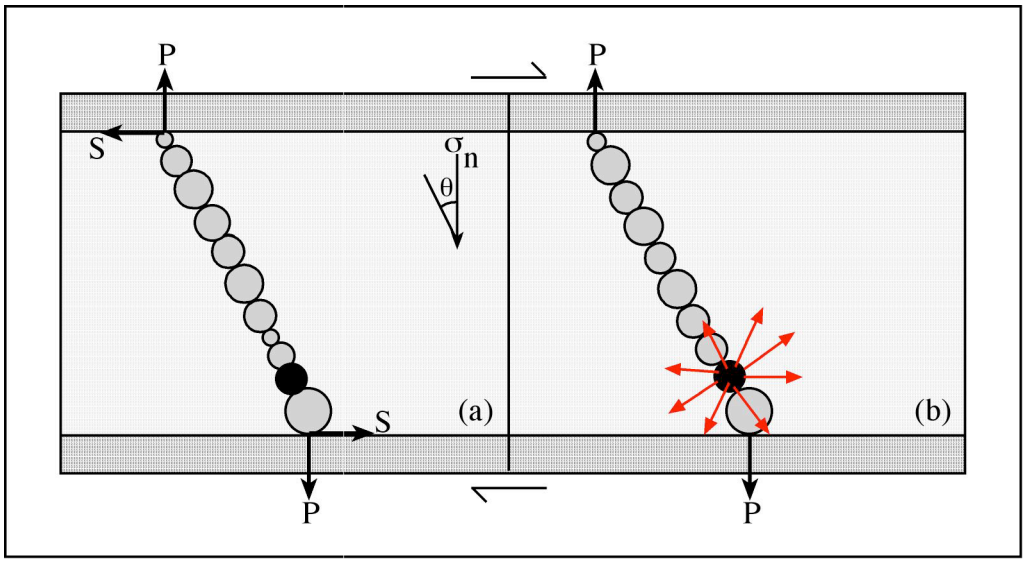

Fig. 4. (a) Forces on a force-chain just prior to fragmentation. Like Fig. 3, grains within a fault gouge would likely have fractally distributed shapes and sizes. P is the failure strength of the weakest grain in the force chain and S its resistance to shear. θ is the angle between the force chain at failure and the resolved normal stress σ_n. The value of θ is generally between 0 and 45º. Lockner (1995) showed, to a first approximation, that at high confining stress, the confined strength of a grain is equal to its unconfined strength plus the confining pressure.

$P\cos\theta + S\sin\theta \sim \Sigma\sigma_n$; $S\cos\theta + P\sin\theta \sim \Sigma\tau$

(b) Forces on a force-chain during fragmentation. As stored elastic strain energy is released as kinetic energy, the fragmenting grain generates a pressure on other grains. S = 0 because a fragmenting grain has no shear strength.

$P\cos\theta = P_f\cos\theta \sim \Sigma\sigma_n$; $P\sin\theta << \Sigma\tau$

Dynamic fragmentation is a well-known phenomenon of rock mechanics (e.g. Grady and Kipp 1984), but it has been studied mainly in the context of the need to crush rocks to produce aggregate for concrete. The energy input required for this process is a cost to that industry, so is considered wasted; in the context of fragmenting granular shear, however, the energy input required to cause the rock to fail is recovered instantaneously as kinetic energy of fragments, and immediately as a high pressure on the surrounding grains.

The major criticism that has been raised with respect to the role of fragmentation in landsliding is that fragmentation is an energy sink, so it must increase rather than reduce friction. This is usually deduced from the common perception, originally proposed by Griffith (1920), that a certain quantity of energy is required to create a given area of new grain surface, and this energy instantly becomes unavailable for dynamic effects because it somehow attaches itself to the new surface. Fracture energy does correlate well with new area created, but there is no physical justification for assuming that it is instantaneously lost to the system dynamics. In fact, the elastic strain energy released at fragmentation is instantaneously available as kinetic or pressure energy. Although the released elastic strain energy degrades rapidly to heat with friction and other processes its immediate effect on fragment velocities and hence intergranular dynamics is very important (McSaveney and Davies 2008).

Dynamic fragmentation thus appears to be a mechanism that is capable of reducing frictional resistance to granular shear, and has been shown to be capable of explaining quantitatively a range of field and laboratory data (Davies *et al*. 2007; Davies and McSaveney 2008*a*). We suggest that dynamic fragmentation occurs during the shearing of granular materials such as fault gouge; in the following we shall show that it can also explain the low *static* strength of large faults.

Fragmentation and the static strengths of faults. The basis of this concept is that the local stress in any fault is spatially non-uniform; and the nature of this variation can be described by extrapolating to fault-scale from laboratory and theoretical data on the distribution of interparticle stresses in static granular media. Figure 5 shows the

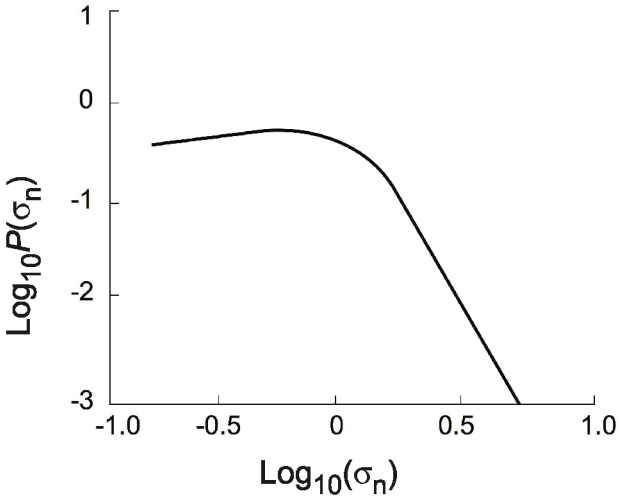

Fig. 5. Probability distribution $P(\sigma_n)$ of normal stress (σ_n) normalized with respect to the mean stress (i.e. local stress divided by mean stress) (after Løvoll *et al.* 1999).

distribution of normal static contact stresses in particles within a volume of granular material; the distribution has been verified by several experimental (Mueth *et al.* 1998; Løvoll *et al.* 1999; Blair *et al.* 2001) and computational (Radjaie *et al*. 1996; Silbert *et al.* 2002) studies. Behringer *et al* (2008) have shown that dynamic force distributions are similar in shape. Of interest to us is the distribution of forces larger than the mean, which is the well-defined exponential tail to the right of $\sigma_n \approx \log_{10}1$. Ngan (2003) and Van Eerd *et al.* (2007) show that the relationship between probability and stress in this region is:

$$P(\sigma_n) = \exp(-\sigma_n)^{\beta} \qquad (5)$$

with the value of $\beta \sim 5/3$.

Equation (5) implies a fractal scaling relationship between the maximum normal stress acting on a grain within a force chain and the mean normal stress acting

on the granular material. Assuming that the probability of a grain experiencing a given stress increases with the number of grains and that fault thickness remains constant, (5) can be written

$$\sigma_{n\ max} \sim -(\ln P_{\sigma n})^{0.6} = (\ln L)^{0.6} \qquad (6)$$

where L is the length of the fault. This relationship indicates that longer faults should have higher values of maximum local stress. When a grain fails due to local stress, the higher this stress, the higher the stress that is immediately transferred to adjacent grains. If the adjacent grains are sufficiently stressed, then the stress transfer will cause them to fail in turn. Here again we use the concept that a fragmenting grain generates a local pressure equal to its strength, but in static failure, the applied strain rate is very low so the rock strength is probably lower than in the dynamic case.

Earthquake ruptures are unstable episodes of irreversible slip during which stored elastic strain energy is released and seismic waves are radiated. On a microscopic scale, fragmentation of highly stressed grains may release enough elastic strain energy (~ 1 GPa) to nucleate a self-propagating earthquake rupture. This suggestion follows from experimental, numerical, and geological evidence gathered by Sammis et al. (1986), Lockner et al. (1991), Reches and Lockner (1994), Reches (1999), Ben-Zion and Lyakhovsky 2002, Hamiel et al. (2004) and Reches and Dewers (2005) that the nucleation and dynamic propagation of earthquake ruptures involves interacting fractures in a small volume of intact and/or granular rock. Our analysis of the statistical distribution of grain strength evolution with time indicates that larger faults, with a greater volume of granular material in the fault core, have a greater likelihood of a strong grain fragmenting at a low mean applied stress. A small fault will require correspondingly higher mean applied stress to cause sufficiently high local stresses to cause grain fragmentation. Thus, a self-propagating rupture is more likely to initiate at lower regional stresses on a large fault than on a small one experiencing a similar stress state.

He *et al.* (1990) show that heterogeneity of the strength distribution over the fault reduces the ability of an initial failure to propagate. We suggest that two changes will occur with time after a fault rupture that will decrease its heterogeneity: First,

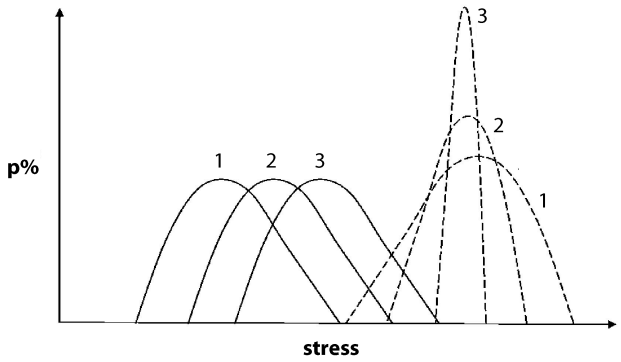

Fig. 6. Increase of tectonic stress distribution (full lines) and evolution of granular material strength distribution (broken lines) with time in temporal sequence 1, 2, 3, where p(%) indicates the proportion of grains within a volume of granular material.

tectonic stress buildup will cause progressive failure of weak force chains, which increases the minimum local strength of granular material along a fault. Second, stress corrosion (Sornette 1999) will progressively reduce the strength of the most-stressed force-chains, leading to a reduction in maximum strength. As shown in Figure 6, this results in a reduction in the overall strength of granular material along the fault (McSaveney and Davies, submitted). It also results in a significant reduction in strength heterogeneity. We believe that as time passes and stress builds up, a fault becomes progressively more likely to experience a large-scale rupture as its strength distribution alters.

In terms of the evaluation Table 1, the fragmentation mechanism meets all the required criteria. We postulate that dynamic fragmentation is the most plausible mechanism presented to date for explaining the static and dynamic weakness of faults.

Discussion

Do LANF initiate at anomalous inclinations?

The initiation of LANF in intact rock at angles that depart from the Andersonian-Byerlee fault mechanics remains an outstanding problem in structural geology. Wong and Gans (2008) recently reviewed the rolling-hinge model of Wernicke and Axen (1988) and presented a thorough discussion of new geological tests for the model. Another outstanding question remains the role of the ductile lower crust in initiating new faults. Echoing the original ideas of Wernicke (1981), Wernicke (1985) and Lister and Davis (1989) argued that low angle detachment faults are rooted in the ductile lower crust and propagate upward as loci of simple shear extending the entire thickness of the brittle crust. Axen (1992) developed this idea and presented a model showing that LANFs bounding metamorphic core complexes could initiate because of mechanical and permeability anisotropies that develop due to ductile shearing.

Vanderhaeghe *et al*. (1999) suggested that models with a brittle crust overlying a ductile crust (Brun *et al*. 1994) are more relevant to detachment faults formed in thickened and thermally weakened crust. In these models, brittle extension in the upper crust is accommodated by pervasive ductile flow in the lower crust. The style of extension of the upper brittle crust controls fault zone geometry, and the low angle detachment fault corresponds to a zone of mechanical decoupling between the brittle upper and ductile middle crust, which is equated with the 450^{o}C isotherm within the continental crust (Brace and Kohlstedt 1980). Recent advances in our understanding of the strength of the lithosphere summarized by Jackson *et al*. (2008) have renewed debate on the role of the ductile crust in nucleating crustal scale fault zones through transient brittle instabilities (e.g. Handy *et al*. 2007). This new interpretation of a strong, thick continental lithosphere may lead to a better understanding of the growth and development of crustal-scale faults like LANF through advances in the field of geodynamics.

Seismic rupture or aseismic slip?

Faults are highly heterogeneous and the true static strength of an individual fault is likely to be an average of its many different asperities or frictional contacts. Asperity type changes with time as faults accrue displacement. This occurs because of a

gradual evolution in fault geometry, fault rock lithology, and fault rock mineralogy. Three primary processes affect the nature of strain accommodation in the cores of large-displacement faults. First, faults increase in length through the linkage of irregular fault surfaces and fault segments, generally leading to a more planar fault with time (e.g. Peacock and Sanderson 1991; Anders and Schlische 1994; Childs et al. 1995, 2008). Second, wear processes result in the progressive accumulation of granular material in the fault core (Robertson 1982; Scholz 1987). Compilations of data over several orders of magnitude of displacement show general linear trends of fault zone thickness increasing with displacement. Although fault zone thickness varies with lithology, fault zones appear to reach maximum thicknesses of about 100 m after a displacement of between 1 and 10 km. Third, fault cores commonly channel chemically active fluids that promote the syntectonic metamorphic alteration of feldspar to weak phyllosilicates (e.g Janecke and Evans 1988). These minerals may alter the frictional strength of faults by forming an interconnected network of shear planes with low frictional strength (Bos and Spiers 2002; Collettini and Holdsworth 2004; Imber et al. 2008).

Because of these spatial, geometrical, mineralogical, and temporal variables, mature crustal-scale faults have highly heterogeneous fault cores, which appear to accommodate slip on a variety of structures, including: very thin 100 μm- to cm-thick ultracataclasite shear surfaces in a single fault core (e.g. Punchbowl Fault, Chester and Logan 1987); along multiple creeping subparallel fault cores cutting a wider, up to 1 km- thick, damage zone (e.g. San Andreas Fault, Hickman et al. 2005); or along multiple strands phyllosilicate-rich fault gouge forming a fault core up to 1 km- thick (e.g., Carboneras Fault, Spain, Faulkner et al. 2003, and Zuccale Fault, Italy, Collettini and Holdsworth 2004). Heterogeneity in the core of mature, large displacement faults helps to explain the various types of seismic behaviour ranging the complete spectrum between aseismic creep, slow slip events and seismic slip (see Schwartz and Rokoksky 2007 and Wibberley *et al.* 2008 for reviews); this assumption is supported by recent numerical and experimental models (e.g., Bos and Spiers, 2002; Giger *et al.* 2008; Hillers *et al.* 2007; Ben-Zion 2008).

While syntectonic chemical alteration and development of an interconnected network of weak shear planes may promote aseismic creep along mature, crustal-scale

faults, in order for a fault to rupture, two conditions must be satisfied: (1) the applied shear stress must be sufficient to overcome the frictional strength– that is, the static fault friction plus any cohesion present and (2) once this is satisfied, the dynamic frictional shear resistance must also be overcome.

If a fault comprises weak material everywhere, the rocks surrounding the fault cannot store sufficient elastic strain energy to drive an earthquake rupture (e.g. Reid 1910). If a rupture nucleates in a strong asperity on such a fault, the propagating rupture tip would granulate the weak fabric and form a material with a normal friction coefficient. Microseismicity might ensue, but a propagating rupture would halt before large strains could be accommodated. Apparent friction must be low at both static and dynamic strain rates for a large fault rupture to occur at low driving stresses. To this end, the interaction of different fault weakening mechanisms discussed above may account for the time-averaged weakness of some faults with spatially heterogeneous strength and pore fluid pressure distributions.

The required conditions for a far-reaching, self-sustaining fault rupture have been investigated by He *et al* (1990) and Pan *et al* (2006), who found that self-sustaining failure is more likely in to occur materials with less variability in component strength. These analyses also indicate that localised areas of markedly low strength are not conducive to large-scale fault rupture. We suggest that two changes will occur with time after a fault rupture that will decrease its heterogeneity. First, tectonic stress buildup will cause progressive failure of weak force chains, which increases the minimum local strength of granular material along a fault. Second, stress corrosion (Sornette 1999) will progressively reduce the strength of the most-stressed force-chains, leading to a reduction in maximum strength. As shown in Figure 5, this results in a reduction in the overall strength of granular material along the fault. We believe that as time passes and stress builds up, a fault becomes progressively more likely to experience a large-scale rupture because of a reduction in the overall strength and strength heterogeneity of granular material within its core.

The role of granular material

Some insight into the importance of brittle faulting in accommodating large strains on LANF comes from the work of John and Foster (1993) on the Chemehuevi low-angle

normal fault, southeastern California, USA. $^{40}Ar/^{39}Ar$ and fission-track thermochronology, combined with structural data constrain the initiation angle of the regionally developed normal fault to a low angle (< 30º). Formation of ductile mylonites occurred prior to displacement on the Chemehuevi LANF, which always truncates high-angle normal faults in the hangingwall and appears to have accommodated ≥ 15 km displacement by brittle deformation processes such as cataclastic flow and frictional sliding in fault gouge, crush breccias, and cataclasites with rare transitional brittle-ductile protomylonite and pseudotachylyte. These observations indicate that the Chemehuevi LANF: (1) is not an exhumed brittle-ductile transition that has experienced only minor displacement (see Miller et al. 1983); (2) initiated and slipped at a high angle to the vertical maximum compressive stress (see Anderson 1951; Wernicke and Axen 1988); (3) was seismically active. Hayman (2006) similarly concluded that fault rocks within the Black Mountain detachments, Death Valley, USA were deformed by granular flow resulting in extreme comminution of granular gouge and strain localization. These observations are consistent with our description of granular flow with dynamic fragmentation.

Unfortunately, geologists still lack criteria for distinguishing cataclasites formed at high seismic strain rates from cataclasites formed at low aseismic strain rates (Sibson 1977, 1989; Cowan 1999). Fundamentally, this inhibits our understanding of how LANFs accommodate slip (e.g., Hayman 2006; Smith *et al*. 2007). Imber *et al.* (2008) outlined experimental, geological, and seismic evidence that indicates a interconnected network of alteration minerals deforms aseismically in weak fault cores by diffusion-assisted pressure solution creep; corresponding fault rocks include phyllonite and foliated cataclasite formed at depths ≥ 3 km. This paper suggests that a better understanding of the mechanics of granular flow must be obtained before the rheological significance of fault gouge, fault breccia and cataclasite can be evaluated.

According to the dynamic rock fragmentation theory, the high strain rates produced during a seismic rupture should result in more, smaller fragments being generated by each fragmentation event (e.g. Zhang and Hao 2003). Thus, grain-size distributions might differ between the aseismically and seismically formed brittle fault rocks. However, given that grains in cataclasites will be very small, the recently

reported alteration in fractal dimension as grain diameter decreases below about 1 μm (Heilbronner and Kuelen 2006) might obscure the distinction. Chemical alteration effects and analytical difficulties are also encountered when measuring the mineralogy and particle size distribution of very fine grained (nanometers) material in fault gouge (e.g. Reches *et al*. 2007).

Detailed petrographic and geochemical investigations of fault gouge, protocataclasite, cataclasite, and ultracataclasite similar to studies by Chester et al. (1985), Chester and Logan (1987), Goodwin (1999), Cladouhos (1999) and Hayman (2006) will provide more information about respective micromechanical deformation process occurring during slip on LANF. In particular, grains within fault gouge and cataclasite that have deformed via pressure solution and dislocation creep contrast texturally with brittle fracturing mechanisms. Pressure solution creep should lead to compaction and high pore fluid pressures through time and corollary dynamic weakening mechanisms. Petrographically, microfractures in quartz containing fluid inclusion planes may indicate brittle instability through dynamic fragmentation (e.g. Faulkner *et al*. 2006).

Mechanisms of fault weakening

We have focused primarily on the mechanisms that might lead to the formation and reactivation of low angle normal faults in the seismogenic crust at depths less than ~ 12 km. In the brittle crust, fault zones that contain weak materials or weak fault fabric do not violate the tenets of fault mechanics and may slide stably under very low frictional resistance (e.g., Bos and Spiers 2001; Moore and Rymer 2007; Imber *et al.* 2008). However, evidence for this behaviour is rare, and other weakening mechanisms must operate on faults that fail both seismically and aseismically. In the field, some geological evidence for dynamic fault weakening includes:

1. fault parallel veins and vein networks indicative of pore fluid overpressures (e.g. Sibson 2001);
2. fluid inclusion data indicative of coseismic variations in pore fluid pressure (e.g. Parry and Bruhn 1990);
3. pseudotachylyte formed from frictional melt (e.g. Goodwin 1999);

4. intense rock pulverization and damage asymmetry indicative of dynamic normal interface separation (e.g. Ben-Zion 2001; Dor *et al*. 2006);
5. intensely comminuted fault rocks showing evidence of fluidization (e.g. Hayman 2006)

This paper has outlined experimental and numerical evidence for each mechanism. In our view, dynamic rock fragmentation leading to rapid comminution of fault rocks offers the best explanation available at this time for both the static and dynamic weakness of large-scale crustal rocks. Although little studied in the fault context as yet, dynamic fragmentation appears in principle capable of resolving several of the issues that other mechanisms leave unresolved.

Conclusions

1. There is reason to consider seriously the possibility that LANF can both form and rupture seismically at the low inclinations they show in outcrop. These abilities require that frictional resistance to both static rupture and subsequent slip must be less than rock friction values measured in the laboratory and at small-scale in the field.
2. The mechanisms that give rise to this reduced friction in LANF are likely to be the same as those that cause reduced friction in other large-scale faults.
3. To be realistic, potential fault weakening mechanisms must explain both reduced static and dynamic frictional resistances to shear, and must operate predominantly at large scale. Truly aseismic faults that creep continuously at low strain rates on a spatially continuous weak fabric or mineral phase are exceptions.
4. On this basis, for faults that accommodate slip both seismically and microseismically or aseismically, dynamic rock fragmentation appears to be the most applicable mechanism so far proposed.

Acknowledgements

The authors would like to thank B. Wernicke and G. Axen for thoughtful reviews of the original manuscript.

References

Abbott, R.E., Louie, J. N., Caskey, S.J. & Pullammanappallil, S. 2001. Geophysical confirmation of low-angle normal slip on the historically active Dixie Valley fault, Nevada. *Journal of Geophysical Research*, 106, 4169-4181.

Aki, K. 1984. Asperities, barriers, characteristic earthquakes and strong motion prediction. *Journal of Geophysical Research*, 89, 5867-5872.

Anders, M.H. & Schlische, R.W. 1994. Overlapping faults, intrabasin heights and the growth of normal faults. *Journal of Geology* 102, 165-180.

Anderson, E.M. 1951. *The Dynamics of Faulting*. Edinburgh: Oliver and Boyd.

Andrews, D.J. 2002. Rupture dynamics with energy loss outside the slip zone. *Journal of Geophysical Research*, 110, B01307, doi:10.1029/2004JB003191.

Andrews, D.J. & Ben-Zion, Y. 1997. Wrinkle-like slip pulse on a fault between different materials. *Journal of Geophysical Research*, 107(B12), 2363, doi:10.1029/2002JB001942.

Anooshehpoor, A. & Brune, J.N. 1999. Wrinkle-like Weertman pulse at the interface between two blocks of foam rubber with different velocities. *Geophysical Research Letters,* 26(13), 2025-2028.

Anthony, J.L. & Marone, C. 2005. Influence of particle characteristics on granular friction. *Journal of Geophysical Research*, 110, B08409, doi:10.1029/2004JB003399.

Axen, G.J. 2004. Mechanics of low-angle normal faults. *In* Karner, G.D., Morris, J.D., Driscoll, N.W., and Silver, E.A., eds. *Rheology and Deformation of the Lithosphere at Continental Margins*. MARGINS Theoretical and Experimental Earth Science Series, 46-91.

Axen, G.J. 1992. Pore pressure, stress increase, and fault weakening in low-angle normal faulting. *Journal of Geophysical Research*, 97, 8979-8991.

Axen, G.J. & Selverstone, J. 1994. Stress state and fluid pressure level along the Whipple detachment fault, California. *Geology*, 22, 835-838.

Balfour, N.J., Savage M.K. & Townend, J (2005), Stress and crustal anisotropy in Marlborough, New Zealand: evidence for low fault strength and structure-controlled anisotropy. *Geophysical Journal International*, 163, 1073-1086.

Behringer, R.P., Daniels, K.E., Majmudar, T.S. & Sperl, M. 2008. Fluctuations, correlations and transitions in granular materials: statistical mechanics and a non-conventional system. *Philosophical Transactions of the Royal Society*, A366, 493-504.

Ben-Zion, Y. 2001. Dynamic ruptures in recent models of earthquake faults. *Journal of the Mechanics and Physics of Solids,* 49, 2209-2244.

Ben-Zion, Y. 2008. Collective Behaviour and Earthquakes and Faults: Continuum-Discrete Transitions, Progressive Evolutionary Changes, and Different Dynamic Regimes. *Reviews of Geophysics*, 46(4), RG4006.

Ben-Zion, Y. & Lyakovsky, V. 2002. Accelerated seismic release and related aspects of seismicity patterns in earthquake faults. Pure and Applied Geophysics, 159, 2385-2412.

Benz, W. & Ausphaug, E. 1995. Simulations of brittle solids using smooth particle hydrodynamics. *Computer Phys. Comm*. 87, 253-265.

Biegel, R.L., Sammis, C.G. & Dieterich, J.H. 1989. Frictional properties of simulated debris. *Journal of Structural Geology*, 11, 827-846.

Blair, D.L., Mueggenburg, N.W., Marshall, A.H., Jaeger, H.M. & Nagel, S.R. 2001. Force distribution in three-dimensional granular assemblies, effects of packing order and interparticle friction. *Physical Review E*, 63, 041304/1-8.

Bos, B. & Spiers, C.J. 2001. Experimental investigation into the microstructural and mechanical evolution of phyllosilicate-bearing fault rock under conditions favouring pressure solution. *Journal of Structural Geology*, 23, 1187-1202.

Boutareaud, S., Calugaru, D.-G., Han, R., Fabbri, O., Mizoguchi, K. Tsutsumi, A. & Shimamoto, T. 2008. Clay-clast aggregates: a new textural evidence for seismic fault sliding? *Geophysical Research Letters*, 35, L05302, doi:10.1029/2007GL032554.

Bowden, F. & Tabor, D. 1986. *The Friction and Lubrication of Solids.* Clarendon Press, Oxford.

Brace, W.F. & Byerlee, J.D. 1966. Stick-slip as a mechanism for earthquakes. *Science*, 168, 990-992.

Brace, W.F. & Kohlstedt, D. 1980. Limits on lithospheric stress imposed by laboratory experiments. *Journal of Geophysical Research*, 85, 6248-6252.

Brantut, N., Schubnel, A., Rouzeaud, J., Brunet, F. & Shimamoto, T. 2007. High velocity frictional properties of clay-bearing fault gouge: experiments and modeling. *EOS Transactions AGU Fall Meeting Supplement*: Abstract T11A-0333.

Brodsky, E.E. & Kanamori, H. 2001. Elastohydrodynamic lubrication of faults. *Journal of Geophysical Research* 106, 16357–16374.

Brown, K.M., Kopf, A., Underwood, M.B. & Weinberger, G.L. 2003. Compositional and fluid pressure controls on the state of stress on the Nankai subduction thrust: A weak plate boundary. *Earth and Planetary Science Letters*, 214, 589-603.

Brudy, M., Zoback, M.D., Fuchs, K., Rummel, F. & Baumgartner, J. 1997. Estimation of the complete stress tensor to 8 km in the KTB scientific drilling holes; implications for crustal strength. *Journal of Geophysical Research*, 102, 18453-18475.

Brun, J.-P., Sokoutis, D. & van den Driessche, J., 1994. Analogue modeling of detachment fault systems and core complexes. *Geology*, 22(4), 319-322.

Brune, J.N. 1976. The physics of earthquake strong motion. *In*: Lomnitz, C. & Rosenbleuth, E. (eds) *Seismic Risk and Engineering Decision.* Elsevier, Amsterdam. 141-177.

Byerlee, J. 1978. Friction of rocks. *Pure and Applied Geophysics* 116: 4-5, 615-626.

Byerlee, K. 1990. Friction, overpressure and fault normal compression. Geophysical Research Letters, 17, 2109-2112.

Caine, J.S., Evans, J.P. & Forster, C.B. 1996. Fault zone architecture and permeability structure. *Geology*, 24 (11), 1025-1028.

Campbell, C.S. 2002. Granular shear flows at the elastic limit. *Journal of Fluid Mechanics*, 465, 261-291.

Carpenter, B.M, Marone, C.J. & Saffer, D.M 2007. Frictional Behavior of Materials in the 3D SAFOD Volume. *Eos Trans. AGU, 88*(52), Fall Meet. Suppl., Abstract T41B-0580.

Cates, M., Wittmer, J., Bouchard, J.-P., & Claudin, P. 1998. Jamming, force chains, and fragile matter. *Physical Review Letters*, 81, 1841-1844.

Chester, F.M., Friedman, M. & Logan, J.M. 1985. Foliated cataclasites. *Tectonophysics*, 111, 139-146.

Chester, F.M. & Logan, J.M. 1987. Composite planar fabric of gouge from the Punchbowl Fault, California. *Journal of Structural Geology*, 9, 621-634.

Childs, C., Watterson, J. & Walsh, J.J. 1995. Fault overlap zones within developing normal fault systems. *Journal of the Geological Society, London*, 152, 535-549.

Childs, C., Manzocchi, T., Walsh, J.J., Bonson, C.G., Nicol, A. & Schöpfer, M.P.J. 2008. A geometric model of fault zone and fault rock thickness variations. *Journal of Structural Geology*, doi:10.1016/j.jsg.2008.08.009.

Cladouhos, T.T. 1999. Shape preferred orientations of survivor grains in fault gouge. *Journal of Structural Geology*, 21, 419-436.

Collettini, C. & Barchi, M.R. 2004. A comparison of structural data and seismic images for low-angle normal faults in the Northern Apennines (Central Italy): constraints on activity. *In*: Alsop, G.I., Holdsworth, R.E., McCaffrey, K.J.W. &

Hand, M. (eds) *Flow Processes in Faults and Shear Zones*. Geological Society, London, Special Publications, 224, 95-112.

Collettini, C. & Holdsworth, R.E. 2004. Fault zone weakening and character of slip along low-angle normal faults: insights from Zuccale fault, Elba, Italy. *Journal of the Geological Society, London*, 161, 1039-1051.

Collettini, C. & Sibson, R.H. 2001. Normal faults, normal friction? *Geology*, 29(10), 927-930.

Collins, G.S. & Melosh, H.J. 2003. Acoustic fluidisation and the extraordinary mobility of sturzstroms. *Journal of Geophysical Research*, 108 B10: 2473, doi:10.1029/2003JB002465.

Coney, P.J. 1980. Cordilleran metamorphic core complexes: An overview. *In*: Crittenden, M.D., Jr., Coney, P.J., & Davis, G.H. (eds) *Cordilleran Metamorphic Core Complexes*. Memoir 153, Geological Society of America, Boulder, Colorado, 7-31.

Cowan, D.S. 1999. Do faults preserve a record of seismic slip? A field geologist's opinion. *Journal of Structural Geology*, 21, 437-448.

Cowan, D.S., Cladouhos, T.T. & Morgan, J. 2003. Structural geology and kinematic history of rocks formed along low-angle normal faults, Death Valley, California. *Geological Society of America Bulletin*, 115, 1230-1248.

Crampin, S. & Chastin, S. 2003. A review of shear-wave splitting in the crack-critical crust. *Geophysics Journal International*, *155*; 221-240.

Crittenden, M.D., Jr., Coney, P.J., & Davis, G.H. (eds). 1980. *Cordilleran Metamorphic Core Complexes*. Memoir 153, Geological Society of America, Boulder, Colorado.

Cundall, P.A. & Strack, O.D.A. 1979. A discrete numerical model for granular assemblies. *Geotechnique*, 29, 47-65.

Davies T.R. & McSaveney, M.J. 2002. Dynamic simulation of the motion of fragmenting rock avalanches. *Canadian Geotechnical Journal*, 39, 789-798.

Davies, T.R. & McSaveney, M.J. 2005. Runout of rock avalanches and volcanic debris avalanches. *In:* Pacarelli, L. (ed.) *Proceedings of the International Conference on Fast Slope Movements: Prediction and Prevention for Rish Mitigation*. Patron Editore, Bologna, May 11-13, 2003, 81-87.

Davies, T.R. & McSaveney, M.J. 2008*a*. The role of rock fragmentation in the motion of large landslides. *Engineering Geology,* doi:10.1016/j.enggeo.2008.11.004.

Davies, T.R.H. & McSaveney, M.J. 2008*b*. A mechanical explanation for the Socompa debris avalanche runout. Symposium on Volcanic sector collapse:

Origin, transformation to debris flows and tsunami. *IAVCEI General Assembly, Reykjavik, Iceland.*

Davies, T.R.H., McSaveney, M.J. & Hodgson, K.A. 1999. A fragmentation-spreading model for long-runout rock avalanches. *Canadian Geotechnical Journa*l, 36, 1096-1110.

Davies, T. R.H. McSaveney, M.J. & Beetham, R. D. 2006. Rapid block glides – slide-surface fragmentation in New Zealand's Waikaremoana landslide. *Quarterly Journal of Engineering Geology and Hydrogeology*, 39, 115–129.

Davies, T.R.H., McSaveney, M.J. & Deganutti, A.M. 2007. Dynamic rock fragmentation causes low rock-on-rock friction. *In* Eberhardt, E. Stead, D. & Morrison, T. (eds) *Rock Mechanics – meeting society's challenges and demands*. Taylor & Francis, London, 959-966.

Dean, S.M., Minshull, T.A., & Whitmarsh, R.B. 2008. Seismic constraints on the three- dimensional geometry of low-angle intracrustal reflectors in the Southern Iberia Abyssal Plain. *Geophysical Journal International*, 175, 571-586.

Di Toro, G., Goldsby, G.L. & Tullis, T.E. 2004. Friction falls towards zero in quartz rock as slip velocity approaches seismic rates. *Nature*, 227: 436-430.

Dor, O., Rockwell, T.K. & Ben-Zion, Y. 2006. Geologic observations of damage asymmetry in the structure of the San Jacinto, San Andreas and Punchbowl faults in southern California: a possible indicator for preferred rupture propagation direction. *Pure and Applied Geophysics*, 163, doi:10.1007/s00024-005-0023-9.

Evans, J.P. & Chester, F.M. 1995. Fluid-rock interaction and weakening of faults of the San Andreas system: inferences from San Gabriel fault-rock geochemistry and microstructures. *Journal of Geophysical Research*, 100, 13007-13020.

Faulkner, D.R., Mitchell, T.M., Healy, D. & Heap, M.J. 2006. Slip on 'weak' faults by the rotation of regional stress in the fracture damage zone. *Nature*, 444, 922-925, doi:10.1038/nature053353.

Fialko, Y. & Khazan, Y. 2005. Fusion by earthquake faulting: stick or slip? *Journal of Geophysical Research*, 110: B12407 doi: 10.1029/2005B003869.

Forster, M.A. & Lister, G.S. 1999. Detachment faults in the Aegean core complex of Ios, Cyclades, Greece. *In:* Ring, U., Brandon, M.T., Lister, G.S. & Willett, S.D. (eds) *Exhumation Processes: Normal Faulting, Ductile Flow and Erosion*. Geological Society, London, Special Publications, 154, 305-323.

Francois, B., Lacombe, F. & Herrmann, H.J. 2002. Finite width of shear zones. *Physical Review E*, 65, 031311.

Garagash, D.I. & Rudnicki, J.W. 2003*a*. Shear heating of a fluid-saturated slip-weakening dilatant fault zone 1. Limiting regimes. *Journal of Geophysical Research*, 108(B2), 2121, doi:10.1029/2001JB001653.

Garagash, D.I. & Rudnicki, J.W. 2003*b*. Shear heating of a fluid-saturated slip-weakening dilatant fault zone 2. Quasi-drained regime. *Journal of Geophysical Research*, 108(B10), 2472, doi:10.1029/2002JB002218.

Garcia, X. & Medina, E. 2008. Strong-weak network anisotropy switching and hysteresis in three-dimensional granular materials. *Physical Review E*, 78, 021305.

Giger, S.B, Tenthorey, E. Cox, S.F. & Fitz Gerald, J.D. 2007. Permeability evolution in quartz fault gouges under hydrothermal conditions. *Journal of Geophysical Research*, 112, B07202, doi:10.1029/JB004828.

Goldsby, D.L. & Tullis, T.E. 2002. Low frictional strength of quartz rocks at subseismic slip rates. *Geophysical Research Letters,* 29(17), 1844, doi:10.1029/2002GL015240.

Goldsby, D.L. & Tullis, T.E. 2007. Flash heating and weakening of crustal rocks during coseismic fault slip. *EOS Transactions AGU Fall Meeting Supplement*: Abstract T11A-0352.

Goodwin, L.B. 1999. Controls on pseudotachylyte formation during tectonic exhumation in the South Mountains metamorphic core complex, Arizona. *In:* Ring, U., Brandon, M.T., Lister, G.S. & Willett, S.D. (eds) *Exhumation Processes: Normal Faulting, Ductile Flow and Erosion*. Geological Society, London, Special Publications, 154, 325-342.

Grady, D.E. & Kipp, M.E., 1987. Dynamic rock fragmentation. In *Fracture Mechanics of Rock*, Academic Press, London, 429–475.

Gratier, J.-P. & Gueydan, F. 2007. Deformation in the Presence of Fluids and Mineral Reactions, in, Handy, M.R., Hirth, G., & Hovius, N., (eds). *Tectonic Faults: Agents of Change on a Dynamic Earth*. MIT Press, Cambridge, Massachusetts, 319-356.

Griffith, A.A. 1920. The phenomenon of rupture and flow in solids. *Philosophical Transactions of the Royal Society of London*, A221, 163-198.

Guo, Y. & Morgan, J.K. 2006. The frictional and microchemical effects of grain comminution in fault gouge from distinct element simulations. *Journal of Geophysical Research*, 111, B12406, doi:10.1029/2005JB004049.

Hamiel, Y., Lyakhovsky, V., & Agnon, A. 2004. Coupled evolution of damage and porosity in poroelastic media: theory and applications to deformation of porous rocks. Geophysical Journal International, 156, 701-713.

Han, R., Shimamoto, T., Hirose, T., Ree, J.-H. & Ando, J. 2007. Ultralow friction of carbonate faults caused by thermal decomposition. *Science*, 316 (5826), 878-881.

Handy, M.R., Hirth, G. & Burgmann, R. 2005. Continental Fault Structure and Rheology from the Frictional-to-Viscous Transition Downward. 2007. *In*, Handy, M.R., Hirth, G., & Hovius, N., eds. *Tectonic Faults: Agents of Change on a Dynamic Earth*. MIT Press, Cambridge, Massachusetts, 139-181.

Hayman, N. W. 2006. Shallow crustal fault rocks from the Black Mountain detachments, Death Valley, CA. *Journal of Structural Geology* 28; 1767-1784.

Hazzard, J.F., Young, R.P. & Maxwell, S.C. 2000. Micromechanical modelling of cracking and brittle failure of rocks. *Journal of Geophysical Research*, 105, B7: 16683-16697.

He, C. Okubo, S. & Nishimatsu, Y. 1990. A study on the Class II behaviour of rock. *Rock Mechanics and Rock Engineering*, 23, 261-273.

Healy, D. 2008. Damage patterns, stress rotations and pore fluid pressures in strike-slip fault zones. *Journal of Geophysical Research*, 113, B12407, doi:10.1029/2008JB005655.

Heaton, T.H. 1990. Evidence for and implications of self-healing pulses of slip in earthquake rupture. *Physics of the Earth and Planetary Interiors*, 64, 1-20.

Heilbronner, R. & Kuelen, N. 2006. Grain size and grain shape analysis of fault rocks. *Tectonophysics*, 427, 199–216.

Hickman, S.H., Zoback, M.D. & Ellsworth, W.L. 2005. Structure and composition of the San Andreas fault zone at Parkfield: Initial results from SAFOD phases 1 and 2. *Eos Trans. AGU, 87*. Fall Meeting Supplement, Abstract T23E-25.

Hillers, G. & Miller, S.A. 2007. Dilatancy controlled spatiotemporal slip evolution of a sealed fault with spatial variations of the pore pressure. *Geophysics Journal International*, 168, 431-445.

Hillers, G., Mai, P.M., Ben-Zion, Y. & Ampuero, J.-P. 2007. Statistical properties of seismicity of fault zones at different evolutionary stages. *Geophysics Journal International*, 169, 515-533.

Hirose, T. & Bystricky, M. 2007. Extreme dynamic weakening of faults during dehydration by coseismic shear heating *Geophysical Research Letters*, 34, L14311, doi:10.1029/2007GL030049.

Hirose, T. & Shimamoto, T. 2005. Growth of molten zone as a mechanism of slip weakening of simulated faults in gabbro during frictional melting. *Journal of Geophysical Research*, 110, B05202, doi:10.1029/2004JB003207.

Hooke, R. L. & Iverson, N.R. 1995. Grain-size distribution in deforming subglacial tills: Role of grain fracture. *Geology*, 23(1), 57-60.

Hubbert, M.K. & Rubbey, W.W. 1959. Role of fluid pressure in the mechanics of overthrust faulting., 1., Mechanics of fluid-filled porous solids and its application to overthrust faulting. *Geological Society of America Bulletin*, 70, 115-166.

Imber, J., Holdsworth, R.E., Smith, S.A.F., Jefferies, S.P. & Collettini, C. 2008. Frictional-viscous flow, seismicity and the geology of weak faults: a review and future directions. *In*: Wibberley, C.A.J., Kurz, W., Imber, J., Holdsworth, R.E. & Collettini, C. (eds) *The Internal Structure of Fault Zones: Implications for Mechanical and Fluid-Flow Properties.* Geological Society, London, 299. 151-173.

Jackson, J.A. & White, N.J. 1989. Normal faulting in the upper continental crust: observations from regions of active extension. *Journal of Structural Geology*, 11, 15-36.

Jackson, J., McKenzie, D., Priestley, K. & Emmerson, B. 2008. New views on the structure and rheology of the lithosphere. *Journal of the Geological Society, London*, 165, 453-465.

Janecke, S.U. & Evans, J.P. 1988. Feldspar-influenced rock rheologies. *Geology*, 16, 1064-1067.

John, B.E. & Foster, D.A. 1993. Structural and thermal constraints on the initiation angle of detachment faulting in the southern Basin and Range: the Chemehuevi Mountains study. *Geological Society of America Bulletin*, 105, 1091-1108.

Kopf, A. 2001. Permeability variation across an active low angle normal fault, Western Woodlard Basin (ODP leg 180) and its implication for fault activation, in, Holdsworth, R.E.; Strachan, R.A.; Macloughlin J.F.; Knipe, R.J. (eds).*The Nature and Tectonic Significance of Fault Zone Weakening,* Geological Society of London Special Publication 186, 23-41.

Lin, A., Maruyama, T. & Kobayashi, K., 2007. Tectonic implications of damage zone-related fault-fracture networks revealed in drill core through the Nojima fault, Japan. *Tectonophysics*, 443, 161-173.

Lister, G.S. & Davis, G.A. 1989. The origin of metamorphic core complexes and detachment faults formed during tertiary continental extension in the northern Colorado River region, USA. *Journal of Structural Geology*, 11, 65-94.

Lockner, D.A. 1995. Rock Failure. *In*, Ahrens, T.J. (ed). *Rock Physics and Phase Relations: A Handbook of Physical Constants*. American Geophysical Union, Washington, DC. 127-145.

Losh, S. 1997. Stable isotope and modeling studies of fluid-rock interaction associated with the Snake Range and Mormon Peak detachment faults, Nevada. *Geological Society of America Bulletin*, 109, 300-323.

Løvoll, G. Måløy, K.J. & Flekkøy, E.G. 1999. Force measurements on static granular materials *Physical Review E* 60: 5872-5878.

Majmudar, T.S. & Behringer, R.P. 2005. Contact force measurements and stress-induced anisotropy in granular materials. *Nature*, 435, 1079-1082.

Manatschal, G., Marquer, D., & Fruh-Green, G. 2000. Channelized fluid flow and mass transfer along a rift-related detachment fault (eastern Alps, southeast Switzerland). *Geological Society of America Bulletin* 112(1), 21-33.

Marone, C. & Scholz, C.H. 1989. Particle-size distribution and microstructures within simulated fault gouge. *Journal of Structural Geology* 11(7); 799-814.

Matsuoka, H. 1974. A microscopic study on shear mechanism of granular materials. *Soils and Foundations*, 14(1), 29-43.

McGarr, A. & Gay, N.C. 1978. State of stress in the earth's crust. *Annual Review of Earth and Planetary Sciences*, 6, 405-436.

McSaveney, M.J. & Davies, T.R.H. 2005. Dynamics of large high-speed blockslides. *In*: Senneset, K., Flaate, K. & Larsen, J.-O. (eds) *Landslides and Avalanches*. ICFL 2005, Norway. Taylor & Francis Group, London, 257-264.

McSaveney, M.J. & Davies, T.R.H. 2006. Rapid rock-mass flow with dynamic fragmentation. *In*: Evans, S.G., Scarascia-Mugnozza, G., Strom, A. & Hermanns, R.L. (eds) Advanced Research Workshop: Landslides from Massive Rock Slope Failure. NATO Science Series, IV Earth and Environmental Sciences, 49, 285–304. Celano, Italy, June 16–21.

McSaveney, M.J. & Davies, T.R.H. 2007. Rockslides and their motion. *In*: Sassa, K., Fukuoka, H., Wang, F. & Wang G. (eds) *Progress in Landslide Science*. Springer-Verlag, Berlin, 113-134.

McSaveney, M.J. & Davies, T.R. 2008. No energy loss to surface energy in rock comminution. *Engineering Geology*, doi:10.1016/j.enggeo.2008.11.001.

McSaveney, M.J., Davies, T.R.H. & Hodgson, K.A. 2000. A contrast in deposit style and process between large and small rock avalanches. *In*: Bromhead, E., Dixon, N. & Ibsen, M.-L. (eds) Landslides in Research, Theory and Practice. Thomas Felford Publishing, London, 1053–1058.

Maveyraud, C. Benz, W., Sornette, A. & Sornette, D. (1999). Solid friction at high sliding velocities: an explicit three-dimensional dynamical smoothed particle hydrodynamics approach. *Journal of Geophysical Research*, 104, B12: 28769-28788.

Melosh, H.J. 1976. Acoustic fluidisation – a new geologic process? *Journal of Geophysical Research*, 84, 7513-7520.

Melosh, H.J. 1993. Meteorite origins- blasting rocks off planets. *Nature*, 363, 498-499.

Melosh, H.J. 1996. Dynamical weakening of faults by acoustic fluidization. *Nature,* 379, 601-606.

Melosh, H.J., Ryan, E.V. & Ausphaug, E. 1992. Dynamic fragmentation in Impacts: hydrocode simulation of laboratory impacts. *Journal of Geophysical Research*, 97, 14,735-14,759.

Miller, E.L., Gans, P.B. & Garing, J. 1983. The Snake Range decollement: An exhumed mid-Tertiary ductile-brittle transition. *Tectonics*, 2, 239-263.

Miller, S.A., Collettini, C., Chiaraluce, L., Cocco, M., Barchi, M. & Kaus, J.P. 2004. Aftershocks driven by a high pressure CO_2 source at depth. *Nature,* 427, 724-727.

Mizoguchi, K., Hirose, T., Shimamoto, T. & Fukuyama, E. 2007. Reconstruction of seismic faulting by high-velocity friction experiments: An example of the 1995 Kobe earthquake. *Geophysical Research Letters*, 34, L01308, doi10.1029/2006GL027931.

Moore, D.E. & Lockner, D.A. 2004. Talc friction in the temperature range 25º-400 ºC: relevance for fault-zone weakening. *Tectonophysics*, doi:10.1016/j.tecto.2007.11.039.

Moore, D.E. & Rymer, M.J. 2007. Talc-bearing serpentinite and the creeping section of the San Andreas fault. *Nature*, 448, 795-797, doi:10.1038/nature06064.

Morley, C.K. 1999. Marked along-strike variations in dip of normal faults- the Lokichar fault, N. Kenya rift: a possible case for metamorphic core complexes. *Journal of Structural Geology*, 21, 479-492.

Morgan, J. & Boettcher, M. 1999. Numerical simulations of granular shear zones using the distinct element method: 1. Shear zone kinematics and the micromechanics of localization. *Journal of Geophysical Research*, 104 (B2), 2703-2719.

Morrison, J., 1994. Meteoric water-rock interaction in the lower plate of the Whipple Mountain metamorphic core complex, California. *Journal of Metamorphic Geology*, 12, 827-840.

Mueth, D.M., Jaeger, H.M. & Nagel, S.R. 1998. Force distribution in a granular medium. *Physical Review E*, 57, 3164-3169.

Ngan A. H. W. 2003. Mechanical analog of temperature for the description of force distribution in static granular packings *Physical Review E,* 68, 011301 1-10.

Numelin, T., Marone, C. & Kirby, E. 2007. Frictional properties of natural fault gouge from a low-angle normal fault, Panamint Valley, California. *Tectonics*, 26, doi: 10/1029/2005TC001916.

O'Hara, K.O. 2005. Evaluation of asperity-scale temperature effects during seismic slip. *Journal of Structural Geology*, 27, 1892-1898.

O'Hara, K., Mizoguchi, K., Shimamoto, T. & Hower, J.C. 2006. Experimental frictional heating of coal gouge at seismic slip rates: Evidence for devolatilization and thermal pressurization of gouge fluids. *Tectonophysics*, 424, 109-118.

Ohnaka, M. 2003. A constitutive scaling law and a unified comprehension for frictional slip failure, shear fracture of intact rock, and earthquake rupture. *Journal of Geophysical Research*, 108 (B2), 2080, doi: 10.1029/2000JB000123.

Ozawa, K. & Takizawa, S. 2007. Amorphous material formed by mechanochemical effect in natural pseudotachylyte of crushing origin: A case study of the Iida-Matsukawa Fault, Nagano Prefecture, Central Japan. *Journal of Structural Geology*, 29, 1855-1869.

Pan, P-Z. Feng, X-T. & Hudson, J.A., 2006. Numerical simulations of Class I and Class II uniaxial compression curves using an elasto-plastic cellular automaton and a linear combination of stress and strain as the control method. *International Journal of Rock Mechanics & Mining Sciences*, 43, 1109–1117.

Parry, W.T. & Bruhn, R.L., 1990. Fluid pressure transients on seismogenic normal faults. *Tectonophysics*, 179, 335-344.

Paterson, M.S. 1978. *Experimental Rock Deformation. The Brittle Field.* Springer-Verlag, Berlin. 254 pp.

Peacock, D.C & Sanderson, D.J. 1991. Displacements, segment linkage, and relay ramps in normal fault zones. *Journal of Structural Geology* 13, 721-733.

Philpotts, A.R., 1964. Origin of pseudotachylytes. *American Journal of Science*, 262, 1008-1035.

Potyondi, D.O. & Cundall, P.A. 2000. A particle-bonded model for rock. *International Journal of Rock Mechanics and Mining Sciences*, 41, 1329-1364.

Proffett, J.M., Jr. 1977. Cenozoic geology of the Yerington district, Nevada, and implication for the nature and origin of Basin and Range faulting. *Geological Society of America Bulletin*, 88, 247-266.

Rabinowicz, E. 1951. The Nature of the Static and Kinetic Coefficients of Friction. *Journal of Applied Physics,* 22(11), 1373-1379.

Rabinowicz, E. 1995. *Friction and Wear of Materials*. John Wiley & Sons, Inc., New York, NY.

Radjai, F., Jean, M., Moreau, J. & Roux, S. 1996. Force distribution in dense two-dimensional granular systems. *Physical Review Letters* 77, 274-277.

Rawling, G.C. & Goodwin, L.B. 2003. Cataclasis and particulate flow in faulted, poorly lithified sediments. Journal of Structural Geology 25, 317-331.

Reches, Z. 1999. Mechanisms of slip nucleation during earthquakes. *Earth and Planetary Science Letters*, 170, 475–486.

Reches, Z., & Dewers, T.A. 2005. Gouge formation by dynamic pulverization during earthquake rupture. *Earth and Planetary Science Letters*, 235, 361–374.

Reches, Z., & Lockner, D.A. 1994. Nucleation and growth of faults in brittle rocks. *Journal of Geophysical Research – Solid Earth*, 99, 18159–18173.

Reches, Z., Mishima, T.D., Strout, G., Lockner, D.A., Hamilton, M. & Heesakkers, V. 2007. Gouge Powder from Earthquakes Rupture-zones and Laboratory Rupture Experiments: Sub-microscopic Observations and particle size Distribution. *EOS Transactions AGU,* 88(52), Fall Meeting Supplement, Abstract T11A-0338.

Reid, H.F. 1910. The mechanism of the earthquake. *In*, *The California Earthquake of April 18, 1906, Report of the State Earthquake Investigation Commission, Vol. 2*. Carnegie Institution, Washington, D.C. 1-192.

Rempel, A.W. 2006. The Effects of Flash-Weakening and Damage on the Evolution of Fault Strength and Temperature. *In*, Abercrombie, R.E, McGarr, A., Di Toro, G.D. & Kanamori, H., eds. *Earthquakes: Radiated Energy and the Physics of Faulting*. Geophysical Monograph Series 170, 263-270.

Reynolds, S.J. & Lister, G.S. 1987. Structural aspects of fluid-rock interaction in detachment zones. *Geology*, 15, 362-366.

Rietbrock, A., Tiberi, C, Scherbaum, F. & Lyon-Caen, H. 1996. Seismic slip on a low-angle normal fault in the Gulf of Corinth: evidence from high-resolution cluster analysis of microearthquakes. *Geophysical Research Letters*, 23, 1817-1820.

Rice, J.R. 1992. Fault stress states, pore pressure distributions, and the weakness of the San Andreas Fault. *In*, Evans, B. & Wong, T.-F. (eds) *Fault Mechanics and Transport Properties of Rocks: A Festschrift in Honor of W.F. Brace*. Academic Press, New York, New York. 475-504.

Rice, J.R. 1999. Flash heating at asperity contacts and rate-dependent friction. *Eos Trans AGU* 80(46) Fal Meeting Suppl., F6811.

Rice, J.R. 2006. Heating and weakening of faults during earthquake slip. *Journal of Geophysical Research*, 111: B05311, doi:10.1029/2005BJ004006.

Rigo, A., Lyon-Caen, H., Armijo, R., Deschamps. A., Hatzfield, D., Makropoulos, K., Papadimitriou, P. & Kassaras, I. 1996. A microseismic study in the western part of the Gulf of Corinth (Greece): implications for large-scale normal faulting mechanisms. *Geophysical Journal International*, 126, 663-688.

Ring, U., Layer, P.W. & Reischmann, T. 2001. Miocene high-pressure metamorphism in the Cyclades and Crete, Aegean Sea, Greece: evidence for large-magnitude displacement on the Cretan detachment. *Geology*, 29: 395-398.

Robertson, E.C. 1982. Continuous formation of gouge and breccia during fault displacement. *In*: Goodman, R.E. & Hulse, F. (eds) *Issues in Rock Mechanics, Proc. Symp. Rock. Mech. 23rd*. American Institute of Mining Engineers, New York, New York. 397-404.

Rubinstein, S.M., Cohen, G. & Fineberg, J. 2004. Detachment fronts and the onset of dynamic friction. *Nature*, 430, 1005-1010.

Rudnicki, J.W & Rice, J.R. 2006. Effective normal stress alterations due to pore pressure changes induced by dynamic slip propagation on a plane between dissimilar materials. *Journal of Geophysical Research*, 111, B10308, doi:10.1029/2006JB004396.

Sammis, C.G. & Ben-Zion, Y. 2008. Mechanics of grain-size reduction in fault-zones. *Journal of Geophysical Research*, 113: doi:10.1029/2006BJ004892.

Sammis, C.G. & King, G.C.P. 2007. Mechanical origin of power law scaling in fault zone rock. *Geophysical Research Letters*, 34, 04312, doi:10.1029/2006GL028548.

Sammis, C. G., Osbourne, R. H., Anderson, J. L., Banerdt, M. & White, P. 1986. Self-similar cataclasis in the formation of fault gouge. *Pure and Applied Geophysics*, 124, 53–78.

Scholz, C.H. 1987. Wear and gouge formation in brittle faulting. *Geology*, 15, 493-495.

Scholz, C.H. 1992. Weakness amidst strength. *Nature*, 359, 677-678.

Scholz, C.H. 1998. Earthquakes and friction laws. *Nature*, 391: N6662, 37-42.

Scholz, C.H. & Hanks, T.C. 2004. The strength of the San Andreas fault: a discussion, in, Karner, G.D, Taylor, B., Driscoll, N., & Kohlstedt, D. , eds. *Rheology and deformation of the lithosphere at continental margins.* Columbia University Press, New York, 261-283.

Schwartz, S.Y. & Rokosky, J.M. 2007. Slow Slip Events and Seismic Tremor at Circum-Pacific Subduction Zones. *Reviews of* Geophysics, 45, RG3004.

Shipton, Z.K., Soden, A.M., Kirkpatrick, J.D., Bright, A.M. & Lunn, R.J. 2006. How thick is a fault? Fault displacement-thickness scaling revisited, in, Abercrombie, R.E, McGarr, A., Di Toro, G.D., & Kanamori, H. (eds) *Earthquakes: Radiated Energy and the Physics of Faulting*. Geophysical Monograph Series 170, 193-198.

Sibson, R.H. 1973. Interactions between temperature and fluid pressure during earthquake faulting- A mechanism for partial of total stress relief. *Nature Physical Sciences*, 243, 66-68.

Sibson, R.H. 1975. Generation of pseudotachylyte by ancient seismic faulting. *Geophysical Journal of the Royal Astronomical Society,* 43, 775-794.

Sibson, R.H. 1977. Fault rocks and fault mechanisms. *Journal of the Geological Society of London* 133, 191-213.

Sibson, R.H. 1983. Continental fault structure and the shallow earthquake source. *Journal of the Geological Society, London*, 140, 741-767.

Sibson, R.H. 1986. Earthquakes and rock deformation in crustal fault zones. *Annual Review of Earth and Planetary Sciences*, 14, 149-175.

Sibson, R.H. 1989. Earthquake faulting as a structural process. *Journal of Structural Geology*, 11, 1-14.

Sibson, R.H. 2001. Fluid involvement in normal faulting. *Journal of Geodynamics*, 29, 469-499.

Sibson, R.H. & Toy, V.G. 2006. The Habitat of Fault-Generated Pseudotachylyte: Presence vs. Absence of Friction-Melt, in, Abercrombie, R.E, McGarr, A., Di Toro, G.D., & Kanamori, H., eds. *Earthquakes: Radiated Energy and the Physics of Faulting*. Geophysical Monograph Series, 170, 153-166.

Silbert, L.E., Grest, G.S., & Landry, J.W. 2002. Statistics of the contact network in frictional and frictionless granular packings. *Physical Review E*, 65, 031304/1-6.

Sleep, N.H. 1995. Frictional heating and the stability of rate and state dependent frictional sliding. *Geophysical Research Letters*, 22, 2785-2788.

Sleep, N.H. & Blanpied, M.L. 1992. Creep, compaction, and the weak rheology of major faults. *Nature*, 359, 687-692.

Smith, G.M., Davies, T.R.H., McSaveney, M.J. & Bell, D.H. 2006. The Acheron rock avalanche, Canterbury, New Zealand – morphology and dynamics. *Landslides*, 3: 62-72.

Smith, S.A.F., Holdsworth, R.E., Collettini, C. & Imber, J. 2007. Using footwall structures to constrain the evolution of low-angle normal faults. *Journal of the Geological Society, London*, 164, 1187-1191.

Smith, S.A.F., Collettini C. & Holdsworth, R.E. 2008. Recognizing the seismic cycle along ancient faults: CO_2- induced fluidization of breccias in the footwall of a sealing low-angle normal fault. *Journal of Structural Geology*, 30, 1034-1046.

Sornette, D. 1999. Earthquakes: from chemical alteration to mechanical rupture. *Physics Reports*, 313, 237-291.

Spencer, J.E. & Welty, J.W. 1986. Possible controls of base-metal and precious mineralization associated with Tertiary detachment faults in the lower Colorado River trough, Arizona and California. *Geology*, 14, 195-198.

Spray, J.G. 1995. Pseudotachylyte controversy: fact or friction? *Geology*, 23, 1119-1122.

Sulem, J., Llazar, P. & Vardoulakis, Ii. 2007. Thermo-poro-mechanical properties of clayey gouge and application to rapid fault shearing. *International Journal for Numerical and Analytical Methods in Geomechanics*, 31, 523-540.

Takahashi, M., Mizoguchi, K., Kitamura, K. & Masuda, K. 2007. Efect off clay content on the frictional strength and fluid transport property of faults. *Journal of Geophysical Research*, 112, B08206, doi:10.1029/JB004678.

Tembe, S., Lockner, D.A., Solum, J.G., Morrow, C.A., Wong, T-f. & Moore, D.E. 2006. Frictional strength of cuttings from the SAFOD drillhole phases 1 and 2. *Geophysical Research Letters*, 33, L22307, doi:10.1029/2006GL027626.

Terzhagi, K. & Peck, R.B. 1948. *Soil Mechanics in engineering practice.* Chichester: Wiley.

Townend, J. 2006. What do Faults Feel? Observational Constraints on the Stresses Acting on Seismogenic Faults. *In*, Abercrombie, R.E, McGarr, A., Di Toro, G.D., & Kanamori, H., eds. *Earthquakes: Radiated Energy and the Physics of Faulting*. Geophysical Monograph Series 170, 313-328, doi:10.1029/170GM31.

Townend, J., & Zoback, M. D. 2004. Regional tectonic stress near the San Andreas fault in central and southern California. *Geophysical Research Letters*, 31, L15S11, doi:10.1029/2003 GL018918.

Townend, J., & Zoback, M.D. 2001. Implications of earthquake focal mechanisms for the frictional strength of the San Andreas fault system. *In*, Holdsworth, R.E.; Strachan, R.A.; Macloughlin J.F.; Knipe, R.J., eds. *The Nature and Tectonic Significance of Fault Zone Weakening.* Geological Society of London Special Publication 186, 13-21.

van Eerd, A.R.T., Ellenbroek, W.G., van Hecke, Snoeijer, M.J.H. & Vlugt, T.J.H. 2007. The tail of the contact force distribution in static granular materials. *Condensed Matter e-prints,* cond-mat/0702520.

Vanderhaeghe, O., Burg, J-P. & Teyssier, C. 1999. Exhumation of migmatites in two collapsed orogens: Canadian Cordillera and French Variscides. *In:* Ring, U., Brandon, M.T., Lister, G.S. & Willett, S.D. (eds) *Exhumation Processes: Normal Faulting, Ductile Flow and Erosion*. Geological Society, London, Special Publications, 154, 181-204.

Vendeville, B. 1991. Mechanisms generating normal fault curvature: a review illustrated by physical models. *In*, Roberts, A.M., Yielding, G., Freeman, B., eds. *The Geometry of Normal Faults*. Geological Society, London, 56, 241-249.

Wang, K., Mulder, T., Rogers G.C. and, Hyndman, R.D. 1995. Case for very low coupling stress on the Cascadia subduction fault. *Journal of Geophysical Research*, 100, B7: 12907-12918.

Warr, L.N. & van der Pluijm, B.A. 2005. Crystal fractionation in the friction melts of seismic faults (Alpine Fault, New Zealand). *Tectonophysics*, 402, 111-124.

Weertman, J.J. 1980. Unstable slippage across a fault that separates elastic media of different elastic constants. *Journal of Geophysical Research*, 85, 1455-1461.

Wernicke, B.P. 1981. Low-angle normal faults in the Basin and Range Province-Nappe tectonics in an extending orogen. *Nature*, 291, 645-648.

Wernicke, B. 1985. Uniform-sense normal simple shear of the continental lithosphere. *Canadian Journal of Earth Science*, 22, 108-125.

Wernicke, B. 1992. Cenozoic extensional tectonics of the Cordillera, U.S. *In,* Burchfiel, B.C., Lipman, P.W., Zoback, M.L., eds., *The Cordilleran Orogen; Conterminous U.S.* Geological Society of America: Boulder, Colorado, 553-582.

Wernicke, B. 1995. Low-angle normal faults and seismicity: a review. *Journal of Geophysical Research,* 100, B10: 20159-20174.

Wernicke, B. & Axen, G.J. 1988. On the role of isostasy in the evolution of normal fault systems. *Geology*, 16, 848-851.

White, N. & Yielding, G. 1991. Calculating normal fault geometries at depth: theory and examples. *In*, Roberts, A.M., Yielding, G., Freeman, B., eds. *The Geometry of Normal Faults*. Geological Society, London, 56, 251-260.

Wibberley, C. 1999. Are feldspar-to-mica reactions necessarily reaction-softening processes in fault zones? *Journal of Structural Geology*, 21, 1219-1227.

Wibberley, C. A.J., Yielding, G., and Di Toro, G. 2008. Recent advances in the understanding of fault zone internal structure: a review. *In*: Wibberley, C.A.J., Kurz, W., Imber, J., Holdsworth, R.E. & Collettini, C. (eds) *The Internal Structure of Fault Zones: Implications for Mechanical and Fluid-Flow Properties.* Geological Society, London, 299. 5-33.

Wintsch, R.P., Christoffersen, R. & Kronenberg, A.K., 1995. Fluid-rock reaction weakening of fault zones. *Journal of Geophysical Research*, 100, 13021-13032.

Wong, M.S. & Gans, P.B. 2008. Geologic, structural, and thermochronologic constraints on the tectonic evolution of the Sierra Mazatán core complex, Sonora, Mexico: New insights into metamorphic core complex formation. *Tectonics*, 27, TC4013, doi: 10.1029/2007TC002173.

Yuan, F. & Prakash, V., 2007. Slip weakening in rocks and analog materials at co-seismic slip rates. *J. Mech. Phys. Solids*, doi:10.1016/j.jmps.2007.05.007.

Zhu, H.P., Zhou, Z.Y., Yang, R.Y. & Yu, A.B. 2008. Discrete particle simulation of particulate systems: A review of major applications and findings. *Chemical Engineering Science*, 63, 5728-5770.

Yund, R.A., Blanpied, M.L., Tullis T.E. & Weeks, J.D. 1990. Amorphous material in high strain experimental fault gouges. *Journal of Geophysical Research*, 95, 15589-15602.

Zhang, Y.-Q., Lu, Y. & Hao, H. 2004. Analysis of fragment size and ejection velocity at high strain rate. *International Journal of Mechanical Sciences*, 46, 27-34.

Zhu, H. P., Zhou, Z. Y., Yang, R. Y. & Yu, A. B. 2008. Discrete particle simulation of particulate systems: a review of major applications and findings. *Chemical Engineering Science*, 63, 5728–5770.

Zik, O. Stavans, J. & Rabin, Y., 1992. Mobility of a sphere in vibrated granular media. *Europhys. Lett.*, 17, 315-319.

Zoback, M.D & Townend, J. 2001. Implications of hydrostatic pore pressures and high crustal strength for the deformation of intraplate lithosphere. *Tectonophysics*, 336, 19-30.

Zoback, M.D., Hickman, S.H., Ellsworth, W., Kirschner, D., Pennell, N..B., Chery, J. & Sobolev, S. 2007. Preliminary Results from SAFOD Phase 3: Implications for the state of stress and shear localization in and near the San Andreas Fault at depth in central California. *Abstract* T13G-03, AGU Fall Meeting, San Francisco.

Appendix B

Chapter 2 Geochemistry and Mineralogy Data

B.1 Chapter 2 Documentation

Deputy Vice-Chancellor's Office
Postgraduate Office

UNIVERSITY OF CANTERBURY
Te Whare Wānanga o Waitaha
CHRISTCHURCH NEW ZEALAND

Co-Authorship Form

This form is to accompany the submission of any thesis that contains research reported in co-authored work that has been published, accepted for publication, or submitted for publication. A copy of this form should be included for each co-authored work that is included in the thesis. Completed forms should be included at the front (after the thesis abstract) of each copy of the thesis submitted for examination and library deposit.

Please indicate the chapter/section/pages of this thesis that are extracted from co-authored work and provide details of the publication or submission from the extract comes:

Chapter 2, Alpine Fault architecture at Gaunt Creek: integrated field, drilling, and laboratory results, contains material published in the following articles:

Sutherland R, Toy VG, Townend J, Cox SC, Eccles JD, Faulkner DR, Prior DJ, Norris RJ, Mariani E, ***Boulton C****, Carpenter BM, Menzies CD, Little TA, Hasting M, De Pascale G, Langridge RM, Scott HR, Reid-Lindroos Z, Fleming B 2012. Drilling reveals fluid control on architecture and rupture of the Alpine Fault, New Zealand. Geology 40: 1143-1146, doi:10.1130/G33614.1.*

Townend J, Sutherland R, Toy VG, Eccles JD, ***Boulton C****, Cox SC, McNamara D 2013. Late-interseismic state of a continental plate-bounding fault: petrophysical results from DFDP-1 wireline and core analysis, Alpine Fault, New Zealand. Geochemistry, Geophysics, Geosystems: doi:10.1029/2013GC004772.*

Please detail the nature and extent (%) of contribution by the candidate:

Sutherland et al. (2012). This was the first article published on the results of Phase 1 of the Deep Fault Drilling Project (DFDP-1). The candidate contributed, in total, c. 6% of the research, manuscript drafting, manuscript writing, and manuscript revision. Results are summarized in 1 figure and 1 paragraph in Chapter 2. Details of manuscript reviewers can be found in the acknowledgements section of the publication, reprinted in its entirety in Appendix G.

Townend et al. (2012). The manuscript contained a detailed analysis of the geochemical and geophysical properties of the two drillholes completed in the first phase DFDP-1, Alpine Fault. The candidate contributed, in total, c. 15% to the manuscript research, manuscripting drafting, manuscript writing, and manuscript revision. Details of manuscript reviewers can be found in the acknowledgements section of the publication, reprinted in its entirety in Appendix G.

Certification by Co-authors:

If there is more than one co-author then a single co-author can sign on behalf of all

The undersigned certifys that:

- The above statement correctly reflects the nature and extent of the PhD candidate's contribution to this co-authored work
- In cases where the candidate was the lead author of the co-authored work he or she wrote the text

Name: John Townend Signature: 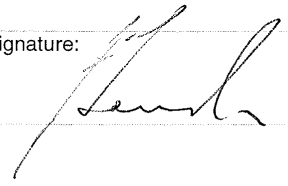 Date: 18 October 2013

Deputy Vice-Chancellor's Office
Postgraduate Office

UNIVERSITY OF CANTERBURY
Te Whare Wānanga o Waitaha
CHRISTCHURCH NEW ZEALAND

Co-Authorship Form

This form is to accompany the submission of any thesis that contains research reported in co-authored work that has been published, accepted for publication, or submitted for publication. A copy of this form should be included for each co-authored work that is included in the thesis. Completed forms should be included at the front (after the thesis abstract) of each copy of the thesis submitted for examination and library deposit.

Please indicate the chapter/section/pages of this thesis that are extracted from co-authored work and provide details of the publication or submission from the extract comes:

Figures that I made for Chapter 2, and some concepts presented in the discussion of Chapter 2, are also located in the following manuscript submitted for publication.

Toy VG, **Boulton C**, Sutherland R, Townend J, Norris RJ, Little TA, Prior DJ, Mariani E, Faulkner D, Menzies C, Scott H, Carpenter BM (in prep). Rock types, deformation mechanisms, and architecture of the Alpine Fault, revealed by DFDP-1 drilling, New Zealand. Earth and Planetary Science Letters.

Please detail the nature and extent (%) of contribution by the candidate:

In total, I contributed c. 30% to the data gathering, manuscript drafting and manuscript writing.

Certification by Co-authors:

If there is more than one co-author then a single co-author can sign on behalf of all

The undersigned certifys that:

- The above statement correctly reflects the nature and extent of the PhD candidate's contribution to this co-authored work
- In cases where the candidate was the lead author of the co-authored work he or she wrote the text

Name: VIRGINIA TOY Signature: Date: 19 NOV 2013

B.2 Introduction to Digitally Archived Data

Data presented in Chapter 2 are digitally archived in Appendix G. Details about the files are given below.

B.2.1 Major element analysis tables

Appendix G contains text files of major element geochemical results listed in Table 2.4, Table 2.5, and Table 2.6. Columns in the text files are described below. NSS denotes not sufficient sample. NA denotes not analyzed.

Column1 "Sample" gives the each sample's unique identifier. All "DFDP" samples were analyzed with ICP-AES; instrument precision for this method is ±0.02 wt.%. All "AFUC" and "RW_XRF" samples were analyzed with XRF. Instrument precision for this method was not available.

Column2 In Table 2.4 and Table 2.5, "Hole depth" denotes depth below ground surface at the DFDP-1 drill site, Gaunt Creek. In Table 2.6, "Location" denotes location along-strike of the Alpine Fault. Location latitude/longitude co-ordinates are: Little Man River 43.1400°S/170.2818°E; Gaunt Creek Terrace and Gaunt Creek Scarp 43.3141°S/170.3259°E; Stoney Creek 43.2290°S/170.1239°E; Waikukupa River 43.2622°S/170.0490°E; Robinson Creek 43.4956°S/169.1350°E; Martyr River 44.1326°S/168.5536°E; McKenzie Creek 44.3599°S/168.1390°E; Hokuri Creek 44.4062°S/168.0648°E.

Column3 "Lithology" denotes the characteristic lithological unit that corresponds to the sampled fault rock. Characteristic lithologies are defined in Chapter 2.

Column4 "SiO_2" is in units of wt.%. For samples analysed with ICP-AES, repeat standard analyses yield the following maximum analytical error: SiO_2 ±2.20%. For samples analysed with XRF, repeat standard analyses yield the following maximum analytical error: SiO_2 ±0.20%.

Column5 "TiO_2" is in units of wt.%. For samples analysed with ICP-AES, repeat standard analyses yield the following maximum analytical error: TiO2 ±1.55%. For samples analysed with XRF, repeat standard analyses yield the following maximum analytical error: TiO_2 ±0.44%.

Column6 "Al_2O_3" is in units of wt.%. For samples analysed with ICP-AES, repeat standard analyses yield the following maximum analytical error: Al_2O_3 ±2.68%. For samples analysed with XRF, repeat standard analyses yield the following maximum analytical error: Al_2O_3 ±0.34%.

Column7 "Fe_2O_3t" denotes total Fe_2O_3, and units are wt.%. For samples analysed with ICP-AES, repeat standard analyses yield the following maximum analytical error: Fe_2O_3 ±2.52%. For samples analysed with XRF, repeat standard analyses yield the following maximum analytical errors: Fe_2O_3 ±0.21%.

Column8 "MnO" is in units of wt.%. For samples analysed with ICP-AES, repeat standard analyses yield the following maximum analytical error: MnO ±0.01%. For samples analysed with XRF, repeat standard analyses yield the following maximum analytical error: MnO ±10.88%.

Column9 "MgO" is in units of wt.%. For samples analysed with ICP-AES, repeat standard analyses yield the following maximum analytical error: MgO ±1.60%. For samples analysed with XRF, repeat standard analyses yield the following maximum analytical error: MgO ±2.32%.

Column10 "CaO" is in units of wt.%. For samples analysed with ICP-AES, repeat standard analyses yield the following maximum analytical error: CaO ±5.44%. For samples analysed with XRF, repeat standard analyses yield the following maximum analytical error: CaO ±0.44%.

Column11 "Na_2O" is in units of wt.%. For samples analysed with ICP-AES, repeat standard analyses yield the following maximum analytical error: Na_2O ±9.00%. For samples analysed with XRF, repeat standard analyses yield the following maximum analytical error: Na_2O ±8.32%.

Column12 "K_2O" is in units of wt.%. For samples analysed with ICP-AES, repeat standard analyses yield the following maximum analytical error: K_2O ±2.53%. For samples analysed with XRF, repeat standard analyses yield the following maximum analytical error: K_2O ±0.60%.

Column13 "P_2O_5" is in units of wt.%. Oxide abundance was within instrument precision, and analytical errors range up to 100%.

Column14 "Cr_2O_5" is in units of wt.%. Oxide abundance was within instrument precision, and analytical errors range up to 100%.

Column15 "SrO" is in units of wt.%. Oxide abundance was within instrument precision, and analytical errors range up to 100%.

Column16 "BaO" is in units of wt.%. Oxide abundance was within instrument precision, and analytical errors range up to 100%.

Column17 "LaO" is in units of wt.%. A maximum LOI analytical error ±11.55% was calculated from repeat standard analyses provided by ALS Minerals.

Column18 "Total" is the sum of the oxides reported (wt. %).

Column19 "CIA" is the chemical index of alteration, calculated following

$$\mathrm{CIA} = \left[\frac{\mathrm{Al_2O_3}}{\mathrm{Al_2O_3} + \mathrm{Na_2} + \mathrm{K_2O} + \mathrm{CaO}}\right] \times 100$$

where the major element oxides are given in molecular proportions (wt. %) (Nesbitt & Young 1982, 1989).

B.2.2 Qualitative X-ray diffraction (XRD) data

Appendix G also contains text files of the results of qualitative X-ray diffaction (XRD) analyses conducted on 34 clean characteristic lithology samples collected from DFDP-1A and DFDP-1B drillcore. Samples were first ground for 10 minutes in a McCrone micronizing mill under ethanol and dried

overnight at 60°C. Approximately 3 g of milled and dried sample powder was then lightly ground with a mortar and pestle and lightly back pressed into stainless steel sample holders. Powder XRD measurements were performed on a PANalytical X'Pert PRO MPD PW 3040/60 X-ray diffractometer in the Department of Geology, University of Otago. Measurement conditions were 40 kV, 30 mA, CuK_{α} radiation with 0.125° divergence slit size. XRD patterns were recorded in steps of 0.0080°2_{θ}using X'Pert Data Collector version 2.0e and processed with X'Pert HighScore version 2.2b. Results are listed in Table 2.1. Raw XRD trace data are listed in individual text files labeled with the sample name as it appears in Table 2.1. Raw data are given so that the traces can be manipulated in whichever (usually proprietary) software the user wishes to use. Column values are described below.

Column1 "No." denotes the scan increment during which the recorded data were acquired.

Column2 "Pos. [°2θ]" denotes the angle of diffraction.

Column3 "Iobs [cts]" gives the observed raw intensity of the diffracted X-ray beams recorded by the detector.

Column4 "Icalc [cts]" gives the observed raw intensity of the diffracted X-ray beams recorded by the detector. If data had been treated, this value would be different from Column 3.

Column5 "CT [s]" the counting time per data point, in seconds.

Column5 "Iback [cts]" gives the calculated background intensity.

Column6 "ESD" this column, the Estimated Standard Deviation, is blank because the data are raw and background intensity has not been subtracted.

Column7 "D spacings" is the interlattice spacing, calculated using Bragg's Law such that $n\lambda = 2d\sin\theta$where n is an integer, λ is the wavelength of the incident X-ray, d is the interlattice spacing, or spacing between

planes in the crystal lattice, and θ is the angle between the incident X-ray and the scattering planes.

B.2.3 Quantative X-ray diffraction (XRD) data

Quantitative XRD analyses were on Alpine Fault gouges and cataclasites in DFDP-1B by Mark Raven, CSIRO Land and Water, Urrbrae, South Australia, Australia. For these analyses, approximately 1.5 g of each sample was ground for 10 minutes in a McCrone micronizing mill under ethanol. The resulting slurries were oven-dried at 60°C, thoroughly mixed with mortar and pestle, and lightly back pressed into stainless steel sample holders. XRD patterns were recorded in steps of 0.017°2θ on a PANalytical X'Pert Pro Multipurpose Diffractometer using Fe-filtered Co K_α radiation (1.78897 Å radiation), 2θ-compensating variable divergence slit, 1° antiscatter slit and fast X'Celerator Si multi-strip detector with 128 elements. Smectite identification was done using XRD patterns obtained from oriented slides of Mg-saturated, glycerolated <2 μm clay separates. Since variable hydration of interlayer water causes problems with quantification, smectite-bearing samples were calcium saturated and re-analyzed. Quantitative analysis was performed using SIROQUANT, a commercially available software package from Sietronics Pty Ltd. The raw data for each analysis reported in Chapters 2, 3, 4, 5, and 6 are listed in separate text files labeled according to each analysis' unique CSIRO identifier. All samples were microionized, but specific treatments varied. Raw data are given so that the traces can be manipulated in whichever (usually proprietary) software the user wishes to use. All raw data are presented as text files in Appendix G. The following abbreviations denote how the sample was treated and correspond to column headings.

No abbreviation indicates microionized only.

"MCa" indicates samples were microionized and Ca saturated.

"Ca" and "Ca_1" indicates samples were Ca saturated.

"I2um_Mg_Gly" indicates sample was a <2 μm separate, was oriented, Mg saturated and glycerolated.

"gly" indicates sample was oriented, Mg saturated, and glycerolated.

"a_gly" indicates sample was acetic acid washed, oriented, Mg saturated, and glycerolated.

"ac" indicates sample was acetic acid washed and Ca saturated.

Appendix C

Chapter 3 Friction and Permeability Data

C.1 Chapter 3 Documentation

UNIVERSITY OF CANTERBURY
Te Whare Wānanga o Waitaha
CHRISTCHURCH NEW ZEALAND

Deputy Vice-Chancellor's Office
Postgraduate Office

Co-Authorship Form

This form is to accompany the submission of any thesis that contains research reported in co-authored work that has been published, accepted for publication, or submitted for publication. A copy of this form should be included for each co-authored work that is included in the thesis. Completed forms should be included at the front (after the thesis abstract) of each copy of the thesis submitted for examination and library deposit.

Please indicate the chapter/section/pages of this thesis that are extracted from co-authored work and provide details of the publication or submission from the extract comes:

Chapter 3, Physical properties of surface outcrop cataclastic fault rocks, Alpine Fault, New Zealand, is reprinted in its entirety from:

***Boulton C**, Carpenter BM, Toy VG, Marone C 2012. Physical properties of surface outcrop cataclastic fault rocks, Alpine Fault, New Zealand. Geochemistry Geophysics Geosystems 13(1): Q01018, doi:10.1029/2011GC003872.*

Please detail the nature and extent (%) of contribution by the candidate:

The candidate contributed, in total, 85% of the experiment design, data collection (including fieldwork and laboratory experiments), data interpretation, manuscript drafting, manuscript writing, and manuscript revision. Details of analytical work done by technical staff, and manuscript reviewers, can be found in the acknowledgements section of Chapter 3.

Certification by Co-authors:

If there is more than one co-author then a single co-author can sign on behalf of all

The undersigned certifys that:

- The above statement correctly reflects the nature and extent of the PhD candidate's contribution to this co-authored work
- In cases where the candidate was the lead author of the co-authored work he or she wrote the text

Name:	Signature:	Date:
Brett M. Carpenter	Brett M. Carpenter	24/06/2013

Subject: RE: G3 permission
From: "Goldweber, Paulette - Hoboken" <pgoldweb@wiley.com>
Date: 31/10/13 7:58 AM
To: Carolyn Boulton <cjb205@uclive.ac.nz>

Dear Carolyn:

Thank you for your request. John Wiley & Sons, Inc. has no objections to your proposed reuse of this material.

Permission is hereby granted for the use requested subject to the usual acknowledgements (title, volume number, issue number, year, page numbers. Copyright [year and owner]. And the statement "This material is reproduced with permission of John Wiley & Sons, Inc."). Any third party material is expressly excluded from this permission. If any of the material you wish to use appears within our work with credit to another source, authorization from that source must be obtained.

This permission does not include the right to grant others permission to photocopy or otherwise reproduce this material except for accessible versions made by non-profit organizations serving the blind, visually impaired and other persons with print disabilities.

Sincerely,

Paulette Goldweber
Associate Manager/Permissions-Global Rights
Professional Development

Wiley
111 River Street, 4-02
Hoboken, NJ 07030-5774
U.S.
www.wiley.com

T +1 201-748-8765
F +1 201-748-6008
pgoldweb@wiley.com
PermissionsUS@wiley.com

-----Original Message-----
From: Carolyn Boulton [mailto:cjb205@uclive.ac.nz]
Sent: Monday, October 14, 2013 8:29 PM
To: RightsLink; Tim Davies
Subject: G3 permission

Dear John Wiley & Sons, Ltd.,

I am writing to ask for permission to include a publication in my dissertation document. I have cc'd my senior supervisor, who supports the use of this publication in my dissertation. I have also obtained permission from the publication co-authors.

According to the attached document, wherein I have highlighted the pertinent

regulation, the University of Canterbury requires written permission from the journal in which the article is published.

I would like to use the following publication, on which I am first author, in my PhD dissertation:

http://onlinelibrary.wiley.com/doi/10.1029/2011GC003872/abstract

The document will not be formatted as is it appears in the journal, but rather it will be formatted as part of the coherent thesis document.

If you require any additional information regarding the use of this publication, please do not hesitate to ask.

Thank you for your help,
Carolyn

--
PhD Candidate
Department of Geological Sciences
University of Canterbury
PB 4800, Christchurch 8140
New Zealand
Phone: +64 3 3642700
Email: cjb205@uclive.ac.nz

C.2 Chapter 3 Friction Plots

This appendix contains run plots of all experiments presented in Chapter 3. All data are located in text files in Appendix G.3. All experiments were conducted on the double direct shear apparatus at Pennsylvania State University, Pennsylvania, USA. A detailed diagram of the experimental apparatus and sample assembly is provided in Figure **??**. Plots of coefficient of friction (μ) against elastically corrected displacement (μm) are provided in Figures C.2, C.3, and C.4. The displacement plots are presented in the order that they appear in Table 3.2. Vertical lines in some displacement plots indicate where shearing stopped and the load point displacement transducer was reset to stay within optimal range. Detailed methods and data archives are located in Appendix C.

Figure C.1 (over). **(a)** Diagrammatic sketch of the double direct shear apparatus, including pressure vessel, used in experiments presented in Chapters 3 and 4. In the double direct shear configuration, two sample layers are bracketed by two outer steel blocks across which the normal force is applied with a horizontal piston. Shear is established in the layers by driving a central steel block downward with a vertical piston. Confining fluid (food grade vegetable oil) within the vessel applies a pressure to the sample assembly. **(b)** Detailed diagram of the sample assembly, including forcing blocks, horizontal and vertical displacement transducers (DCDTs), internal pore fluid (tap water) lines, pore fluid reservoirs, and sintered porous stainless steel fluid distribution frits (dark gray toothed objects). **(c)** Detailed diagram of the materials used to isolate the pore fluid from the confining fluid inside the pressure vessel. The sample and sample blocks are first jacketed with a 3.2 mm-thick latex rubber sheet and covered with 2 0.9 mm-thick rubber sleeves, followed by 2 dip-molded rubber jackets. The jacketed sample assembly is sealed with an O-ring and steel wire. The effective permeability of the porous frits is $\geq 4.2 \times 10^{-14}$ m^2. Calibrations that account for the effects of the fluid tubing and finite response time of the pressure intensifiers show that the fluid pressure at the boundary layers is constant for effective layer permeabilities below about 5×10^{-15} m^2. Thus, drained conditions are maintained during shearing. Figure and caption after Samuelson et al. (2009).

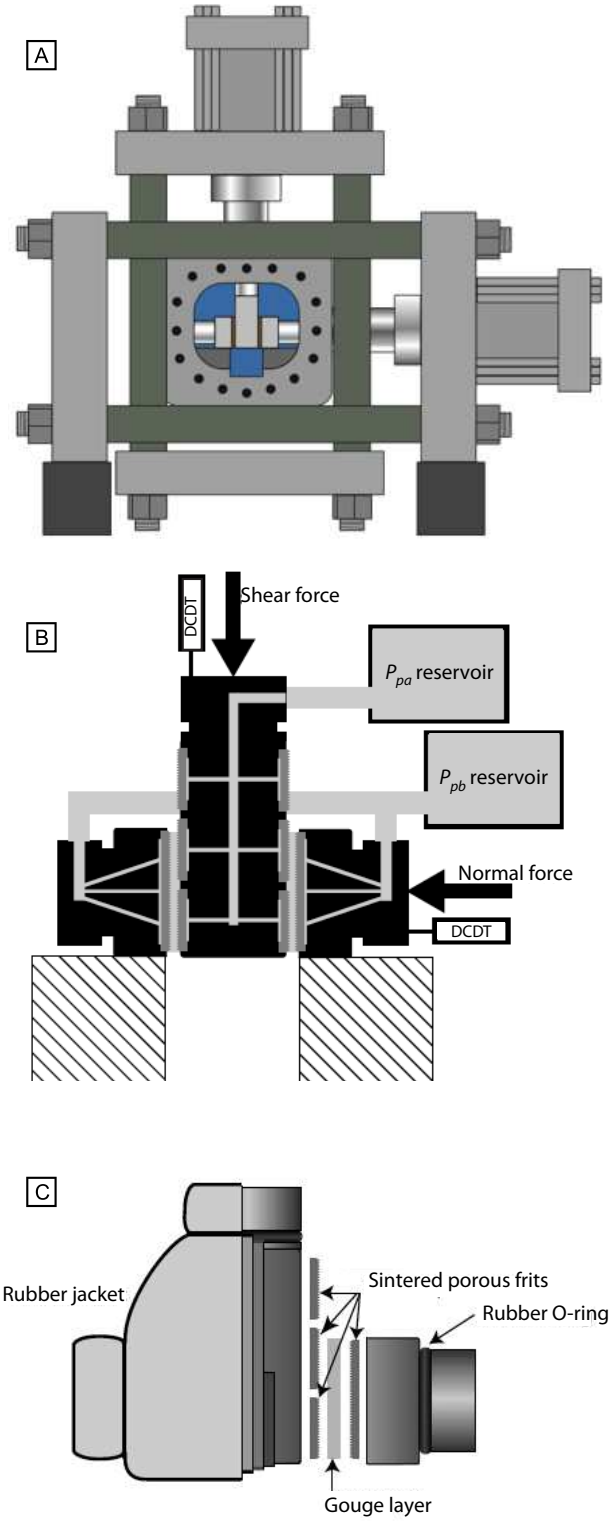
A
B
DCDT
Shear force
P_{pa} reservoir
P_{pb} reservoir
Normal force
DCDT
C
Rubber jacket
Sintered porous frits
Rubber O-ring
Gouge layer

Figure C.1:

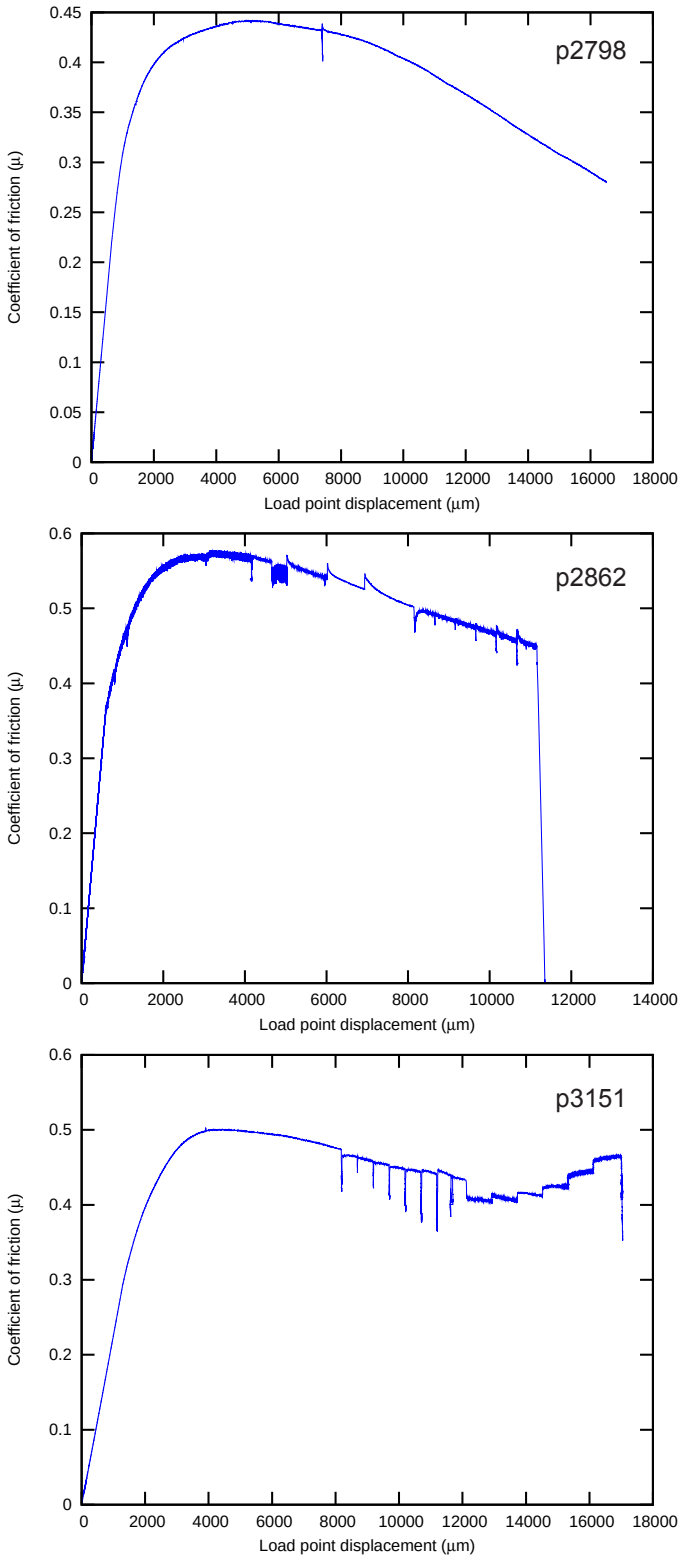

Figure C.2: Experiments p2798, p2862, and p3151.

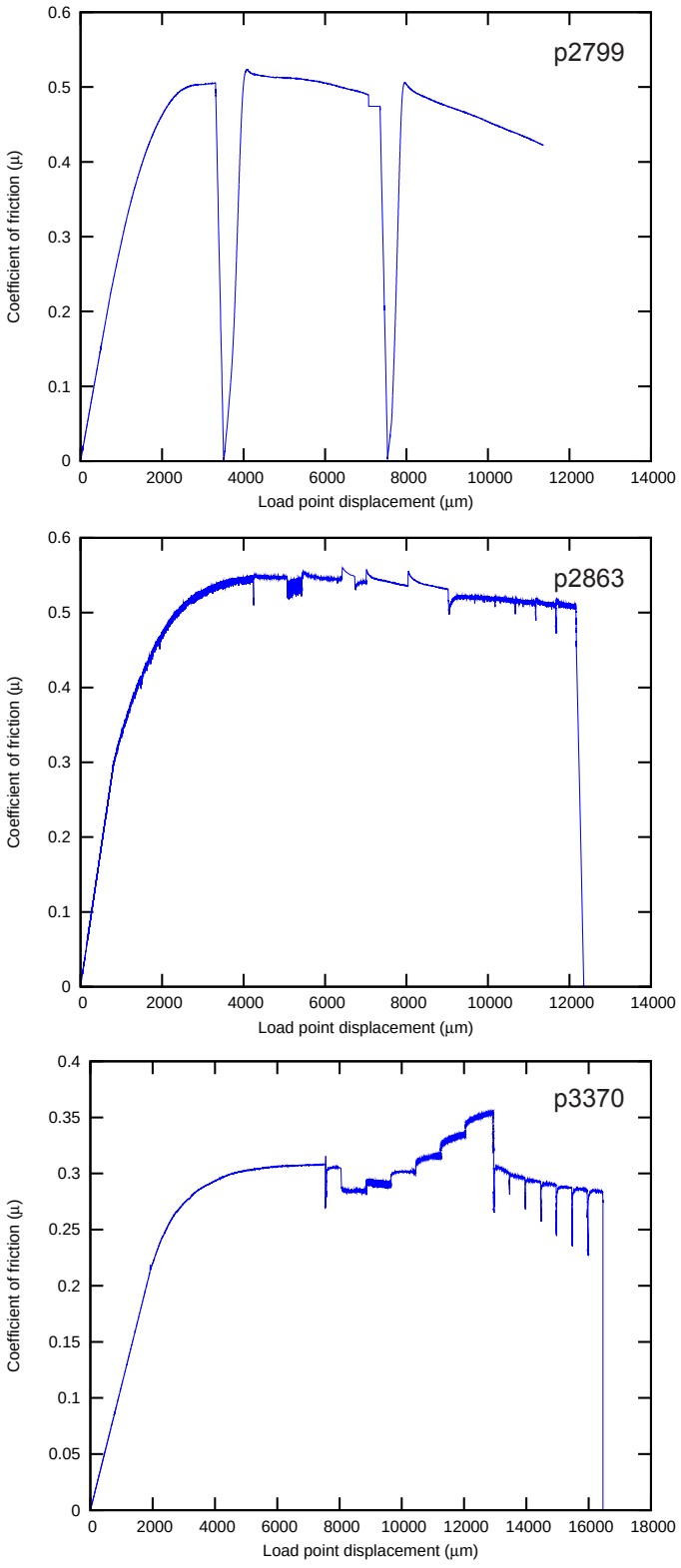

Figure C.3: Experiments p2799, p2863, and p3370.

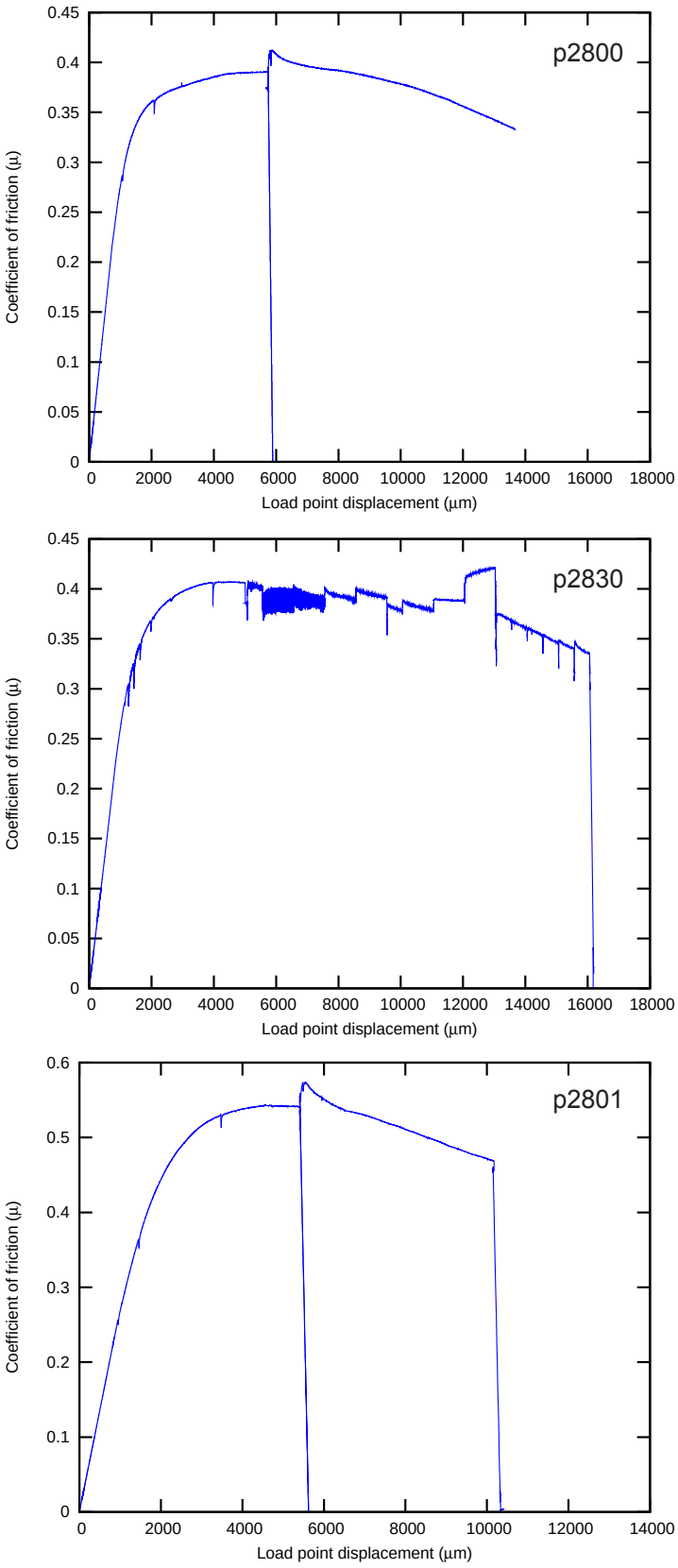

Figure C.4: Experiments p2800, p2830, and p2801.

C.3 Introduction to Digitally Archived Data

Complete records of the double direct shear experiments presented in Chapter 3 are digitally archived in Appendix G.3. Details about the files are given below.

Text files of data recorded during 10 double direct shear experiments conducted on the biax, Pennsylvania State University, Pennsylvania, USA, are contained in this appendix. Surface-outcrop samples of Alpine Fault gouges and cataclasites were deformed in a servo-hydraulic controlled biaxial testing apparatus fitted with a pressure vessel (Samuelson et al. 2009; Ikari et al. 2011b). All samples were sheared under saturated, drained conditions at room temperature with a constant pore pressure boundary condition. Normal and shear stresses were calculated from applied loads by dividing by the contact area of the forcing block for normal stress, and dividing by twice the contact area for shear stress. Two intact wafers of fault gouge or cataclasite were used for each experiment, and wafer dimensions were: 6-8 mm-thick, 54 mm-wide, 61 mm-long. The long axis of each wafer was cut parallel to the fault shear direction as indicated by slickenside striations measured in the field. Effective normal stress (σ_n'), confining pressure (P_c), and pore fluid pressure (P_p) were held constant at ~ 31 MPa, 25 MPa, and 10 MPa, respectively (Table 3.2). Effective normal stress was determined from measurements of applied normal stress, a fraction of the confining pressure equal to the ratio of the piston contact area (44 mm diameter) to the sample area, and the measured pore fluid pressure following:

$$\sigma_n' = \sigma_n + 0.506P_c - P_p \tag{C.1}$$

Pore fluid used in the experiments was University Park, Pennsylvania, USA tap water with pH = 7 and total cation concentration $\left[Ca_2^+ + Mg_2^+\right]$ = 2–4 mmol/L. Corrections for jacket stretching and rubber compression were made following Samuelson et al. (2009). Each data file contains 20 columns, and each column is described below.

Column1 "rc_disp" gives the load point displacement in μm. Displacement of the vertical ram (load point) was measured outside of the pressure vessel using a displacement transducer with ±0.1 μm precision.

Column2 "Shear_stress" gives the shear stress resolved on the deforming samples in MPa. Shear stress was measured by a load cell outside of the pressure vessel with an accuracy of ±0.002 MPa.

Column3 "layer-thick" gives the instantaneous thickness of the deforming samples in μm. It is calculated from the displacement of the horizontal ram (load point) was measured outside of the pressure vessel using a displacement transducer with ±0.1 μm precision.

Column4 "Nor_Stress" gives the normal stress resolved on the deforming samples in MPa. Normal stress was measured by a load cell outside of the pressure vessel with an accuracy of ±0.002 MPa.

Column5 "Pc_disp" gives the displacement of the piston within the pressure intensifier that controls the confining pressure (P_c); units are μm. During the experiments, the piston is load-controlled to maintain a constant confining pressure. The movement of the piston is measured with a linear variable differential transformer (LVDT).

Column6 "Pc_load" gives the confining pressure in MPa. Confining pressure was monitored with a Stellar Technology pressure transducer with a resolution greater than ±0.007 MPa.

Column7 "Ppa_disp" gives the displacement of the piston within the pressure intensifier that controls the upstream pore fluid pressure (P_{pa}); units are μm/s. The movement of the piston is measured with a linear variable differential transformer (LVDT). During the shearing part of each friction experiment, the upstream (P_{pa}) and downstream (P_{pb}) pore fluid intensifiers are controlled independently to maintain constant pore fluid pressure boundary conditions. During each permeability experiment, the upstream (P_{pa}) and downstream (P_{pb}) pore fluid inten-

sifiers act together to create a pressure differential across the samples (perpendicular to the shearing direction).

Column8 "Ppa_load" gives the upstream pore fluid pressure (P_{pa}) in MPa. P_{pa} was monitored with a Stellar Technology pressure transducer with a resolution greater than ± 0.007 MPa.

Column9 "Ppb_disp" gives the displacement of the piston within the pressure intensifier that controls the downstream pore fluid pressure (P_{pb}); units are μm/s. The movement of the piston is measured with a linear variable differential transformer (LVDT).

Column10 "Ppb_load" gives the downstream pore fluid pressure (P_{pb}) in MPa. P_{pb} was monitored with a Stellar Technology pressure transducer with a resolution greater than ± 0.007 MPa.

Column11 "Time" gives the time, in seconds, elapsed since the start of the experiment.

Column12 "ec_disp" gives the load point displacement corrected for elastic stretching of the apparatus and sample assembly, including the elastic and rubber jackets. Units are μm.

Column13 "shear_strain" gives the instantaneous engineering shear strain. Shear strain is calculated from the displacement (Column 12) divided by the instantaneous layer thickness (Column 3).

Column14 "Eff_Stress" gives the effective normal stress (σ_n'), in MPa, calculated following equation C.1.

Column15 "mu" gives the coefficient of friction, calculated by dividing shear stress (Column 2) by effective normal stress (Column 14) assuming no cohesion.

Column16-20 are columns created during the calculation of permeability.

Column16. "Qa" is the displacement rate of the P_{pa} piston, calculated from data in Columns 7 and 11, converted into a flow rate or dischage using the area of the piston (2.54 cm area piston). Units are m^3.

Column17 "Qb" is the displacement rate of the P_{pb} piston, calculated from data in Columns 9 and 11, converted into a flow rate or dischage using the area of the piston (2.54 cm area piston). Units are m^3.

Column18 "percentQdiff" is the percent different between the two flow rates. If the calculated value is greater than 5%, the results are invalid.

Column19 "Qx" is the average discharge multiplied by the layer thickness (Column 3 converted to m). Units are m^3.

Column20 "perm" is permeability in units of m^2. This is calculated by solving Darcy's law, letting permeability $k = \frac{Qx \times \eta}{A \times \left(P_{pb} - P_{pa}\right)}$ where Qx is the average discharge, η is the dynamic viscosity of water (in MPa), A is cross-sectional area of the sample, and (P_{pb}–P_{pa}) is the measured pressure differential, in MPa.

Appendix D

Chapter 4 Friction and Permeability Data

D.1 Chapter 4 Documentation

UNIVERSITY OF CANTERBURY
Te Whare Wānanga o Waitaha
CHRISTCHURCH NEW ZEALAND

Deputy Vice-Chancellor's Office
Postgraduate Office

Co-Authorship Form

This form is to accompany the submission of any thesis that contains research reported in co-authored work that has been published, accepted for publication, or submitted for publication. A copy of this form should be included for each co-authored work that is included in the thesis. Completed forms should be included at the front (after the thesis abstract) of each copy of the thesis submitted for examination and library deposit.

Please indicate the chapter/section/pages of this thesis that are extracted from co-authored work and provide details of the publication or submission from the extract comes:

Chapter 4, Slip localization on the southern Alpine Fault, New Zealand, is reprinted in its entirety from:

*Barth NC, **Boulton C**, Carpenter BM, Batt GE, Toy VG 2013. Slip localization on the southern Alpine Fault, New Zealand. Tectonics 32: 1-21, doi:10.1002/tect.20041.*

Please detail the nature and extent (%) of contribution by the candidate:

The candidate contributed, in total, 40% of the experiment design, data collection, data interpretation, manuscript drafting, manuscript writing, and manuscript revision. Details of analytical work done by technical staff, and manuscript reviewers, can be found in the acknowledgements section of Chapter 4.

Certification by Co-authors:

If there is more than one co-author then a single co-author can sign on behalf of all

The undersigned certifies that:

- The above statement correctly reflects the nature and extent of the PhD candidate's contribution to this co-authored work
- In cases where the candidate was the lead author of the co-authored work he or she wrote the text

Name: *Nicolas Barth* Signature: Nicolas Barth Date: *19 June 2013*

NOTWITHSTANDING ANY FAILURE OF ESSENTIAL PURPOSE OF ANY LIMITED REMEDY PROVIDED HEREIN.
9. Should any provision of this Agreement be held by a court of competent jurisdiction to be illegal, invalid, or unenforceable, that provision shall be deemed amended to achieve as nearly as possible the same economic effect as the original provision, and the legality,
validity and enforceability of the remaining provisions of this Agreement shall not be affected or impaired thereby.
10. The failure of either party to enforce any term or condition of this Agreement shall not constitute a waiver of either party's right to enforce each and every term and condition of this Agreement. No breach under this agreement shall be deemed waived or excused by either party unless such waiver or consent is in writing signed by the party granting such waiver or consent. The waiver by or consent of a party to a breach of any provision of this Agreement shall not operate or be construed as a waiver of or consent to any other or subsequent breach by such other party.
11. This Agreement may not be assigned (including by operation of law or otherwise) by you without WILEY's prior written consent.
12. Any fee required for this permission shall be non-refundable after thirty (30) days from receipt
13. These terms and conditions together with CCC's Billing and Payment terms and conditions (which are incorporated herein) form the entire agreement between you and WILEY concerning this licensing transaction and (in the absence of fraud) supersedes all prior agreements and representations of the parties, oral or written. This Agreement may not be amended except in writing signed by both parties. This Agreement shall be binding upon and inure to the benefit of the parties' successors, legal representatives, and authorized
assigns.
14. In the event of any conflict between your obligations established by these terms and conditions and those established by CCC's Billing and Payment terms and conditions, these
terms and conditions shall prevail.
15. WILEY expressly reserves all rights not specifically granted in the combination of (i) the license details provided by you and accepted in the course of this licensing transaction, (ii)
these terms and conditions and (iii) CCC's Billing and Payment terms and conditions.
16. This Agreement will be void if the Type of Use, Format, Circulation, or Requestor Type was misrepresented during the licensing process.
17. This Agreement shall be governed by and construed in accordance with the laws of the State of New York, USA, without regards to such state's conflict of law rules. Any legal action, suit or proceeding arising out of or relating to these Terms and Conditions or the breach thereof shall be instituted in a court of competent jurisdiction in New York County I the State of New York in the United States of America and each party hereby consents and submits to the personal jurisdiction of such court, waives any objection to venue in such court and consents to service of process by registered or certified mail, return receipt requested, at the last known address of such party.

Wiley Open Access Terms and Conditions

Wiley publishes Open Access articles in both its Wiley Open Access Journals program[http://www.wileyopenaccess.com/view/index.html] and as Online Open articles in its subscription journals. The majority of Wiley Open Access Journals have adopted the Creative Commons Attribution License (CC BY) which permits the unrestricted use,
distribution, reproduction, adaptation and commercial exploitation of the article in any medium. No permission is required to use the article in this way provided that the article is properly cited and other license terms are observed. A small number of Wiley Open Access journals have retained the

D.2 Chapter 4 Friction Experiment Plots

This appendix contains run plots of all experiments presented in Chapter 4. All experiments were conducted on the double direct shear apparatus at Penn State University, Pennsylvania, USA. A detailed diagram of the experimental apparatus and sample assembly is provided in Figure C.1. Plots of coefficient of friction (μ) against elastically corrected displacement (μm) are provided in Figures D.1 and D.2. The displacement plots are presented in the order that they appear in Table 4.3. Vertical lines in some displacement plots indicate where shearing stopped and the vertical displacement transducer was reset to stay within optimal range. Detailed methods and data archives are located in Appendices D.3 and G.4, respectively.

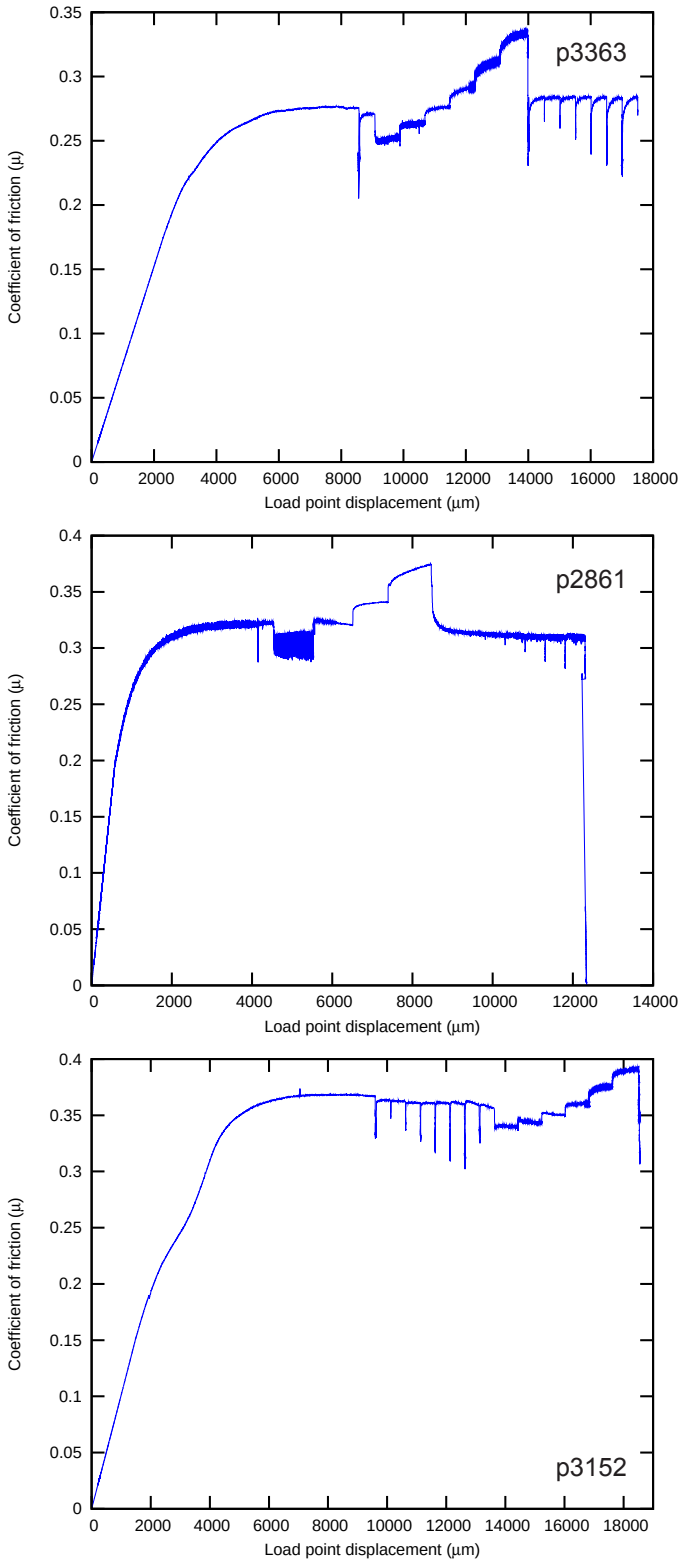

Figure D.1: Experiments p3363, p2861, and p3152.

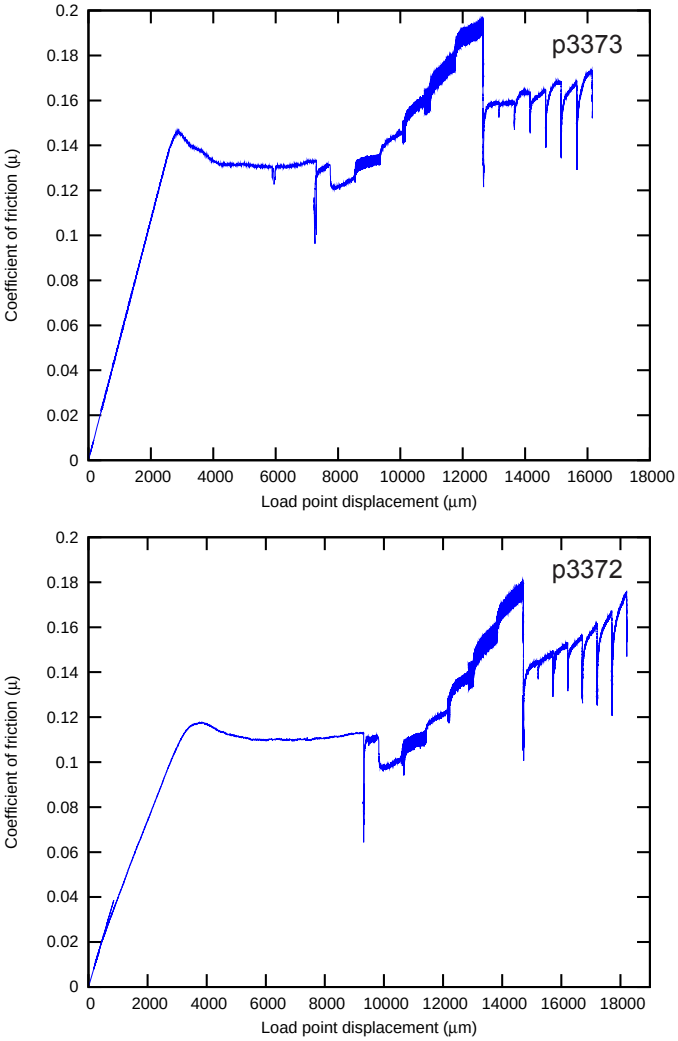

Figure D.2: Experiments p3373 and p3372.

D.3 Introduction to Digitally Archived Data

Complete records of the double direct shear experiments presented in Chapter 4 are digitally archived in Appendix G.4. Details about the files are given below.

Text files of data recorded during 5 double direct shear experiments conducted using the biax, Penn State University, Pennsylvania, USA, are contained in this appendix. Surface-outcrop samples of southern Alpine Fault gouges were deformed in a servo-hydraulic controlled biaxial testing apparatus fitted with a pressure vessel (Samuelson et al. 2009; Ikari et al. 2011b). All samples were sheared under saturated, drained conditions at room temperature with a constant pore pressure boundary condition. Normal and shear stresses were calculated from applied loads by dividing by the contact area of the forcing block for normal stress, and dividing by twice the contact area for shear stress. Two intact wafers of fault gouge or cataclasite were used for each experiment, and wafer dimensions were: 6-8 mm-thick, 54 mm-wide, 61 mm-long. The long axis of each wafer was cut parallel to the fault shear direction as indicated by slickenside striations measured in the field. Effective normal stress (σ_n'), confining pressure (P_c), and pore fluid pressure (P_p) were held constant at 6 MPa, 4 MPa, and 1 MPa, respectively, for experiments p3673, p3373, and p3372. Effective normal stress (σ_n'), confining pressure (P_c), and pore fluid pressure (P_p) were held constant at ~ 31 MPa, 15 or 25 MPa, and 10 MPa, respectively, for experiments p2861 and p3152 (Table 4.3). Effective normal stress was determined from measurements of applied normal stress, a fraction of the confining pressure equal to the ratio of the piston contact area (44 mm diameter) to the sample area, and the measured pore fluid pressure following:

$$\sigma_n' = \sigma_n + 0.506P_c - P_p \tag{D.1}$$

Pore fluid used in the experiments was University Park, Pennsylvania, USA tap water with pH = 7 and total cation concentration $\left[Ca_2^+ + Mg_2^+\right]$ = 2–4 mmol/L. Corrections for jacket stretching and rubber compression were made following Samuelson et al. (2009). Each data file contains 20 columns, and each column is described below.

Column1 "rc_disp" gives the load point displacement in μm. Displacement of the vertical ram (load point) was measured outside of the pressure vessel using a displacement transducer with $\pm$0.1 mm precision.

Column2 "Shear_stress" gives the shear stress resolved on the deforming samples in MPa. Shear stress was measured by a load cell outside of the pressure vessel with a precision of $\pm$0.1 kN.

Column3 "layer-thick" gives the instantaneous thickness of the deforming samples in mm. It is calculated from the displacement of the horizontal ram (load point) was measured outside of the pressure vessel using a displacement transducer with $\pm$0.1 μm precision.

Column4 "Nor_Stress" gives the normal stress resolved on the deforming samples in MPa. Normal stress was measured by a load cell outside of the pressure vessel with a precision of $\pm$0.1 kN.

Column5 "Pc_disp" gives the displacement of the piston within the pressure intensifier that controls the confining pressure (Pc); units are μm. During the experiments, the piston is load-controlled to maintain a constant confining pressure. The movement of the piston is measured with a linear variable differential transformer (LVDT).

Column6 "Pc_load" gives the confining pressure in MPa. Confining pressure was monitored with a Stellar Technology pressure transducer with a resolution greater than $\pm$0.007 MPa.

Column7 "Ppa_disp" gives the displacement of the piston within the pressure intensifier that controls the upstream pore fluid pressure (Ppa); units are mm/s. The movement of the piston is measured with a linear variable differential transformer (LVDT). During the shearing part of each friction experiment, the upstream (P_{pa}) and downstream (P_{pb}) pore fluid intensifiers are controlled independently to maintain constant pore fluid pressure boundary conditions. During each permeability experiment, the upstream (P_{pa}) and downstream (P_{pb}) pore fluid inten-

sifiers act together to create a pressure differential across the samples (perpendicular to the shearing direction).

Column8 "Ppa_load" gives the upstream pore fluid pressure (P_{pa}) in MPa. P_{pa} was monitored with a Stellar Technology pressure transducer with a resolution greater than ± 0.007 MPa.

Column9 "Ppb_disp" gives the displacement of the piston within the pressure intensifier that controls the downstream pore fluid pressure (P_{pb}); units are μm/s. The movement of the piston is measured with a linear variable differential transformer (LVDT).

Column10 "Ppb_load" gives the downstream pore fluid pressure (P_{pb}) in MPa. P_{pb} was monitored with a Stellar Technology pressure transducer with a resolution greater than ± 0.007 MPa.

Column11 "Time" gives the time, in seconds, elapsed since the start of the experiment.

Column12 "ec_disp" gives the load point displacement corrected for elastic stretching of the apparatus and sample assembly, including the elastic and rubber jackets. Units are μm.

Column13 "shear_strain" gives the instantaneous engineering shear strain. Shear strain is calculated from the displacement (Column 12) divided by the instantaneous layer thickness (Column 3).

Column14 "Eff_Stress" gives the effective normal stress (σ_n'), in MPa, calculated following equation D.1.

Column15 "mu" gives the coefficient of friction, calculated by dividing shear stress (Column 2) by effective normal stress (Column 14) assuming no cohesion.

Column16-20 are columns created during the calculation of permeability.

Column16 "Qa" is the displacement rate of the P_{pa} piston, calculated from data in Columns 7 and 11, converted into a flow rate or dischage using the area of the piston (2.54 cm area piston). Units are m^3.

Column17. "Qb" is the displacement rate of the P_{pb} piston, calculated from data in Columns 9 and 11, converted into a flow rate or dischage using the area of the piston (2.54 cm area piston). Units are m^3.

Column18 "percentQdiff" is the percent different between the two flow rates. If the calculated value is greater than 5%, the results are invalid.

Column19 "Qx" is the average discharge multiplied by the layer thickness (Column 3 converted to m). Units are m^3.

Column20 "perm" is permeability in units of m^2. This is calculated by solving Darcy's law, letting permeability $k = \frac{Qx \times \eta}{A \times \left(P_{pb} - P_{pa}\right)}$ where Qx is the average discharge, η is the dynamic viscosity of water (in MPa), A is cross-sectional area of the sample, and (P_{pb}–P_{pa}) is the measured pressure differential, in MPa.

Appendix E

Chapter 5 Particle Size Analysis and Friction Data

E.1 Chapter 5 Documentation

Deputy Vice-Chancellor's Office
Postgraduate Office

UNIVERSITY OF CANTERBURY
Te Whare Wānanga o Waitaha
CHRISTCHURCH NEW ZEALAND

Co-Authorship Form

This form is to accompany the submission of any thesis that contains research reported in co-authored work that has been published, accepted for publication, or submitted for publication. A copy of this form should be included for each co-authored work that is included in the thesis. Completed forms should be included at the front (after the thesis abstract) of each copy of the thesis submitted for examination and library deposit.

Please indicate the chapter/section/pages of this thesis that are extracted from co-authored work and provide details of the publication or submission from the extract comes:

Chapter 5, Frictional strength and stability of exhumed fault gouges in DFDP-1 cores, Alpine Fault, New Zealand comprises material submitted for publication to Geophysical Research Letters. The full citation is as follows:

***Boulton C**, Moore DE, Lockner DA, Toy VG, Townend J, Sutherland R, In review. Frictional strength and stability of exhumed fault gouges in DFDP-1 cores, Alpine Fault, New Zealand. Geophysical Research Letters.*

Please detail the nature and extent (%) of contribution by the candidate:

The candidate contributed, in total, 80% of the research, manuscript drafting, and manuscript writing.

Certification by Co-authors:

If there is more than one co-author then a single co-author can sign on behalf of all

The undersigned certifys that:

- The above statement correctly reflects the nature and extent of the PhD candidate's contribution to this co-authored work
- In cases where the candidate was the lead author of the co-authored work he or she wrote the text

Name:	Signature:	Date:
Diane E. Moore	Diane E. Moore	October 31, 2013

E.2 Chapter 5 Friction Experiment Plots

This appendix contains run plots of all experiments presented in Chapter 5. All experiments were conducted on a triaxial compression apparatus at the United States Geological Survey, Menlo Park, California, USA. A detailed diagram of the experimental apparatus and sample assembly is provided in Figure E.1. Plots of coefficient of friction (μ) against elastically corrected axial displacement (μm) are provided in Figures E.2, E.3, E.4, E.5, E.6, E.7 and E.8. The displacement plots are presented in the order that they appear in Table 5.1. Plots of two additional experiments, AFHT 21 and AFHT 22 are also provided. These experiments were conducted to test the effective pressure law. The effective normal stress (σ_n' = 93.6 MPa), temperature (T = 210^{o}C), and jacket type (lead) were identical to AFHT15. However, confining pressure (P_c) and pore fluid pressure (P_p) were manipulated to simulate a pore fluid factor of λ_v = 0.18 (P_c = 114.4 MPa and P_p = 20.8 MPa) for experiment AFHT21 and λ_v=0.6 (P_c = 234 MPa and Pp=140.4 MPa) for experiment AFHT22. Detailed methods and data archives are located in Appendices E.3 and G.5, respectively.

E.3 Introduction to Digitally Archived Data

In Chapter 5, quantitative X-ray diffraction, particle size analysis, and hydrothermal friction experiment data on two DFDP-1 gouges, 1A blue gouge and 1B brown gouge, were presented. Text files containing the X-ray diffraction traces are located in Appendix G.2.3. Text files containing particle size analysis data can be found in Appendix G.5.1; data and methods are described below. Text files for hydrothermal friction experiments are located in Appendix G.5.2; data and methods are described below.

E.3.1 Particle size analysis

I conducted laser diffraction particle size analysis of two fault gouges collected from DFDP-1A and DFDP-1B core following the recommended methods of Storti & Balsamo (2010). Low strength materials, such as cataclastic fault rock containing abundant microfractures, and cohesive materials, such

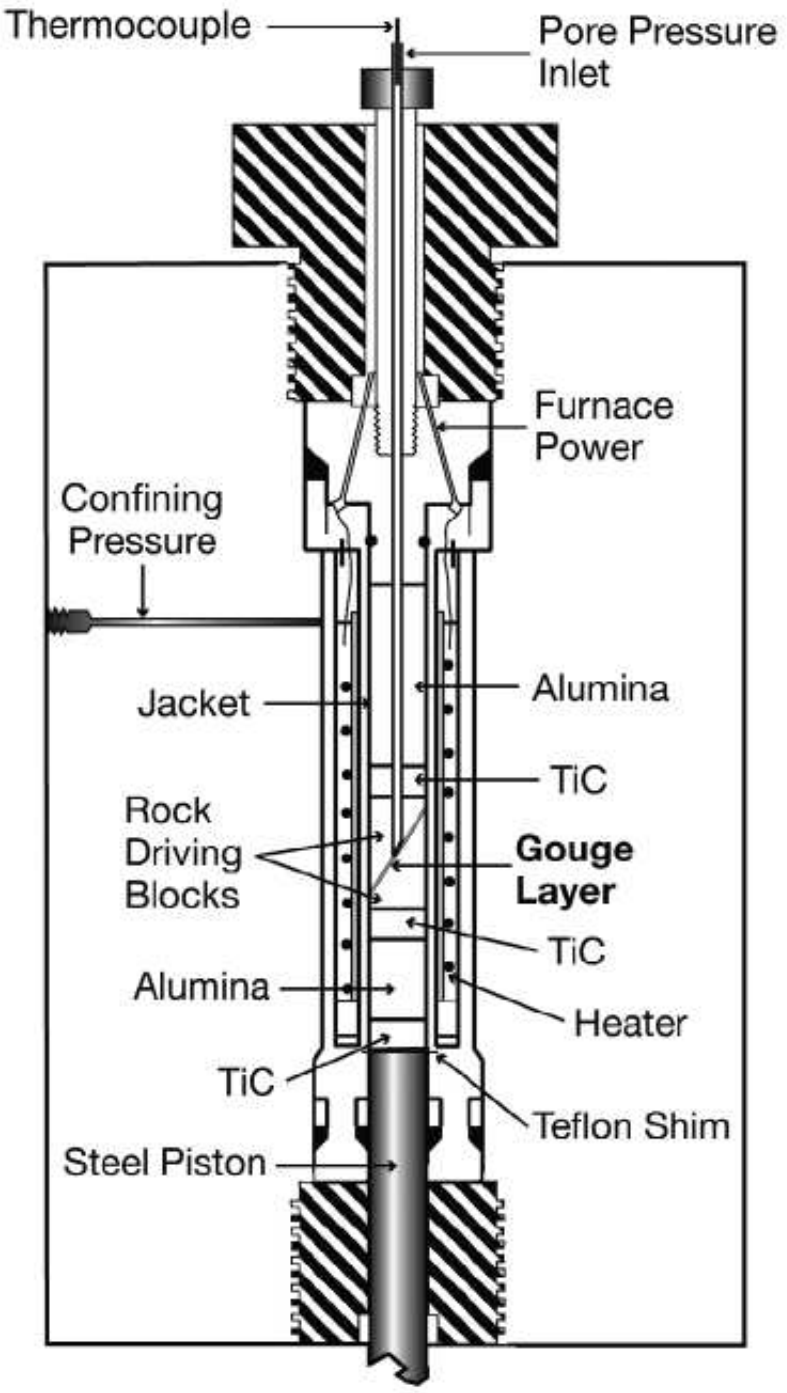

Figure E.1: Triaxial compression apparatus assembly. Figure reproduced from Moore & Lockner (2011)

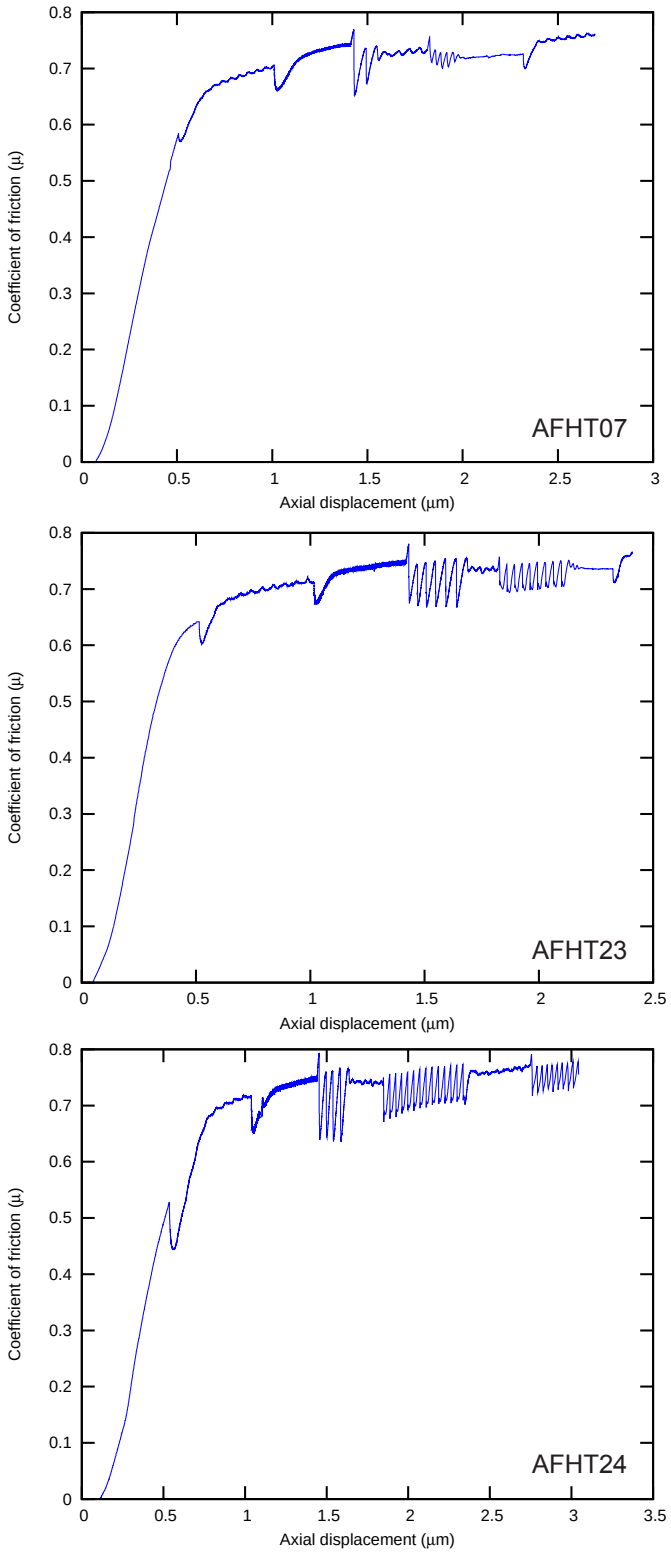

Figure E.2: Experiments AFHT07, AFHT23, and AFHT24.

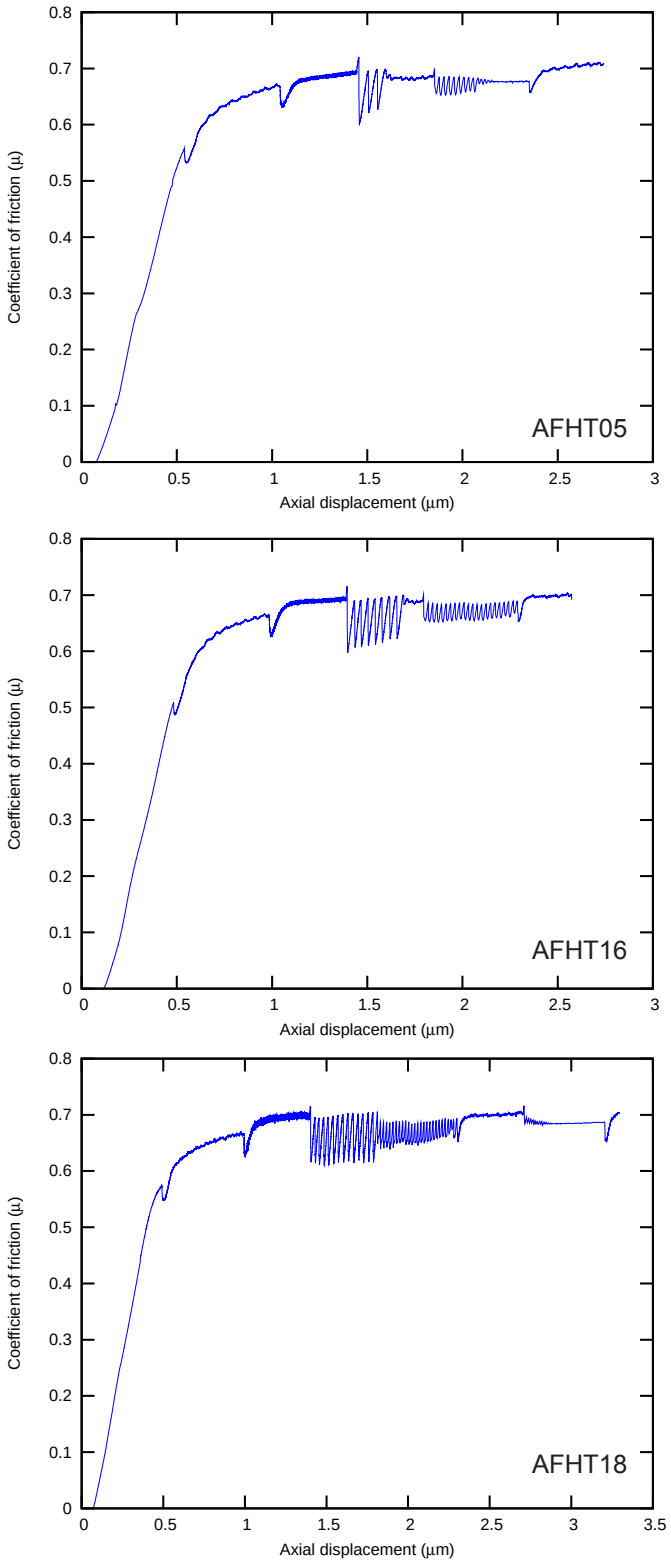

Figure E.3: Experiments AFHT05, AFHT16, and AFHT18.

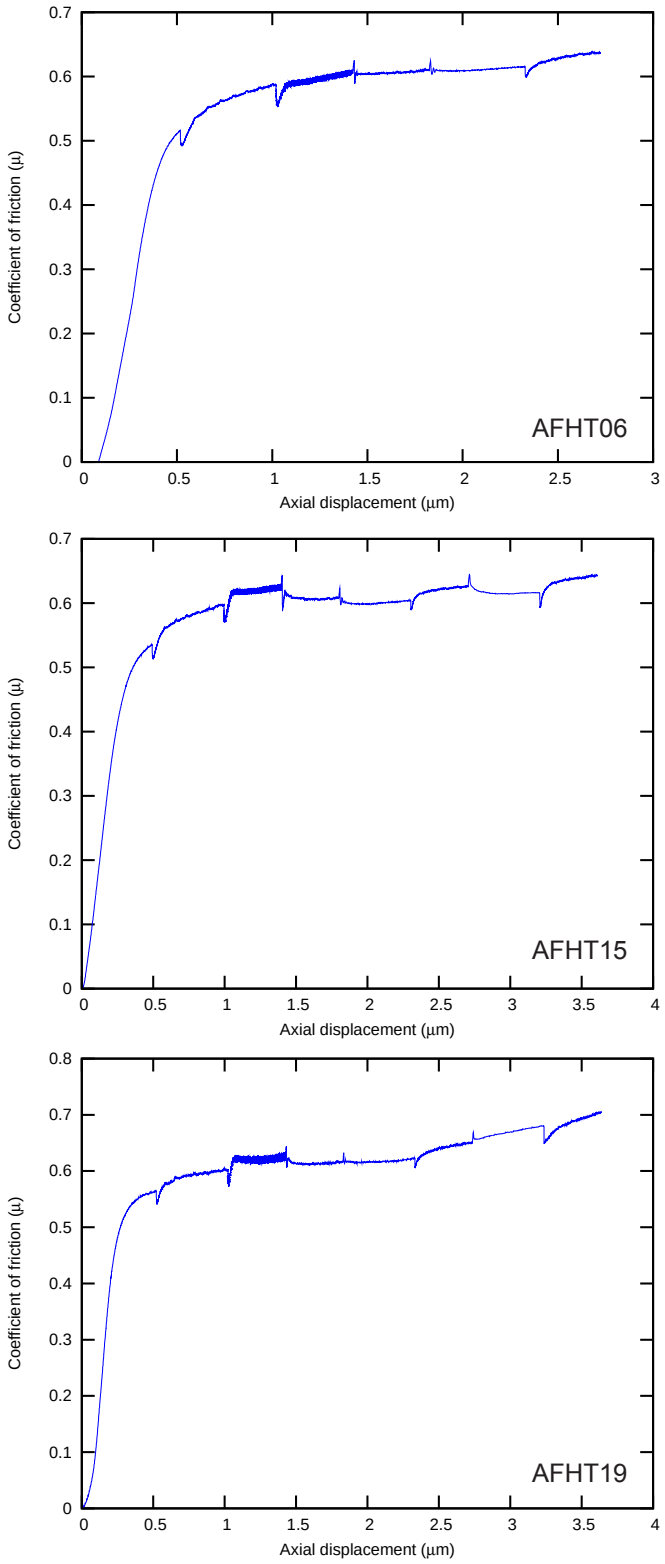

Figure E.4: Experiments AFHT06, AFHT15, and AFHT19.

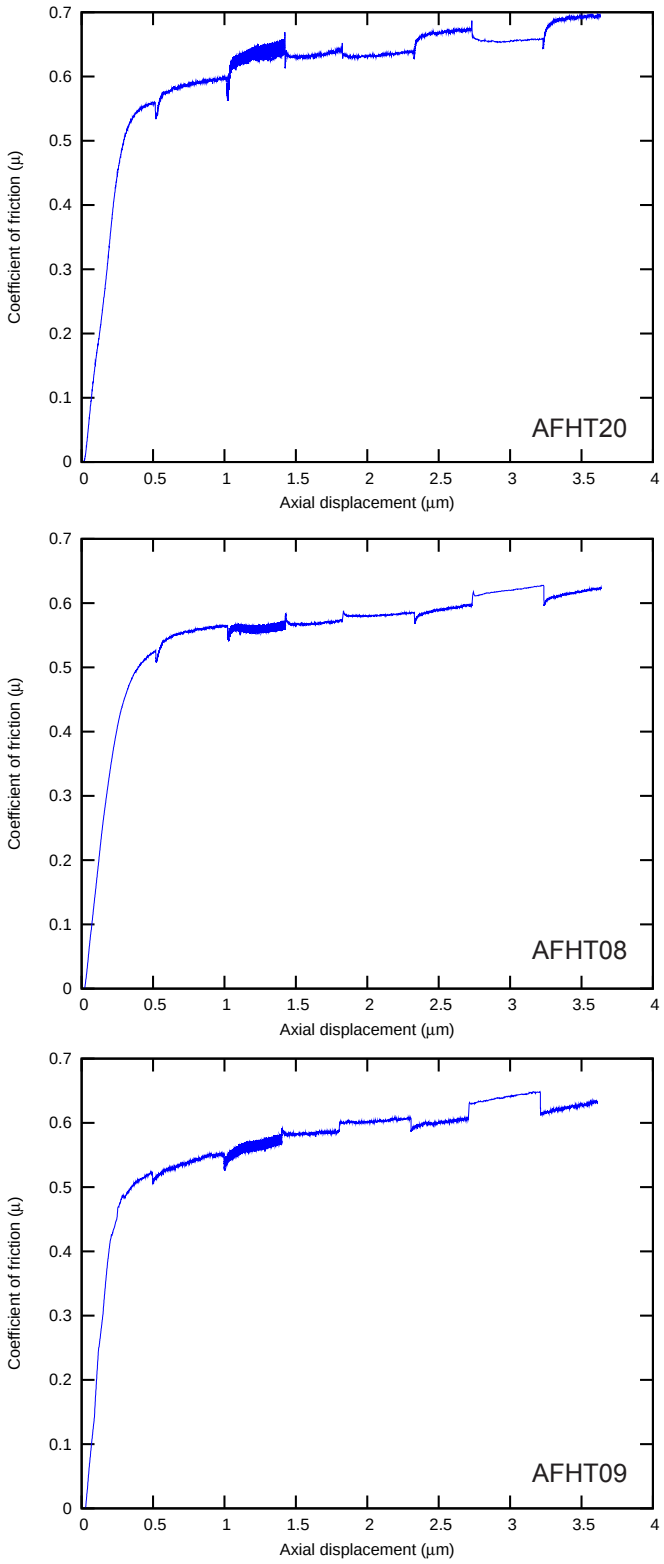

Figure E.5: Experiments AFHT20, AFHT08, and AFHT09.

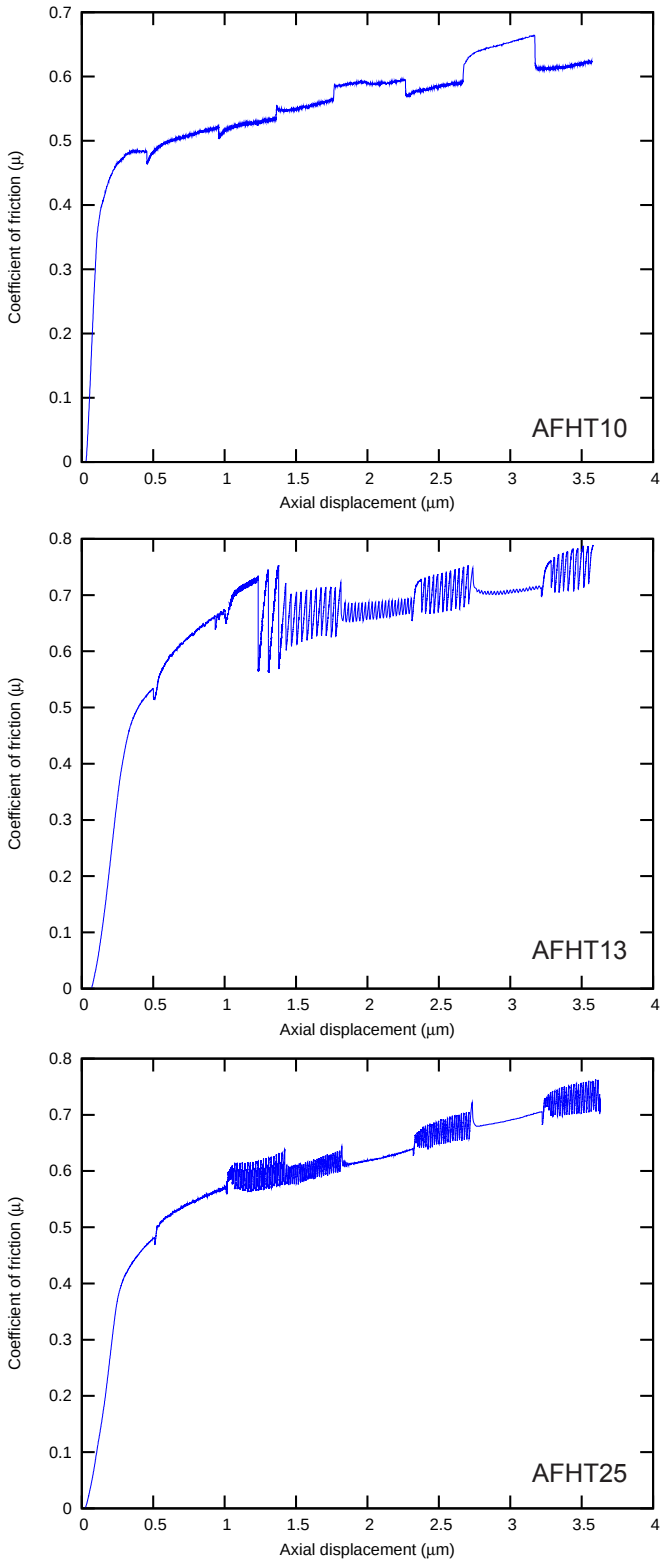

Figure E.6: Experiments AFHT10, AFHT13, and AFHT25.

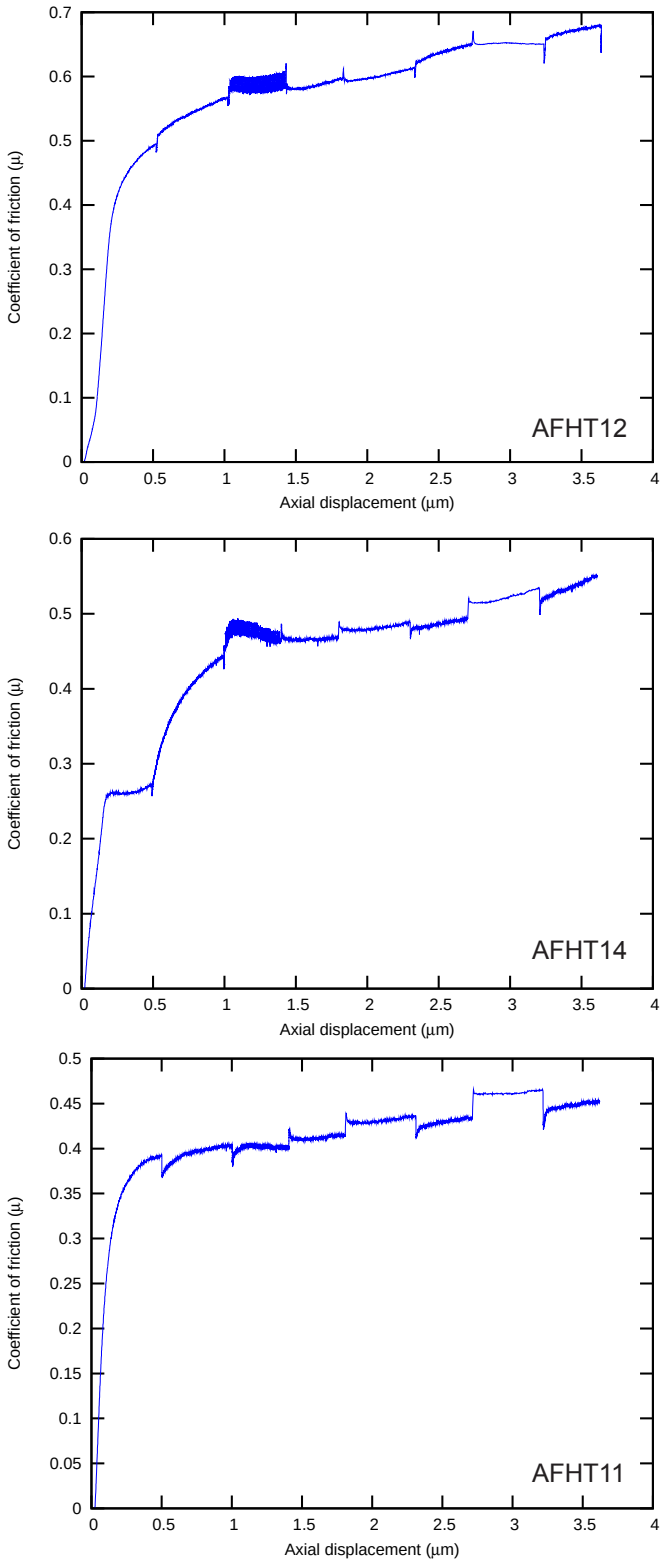

Figure E.7: Experiments AFHT12, AFHT14, and AFHT11.

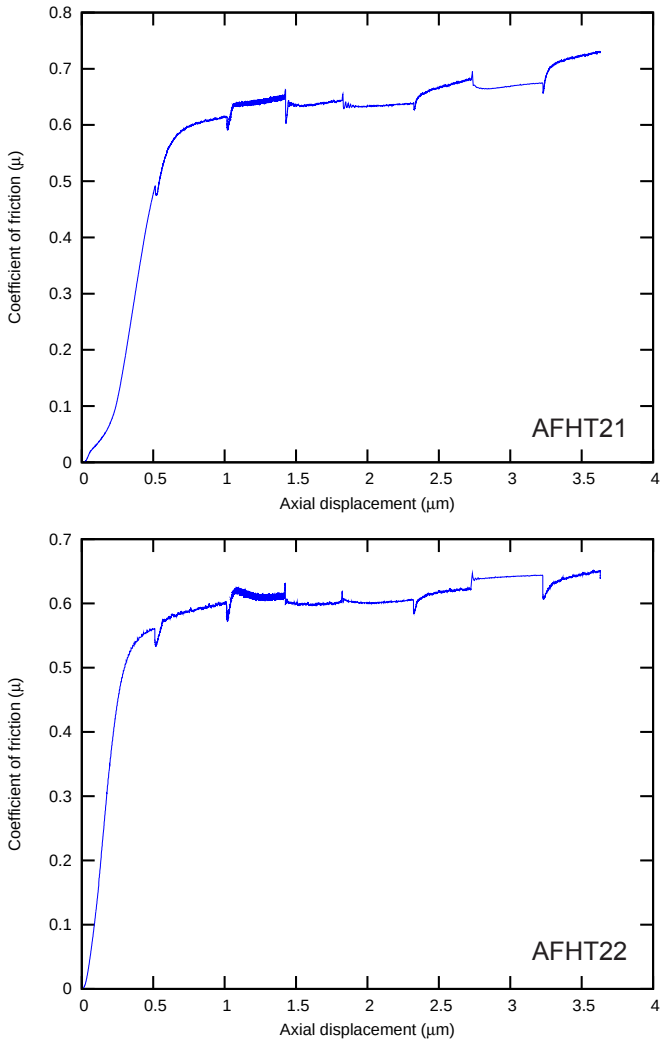

Figure E.8: Experiments AFHT21 and AFHT22.

as phyllosilicates with high surface charges, require careful preparation and analytical techniques when examined using laser diffraction particle size analysis.

Following Storti & Balsamo (2010), each sieved separate ($< 150\mu$m) was dispersed in 5.5 g/L sodium hexametaphosphate for $>$ 24hours prior to analysis. To avoid subsampling errors, the entire solution was added the sample chamber of a Saturn Digisizer 5205 laser digisizer, which has a 10% accuracy in the size range 0.1 to 1 mm and a 3% accuracy in the size range 1 to 1000 μm. I adjusted the laser beam angle to 65 degrees, as recommended for materials with particle sizes less than 0.3 μm.

Within the sample chamber, samples were dispersed for 60 seconds using ultrasonication. Pump speed was automatically adjusted to the maximum particle size analyzed, 150 mm, to ensure adequate circulation, and ultrasonication was not used during measurements or between repeat analyses. Samples were analyzed at several obscuration ratios to ensure an absence of multiple scattering and then autodiluted to the obscuration ratio at which I observed the least variability between repeat analyses, 25.2% for the 1a blue gouge, and 23.1% for the 1b brown gouge. Using the manufacturer's settings, I set the optical properties to model analyzed material as kaolinite (RI = 1.55, ρ = 2.65 g/cm^3). Results were modeled using Mie theory, which uses material-specific input values of refractive index and absorption and accounts for variation in extinction efficiency as a function of particle size. The 1A blue gouge has a mean diameter of 19.8 μm ($\pm$0.2 μm) and a median diameter of 4.3 μm ($\pm$0.02 μm). The 1B brown gouge is finer grained, with a mean diameter of 13.9 μm ($\pm$0.7 μm) and a median diameter 2.6 μm ($\pm$0.03 μm). Results of 3 individual analyses, and the average of 3 individual analyses, are presented in two text files. Columns are:

Column1 "Particle diameter" is the particle diameter, in μm.

Column2 "Cumulative Volume Finer Percent" is as stated, in %.

E.3.2 Hydrothermal friction experiments

In Chapter 5, I presented the results of 18 hydrothermal friction experiments conducted on two mineralogically distinct fault gouges recovered during the Deep Fault Drilling Project (DFDP-1). Shearing experiments were conducted on the two fault gouges using a triaxial deformation apparatus: ten following a lithostatic pressure gradient (average crustal density, ρ, = 2650 kg/m^3), hydrostatic pore fluid pressure (pore fluid factor, λ, = 0.4), and a 35°C/km geothermal gradient; six at equivalent effective normal stresses with elevated temperatures; and two at room temperature, σ_n' = 31.2 MPa. Experiments were conducted using an inclined sawcut configuration, furnace assembly, and methods described in Moore & Lockner (2011).

For each experiment, the test sample, a 1 mm-thick layer of gouge, was applied to a 30° inclined plane cut in a 19.1 mm-diameter by 41 mm-long Westerly Granite cylinder. Sawcut surfaces were roughened with 120 grit SiC to avoid boundary slippage. Deionized water was used as pore fluid and maintained at constant pressure with access to the fault by a 2.4 mm-diameter hole. Servo-controlled confining pressure was adjusted once per second in response to changes in axial load to maintain constant normal stress on the inclined sawcut. Furnace heating took 30 minutes, and temperature varied less than 2°C during each experiment. To determine the friction rate parameter (a–b), velocity steps between 0.01 and 3 μm/s were imposed according to predefined scripts. Total axial displacement varied between 2.41 and 3.63 mm. For a 30° inclined sawcut, fault-parallel displacement is approximately 15% larger.

Corrections were made for seal friction, the pressure- and velocity-dependence of seal friction, changes in contact area of the sawcut surfaces, elastic deformation of the loading system, copper and lead jacket shear resistance, and Teflon shim friction (see Tembe et al. (2010); Moore & Lockner (2008, 2011)). Below 250°C, shear stress corrections for Cu jackets are 6 to 10 MPa; therefore, tests in this temperature range are performed with Pb jackets (corrections are less than 2 MPa). Typical uncertainties in μ for tests from room temperature to 210° (using Pb jackets) are ±0.02 while uncertainties at higher temperatures (with Cu jackets) are ±0.03. A repeat experiment

conducted on DFDP-1a gouge at 210°C, 93.6 MPa effective normal stress, revealed a difference in μ for copper and lead jackets of 0.01. Cu jackets exhibit rate-dependent strength variations in the range of (a–b) = 0.01. Lead jackets do not have measureable velocity sensitivity.

Text files of all experimental results are located in Appendix G.5.2. Also included are the results of two additional experiments, AFHT21 and AFHT22. These experiments were conducted to test the effective pressure law. The effective normal stress (σ_n' = 93.6 MPa), temperature (T = 210°C), and jacket type (lead) were identical to AFHT15. However, confining pressure (P_c) and pore fluid pressure (P_p) were manipulated to simulate a pore fluid factor of λ_v = 0.18 (P_c = 114.4 MPa and P_p = 20.8 MPa) for experiment AFHT21 and λ_v = 0.6 (P_c = 234 MPa and P_p = 140.4 MPa) for experiment AFHT22. Run-plots for each experiment are found in Appendix E.2. Details of the column values in each text file located in Appendix G.5.2 are given below.

Column1 "Time_s" is the time elapsed since the start of the experiment in seconds.

Column2 "35-Pp_b" is the pore fluid pressure in bars.

Column3 "38-Pvol_cc" is the volume of fluid, in cubic centimeters, within the entire sample assembly, including the fluid occupying the gouge sample pore space.

Column4 "39-Temp_C" is the ambient temperature in the sample gouge layer, in °C.

Column5 "63-DifStr_b" is the differential stress, in bars. The differential stress is $\sigma_1 - \sigma_2 = \sigma_3 = P_c$.

Column6 "64-ShrStr_b" is the recorded shear stress, in bars. This column has been corrected for seal friction following the methods outlined above.

Column7 "67-NorStr_b" is the recorded normal stress, in bars. This column has been corrected for changes in contact area of the sawcut surfaces. The method is outlined in Tembe et al. (2010), Appendix A2.

Column8 "68-EfNorStr_b" is the recorded effective normal stress, in bars. The number recorded is Column 7 less Column 2.

Column9 "Mu_eff" is the coefficient of friction calculated in real time during the experiment. The calculation is done by dividing Column 6 by Column 8, assuming no cohesion.

Column10 "CorrNor_b" is the normal stress, Column 7, plus 7 bars. As Tembe et al. (2010), Appendix A4, showed, a small increase in force on the sawcut results from the shear traction the piston and the lower driving block. A greased Teflon® shim decreases the increase in force by reducing the shear traction between the piston and lower driving block. Units are in bars.

Column11 "CorrEffNor_b" is the corrected normal stress, Column 10, less the pore fluid pressure, Column 2. Units are in bars.

Column12 "Displacement_mm" is the corrected load point (also called axial) displacement, in mm. Corrections for the elastic deformation of the loading system and driving blocks have been applied. The correction is outlined in Tembe et al. (2010), Appendix A5. The displacement recorded by the DCDT has also been zeroed at the point where the piston makes contact with the sample assembly.

Column13 "CorrShrStr_b" is the corrected shear stress, in bars. Shear stress is zeroed at the point where the driving piston makes contact with the sample assembly. Shear stress is also corrected for the jacket strength. Copper jackets have temperature- and displacement-dependent strengths. The strength of lead jackets only varies with temperature. The equations used for the corrections are given below.

- *Copper jackets.* Corrections were calculated for a 1 μm/s sliding rate. Displacement (dz) is the value measured in Column 12, in mm. Shear stress, τ, the value recorded in Column 6, in bars.

Temperature (°C)	**Corrected shear strength (bars)**
25	$\tau_{corr} = \tau - (28.5 + 19.22 \times dz)$
100 and 150	$\tau_{corr} = \tau - (44.4 + 15.61 \times dz)$
200	$\tau_{corr} = \tau - (52.2 + 10.79 \times dz)$
210	$\tau_{corr} = \tau - (52.1 + 10.32 \times dz)$
250	$\tau_{corr} = \tau - (50.3 + 8.38 \times dz)$
280	$\tau_{corr} = \tau - (47.3 + 6.93 \times dz)$
300	$\tau_{corr} = \tau - (44.5 + 5.97 \times dz)$
350	$\tau_{corr} = \tau - (34.9 + 3.56 \times dz)$
400	$\tau_{corr} = \tau - (21.5 + 1.15 \times dz)$

- *Lead jackets.* Corrections were calculated for a 1 μm/s sliding rate. Shear stress, τ, is the value recorded in Column 6, in bars.

Temperature (°C)	**Corrected shear strength (bars)**
25	$\tau_{corr} = \tau - 9$
70	$\tau_{corr} = \tau - 7.2$
100	$\tau_{corr} = \tau - 6$
140	$\tau_{corr} = \tau - 4.4$
150	$\tau_{corr} = \tau - 4$
175	$\tau_{corr} = \tau - 3$
200	$\tau_{corr} = \tau - 2$
210	$\tau_{corr} = \tau - 1.6$
250	$\tau_{corr} = \tau$ (no correction)

Column14 "CorrMu" is the corrected coefficient of friction, the corrected shear stress (Column 13) divided by the corrected effective normal stress (Column 11).

Appendix F

Chapter 6 Friction Data

F.1 Introduction to Digitally Archived Data

Data from 15 high velocity friction experiments were presented in Chapter 6. As Chapter 6 has not been submitted for publication, no co-authorship form is required. In addition, run plots for every experiment were presented previously in Figure 6.4, Figure 6.5, and Figure 6.6. Experiments were conducted on the low to high velocity (LHV) apparatus at the Institute of Geology, China Earthquake Administration, Beijing, China (Figure F.1). The methods presented in section 6.3.1 are summarised here. In every experiment, an air actuator applied an axial force of 1.25 kN to a solid cylindrical sample 40 mm in diameter, yielding an applied normal stress (σ_n) of 0.995 MPa. Prior to imposing shear, samples were left under load until the displacement transducer recorded steady state thickness, typically less than 1 hour.

To establish shear, a 22 kW servo-motor rotated one side of the sample assembly while the other side was kept stationary. For a solid cylinder, velocity varies with position, and the equivalent slip velocity (v_{eq}) is calculated following:

$$v_{eq} = \frac{4\pi R r_o}{3} \tag{F.1}$$

where r_0 is the outer radius and R is the revolution speed in revolutions per second. Equivalent slip velocity was defined such that the rate of frictional work is τv_{eq}S if the shear stress is assumed to be constant over the sliding surface of area S (Tsutsumi & Shimamoto 1997; Hirose & Shimamoto 2005a; Mizoguchi et al. 2007). Experiments were conducted at a v_{eq} of 1.0 m/s. Torque, axial force, axial displacement, and rotary motion data were recorded at a sampling rate of 200 Hz.

Each sample assembly comprised two cylinders of Indian gabbro, a Teflon® sleeve, and 2.5 g of air-dry (dry) 150 μm fault rock separate (the 1B 144.04 m gouge was not sieved). Relative humidity in the laboratory ranged between 40% and 60%. Initial sample thickness ranged between 1.0 mm and 1.3 mm. For the water-saturated (wet) experiments, 0.625 mL (25 wt.%) of de-ionized water was added to the fault rock powder. Fault rock powders were placed between two 39.980-39.990 mm-diameter Indian gabbro cylinders (permeability $< 10^{-22}$ m^2) with sliding surfaces ground on a 150# (100 μm) diamond-grinding wheel to make them planar. Sliding surfaces were also roughened with 80# SiC (180 mm) to inhibit slippage. Each fault rock powder was contained by a Teflon® sleeve. It remains impossible to directly measure the pore fluid pressure during high velocity water-saturated experiments. Text files for the high velocity friction experiments are located in Appendix G.6.

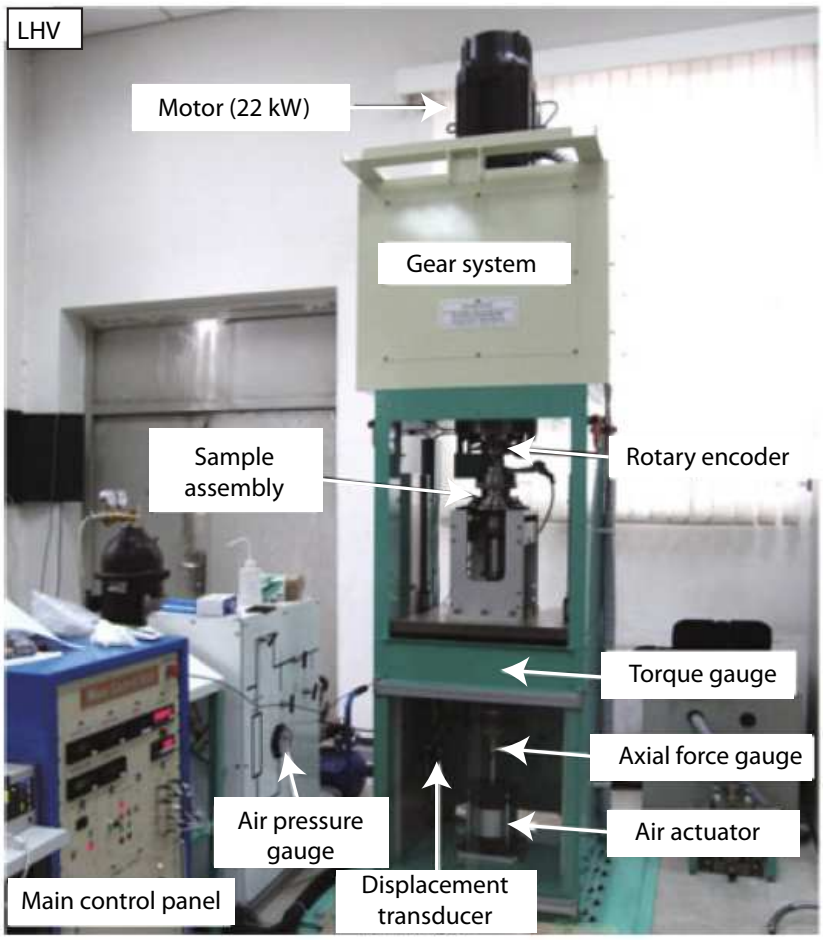

Figure F.1: Labeled photograph of the low-to-high velocity rotary shear apparatus, Institute of Geology, China Earthquake Administration from Hou et al. (2012).

F.1.1 LHV processed data

While data were recorded at 200 Hz, data in the text files located in Appendix G.6.1 are 2-point averages (e.g., data have been averaged to yield an effective recording frequency of 100 Hz). These data were used in the plots and tables presented in Chapter 6. All data have not been corrected for Teflon® friction. Column values are given below.

Column1 "Time_s" is time elapsed since the start of recording, in seconds. For each experiment, 10 seconds of data are recorded before the servo-controlled motor starts rotating the sample.

Column2 "EquivV_ms" is equivalent slip velocity in m/s. Using the recorded revolution speed of the motor, in rps, this is calculated using equation 1. The equivalent slip rate occurs at $r = \frac{2}{3r_o}$ on the sample surface. The outer radius (r_o) is 20 mm in the sample, and the equivalent slip velocity occurs at $r = 13.33$ mm.

Column3 "Displacement_m" is equivalent displacement at $r = \frac{2}{3r_o}$ on the sample surface in m. The outer radius (r_o) is 20 mm in the sample, and the equivalent displacement given occurs at $r = 13.33$ mm.

Column4 "Mu" is the coefficient of friction, obtained by dividing recorded shear stress by normal stress.

Column5 "Axial-displacement_mm" is the axial (vertical) displacement of the sample, sample assembly, and loading column in mm.

F.1.2 LHV unprocessed data

Appendix G.6.2 contains the raw data recorded during each LHV experiments at a recording frequency of 200 Hz. Column values are given below.

Column1 "Unit" is time since the start of data acquisition, in seconds.

Column2 "Axial-load_kN" is the force applied to the specimen in kN. Normal stress is calculated by dividing this value by the area of the specimen in m.

Column3 "Axial-displ_mm" is the axial (vertical) displacement of the sample, sample assembly, and loading column in mm. This value has not been zeroed.

Column4 "Torque-Nm" is the torque recorded, in Nm. Shear stress is calculated following:

$$torque = \int_{r_i}^{r_o} r\left(t \times 2\pi r dr\right) = \frac{2\pi}{3} t\left(r_o^3 - r_i^3\right)$$

Where r_o and r_i are outer and inner radius, respectively.

Column5 "Rotation-angle" is the angular rotation recorded by the rotary encoder. This value is not zeroed in the raw data files.

Column6 "Rev-rate_rpm" is the revolution rate of the servo-motor, in rpm.

Column7 "Cumul-rotation" is the cumulative rotation. This value is not zeroed in the raw data files. Equivalent displacement is calculated by multiplying Column 6, when zeroed, by the circumference of a circle with a radius (r) of $13\frac{1}{3}$ mm.

Appendix G

Digital Data Archive

Data files of analyses and experiments conducted are located on an attached compact disc.